SELECTED PAPERS

1984 - 1994

Colorado State University

Pierre Y. Julien

September, 1994

LIBRARIES
OCT 26 1994
COLORADO STATE UNIVERSITY

CER94-95-PYJ-1

SELECTED PAPERS

1984 - 1994

DATE DUE 5/7
Spring Res 96
CE 707 - 2hrs
MAY 07 1998
JAN 15 1997
Spring Res 97
CE 707 - 24hrs
NOV MAR 1998 1998
OCT 28 2002
SEP 14 2006
261-2500
Printed in USA

Colorado State University

Pierre Y. Julien

September, 1994

CER94-95-PYJ-1

U18401 0337611

TA7
.C6
CER
94-95-1
copy 2

PREFACE

This report has been prepared with the intent to compile papers written over the years and scattered throughout the literature. Considering the profuse literature and the scarcity of reprints remaining for most papers, I find helpful to assemble the key contributions into a single volume. Graduate students in the field of sediment transport, river mechanics and geosciences will find herewith detailed answers to questions formulated in the classroom - CE716 and CE717. The papers are combined by topic rather than in chronological order, thus attempting to maintain the logical sequence under which technological developments unfolded. The most interesting contributions may well be in the field of upland erosion modeling and the analysis of hyperconcentrations. Yet, other contributions in surface runoff, local scour, river morphology and sedimentation are forthcoming.

I wish to take this opportunity to thank all my graduate students for their assistance in forging new ideas, testing new hypotheses, developing new technology and seeking scientific advances in the fields of sediment transport, river mechanics and geosciences.

Pierre Y. Julien

COLORADO STATE UNIVERSITY LIBRARIES

SELECTED PAPERS

Surface runoff

1. Richardson, J.R. and P.Y. Julien, "Suitability of simplified overland flow equations." Water Resources Research, AGU, Vol. 30, No. 3, 1994, pp. 665-671. *Page 1-7.*

2. Julien, P.Y. and D.M. Hartley. "Formation of roll waves in laminar sheet flow." Journal of Hydraulic Research, IAHR, Vol. 24, No. 1, 1986, pp. 5-17. *Page 8-20.*

3. Hartley, D.M. and P.Y. Julien. "Boundary shear stress induced by raindrop impact." Journal of Hydraulic Research, IAHR, Vol. 30, No. 3, 1992, pp. 341-359. *Page 21-39.*

4. Julien, P.Y. and G.E. Moglen, "Similarity and length scale for spatially varied overland flow." Water Resources Research, AGU, Vol. 26, No. 8, 1990, pp. 1819-1832. *Page 40-53.*

5. Ogden, F.L. and P.Y. Julien, "Runoff sensitivity to temporal and spatial rainfall variability at runoff plane and small basin scale." Water Resources Research, AGU, Vol. 29, No. 8, 1993, pp. 2589-2597. *Page 54-62.*

6. Ogden, F.L. and P.Y. Julien, "runoff model sensitivity to radar rainfall resolution." Journal of Hydrology, Vol. 158, 1994, pp. 1-18. *Page 63-80.*

7. Cline, T.J., A. Molinas and P.Y. Julien. "An AutoCAD-based watershed information system for the hydrologic model HEC-1." Water Resources Bulletin, AWRA, Vol. 25, No.3, June 1989, pp. 641-652. *Page 81-92.*

8. Thorne, C.R., L.W. Zevenbergen, J.E. Pitlick, S. Rais, J.B. Bradley and P.Y. Julien. "Direct measurements of secondary currents in a meandering sand-bed river." Nature, Vol. 315, June 1985, pp. 746-747. *Page 93-94.*

9. Julien, P.Y. "Downstream hydraulic geometry of noncohesive alluvial channels." International Conference on River Regime, Wallingford, England, May 18-20, 1988, pp. 9-16. *Page 95-102.*

Upland erosion

10. Julien, P.Y. and D.B. Simons. "Sediment transport capacity of overland flow." Transactions of the ASAE, Vol. 28 (3), May-June 1985, pp. 755-762. (Winner of the 1986 ASAE Paper Award.) *Page 103-110.*

11. Julien, P.Y. and M. Frenette. "Modelling of rainfall erosion." Journal of Hydraulic Engineering, ASCE, Oct. 1985, Vol. 111 (10), pp. 1344-1359. *Page 111-126.*

12. Julien, P.Y. and A.M. Dawod. "On predicting upland erosion losses from rainfall depth. 1. Probabilistic approach." Stochastic Hydrology and Hydraulics Journal, Vol. 1, 1987, pp. 127-134. *Page 127-134.*

13. Dawod, A.M. and P.Y. Julien. "On predicting upland erosion losses from rainfall depth. 2. Field applications in Iraq." Stochastic Hydrology and Hydraulics Journal, Vol. 1, 1987, pp. 135-140. *Page 135-140.*

14. Julien, P.Y. and M. Frenette. "Macroscale analysis of upland erosion." Hydrological Sciences Journal, IAHS, Vol. 32, No. 3, 1987, pp. 347-358. *Page 141-152.*

15. Julien, P.Y. and M. Gonzalez del Tanago, "Spatially varied soil erosion under different climates." Hydrologic Sciences Journal, IAHS, Vol. 36, No. 6, Dec. 1991, pp. 511-524. *Page 153-166.*

16. Frenette, M. and P.Y. Julien. "LAVSED I - A model for predicting suspended load in northern streams." Canadian Journal of Civil Engineering, CSCE, Vol. 13, 1986, pp. 150-161. (French). *Page 167-178.*

17. Julien, P.Y. and M. Frenette. "LAVSED II - A model for predicting suspended load in northern streams." Canadian Journal of Civil Engineering, CSCE, Vol. 13, 1986, pp. 162-170. *Page 179-187.*

18. Frenette, M. and P.Y. Julien. "Computer modelling of soil erosion and sediment yield from large watersheds." International Journal of Sediment Research, Vol. 1, 1987, pp. 39-68. *Page 188-217.*

Sediment transport

19. Richardson, E.V., H.S. Woo and P.Y. Julien. "Research trends in sedimentation." Keynote Paper in Megatrends in Hydraulic Engineering, Colorado State University, 1986, pp. 299-330. *Page 218-234.*

20. Woo, H.S., P.Y. Julien and E.V. Richardson. "Washload and fine sediment load." Technical Note, Journal of Hydraulic Engineering, ASCE, June 1986, Vol. 112, No. 6, pp. 541-545. *Page 235-239.*

21. Woo, H.S., P.Y. Julien and E.V. Richardson. "Transport of bed sediment in clay suspensions." Technical Note, Journal of Hydraulic Engineering, ASCE, August 1987, Vol. 113, No. 8, pp. 1061-1066. *Page 240-245.*

22. Williams, D.T. and P.Y. Julien. "Applicability index for sand transport equations." Technical Note, Journal of Hydraulic Engineering, ASCE, Nov. 1989, Vol. 115, No. 11, pp. 1578-1581. *Page 246-249.*

23. Julien, P.Y. "Concentration of fine sediment particles in a vortex." Journal of Hydraulic Research, IAHR, Vol. 24, No. 4, 1986, pp. 255-264. *Page 250-259.*

24. Woo, H.S. and P.Y. Julien, "Turbulent shear stress in heterogeneous sediment-laden flows." Technical Note, Journal of Hydraulic Engineering, ASCE, Nov. 1990, Vol. 116, No. 11, pp. 1416-1421. *Page 260-265.*

Hyperconcentrations

25. Woo, H.S., P.Y. Julien and E.V. Richardson. "Suspension of large concentrations of sands." Journal of Hydraulic Engineering, ASCE, Vol. 114 (8), August 1988, pp. 888-898. *Page 266-276.*

26. O'Brien, J.S. and P.Y. Julien. "Physical properties and mechanics of hyperconcentrated sediment flows." Proceedings of the ASCE Specialty Conference on the Delineation of Landslide, Flash Flood and Debris Flow Hazards in Utah, 1985, Utah Water Research Lab. Series UWRL/G-85/03, pp. 260-279. *Page 277-296.*

27. O'Brien, J.S. and P.Y. Julien. "Laboratory analysis of mudflow properties." Journal of Hydraulic Engineering, ASCE, Vol. 114 (8), August 1988, pp. 877-887. *Page 297-307.*

28. Julien, P.Y. and Y.Q. Lan. "Rheology of hyperconcentrations." Journal of Hydraulic Engineering, ASCE, Vol. 117, No.3, March 1991, pp. 346-353. *Page 308-315.*

29. O'Brien, J.S., P.Y. Julien and W.T. Fullerton, "Two-dimensional water flood and mudflow simulation." Journal of Hydraulic Engineering, ASCE, Vol. 119, No. 2, Feb. 1993, pp. 244-261. *Page 316-333.*

Scour

30. Santoro, V.C., P.Y. Julien, E.V. Richardson, and S.R. Abt. "Velocity profiles and scour depth measurements around bridge piers." Transportation Research Board, National Research Council, Transportation Research Record, No. 1319, Bridge and Hydrology Research 1991, pp. 137-142. *Page 334-347.*

31. Bormann, N.E. and P.Y. Julien. "Scour downstream of grade-control structures." Journal of Hydraulic Engineering, ASCE, Vol. 117, No.5, May 1991, pp. 579-594. *Page 348-363.*

32. Stein, O.R. and P.Y. Julien, "Criterion delineating the mode of headcut migration." Journal of Hydraulic Engineering, ASCE, Vol. 119, No. 1, Jan. 1993, pp. 37-50. *Page 364-377.*

33. Stein, O.R., P.Y. Julien and C.V. Alonso. "Mechanics of jet scour downstream of a headcut." Journal of Hydraulic Research, IAHR, Vol. 31, No. 6, 1993, pp. 723-738. *Page 378-393.*

34. Stein, O.R. and P.Y. Julien. "Sediment concentration below free overfall." Journal of Hydraulic Engineering, ASCE, Vol. 120, No. 9, Sept. 1994, pp. 1043-1058. *Page 394-410.*

Sedimentation

35. Frenette, M. and P.Y. Julien. "Advances in predicting reservoir sedimentation." General Lecture, Third International Symposium on River Sedimentation, ISRS-III, Jackson, Mississippi, March 31-April 4, 1986, pp. 26-46. *Page 411-430.*

36. Julien, P.Y., Y.Q. Lan and G. Berthault. "Experiments on segregation, lamination, stratification and desiccation of heterogeneous sand mixtures." Bulletin de la Societe Geologique de France, Tome 164, No, 5, 1993, pp. 649-660. *Page 431-442.*

37. Frenette, M., M. Caron, P.Y. Julien, and R.J. Gibson. "Interaction between salmon parr population and discharge in the Matamec River." Canadian Journal of Fisheries and Aquatic Sciences, Vol. 41, No. 6, 1984, pp. 954-964. (French). *Page 443-452.*

WATER RESOURCES RESEARCH, VOL. 30, NO. 3, PAGES 665–671, MARCH 1994

Suitability of simplified overland flow equations

J. R. Richardson and P. Y. Julien
Engineering Research Center, Colorado State University, Fort Collins

Abstract. A dimensionless formulation of the acceleration terms of the Saint-Venant equations is presented for one-dimensional overland flows under either laminar or turbulent conditions. For stationary storms over a plane surface of uniform roughness, dimensionless analytical expressions are derived during the rising limb for the local acceleration a_l^*, and during equilibrium for the convective acceleration a_c^* and the pressure gradient a_p^* ((13), (14), and (15), respectively). In terms of the order of magnitude, the three acceleration terms are inversely proportional to the kinematic flow number K. At equilibrium, the pressure gradient a_p^* is also inversely proportional to the square of the Froude number Fr. The relative magnitude of the acceleration terms for supercritical overland flow ($a_l^* > a_c^* > a_p^*$) differs from subcritical overland flow ($a_p^* > a_l^* > a_c^*$), which in all cases contrasts with open-channel flows ($a_p^* > a_c^* > a_l^*$). The kinematic wave approximation is therefore only suitable when both K and Fr are large. Improvements using the diffusive wave approximation are only possible for subcritical overland flow. Both the diffusive wave and the quasi-steady dynamic wave approximations are not suitable for supercritical overland flow. The analysis of moving storms corroborates these findings in that the local acceleration exceeds the convective acceleration. These effects are particularly pronounced during the rising limb of overland flow hydrographs for downstream moving rainstorms.

Introduction

The solution to overland flow problems is crucial because upland areas generally provide a significant source of water for surface runoff. In turn, knowledge of surface runoff is essential to determine the timing and magnitude of floods and to estimate soil erosion losses and nonpoint source pollutant transport from upland areas. Overland flow originates from rainfall, snowmelt, or saturation excess on the soil surface. Rainfall excess over a surface of slope S_0 and length L_0 generates surface runoff of thickness H_0 and Froude number F_0 at the downstream end of the upland surface. Complete equilibrium hydrographs occur when the rainfall duration exceeds the time to equilibrium T_e, while rainstorms shorter than T_e generate partial equilibrium hydrographs.

The governing equations for one-dimensional overland flow derived by Saint-Venant are unfortunately not prone to simple analytical solutions, except in very simplified cases. Prior analyses of the relative magnitude of the terms of the momentum equation for open channels lead to several levels of approximation depending on the desired level of accuracy. In their early treatment of flood movement in long rivers, *Lighthill and Whitham* [1955] concluded that all acceleration terms of the momentum equation could be neglected when the Froude number is less than two. Investigations focused primarily on the role played by three acceleration terms: (1) the local acceleration term denoted as a_l describing the temporal variability in velocity, (2) the convective acceleration term a_c describing the spatial variability in velocity, and (3) the pressure gradient term a_p describing the spatial variability in flow depth. Subsequent reviews of the relative magnitude of these acceleration terms by *Henderson* [1966], *Ponce and Li* [1979], and *Weinmann and Laurenson* [1979] suggested that $a_p > a_c > a_l$ for open-channel flows.

Copyright 1994 by the American Geophysical Union.

Paper number 93WR03098.
0043-1397/94/93WR-03098$05.00

Simplifications of the momentum equation, for computation of overland and channel flow, have been developed based upon the relative magnitude of the acceleration terms. These simplifications are known as (1) the quasi-steady dynamic wave, which neglects the local acceleration term a_l, (2) the diffusive wave, which neglects both the local and convective acceleration terms a_l and a_c, and (3) kinematic wave approximation, which neglects all three acceleration terms.

Woolhiser and Liggett [1967] normalized the momentum equation to simplify overland flow investigations and defined the kinematic flow number $K_0 = S_0 L_0 / H_0 F_0^2$; they found that the kinematic wave approximation is suitable to overland flow when K_0 is greater than 10, which describes most actual flow situations. *Woolhiser* [1975] also showed that the rising outflow hydrograph compares favorably with the kinematic wave approximation even when $F_0 < 2$.

Al-Mashidani and Taylor [1974] solved the Saint-Venant equations for subcritical, critical, and supercritical flows while imposing critical flow conditions at the lower boundary; they confirmed the findings of *Woolhiser and Liggett* [1967] regarding the suitability of the parameter K_0, although higher values of K_0 were needed to use the kinematic wave approximation. *Al-Mashidani and Taylor* [1974] also showed that it is not necessary to impose the condition that $F_0 < 2$ to justify the kinematic wave approximation and that the downstream boundary condition has little or no influence on the outflow hydrograph.

Morris [1979] compared the solution for the zero-depth

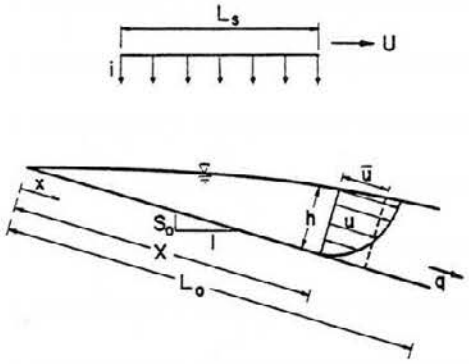

Figure 1. One-dimensional overland flow diagram for a block moving storm.

gradient to the critical flow lower boundary condition. The difference between the two solutions decreases as the value of K_0 increases. *Morris* [1979] concluded that for a range of F_0 and K_0 which covers most practical overland flow situations, the effect of the choice of lower boundary condition has no significant effect on flow depth and velocity profiles. *Morris and Woolhiser* [1980] introduced the additional criterion which combines F_0 and K_0 and reported that the kinematic wave approximation fails when $F_0 < 0.5$ and when $F_0^2 K_0 < 5$. *Morris and Woolhiser* [1980] recommended using the different wave approximation for some cases where $F_0^2 K_0 < 5$, and they showed that the diffusive wave approximation is satisfactory at low values of F_0 when K_0 is large. *Vieira* [1983] recommended using the kinematic wave approximation when $K_0 > 50$, and when $5 < K_0 < 20$ the kinematic wave or the diffusive wave approximations are suitable solutions to overland flow. *Govindaraju et al.* [1988] confirmed that the diffusive wave approximation is valid for small F_0 and large K_0.

More recently, *Hromadka and De Vries* [1988] recommended that use of the kinematic wave method for channel routing in watershed models be reconsidered. The controversial discussions to the paper led to the analysis of *Ponce* [1991], who concluded that the kinematic wave theory can be improved by extending it to the realm of diffusion waves.

These studies suggest that selection criteria based on the factors K_0 or F_0 are not as simple as originally perceived, and that the downstream boundary condition can influence the selection of appropriate simplifications of the momentum equation. The complications arising in the analysis of overland flow justifies a second look at the relative magnitude of the acceleration terms of the momentum equation.

The objective of this paper is to examine the relative magnitude of the terms of the momentum equation for one-dimensional overland flow over a plane surface with constant surface roughness. More specifically, the local acceleration term during the rising limb is compared with the convective acceleration and pressure gradient terms under complete equilibrium. The approach differs from *Woolhiser and Liggett*'s [1967] normalizing procedure in that the analysis is applicable at any location on the overland flow plane and encompasses laminar and turbulent flow conditions for both stationary and moving storms.

Overland Flow Dynamics

A simplified diagram for one-dimensional overland flow over a plane of length L_0 and slope S_0 with constant roughness is presented in Figure 1. A block moving storm of length L_s with velocity U generates surface runoff from the excess rainfall rate i. At a distance X from the upper boundary, the unit discharge q varies in time and reaches a maximum value of $q_m = iX$ under equilibrium conditions. The flow depth h and the average flow velocity $\bar{u} = q/h$ depend on the friction slope S_f. Additional variables include the gravitational acceleration g and the kinematic viscosity ν of the fluid.

The governing one-dimensional overland flow equations derived by Saint-Venant describe conservation of mass and momentum in space x and time t:

$$\frac{\partial h}{\partial t} + \frac{\partial q}{\partial x} = i(x, t) \tag{1}$$

$$\frac{1}{g}\frac{\partial \bar{u}}{\partial t} + \frac{\bar{u}}{g}\frac{\partial \bar{u}}{\partial x} + \frac{\partial h}{\partial x} = S_0 - S_f \tag{2}$$

respectively.

The three partial derivatives on the left-hand side of (2) denote dimensionless forms of local acceleration $a_l = (1/g)(\partial \bar{u}/\partial t)$, convective acceleration $a_c = (\bar{u}/g)(\partial \bar{u}/\partial x)$, and pressure gradient $a_p = \partial h/\partial x$, respectively. This one-dimensional formulation of the momentum equation neglects both lateral inflow and the momentum contribution due to rainfall intensity $\bar{u}i/h$. It can be demonstrated by multiplying and dividing $\bar{u}i/h$ by $\bar{u}X$ that the rainfall momentum is proportional to the convective acceleration term through $\bar{u}i/h = \bar{u}\bar{u}iX/X\bar{u}h = \bar{u}^2/X \cong \bar{u}\partial\bar{u}/\partial x$. Since both terms yield similar results, the following analysis focuses on the convective acceleration term.

An additional relationship such as the Darcy-Weisbach equation relates resistance to flow with the friction slope S_f and can be rewritten in the following stage-discharge relationship:

Table 1. Parameters α and β for Four Types of Overland Flow [*Julien and Simons*, 1985]

Flow Type	α	β
Laminar	$8gS_f/k\nu$	3.0
Turbulent flow, smooth boundary, (Blasius)	$1/\nu^{0.14}\ [8gS_f/0.22]^{0.57}$	1.72
Turbulent flow, rough boundary (Manning)	$S_f^{0.5}/n$	1.67
Turbulent flow, rough boundary (Chezy)	$CS_f^{0.5}$	1.5

$$q = \alpha h^{\beta} \tag{3}$$

The parameters α and β are summarized in Table 1 for four overland flow types: (1) laminar sheet flow with constant value of the resistance parameter k, (2) turbulent flow over a smooth boundary as described by the Blasius equation, (3) turbulent flow over a rough boundary with a constant value of Manning n, and (4) turbulent flow over a rough boundary with very small relative roughness with constant value of the Chezy coefficient C. It is important to notice that by definition of the resistance relationship, the coefficient α is a function of the friction slope S_f.

Normalization of the Governing Equations

Woolhiser and Liggett [1967] normalized the momentum equation after dividing each parameter in (1) and (2) by a combination of the normal depth H_0 at the downstream end of the plane L_0, the corresponding normal flow velocity V_0, and the maximum rainfall intensity i_0. The resulting dimensionless parameters (denoted with an asterisk) are defined: $h_0^* = h/H_0$, $u_0^* = \bar{u}/V_0$, $X_0^* = x/L_0$, $t_0^* = V_0 t/L_0$, and $i_0^* = i/i_0 = 1$. With this normalization, both the continuity equation (1) and the momentum equation (2) can be rewritten in the following normalized dimensionless form:

$$\frac{\partial h_0^*}{\partial t_0^*} + \frac{\partial u_0^* h_0^*}{\partial x_0^*} = 1 \tag{4}$$

$$\frac{\partial u_0^*}{\partial t_0^*} + u_0^* \frac{\partial u_0^*}{\partial x_0^*} + \frac{1}{F_0^2}\frac{\partial h_0^*}{\partial x_0^*} = \frac{S_0 L_0}{H_0 F_0^2}\left(1 - \frac{u_0^{*2}}{h_0^*}\right) \tag{5}$$

Note that the kinematic flow parameter $K_0 = S_0 L_0/H_0 F_0^2$ appears on the right-hand side of (5). This normalization provides tremendous insight into overland flow characteristics, particularly regarding the role played by the parameters F_0 and K_0. The analysis of the relative magnitude of the acceleration terms on the left-hand side of (5) is somewhat difficult because the values of the derivatives, such as $\partial u_0^*/\partial t_0^*$, are unknown even though u_0^*, h_0^*, x_0^*, and t_0^* can be determined at the downstream end under equilibrium conditions. The following treatment introduces modifications of the parameters F_0 and K_0. The proposed analysis evaluates the relative magnitude of the acceleration terms of the momentum equation for the rising and equilibrium portions of an overland flow hydrograph including laminar and turbulent overland flows under stationary and moving rainstorms.

Stationary Storms

With reference to Figure 1, analytical expressions for flow depth and velocity are derived for long ($L_s > L_0$) stationary storms ($U = 0$) over a plane surface (constant slope S_0) under a constant rainfall intensity i. It is assumed that the overland flow plane is initially dry ($h = 0$ and $q = 0$) prior to the beginning of precipitation at time $t = 0$. *Woolhiser and Liggett* [1967] clearly demonstrated that according to the kinematic wave approximation at high values of K_0, the flow depth increases linearly with time $h = it$ during the rising limb until the flow depth conveys the equilibrium discharge ($q_m = iX$). At the inception of runoff, the statement $h = it$ is always exact regardless of the momentum equation because it stems solely from continuity (1). Generally speaking, $h = it$ is considered a reasonable approximation during the rising limb, except near the time to equilibrium.

The time to equilibrium T_e is obtained from (3) with $h = iT_e$ under equilibrium discharge $q_m = iX = \alpha(iT_e)^{\beta}$, or

$$T_e = i^{((1/\beta)-1)}(X/\alpha)^{1/\beta} \tag{6}$$

Note that this general form of the time to equilibrium is valid at any location on the plane for any of the four flow conditions summarized in Table 1. The time to equilibrium from (6) is consistent with the full dynamic momentum equation because α is defined in terms of the friction slope.

Under equilibrium conditions, the flow depth is space dependent but time invariant. The relationships for flow depth and velocity ($\bar{u} = q/h$) obtained from (3) under equilibrium discharge ($q = iX = \alpha h^{\beta}$) are

$$h = (iX/\alpha)^{1/\beta} \tag{7}$$

$$\bar{u} = \alpha(iX/\alpha)^{(\beta-1)/\beta} \tag{8}$$

respectively.

The Froude number $Fr = \bar{u}/(gh)^{1/2}$, obtained from (7) and (8), and the kinematic flow number $K = S_0 X/hFr^2$ obtained from (7) and (9), are written as a function of the dimensionless distance from the upstream end of the overland flow plane ($X^* = X/L_0$):

$$Fr = g^{-1/2}\alpha^{3/2\beta}(iX)^{(1-(3/2\beta))} = F_0 X^{*(1-(3/2\beta))} \tag{9}$$

$$K = gS_0\alpha^{-2/\beta} i^{((2/\beta)-2)} X^{((2/\beta)-1)} = K_0 X^{*((2/\beta)-1)} \tag{10}$$

respectively. Both Fr and K from (9) and (10) vary along the plane. They are slightly different from F_0 and K_0 previously defined at the downstream end of the plane by *Woolhiser and Liggett* [1967]. Both formulations are equivalent when $X^* = 1$. Example calculations of the Froude number using (9) indicate that overland flow generated by uniform excess rainfall intensities of 1 in/hour (7.05×10^{-6} m/s) are supercritical ($Fr > 1$) at any slope steeper than 0.01 over a smooth surface longer than 50 m. The corresponding kinematic flow number is large ($K > 150$). In supercritical flow, backwater effects cannot propagate upstream and downstream boundary conditions are not required.

Analytical Description of Acceleration Terms

A normalized dimensionless form of the momentum equation is obtained after dividing (2) by the bed slope S_0:

$$[a_l^* + a_c^* + a_p^*] = 1 - S_f/S_0 \tag{11}$$

where

$$a_l^* = \frac{1}{gS_0}\frac{\partial \bar{u}}{\partial t} \qquad a_c^* = \frac{\bar{u}}{gS_0}\frac{\partial \bar{u}}{\partial x} \qquad a_p^* = \frac{1}{S_0}\frac{\partial h}{\partial x}$$

The local acceleration term a_l^* is zero during equilibrium but varies during the rising and falling limbs. On the other hand, the convective acceleration term a_c^* and the pressure gradient term a_p^* vanish when $h = it$ during the rising limb because h does not vary with x at the downstream end of the plane. The following analysis first focuses on defining the maximum values of each term and then compares the

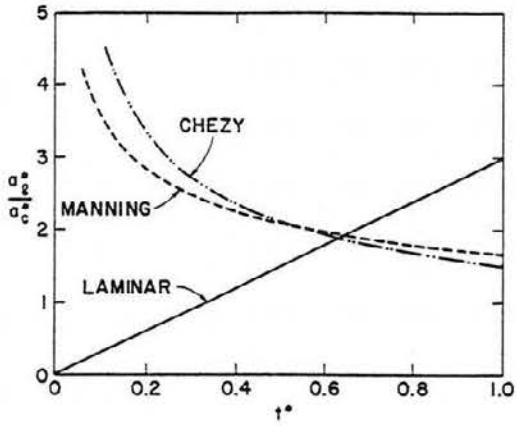

Figure 2. Ratio of a_l^*/a_c^* for stationary storms.

relative magnitude of these maximum values. Therefore the local acceleration term a_l^* which is largest during the rising limb is compared with the convective acceleration term a_c^* and the pressure gradient term a_p^* which are largest at equilibrium.

During the rising limb of a hydrograph, the flow depth, velocity, and discharge at a given point change primarily with time, while space derivatives are comparatively small. The depth-averaged velocity $\bar{u} = q/h$ varies with time from $h \cong it$. The following expression for the local acceleration a_l^* is obtained from (8) after neglecting $\partial\alpha/\partial t$:

$$a_l^* \cong \frac{(\beta - 1)}{gS_0}\,\alpha i^{\beta-1} t^{\beta-2} \tag{12}$$

This approximate relationship deviates from an identity only because of two approximations, $h \cong it$ and $\partial\alpha/\partial t \cong 0$. The first approximation is valid at the beginning of the storm because both $q = 0$ and $\partial q/\partial x = 0$ at the early rise. The second approximation relates to changes in friction slope and α with time. The time derivative of the friction slope, which is nearly constant, remains small compared to the time derivative of flow depth, which is the dominant factor during the rising limb.

The local acceleration term a_l^* from (12) can be rewritten as a function of the following dimensionless parameters: (1) the kinematic number K from (10), (2) the dimensionless time $t^* = t/T_e$, with T_e from (6), and (3) the distance $X^* = X/L_0$:

$$a_l^* \cong \frac{(\beta - 1)}{K}\,t^{*\beta-2} = \frac{(\beta - 1)}{K_0}\,t^{*\beta-2}X^{*(1-(2/\beta))} \tag{13}$$

Notice in (13) that the formulation using K does not involve the parameter X^*, which justifies our preference for using K instead of K_0.

After equilibrium, the flow depth, velocity, and discharge at a given point change primarily with space, while time derivatives vanish. Analytical relationships for a_c^* and a_p^* follow from $q = iX$ and (7) after considering that α is nearly constant, or neglecting $\partial\alpha/\partial x$:

$$a_c^* \cong \frac{\beta - 1}{\beta K} = \left(\frac{\beta - 1}{\beta K_0}\right)X^{*(1-(2/\beta))} \tag{14}$$

$$a_p^* \cong \frac{1}{\beta K Fr^2} = \left(\frac{1}{\beta K_0 F_0^2}\right)X^{*((1/\beta)-1)} \tag{15}$$

These two approximate relationships deviate from strict identities only because α, or the friction slope, is nearly constant. It is acknowledged that the friction slope and α vary with space. The space derivative of the friction slope, which is nearly constant, remains small compared to the space derivatives of flow depth and velocity, which are the dominant factors during equilibrium because $\partial\bar{u}h/\partial x = i$.

All three dimensionless acceleration terms a_l^*, a_c^*, and a_p^* from (13), (14), and (15) are inversely proportional to the kinematic flow number K, or K_0, and only a_p^* depends on the Froude number Fr, or F_0. These three expressions can be used to assess the friction slope for overland flow with stationary storms. Furthermore, a_l^* can be related to the friction slope by $a_l^* = 1 - (S_f/S_0)$ during the rising limb of the hydrograph (when $0 < t^* < 1$), while a_c^* in conjunction with a_p^* can be related to the friction slope by $a_c^* + a_p^* = 1 - (S_f/S_0)$ when the flow is steady and nonuniform under equilibrium conditions ($t^* \geq 1$).

Relative Magnitude of Acceleration Terms

The ratio of a_l^* during the rising limb to a_c^* at equilibrium is obtained from (13) and (14):

$$a_l^*/a_c^* = \beta t^{*\beta-2} \tag{16}$$

Note that this ratio is independent of both the kinematic flow number and the Froude number but varies solely with dimensionless time and the exponent β of the resistance equation. For turbulent flow, as represented by either the Chezy or Manning equations, β is less than two, which indicates that the minimum value of the ratio a_l^*/a_c^* for turbulent flows must be larger than β. This minimum value (1.5 for Chezy and 1.67 for Manning) will occur when the dimensionless time is unity. For laminar flow, the ratio of a_l^*/a_c^* has a minimum value of zero, when $t^* = 0$. The implication of this observation is that a_l^* will be greater than a_c^*, as is illustrated in Figure 2, except for laminar flow when t^* is less than about 0.3. For a complete equilibrium hydrograph on a plane surface with uniform roughness, the ratio of the two largest acceleration terms is obtained when $t^* = 1$. The largest value of a_l^* always exceeds the maximum value of a_c^* in all cases because $\beta > 1$ for both laminar and turbulent flows. It is concluded that for complete equilibrium hydrographs, the local acceleration term always exceeds the convective acceleration term regardless of the kinematic flow number. This demonstrates that the quasi-steady wave approximation does not necessarily improve upon the diffusive wave approximation because the neglected term a_l^* is larger than the term a_c^* retained in this simplification.

The ratio of the convective acceleration a_c^* to the pressure gradient term a_p^* under complete equilibrium conditions is obtained from (14) and (15):

$$a_c^*/a_p^* = (\beta - 1)Fr^2 = (\beta - 1)F_0^2 X^{*(2-(3/\beta))} \tag{17}$$

This ratio does not depend on the kinematic flow number but varies with the exponent β and the Froude number. The values of the Froude number above which a_c^*/a_p^* exceeds unity are $Fr > 0.7$ for laminar flow ($\beta = 3$); $Fr > 1.22$ for Manning equation ($\beta = 5/3$); and $Fr > 1.4$ for Chezy equation ($\beta = 1.5$). Considering all cases, a_c^* exceeds a_p^*

when the flow is supercritical with $Fr > 1.4$, while $a_c^* < a_p^*$ for subcritical flows with $Fr < 0.7$.

The ratio of the local acceleration a_l^* during the rising limb to the pressure gradient a_p^* at equilibrium is obtained from (13) and (15):

$$a_l^*/a_p^* = \beta(\beta - 1)Fr^2 t^{*\beta-2} = \beta(\beta - 1)F_0^2 t^{*\beta-2} X^{*(2-(3/\beta))} \quad (18)$$

This ratio is independent of the kinematic flow number but varies with flow type, Froude number, and dimensionless time t^*. For complete equilibrium hydrographs ($t^* \geq 1$), the values of the Froude number above which $a_l^* > a_p^*$ are $Fr > 0.4$ for laminar flow ($\beta = 3$); $Fr > 0.95$ for Manning equation ($\beta = 5/3$); and $Fr > 1.15$ for Chezy equation ($\beta = 1.5$). These criteria are similar to those for a_c^*/a_p^*. Therefore a_l^* exceeds a_p^* when the flow is supercritical with $Fr > 1.4$, while $a_l^* < a_p^*$ for subcritical flows with $Fr < 0.4$.

The results can be summarized as follows: (1) $a_l^* > a_c^* > a_p^*$ for supercritical flows with $Fr > 1.4$ and (2) $a_p^* > a_l^* > a_c^*$ for subcritical flows with $Fr < 0.4$.

Moving Storms

The relative magnitude of the acceleration terms of the momentum equation for block moving rainstorms is analyzed numerically, as analytical solutions become overly complex. The one-dimensional full-dynamic wave model FDCASC tested by *Richardson* [1989] simulates runoff under spatially and temporally varied rainfall precipitation. This model simulates one-dimensional overland flow for upslope and downslope block moving storms, as is sketched in Figure 1. The dimensionless discharge $q^* = q/iL_0$ varies with dimensionless time $t^* = t/T_e$. Two dimensionless storm parameters define the length of the storm $L_* = L_s/L_0$ and the storm celerity $U^* = UT_e/L_0$. Positive and negative values of U^* correspond to storms moving down and up the plane, respectively.

Downslope Moving Storms

This analysis summarizes typical results from *Richardson*'s [1989] investigation on one-dimensional moving rainstorms. For instance, the acceleration terms for the rising and equilibrium portions of a downslope moving storm with celerity $U^* = 1$ and storm length $L^* = 1.5$ are shown in Figure 3. The other parameters for this case are $F_0 = 1.63$ and $K_0 = 105$. Under these conditions, the values of the acceleration terms for stationary storms from (13), (14), and (15) are $a_l^* \sim 0.006$, $a_c^* \sim 0.004$, and $a_p^* \sim 0.002$, respectively; thus $a_l^* > a_c^* > a_p^*$.

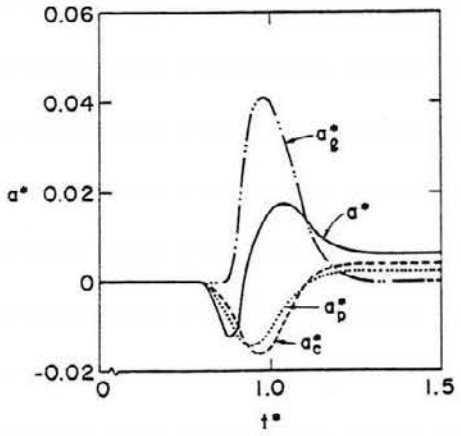

Figure 3. Acceleration terms for a downslope moving storm ($U^* = 1$).

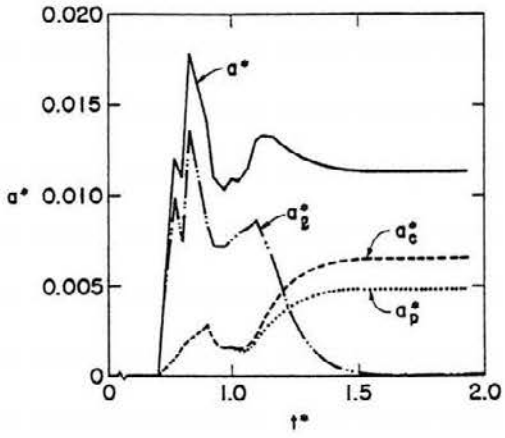

Figure 4. Acceleration terms for an upslope moving storm ($U^* = -1$).

For the downslope moving storm in Figure 3, all three acceleration terms are zero prior to runoff, after which the term a_l^* increases rapidly as soon as the flood wave reaches the downstream end of the plane. It is found that the maximum value of $a_l^* = 0.04$ is roughly an order of magnitude larger than the corresponding value for an equivalent stationary storm $a_l^* = 0.006$. Both values of a_c^* and a_p^* are negative, and their absolute magnitude is smaller than a_l^* as predicted for supercritical stationary storms ($a_l^* > a_c^* > a_p^*$). It is clear from Figure 3 that for downslope moving storms, all the acceleration terms reach a maximum during the rising limb of the hydrograph. Equilibrium conditions are reached for sufficiently large storms. Figure 3 shows that the analytical expressions of a_c^* and a_p^* for stationary storms are reached asymptotically as $t^* > 1.3$. The numerical sum of all three acceleration terms ($a^* = a_l^* + a_c^* + a_p^*$) is also presented on the plots for a storm moving down a plane. During the rising limb, the sum of all three acceleration terms a^* is smaller than the single contribution because the values of a_l^* oppose those of a_c^* and a_p^*.

This analysis contrasts with the previous discussion pertaining to stationary storms. It is important to note that each acceleration term contributes to the value of the friction slope during the rising limb. The term a_l^* peaks at a positive value while the other two acceleration terms are negative, which indicates that using either the quasi-steady dynamic wave or the diffusive wave approximation results in "false improvement" of the computation of the friction slope. Indeed, a friction slope greater than the bed slope is calculated when it actually should be less than the bed slope.

Upslope Moving Storms

Upslope moving storms produce gradually rising limbs when compared with downslope moving storms. The time to equilibrium is consequently delayed, and a value of $L^* = 2$ ensures that the discharge reaches equilibrium. The values of the acceleration terms are plotted on Figure 4 for a storm

moving up the plane at a dimensionless storm speed ($U^* = -1$). The other parameters for these simulations are the same as for the simulation of upslope moving storms.

The magnitude of acceleration terms for upslope moving storms differs largely from downslope moving storms. Runoff immediately increases at the downstream end of the plane and consequently, the flow depth, velocity, and discharge at the terminus of the plane are larger than for locations further upstream. All three acceleration terms are positive during the rising limb, the dominant term being a_l^*. As equilibrium conditions are approached, the value of a_l^* decreases to zero and the values of a_c^* and a_p^* approach the analytical values obtained for stationary storms as shown in Figure 4 when $t^* > 1.5$.

As in the case of downslope moving storms, all three acceleration terms contribute to the determination of the friction slope during the rising limb with downslope moving storms. However, for upslope moving storms, all acceleration terms are positive during the rise, and the use of either the quasi-steady or the diffusive wave approximation will adjust the friction slope in the right direction. The use of either approximation, however, is insufficient because the largest acceleration term a_l^* is neglected.

Conclusion

This investigation focuses primarily on the relative magnitude of the acceleration terms of the Saint-Venant equations applied to one-dimensional overland flow on a plane surface with uniform roughness. Both stationary and block moving rainstorms are considered and the analysis is applicable to laminar and turbulent flows. In absolute value, all acceleration terms (a_l^*, a_c^*, a_p^*) become small compared to S_0 when K is large, as given by (13), (14), and (15). When considering the relative magnitude of the acceleration terms for complete equilibrium hydrographs under stationary rainstorms, it is found that (1) the local acceleration term a_l^* during the rising limb is always larger than the convective acceleration term a_c^* at equilibrium, (2) $a_l^* > a_c^* > a_p^*$ for supercritical overland flow with $Fr > 1.4$, and (3) $a_p^* > a_l^* > a_c^*$ for subcritical overland flow with $Fr < 0.4$. These results on the relative magnitude of the acceleration terms are independent of the kinematic flow number K.

In supercritical overland flow, these results ($a_l^* > a_c^* > a_p^*$) are opposite to those for open channels ($a_l^* < a_c^* < a_p^*$) in that the diffusive wave approximation and the quasi-steady dynamic wave approximation do not improve upon the kinematic wave approximation because the additional term considered is smaller than the terms deleted from the approximation. On the other hand, the results for subcritical overland flow ($a_p^* > a_l^* > a_c^*$) support the use of the diffusive wave approximation but prohibit the use of the quasi-steady dynamic wave formulation.

The findings for moving rainstorms corroborate those of stationary storms in that $a_l^* > a_c^* > a_p^*$ for supercritical overland flow. Individual values of the acceleration terms for moving rainstorms can be up to one order of magnitude larger than for an equivalent stationary storm. Figures 3 and 4 clearly show that either the quasi-steady dynamic wave approximation (neglecting the term a_l^*) or the diffusive wave approximation (neglecting both a_l^* and a_c^*) would neglect terms significantly larger than a_p^*. This effect is found to be more pronounced during the rising limb of overland flow hydrographs for downslope moving storms.

Notation

a^*	sum of three dimensionless acceleration terms.
a_c	convective acceleration.
a_c^*	dimensionless convective acceleration.
a_l	local acceleration.
a_l^*	dimensionless local acceleration.
a_p	pressure gradient.
a_p^*	dimensionless pressure gradient.
C	Chezy resistance coefficient.
Fr	Froude number.
F_0	downstream Froude number.
g	gravitational acceleration.
h	flow depth.
h_0^*	dimensionless flow depth.
H_0	downstream normal flow depth.
i	excess rainfall intensity.
i_0	maximum rainfall intensity.
i_0^*	dimensionless rainfall intensity.
k	laminar resistance parameter.
K	kinematic flow number.
K_0	downstream kinematic flow number.
L_s	storm length.
L^*	dimensionless storm length.
L_0	runoff length.
n	Manning resistance coefficient.
q	unit discharge.
q^*	dimensionless unit discharge.
q_m	equilibrium unit discharge.
S_0	bed slope.
S_f	friction slope.
t	time.
t^*	dimensionless time.
t_0^*	dimensionless time from *Woolhiser and Liggett* [1967].
T_e	time to equilibrium.
U	storm velocity.
U^*	dimensionless storm velocity.
$\bar{u}$	average flow velocity.
u_0^*	dimensionless flow velocity.
V_0	downstream normal flow velocity.
X	distance from upstream boundary.
x	downstream coordinate.
x_0^*	dimensionless downstream distance.
α	coefficient of the stage-discharge relationship.
β	exponent of the stage-discharge relationship.
ν	kinematic viscosity of water.

Acknowledgments. This study has been part of the hydrologic modeling activities at the Colorado State University Center for Geosciences. The financial support granted by the U.S. Army Research Office (grant ARO/DAAL 03-86-K-0175) is gratefully acknowledged. The authors are indebted to K. Marcus for his thoughtful assistance during the early developments of this analysis.

References

Al-Mashidani, G., and C. Taylor, Finite element solutions of the shallow water equations-surface runoff, in *Finite Element Methods in Flow Problems*, edited by J. T. Oden et al., pp. 385–398, UAH Press, Huntsville, Ala., 1974.

Govindaraju, R. S., S. E. Jones, and M. L. Kavvas, On the diffusion wave model for overland flow, 1, Solution for steep slopes, *Water Resour. Res.*, *24*(5), 734–744, 1988.

Henderson, F. M., *Open Channel Flows*, MacMillan, New York, 1966.

6

Hromadka, T. V., II, and J. J. De Vries, Kinematic wave routing and computational error, *J. Hydraul. Eng.*, *114*(2), 207–217, 1988.

Julien, P. Y., and D. B. Simons, Sediment transport capacity of overland flows, *Trans. Am. Soc. Agric. Eng.*, *28*(3), 755–762, 1985.

Lighthill, F. R. S., and G. B. Whitham, On kinematic waves, I, Flood measurements in Long Rivers, *Proc. R. Soc. London, Ser. A*, *229*, 281–316, 1955.

Morris, E. M., The effect of the small slope approximation and lower boundary conditions on solutions of the Saint-Venant equations, *J. Hydrol.*, *40*, 31–47, 1979.

Morris, E. M., and D. A. Woolhiser, Unsteady one-dimensional flow over a plane: Partial equilibrium and recession hydrographs, *Water Resour. Res.*, *16*(2), 355–360, 1980.

Ponce, M. V., The kinematic wave controversy, *J. Hydraul. Eng.*, *117*(4), 511–525, 1991.

Ponce, M. V., and R. M. Li, Overview of flood routing methods, in *Analysis of Watershed and River Systems*, edited by D. B. Simons and R. M. Li, chap. 6, Colorado State University, Fort Collins, 1979.

Richardson, J. R., The effects of moving rainstorms on overland flow using one-dimensional finite elements, Ph.D. dissertation, Dep. of Civ. Eng., Colo. State Univ., Fort Collins, 1989.

Vieira, J. H. D., Conditions governing the use of approximations for the Saint-Venant equations for shallow surface water, *J. Hydrol.*, *60*, 43–58, 1983.

Weinmann, P. E., and E. M. Laurenson, Approximate flood routing methods: A review, *J. Hydraul. Eng. Am. Soc. Civ. Eng.*, *105*(HY12), 1521–1536, 1974.

Woolhiser, D. A., Simulation of unsteady overland flow, in *Unsteady Flow in Open Channels*, chap. 12, pp. 485–508, Water Resources Publications, Fort Collins, Colo., 1976.

Woolhiser, D. A., and J. A. Liggett, Unsteady one-dimensional flow over a plane: The rising hydrograph, *Water Resour. Res.*, *3*(3), 753–771, 1967.

P. Y. Julien and J. R. Richardson, Engineering Research Center, Foothills Center, Foothills Campus, Colorado State University, Fort Collins, CO 80523.

(Received August 9, 1993; revised August 19, 1993; accepted October 19, 1993.)

Formation of roll waves in laminar sheet flow

Formation d'un train d'ondes dans les écoulements superficiels laminaires

P. Y. JULIEN
Faculty Affiliate, Colorado State University, Fort Collins, CO, U.S.A.

D. M. HARTLEY
Research Hydraulic Engineer, USDA-Agricultural Research Service, Fort Collins, CO, U.S.A.

SUMMARY
The formation of a series of roll waves in laminar sheet flows in a smooth channel is examined both theoretically and experimentally. Roll waves were observed in subcritical flows at a Froude number as low as 0.74. The recommended theoretical relationship for the celerity of roll waves is a function of the momentum correction factor. This relationship is in good agreement with measured celerities of roll waves. The period of roll waves remained fairly constant throughout these experiments. Previous derivations of the length required for the formation of roll wave were modified because experimental evidence demonstrates that the simplified relationship for the celerity of roll waves does not hold true for laminar sheet flows. Using the modified relationship, the dimensionless distance displays an hyperbolic variation with the Froude number and good agreement is obtained with experimental data. This analysis also demonstrates that for supercritical flows the distance is proportional to the ratio of flow depth and slope. Alternatively an equivalent function of Reynolds number and slope can be used.

RÉSUMÉ
La formation d'un train d'ondes dans les écoulements superficiels sur surface lisse est étudiée analytiquement et expérimentalement. Des trains d'ondes ont été observés dans des écoulements fluviaux à des nombre de Froude aussi faibles que 0,74. Une expression analytique fonction du coefficient de Boussinesq est recommandée pour décrire la vitesse de propagation des ondes. La période des ondes demeure constante sous les diverses conditions hydrauliques de cette étude. Les équations existantes décrivant la distance de développement des ondes ont dû être modifiées puisque cette étude expérimentale démontre que certaines hypothèses relatives à la vitesse de propagation des ondes ne sont pas valables pour les écoulements laminaires. Les modifications apportées aux équations donnent des résultats en accord avec les résultats expérimentaux. De plus, l'analyse démontre que pour les écoulements torrentiels, la distance est proportionelle au rapport de la profondeur d'écoulement sur la pente. Une expression équivalente en termes de pente et du nombre de Reynolds peut également être utilisée.

1 Introduction

Sheet flows in steep channels often exhibit surface instabilities which grow until a series of breaking or roll waves are formed. In this study the formation of roll waves under laminar conditions is discussed. Previous treatments of the laminar case have neglected the minimum channel length necessary for roll wave development. Theoretical derivations for turbulent flow [Montuori, 1963 and Liggett, 1975] indicate that simple criteria based on the Froude number are necessary though insufficient since the length required for the formation of roll waves is not considered. In the first part of this study, previous theories on the formation of roll waves are

Revised version received July 11, 1985. Open for discussion July 1, 1986.

8

examined and modified in the light of laminar sheet flow characteristics. The experimental part of this study has been conducted in order to provide information regarding the validity of the derived theoretical relationships.

2 Steady uniform laminar sheet flow characteristics

The analysis of the free surface stability of laminar sheet flows assumes that steady uniform flow conditions exist prior to the occurrence of a small perturbation of the water surface. Two non-linear partial differential equations were derived by Saint-Venant to describe gradually varied unsteady flows. These are respectively the continuity and the momentum relationships. For steady uniform sheet flows, the continuity equation can be written as:

$$q = \bar{u}h \tag{1}$$

in which

q = unit discharge
$\bar{u}$ = mean velocity
h = flow depth

The momentum equation reduces to the so-called kinematic wave approximation for which the bed slope S is equal to the friction slope S_f. The friction slope is given by the Darcy-Weisbach equation:

$$S_f = \left(\frac{K\upsilon}{8g}\right)\frac{\bar{u}}{h^2} \tag{2}$$

in which

g = gravitational acceleration
υ = kinematic viscosity
K = the friction coefficient

After combining equations (1) and (2), the mean velocity and flow depth are:

$$\bar{u} = \left(\frac{8g}{K\upsilon}\right)^{1/3} S_f^{1/3} q^{2/3} \tag{3}$$

$$h = \left(\frac{K\upsilon}{8g}\right)^{1/3} S_f^{-1/3} q^{1/3} \tag{4}$$

The relationships are valid for uniform or gradually varied laminar sheet flows only. The velocity distribution with the distance y from the water surface is given by:

$$u = \frac{12g}{K\upsilon} S_f (h^2 - y^2) \tag{5}$$

This velocity profile decreases parabolically from a maximum of 1.5 times the mean velocity at the free surface to zero at the boundary.

3 Theory on the stability of laminar sheet flow

In deriving a fundamental stability criteria for the water surface, several approaches were used by different researchers. Early investigations by Thomas (1939) and Stoker (1957) suggested that the flow is unstable when $S > 4g/C^2$ in which C is the Chézy coefficient. The foremost criterion for instability published in the Russian literature was derived by Vedernikov (1945, 1946). For laminar flows, the Vedernikov number Ve can be written as:

$$Ve = 2F\left(1 - R_h \frac{\partial P}{\partial A}\right) \tag{6}$$

in which

R_h = the hydraulic radius
P = the wetted perimeter
A = the cross-sectional area

The Froude number F defined as $\bar{u}/\sqrt{gh}$ represents the ratio of inertia to gravity forces. For an infinitely wide channel, the Vedernikov number is equal to twice the Froude number and the flow becomes unstable ($Ve > 1$) when the Froude number exceeds 0.5 for laminar flow as compared to 2.0 for turbulent flow. This critical Froude number was also reported by Robertson and Rouse (1941) and Powell (1948). Mayer (1961) observed roll waves in subcritical laminar sheet flows but mistakenly concluded that roll waves can form only when the slope is larger than 3%. Yih (1954, 1963, 1977) and Benjamin (1975) solved the problem of stability of sheet flows down an inclined plane using the Orr-Sommerfeld equation. For very long waves the flow is unstable when:

$$Re \geq \frac{5}{6S} \tag{7}$$

in which Re = the Reynolds number

This criterion was also suggested by Taylor and Kennedy (1961). If equation (2) is substituted into equation (7), uniform flow ($S = S_f$) and a K value of 24 are assumed, a critical Froude number of $F_c = 0.53$ results which is close to the Vedernikov criteria for wide rectangular channels. Ishihara et al. (1961) also suggested the critical value $F_c = 0.577$.

Unfortunately, these criteria based on the Froude number ignore the distance along the channel required for the formation of roll waves. This factor becomes particularly important for subcritical sheet flows since previous studies for turbulent flows [Montuori, 1963] demonstrate that the distance at which the waves are fully developed increases to infinity as the Froude number approaches the critical value.

3.1 *Formation and celerity of roll waves*

When the flow is unstable ($Ve > 1$) a minor perturbation of the water surface induces the formation of small waves. The amplitude of these waves increases gradually as they move downstream until a bore is formed and the wave breaks. The distance travelled between the point at which the perturbation is initiated and the breaking point of the wave defines the distance required for the formation of roll waves. This distance, ξ_c, is determined theoretically from the following procedure using the celerity of roll waves.

The total celerity, c, of a small gravity wave moving in a fluid with a uniform velocity distribution along the vertical is:

$$c = \bar{u} + \sqrt{gh} \tag{8}$$

In the more general case of a nonuniform vertical velocity distribution, the celerity can be theoretically derived from the momentum equation. After the momentum correction factor β_m is used instead of an empirical coefficient, the equation for celerity suggested by Arsenishvili (1965) can be written as:

$$c = \bar{u} + c_0 = \beta_m \bar{u} + \sqrt{gh + \beta_m(\beta_m - 1)\bar{u}^2} \tag{9}$$

in which c_0 is the celerity of the wave relative to the mean velocity $\bar{u}$; and

$$\beta_m = \frac{1}{\bar{u}^2 h} \int_0^h u^2 \, dy \tag{10}$$

When $\beta_m = 1$, equation (9) reduces to equation (8). For sheet flows, however, the momentum correction factor $\beta_m = 1.2$ is obtained from equations (5) and (10). The ratio of celerities $c/\sqrt{gh}$ is:

$$\frac{c}{\sqrt{gh}} = \beta_m F + \sqrt{1 + \beta_m(\beta_m - 1)F^2} \tag{11}$$

Equations (9) or (11) can be used to compute the celerity of roll waves in laminar sheet flows.

3.2 *Perturbation analysis*

The following analysis of the channel length required for a small disturbance to become a breaking wave resembles the mathematical treatment used by Liggett (1975) and Dracos and Glenne (1967). First, time is removed from the momentum and continuity equations written in terms of x and t by introducing a moving coordinate system in ξ and η which travels at the constant wave speed, $\bar{u} + c_0$. The variable ξ replaces the original space coordinate x and defines position with respect to a fixed point, while the second coordinate, η, defines position relative to the moving coordinate system and is written:

$$\eta = (\bar{u} + c_0)t - \xi \tag{12}$$

A small perturbation moving at the wave speed $(\bar{u} + c_0)$ is imposed at $\xi = 0$ on an initially steady uniform flow. This is mathematically simulated by writing the equations for conservation of mass and momentum as follows:

$$B'(\bar{u} + c_0)\frac{\partial h'}{\partial \eta} + \bar{u}'B'\left(\frac{\partial h'}{\partial \xi} - \frac{\partial h'}{\partial \eta}\right) + A'\left(\frac{\partial u'}{\partial \xi} - \frac{\partial \bar{u}'}{\partial \eta}\right) = 0 \tag{13}$$

and

$$(\bar{u} + c_0)\frac{\partial \bar{u}'}{\partial \eta} + \bar{u}'\left(\frac{\partial \bar{u}'}{\partial \xi} - \frac{\partial \bar{u}'}{\partial \eta}\right) + g\left(\frac{\partial h'}{\partial \xi} - \frac{\partial h'}{\partial \eta}\right) = g(S - S_f') \tag{14}$$

in which the variables h', $\bar{u}'$, B', A' and S_f' represent perturbations in the neighborhood of the uniform flow values of flow depth h, velocity $\bar{u}$, top width B, cross-sectional area A and bed slope S. The perturbed variables, denoted by primes, are defined as follows:

$$h' = h + \frac{\partial h'}{\partial \eta}\eta + \frac{1}{2}\frac{\partial^2 h'}{\partial \eta^2}\eta^2 + 0(\eta^3) \tag{15}$$

$$\bar{u}' = \bar{u} + \frac{\partial \bar{u}'}{\partial \eta}\eta + \frac{1}{2}\frac{\partial^2 \bar{u}'}{\partial \eta^2}\eta^2 + 0(\eta^3) \tag{16}$$

$$B' = B + \frac{\partial B'}{\partial h'}\frac{\partial h'}{\partial \eta}\eta + 0(\eta^2) \tag{17}$$

$$A' = A + \frac{\partial A'}{\partial h'}\frac{\partial h'}{\partial \eta}\eta + 0(\eta^2) \tag{18}$$

$$S_f' = S + S\eta\left(\frac{1}{\bar{u}}\frac{\partial \bar{u}'}{\partial \eta} - \frac{2}{h}\frac{\partial h'}{\partial \eta}\right) + 0(\eta^2) \tag{19}$$

The truncated series are valid for small values of η and the solution is examined in the neighborhood of $\eta = 0$. An analysis of equations (13) and (14) using the perturbation defined by equations (15) through (19) as presented in Julien and Hartley (1985) results in the following relationship

$$\frac{\partial^2 h'}{\partial \xi \partial \eta} - \beta\left(\frac{\partial h'}{\partial \eta}\right)^2 + \gamma\frac{\partial h'}{\partial \eta} = 0 \tag{20}$$

in which for rectangular channels ($B = B'$ and $\partial B'/\partial h' = 0$), the coefficients β and γ are respectively:

$$\beta = \frac{3g}{c_0^2 + 2\bar{u}c_0 + gh} \tag{21}$$

and,

$$\gamma = \frac{gS}{\bar{u}^2}\left(1 - \frac{2c_0F^2}{\bar{u}}\right)\left[\frac{1}{2 + \frac{c_0}{\bar{u}} + \frac{\bar{u}}{c_0F^2}}\right] \tag{22}$$

This derivation improves the one given by Liggett (1975) since the wave celerity defined by equation (9) accounts for the velocity distribution present in laminar sheet flow. If a uniform velocity distribution is assumed (i.e. $c_0 = \sqrt{gh}$), equations (21) and (22) reduce to the relationship proposed by Liggett.

The solution of equation (20) is:

$$\frac{\partial h'}{\partial \eta} = \frac{\varepsilon}{\frac{\beta\varepsilon}{\gamma} + e^{\gamma\xi}} \tag{23}$$

in which ε is a constant of integration along the longitudinal distance ξ.

3.3 *Distance for the formation of roll waves*

The critical distance ξ_c at which the wave breaks is assumed to occur when the water surface is vertical. Mathematically, this condition is obtained when the denominator of equation (23) is set equal to zero, or when:

$$\xi_c = \frac{1}{\gamma} \ln \left(-\frac{\beta}{\gamma} \varepsilon \right) \tag{24}$$

Liggett (1975) derived a relationship between ε and the variables β, γ and the value of $\partial h/\partial \eta$ at the origin. Unfortunately this latter quantity is an unknown which is practically impossible to measure. The following approach which avoids the necessity of directly evaluating ε is recommended.

After combining equations (21), (22) and (24), the distance ξ_c can be written as follows:

$$\xi_c = \frac{h}{S} \left\{ \Psi \left[\Phi + \ln \left(\frac{S}{3\varepsilon} \right) \right] \right\} \tag{25}$$

in which,

$$\Psi = \left[\frac{F^2}{\frac{2c_0 F^2}{\bar{u}} - 1} \right] \left(2 + \frac{c_0}{\bar{u}} + \frac{\bar{u}}{c_0 F^2} \right) \tag{26}$$

and,

$$\Phi = \ln \left(2 \frac{c_0^2 F^2}{\bar{u}^2} - \frac{c_0}{\bar{u}} \right) \tag{27}$$

From equation (11), $c_0/\bar{u}$ can be written as a function of the Froude number for a given value of β_m. Taking $\beta_m = 1.2$ for laminar sheet flows, the variable Ψ and Φ from equations (26) and

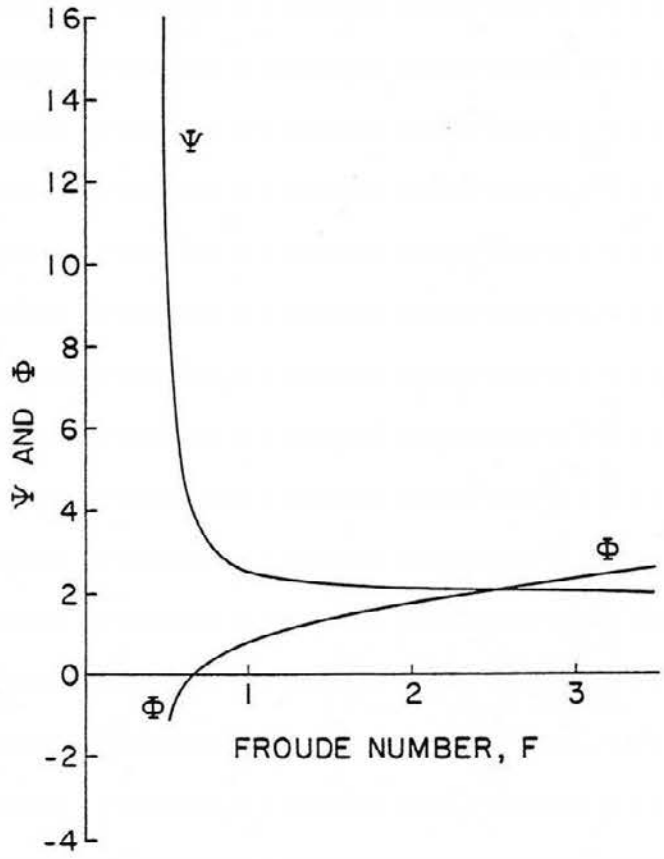

Fig. 1. Dimensionless variables Φ and Ψ as a function of Froude number.
Variables adimensionnelles Φ et Ψ en fonction du nombre de Froude.

(27) are dimensionless and unique functions of the Froude number as plotted in Fig. 1. For supercritical flows, Ψ has a nearly constant value of 2.0 while Φ increases gradually with the Froude number. It can also be demonstrated that over a fairly wide range of slopes the expression $\ln(S/3\varepsilon)$ will be substantially constant. If Φ is small compared to $\ln(S/3\varepsilon)$ then the following approximate relationship for ξ_c can be written:

$$\xi_c \cong D\frac{h}{S} \tag{28}$$

in which D is equivalent to the factor in braces in equation (25) and is approximately constant. Equations (24) is general while equation (28) represents a simplified expression applicable only to supercritical flows. The ability of equations (24) and (28) to predict the distance ξ_c is evaluated with laboratory data described in the following section.

Table 1. Data summary

S	Re	c m/s	T s	ξ_c m	F	$\frac{gS\xi_c}{\bar{u}^2}$	D	E mm
(1)	(2)	(3)	(4)	(5)	(6)	(7)	(8)	(9)
0.040	335	0.46	1.33	0.91	2.11	6.03	26.6	1.80
0.040	400	0.50	1.61	0.91	2.31	4.74	25.4	1.71
0.040	500	0.57	1.96	0.91	2.58	3.53	23.5	1.59
0.035	68	0.22	1.27	2.74	0.89	147.30	-	-
0.035	95	0.26	1.28	1.52	1.05	51.20	56.6	3.81
0.035	141	0.34	1.45	1.52	1.28	30.50	49.7	3.35
0.035	188	0.34	1.32	2.13	1.48	28.70	62.6	4.26
0.035	265	0.42	1.37	2.13	1.76	18.40	56.9	3.81
0.035	380	0.43	1.19	2.74	2.11	14.40	64.4	4.33
0.030	90	0.24	1.35	2.13	0.95	72.70	-	-
0.030	122	0.25	1.43	2.13	1.10	49.60	59.7	4.02
0.030	200	0.36	1.47	2.74	1.41	33.10	65.8	4.36
0.030	260	0.41	1.25	2.13	1.61	23.10	46.6	3.99
0.030	340	0.42	1.37	2.13	1.84	16.30	42.9	3.66
0.030	360	0.48	1.35	1.52	2.15	5.90	27.1	1.83
0.030	550	-	-	1.52	2.35	4.68	25.8	1.74
0.025	65	-	-	7.62	0.74	380.00	-	-
0.025	71	-	-	7.62	0.77	340.00	-	-
0.025	85	0.22	1.52	3.35	0.84	118.00	-	-
0.025	104	0.24	1.52	3.35	0.93	91.00	-	-
0.025	130	0.33	1.54	2.74	1.04	54.70	59.1	3.96
0.025	200	0.34	1.61	2.74	1.29	30.70	51.1	3.44
0.025	246	0.38	1.75	2.13	1.43	18.20	37.2	2.50
0.025	320	0.44	1.52	1.52	1.63	9.20	24.5	1.62
0.025	420	0.47	1.19	0.91	1.87	3.83	13.3	0.88
0.025	530	0.50	1.15	1.52	2.10	4.65	20.4	1.37
0.015	140	0.26	1.72	2.74	0.84	41.60	-	-
0.015	173	0.27	1.33	2.13	0.93	24.30	-	-
0.015	260	0.33	1.43	2.13	1.14	14.20	18.4	1.25
0.015	320	0.40	1.23	2.13	1.26	10.80	17.2	1.16
0.015	450	0.43	1.08	1.52	1.50	5.90	11.0	0.88
mean			1.41				38.5	2.67
standard deviation			0.20				18.5	1.28

4 Experimental investigation

Laboratory experiments were conducted to determine laminar flow conditions which produced roll waves. The measurements of roll waves included the length required for their formation, wave frequency and wave celerity.

A 0.21 m wide by 9.75 m long rectangular flume was utilized for these experiments. The slope was adjusted between 1.5 and 4% and the unit discharge varied between 6.5×10^{-5} to 5.5×10^{-4} m^2/s. The water temperature was measured and the theoretical friction factor $K = 24$ was verified. Inlet conditions were shown by Brock (1965) to be important in the evaluation of the distance ξ_c. In our experiments a honeycomb flow straightener was placed at the entrance of the channel to break up any large eddies. The initial perturbation triggering the formation of roll waves was assumed to occur immediately downstream of the straightener. The distance ξ_c was measured from this point to the location where a well-defined breaking wave was observed. All the data collected in this experimental investigation were reported by Julien and Hartley (1985). A summary of the experimental data is presented in Table 1. The first five columns read as follows: slope, Reynolds number, wave celerity, wave period and distance for roll wave formation. In column six the Froude number was computed from the Reynolds number and slope.

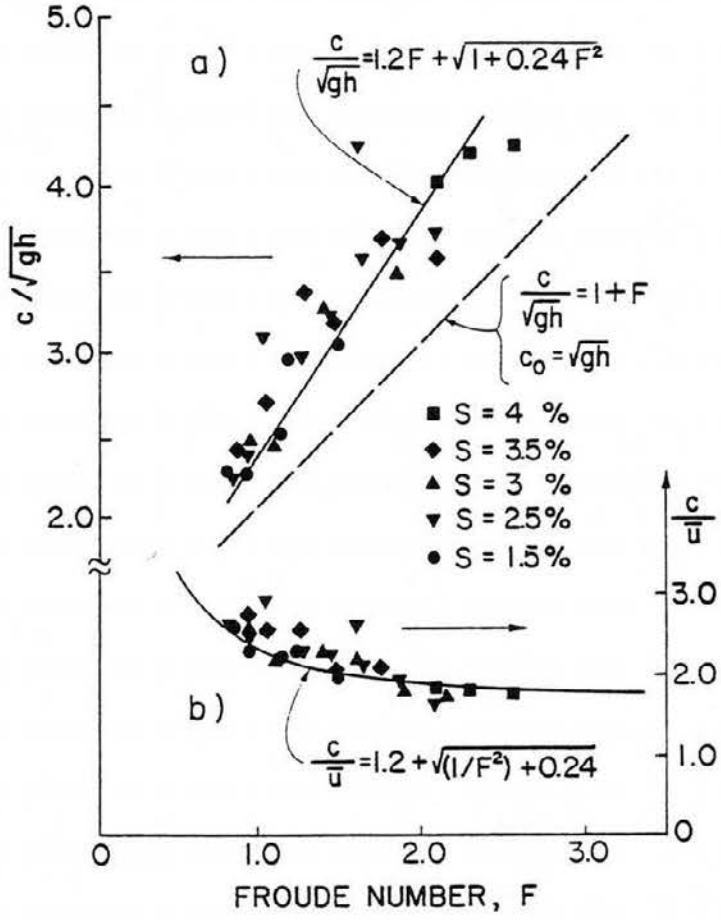

Fig. 2. Dimensionless celerity as a function of Froude number.
Vitesse de propagation adimensionnelle en fonction du nombre de Froude.

15

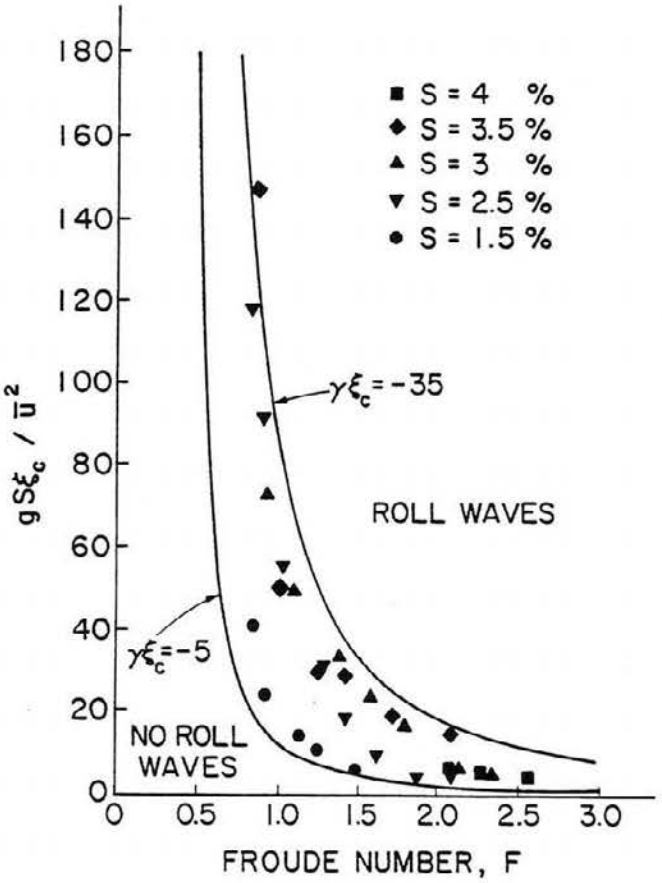

Fig. 3. Dimensionless critical distance as a function of Froude number.
Distance critique adimensionnelle en fonction du nombre de Froude.

4.1 *Analysis of wavelength, period and celerity*

The wavelength can be evaluated from the wave celerity and the period. The observed values of the ratio $c/\sqrt{gh}$ have been plotted against the Froude number on Fig. 2a along with solid and dashed lines representing equation (11) with $\beta_m = 1.2$ and equation (8) for which $\beta_m = 1.0$. The superiority of equation (11) is well supported by the data. Equation (11) can also be written as the ratio of the wave celerity to the mean flow velocity $\bar{u}$ as follows:

$$\frac{c}{\bar{u}} = \beta_m + \sqrt{\frac{1}{F^2} + \beta_m(\beta_m - 1)} \tag{29}$$

For unstable flows ($F > 0.5$), the ratio $c/\bar{u}$ calculated from equation (29) ($\beta_m = 1.2$) decreases from 3.26 to a minimum of 1.69 as shown in Fig. 2b.

The measured wave periods T shown in Table 1 (Col. 4) were fairly constant with a mean value of $\bar{T} = 1.41$ seconds and a standard deviation of 0.20 seconds.

The wavelength L can be obtained from equation (29) in which c is replaced by L/T:

$$\frac{L}{\bar{u}T} = 1.20 + \sqrt{\frac{1}{F^2} + 0.24} \tag{30}$$

For a given mean velocity, the wavelength increases with decreasing Froude number and a first approximation of the wavelength is obtained from the mean value of wave period $\bar{T} = 1.41s$.

4.2 *Critical distance for the formation of roll waves*

Two relationships (equations (24) and (28)) for the distance required for the formation of roll waves are examined in the light of experimental data for laminar sheet flows. In equation (24), the distance ξ_c is a function of β, γ, and ε. The parameters β and γ are computed from equations (21) and (22). The values of ln ε calculated from equation (24) using measured values of ξ_c ranged from -61 to -9.4 with a mean value of -25.7. As suggested by Montuori (1963) and Liggett (1975), the values of ln $(-\beta\varepsilon/\gamma)$ or $\gamma\xi_c$ were computed. Measured values of ξ_c were converted to the dimensionless parameter $gS\xi_c/\bar{u}^2$ in Table 1 (Col. 7) and plotted againt the Froude number in Fig. 3. This figure clearly defines a region where roll waves were observed $(\xi > -35/\gamma)$ and a region where roll waves were not completely developed $(\xi < -5/\gamma)$. Between these limits exists a zone of uncertainty defined by $-35/\gamma > \xi_c > -5/\gamma$. This figure can be used to estimate the distance for the formation of roll waves from the parameter γ. The evaluation of γ from equation (22) is possible provided the variables S, $\bar{u}$, c_0 and F are known.

If the flow is supercritical, the evaluation of ξ_c from equation (28) involves only the flow depth, slope and the coefficient D. From the experimental data, it was demonstrated that Φ is small compared to ln $(S/3\varepsilon)$ and therefore D is expected to be substantially constant. The values of D presented in Table 1 (Col. 8) were computed from the experimental values of ξ_c, S and h using equation (28). The mean value for D is 38.5 with a standard deviation equal to 18.5. Equation (28) is therefore recommended to estimate ξ_c for supercritical flows, when depth and slope are known. The flow depth in equation (28) can also be replaced by a function of the slope $(S \cong S_f)$ and the Reynolds number from equation (4):

$$\xi_c \cong E \frac{Re^{1/3}}{S^{4/3}} \tag{31}$$

in which,

$$E = D\left(\frac{Kv^2}{8g}\right)^{1/3} \tag{32}$$

These relationships indicate that for the same slope and Reynolds number, the constant E, and therefore the critical distance ξ_c increases with increasing viscosity and surface roughness K. The parameter E has dimensions of length. Values of E from the experiments are tabulated in Table 1 (Col. 9). This parameter has a mean value of 2.67 mm and a coefficient of variation of 48%. Equation (31) is recommended for supercritical laminar sheet flows over smooth surfaces. It should be noted that the mean values of the coefficients $D = 38.5$ and $E = 2.67$ mm apply to the range of conditions used in this experimental study. These values may not be applicable beyond this range.

5 Applications

It is recognized that this study is mainly of theoretical interest. However, roll waves in highly viscous mudflows have been observed in steep mountain channels. Investigations of these flows should benefit from the analysis presented in this paper.

6 Summary and conclusions

The formation of roll waves in laminar sheet flows is examined using a theoretical analysis supported by experimental data. Previous investigations indicate that roll waves are theoretically

possible in laminar sheet flows at Froude numbers as low as 0.50 as compared with 2.0 in turbulent flow. The existence of roll waves at Froude numbers near the lower limit is difficult to verify experimentally because of the extreme channel lengths required. However, in this study, roll waves were observed in laminar, subcritical flow at a Froude number as low as 0.74.

The parabolic velocity distribution in laminar sheet flows implies that the momentum correction factor is larger than unity ($\beta_m = 1.2$). This suggests that the relationship $c = \bar{u} + \sqrt{gh}$ used in previous studies is not applicable to laminar sheet flows and should be replaced by one which uses β_m. The proposed relationship (equation (11)) reduces to $c_0 = \sqrt{gh}$ when $\beta_m = 1$ and is in good agreement with the measured celerities of roll waves when $\beta_m = 1.2$ as shown in Fig. 2. The measured periods of roll waves remained fairly constant in the experimental study at $\bar{T} = 1.41$ second. The wavelength is shown to vary between $1.69\overline{uT} < L < 3.26\overline{uT}$.

The linearized derivation by Liggett (1975) of the length, ξ_c, required for the formation of roll waves has been modified to account for the parabolic velocity distribution of laminar sheet flows. The modified derivation gives more general expressions for the coefficients β and γ which reduce to those proposed by Liggett when $\beta_m = 1$. The results indicate that the length ξ_c is a function of several flow variables and a constant of integration ε which could be calculated from experiments. Though the parameter $\ln \varepsilon$ varies widely ($-61 < \ln \varepsilon < -9.4$), the dimensionless distance shown in Fig. 3 displays a similar relationship to the Froude number as found by Montuori (1963) for turbulent flows. For supercritical flows, ξ_c is proportional to the ratio of flow depth and slope. Alternatively, an equivalent function of Reynolds number and slope may be used.

Acknowledgement

This study has been completed at the Engineering Research Center at Colorado State University. The support of a NATO post-doctoral fellowship to the first author provided by the Natural Sciences and Engineering Research Council of Canada is gratefully acknowledged. The authors would also like to thank the U.S. Department of Agriculture, Agricultural Research Service for providing additional resources for this study.

Notations

A	cross-sectional area for uniform flow
A'	cross-sectional area for flow with a small perturbation
B	top channel width for uniform flow
B'	top channel width for flow with a small perturbation
c	wave celerity
c_0	velocity of the wave relative to the mean velocity $\bar{u}$
C	Chézy coefficient
D, E	empirical constants in equations (28) and (32)
F	Froude number
F_c	critical Froude number
g	gravitational acceleration
h	uniform flow depth
h'	flow depth for flow with a small perturbation
K	friction parameter
L	wavelength

q	unit discharge
R	ratio of two functions of the Froude number
Re	Reynolds number
R_h	hydraulic radius
S	channel slope
S_f	friction slope
S'_f	friction slope for flow with a small perturbation
t	time
T	wave period
$\bar{T}$	mean wave period
u	velocity
$\bar{u}$	mean velocity for uniform flow
$\bar{u}'$	mean velocity for flow with a small perturbation
Ve	Vedernikov number
y	distance from the water surface
β, γ	functions of flow variables in equations (21) and (22)
β_m	momentum correction factor
ε	constant of integration
η	transformed distance moving with the wave
υ	kinematic viscosity of water
ξ	distance downslope
ξ_c	critical distance at which roll waves are formed
Φ, Ψ	functions of the Froude number

References / Bibliographie

ARSENISHVILI, K. I., *Effect of wave formation on hydro-engineering structures*, Translated from Russian, 1965, 134 p.

BENJAMIN, T. B., Wave formation in laminar flow down on inclined plane, Journal of Fluid Mechanics, Vol. 2, 1975, pp. 554–574.

BROCK, R. R., Development of roll-wave trains in open channels, Journal of the Hydraulics Division, ASCE, Vol. 95, No. HY4, 1969, pp. 1401–1427.

CHOW, V. T., *Open channel hydraulics*, McGraw-Hill, 1959, 680 p.

DRACOS, T. A. and GLENNE B., Stability criteria for open-channel flow, Journal of the Hydraulics Division, Vol. 93, No. HY6, November 1967, pp. 79–101.

ISHIHARA, T., IWAGAKI, Y. and IWASA, Y., Discussion on "Roll waves and slug flows in inclined open channels", Transactions of the ASCE, 1961, pp. 548–563.

JULIEN, P. Y. and HARTLEY, D. M., Formation of roll waves in laminar sheet flow, Report CER84-85PYJ-DMH18, Department of Civil Engineering, Colorado State University, 1985, 34 p.

LIGGETT, J. A. Stability, Chapter 6 in *Unsteady Flow in Open Channels*, WRP, 1975, pp. 259–282.

MAYER, P. G., Roll waves and slug flows in inclined open channels, Transactions of the ASCE, 1961, pp. 505–535.

MONTUORI, C., Discussion on "Stability aspects of flow in open channels", (by F. F. Escoffier and M. B. Boyd) Journal of the Hydraulics Division, ASCE, Vol. 89, No. HY4, July 1963, pp. 264–273.

POWELL, R. W., Vedernikov's criterion for ultra-rapid flow, Transactions of AGU, Vol. 29, No. 6, 1948, pp. 882–886.

ROBERTSON, J. M. and ROUSE, H., On the four regions of open channel flow, Civ. Eng., Vol. 11, 1941, pp. 169–171.

STOKER, J. J., Mathematical hydraulics, in *Water waves*, Wiley Interscience, 1957, pp. 451–509.

TAYLOR, R. H. and KENNEDY, J. F., Discussion on roll waves and slug flows in inclined open channels by P. G. Mayer, Transactions of the ASCE, 1961, pp. 541–548.
THOMAS, H. A., The propagation of waves in steep prismatic conduits, Proc. Hydraulic Conference, Univ. of Iowa, 1939, pp. 214–229.
VEDERNIKOV, V. V., Conditions at the front of a translation wave disturbing a steady motion of a real fluid, USSR Academy of Sciences, Vol. 48, No. 4, 1945, pp. 239–242.
VEDERNIKOV, V. V., Characteristic features of a liquid flow in an open channel, USSR Academy of Sciences, Vol. 52, 1946, pp. 207–210.
YIH, C. S., Stability of parallel laminar flow with a free surface, Proc. 2nd U.S. Congress in Applied Mechanics, 1954, pp. 623–628.
YIH, C. S., Stability of liquid flow down an inclined plane, Physics Fluids, Vol. 6, 1963, pp. 321–334.
YIH, C. S., *Fluid mechanics,* West River Press, 1977, pp. 502–507.

Boundary shear stress induced by raindrop impact

Contrainte de cisaillement due a l'impact de gouttes d'eau sur une nappe liquide

D. M. HARTLEY
Research Hydraulic Engineer,
Hydro-Ecosystems Research Group,
USDA-Agricultural Research Service,
Fort Collins, CO 80522, USA

P. Y. JULIEN
Associate Professor of
Civil Engineering,
Colorado State University,
Fort Collins, CO 80523, USA

SUMMARY
An efficient mathematical model for calculation of the boundary shear stress field induced by raindrop impact is developed and tested using numerical and experimental data. The model comprises a series of dimensionally consistent, closed-form, algebraic equations, written in terms of physically meaningful parameters describing the fluid properties and initial conditions at the instant of drop impact. The relationships in the model are derived from the analysis of data generated by a computer code which numerically solves the Navier-Stokes equations for two-dimensional flow of a viscous, incompressible fluid with a free surface. The resulting simplified, algebraic model is validated using data from laboratory experiments which employ hot-film anemometry to measure drop induced boundary shear stresses. Substantial agreement is found between model and experimental results with regard to the boundary shear stress magnitudes and sensitivity of magnitudes to different water layer depths, drops sizes, drop velocities and distances from the center of drop impact.

RÉSUMÉ
Un modèle mathématique de calcul de contraintes de cisaillement lors de l'impact de gouttes d'eau sur une nappe liquide est développé et vérifié à l'aide de données numériques et expérimentales. Le modèle consiste en une série d'équations algébriques en function des principaux paramètres physiques décrivant l'impact de gouttes d'eau. Les relations du modèle sont basées sur une analyse de données obtenues par une solution numérique des équations de Navier-Stokes appliquées à l'analyse bi-dimensionnelle d'un écoulement visqueux incompressible lors d'un impact de gouttes d'eau sur une nappe liquide. Le modèle algébrique simple qui en résulte est validé à partir de données de contraintes de cisaillement mesurées en laboratoire à l'aide d'une technique anémométrique à film chaud. Il existe un bon accord entre le modèle et les mesures expérimentales relativement à l'amplitude des contraintes de cisaillement ainsi que la sensibilite du modèle aux paramètres tels la taille et la vitesse des gouttes d'eau, la profondeur de la nappe d'eau et la distance du point d'impact.

1 Introduction

The deformation of a liquid surface struck by a droplet was first photographed and studied systematically by Worthington (1882) at the end of the 19th century. His classic monograph (1908), republished posthumously just a few decades ago (1963) described experiments involving droplet impact on both dry, smooth surfaces and deep liquid pools. Worthington was primarily concerned with the evolution of the splash structure as affected by droplet impact velocity and surface tension. Later, Laws (1939, 1940) applied high-speed motion picture photography techniques to the study of raindrop splashes on soil covered by thin layers of water. He identified the lateral jet of the expanding splash crater and the ejection of numerous droplets from the splash

Revision received March 1, 1991. Open for discussion till December 31, 1992

crown as mechanisms of soil particle detachment and transport. Photographs from this study show that when a large drop strikes a water layer, a crater expands horizontally over a period of approximately 35 msec and collapses over a period twice that long. The vertical motion forming the cylindrical shell of the splash crown is superimposed on this horizontal motion. The rise of the shell occurs over approximately 1/5 and the collapse over 4/5 of the cycle.

Other investigators (Hobbs and Kezweeny, 1967; Hobbs and Osheroff, 1967; Macklin and Hobbs, 1969; Mutchler and Hansen, 1970; Macklin and Metaxes, 1976) used photographs to correlate various aspects of drop morphology such as crown droplet formation, crater shape, maximum crater size and height of the recoil jet with initial conditions such as drop size, impact velocity and pool depth. Macklin and Hobbs (1969) observed that when a 2.3 mm drop impacted a pool with a depth greater than 4 drop diameters at about 50% of terminal velocity, a hemispherical crater formed and fluid motion was predominantly vertical. At depths less than 2.5 drop diameters, the splash crater contacted the bed and became conical in shape. At the shallowest depths, the crater was cylindrical and fluid motion was predominantly horizontal. Mutchler and Hansen (1970) found that splash diameter and height increased from zero to a maximum as pool depth increased from zero to 1/3 drop diameters. These splash dimensions decreased as pool depth increased from 1/3 to 3 drop diameters, and then remained constant for depths greater than 3 diameters. Later Mutchler and Young (1975) used Mutchler and Hansen's data to develop empirical relationships for crater expansion rates and infer rough estimates of the variation of bed shear with time after drop impact. They also suggested that water depths greater than 3 drop diameters were sufficient to protect the soil surface from raindrop action. This rule of thumb was based on the observation of the invariance of splash size with pool depth at depths greater than 3 drop diameters and the hypothesis that forces on the bed would be negligible under these conditions.

Both analytical and numerical studies have complemented experimental research into the dynamics of the drop impact phenomenon. Engel (1966) derived an energy balance for the instant of maximum crater size and derived an expression for the maximum crater radius which compared well with experimental data. At about the same time, numerical simulations of the drop impact problem were being performed which provided both synthetic pictures of dynamic splash morphology and evaluation of the dynamic pressure and velocity fields within the fluid. Harlow and Shannon (1967) used the MAC or "Marker and Cell" (Welch at al., 1965) technique to numerically solve the Navier-Stokes equation for drop impact on a free surface. Their simulations were restricted to low velocity impact in the absence of surface tension and viscosity. For these conditions, the simulation showed that the drop material tended to line the bottom and sides of the crater.

Wang (1970) modified the model used by Harlow and Shannon and applied it to more realistic drop impact conditions which included surface tension and viscous forces. Wang's objective was to numerically investigate the pressure field generated by single drop impacts on shallow pools with drop sizes and velocities similar to those found in natural rainfall. Using results of numerical simulations, Wang developed an equation describing peak pressure on the boundary as a function of the drop stagnation pressure at impact and a ratio of drop size to pool depth. This equation agreed well with experimental data obtained with a pressure cell. He found that boundary pressure generally built up to a maximum within 1.0 msec and that at the instant of peak pressure, the spatial distribution of the pressure was Gaussian and centered on the axis of impact. Wang made a few rough calculations of peak shear based on simulated velocity differences between computional cells adjacent to the lower boundary but the computational grid was too coarse to allow a good estimate of the velocity gradient.

Further numerical simulation using the MAC method was carried on by Huang et al. (1982) for drop impacts in the absence of viscosity and surface tension. They found that a 4.0 mm drop impacting a solid surface produced pressures lasting a few microseconds which were 20 times the stagnation pressure and that radial jet velocities were twice the impact velocity. More recently, Tan (1990) reviewed many of the experimental and numerical studies of raindrop splash and erosion. He also proposed a raindrop erosion model which suggested that erosive pressures on the soil surface are maximized when a water layer equal to the drop diameter is present.

2 Focus and methodology

This study focuses on the boundary shear stress induced by raindrop impact on layers of water which are less than 3.0 raindrop diameters because past research indicates that erosive forces become practically insignificant at larger water depths (Wang, 1970; Mutcher and Young, 1975). Additionally, analysis is confined to the initial period of drop penetration and crater expansion when drop momentum is concentrated in a relatively small area around the impact site. During this period, pressure gradients, fluid velocities and boundary shear stresses are large in comparison to later stages of splash (Worthington, 1963; Laws, 1939; Wang, 1970; Harlow and Shannon, 1967).

Based on physical considerations and a dimensional analysis, Hartley (1990) showed that a general equation for the time and space varying boundary shear stress field can be written in terms of a Reynolds number R, Weber number W, Froude number F, dimensionless pool depth y_0^* and dimensionless space and time values x^* and t^* as follows:

$$\tau^* = f(R,\ W,\ F,\ y_0^*,\ x^*,\ t^*) \tag{1}$$

in which $\tau^* = \tau/\varrho V_0^2$, $R = \varrho V_0 r/\mu$, $W = \varrho V_0^2 r/\sigma$, $F = V_0/(gr)^{0.5}$, $y_0^* = y_0/r$, $x^* = x/r$, and $t^* = V_0 t/r$. Here τ is the boundary shear stress, ϱ is the fluid density, V_0 is drop impact velocity, r is the radius of the drop, μ is the fluid dynamic viscosity, σ is the surface tension, g is the gravitational acceleration, y_0 is the initial depth of the pool at the instant of impact, x is the radial distance from the vertical axis of symmetry and t is the time since the instant of impact. As noted by Harlow and Shannon (1967), gravity and surface tension forces both tend to restore the water surface to a horizontal or rest position. Numerical simulations conducted by Hartley (1990) corroborated this analysis and lead to the simplification of equation (1) by merging F and W into a single parameter θ as follows:

$$\tau^* = f(R, \theta, y_0^*, x^*, t^*) \tag{2}$$

in which

$$\theta = F W^{0.5}/(F + W^{0.5}) \tag{3}$$

This simplification is justified by Hartley's results which showed a similar sensitivity of the boundary shear stress field to F and $W^{0.5}$ when either or both parameters were small. This trend is represented by equation (3). Additionally, it is shown in the following analysis that gravity and surface tension forces have only a minor effect on shear stress magnitudes.

Equation (2) describes drop induced boundary shear stress in terms of dimensionless variables which use the drop impact velocity and drop radius as space and time scaling factors. The functional dependence of the dimensionless boundary shear stress on the independent dimensionless variables defined in equation (2) was investigated using a numerical solution to the equations of

23

fluid motion. A set of empirical relationships for the boundary shear stress was developed from the results of the numerical experiments. Subsequently, the numerically derived empirical relationships were compared with results from laboratory experiments.

3 Numerical model

The numerical model employed in this study is a modified version of the SOLA-VOF model (Nichols et al., 1980). SOLA-VOF is a generic code for the finite difference solution of two-dimensional, viscous, incompressible flow problems involving free surfaces or boundaries between two immiscible fluids. Particular flow problems are defined through the specification of appropriate boundary and initial conditions by the code user. Consequently, SOLA-VOF has been applied to a wide range of flow problems (Nichols et al., 1980) including a jet impinging on a wall, collapse of a tank surrounded by a retaining wall, and instability of a thin liquid column due to surface tension. Additionally, Hartley (1990) validated the model's ability to solve unsteady viscous flow problems by comparing simulation results with the analytical solution for the problem of a suddenly accelerated plate in an unbounded fluid medium.

The basic numerical procedure used to solve the equations of motion by SOLA-VOF employs an explicit difference scheme to obtain estimates of the entire velocity field at the advanced time step. These velocities are checked by computing the divergence or error in continuity which in turn is used to correct pressure values throughout the domain. Velocities are recomputed and the iterations continue until the divergences at all locations are smaller than a user-defined tolerance. Unlike earlier hybrid Eulerian-Lagrangian techniques such as the MAC method (Welch et al., 1965) which used massless marker particles to track the movement of free surfaces, SOLA-VOF is purely Eulerian. Fluid interfaces or free surfaces are tracked using a step function which defines the presence or absence of fluid at a point. Details of this method and other features of the numerical solution employed by SOLA-VOF are presented elsewhere (Nichols et al., 1980; Hirt and Nichols, 1981) and will not be repeated here. Hartley (1990) and Hartley and Alonso (1990) discuss modifications of the SOLA-VOF code and its application to the problem of raindrop impact.

4 Simulation experiments

A set numerical experiments was conducted using the modified SOLA-VOF numerical code described by Hartley (1990) in which the dependence of the dimensionless boundary shear stress on the independent variables identified in equation (1) was investigated. Numerical simulation of natural raindrop conditions was considered desirable, but the large Reynolds numbers of these drops required prohibitively small computional cells and time steps to define boundary layers and maintain numerical stability (Hartley, 1990). Thus, simulations were conducted at lower Reynolds numbers than occur during the impact of natural raindrops. Table 1 compares Reynolds number and other parameter values for natural raindrops and the laboratory and numerical simulation conditions of this study.

Fig. 1 represents typical results of the numerically calculated boundary shear stress field. As shown in the figure, the boundary shear stress field can be described by a family of curves in which each curve represents the spatial distribution of the boundary shear stress at a particular instant in time. In this study, "peak boundary shear stress" (τ_p) refers to the peak of a spatial distribution at an instant in time (i.e. peak of any curve in Fig. 1) while "maximum peak boundary

Table 1. Comparison of parameters ranges

parameter	natural rainfall[1]	laboratory experiment	computer simulations
R	6500. - 23000.	1600. - 7700.	50. - 500.
y_0^*	0.00 - infinity	0.88 - 5.00	0.50 - 6.00
θ	18.0 - 28.0	3.1 - 10.1	2.8 - 22.6

[1] Raindrop diameters assumed to range from 2.0 mm to 5.0 mm.

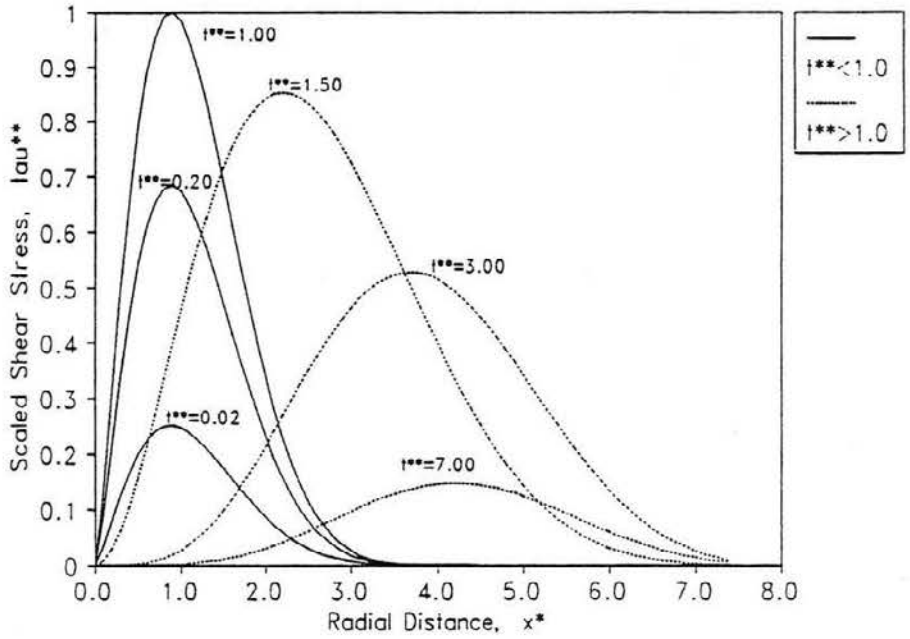

Fig. 1. Typical simulated boundary shear stress distributions at different times after drop impact.
Distributions typiques des contraintes de cisaillement simulées à différents intervalles de temps après impact.

shear stress" ($\tau_{p\,max}$) refers to the global maximum or largest of the peaks (peak value of distribution represented by bold line in Fig. 1) The double asterisk superscript (τ^{**}) on the y-axis of Fig. 1 denotes boundary shear stress magnitudes normalized by the magnitude of the maximum peak boundary shear stress ($\tau_{p\,max}$) while the time labels above the curves (t^{**}) indicate time values scaled by the time to reach the maximum boundary shear stress magnitude ($t_{p\,max}$).
Although details of the pattern vary depending on values of controling parameters, the trend shown in Fig. 1 is typical. That is, the rise to maximum shear was generally quite rapid (curves with solid lines) in comparison with a longer period of shear decay (curves with dashed lines). Also, prior to the time of the maximum boundary shear stress ($t^{**} < 1.0$), spatial distributions of the shear tended to be geometrically similar and spatially concurrent. During the relatively extended period of decay (dashed curves) the shear tended to diffuse further from the center of impact and to become more symmetrically distributed. Fig. 2 shows how shear magnitudes varied in time by plotting peak values from the curves in Fig. 1 and simply reinforces the point that the entire shear pulse reaches a maximum value within a very short period compared to duration of the entire pulse.

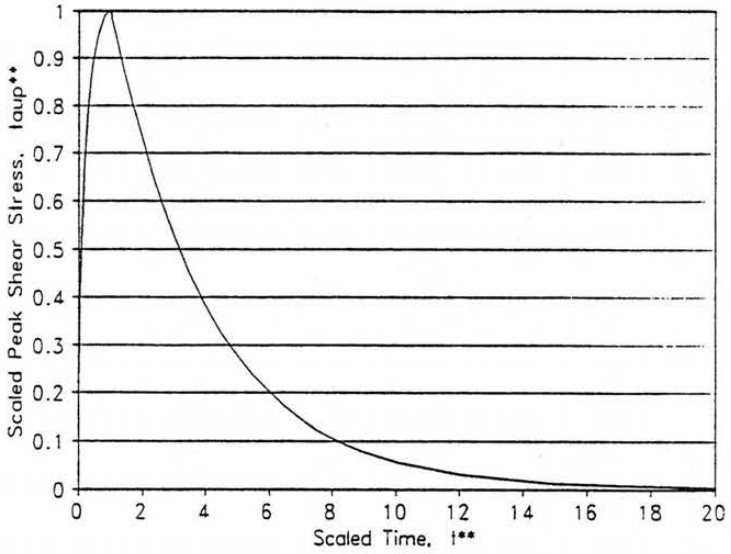

Fig. 2. Typical simulated temporal variation in magnitude of peak shear stress.
Variation temporelle typique des pointes de cisaillement simulées.

5 Simplified equations for the boundary shear stress field

In order to arrive at a set of simplified algebraic equations which could be used to generate the dynamic boundary shear stress field represented in Fig. 1, the entire numerically generated data set was analyzed and various functions of the independent variables in equation (2) were optimized using a nonlinear optimization routine (DeCoursey and Snyder, 1969). As a result of this analysis, it was found that the boundary shear stress distributions at various instants in time could be well-approximated by beta functions. Additionally, these beta functions remained constant in shape and range prior to the instant of maximum peak shear but change shape and range thereafter. Detailed discussion and comparison of individual equations with numerical model results are given by Hartley (1990). A summary of the relationships which make up the algebraic model are presented below.

5.1 *Maximum peak boundary shear stress*

The variation in magnitude of the maximum peak boundary shear stress ($\tau^*_{p\,max}$) was studied using the numerical model over a range of the dimensionless parameters identified above. Results of these simulations are given in Table 2. Simulated maximum peak boundary shear stress declined steeply with increased water layer depth. For example, maximum peak boundary shear stresses at depths of 6.0 radii were only about one percent as large as at a depth of 0.50 radii. This agrees qualitatively with the suggestion of Mutchler and Young (1975) that a depth of 6.0 radii would protect the soil surface from erosion. Wang (1970) noted a similar dramatic reduction in maximum peak boundary pressure with increasing water layer depth in his raindrop splash study. Evidently, both the pressure and shear stress attenuation reflect the cushioning effect of the water layer.

Simulated maximum peak boundary shear stresses also consistently declined with Reynolds number. This trend is similar to the one reported by Rajaratnam (1976) for peak boundary shear stress caused by an impinging circular jet, a steady flow case which is quite simular to drop impact. There was also a small effect of gravity and surface tension over the range of numerically simulated conditions.

Table 2. Modified SOLA-VOF simulation of maximum peak boundary shear stress

run #	y_0^*	R	θ	$\tau^*_{p\,max}$
1	0.50	50	3	7.900E-02
2	0.50	50	6	7.227E-02
3	0.50	50	12	7.083E-02
4	0.50	50	24	6.960E-02
5	1.00	50	3	4.505E-02
6	1.00	50	6	3.838E-02
7	1.00	50	12	3.454E-02
8	1.00	50	24	3.454E-02
9	1.00	150	3	2.562E-02
10	1.00	150	6	2.052E-02
11	1.00	150	12	1.847E-02
12	1.00	150	24	1.741E-02
13	1.00	500	3	1.446E-02
14	1.00	500	6	1.133E-02
15	1.00	500	12	9.296E-03
16	1.00	500	24	9.296E-03
17	2.00	50	3	1.171E-02
18	2.00	50	6	1.271E-02
19	2.00	50	12	1.271E-02
20	2.00	50	24	1.271E-02
21	2.00	150	3	6.038E-03
22	2.00	150	6	6.793E-03
23	2.00	150	12	6.793E-03
24	2.00	150	24	6.793E-03
25	2.00	500	3	2.760E-03
26	2.00	500	6	3.240E-03
27	2.00	500	12	3.240E-03
28	2.00	500	24	3.140E-03
29	4.00	50	3	1.820E-03
30	4.00	50	6	2.000E-03
31	4.00	50	12	2.484E-03
32	4.00	50	24	2.484E-03
33	4.00	150	3	8.172E-04
34	4.00	150	6	1.124E-03
35	4.00	150	12	1.330E-03
36	4.00	150	24	1.328E-03
37	4.00	500	3	2.900E-04
38	4.00	500	6	4.300E-04
39	4.00	500	12	5.143E-04
40	4.00	500	24	5.657E-04
41	6.00	50	3	5.430E-04
42	6.00	50	6	6.723E-04
43	6.00	50	12	7.499E-04
44	6.00	50	24	8.016E-04

However, for erosive natural rainfall conditions, sensitivity of the maximum peak boundary shear stress to the gravity and surface tension parameter would be negligible. Optimization using the numerically simulated data resulted in the following relationship:

$$\tau^*_{p\,max} = 2.85\,(y_0^* + 1)^{-3.16}\,R^{-.55}\,C_1 \tag{4}$$

with a coefficient of determination $r^2 = 0.99$. The term in parenthesis in this relationship is equal to the sum of the pool depth and drop radius scaled by the radius. The factor C_1 is defined by:

$$C_1 = [1.0 - \exp(-1.6\,\theta/y_0^*)] \tag{5}$$

It represents the effect of gravity and surface tension but deviates very little from a value of 1.0 for erosive natural rainfall conditions in which θ is generally larger than 9.0 and y_0^* less than 6.0. This suggests C_1 values ranging from .91 to 1.0 and supports the earlier contention that gravity and surface tension have a minor influence on the boundary shear stress.

5.2 *Time to reach maximum peak boundary shear stress*

Simulated values of the dimensionless time to reach maximum peak boundary shear stress $t^*_{p\,max}$, were found to be primarily a function of the dimensionless depth y_0^* and secondarily a function of θ, the combined gravity and surface tension parameter. The effects of gravity and surface tension appear to be small for low values of y_0^*, but much larger for larger depths. The variation of $t^*_{p\,max}$ with y_0^*, and θ can be described by the following optimized relationship (coefficent of determination $r^2 = 0.99$):

$$t^*_{p\,max} = 1.4\,(y_0^* + 1)\,C_2 \tag{6}$$

in which

$$C_2 = [1. - \exp(-.60\,\theta/y_0^*)] \tag{7}$$

Similar to C_1, the factor C_2 is of minor importance, varying between 0.88 and 1.0 for most cases of practical interest ($\theta > 18$ and $y_0^* < 5$). Thus, equation (6) indicates that the time interval between drop impact and maximum peak boundary shear stress is approximately proportional to the travel time at the impact velocity over a distance equal to the drop radius plus the pool depth – a physically reasonable result.

5.3 *Growth and decay of peak boundary shear stress*

Fig. 2 shows the typical numerical simulation results for the variation in peak boundary shear stress magnitudes with time. As shown in the figure, peak boundary shear stress magnitudes increased rapidly to a maximum value following impact. The rate of boundary shear stress growth depended mainly on the dimensionless depth y_0^* and could be represented by a gamma function (coefficient of determination $r^2 = 0.80$) as follows:

$$\tau_p^{**} = (t^{**})^{\gamma} \exp[\gamma(1. - t^{**})], \text{ for } t^{**} \leq 1.0 \tag{8}$$

Here the double asterisk superscripts indicated that the dimensionless time t^* has been scaled by the dimensionless time to reach the maximum peak $t^*_{p\,max}$ and the peak boundary shear stress τ_p^* has been scaled by the maximum peak boundary shear stress $\tau^*_{p\,max}$. The single parameter γ can be estimated by:

$$\gamma = 0.7\,(y_0^*)^{.55} \tag{9}$$

Equation (8) represents the initial part of the curve shown in Fig. 2 prior to the occurrence of the maximum peak boundary shear stress. The rate of decay of peak boundary shear stress magnitudes following the maximum peak was found to depend most strongly on gravity and surface tension forces as represented by the parameter θ. When θ was small, decay tended to be rapid, reflecting the restoring effect of gravity and surface tension forces. Conversely, when θ was large, decay of the peaks proceeded more slowly. The decay of peak boundary shear stresses could be described by the following exponential relationship (coefficient of determination $r^2 = 0.85$):

$$\tau_p^{**} = \exp - [\lambda_d (t^{**} - 1.)] \tag{10}$$

in which the λ_d is given by

$$\lambda_d = 1.35\,\theta^{.64} + .12. \tag{11}$$

λ_d varies from 0.33 to 0.28 for natural raindrops ranging in size from 2.0 to 5.0 mm in diameter. It may be taken as a constant at 0.31 for these conditions with less than a 20% deviation in τ_p^{**} for $t^{**}<8.5$. Thus, it can be seen that θ gains in importance as shear stress magnitudes subside, but may be neglected in the determination of the earlier, larger stresses under natural rainfall conditions.

5.4 *Spatial distribution of boundary shear stress*

The spatial distributions of boundary shear stresses at various instants during the growth and decay of boundary shear stress magnitudes was examined using the graphical output from the numerical model. Various distribution functions including gamma, lognormal, and beta distributions were fitted to the simulated boundary shear stress values. Nonlinear optimization results demonstrated that a beta distribution with a left boundary at the axis of impact did an excellent job of representing the finite difference results. The beta function is defined:

$$\tau^{**} = C_\beta\,(x^*/x_r^*)^{p1}(1 - x^*/x_r^*)^{p2} \tag{12}$$

in which τ^{**} is the boundary shear stress at any instant scaled by the maximum peak boundary shear stress, C_β is a beta constant, x^* is the radial distance from the axis of drop impact scaled by the drop radius, x_r^* is the right-hand boundary of the distribution and $p1$ and $p2$ are beta distribution shape parameters. The parameters of the distribution are C_β, $p1$, and $p2$ and x_r^*. The first parameter controls the magnitude of the τ^{**} values, while the powers $p1$ and $p2$ control skewness and kurtosis. The following relationships among the beta parameters, the scaled peak magnitude τ_p^{**} and position x_p^* can be shown to hold identically:

$$p2 = p1\,(x_r^* - x_p^*)/x_p^*, \tag{13}$$

and

$$C_\beta = \tau_p^{**}\,(x_p^*/x_r^*)^{-p1}\,(1 - x_p^*/x_r^*)^{-p2}. \tag{14}$$

Finite difference model results were used to optimize relationships which completed the description of the spatial distribution of the boundary shear stress. For the period between the instant of impact and the occurrence of the maximum peak boundary shear stress ($t^{**} < 1.0$) the shape of the spatial distribution remained essentially constant and the following equations were found to produce an accurate facsimile of the finite difference results:

$$p1 = 1 + \exp(-1.25\,y_0^*), \tag{15}$$

$$x_r^* = 1 + 7.5\,[1 - \exp\,(-1.25\,y_0^*)], \tag{16}$$

$$x_p^* = .88 + 5\,\exp\,(-3.7/y_0^*). \tag{17}$$

Equations 15–17 together with identities 12–14 represent the spatial distribution of the boundary shear stress field for $t^{**} < 1.0$. These relationships fit the finite difference model results very closely ($r^2 > 0.95$) over the entire range of conditions simulated. An example of the fit between these equations and the finite difference model is shown in Fig. 3 in which the solid lines

represent the equations and the symbols represent finite difference model results for $t^{**} \leq 1.00$. These results indicate that according to the model, the dimensionless depth y_0^* is the only parameter controlling the spatial distribution during the period of boundary shear stress build-up to the maximum peak boundary shear stress.

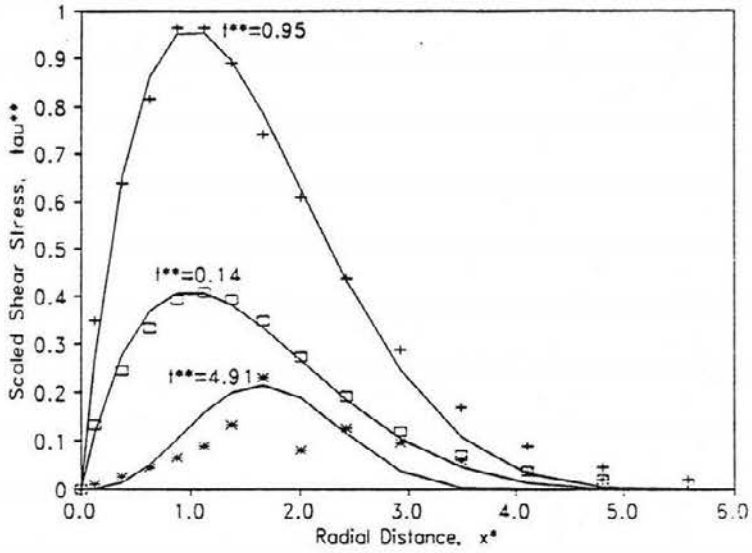

Fig. 3. Typical comparison of algebraic and numerical results.
Comparaison typique des résultats des modèles algébrique et numérique.

For period of shear decay ($t^{**} > 1.0$), equations 15–17 are replaced by

$$x_{pd}^* = x_p^* \{1. + (.21\,\theta - 20.\,R^{-0.5}) \cdot \exp[-y_0^*/(t^{**} - 1)]\} \tag{18}$$

$$p1_d = p1 + (p2 - p1)\exp[-1./(t^{**} - 1.)] \cdot \exp(-.30 y_0^{*2}) \tag{19}$$

$$p2_d = p2 \tag{20}$$

and

$$x_{rd}^* = x_{pd}^*(p2_d/p1_d + 1) \tag{21}$$

All variables are as previously defined. The subscript d is added to the parameters to show that they apply to decay period. For this period, the optimization of the equations (12–14 plus 18–21) to the finite difference model results in $r^2 > 0.85$ over the range of simulation conditions given in Table 2. While still good, this fit is inferior to the earlier period of shear build-up. Also in contrast to the earlier period, dimensionless time t^{**} and the parameters θ and R affect the spatial distribution of the shear. An example of the fit between the equations and the finite difference model is shown by the $t^{**} = 4.91$ in Fig. 3.

Equations (1) through (21) provide a complete algebraic description of the boundary shear stress field during the period of splash crater expansion. In summary, the boundary shear stress field simulated with the finite difference model can be approximated from the drop radius r, the impact velocity V_0, the pool depth y_0^* and the physical constants ϱ, ν, σ and g.

6 Experimental validation of the algebraic model

The set of approximate equations for estimation of the boundary shear stress field were tested using laboratory data collected with a hot-film anemometry system. In these tests water drops of various sizes and velocities were imposed upon low velocity flows in a rectangular flume. Boundary shear stress pulses caused by the drops were measured using a flush-mounted, hot-film boundary shear stress probe.

6.1 *Methods and materials*

Laboratory experiments were conducted in a 0.21 m wide by 9.75 m long rectangular flume using filtered and deionized water which was maintained at a constant temperature. A schematic of the experimental equipment is shown in Fig. 4. The probe with a 0.25 by 1.00 mm hot-film sensor was mounted so that the sensor was flush with the bed of the flume. The probe was connected by a cable to a constant temperature anemometer. The anemometer is designed to supply sufficient power to the hot-film sensor to maintain it at a constant temperature. Voltage output from the anemometer indicates the instantaneous boundary shear stress on the sensor through a well defined calibration relationship (Sandborn, 1972). Anemometer voltage output was automatically stored in a minicomputer.

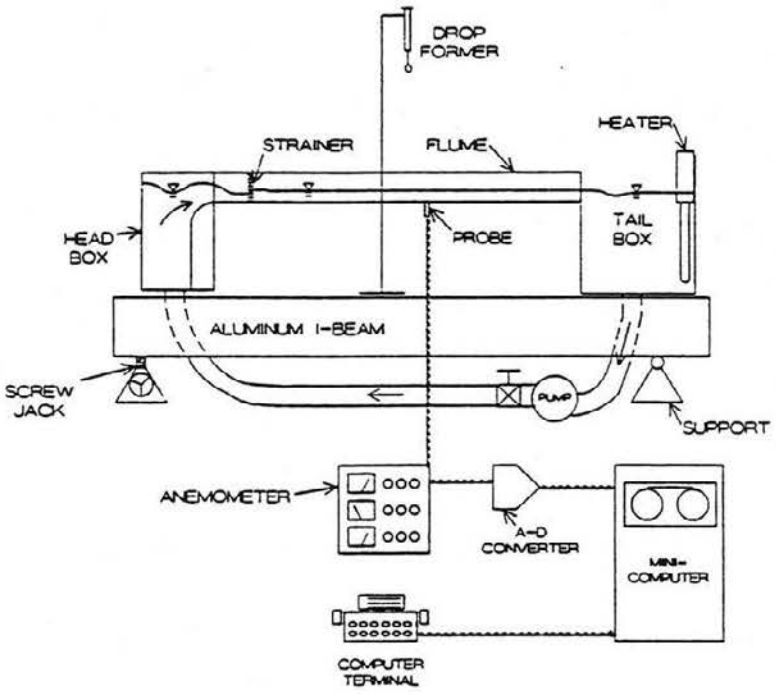

Fig. 4. Schematic of experimental setup.
Schema des conditions expérimentales.

Water droplets were formed using a hypodermic syringe. Three drop diameters were used: 3.2, 3.8 and 4.5 mm. The two smaller drop sizes were generated using hypodermic needles with the points cut off and ends filed. The largest drop size was generated using the plastic syringe without an attached needle. Gravimetric tests verified that drops generated using these orifices were quite uniform with sample standard deviations of approximately 1% of the nominal size. The syringe

was attached to a ring stand at a location designed to produce impact at a specified distance from the hot-film sensor and at a known impact velocity.

The flush mount hot-film sensor obeys the standard calibration relationship (Sandborn, 1972):

$$\tau^{1/3} = A E^2 - B \tag{23}$$

in which τ is the instantaneous boundary shear stress, E is the anemometer voltage output and A and B are constants which must be determined by calibration. The calibration constants are sensitive to water temperature and can also be effected by water quality which is the reason for using temperature controlled, filtered and deionized water in the experiments. These features of the measurement system are discussed in more detail by Schall (1979). The constants A and B must be determined using a flow with a known boundary shear stress value. This was accomplished by establishing uniform flow in the laboratory flume over the range of slopes and flow depths and estimating the average boundary shear stress using the relationship:

$$\tau = \gamma y S \tag{24}$$

in which τ is the time average boundary shear stress, γ is the specific weight of water, y is the flow depth and S is the friction slope which is equal to the slope of the flume bed for uniform flow conditions.

Measurements of boundary shear stress pulses caused by impacting water drops were designed to investigate effects of water layer depth, drop impact velocity, drop size and distance from the point of drop impact. Ranges of experimental variables are shown in Table 3 and the resultant range of dimensionless variables are shown in Table 4.

Table 3. Range of dimensional variables investigated

variable	values
water depth, y_0	2.0, 4.0, 6.0, 8.0 mm
drop impact velocity, V_0	1.0, 1.7, 3.4 m/s
drop diameter, d	3.2, 3.8, 4.5 mm
distance from impact, x	5.0, 10.0, 15.0 mm

All drop induced boundary shear stress pulse measurements were conducted with a small uniform discharge flowing in the flume. The presence of a base flow was considered necessary in order to maintain constant temperature of fluid over the hot-film sensor. Base flows were in the laminar to transitional range ($100 < Re < 1200$) and velocities were small ($0.05 < V_x < 0.17$ m/s). Hartley (1990) used a force balance to demonstrate that the base flows have a negligible effect on the boundary shear stress measurements because of the comparitively short duration of the shear stress pulses.

After daily calibration runs, the flume slope was set at .004 and flow rate was adjusted until the desired uniform flow depth was achieved. A ring stand was used to position the water drop former at a height which would result in the proper drop impact velicity. This height was determined using the method presented by Wang (1970). The horizontal position of the drop former was adjusted by sight and touch with the aid of a 2.0 mm diameter plastic rod. Drop impacts were sited within 1.0 mm of the desired impact point with this method. When the drop former was located at the proper location, static head was adjusted on the drop former so that drops fell at approximately 2.0 seconds intervals. This rate guaranteed that boundary shear stress pulses from

successive drops would be independent. When the desired rate of drop impacts had been achieved, the anemometer output was sampled for 10 seconds at a frequency of 1000 hertz (1–2% of the cut-off frequency of the system) and 4 to 5 replicate boundary shear stress pulses were recorded.

Table 4. Range of dimensionless variables investigated

variable	range
dimensionless depth, y_0^*	0.88 - 5.00
Reynolds number, R	1600 - 7700
gravity-surface tension parameter, θ	3.1 - 10.1
dimensionless distance, x^*	2.22 - 9.38

6.2 *Comparison of algebraic model and experimental data*

The previously described algebraic model for the boundary shear stress field was used to simulate boundary shear stress pulses corresponding to the experimental conditions. Comparisons of model and experimental results are summarized in Figs. 5 through 7. Fig. 5 compares results of the model and experiments at three different flow depths for a period of 50 msec. As indicated by Fig. 5, the model generally follows the trend in the experimental data of decreasing boundary shear stress peaks with flow depth. At the 2.0 mm depth, the model estimates a boundary shear stress peak which is nearly twice as large as the measured value. However, it should be noted that estimated inaccuracies in the setting of flow depth and positioning the drop impact point would be sufficient to account for this discrepancy.

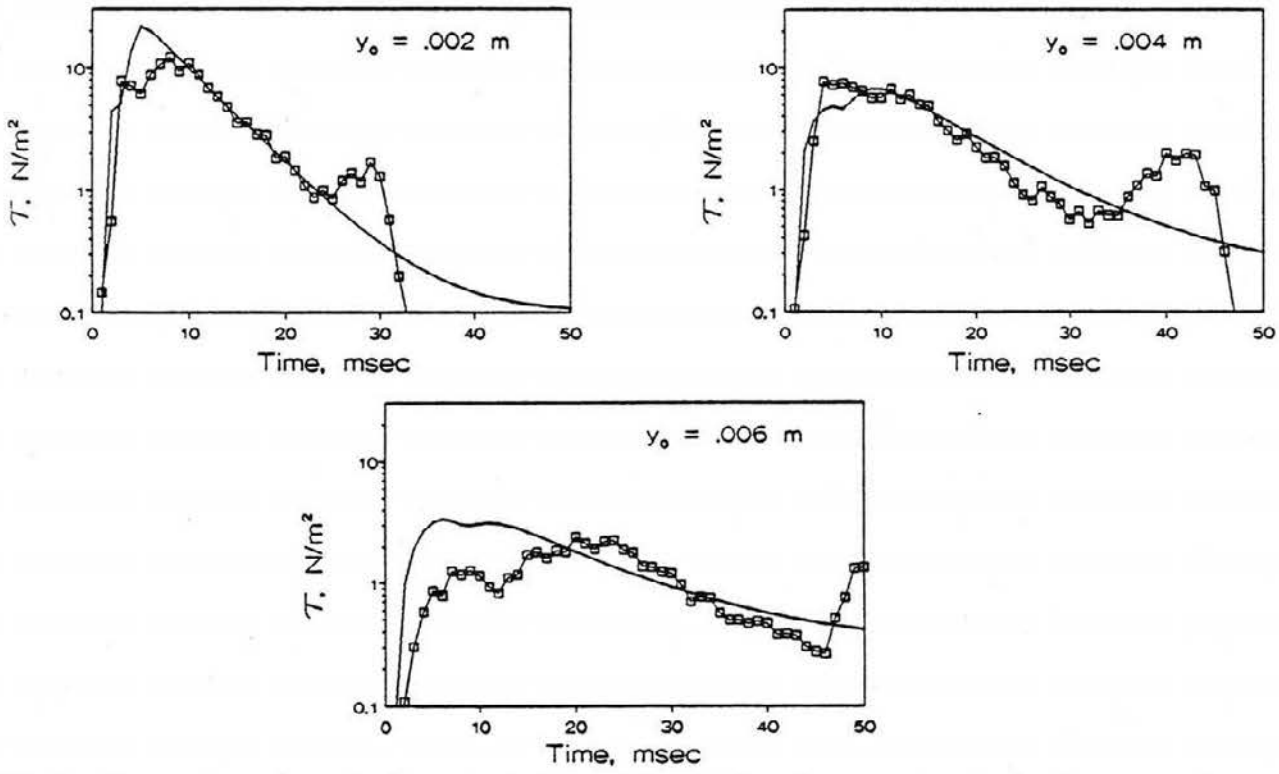

Fig. 5. Comparison of results from algebraic model and laboratory experiments for three water layer depths.

Comparaison des résultats du modèle algébrique et des mesures expérimentales pour trois profondeurs d'écoulement.

Fig. 6 illustrates the agreement between the model and the measured data with respect to the effect of distance from the center of drop impact. The series of graphs clearly shows that both the model and the measured data indicate an order of magnitude reduction in boundary shear stress for a distance of .010 m as compared with .005 m.
Additionally, both model and experimental data indicate that the effect of the drop is nonexistent at a distance of .015 m.

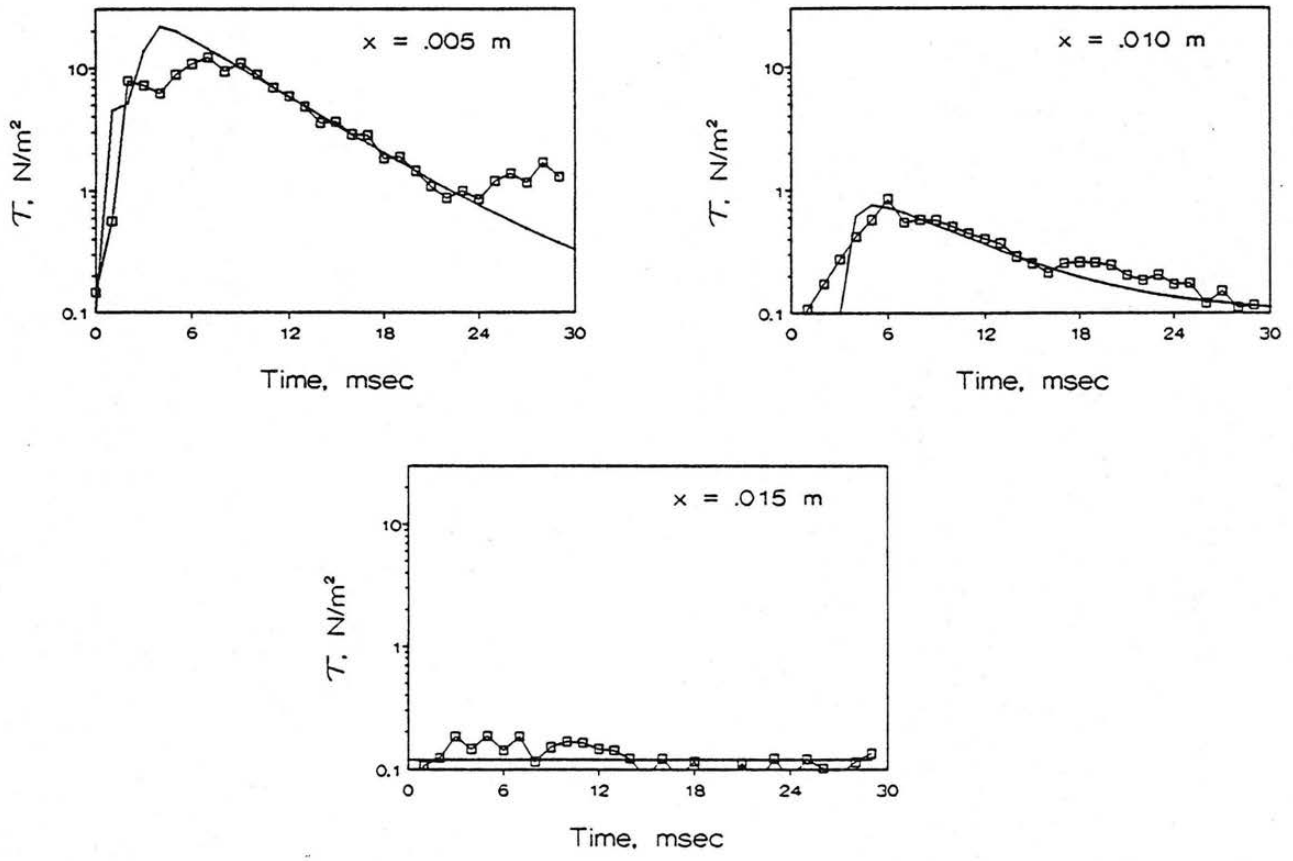

Fig. 6. Comparison of results from algebraic model and laboratory experiments for three radial distances.
Compariason des résultats du modèle algébrique et des mesures expérimentales à trois distances radiales.

A comparison of results for three different drop impact velocites is shown in Fig. 7. For the first graph ($V_0 = 1.0$ m/s), the match between model and experimental data appears quite good during the initial 15 msec. However, at later times, measured boundary shear stress values exceed predicted ones. This may result from the entrainment of air bubbles during the collapse of the splash crater which can cause the hot-film probe to register an erroneously high boundary shear stress readings. This effect is not evident in the other two graphs in the figure because the higher impact velocities extend the period of splash crater expansion. At the intermediate drop impact velocity, both the simulated and measured boundary shear stress peaks are larger than at the lowest impact velocity, however, the simulated value is about half as large as the measured one. At the largest impact velocity, both peaks again exhibit an increase over peaks at the intermediate value; however, in this case the simulated value is larger than the measured value. Thus, in this

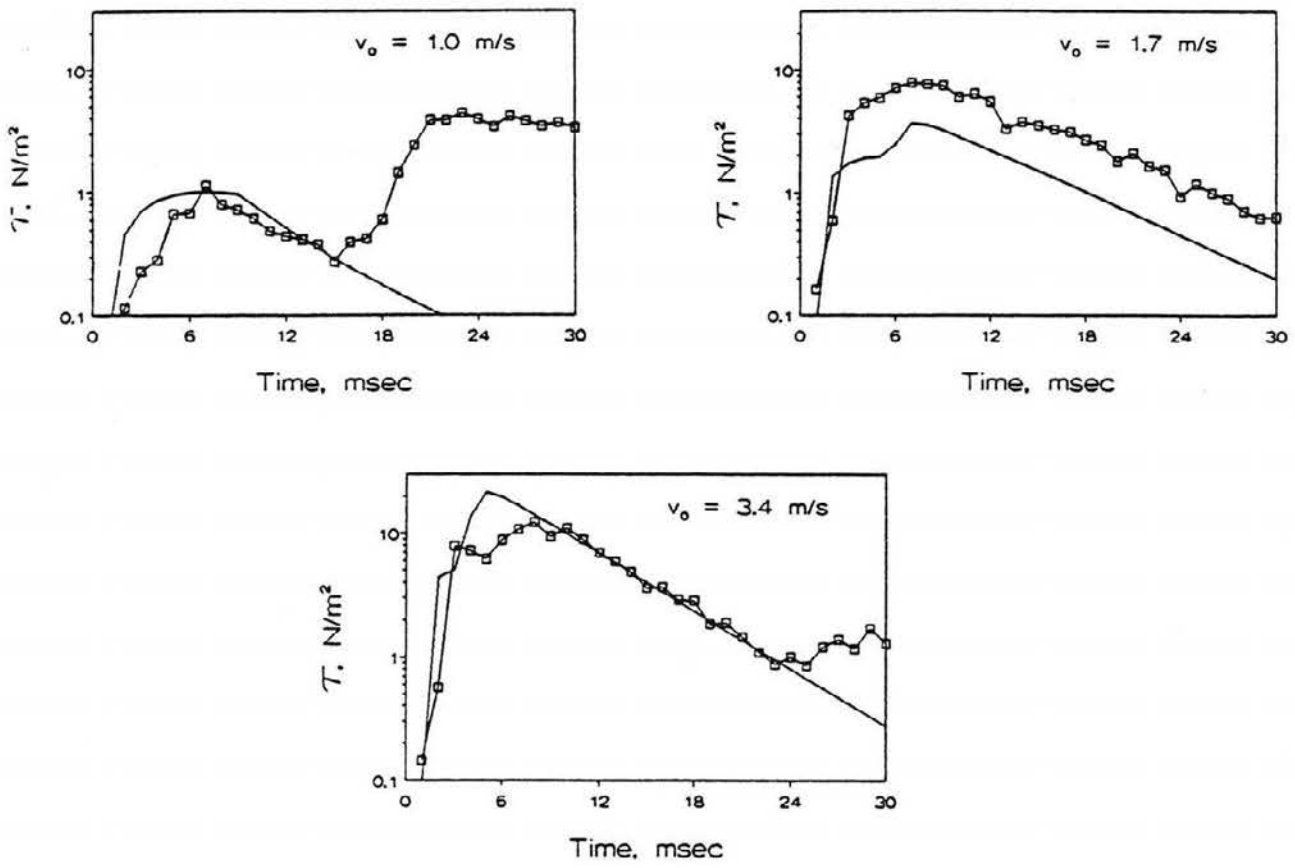

Fig. 7. Comparison of results from algebraic model and laboratory experiments for three impact velocities.
Comparaison des résultats du modèle algébrique et des mesures expérimentales pour trois vitesses de chute.

set of comparisons, the model and measured data display the same trend with respect to impact velocity if only the initial measured boundary shear stress pulse is considered.

Fig. 8 presents a comparison of measured and simulated results for three different drop diameters. Although peak values of the simulated pulses are somewhat higher than measured peaks, the trend toward larger peak boundary shear stresses at larger drop sizes is evident in both the measured and simulated results. Additionally, boundary shear stress pulse durations of the simulated and measured pulses are quite similar.

Fig. 9 represents a summary comparison of all 150 experimentally measured peak boundary shear stresses with model estimates. Although there is scatter about the line of perfect agreement, the model estimates peak boundary shear stresses which are within a factor of 2.0 of the measured values for about 79% of the data. The model appears to underestimate peak boundary shear stresses for conditions which produce small values i.e. large flow depths and small impact velocities. However, these are of less practical interest than larger values. For peak boundary shear stresses greater than 1.0 N/m^2, the number of estimates which are within a factor of two of the measured values rises to 85%.

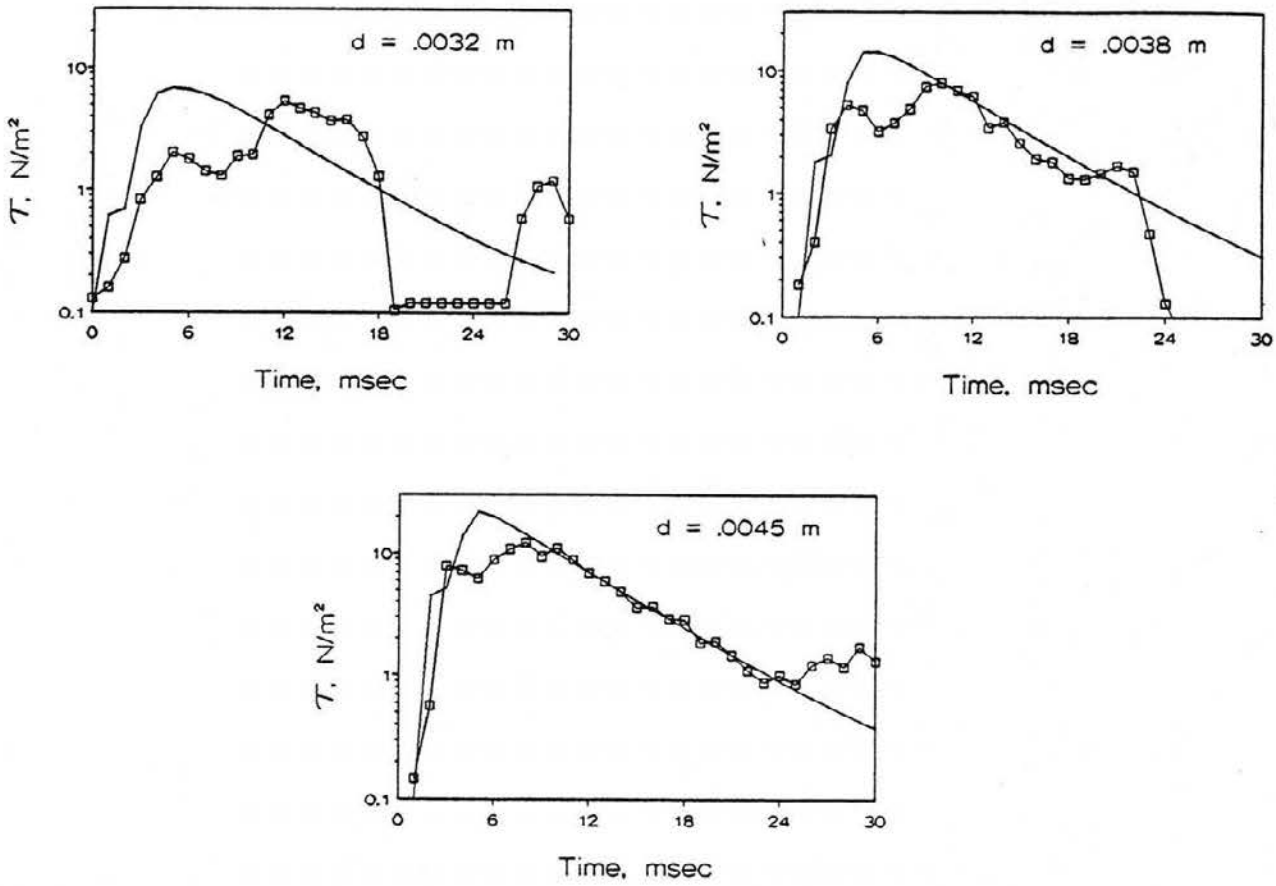

Fig. 8. Comparison of results from algebraic model and laboratory experiments for three raindrop sizes.
Comparaison des ré
mètres de gouttes.

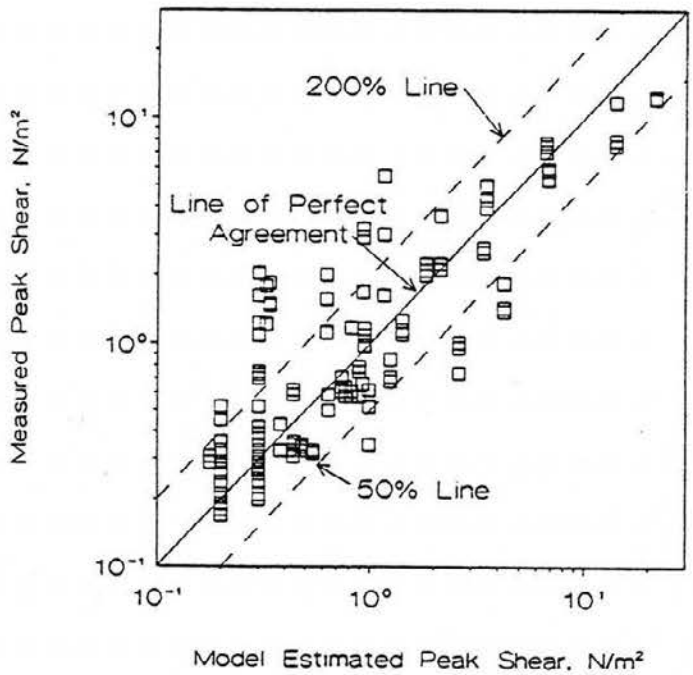

Fig. 9. Comparison of peak shear estimates from algebraic equations with measured values for all experimental runs.

Comparaison des pointes de cisaillement tirées des équations algébriques avec les valeurs mesurées pour toutes les expériences.

7 Summary and conclusions

A set of dimensionless algebraic equations which approximately describe the boundary shear stress field induced by raindrop impact during the period of splash crater expansion has been developed. The independent variables in these equations were derived from physical reasoning and dimensional analysis and their specific functional forms were developed empirically using data generated from a series of numerical experiments. The numerical model used to generate these data utilizes a finite difference solution to the equations of two-dimensional motion for a viscous, incompressible fluid, with a free surface. Excellent agreement between the simplified algebraic model and the numerical model is demonstrated over a wide range of values of the specified, dimensionless, independent variables.

Subsequently, the algebraic relationships were validated using laboratory experiments involving a range of drop sizes, impact velocities and water layer depths. For the shallowest depths investigated in the experiments, peak boundary shear stresses in excess of 10 N/m^2 were measured and duly estimated by the algebraic model. Given the larger impact velocities and smaller depths which may exist under natural rainfall conditions, maximum peak boundary shear stresses may be 5 to 10 times as great as the largest values measured in the experiments.

Results of this study indicate that the magnitude of the dimensionless boundary shear stress is strongly and inversely dependent on the dimensionless depth and also to a lesser extent inversely dependent on the drop Reynolds number. Gravity and surface tension forces appear to exert a minor influence in the generation of large boundary shear stresses caused by raindrops impacting shallow layers of water. However, these forces tend to affect the boundary shear stress field as the fluid decelerates and the boundary shear stress magnitudes decay. The spatial distribution of the boundary shear stress at any time during the crater expension period can be estimate by a beta distribution. The parameters of the distribution are functions of the dimensionless variables defined in the analysis.

This study focused on the boundary shear stress caused by a single, isolated raindrop. Knowledge gained concerning the spatial and temporal scales of the shear field should be useful in analysing the degree of raindrop interaction under natural rainfall conditions. However, if independence of raindrops is assumed, the algebraic relationships developed in this study provide a convenient and efficient first approximation for the magnitude, spatial extent and duration of boundary shear stresses caused by rainfall on overland flow. The determination of these boundary shear stress distributions represents an important component in the mathematical modeling of soil detachment and sediment transport from upland surfaces.

Acknowledgment

The authors wish to thank Dr. Donn Decoursey and Dr. Carlos Alonso of the United States Department of Agriculture Research Service for their support and assistance throughout the course of this study. The experiments were carried out at the Hydraulic Laboratory of the Engineering Research Center of Colorado State University.

Notations

Symbol[1/2]

A	coefficient in probe calibration equation
B	constant in probe calibration equation, $(M/LT^2)^{1/3}$
C_1	correction factor in dimensionless maximum peak boundary shear stress equation
C_2	correction factor in equation for dimensionless time to reach maximum peak shear stress
C_β	beta function coefficient
d	drop diameter, L
E	anemometer output- electrical potential, $L^2 M/(T^3 I)$
F	drop Froude number
g	gravitational acceleration, L/T^2
$p1$	first power of beta function
$p2$	second power of beta function
$p1_d$	first power of beta function during decay period
$p2_d$	second power of beta function during decay period
R	drop Reynolds number
R_e	base flow Reynolds number
r	radius of drop
S	channel friction slope
t	point in time after drop impact, T
t^*	dimensionless time after drop impact
t^{**}	dimensionless time scaled by dimensionless time to reach maximum peak boundary shear stress
$t^*_{p\,max}$	dimensionless time to reach maximum peak boundary shear stress
V_0	drop impact velocity, L/T
V_x	base flow velocity, L/T
W	drop Weber number
x	distance from center of drop impact
x^*	dimensionless distance from center of drop impact, L
x^*_p	dimensionless position of peak boundary shear stress
x^*_{pd}	dimensionless position of peak boundary shear stress during boundary shear decay
x^*_r	dimensionless right boundary of beta function
x^*_{rd}	dimensionless right boundary of beta function during boundary shear stress decay
y	vertical space coordinate and flow depth, L
y_0	water layer depth, L
y^*_0	dimensionless water layer depth
ϱ	fluid density, M/L^3
σ	surface tension, M/T^2
ν	kinematic viscosity, L^2/T
γ	specific weight of fluid, $M/(T^2 L^2)$
θ	combined gravity and surface tension parameter
τ	boundary shear stress, $M/(LT^2)$

[1] M = mass, L = length, T = time, I = unit of electrical current.

[2] (boundary shear stress dimensions)$^{1/3}$/(electrical potential dimensions)^2

τ^* dimensionless boundary shear stress

τ_p peak boundary shear stress, $M/(LT^2)$

τ_p^{**} dimensionless peak boundary shear stress scaled by dimensionless maximum peak boundary shear stress

$\tau_{p\,max}$ maximum peak boundary shear stress, $M/(LT^2)$

$\tau_{p\,max}^*$ dimensionless maximum peak boundary shear stress

λ gamma functional parameter

λ_d Exponential decay parameter

References / Bibliography

DECOURSEY, D. G. and SNYDER, W. M. (1969), Computer-oriented method of optimizing hydrologic model parameters, Journal of Hydrology, 9, pp. 34–56.

ENGEL, O. G. (1966), Crater depth in fluid impacts, Journal of Applied Physics 37(4), pp. 1798–1808.

HARLOW, F. H. and SHANNON, J. P. (1967), The splash of a liquid drop, Journal of Applied Physics, 38(10), pp. 3855–3866.

HARTLEY, D. M. (1990), Boundary shear stress induced by raindrop impact, Ph.D. dissertation, Dept of Civ. Engr., Colorado State Univ., Fort Collins, 193 pp.

HARTLEY, D. M. and ALONSO, C. V. (1991), Numerical study of maximum boundary shear stress induced by raindrop impact, Water Resources Research 27(8), pp. 1819–1826.

HIRT, C. W. and NICHOLS B. D. (1981), Volume of fluid (VOF) method for the dynamics of free boundaries, Journal of Computational Physics, 39, pp. 210–225.

HOBBS, P. V. and KEZWEENY, A. J. (1967), Splashing of a water drop, Science 155, pp. 1112–1114.

HOBBS, P. V. and OSHEROFF, T. (1977), Splashing of drops on shallow liquids, Science 158, pp. 1184–1186.

HUANG, C., BRADFORD, J. M. and CUSHMAN, J. M. (1982), A numerical study of raindrop impact phenomena, SSSA Journal 46, pp. 14–20.

LAWS, J. O. (1939), Short exposure photographs of water-drops striking soil, U.S. Department of Agriculture, Soil Conservation Service, 12 pp.

LAWS, J. O. (1940), Recent studies of raindrops and erosion. Agricultural Engeneering, 21. p. 431.

MACKLIN, W. C. and HOBBS, P. V. (1969), Subsurface phenomena and splashing of drops on shallow liquids, Science 166, pp. 107–108.

MACKLIN, W. C. and METAXES, G. J. (1976), Splashing of drops on liquid layers, Journal of Applied Physics 47(9), pp. 3963–3969.

MUTCHLER, C. M. and HANSEN, L. M. (1970), Splash of a waterdrop at terminal velocity, Science 169, pp. 1311–1312.

MUTCHLER, C. M. and YOUNG, R. A. (1975), Soil detachment by raindrops, In: Present and Prospective Technology for Predicting Sediment Yields and Sources, U.S. Department of Agriculture, Agricultural Research Service, ARS-S-40, pp. 113–117.

NICHOLS, B. D., HIRT, C. W. and HOTCHKISS, R. S. (1980), SOLA-VOF, A solution algorithm for transient fluid flow with multiple free boundaries, Report LA-8355, Los Alamos Scientific Laboratory, 119 pp.

RAJARATNAM, N. (1976), Turbulent jets, (Developments in water science; 5), American Elsevier, New York.

SANDBORN, V. A. (1972), Resistance and temperature transducers, Metrology Press, Fort Collins, 545 pp.

SCHALL, J. D. (1979), Spatial and time distribution of boundary shear stress in open channel flows, M.S. thesis, Department of Civil Engineering, Colorado State University, Fort Collins, Colorado, 156 pp.

TAN, S. (1990), Rainfall and soil detachment, Journal of Hydraulic Research, 27(5), pp. 699–715.

WANG, R. C. (1970), The mechanics of a drop after striking a stagnant water layer, Ph.D. dissertation, Dept. Civ. Eng., Univ. of Illinois, Urbana, 131 pp.

WELCH, J. E., HARLOW, F. H. SHANNON, J. P. and DALY, B. J. (1965), The MAC method: a computing technique for solving viscous, incompressible, transient fluid-flow problems involving free surfaces, Report LA-3425, Los Alamos Scientific Laboratory, Los Alamos, New Mexico, 146 pp.

WORTHINGTON, A. M. (1882), On impact with a liquid surface. Proceedings of the Royal Society (London), 32, p. 217.

WORTHINGTON, A. M. (1908), A study of Splashes, Longmans, Green and Co.

WORTHINGTON, A. M. (1963), A Study of Splashes, MacMillan, New York.

WATER RESOURCES RESEARCH, VOL. 26, NO. 8, PAGES 1819–1832, AUGUST 1990

Similarity and Length Scale for Spatially Varied Overland Flow

PIERRE Y. JULIEN AND GLENN E. MOGLEN

Department of Civil Engineering, Colorado State University, Fort Collins

One-dimensional finite element models enable physically based investigations of overland flow generated under spatially varied surface slope, width, roughness, and excess rainfall intensity. Simulated results of 8400 dimensionless hydrographs under spatially varied input parameters indicate that runoff discharge variations depend primarily on the ratio of rainfall duration t_r to the time to equilibrium t_e. Peak discharge distributions change drastically as the dimensionless rainfall duration t_r/t_e approaches unity. Similarity conditions exist for all four parameters regardless of whether the spatial variability is correlated or uncorrelated. A length scale function of not only the spatially averaged values of surface parameters but also depending on rainstorm duration and intensity delineates similarity conditions for spatially varied surface runoff. For surface runoff lengths much shorter than this length scale, the rainfall-runoff relationship becomes nearly independent of the spatial variability in hydrologic parameters. Conversely, for surface runoff lengths exceeding the length scale, the rainfall-runoff relationship is sensitive to spatial variability. This length scale can serve as a basis for the determination of grid sizes in hydrologic models.

INTRODUCTION

The influence of the spatial variability of rainfall precipitation, infiltration, surface roughness and surface topography on surface runoff characteristics has been widely recognized in hydrology. Rainfall precipitation has received considerable attention in the recent literature, *Amorocho and Wu* [1977] simulated spatially distributed precipitation fields using a randomization process to generate clusters of short-lived and high intensity rain cells within a storm band. *Gupta and Waymire* [1979] investigated the stochastic structure of space-time rainfall fields. *Woolhiser and Osborn* [1985] examined the temporal features of accumulated point rainfall precipitation in dimensionless form while *Valdes et al.* [1985] considered three one-dimensional models of point rainfall precipitation. More recently, *Rodriguez-Iturbe and Eagleson* [1987] demonstrated the feasibility of modeling the spatial and temporal structure of rainfall events through mathematical multidimensional point process techniques.

The spatial variability of infiltration characteristics has also been examined by *Smith and Hebbert* [1979], in which Monte Carlo simulations of the random distribution of soil properties lead to the conclusion that gradual S-shaped infiltration curves result from randomly nonuniform soil surfaces. *Maller and Sharma* [1981] extended previous investigations in light of Philip's infiltration equation. *Sivapalan and Wood* [1986] derived quasi-analytical expressions for the ponding time and infiltration rate under two conditions: (1) spatially variable soils and uniform rainfall, and (2) constant soil properties and spatially variable rainfall. They concluded that rainfall is expected to play a more critical role in rainfall-runoff modeling since the correlation length of rainfall is usually larger than that of soil hydraulic conductivity. It has also been suggested that biased mean areal infiltration responses result from spatially variable soil and rainfall when average soil properties and rainfall intensity are used. Comprehensive treatments of runoff prediction errors and bias in parameter estimation induced by spatially varied precipitation together with a Green-Ampt infiltration equation have been pursued by *Troutman* [1983, 1985*a*, *b*].

Routing surface runoff exhibits several intricacies. For instance, *Wilson et al.* [1979] stated that nobody will dispute the effect of spatial distribution of rainfall on the amount of surface runoff. They also pointed out that their experiments do not support the argument made in the past that errors in the rainfall input will be dampened when routed through a basin. They concluded that not only the spatial distribution of rainfall has a marked influence on the behavior of the runoff hydrograph from a small catchment, but the application of rainfall-runoff models without an appropriate description of the spatial character of the input may lead to unacceptable errors. If linear models for the simulation of rainfall-runoff relationships are widely used in regard of their simplified mathematical structure, it remains that surface runoff routing is highly nonlinear as recognized by *Diaz-Granados et al.* [1986]. It has long been known that the response time of a basin tends to decrease as storm intensity increases. *Dawdy* [1982] states that kinematic wave models constitute one step away from the linear storage assumption toward the use of a dynamic routing equation. He added that the kinematic wave equation tends to overcome the shortcoming that linear techniques, such as instantaneous unit hydrographs, are not identical for small and large storms. Major advantages of kinematic wave models are that parameters relate to the physical world, and these models are perfectly suited for use in distributed parameter models. He explains the disadvantage of distributed models in that they require more data and much more computer time to run when compared with lumped-parameter models. As computers get larger, faster and cheaper, however, this disadvantage decreases in importance. He finally concluded that the trend in rainfall-runoff modeling is toward physically based distributed-parameter models.

Spatially varied overland flow has been investigated extensively by a number of researchers using both physical and analytical models. *Kibler and Woolhiser* [1970] used a kinematic cascade of planes and a converging conical surface to examine the effects of varying slope and width on computed discharge. *Machado and O'Donnell* [1977] analyzed the influence of spatial and temporal variability of model param-

Copyright 1990 by the American Geophysical Union.

Paper number 90WR00499.
0043-1397/90/90WR-00499$05.00

40

eters and rainfall input with given probability distributions on overland flow treated as a stochastic variable. Their analysis permits calculations of the variance of the outflow in terms of the sampling variance of the parameters. *Wu et al.* [1978] used a physical model to examine several different spatial distributions of roughness elements in an effort to develop criteria for the valid use of lumped parameters.

Self-similarity and scale problems have more recently been looked into. The investigation of *Sharma et al.* [1983] implies the definition of a zone of influence, or a spatial scale beyond which the spatial correlation for a given property could be neglected. *Milly and Eagleson* [1987] inferred that the problem of spatial integration to the catchment scale is not trivial because the analysis of small-scale physical processes in catchments suggest that the local response is a nonlinear function of these variables. They examined the extent to which the spatial variability of soil and vegetation affect the temporal-spatial averages of the major hydrologic fluxes. They sought the existence of an equivalent homogeneous soil capable of reproducing the average behavior of an inhomogeneous area. *Caroni et al.* [1986] dealt with the problem of detecting nonlinearity and time-variance at the basin scale. The analysis has been performed where spatial variability of rainfall patterns, soil properties and vegetation cover would not appreciably affect the rainfall-runoff process. The integrating effects of variability should not dominate at such a drainage basin scale. *Sivapalan et al.* [1987] described a simple conceptual model of runoff production based on catchment topography and the spatial variability of rainfall and soil properties. They formulated five similarity parameters and three dimensionless variables representing initial conditions and storm characteristics. *Wood et al.* [1988] reported results of a preliminary investigation into the existence of a representative elementary area (REA). They believe that at a small scale, actual patterns of topography, soil and rainfall characteristics are important in governing runoff production. Differences in actual patterns of variability between areas at this scale will produce different responses. However, as scale increases, all areas will yield almost identical responses for the case of stationary distributions. They consider that the hydrologic variables at every location within each catchment are related to its average value through some probability distribution. Each mathematical point in the continuum is associated with the area over which the average values are taken. The REA is defined as the averaging area acting as the smallest discernible point which is representative of the continuum. They concluded that the REA is strongly influenced by the topography.

As mentioned by *Amorocho* [1982], the simulation of spatially varied precipitation fields should not be considered as a necessary prescription for all catchments and all applications. Depending on the catchment response to storm field variabilities, these simulations may not be justified from practical and economical standpoints; to omit the simulations in other cases may lead to gross inaccuracies in hydrological applications. We concur with his conclusion that research on objective methods to make this determination is urgently needed. Not only is research needed for spatially varied precipitation fields, but it should be extended to the analysis of topography, infiltration and excess rainfall, vegetation and surface roughness.

The specific objective of this study is to quantify the influence of spatial variability in slope, surface roughness, surface width, and excess rainfall intensity on surface runoff characteristics. Reference systems are modeled with spatially averaged values of the hydrologic parameters. The differences between computed surface runoff hydrographs for reference systems versus spatially varied systems are examined in dimensionless form for complete and partial equilibrium hydrographs. The analysis of the rainfall-runoff response under spatially varied hydrologic conditions serves to define a length scale describing similar surface runoff conditions.

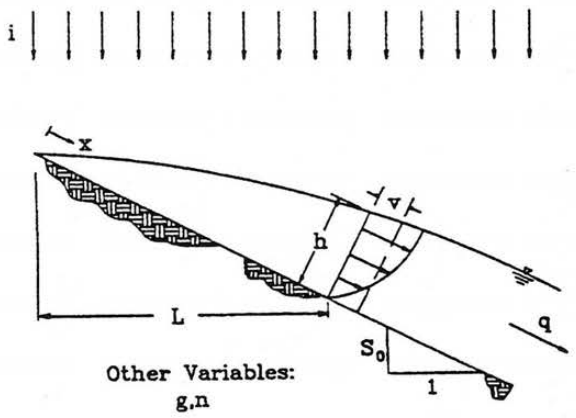

Fig. 1. Overland flow parameters.

The methodology proposed for this analysis of spatially varied conditions differs from the above cited studies. Numerical models are called for because analytical solutions to spatially varied nonlinear systems cannot be derived even for the most simple case. The selected one-dimensional finite element model solves the kinematic wave approximation of the St-Venant equations. The results are expressed in dimensionless form after considering that the time to equilibrium serves as an important physical characteristic. Similarities are preserved by keeping the same spatially averaged input parameters for each system. Also, the same excess rainfall volume is maintained in each system in order to avoid the error and bias problems discussed in the recent literature.

FUNDAMENTALS OF OVERLAND FLOW

The overland flow system shown in Figure 1 illustrates the following overland flow parameters: L is the length of the horizontal projection of the overland flow plane, h is the flow depth, v is the average flow velocity, S_0 is the average slope gradient, i is the excess rainfall intensity, and q is the discharge per unit width. Note that excess rainfall intensity obtained by subtracting the rate of infiltration from rainfall intensity is considered in the analysis. Infiltration combines both the conventional Hortonian infiltration excess mechanism with Dunne's saturation excess runoff production mechanism. In the following the interaction between surface and subsurface flow is not being separately considered but treated as excess rainfall intensity. Four additional parameters are the plane width w, the gravitational acceleration g, the Manning roughness coefficient n, and the total discharge $Q = wq$.

The governing equations for overland flow are the St-Venant momentum and continuity equations. Derivations of these equations may be found in the works by *Henderson and Wooding* [1964], *Woolhiser and Liggett* [1967], *Eagle-*

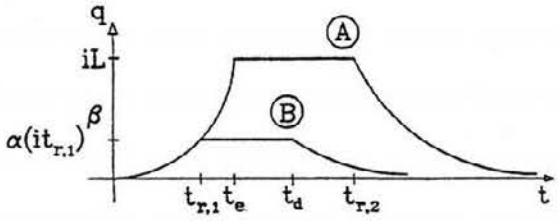

Fig. 2. Complete and partial equilibrium hydrographs.

son [1970] and *Overton and Meadows* [1976]. The St-Venant equations which account for unsteady nonuniform flow may be simplified to the kinematic wave approximation which is applicable under most overland flow conditions.

Conservation of mass for one-dimensional overland flow with variable surface width yields the following form of the continuity equation:

$$w\frac{\partial h}{\partial t}+\frac{\partial Q}{\partial x}-wi=0 \tag{1}$$

Notice that under spatially varied width, a two-dimensional system is actually considered.

Resistance to flow is expressed in terms of a stage-discharge relationship:

$$Q=\alpha h^{\beta} \tag{2}$$

Several resistance equations describe the various types of overland flow conditions depending on whether the flow is laminar or turbulent, and whether the boundary is smooth or rough. These conditions have been examined by *Julien and Simons* [1985], and the Manning resistance equation has been arbitrarily selected for the purpose of this study. Preliminary investigations by *Julien et al.* [1988] and *Moglen* [1989] showed comparable results with other resistance equations. After combining the Manning resistance equation with the kinematic wave approximation, the following expressions for α and β are obtained:

$$\alpha=\frac{S_0^{1/2}w}{n} \tag{3}$$

$$\beta=\frac{5}{3} \tag{4}$$

It can be noted that the kinematic wave approximation requires that slopes cannot be negative or zero.

An important physical characteristic of overland flow planes with constant slope, width, roughness and rainfall intensity is the time to equilibrium t_e given by the relationship:

$$t_e=\left(\frac{wL}{\alpha i^{\beta-1}}\right)^{1/\beta} \tag{5}$$

As shown in Figure 2, a complete equilibrium hydrograph (hydrograph A), is obtained when the rainfall duration $t_{r,2}$ exceeds the time to equilibrium t_e. For rainfall durations $t_{r,1}$ shorter than the time to equilibrium t_e the resulting partial equilibrium hydrograph is sketched as hydrograph B.

In terms of the linearity of the rainfall-runoff response, the hydrographs in Figure 2 indicate that partial equilibrium hydrographs are nonlinear because the magnitude of the peak discharge depends on both the duration and intensity of rainfall. Similarly, the duration of peak discharge for partial equilibrium hydrographs $t_d - t_{r,1}$ also depends on a complex function of rainfall duration and intensity. On the other hand, as the rainfall duration t_r becomes much larger than the time to equilibrium t_e, the response of complete hydrographs becomes asymptotically linear, because the magnitude of peak discharge increases linearly with rainfall intensity. Also, the duration of complete equilibrium peak discharge $t_r - t_e$ becomes asymptotically equal to rainfall duration t_r when $t_r \gg t_e$.

In the following analysis, excess rainfall intensity is allowed to vary in space but not in time. The additional effects of spatial variability in slope, width, and surface roughness are accounted for after substituting (2) into (1):

$$w\frac{\partial h}{\partial t}+\alpha\beta h^{\beta-1}\frac{\partial h}{\partial x}+h^{\beta}\frac{\partial \alpha}{\partial x}-wi=0 \tag{6}$$

where the second and third terms from the left account for the spatial variation in discharge. From (6) and (3) the spatial variability of both slope S_0 and surface roughness n is reflected in the second and third terms of (6). On the other hand, the spatial variability of excess rainfall intensity i is accounted for in the last term of (6), while surface width w is included in all terms of (6). Equation (6) is solved for flow depth as a function of space and time, then converted into runoff discharge from (2).

Finite Element Formulation

Numerical modeling of overland flow has evolved considerably as digital computers have become faster and more common. Originally, the method of characteristics was used to find "the space-time locus of discontinuity in the partial derivatives" [*Eagleson*, 1970]. In recent years, finite difference and finite element schemes have been used to solve the equations of motion for overland flow. These techniques are very flexible, allowing for a wider range of conditions while avoiding problems incurred by kinematic shocks as described by *Lighthill and Whitham* [1955]. A finite element scheme has been arbitrarily preferred for the following analysis. It is acknowledged that similar conclusions should be obtained from equivalent finite difference schemes. The comparison between finite difference and finite element schemes is, however, beyond the scope of this paper.

The one-dimensional finite element model CASC, briefly described here, provides numerical solutions to (6) from the Galerkin weighted residual method:

$$\int_L(\delta h)\frac{\partial h}{\partial t}w\,dx+\int_L(\delta h)\alpha\beta h^{\beta-1}\frac{\partial h}{\partial x}\,dx+\int_L(\delta h)h^{\beta}\frac{\partial \alpha}{\partial x}\,dx-\int_L(\delta h)wi\,dx=0 \tag{7}$$

where δh is a small variation from the flow depth h. Making use of the Jacobian determinant $|J|$, the shape function N, and the derivative of the shape function $\partial N/\partial\xi$ with respect to the local coordinate ξ, the following discretized form of (7) is obtained:

$$\int_L \langle \delta \mathbf{h} \rangle \{\mathbf{N}\}\langle \mathbf{N}\rangle \left\{ \mathbf{w} \frac{\Delta \mathbf{h}}{\Delta \mathbf{t}} \right\} |J|\, d\xi + \int_L \langle \delta \mathbf{h} \rangle \{\mathbf{N}\}\langle \mathbf{N}\rangle \{\boldsymbol{\alpha}\boldsymbol{\beta}\mathbf{h}^{\beta-1}\} \left\langle \frac{\partial \mathbf{N}}{\partial \xi} \right\rangle \{\mathbf{h}\}\, d\xi + \int_L \langle \delta \mathbf{h} \rangle \{\mathbf{N}\}\langle \mathbf{N}\rangle \{\mathbf{h}^{\beta}\} \left\langle \frac{\partial \mathbf{N}}{\partial \xi} \right\rangle \{\boldsymbol{\alpha}\}\, d\xi - \int_L \langle \delta \mathbf{h} \rangle \{\mathbf{N}\}\langle \mathbf{N}\rangle \{\mathbf{wi}\} |J|\, d\xi = 0 \tag{8}$$

Note that braces indicate a column vector, while angle brackets indicate a row vector. Using Gaussian quadrature for each element, (8) is integrated and assembled into two global matrices $[C]$ and $[K]$, and one vector $\{\mathbf{F}\}$:

$$[C] = \{\mathbf{N}\}[\langle \mathbf{N}\rangle \{\mathbf{w}\}]\langle \mathbf{N}\rangle |J| \tag{9}$$

$$[K] = \{\mathbf{N}\}\left[\langle \mathbf{N}\rangle \{\mathbf{h}^{\beta-1}\} \left(\left\langle \frac{\partial \mathbf{N}}{\partial \xi} \right\rangle \{\boldsymbol{\alpha}\}\langle \mathbf{N}\rangle + \langle \mathbf{N}\rangle \{\boldsymbol{\alpha}\boldsymbol{\beta}\} \left\langle \frac{\partial \mathbf{N}}{\partial \xi} \right\rangle \right) \right] \tag{10}$$

$$\{\mathbf{F}\} = \{\mathbf{N}\}\langle \mathbf{N}\rangle \{\mathbf{wi}\} |J| \tag{11}$$

The resulting matrix formulation is

$$[C] \left\{ \frac{\Delta \mathbf{h}}{\Delta \mathbf{t}} \right\} + [K]\{\mathbf{h}\} - \{\mathbf{F}\} = 0 \tag{12}$$

The initial boundary condition imposes no flow depth at all nodes for the first time step, and the upstream boundary is held fixed at zero flow depth at subsequent time steps. The following implicit numerical scheme [*Dhatt and Touzot*, 1984] is solved iteratively:

$$\{\Delta \mathbf{h}^j_{t+\Delta t}\} = ([C] + \Delta t[K])^{-1}((\{\mathbf{F}\} - [K]\{\mathbf{h}^j_{t+\Delta t}\})\Delta t + [C](\{\mathbf{h}_t\} - \{\mathbf{h}^j_{t+\Delta t}\})) \tag{13}$$

where the depth vector $\{\mathbf{h}\}$ is incremented by an amount $\{\Delta \mathbf{h}\}$ using

$$\{\mathbf{h}^1_{t+\Delta t}\} = \{\mathbf{h}_t\} \qquad j = 0 \tag{14}$$

$$\{\mathbf{h}^{j+1}_{t+\Delta t}\} = \{\mathbf{h}^j_{t+\Delta t}\} + \{\Delta \mathbf{h}^j_{t+\Delta t}\} \qquad j > 0 \tag{15}$$

Calculations at iteration j are performed between (13) and (15) until the vector $\{\Delta \mathbf{h}\}$ becomes negligible.

This algorithm enables the simulation of stationary storms (this paper) or moving storms [*Richardson*, 1989]. The interested reader is referred to *Julien et al.* [1988] for more details regarding the mathematical formulation, code description, simulation examples for stationary and moving rainstorms, and comparison with observed data.

In the following sections, two sets of conditions are considered for the spatially varied analysis in slope, width, surface roughness and excess rainfall precipitation: (1) in the next section, each parameter is examined separately under spatially uncorrelated random fields; and (2) the effects of spatially varied slope are then examined separately under correlated conditions given from field spectral density data.

Uncorrelated Spatial Variability

The effects of each parameter variation on the discharge hydrograph are investigated separately for uncorrelated spatially varied slope, Manning n, width, and excess rainfall intensity. The terminology "uncorrelated" spatial variability refers to the selection of nodal parameter values which are independent of the values at adjacent nodes. The use of excess rainfall intensity instead of rainfall intensity accommodates the following two situations: (1) spatially varied rainfall precipitation and constant infiltration; and (2) constant rainfall precipitation and spatially varied infiltration. Infiltration here refers to both the Hortonian infiltration mechanism with Dunne's saturation excess runoff production mechanism treated jointly as excess rainfall. One may appropriately notice that the model CASC cannot simulate negative values of excess rainfall intensity. Dimensionless hydrographs are obtained from dimensionless discharge q/iL and dimensionless time t/t_e. The dimensionless rainfall duration t_r/t_e defines the ratio of rainfall duration t_r to the time to equilibrium t_e. When this parameter is less than 1, the hydrograph is said to reach partial equilibrium. Complete equilibrium hydrographs corresponds to $t_r/t_e > 1$.

Similar systems are simulated with identical time steps, number of nodes, and probability density functions of the spatially varied parameter. Preliminary investigations by *Julien et al.* [1988] and *Moglen* [1989] showed that (1) a constant time step equal to one-fourth of the time to equilibrium t_e is more than adequate to define a discharge hydrograph; (2) runoff discharge is relatively unaffected by the number of nodes, provided there is a minimum of seven nodes; and (3) the results of the forthcoming analysis are not sensitive to the probability density function selected for the variability of each parameter. Accordingly, the model CASC is applied with a spatial resolution of 11 equidistant nodes and a time resolution equal to one-tenth of the time to equilibrium.

Spatial perturbations are introduced when the nodal values X'_l of one of the four spatially varied parameters are randomly selected based on a uniform distribution around the reference value μ_x. The magnitude of the spatial variability of each parameter is defined by the perturbation scaling factor ϕ which describes the maximum allowable nodal value X'_l from

$$\mu_x \left(1 - \frac{\phi - 1}{\phi + 1} \right) \le X'_l \le \mu_x \left(1 + \frac{\phi - 1}{\phi + 1} \right) \tag{16}$$

The perturbation scaling factor ϕ controls the magnitude of the spatial variability. From (16) the transformation imposes that all values of plane width, surface slope, Manning n, and rainfall intensity are nonzero and positive, computer simulations being impossible otherwise. Notice that the quantity $(\phi - 1)/(\phi + 1)$ reduces to zero when $\phi = 1$, which defines a nonperturbed system. For very large ϕ values the same ratio approaches unity and the maximum variation from the mean is therefore $2\mu_x$. For systems discretized with 11 nodes the spatially averaged values of each parameter X are set equal to their respective constant reference value μ_x from the following modification of the previously assigned values of X'_l:

$$X_l = \left(\frac{11\mu_x}{X_1 + X_2 + X_3 + \cdots + X_{11}} \right) X'_l \tag{17}$$

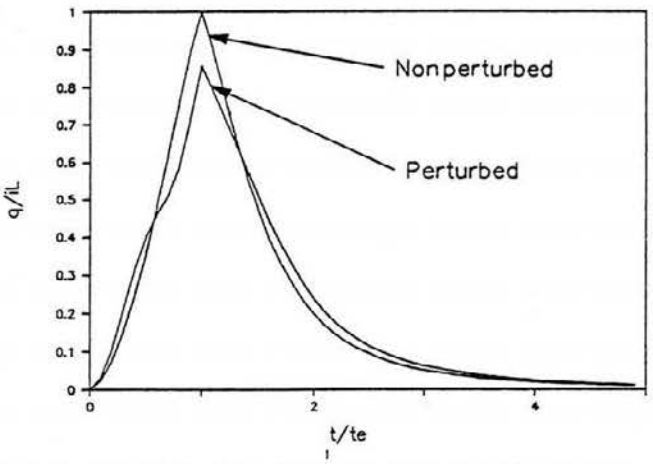

Fig. 3. Spatially varied and nonperturbed overland flow hydrographs.

Consequently, the spatially averaged properties of each parameter are preserved in order to compare systems which are strictly equivalent in terms of average properties, but variable only in terms of spatial distribution.

Consider the simulation of a single perturbed system as shown in Figure 3. While the nonperturbed system produces smooth rising and falling limbs, the spatially varied system creates fluctuations in discharge about the nonperturbed hydrograph.

Several sets of 100 perturbed systems are generated. Identical volumes of water are routed through each of the 100 systems in order to provide comparisons of similar systems. The input parameter envelopes describe the maximum and minimum of those 100 parameter perturbations at each node. They are nondimensionalized after dividing by the reference value. Thus x^*, z^*, n^*, w^*, and i^*, respectively, denote dimensionless space, elevation, Manning coefficient, surface width, and excess rainfall intensity. Figures 4*a*–4*d* show the input parameter envelopes as a function of dimensionless space from upstream $x^* = 0$ to downstream $x^* = 1$. For instance, when $\phi = 2$, the highest and lowest value of the perturbed parameter at each node defines the input parameter envelope denoted with $\phi = 2H$ for the highest and $\phi = 2L$ for the lowest values. Similarly, the lines $\phi = 4H$ and $\phi = 4L$ define the input parameter envelopes when $\phi = 4$. These figures illustrate the effects of the parameter ϕ; envelopes are small when $\phi = 2$ and large when $\phi = 6$.

In order to investigate all possible permutations of the single parameter variability, it is important to recognize that there are three types of input parameters: (1) the duration of rainfall (partial or complete equilibrium), (2) the magnitude of parameter perturbation ϕ, and (3) the overland flow parameter to be varied (slope, Manning n, surface width, and excess rainfall intensity). Three different rainfall durations covering the range from partial to complete equilibrium

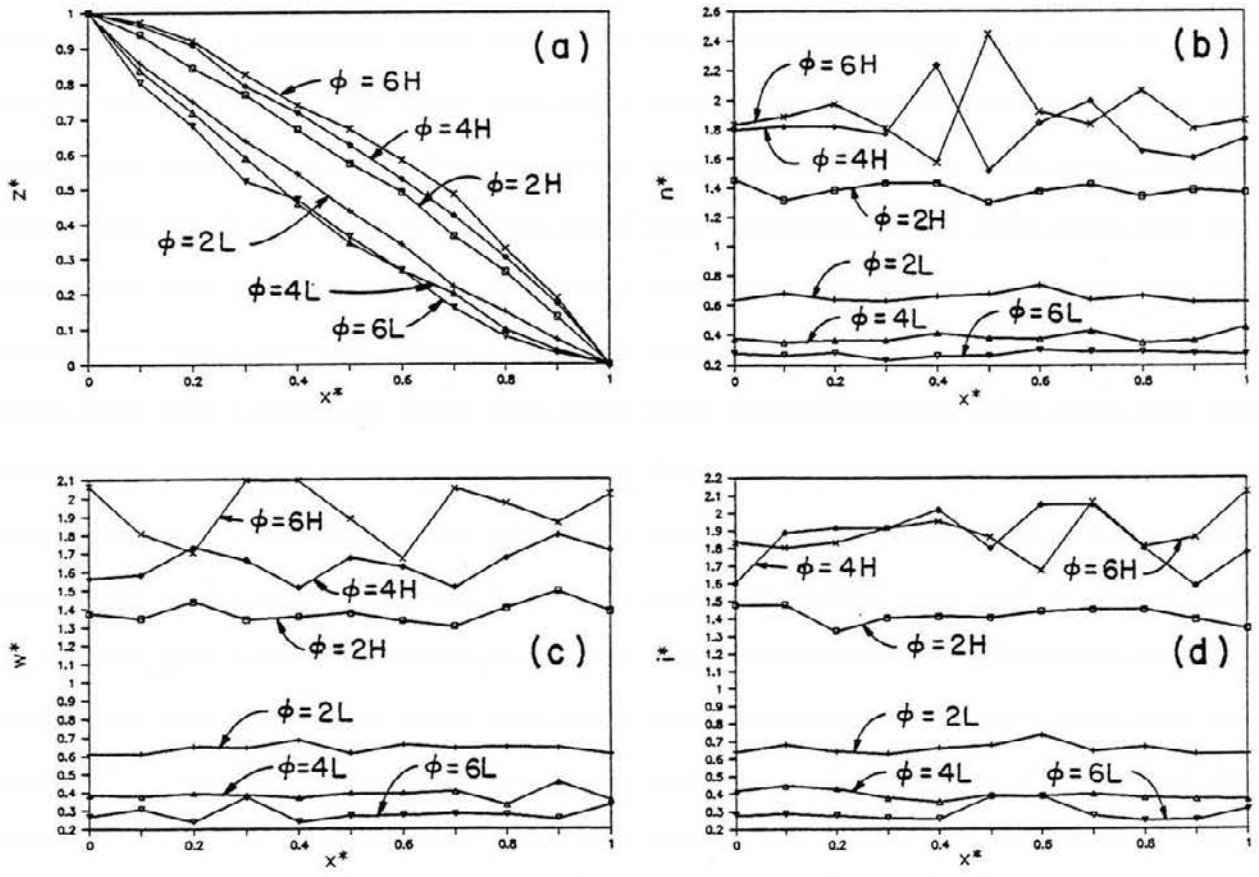

Fig. 4. Input Envelopes for (*a*) slope, (*b*) Manning n, (*c*) surface width, and (*d*) rainfall intensity.

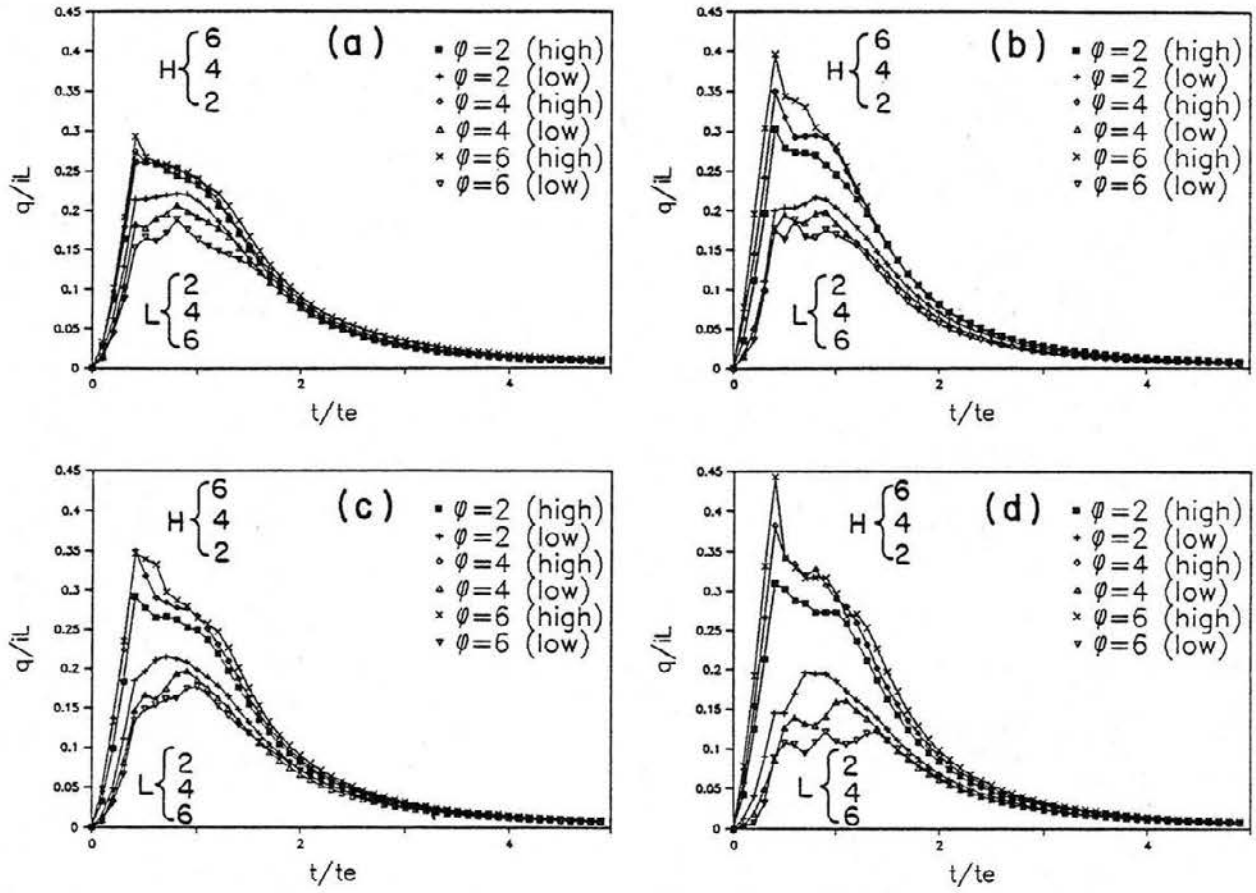

Fig. 5. Hydrograph envelopes for (*a*) slope at $t_r/t_e = 0.4$, (*b*) Manning n at $t_r/t_e = 0.4$, (*c*) surface width at $t_r/t_e = 0.4$, (*d*) rainfall intensity at $t_r/t_e = 0.4$, (*e*) slope at $t_r/t_e = 1.0$, (*f*) Manning n at $t_r/t_e = 1.0$, (*g*) surface width at $t_r/t_e = 1.0$, (*h*) rainfall intensity at $t_r/t_e = 1.0$, (*i*) slope at $t_r/t_e = 5.0$, (*j*) Manning n at $t_r/t_e = 5.0$, (*k*) surface width at $t_r/t_e = 5.0$, and (*l*) rainfall intensity at $t_r/t_e = 5.0$.

hydrographs are selected: $t_r/t_e = 0.4$, 1.0, and 5.0. Simulations are repeated for three different values of ϕ: 2, 4, and 6. The individual effects of the four overland flow parameters are investigated. For each permutation (4 parameters × 3 values of ϕ × 3 values of t_r/t_e), 100 simulations are performed, thus totaling 3600 simulated hydrographs. Given the large amount of data generated from these 3600 hydrographs, the pertinent hydrologic data have been reduced into an interpretable form. First, hydrograph envelopes are considered, followed by deviation hydrographs, relative spatial sensitivity, and finally, distribution of peak discharge.

Hydrograph Envelopes

For each set of 100 equivalent hydrographs a hydrograph envelope is determined from the highest and lowest simulated discharges at each time step. These envelopes, in Figures 5*a*–5*l*, show the maximum variation in discharge as a function of time along the hydrograph. For instance, when $\phi = 2$, all the 100 simulated hydrographs were comprised between the curves $2L$ and $2H$. It is observed that the general shape of these envelopes is primarily a function of the dimensionless ratio t_r/t_e. The degree of variation within a set of hydrographs is quite large for $t_r/t_e = 0.4$, but very small when $t_r/t_e = 5.0$. Interesting results include the following:

1. Figures 5*a*–5*d* show partial equilibrium hydrograph results with the highest simulated discharge occurring at the last time interval experiencing rainfall. The region enclosed by the envelopes is much larger than that for $t_r/t_e = 1.0$ or 5.0 (Figures 5*e*–5*l*).

2. When $t_r/t_e = 1.0$ (see Figures 5*e*–5*h*), a particular case of complete hydrograph is obtained. Notice that these hydrographs exhibit peak discharges near unity at $t/t_e = t_r/t_e = 1.0$ and then begin to recede. In essence, these hydrographs are like the complete hydrographs without an equilibrium plateau and like the partial hydrographs in that the peak discharge occurs during the last time interval with rainfall.

3. When $t_r/t_e \gg 1$ (i.e., $t_r/t_e = 5.0$; see Figures 5*i*–5*l*), complete hydrographs are characterized by an equilibrium plateau region where the dimensionless discharge is unity from $t/t_e \approx 1.0$ to $t/t_e = t_r/t_e$. These Figures 5*i*–5*l* demonstrate that the numerical model reproduces the expected results that the dimensionless equilibrium discharge equals unity regardless of the spatial variability of the hydrologic parameters. The runoff variability during the rising and falling limbs can be better analyzed through deviation hydrographs.

Deviation Hydrographs

With reference to Figure 3, the discharge from a nonperturbed system at any time may be considered as a reference value about which the discharge from a perturbed system varies. When considering a set of 100 simulated hydrographs, the deviation hydrograph measures the standard

48

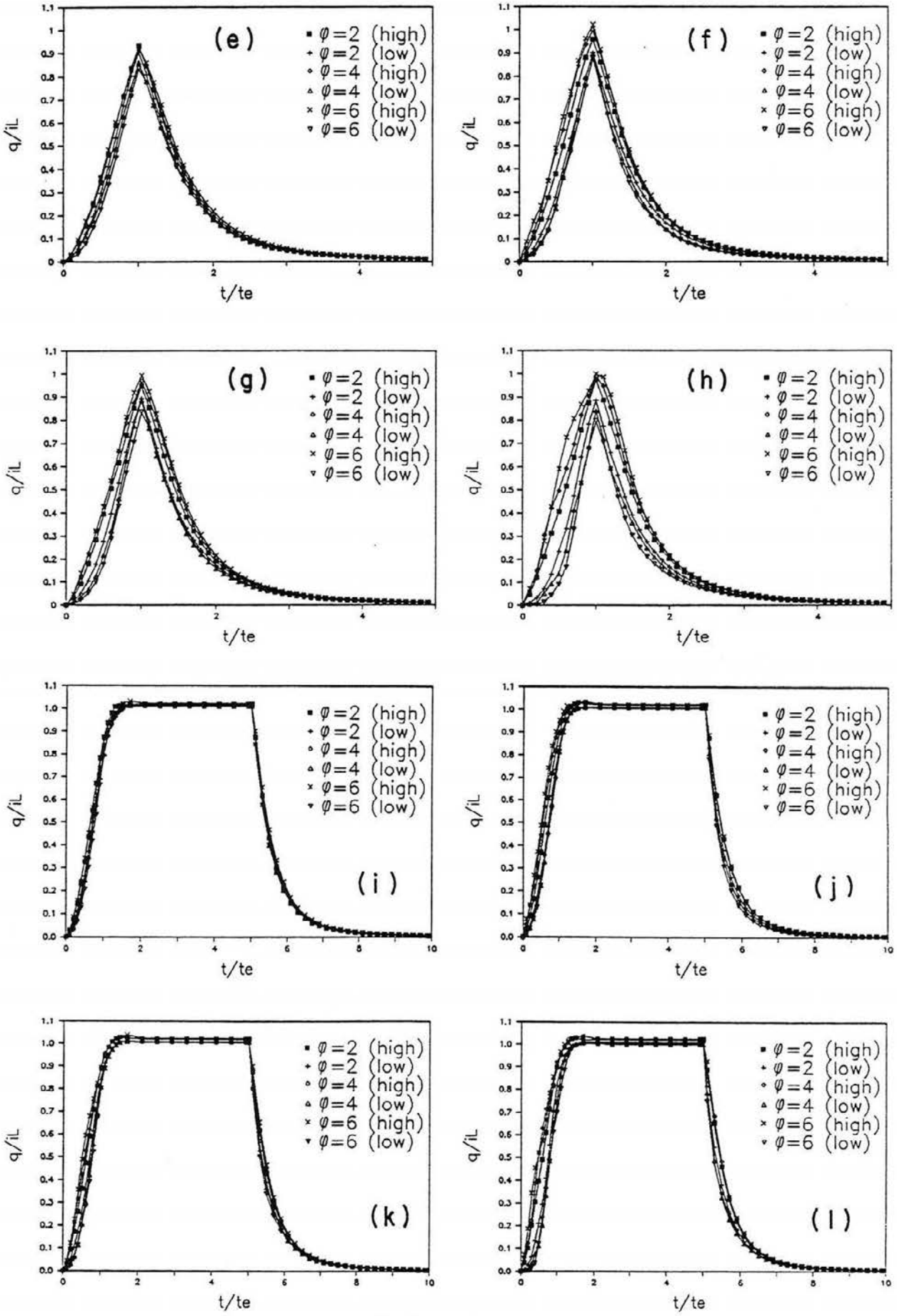

Fig. 5. (continued)

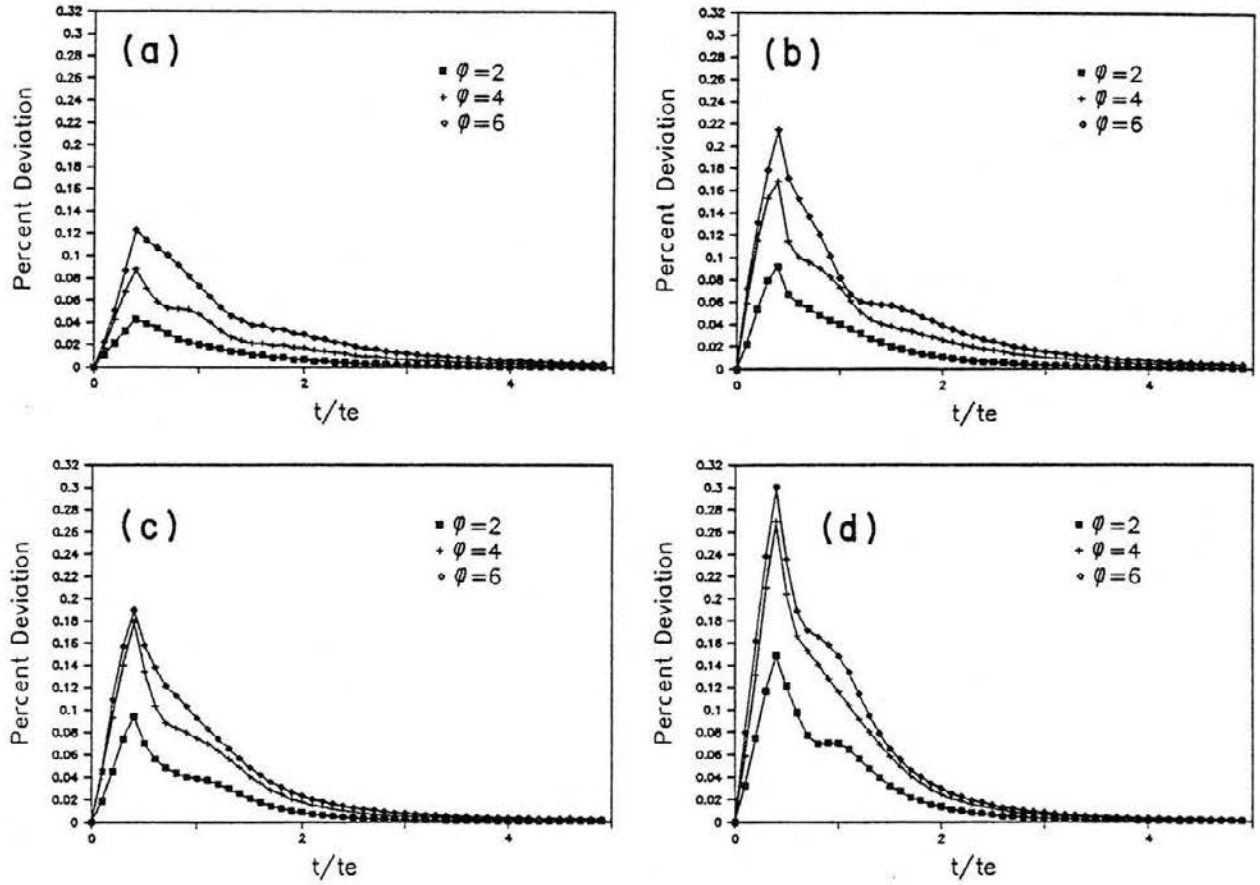

Fig. 6. Deviation hydrographs for (*a*) slope at $t_r/t_e = 0.4$, (*b*) Manning n at $t_r/t_e = 0.4$, (*c*) surface width at $t_r/t_e = 0.4$, (*d*) rainfall intensity at $t_r/t_e = 0.4$, (*e*) slope at $t_r/t_e = 1.0$, (*f*) Manning n at $t_r/t_e = 1.0$, (*g*) surface width at $t_r/t_e = 1.0$, (*h*) rainfall intensity at $t_r/t_e = 1.0$, (*i*) slope at $t_r/t_e = 5.0$, (*j*) Manning n at $t_r/t_e = 5.0$, (*k*) surface width at $t_r/t_e = 5.0$, and (*l*) rainfall intensity at $t_r/t_e = 5.0$.

deviation of the calculated values of discharge about the nonperturbed discharge at each time step:

$$\sigma_t = \sqrt{\frac{1}{m-1}\sum_{k=1}^{m}(q_{k,t} - q_{np,t})^2} \tag{18}$$

where σ_t describes the deviation in output discharge at time t; m is the number of simulated hydrographs (100 in this case); $q_{k,t}$ is the kth perturbed discharge at time t; and $q_{np,t}$ is the nonperturbed discharge at time t. The curve traced out by the deviation hydrograph indicates the magnitude of discharge variation as a function of time.

Dimensionless deviation hydrographs are obtained by dividing the deviation hydrograph σ_t by the partial or complete equilibrium discharge ($\alpha(it_r)^\beta$ when $t_r/t_e < 1.0$; or iL when $t_r/t_e \geq 1.0$). The resulting dimensionless deviation hydrographs in Figures 6*a*–6*l* reflect the percentage variation in discharge relative to the nonperturbed equilibrium discharge. For example, in Figure 6*a* where the slope is spatially varied for a set of 100 equivalent systems, the largest variation in discharge is approximately 0.12 at $t/t_e = 0.4$. This means that the standard deviation of discharges at $t/t_e = 0.4$ is approximately 12% of the peak discharge of the partial equilibrium hydrograph.

Examination of Figures 6*a*–6*l* indicates that the general shape of dimensionless deviation hydrographs is primarily dependent on the value of t_r/t_e regardless of which parameter is spatially varied. The following observations are rather instructive:

1. Figures 6*a*–6*d* exhibit the largest variations in discharge, and therefore the discharge from partial equilibrium systems is highly sensitive to perturbations in any input parameter.

2. The region $t/t_e < 1.0$ in Figures 6*e*–6*l* exhibits a maximum value around $t/t_e = 0.7$. The deviation increases for $t < 0.7t_e$ because the discharges are getting larger. For $0.7t_e < t < t_e$, the deviation decreases with time because the system is approaching equilibrium discharge which, as shown in Figures 5*i*–5*l*, is independent of deviations in the system. Therefore at $t = 0.7t_e$ a balance seems to exist between the opposing trends of near equilibrium behavior and time increasing discharge causing a maximum deviation in discharge. Notice that for $t < 0.4t_e$, the results in Figures 6*a*–6*d* are not directly comparable to those of Figures 6*e*–6*l*. This is because the deviation hydrograph is defined as $\sigma_t/\alpha(it_r)^\beta$ when $t_r < t_e$ and σ_t/iL when $t_r > t_e$.

3. Figures 6*i*–6*l* show the standard deviation in discharge for varying input parameters and $t_r/t_e = 5.0$. Notice again that the maximum deviations in discharge occur at $t/t_e = 0.7$ as was the case for $t_r/t_e = 1.0$. A similar peak is observed for the recession limb, its magnitude in all cases remains smaller than the peak during the rising limb. It can be concluded that spatial variability will primarily affect the rising limb of hydrographs.

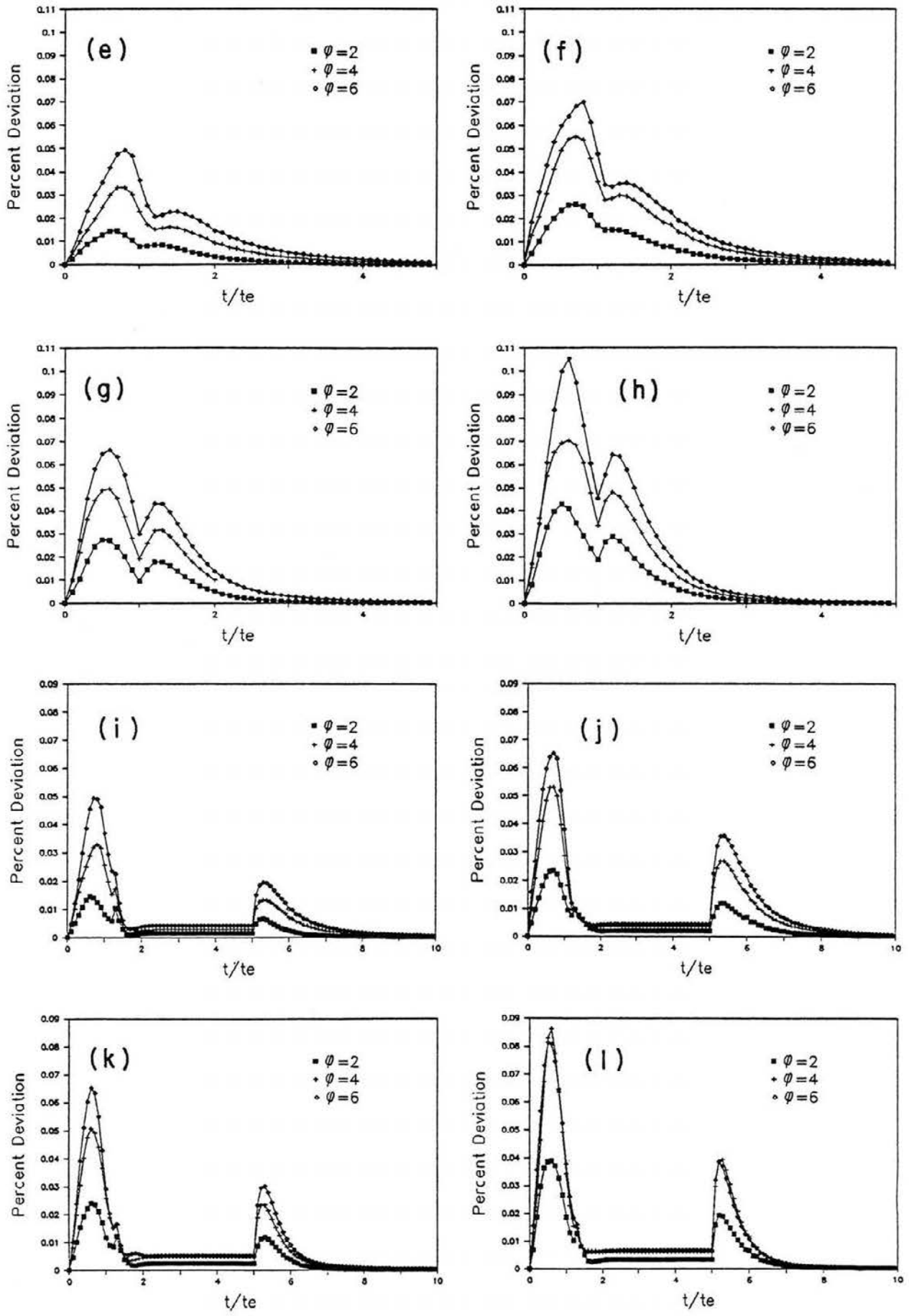

Fig. 6. (continued)

TABLE 1. Relative Spatial Sensitivity $R_{s,l}$

Parameter	ϕ	$t_r/t_e = 0.4$	$t_r/t_e = 1.0$	$t_r/t_e = 5.0$
Slope	2	0.05536	0.03163	0.01005
Slope	4	0.06145	0.03846	0.00948
Slope	6	0.07977	0.04561	0.01161
Manning n	2	0.11648	0.07270	0.02033
Manning n	4	0.11327	0.08260	0.02001
Manning n	6	0.12678	0.08447	0.02048
Surface width	2	0.10987	0.06707	0.01741
Surface width	4	0.11651	0.07523	0.01666
Surface width	6	0.11697	0.07787	0.01860
Rainfall intensity	2	0.19591	0.11301	0.02743
Rainfall intensity	4	0.18717	0.12124	0.02890
Rainfall intensity	6	0.19622	0.12834	0.02522

Relative Spatial Sensitivity

With an understanding of the general behavior of the model response to input variation, the objective of this section is to quantify the spatial sensitivity of the model output to each parameter.

The spatial variability of an input parameter is defined in terms of a coefficient of variation $C_v = \sigma_i/\mu_X$ where σ_i is the standard deviation of the spatially varied input parameter for a set of 100 equivalent systems, and μ_X is the reference value of the same parameter.

The spatial variability of the output discharge is computed with a technique similar in concept to that used by *Wu et al.* [1978]. The hydrograph envelopes presented in Figure 6 can be time-integrated to provide a hydrograph envelope volume ΔV. When divided by the total excess rainfall volume V, the resulting ratio $V^* = \Delta V/V$ describes the spatial variability of the output discharge.

Relative spatial sensitivity $R_{s,l}$ describes the ratio of variation in output per unit variation in input as proposed by *McCuen and Snyder* [1986]:

$$R_{s,l} = \frac{V^*}{C_v} \tag{19}$$

The values of relative spatial sensitivity shown in Table 1 provide a quantitative evaluation of the four input parameters under spatially varied conditions. It is found that excess rainfall intensity shows the highest degree of sensitivity, followed by Manning n, surface width, and finally slope. This is in agreement with the observations of envelope hydrographs in Figure 5 and of deviation hydrographs in Figure 6. This relative spatial sensitivity analysis demonstrates that relative spatial sensitivity values decrease with dimensionless rainstorm duration but remain nearly constant for various ϕ values.

A total of 4800 additional computer simulations (100 runs $\times$ 4 parameters $\times$ 12 values of t_r/t_e = 0.6, 0.8, 1.1, 1.2, 1.3, 1.4, 1.5, 1.6, 1.8, 2.5, 3, 4) were performed to better define the relationship between relative spatial sensitivity $R_{s,l}$ and dimensionless rainstorm duration t_r/t_e in the region of $0.4 \leq t_r/t_e \leq 5.0$. After rescaling the values of $R_{s,l}$ with their reference values at $t_r/t_e = 1.0$, Figure 7 shows the same decrease in sensitivity for each parameter. For example, this general curve shows that the relative spatial sensitivity when $t_r/t_e = 2$ is about 50% of the relative sensitivity when $t_r/t_e = 1$.

Distribution of Peak Discharge

Considering the 100 hydrographs simulated under spatially varied conditions, the values of the peak discharges for each system are ranked and plotted against their nonexceedance probability. Figures 8*a*–8*d* show the distribution of dimensionless peak discharges for several values of t_r/t_e ranging from 0.3 to 2 near the threshold conditions between complete and partial equilibrium hydrographs. These figures clearly illustrate the changes in distribution of peak discharge for perturbed systems when the rainfall duration is approaching time to equilibrium. When $t_r/t_e < 1.0$, peak discharges vary over a wide range of values as indicated by wide-spread distributions in Figures 8*a*–8*d*. As rainfall duration approaches and exceeds the time to equilibrium, the system is forced to peak closer to or at unity as indicated by the steep lines in Figures 8*a*–8*d*.

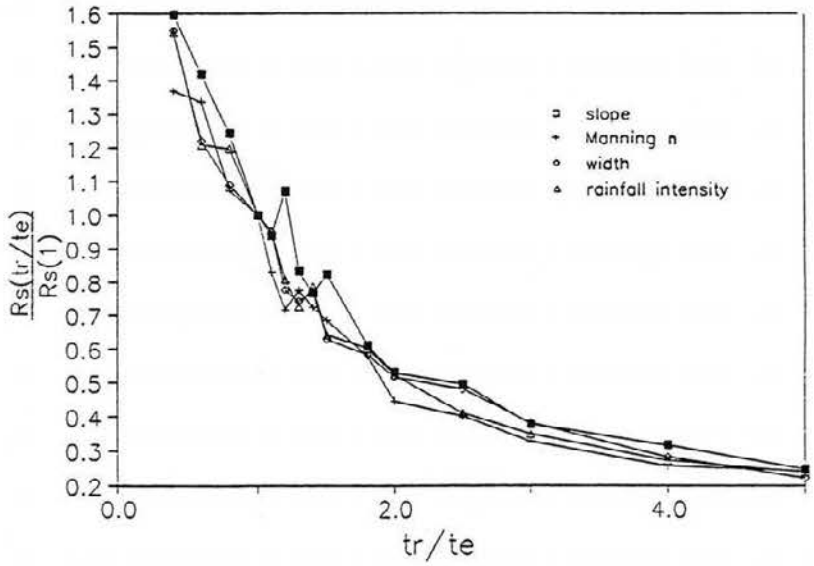

Fig. 7. Relative spatial sensitivity versus dimensionless rainfall duration t_r/t_e.

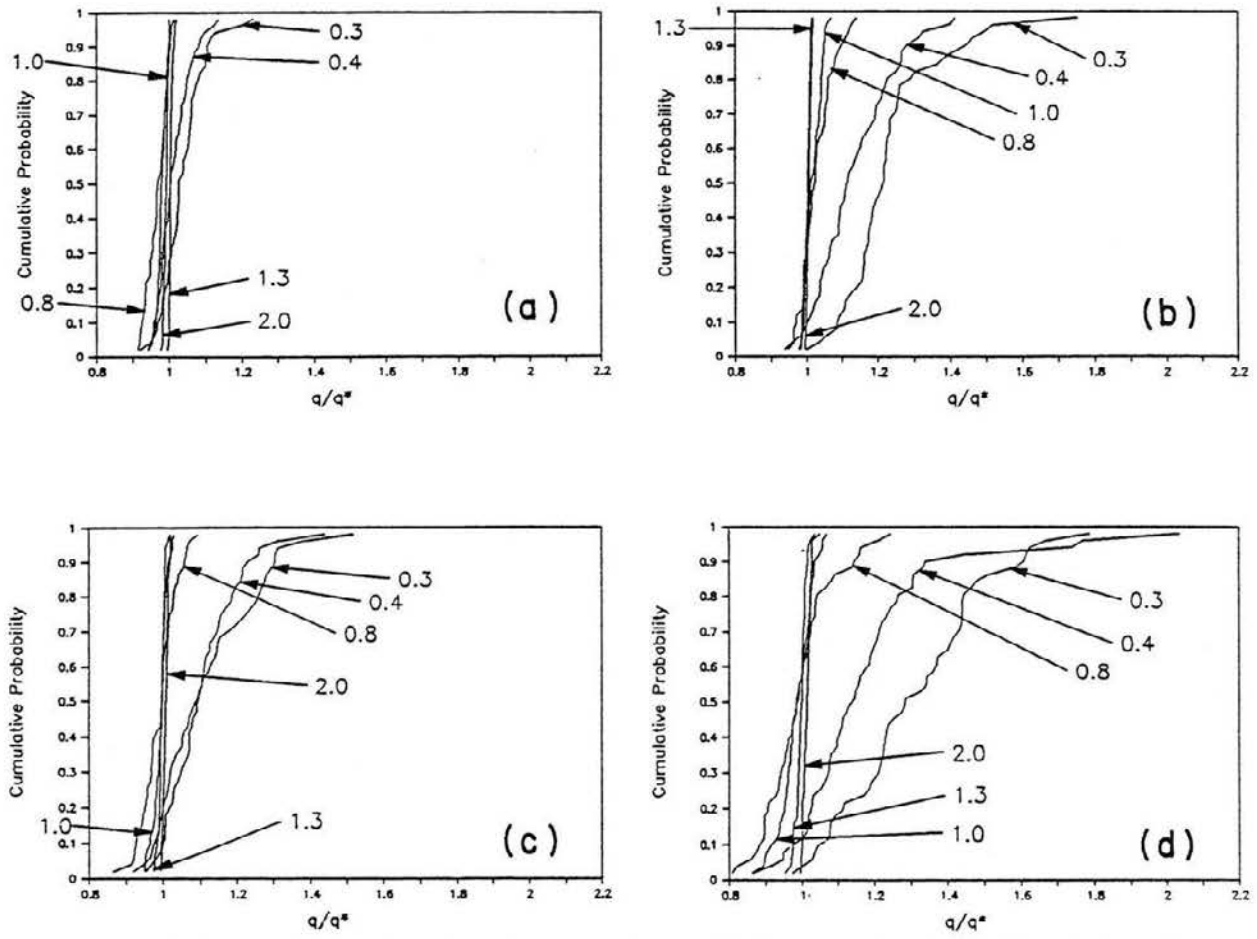

Fig. 8. Distribution of peaks when $0.3 < t_r/t_e < 2$ for (*a*) slope, (*b*) Manning *n*, (*c*) surface width, and (*d*) rainfall intensity.

These figures clearly demonstrate that the distribution of peak discharges changes completely as t_r/t_e approaches unity. For this reason it is concluded that the time to equilibrium under spatially varied conditions remains essentially equal to the time to equilibrium calculated for the nonperturbed system.

Correlated Spatial Variability

The above results for uncorrelated spatially varied hydrologic parameters highlight the primary importance of the time to equilibrium to describe the physical characteristics of a spatially perturbed system. The question of interest in this section regards whether spatial correlation between the perturbed parameters will change the results of the analysis or not. A brief investigation of this problem is presented in this section. The approach taken is based on the reconstitution of surface profiles from spectral density functions of terrain elevation data. Since the results shown in Figure 7 are independent of the parameter selected for the analysis, only surface slope has been selected here, the other parameters being expected to yield similar results.

A terrain height variance spectra is obtained from field measurements of terrain elevations in Steamboat Springs, Colorado. The data sources for this analysis include topographic maps and National Oceanic and Atmospheric Administration/EDIS/NGSDC 30-s average elevation tapes. *Young and Pielke* [1983] converted the data into spectral form using a fast Fourier transform algorithm. Least squares was used to fit the power law relationship:

$$S_z = a\lambda^b \tag{20}$$

where S_z is the terrain height variance in meters squared kilometers, λ is the wavelength of the landform in kilometers, and a and b are the calibrated coefficient and exponent, respectively. For Steamboat Springs, a and b are equal to 2.1 and 0.9, respectively.

The major difference with the random generation scheme described earlier is that spectral data creates spatially correlated slope profiles. By "spatially correlated" it is meant that the slope at one node is somewhat influenced by the slope of adjacent nodes. The result is that the spatially correlated slope profiles have smooth, gradual changes in slope when compared to the rugged randomly generated profiles as shown in Figure 9. Series of 100 spatially correlated slope profiles are generated from (20) for rainfall durations of $t_r/t_e = 0.4$, 1.0, and 5.0. The simulated data are analyzed with the same procedure developed for uncorrelated spatial variability.

A relative sensitivity analysis based on (19) is performed on the spatially correlated profiles for comparison with the spatially uncorrelated profiles. Table 2 shows, again, how R_s decreases as t_r/t_e increases. The absolute values of correlated versus uncorrelated data are meaningless because a larger value of ϕ could have been selected to match the correlated values. Therefore after dividing the values in

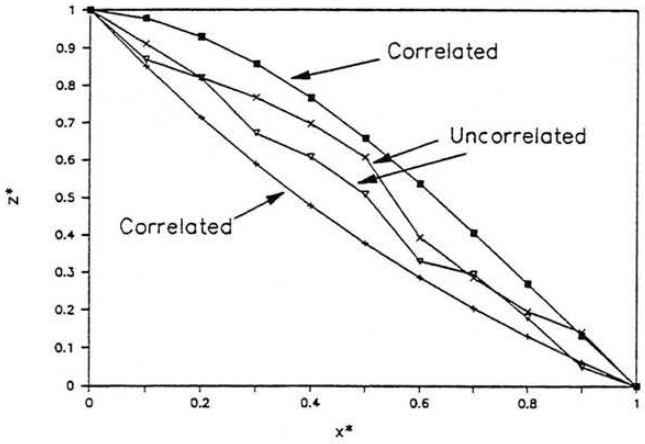

Fig. 9. Comparison of correlated and uncorrelated slope profiles.

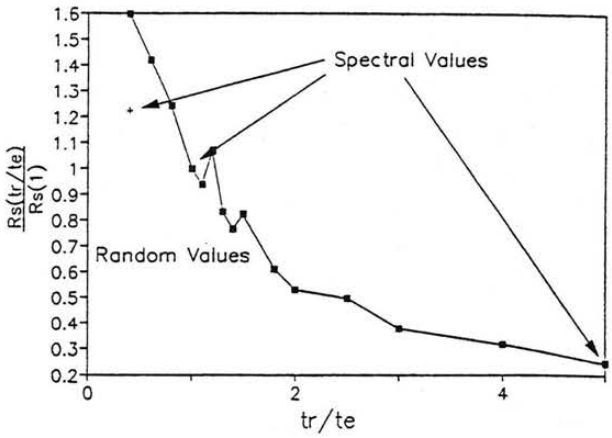

Fig. 10. Relative spatial sensitivity for correlated and uncorrelated ($\phi = 4$) slope profiles.

Table 2 by the relative sensitivity at $t_r/t_e = 1$, the resulting graph in Figure 10 shows the results practically identical to those of Figure 7. From Figure 10 it may be inferred that the decrease of R_s as a function of t_r/t_e is independent of the nature of the slope perturbations.

The primary conclusion is that uncorrelated systems show the same behavior as spatially correlated systems in that the time to equilibrium plays the dominant role in spatially varied surface runoff.

Similarity and Scaling Problems

Similarity conditions for surface runoff generated at different scales can be reassessed considering that spatially varied hydrologic parameters exert little influence on the computed discharge if the duration of rainfall exceeds the time to equilibrium. The criteria used to calculate the time to equilibrium may now be reversed and used to determine the appropriate length scale describing similarity conditions for surface runoff given the rainfall duration t_r, the spatially averaged excess rainfall intensity i, the average slope S, the average surface roughness n, and the average surface width w. The appropriate length scale L_s is then calculated from (5) after considering that $L_s = L$ when $t_r = t_e$:

$$L_s = \frac{\alpha i^{\beta-1}(t_r)^{\beta}}{w} \tag{21}$$

or, specifically for Manning equation,

$$L_s = \left[\frac{t_r^{5/3} S_0^{1/2} i^{2/3}}{n}\right] \tag{22}$$

where the length scale L_s is in meters, the rainfall duration t_r is in seconds, and the rainfall intensity i is in meters per second. Notice that the length scale does not depend solely on the configuration of the catchment but also depends on the characteristics of the storm to be investigated. Indeed, both the rainfall duration t_r and the spatially averaged excess rainfall intensity i are needed for the determination of the length scale. Under these conditions the length scale L_s means that the spatial variability at a field runoff length smaller than L_s has a negligible influence on the computed discharge. At this scale the runoff response to rainfall input also becomes nearly linear as $t_r/t_e \to \infty$. Conversely, field runoff lengths in excess of the length scale produce a nonlinear rainfall-runoff relationship which is highly sensitive to spatial variability of the hydrologic parameters.

The following practical example determines if the spatial variability in topography and surface roughness will largely influence calculations of surface runoff. The spatially averaged values are given for the slope $S_0 = 0.03$, runoff length $L = 500$ m, Manning $n = 0.02$, rainfall duration $t_r = 3600$ s (1 hour) and excess rainfall intensity $i = 7.06 \times 10^{-6}$ m/s (1 inch per hour). The length scale calculated from (22) exceeds the runoff length ($L_s = 2690$ m $> L = 500$ m) which indicates that the spatial variability in topography and surface roughness exerts little influence on the calculations of surface runoff from spatially averaged values of the hydrologic parameters. For this rainstorm the spatial variability effects would be important at runoff lengths $L > L_s = 2690$ m.

TABLE 2. Relative Spatial Sensitivity for Correlated and Uncorrelated ($\phi = 6$) Slope Profiles

Distribution	$t_r/t_e = 0.4$	$t_r/t_e = 1.0$	$t_r/t_e = 5.0$
Correlated	0.2046	0.1672	0.0432
Uncorrelated ($\phi = 6$)	0.0798	0.0456	0.0116

Conclusions

This study quantifies the influence of spatial variability in slope, surface roughness, surface width, and excess rainfall intensity on surface runoff characteristics. Comparisons of similar one-dimensional systems involve finite element surface runoff simulations for stationary rainstorms using the kinematic wave approximation of the St-Venant equations combined with Manning's resistance formula. Similarities between all input parameters are strictly preserved by keeping identical spatially averaged values of all input parameters for each run. Also, the same excess rainfall volume is maintained in all runs in order to avoid the error and bias problems discussed in the recent literature. The results of both correlated and uncorrelated spatial variability are expressed in dimensionless form after considering that the time to equilibrium serves as an important physical characteristic. These similarities in rainfall-runoff response under spatially varied hydrologic conditions serve to define a length scale describing similar sensitivity to spatially varied surface runoff conditions.

This investigation demonstrates that the finite element method is an extremely powerful tool for fundamental hydrologic investigations on overland flow generated under spatially varied conditions. Not only does the finite element method provide efficient solutions (8400 computer simulations are summarized in this paper) to the kinematic wave approximation of the governing surface runoff equations, but it permits quantitative evaluations of the effects of spatial variability in terms of physically based dimensionless parameters such as dimensionless discharge q/iL, dimensionless time t/t_e, and dimensionless rainfall duration t_r/t_e.

The primary conclusions reached from this investigation can be listed as follows:

1. A length scale describing similarity in surface runoff generated under spatially varied hydrologic conditions is defined as a function of both the surface parameters and the duration and excess rainfall intensity of rainstorms.
2. For field runoff lengths much shorter than the length scale, the spatial variability exerts little influence on the runoff hydrograph, and the rainfall-runoff relationship becomes nearly linear. Conversely, at field runoff lengths exceeding the scale length, the spatial variability causes variations in calculated runoff discharges and the rainfall-runoff relationship becomes nonlinear.
3. The time to equilibrium of spatially varied systems remains essentially equal to the time to equilibrium calculated from spatially averaged values of hydrologic parameters.
4. The results of the relative spatial sensitivity in Figure 7 are identical for each of the four parameters considered.
5. The results of relative spatial sensitivity in Figure 10 are remarkably similar for both correlated and uncorrelated spatial variability.
6. The deviation hydrographs in Figure 6 show that the maximum variability in runoff discharge occurs during the rising limb of the hydrograph.
7. The distribution of peak discharges in Figure 8 changes drastically as the dimensionless rainfall duration approaches unity.

The length scale can serve as a basis for the determination of grid size in hydrologic models. Extreme events with large rainfall durations and intensity can be analyzed with coarser grids than most common rainstorms.

Acknowledgments. This study has been completed by the Hydrologic Modeling Group of the Center for Geosciences at Colorado State University. The financial support granted by the U.S. Army Research Office (grant ARO/DAAL 03-86-K-0175) is gratefully acknowledged. We are thankful to R. Pielke from the Department of Atmospheric Sciences at Colorado State University who provided the spectral data and expertise needed for the correlated spatial variability analysis.

REFERENCES

Amorocho, J., Stochastic modeling of precipitation in space and time, in *Statistical Analysis of Rainfall and Runoff*, pp. 3–20, Water Resources Publications, Littleton, Colo., 1982.

Amorocho, J., and B. Wu, Mathematical models for the simulation of cyclonic storm sequences and precipitation fields, *J. Hydrol.*, *32*, 329–345, 1977.

Caroni, E., R. Rosso, and F. Siccardi, Nonlinearity and time-variance of the hydrologic response of a small mountain creek, in *Scale Problems in Hydrology*, pp. 19–37, D. Reidel, Hingham, Mass., 1986.

Dawdy, D. R., A review of deterministic surface water routing in rainfall-runoff models, in *Rainfall-Runoff Relationships*, pp. 23–36, Water Resources Publications, Littleton, Colo., 1982.

Dhatt, G., and G. Touzot, *The Finite Element Method Displayed*, John Wiley, New York, 1984.

Diaz-Granados, M., R. L. Bras, and J. B. Valdes, Incorporation of channel losses in the geomorphologic IUH, in *Scale Problems in Hydrology*, pp. 217–243, D. Reidel, Hingham, Mass., 1986.

Eagleson, P. S., *Dynamic Hydrology*, McGraw-Hill, New York, 1970.

Gupta, V. K., and E. C. Waymire, A stochastic kinematic study of subsynoptic space-time rainfall, *Water Resour. Res.*, *15*(3), 637–644, 1979.

Henderson, F. M., and R. A. Wooding, Overland and groundwater flow from a steady rainfall of finite duration, *J. Geophys. Res.*, *69*(8), 1531–1540, 1964.

Julien, P. Y., and D. B. Simons, Sediment transport capacity of overland flow, *Trans. ASAE*, *28*(3), 755–762, 1985.

Julien, P. Y., G. E. Moglen, and G. U. Sunada, CASC user's manual—A finite element model for spatially varied overland flow simulation, *Rep. CER 87-88 GEO7*, Colo. State Univ., Fort Collins, 1988.

Kibler, D. F., and D. A. Woolhiser, The kinematic cascade as a hydrologic model, *Hydrol. Pap. 39*, Colo. State Univ., Fort Collins, 1970.

Lighthill, M. H., and G. B. Whitham, On kinematic waves, I, Flood movement in long rivers, *Proc. R. Soc. London, Ser. A*, *229*, 281–316, 1955.

Machado, D., and T. O'Donnell, A stochastic interpretation of a lumped overland flow model, in *Proceedings of the Fort Collins Third International Hydrological Symposium on Theoretical and Applied Hydrology*, pp. 259–269, Water Resources Publications, Fort Collins, Colo., 1977.

Maller, R. A., and M. L. Sharma, An analysis of areal infiltration considering spatial variability, *J. Hydrol.*, *52*, 25–37, 1981.

McCuen, R. H., and W. M. Snyder, *Hydrologic Modeling—Statistical Methods and Applications*, Prentice-Hall, Englewood Cliffs, N. J., 1986.

Milly, P. C. D., and P. S. Eagleson, Effects of spatial variability on annual average water balance, *Water Resour. Res.*, *23*(11), 2135–2143, 1987.

Moglen, G. E., The effects of spatial variability of overland flow parameters on runoff hydrographs, M.S. thesis, Civ. Eng. Dep., Colo. State Univ., Fort Collins, 1989.

Overton, D. E., and M. E. Meadows, *Stormwater Modeling*, Academic, San Diego, Calif., 1976.

Richardson, J. R., The influence of moving precipitation fields on rainfall-runoff processes, Ph.D. dissertation, Dep. of Civ. Eng., Colo. State Univ., Fort Collins, 1989.

Rodriguez-Iturbe, I., and P. S. Eagleson, Mathematical models of rainstorm events in space and time, *Water Resour. Res.*, *23*(1), 181–190, 1987.

Sharma, M. L., R. J. W. Barron, and E. S. De Boer, Spatial structure and variability of infiltration parameters, in *Advances in Infiltration*, pp. 113–121, American Society of Agricultural Engineers, St. Joseph, Mich., 1983.

Sivapalan, M., and E. F. Wood, Spatial heterogeneity and scale in the infiltration response of catchments, in *Scale Problems in Hydrology*, pp. 81–106, D. Reidel, Hingham, Mass., 1986.

Sivapalan, M., K. Beven, and E. F. Wood, On hydrologic similarity, 2.A scaled model of storm runoff production, *Water Resour. Res.*, *23*(12), 2266–2278, 1987.

Smith, R. E., and R. H. B. Hebbert, A Monte Carlo analysis of the hydrologic effects of spatial variability of infiltration, *Water Resour. Res.*, *15*(2), 419–429, 1979.

Troutman, B. M., Runoff prediction errors and bias in parameter estimation induced by spatial variability of precipitation, *Water Resour. Res.*, *19*(3), 791–810, 1983.

Troutman, B. M., Errors and parameter estimation in precipitation-runoff modeling, 1, Theory, *Water Resour. Res.*, *21*(8), 1195–1213, 1985*a*.

Troutman, B. M., Errors and parameter estimation in precipitation-runoff modeling, 2, Case study, *Water Resour. Res.*, *21*(8), 1214–1222, 1985*b*.

Valdes, J. B., I. Rodriguez-Iturbe, and V. K. Gupta, Approximations of temporal rainfall from a multidimensional model, *Water Resour. Res.*, *21*(8), 1259–1270, 1985.

Wilson, C. B., J. B. Valdes, and I. Rodriguez-Iturbe, On the influence of the spatial distribution of rainfall on storm runoff, *Water Resour. Res.*, *15*(2), 321–328, 1979.

Wood, E. F., M. Sivapalan, K. Beven, and L. Band, Effects of spatial variability and scale with implications to hydrologic modeling, *J. Hydrol.*, *102*, 29–47, 1988.

Woolhiser, D. A., and J. A. Liggett, Unsteady, one-dimensional flow over a plane: The rising hydrograph, *Water Resour. Res.*, *3*(3), 753–771, 1967.

Woolhiser, D. A., and H. B. Osborn, A stochastic model of dimensionless thunderstorm rainfall, *Water Resour. Res.*, *21*(4), 511–522, 1985.

Wu, Y. H., V. Yevjevich, and D. A. Woolhiser, Effects of surface roughness and its spatial distribution on runoff hydrographs, *Hydrol. Pap. 96*, Colo. State Univ., Fort Collins, 1978.

Young, G. S., and R. A. Pielke, Application of terrain height variance spectra to mesoscale modeling, *J. Atmos. Sci.*, *40*(10), 2555–2560, 1983.

P. Y. Julien and G. E. Moglen, Department of Civil Engineering, Engineering Research Center, Colorado State University, Fort Collins, CO 80523.

(Received October 6, 1989;
revised January 30, 1990;
accepted February 20, 1990.)

WATER RESOURCES RESEARCH, VOL. 29, NO. 8, PAGES 2589–2597, AUGUST 1993

Runoff Sensitivity to Temporal and Spatial Rainfall Variability at Runoff Plane and Small Basin Scales

FRED L. OGDEN

Iowa Institute of Hydraulic Research, University of Iowa, Iowa City

PIERRE Y. JULIEN

Department of Civil Engineering, Colorado State University, Fort Collins

Surface runoff sensitivity to spatial and temporal variability of rainfall is examined using physically based numerical runoff models. Rainfall duration t_r and temporal sampling interval δt are varied systematically, and normalized by the time to equilibrium t_e. The relative sensitivity R_s is defined as the total volume of outflow variability over 50 Monte Carlo simulations normalized by the rainfall volume and the coefficient of variation of rainfall. Relative sensitivity to temporal rainfall variability increases with both t_r and δt. An asymptotic R_s value proportional to $(\delta t/t_e)^{1/2}$ is approached as $t_r \gg t_e$. Two-dimensional surface runoff simulations with spatially variable rainfall, without temporal variability, on two watersheds indicate that R_s decreases as t_r/t_e increases. Normalized R_s versus t_r/t_e curves are identical for two watersheds and a one-dimensional overland flow plane. These findings indicate that spatial variability is dominant when $t_r < t_e$, while temporal variability dominates when $t_r > t_e$, particularly for larger values of $\delta t/t_e$.

INTRODUCTION

When remotely sensed input data is applied to a runoff model, there are discrete temporal and spatial sampling resolutions of the input data which must be considered as possible sources of error. This error will adversely affect the runoff calculated by the model and produce variability in computed outflow due solely to the temporal and spatial resolution of the input data. It is important to explore the sources of this variability before precipitation data from remote sensors such as telemetered rain gauges or weather radar are applied to two-dimensional physically based runoff models. Additionally, it is important that the magnitude of the effect of each factor be determined. This will allow the proper application of remotely sensed input data in the runoff modeling process and provide additional understanding of the relation between model accuracy and input data temporal and spatial resolution.

Overland flow modeling requires information about numerous hydrologic parameters. The parameters most important when physically simulating overland flow are topography, surface roughness, soil infiltration characteristics, and the distribution, duration, and intensity of precipitation. Although the intensity of precipitation varies continuously in space and time, hydrologic models typically incorporate simplifying assumptions which apply single parametric values to rainfall intensity in space and time. The model output therefore fails to reflect the effects of temporal and spatial variability in the input.

Erichsen and Nordseth [1984] examined the validity of existing computational runoff simulation techniques. There are also many existing methods to model spatial and temporal variability of precipitation on watersheds. The literature gives several examples, particularly one-dimensional models which have been modified to simulate two-dimensional watersheds. More recently, physically based two-dimensional runoff models have been developed by *James and Kim* [1990] and *Julien and Saghafian* [1991].

The effect of the temporal variation of rainfall intensity on overland flow was analytically studied by *Hjelmfelt* [1981]. Results indicate that the peak discharge from an overland flow plane will be slightly larger for rainfall at constant intensity than for rainfall with a typical thunderstorm distribution. Hjelmfelt also notes that the correct value for time to equilibrium is essential for the determination of the peak discharge. The study concludes that difficulty in estimating the time to equilibrium for temporally varying precipitation limits the consideration of temporal variability for design purposes.

A linear and nonlinear reservoir routing method, proposed by *Diskin et al.* [1984], is capable of accepting spatially and temporally varying precipitation input. Another approach for modeling rainfall runoff with spatial and temporal variability in precipitation intensity was proposed by *Niemczynowicz* [1984]. This model of a conceptual urban area was based on Manning's equation and the continuity equation and used dimensional analysis to describe the relationship between moving storms and runoff hydrographs. Later, *Niemczynowicz* [1984] applied this model to urbanized catchments in the city of Lund, Sweden. This study showed that the maximum discharge with the steepest rising limb occurred when the storm was moving down the watershed at a speed approximately equal to the average flow velocity. This author's work focuses on the magnitude of the peak discharge and the relationship between storm velocity and peak discharge.

Storm and Jensen [1984] developed a theoretically and physically based runoff model capable of simulating nonurbanized watersheds with spatially and temporally varying precipitation inputs. This model is also capable of modeling subsurface flows; however, the paper presents a limited

Copyright 1993 by the American Geophysical Union.

Paper number 93WR00924.
0043-1397/93/93WR-00924$05.00

54

compilation of results. The effects of spatially variable precipitation on runoff have been studied by many researchers, including *Woo and Brater* [1962], *Jensen* [1984], and *Wood et al.* [1988]. *Richardson* [1989] performed a detailed study of overland flow dynamics using a one-dimensional finite element overland flow runoff model. The finite element runoff model was calibrated using the laboratory data of *Yen and Chow* [1968].

A Monte Carlo technique was used to study the effect of rain gauge sampling resolution on a distributed watershed model by *Krajewski et al.* [1991]. This study used a one-dimensional distributed parameter model based on the kinematic wave approximation. The findings of this study indicated that model response is more sensitive to temporal resolution than spatial resolution of the input precipitation data. Additionally, these researchers found that a lumped parameter model consistently underestimated peak flows. They also concluded that a two-dimensional distributed model would be better suited for modeling the problem of optimal spatial and temporal resolution.

Julien and Moglen [1990] investigated the effects of spatial variability on overland flow hydrographs using a one-dimensional, kinematic wave, finite element model. The specific areas of interest explored were analysis of the differences in model response for the cases of partial and complete equilibrium; comparison of the relative influence of the spatially varying quantities slope, width, rainfall intensity, and roughness coefficient; and a sensitivity analysis of required grid spacing. The effect of parameter variability was examined by randomly perturbing the values of the four spatially varied parameters in both a correlated and uncorrelated fashion. Julien and Moglen found the effect of all perturbations is a function of t_r/t_e, or the ratio of the rainfall duration t_r to the time to equilibrium t_e of the plane under a constant precipitation intensity. One finding of this study was that the relative magnitudes of the effects of perturbations are different, but when each is normalized with respect to the value at $t_r/t_e = 1.0$, the effects were identical. Therefore a scalar multiple of the spatial variability in any one of the four spatially variable parameters can simulate spatial variability in the other three parameters. More importantly, they found that as t_r/t_e exceeds 2.0, the relative sensitivity of the model to perturbations in all spatial runoff plane and rainfall characteristics becomes small.

OBJECTIVES

There are four specific objectives of this study. The first objective is to verify the findings of *Julien and Moglen* [1990] regarding runoff sensitivity to rainfall spatial variability, using two-dimensional simulations. The second objective is to quantitatively determine the sensitivity of one-dimensional overland flow to temporal precipitation variability. The third objective is to verify the one-dimensional temporal variability study in two-dimensional simulations. The fourth and final objective is to draw a conclusion regarding runoff relative sensitivity R_s due to the separate influences of rainfall spatial and temporal variability as a function of rainfall duration, rainfall data temporal resolution, and runoff area time to equilibrium.

GOVERNING EQUATIONS AND MODELING TECHNIQUE

The state variables governing one-dimensional overland flow are the length of the horizontal projection of the overland flow plane L, the depth of flow h, the average velocity of flow $\bar{u}$, the surface slope S_o, the excess rainfall rate in space and time $i(x, t)$, and the discharge per unit width q. The hydraulic roughness of the plane n and the gravitational acceleration g are also important variables.

There are a host of different approaches in the literature for overland flow routing. The partial differential equations which express conservation of mass (1) and momentum (equations (2) and (3)) in two dimensions are expressed as

$$\frac{\partial h}{\partial t} + \frac{\partial q_x}{\partial x} + \frac{\partial q_y}{\partial y} = e \tag{1}$$

$$\frac{\partial u}{\partial t} + u\frac{\partial u}{\partial x} + v\frac{\partial u}{\partial y} = g\left(S_{ox} - S_{fx} - \frac{\partial h}{\partial x}\right) \tag{2}$$

$$\frac{\partial v}{\partial t} + u\frac{\partial v}{\partial x} + v\frac{\partial v}{\partial y} = g\left(S_{oy} - S_{fy} - \frac{\partial h}{\partial y}\right) \tag{3}$$

where

u, v flow velocities in x and y direction, respectively;
S_{ox}, S_{oy} bed slopes in x and y directions, respectively;
S_{fx}, S_{fy} friction slopes in x and y directions, respectively;
g acceleration due to gravity;
h flow depth;
q_x unit discharge in x direction;
q_y unit discharge in y direction;
e excess rainfall rate, equal to i–f;
i incident rainfall intensity;
f infiltration rate.

The left-hand sides of (2) and (3) contain the local and convective acceleration terms, while the right-hand sides of the equations denote the forces per unit mass acting in the x and y directions, respectively.

The applicability of the simplified equations of motion have been discussed in the literature [*Richardson* 1989; *Ponce and Li*, 1979; *Ponce et al.*, 1978]. *Richardson* [1989] has shown that the full dynamic and kinematic forms of the momentum equation are most applicable for the simulation of overland flow. The most widely used overland flow routing technique is the kinematic wave form of the equation of motion, which neglects the acceleration and pressure terms. The diffusive wave formulation neglects all three acceleration terms on the left-hand side of (2) and (3). The advantages of the diffusive wave formulation over the kinematic waveform are its applicability in regions of small slope and/or high roughness, and the ability to store water on the watershed surface. These advantages justify its application in overland flow simulations on natural basin topography.

A resistance equation is required to provide an energy balance. Practical resistance equations are empirically derived from the analysis of flow variables and field data. A widely applicable roughness equation is the Manning equation in SI units:

$$U = \frac{1}{n} R_h^{2/3} S_f^{1/2} \quad (4)$$

where n is the Manning roughness coefficient, $U = (u^2 + v^2)^{1/2}$ is the flow velocity, R_h is the hydraulic radius, and $S_f = (S_{fx}^2 + S_{fy}^2)^{1/2}$.

Roughness equations are typically of the form $q = (q_x^2 + q_y^2)^{1/2} = \alpha h^\beta$, which for the Manning equation $\alpha = S_f^{1/2}/n$ and $\beta = 5/3$.

Numerical modeling of overland flow has evolved considerably in recent years with the proliferation of digital computers. The CASC one-dimensional kinematic wave rainfall runoff model [*Julien et al.*, 1988] provides a finite element numerical solution by the Galerkin weighted residual method. This model employs the Manning equation and neglects infiltration, therefore assuming that all rainfall is excess rainfall. The algorithm enables the simulation of time varying storms, stationary storms with variable overland flow parameters [*Julien and Moglen*, 1990], and one-dimensional moving storms [*Richardson*, 1989]. A more rigorous description of the model formulation, simulation examples for stationary and moving storms, and comparison with observed data is published in the CASC user's manual [*Julien et al.*, 1988].

The CASC2D watershed runoff model employs a raster-based, two-dimensional solution of the diffusive wave formulation of the St. Venant equations [*De St. Venant* 1871] for overland flow. The model was developed at Colorado State University by *Julien and Saghafian* [1991] and includes *Green and Ampt* [1911] infiltration calculation and diffusive wave channel routing routines. Watershed data are stored in raster format at a user defined spatial resolution. Typically, applied spatial resolutions range from 125 to 200 m. Watershed characteristics within each grid element (e.g., roughness coefficient, soil characteristics, etc.) are treated as constant quantities. The CASC2D runoff model can simulate moving storms and incorporate weather radar estimated rainfall rates [*Ogden*, 1992]. Complete details of the model formulation, options, data requirements, and evaluation are published in the CASC2D user's manual [*Julien and Saghafian*, 1991].

The precipitation model by *Rodriguez-Iturbe and Eagleson* [1987] was selected to generate two-dimensional rainfall fields used in this study. This model employs statistical clustering techniques and simulates the birth, growth, and decay of convective precipitation within a large mesoscale area (LMSA) which is several hundreds of kilometers on a side. The model assumes that within the LMSA, smaller regions of intense rainfall occur, which are referred to as small mesoscale areas (SMSA). Rainfall is more intense within the SMSA's because of the clustering of rain cells, in accordance with a Neyman-Scott process. The spatial distribution of rainfall clusters within the LMSA is taken as a Poisson process. The number of spatial points of rainfall within each SMSA is also determined by a Poisson distribution, with rainfall intensity being an exponentially distributed variable.

Topographical data from two basins, namely, Macks Creek and Taylor Arroyo, were used in the tests. The Macks Creek watershed is located in mountainous southwestern Idaho, covers an area of 31.64 km^2, and has a mean slope of 9.4%. The Taylor Arroyo watershed in southeastern Colorado covers an area of 121 km^2 and has a mean watershed slope of 1.6%. Both watersheds are located in semi-arid regions and are dominated by Hortonian runoff production mechanisms.

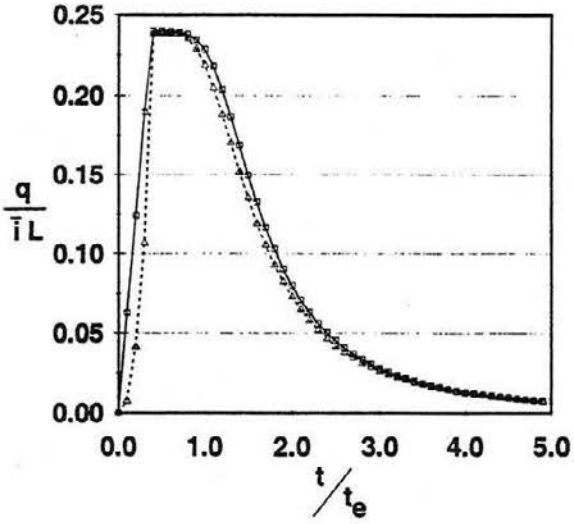

Fig. 1*a*. Hydrograph envelope for $t_r/t_e = 0.4$ and $\delta t/t_e = 0.1$.

Infiltration was neglected in this study. It is impossible to separate the sole effect of rainfall spatial or temporal variability on runoff in the presence of spatially and temporally varying infiltration. By neglecting infiltration, all rainfall is taken as excess rainfall, effectively eliminating separate consideration of the effects of spatial and temporal variability of rainfall and infiltration rate. Furthermore, the selected data analysis method requires conservation of outflow mass, precluding the consideration of infiltration. The applicability of our results is limited to runoff situations where either soils are of very low permeability or rainfall rates are much greater than infiltration rates.

Channel routing was neglected and all flow was modeled as overland flow. The inclusion of channel routing would have added considerable computational effort to this study. The presence of channels would modify the value of t_e for a given rainfall rate. Similarly, the value of the overland flow roughness coefficient affects t_e. The value of Manning's n used in this study was held constant throughout the basin and was equal to 0.04. All results are expressed in terms of t_e, thus enabling the conversion of the results to different runoff geometries which include channel routing or spatially variable roughness coefficient.

HYDROGRAPH ENVELOPES

The hydrograph envelope procedure used by *Julien and Moglen* [1990] was selected to reduce the output data into an interpretable form. Hydrograph envelopes arising from spatially variable rainfall on a one-dimensional runoff plane can be seen in that paper. A hydrograph envelope is generated by finding, for each set of 50 equivalent systems, the highest and lowest simulated discharges at each computational time step. These envelopes show the maximum variation in discharge as a function of time along the hydrograph. Four typical hydrograph envelopes arising from temporally varying rainfall are shown in Figures 1*a* and 1*b* for partial equilibrium hydrographs ($t_r < t_e$) and in Figures 1*c* and 1*d* for complete equilibrium hydrographs ($t_r \geq t_e$). In these

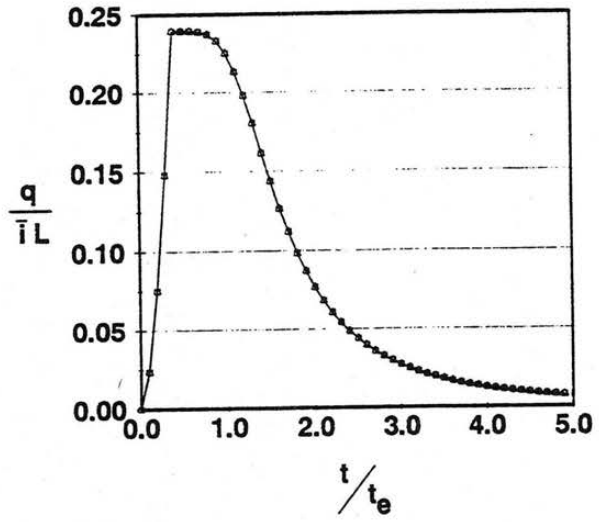

Fig. 1*b*. Hydrograph envelope for $t_r/t_e = 0.4$ and $\delta t/t_e = 1.1$.

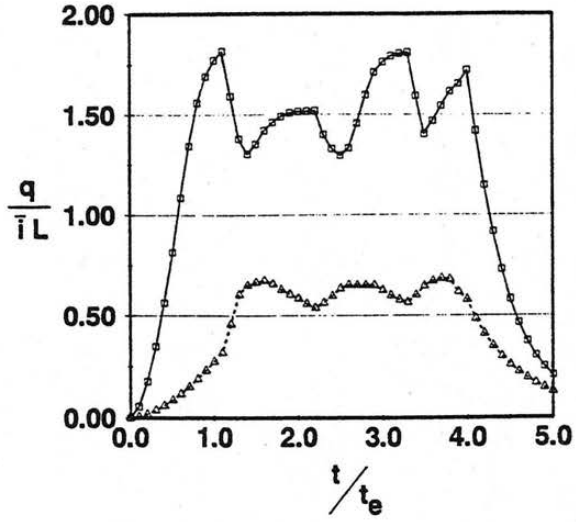

Fig. 1*d*. Hydrograph envelope for $t_r/t_e = 4.0$ and $\delta t/t_e = 1.1$.

four hydrograph envelopes the discharge is made dimensionless by dividing by the steady state system inflow $\bar{i}L$, where $\bar{i}$ represents the mean rainfall rate and L is the overland flow plane horizontal projection.

Sensitivity, a measure of the model response to a change in an input parameter, is used to determine the importance of parameters and to optimize parameter values within a model. With an understanding of the general behavior of the model response to temporal input variability, the goal is to quantify the temporal sensitivity of the model output to each value of temporal sampling resolution $\delta t/t_e$.

With reference to Figures 1*a* through 1*d*, the volume of runoff ΔV, contained within the upper discharge $q_{\max}$ and the lower discharge $q_{\min}$ hydrograph envelopes, is obtained by

$$\Delta V = \sum_{\tau=0}^{\infty} (q_{\max} - q_{\min})_\tau w \Delta t \tag{5}$$

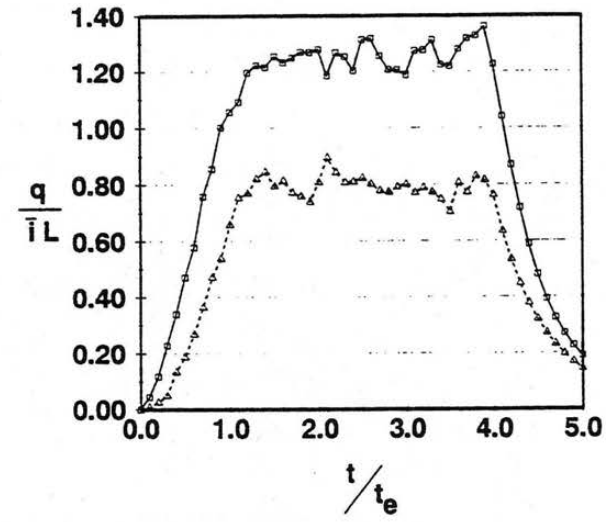

Fig. 1*c*. Hydrograph envelope for $t_r/t_e = 4.0$ and $\delta t/t_e = 0.1$.

where w is the runoff plane width and Δt is the computational time step.

The dimensionless hydrograph envelope volume V^* for the hydrograph envelopes is calculated using

$$V^* = \Delta V / V_r \tag{6}$$

where V_r is the input rainfall volume and is given by:

$$V_r = wL\delta t \sum_{\tau=0}^{t_r} i(\tau) \tag{7}$$

The magnitude of the dimensionless hydrograph envelope volume is indicative of the variability of the 50 Monte-Carlo outflow hydrographs used to generate the envelope.

The coefficient of variation C_v is defined as

$$C_v = \sigma/\mu \tag{8}$$

where σ is the standard deviation of the parameter of interest (in this case the standard deviation of the precipitation time series) and μ is the algebraic mean of the parameter. The value of C_v, 0.319, used throughout these analyses, is the theoretical value for a discrete uniform distribution. Relative sensitivity R_s, which represents the outflow variability normalized by input variability, is represented mathematically by

$$R_s = V^*/C_v \tag{9}$$

This quantity is called the relative sensitivity because the factors μ and V_r in the denominators of (6) and (8) make R_s a dimensionless quantity which is independent of the units used to measure μ and V_r.

The normalized relative sensitivity R_s^*, which represents the R_s function divided by its value at $t_r/t_e = 1.0$, is given by

$$R_s^* = \frac{R_s(t_r/t_e)}{R_s(t_r/t_e = 1.0)} \tag{10}$$

Normalized relative sensitivity is useful for comparing the shape of the R_s versus t_r/t_e function for different runoff geometries.

EFFECTS OF TWO-DIMENSIONAL SPATIAL VARIABILITY OF RAINFALL ON RUNOFF

The objective of this portion of the study is to examine the sensitivity of two-dimensional runoff geometries to the spatial variability of precipitation intensity, an extension of the study by *Julien and Moglen* [1990]. Particularly, this study seeks to verify the findings of the 1990 study using two-dimensional runoff simulations.

A Monte Carlo ensemble of 50 precipitation fields was generated using the precipitation model at the resolution of the watershed elevation data, which is 125 m for Macks Creek and 200 m for Taylor Arroyo. The precipitation model rainfall fields all have similar first- and second-order statistics and identical spatial covariance functions. The precipitation data were applied to the runoff model for different durations of rainfall t_r/t_e to find the relation between R_s and rainfall duration.

Experimental Method

The 50 precipitation fields for each watershed were adjusted to have the same average intensity of 30 mm/hour over the entire watershed by the addition of a constant offset. This adjustment scheme preserved the spatial gradients of rainfall intensity, while providing an equal average intensity. The other precipitation field statistic of interest is the coefficient of variation. The 50 precipitation fields have an average C_v of 1.069 on Macks Creek and 1.099 on Taylor Arroyo.

The testing scheme used the duration of rainfall, defined as a fraction of the time to equilibrium t_r/t_e, as the primary test variable. The values of t_r/t_e tested were 0.1, 0.2, 0.3, 0.4, 0.6, 0.8, 1.0, 1.2, 1.4, 1.8, 2.2, 2.5, 3.0, and 5.0. Hydrograph envelopes were constructed from the 50 outflow hydrographs, as previously described, and the relative sensitivity R_s was calculated.

Two-Dimensional Spatial Variability Results

The distribution of peak outflow magnitude and timing as a function of rainfall duration reveals some aspects of the influence of spatial variability on R_s. These distributions are plotted in Figures 2*a* and 2*b* for the Macks Creek and Taylor Arroyo watersheds, respectively. For all rainfall durations, in no case did the hydrograph peak occur at a time shorter than half the time to equilibrium of the basin. The data also indicate that the variability in hydrograph timing is larger for short ($t_r/t_e < 0.3$) rainfall duration events than the variability in the peak discharge. The variability in peak discharge increases and the variability in peak timing decreases as the rainfall duration increases from $t_r/t_e = 0.3$ to 0.6. As the duration of rainfall increases to $0.8t_e$, the variability in both peak discharge and time to peak decreases, and the data tend to converge on the points $Q_p/Q_e = 1.0$ and $t_p/t_e = 1.0$ as $t_r \rightarrow t_e$. For rainfall durations greater than or equal to the time to equilibrium, the variability in outflow hydrograph peak and time to peak is very small. The distributions of hydrograph Q_p/Q_e and t_p/t_e appear very similar for both study watersheds although they are of considerably different sizes and slopes.

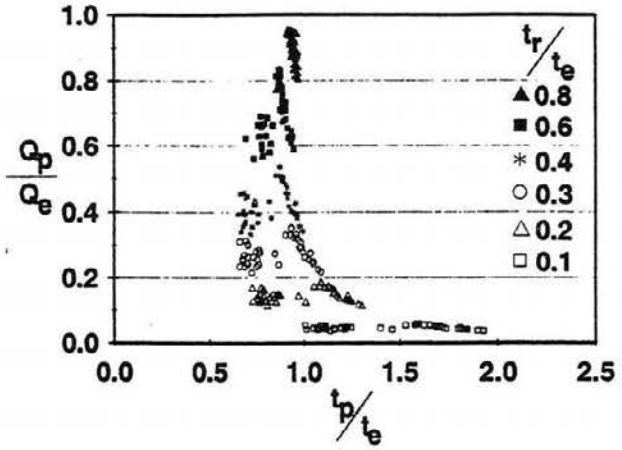

Fig. 2*a*. Dimensionless peak discharge versus dimensionless time to peak for Macks Creek due to spatial rainfall variability.

The relative sensitivity data show that the following runoff geometries are more sensitive to the spatial variability of precipitation in increasing order: 100 m runoff plane of *Julien and Moglen* [1990], Macks Creek watershed, and Taylor Arroyo watershed. The normalized relative sensitivities are plotted in Figure 3. These data provide evidence that the relative sensitivities of geometries as simple as a one-dimensional runoff plane and as complicated as a two-dimensional watershed are similar. The phenomena of runoff sensitivity to the spatial variability of precipitation intensity is therefore independent of scale under the conditions of this study. Of course, the absolute value of the sensitivity is surely geometry dependent; however, the phenomena itself is not. The only difference between the relative sensitivity of a one-dimensional runoff plane and a two-dimensional distributed basin to the variability in space of precipitation intensity appears to be a scaling factor. The scaling factor contains the effects of runoff geometry on the parameter R_s. The R_s scaling factors for the Macks Creek and Taylor Arroyo watersheds, on the basis of the one-dimensional runoff plane are 4.17 and 6.39, respectively.

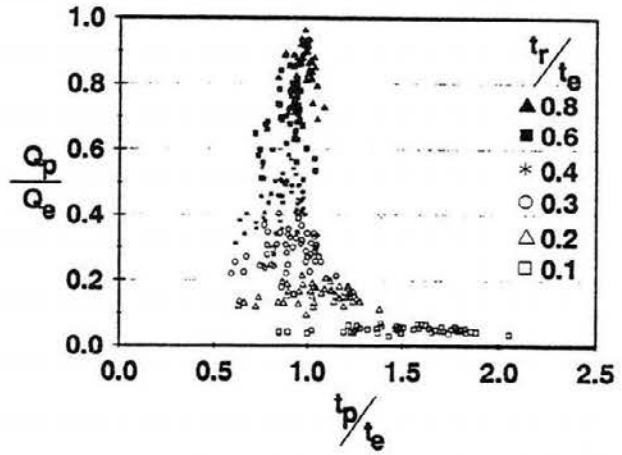

Fig. 2*b*. Dimensionless peak discharge versus dimensionless time to peak for Taylor Arroyo due to spatial rainfall variability.

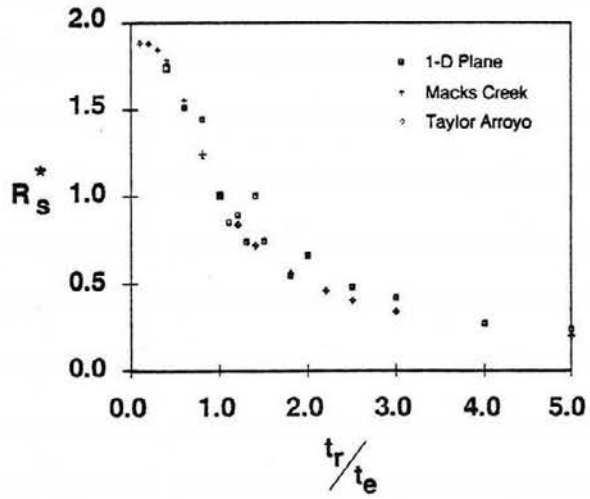

Fig. 3. Normalized R_s due to spatially varied rainfall on Macks Creek, Taylor Arroyo, and one-dimensional runoff plane.

ONE-DIMENSIONAL RUNOFF SENSITIVITY TO RAINFALL TEMPORAL VARIABILITY

The one-dimensional overland flow model CASC was used to determine the effect of the temporal resolution of precipitation on computed outflow hydrographs. The specific parameters of interest were the storm duration t_r, the temporal resolution of precipitation δt, and the time to equilibrium of the overland flow plane t_e. The average rainfall rate over the duration of the rainfall was used to calculate t_e. The testing methodology imposes systematic variability in rainfall duration t_r and temporal resolution of rainfall δt, while all other parameters are held constant. Both of these variables are nondimensionalized by the time to equilibrium t_e of the runoff plane.

The computational time step Δt must always be smaller than the temporal resolution δt of the precipitation data. The temporal resolution must also be evenly divisible by the time step. The computational time step $\Delta t = 0.1t_e$ when $\delta t > 0.1t_e$ or $0.04t_e$ for finer values δt. This choice has been previously shown [*Julien and Moglen* 1990] to more than adequately define the rising limb of the discharge hydrograph. Eleven computational nodes are used to define all systems. Preliminary analyses by *Julien and Moglen* [1990] showed that discharge was relatively unaffected by the number of nodes used, provided there are a minimum of seven present. The length, width, slope, and Manning n values for the overland flow plane are assigned constant values of 100 m, 10 m, 0.1%, and 0.1, respectively. The precipitation intensity varies only in time, not in space. The mean rainfall intensity is 1×10^{-5} m/s (36 mm/hour).

Temporal Variation of Rainfall Intensity

The rainfall time series generation scheme uses a variation factor ϕ and a uniform probability density function. Strictly speaking, a methodology which ignores the time correlation structure in the timewise generation of rain series may not produce realistic rainfall time series. However, this scheme does capture some general behavior of rainfall variability, while maintaining consistency with the previous one-dimensional spatial variability study [*Julien and Moglen*, 1990]. Further refinements to this methodology would include a point rainfall model, which includes a temporal covariance function.

The parameter ϕ describes the maximum allowable variation from the mean value using the following relation:

$$\mu_x\left(1 - \frac{\phi - 1}{\phi + 1}\right) \le X_j \le \mu_x\left(1 + \frac{\phi - 1}{\phi + 1}\right) \qquad (11)$$

where μ_x is the mean value of parameter X, and X_j is the value of parameter X at the jth time. The parameter ϕ should always be chosen to be greater than or equal to one, where $\phi = 1$ indicates no perturbations. The value of ϕ used in this study was 4 and was selected so that the results of this temporal resolution study could be compared with the study of *Julien and Moglen* [1990], which used the same ϕ value, regarding spatial variability of the overland flow parameters. The value $\phi = 4$ produces precipitation intensities ranging from a maximum of 57.6 to a minimum of 14.4 mm/hour.

The above temporal variation scheme was used to generate 50 unique realizations with the same average precipitation intensity, coefficient of variation of the precipitation time series, duration of rainfall, and temporal sampling resolution of the precipitation. Simulations were performed for 17 different durations of rainfall: t_r/t_e = 0.4, 0.6, 0.8, 1.0, 1.1, 1.2, 1.3, 1.4, 1.5, 1.8, 2.0, 2.5, 3.0, 4.0, 5.0, 7.0, and 10.0. For the temporal sampling resolution of the precipitation data, 14 different values were tested. These values of $\delta t/t_e$ were 0.04, 0.1, 0.2, 0.3, 0.4, 0.5, 0.6, 0.7, 0.8, 0.9, 1.0, 1.1, 2.0, and 3.0. The storm duration values cover the range from partial to complete equilibrium. Similarly, the temporal resolution values range from much smaller ($0.04t_e$) than the time to equilibrium to three times the time to equilibrium. For each permutation of the above conditions, 50 simulations were performed. This number was found to yield fairly smooth results in the bounds of all 50 hydrographs when plotted together. A total of 11,900 hydrographs were simulated over all possible permutations of the above conditions.

One-Dimensional Temporal Variability Results

Several observations can be made regarding the sensitivity of the overland flow plane to the temporal resolution of the input data from the four hydrograph envelopes shown in Figures 1*a*–1*d*.

1. When t_r/t_e is less than 1.0, the result is a partial equilibrium hydrograph, with the highest simulated discharge occurring at the last time interval experiencing rainfall, followed by a long recession limb (see Figures 1*a* and 1*b*). The region enclosed by the hydrograph envelope in Figure 1*a* is much smaller than that for t_r/t_e = 4.0 (Figure 1*c*). It is therefore apparent that the sensitivity of overland flow to temporal resolution of the precipitation data is significantly higher for $t_r > t_e$.
2. There is no difference between the maximum and minimum hydrograph envelope in Figure 1*b*. This occurs because the temporal sampling resolution is longer than the time of rainfall. Therefore variation in the outflow hydrograph due to sampling resolution effects cannot be observed. This is, in essence, equal to the constant temporal intensity assumption which is used in many runoff models.
3. When $t_r/t_e \gg 1$ (e.g., t_r/t_e = 4.0), the result is a

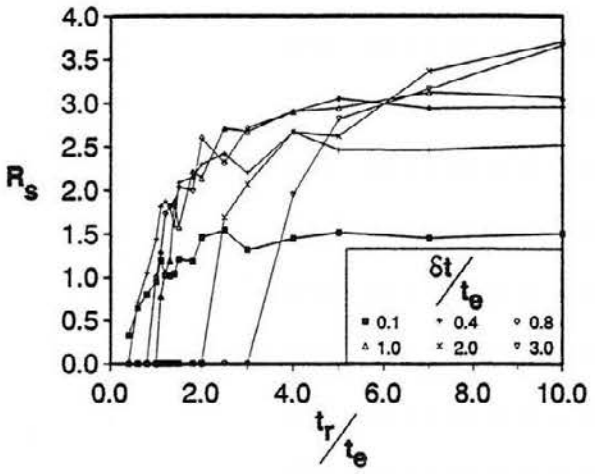

Fig. 4. Relative sensitivity to temporal variability for a one-dimensional runoff plane.

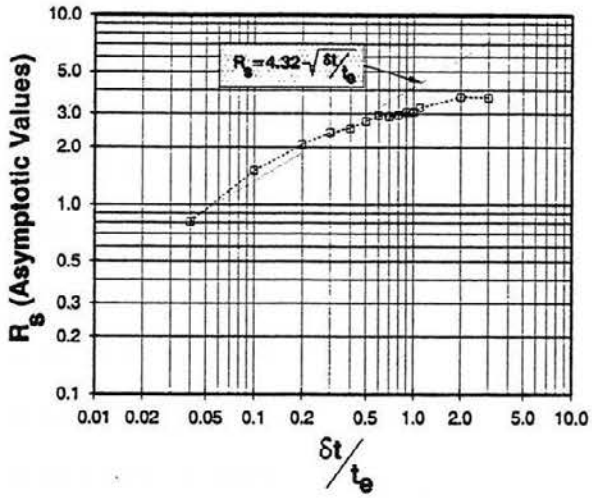

Fig. 5. Asymptotic relative sensitivity values for a one-dimensional runoff plane at $t_r = 10.0t_e$ and various values of $\delta t/t_e$.

complete equilibrium hydrograph, characterized by a non-equilibrium plateau region where the dimensionless discharge varies around 1.0 from $t/t_e \approx 1.0$ to $t = t_r$ (see Figures 1*c* and 1*d*). Temporal variation in the rainfall rate causes the flow from the runoff plane to seek a new equilibrium state after each change in rainfall intensity. This is the reason for the extreme outflow variability around the dimensionless discharge of 1.0.

4. Examination of the hydrograph envelopes indicates that the value of $\delta t/t_e$ has a large effect on the width of the hydrograph envelope when $t_e < t < t_r$. When the temporal resolution is smaller than the time to equilibrium, the hydrograph envelopes tend to be smoother (Figure 1*c*). Values of δt near or greater than t_e produce highly variable hydrograph envelopes where the variability in outflow volume is considerably greater (Figure 1*d*).

The values of R_s for various temporal resolutions are plotted in Figure 4 as a function of t_r/t_e. It is apparent that the magnitude of relative sensitivity increases rapidly for smaller values of t_r/t_e and then changes slowly for larger values of t_r/t_e. In other words, the change in variability in discharge is largest under partial equilibrium conditions and smallest under complete equilibrium conditions. The data in Figure 4 also indicate that the relative sensitivity of the overland flow plane approaches an asymptote as t_r/t_e increases. This can be explained by considering that as t_r/t_e increases considerably beyond 1.0, the upper and lower bounds of the hydrograph envelope becomes roughly parallel. Because the relative sensitivity is an integrated measure of sensitivity, the irregular envelope volumes which occur during the rising and falling limbs of the hydrograph become negligible as $t_r \gg t_e$. This tends to cause R_s to approach an asymptote.

For a given coefficient of variation of the rainfall time series, the asymptotic R_s is thus a function of $\delta t/t_e$, as is shown on Figure 5. Figure 5 shows the dependence of the maximum value of the relative sensitivity on the temporal resolution of the input data. One possible inference from this figure is that the dependence of R_s on $\delta t/t_e$ is not simply a power function. The curvature exhibited in the data on the log-log plot indicates that other variables may play a role. Another, more likely, explanation is that the relative sensitivity reaches a maximum at a value of $\delta t/t_e = 1.0$. This results from the testing methodology employed, which forces the rainfall intensity to vary between two bounds. As $\delta t/t_e$ increases beyond 1.0, the upper and lower limits of the hydrograph become approximately parallel, as in the case of $t_r \gg t_e$.

TWO-DIMENSIONAL RUNOFF SENSITIVITY TO RAINFALL TEMPORAL VARIABILITY

In this portion of the study, the CASC2D runoff model [*Julien and Saghafian* 1991] is used to examine the effects of temporal resolution of rainfall data on two-dimensional surface runoff from a natural watershed. Macks Creek watershed elevation data at 152 m resolution was used as input to the square grid CASC2D runoff model without infiltration or channel routing, as was previously discussed.

A series of simulations were performed to determine the relationship between rainfall intensity and time to equilibrium. Rainfall intensities from 1 to 100 mm/hour were used. The actual equilibrium discharge is an asymptotic value that the outflow discharge approaches as simulation time increases indefinitely. For this reason, 98.5% of the equilibrium discharge was selected to determine the time to equilibrium. The following time to equilibrium relation (12) was determined, with t_e in minutes and i in millimeters per hour:

$$t_e = 497.3i^{-0.428} \tag{12}$$

The two-dimensional methodology is very similar to that used in the one-dimensional analysis. The duration of rainfall t_r was predetermined as a fraction of the time to equilibrium t_e of the basin. As in the one-dimensional study, the precipitation intensity was applied uniformly in space to the entire watershed, while varied in time using a uniform distribution. The same coefficient of variation was chosen for this study on Macks Creek as was applied in the one-dimensional study. Values of t_r/t_e tested were 0.2, 0.4, 0.6, 0.8, 1.0, 1.2, 1.5, 2.0, and 5.0. Values of $\delta t/t_e$ tested included 0.005, 0.01, 0.04, 0.08, 0.16, 0.25, and 0.50.

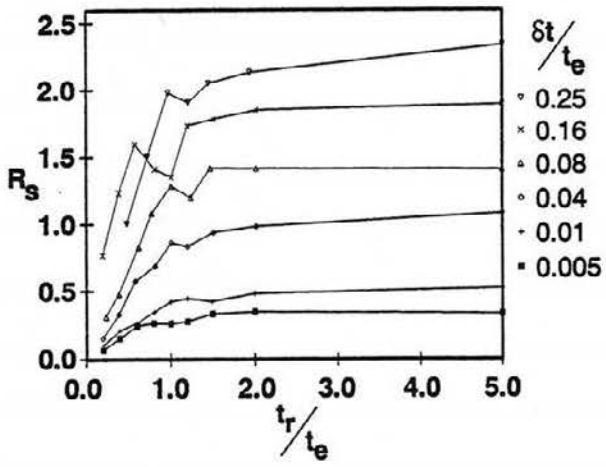

Fig. 6. Relative sensitivity to temporal variability for Macks Creek watershed.

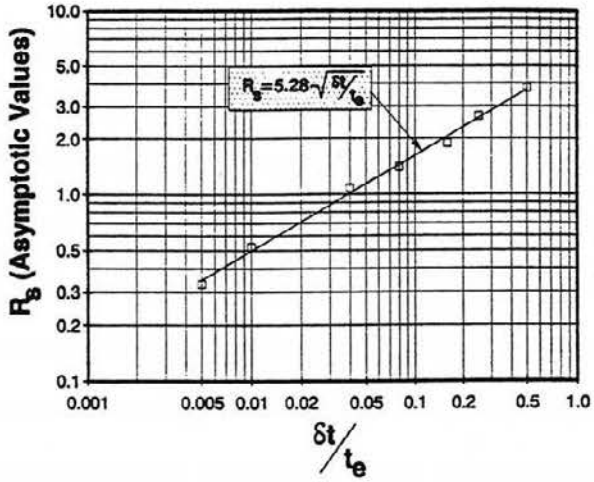

Fig. 7. Asymptotic relative sensitivity values for Macks Creek watershed at $t_r = 5.0t_e$ and various values of $\delta t/t_e$.

TWO-DIMENSIONAL TEMPORAL VARIABILITY RESULTS

The results of this study indicate that the two-dimensional runoff geometry is sensitive to the temporal resolution of precipitation intensity much like the one-dimensional runoff plane in the previous study. The primary difference is the magnitude of the sensitivity. Because of the relatively large time to equilibrium of the two-dimensional system, smaller values of $\delta t/t_e$ were tested on Macks Creek than in the one-dimensional simulations. The hydrograph envelopes produced are very similar to those shown in Figures 1*a* through 1*d*. The relative sensitivity, as shown in Figure 6, increases with both rainfall duration and temporal sampling interval.

From the data in Figure 6 it is apparent that the relative sensitivity to the precipitation data temporal resolution increases substantially as the storm duration increases. This increase is, however, limited. The greatest portion of the increase in relative sensitivity occurs before $t_r/t_e = 2.0$. Beyond this rainfall duration, the increase in R_s is minor. In fact, it appears as though an asymptote is reached as in the one-dimensional study. These asymptotic values represent the maximum relative sensitivity of the model for a given temporal resolution. The asymptotic values from all simulations with $t_r/t_e = 5.0$ are plotted in Figure 7. A regression of the data in Figure 7 show that the relative sensitivity of the Macks Creek watershed to the temporal sampling resolution of the precipitation input data for storms with duration at least 5 times the time to equilibrium is a power function. This function is shown on Figure 7.

CONCLUSIONS

Two-dimensional watershed sensitivity to rainfall spatial variability was explored using the CASC2D runoff model and elevation data from two watersheds. Spatially variable precipitation fields of identical statistics were generated for each watershed using a precipitation model [*Rodriguez-Iturbe and Eagleson*, 1987]. A total of 50 spatially variable rainfall fields were applied to each watershed using a Monte Carlo methodology, for increasing values of rainfall duration t_r/t_e. Results from two-dimensional simulations are compared with one-dimensional results published by *Julien and Moglen* [1990].

The sensitivities of one- and two-dimensional runoff surfaces to temporally varying rainfall were explored. A uniform probability density function was applied to simulate rainfall rate time series in both sets of simulations. The relative sensitivity R_s of both overland flow geometries was examined with respect to the temporal resolution of the rainfall data $\delta t/t_e$ and the duration of rainfall t_r/t_e. The relative sensitivity R_s in both one- and two-dimensional simulations was found to increase with t_r/t_e and $\delta t/t_e$. As t_r exceeds t_e, an asymptotic value of R_s is approached. Asymptotic relative sensitivity values increase approximately with $(\delta t/t_e)^{1/2}$ in both one- and two-dimensional simulations.

With regard to the results, the following conclusions are stated.

1. The duration of spatially varied rainfall on two impervious watersheds affects the magnitude of the relative sensitivity R_s. Simulations using CASC2D under statistically equivalent rainfall fields indicate that R_s decreases with increasing t_r. This finding confirms the one-dimensional simulation results by *Julien and Moglen* [1990]. Curves shown in Figure 3 of R_s versus t_r/t_e normalized by the R_s value at $t_r/t_e = 1.0$ show similarity in the effect of rainfall duration on R_s, independent of watershed size.

2. The effect of temporally variable rainfall on the relative sensitivity R_s of a one-dimensional overland flow plane increases as the temporal sampling interval δt and rainfall duration t_r increase. Asymptotic values of R_s for $t_r \gg t_e$ increase approximately with the square root of $\delta t/t_e$ as shown in Figure 5, for $\delta t/t_e < 1.0$.

3. The effect of the temporal resolution of rainfall data on the R_s for two-dimensional runoff is similar to that for the one-dimensional overland flow plane. Results in Figure 7 show that the asymptotic R_s increases proportionally to the square root of $\delta t/t_e$. The magnitude of R_s also increases with t_r and δt as in the one-dimensional case.

4. The duration of rainfall has opposite effects on the relative sensitivity of runoff to spatial and temporal rainfall variability. The relative sensitivity to spatial variability was found to decrease as the duration of rainfall increases, while

the relative sensitivity to temporal variability increases. Specifically, as the duration of rainfall increases beyond t_e, the relative spatial sensitivity becomes quite small, while the relative temporal sensitivity approaches a large asymptotic value, for all values of $\delta t/t_e \geq 0.01$.

NOTATION

C_v coefficient of variation, dimensionless.
L overland flow plane length, L.
Q total flow rate, L^3/t.
Q_e equilibrium total flow rate, L^3/t.
Q_p peak total flow rate, L^3/t.
R_h hydraulic radius, L.
R_s relative sensitivity, dimensionless.
S_f slope of energy grade line, dimensionless.
S_{fx} slope of energy grade line in the x direction, dimensionless.
S_{fy} slope of energy grade line in the y direction, dimensionless.
S_o slope of overland flow plane, dimensionless.
U two-dimensional velocity magnitude, L/t.
V^* dimensionless hydrograph envelope volume, dimensionless.
V_r volume of rainfall, L^3.
e excess rainfall rate, L/t.
f infiltration rate, L/t.
g acceleration due to gravity, L^2/t.
h overland flow depth, L.
i rainfall intensity, L/t.
$\bar{i}$ rainfall intensity averaged over time, L/t.
n Manning's roughness coefficient.
q unit discharge, L^2/t.
t_e time to equilibrium, t.
t_p time of hydrograph peak discharge, t.
t_r duration of rainfall, t.
u flow velocity in x direction, L/t.
$\bar{u}$ average flow velocity, L/t.
v flow velocity in y direction, L/t.
α empirical coefficient for stage-discharge relation.
β empirical exponent for stage-discharge relation.
δt temporal sampling resolution, t.
μ mean value.
σ standard deviation.
Δt computational time step, t.
ΔV hydrograph envelope volume, L^3.
ϕ variation factor, dimensionless.

Acknowledgments. This study was completed by the Hydrologic Modeling Group of the Center for Excellence in Geosciences at Colorado State University. Financial support by the U.S. Army Research Office (grant ARO/DAAL 03-86-0175) is gratefully acknowledged. We are thankful to Glenn E. Moglen for his initial work on one-dimensional spatial sensitivity. Bahram Saghafian of Colorado State University provided assistance with CASC2D. W. F. Krajewski from the Department of Civil and Environmental Engineering at The University of Iowa provided guidance with the Rodriguez-Iturbe and Eagleson rainfall model. Macks Creek data was provided by the U.S. Department of Agriculture, Agricultural Research Service, in Boise, Idaho. Technical assistance with the Taylor Arroyo data was provided by William Doe of the U.S. Military Academy.

REFERENCES

De St. Venant, B., Theory of unsteady water flow, with application to river floods and to propagation of tides in river channels, English Transl., *Rep. 49-g*, Waterw. Exp. Stat., U.S. Army Corps of Eng., Vicksburg, Miss., 1949.

Diskin, M. H., G. Wyseure, and J. Feyen, Application of a cell model to the Bellebeek watershed, *Nord. Hydrol., 15*, 25–38, 1984.

Erichsen, B., and K. Nordseth, Runoff models—Do they tell what actually happens!, *Nord. Hydrol., 15*, 273–282, 1984.

Green, W. H., and G. A. Ampt, Studies on soil physics, 1, The flow of air and water through soils, *J. Agric. Sci., 4*, 1–24, 1911.

Hjelmfelt, A. T., Jr., Overland flow from time-distributed rainfall, *J. Hydraul. Div. Am. Soc. Civ. Eng., HY2*, 227–238, 1981.

James, W. P., and K. W. Kim, A distributed dynamic watershed model, *Water Resour. Bull., 26*(4), 587–596, 1990.

Jensen, M., Runoff patterns and peak flows from moving block rains based on a linear time-area curve, *Nord. Hydrol., 15*, 155–168, 1984.

Julien, P. Y., and G. E. Moglen, Similarity and length scale for spatially varied overland flow, *Water Resour. Res., 26*(8), 1819–1832, 1990.

Julien, P. Y., and B. Saghafian, CASC2D users manual—A two-dimensional watershed rainfall-runoff model, *Civ. Eng. Rep. CER90-91PYJ-BS-12*, 66 pp., Colo. State Univ., Fort Collins, 1991.

Julien, P. Y., G. E. Moglen, and G. U. Sunada, CASC users manual-A finite element model for spatially varied overland flow simulation, *Cent. for Geosci. Rep. CER 87-88 GEO7*, Colo. State Univ., Fort Collins, September 1988.

Krajewski, W. F., V. Lakshmi, K. P. Georgakakos, and S. C. Jain, A Monte Carlo study of rainfall sampling effect on a distributed catchment model, *Water Resour. Res., 27*(1), 119–128, 1991.

Niemczynowicz, J., Investigation of the influence of rainfall movement on runoff hydrographs, *Nord. Hydrol., 15*, 57–84, 1984.

Ogden, F. L., Two-dimensional runoff modeling with weather radar data, Ph.D. dissertation, 211 pp., Colo. State Univ., Fort Collins, 1992.

Ponce, M. V., and R. M. Li, Overview of flood routing methods, in *Analysis Of Watershed and River Systems*, edited by D. B. Simons and R. M. Li, Colorado State University, Fort Collins, 1979.

Ponce, M. V., R. M. Li, and D. B. Simons, Applicability of the kinematic and diffusion models, *J. Hydaul. Div. Am. Soc. Civ. Eng., 104*(HY3), 353–360, 1978.

Richardson, J. R., The effect of moving rainstorms on overland flow using one-dimensional finite elements, Ph.D. dissertation, 239 pp., Colo. State Univ., Fort Collins, 1989.

Rodriguez-Iturbe, I., and P. S. Eagleson, Mathematical models of rainstorm events in space and time, *Water Resour. Res., 23*(1), 181–190, 1987.

Storm, B., and K. H. Jensen, Experience with field testings of SHE on research catchments, *Nord. Hydrol., 15*, 283–294, 1984.

Woo, D., and E. F. Brater, Spatially varied flow from controlled rainfall, *J. Hydraul. Div. Am. Soc. Civ. Eng., 88*(HY6), 31–56, 1962.

Wood, E. F., M. Sivapalan, K. Bevin, and L. Band, Effects of spatial variability and scale with implications to hydrologic modeling, *J. Hydrol., 102*, 29–48, 1988.

Yen, B. C., and V. T. Chow, A study of surface runoff due to moving rainstorms, *Hydrol. Eng. Ser. Rep. 17*, Dep. of Civ. Eng., Univ. of Ill., Urbana, June 1968.

P. Y. Julien, Department of Civil Engineering, Colorado State University, Fort Collins, CO 80523.

F. L. Ogden, Iowa Institute of Hydraulic Research, The University of Iowa, Iowa City, IA 52242.

(Received September 11, 1992;
revised March 8, 1993;
accepted April 2, 1993.)

ELSEVIER

Journal of Hydrology 158 (1994) 1–18

Journal of Hydrology

[1]

Runoff model sensitivity to radar rainfall resolution

Fred L. Ogden*,[a], Pierre Y. Julien[b]

[a]*Iowa Institute of Hydraulic Research, University of Iowa, Iowa City, IA 52242, USA*
[b]*Department of Civil Engineering, Colorado State University, Fort Collins, CO 80523, USA*

(Received 27 January 1993; revision accepted 16 January 1994)

Abstract

Rainfall rates estimated from polarimetric weather radar measurements of a convective rainstorm are used as input to a two-dimensional physically based rainfall–runoff model. The correlation length of the input rainfall field L_S is 2.3 km. Runoff simulations are performed on two semi-arid watersheds covering 32 km^2 and 121 km^2 at basin data grid sizes L_M of 125 m and 200 m, respectively. The characteristic basin length scale L_W is taken as the square root of the watershed area. Rainfall data at resolutions L_R of 1, 2, 3, 4, 6 and 8 km serve as model input to determine the effect of precipitation data spatial resolution on computed outflow hydrographs. Two dimensionless length parameters are identified which describe the similarity of the effect of rainfall data aggregation on both basins. The first parameter, L_R/L_S, describes 'storm smearing', and the second parameter, L_R/L_W, describes 'watershed smearing'. Results from simulations without infiltration show storm smearing occurring as $L_R \rightarrow L_S$. Watershed smearing causes more significant deviations from simulations using the finest-resolution data when L_R/L_W exceeds 0.4. Results with infiltration reveal that excess rainfall volumes decrease with increasing L_R/L_W. Additionally, excess rainfall volumes do not converge as L_R/L_W is decreased to the practical lower limit provided by contemporary weather radars, which is of the order of 1 km.

1. Introduction

The NEXRAD weather radar network being installed in the USA will provide quantitative digital estimates of the spatial distribution of rainfall. Approximately 160 NEXRAD WSR-88D radars are being deployed throughout the USA and at selected overseas sites (Klazura and Imy, 1993). The radar network will observe approximately 95% of the 48 conterminous USA at beam heights less than 3000 m

* Corresponding author (formerly at Colorado State University).

0022-1694/94/$07.00 © 1994 – Elsevier Science B.V. All rights reserved
SSDI 0022-1694(94)02462-K

List of Symbols

A	Area of watershed (L^2)
K_{DP}	Specific differential propagation phase shift (deg L^{-1})
L_M	Runoff model raster grid size (L)
L_R	Precipitation data grid size (L)
L_S	Rainfall correlation length (L)
L_W	Watershed characteristic length ($= A^{1/2}$) (L)
M_d	Soil moisture deficit
n	Manning roughness coefficient ($L^{1/3}T$)
Q_p	Peak total flow rate ($L^3 t^{-1}$)
$\bar{Q}_p$	Mean normalized peak total flow rate
Q_p^*	Normalized peak total flow rate
R	Rainfall rate (LT^{-1})
S_{Q_p}	Standard deviation of normalized peak outflow
S_{V_o}	Standard deviation of normalized outflow volume
S_{V_r}	Standard deviation of normalized rainfall volume
V_o	Volume of outflow (L^3)
$\bar{V}_o$	Mean normalized outflow volume
V_o^*	Normalized outflow volume
V_r	Volume of rainfall (L^3)
$\bar{V}_r$	Mean normalized rainfall volume
V_r^*	Normalized rainfall volume
Z_{DR}	Differential reflectivity
Z_H	Radar reflectivity factor ($L^6 L^{-3}$)

Greek letters

ϕ_{DP}	Differential propagation phase shift (deg)

above ground level. NEXRAD radars record the spatial distribution of the radar reflectivity factor Z at resolutions ranging from 1 to 4 km, at 15 min temporal resolution. The full hydrologic application of these data requires hydrologic models capable of accepting spatially distributed rainfall. Models of this type, referred to as 'distributed' hydrologic models, are typically physically based and operate on sub-catchments or raster elements which are considerably smaller than the watershed under study.

Given the tremendous quantity of data collected by each NEXRAD site over the course of a year, there is a need to determine if the data may be aggregated and still retain usefulness for hydrologic modeling (National Research Council, 1991, p. 267). Temporal and spatial aggregation tend to reduce rainfall gradients. Physically based rainfall–runoff models are sensitive to the rainfall rate, particularly in determining excess rainfall. The purpose of this study is to examine the sensitivity of a physically based distributed watershed rainfall–runoff model to the spatial resolution of radar rainfall input data. The results of this study have implications for the use of radar-estimated rainfall in real-time flood forecasting, physically based flood frequency analysis using historical radar data, and issues of scale in the rainfall–runoff modeling process.

2. Review of literature

Several recent studies have addressed the issue of remotely sensed precipitation data resolution for watershed modeling. Kouwen and Garland (1989) examined the effect of changing radar rainfall data spatial resolution on a one-dimensional composite square grid distributed parameter watershed model. A 3250 km^2 watershed was simulated using the SIMPLE (Kouwen, 1986) watershed model, with rainfall data grid sizes of 2 km × 2 km and 10 km × 10 km. A total of 30–50 precipitation input grid cells over the watershed were found to model the precipitation field adequately for flood forecasting purposes. A maximum radar resolution of 10 km × 10 km was sufficient for modeling floods produced by either thunderstorms or frontal systems.

Ogden and Turk (1991) examined the effect of radar resolution on the runoff from the 32.2 km^2 Macks Creek, Idaho, watershed using a two-dimensional surface runoff model. Single-parameter (Z) radar data from one storm were gridded at 152 m resolution with a reflectivity–rainfall (Z–R) relationship and applied at successively coarser resolutions. From simulations with only one storm the following conclusions were reached: as the radar grid size was coarsened from 152 m to 5 km, the magnitudes of the peak outflow and outflow volume decreased, whereas the time to peak increased. Hail contamination of the reflectivity signal was noted as a source of unrealistically high rainfall rates.

A Monte Carlo technique was used to study the effect of rain-gauge sampling resolution on a distributed watershed model by Krajewski et al. (1991). The distributed model consisted of a series of one-dimensional distributed stream tube subcatchments, and was based on the kinematic wave overland flow approximation. The findings of this study indicate that model response is more sensitive to temporal resolution than spatial resolution of the input precipitation data. The performance of the distributed model was compared with that of a lumped model. The results indicated that lumped parameter models consistently underestimate peak flows. Krajewski et al. concluded that a two-dimensional square grid model would be better suited to modeling the problem of optimal spatial and temporal resolution.

Dual polarization radar data (Z_H, Z_{DR}) were applied with a linear runoff model by Seliga et al. (1991) to examine the model sensitivity to temporal and spatial variation in precipitation intensity. The runoff model combined elements of unit hydrograph theory and Soil Conservation Service (SCS) curve number analysis. The resolution of the input data, reflected by the size and number of model hydrologic response units (HRUs), was also examined for effect on the runoff model. The results indicated that the watershed response was greatly influenced by the available spatial resolution of the precipitation data, as well as the size of the HRUs used in the model. Seliga et al. concluded that an HRU size of approximately 5 km^2 is adequate. Additionally, the findings indicate that as the HRU size is decreased the magnitudes of the peak outflows do not converge.

The value of weather radar in flood forecasting was examined by Pessoa et al. (1993), in a sensitivity analysis of the distributed basin simulation (DBS) distributed hydrologic model (Cabral et al., 1990) of the 840 km^2 Sieve River basin in Italy. Weather radar data from the MIT C-band radar was transposed and applied to the

Sieve model. The parameters varied include radar data temporal and spatial resolution, the $Z-R$ relationship, and radar signal quantization. The model was found to be most sensitive to the spatial resolution of the radar data, and relatively insensitive to the temporal resolution and data quantization.

Physically based rainfall–runoff model sensitivity to rainfall temporal and spatial variability was examined by Ogden and Julien (1993). The sensitivity of impervious watersheds to the spatial variability of rainfall decreases, inversely with time, to a small value after equilibrium conditions are reached. The opposite is true for rainfall temporal variability, as the sensitivity increases toward an asymptotic value after the time to equilibrium.

3. Objectives

This paper provides a basis for the discussion of radar data spatial resolution requirements for physically based hydrologic modeling of small basins covering less than 150 km^2. The specific objectives of this study are the following: (1) to analyze rainfall data spatial resolution, in the context of length scales, to identify dimensionless similarity parameters which describe conditions where rainfall grid size affects the response of surface runoff models; (2) to examine impervious runoff simulations to determine the effects of precipitation data spatial resolution on peak discharge and rainfall–runoff volumes in terms of dimensionless similarity parameters; (3) to examine runoff simulations of pervious basins to determine the effect of precipitation data resolution on the magnitude of the computed peak discharge, and runoff model sensitivity to rainfall data grid size for various degrees of initial soil saturation.

4. Study watersheds and surface runoff model

The CASC2D (Julien and Saghafian, 1991) watershed rainfall–runoff model was used in this study. CASC2D is a two-dimensional, raster-based, distributed hydrologic model. Overland flow routing is based on a two-dimensional explicit solution of the diffusive wave form of the de St. Venant equations, with friction slopes calculated by the Manning equation. Surface slopes are calculated from digital elevation model (DEM) data. Overland flow is routed in two orthogonal directions within each raster grid element. Channel routing is performed by an explicit diffusive wave formulation.

The three-parameter Green and Ampt (1911) method is used in CASC2D to calculate infiltration rates. The three Green and Ampt parameters (hydraulic conductivity at natural saturation, capillary pressure head at the wetting front, and the soil moisture deficit) can be measured in the field. The head of water on the soil surface was neglected as being much smaller than the capillary pressure head. Soil characteristic data, in the form of SCS textural classifications, were used to define the infiltration parameters of the soils on both Macks Creek and Taylor Arroyo, using the data of Rawls et al. (1983). There are provisions within the model to account for interception and detention storage.

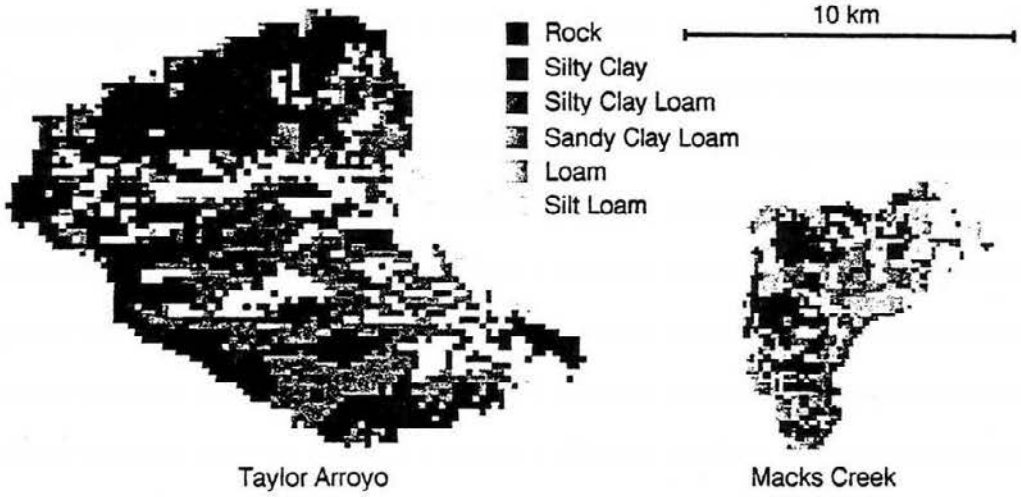

Fig. 1. Soil type maps for Macks Creek and Taylor Arroyo (to scale).

The two semi-arid watersheds selected for this study are the 32 km^2 Macks Creek watershed in southwestern Idaho, and the 121 km^2 Taylor Arroyo watershed in southeastern Colorado. Macks Creek has an average slope of 9.4%, with slopes in some regions in excess of 30%. Macks Creek is an ephemeral stream with flashy response to intense rainstorms. The larger Taylor Arroyo watershed is moderately pervious and has an average slope of 1.6%. Both watersheds can be appropriately modeled using Hortonian runoff production mechanisms. The Macks Creek and Taylor Arroyo elevation data were input to CASC2D at resolutions L_M of 125 m and 200 m, respectively. A watershed characteristic length L_W is taken as the square root of the watershed area. The L_W values for Macks Creek and Taylor Arroyo are 5.7 km and 11.0 km, respectively. The calibration of CASC2D on Macks Creek was performed by Saghafian (1992), and on Taylor Arroyo by Doe (1992). The spatially distributed soil types on Macks Creek and Taylor Arroyo are shown to scale in Fig. 1. The corresponding Green and Ampt soil parameter values are listed in Table 1.

The starting conditions used in all impervious simulations were identical: no surface water, and a constant value of Mannings n of 0.04 over the entire watershed. In simulations with infiltration, the initial soil moisture deficit was varied, and all other soil and basin characteristics remained unchanged. For each

Table 1
Green and Ampt soil parameter values for the soil texture classes shown in Fig. 1

Soil texture class	Total porosity ($cm^3\ cm^{-3}$)	Effective porosity ($cm^3\ cm^{-3}$)	Wetting front capillary pressure (cm)	Hydraulic conductivity ($cm\ h^{-1}$)
Silt loam	0.501	0.486	16.68	0.65
Loam	0.463	0.434	8.89	0.34
Sandy clay loam	0.398	0.330	21.85	0.15
Silty clay loam	0.471	0.432	27.30	0.10
Silty clay	0.479	0.423	29.22	0.05
Rock	–	–	–	0.00

simulation the entire outflow hydrograph was saved in an output file, with the time to peak, peak discharge, total outflow volume, and total rainfall volume in a separate summary file.

5. Advances in radar rainfall estimates

This study required a high-quality spatially distributed rainfall data set. Recent polarimetric weather radar techniques offer an opportunity to record spatially distributed rainfall data with unprecedented accuracy. The weather radar data used in this study were recorded by the CSU-CHILL radar facility, which is located near Greeley, Colorado, and jointly funded by Colorado State University and the National Science Foundation. The radar is a dual linearly polarized coherent radar which operates at 2.750 GHz, corresponding to a wavelength of 10.7 cm in the S band. The beamwidth of the 8 m diameter antenna is approximately 1.0°. Attenuation does not affect S-band weather radars, even in the heaviest rainfall, making them ideal for weather observation. The radar transmits an average power of 1 kW with peak power during transmit pulses of 1 MW, and can measure Doppler velocities.

The dual polarization capabilities of the CSU-CHILL radar allow observation of precipitation in two orthogonal polarization states. The recorded radar observables include the reflectivity factor in horizontal polarization Z_H, the differential reflectivity Z_{DR} (Seliga and Bringi, 1976), and the differential propagation phase ϕ_{DP} (Sachidananda and Zrnic, 1986). The reflectivity factor, Z_H, is an integrated measure of the sixth power of the raindrop size distribution (RSD) over the entire pulse volume. The rainfall rate may be estimated from Z_H by assuming the form and parameters of the RSD and a raindrop fall speed relationship. Such Z–R relationships are often empirically derived. One shortcoming of the use of the reflectivity factor in rain rate estimation is the heavy weighting of the largest particles in the radar pulse volume. Wet hail, for instance, can completely dominate the return signal and mask any useful information from liquid-phase hydrometeors.

Dual linearly polarized radars measure the reflectivity factor in two orthogonal (horizontal and vertical) polarizations, Z_H and Z_V. Differential reflectivity, Z_{DR}, arises because raindrops tend to flatten in their vertical dimension as they grow and fall. The differential reflectivity is given by $Z_{DR} = Z_H - Z_V$, providing an indirect indicator of raindrop oblateness, and therefore size. Using an assumed RSD, Z_{DR} will provide an estimate of one of the RSD parameters. When combined in a relationship with Z_H, a more accurate estimate of the rainfall rate may be obtained. Another appealing aspect of Z_{DR} is in hail identification. Hail particles tend to be nearly spherical, and tumble as they fall. Therefore, the differential reflectivity will tend to be near zero in high-reflectivity regions with hail present, and large if no hail is present. However, if hail is present within a pulse volume, rain rate relationships based on either Z_H or Z_{DR} cannot be used to estimate the rainfall rate (Jameson, 1991), and another method must be applied.

The refractive indices of the atmosphere and of liquid- and ice-phase hydrometeors

are different. As the electromagnetic radiation emitted by the radar passes through a hydrometeor, its speed is changed. Therefore, upon emergence from the hydrometeor, its phase will be lagged somewhat relative to radiation which did not pass through it. As liquid hydrometeors tend to flatten as they become larger, there is a difference between the phase shift of radiation at horizontal and vertical polarization. This differential phase shift, ϕ_{DP}, is an integrated measure of the quantity of liquid water over the entire propagation path, that is, from radar to target and back to the radar. The specific differential propagation phase, K_{DP}, is defined as one-half the spatial derivative of ϕ_{DP}. The parameter K_{DP} is useful in hydrometeorology because it is insensitive to hail, independent of the reflectivity factor, and nearly linearly proportional to the rainfall rate (Sachidananda and Zrnic, 1986).

The expected accuracy of rainfall rates determined using polarimetric techniques was examined by Chandrasekar et al. (1993). In simulations without hail, it was found that the fractional standard deviation (FSD) of rainfall rate estimated from Z_H is approximately 45% for rain rates less than 10 mm h^{-1}, increasing to 55% at 150 mm h^{-1}. The FSD of rain rate estimated with Z_H and Z_{DR} was 60% for rain rates less than 10 mm h^{-1}, and approximately 25% for higher rain rates. Using K_{DP} as the sole rain rate estimator, the FSD was observed to decrease from approximately 80% at 20 mm h^{-1} to 25% at 80 mm h^{-1} and 15% at 200 mm h^{-1}.

The radar data used in this study were recorded on 3 June 1991, and covered the entire lifetime of a convective squall line between 12 and 60 km from the radar. The storm began at approximately 12:00 h MDT. Surface heating and local instability initiated convective activity. The uplifting air created a convergence line along which the most intense thunderstorm cells were located. Data were recorded for 2 h 15 min at 5 min increments. The radar was operated in a volume scan mode, with four elevation angles per volume scan. There was significant beam blockage at the lowest elevation angle scan (0.5°), so the next highest elevation angle (1.6°) was used to estimate the rainfall rates. Ground observers noted large quantities of pea-size hail from this storm.

The following polarimetric algorithm was used to estimate the rainfall rates. In high-reflectivity regions $Z_H > 40$ dBZ, the K_{DP} relationship of Chandrasekar et al. (1990) was used to estimate the rainfall rate. In all other instances, the combined Z_H and Z_{DR} relationship of Chandrasekar et al. (1990) was used, unless $Z_{DR} < 0$. In such cases, rainfall was estimated with Z_H via the Austin (1987) Z–R relationship.

The rainfall fields were converted from radar conical coordinates to rectangular coordinates by interpolation to 1 km × 1 km grid size. Figs. 2 and 3 show multi-parameter estimated rainfall rates within the 80 km × 80 km square data domain, at 12:48 h MDT and 13:56 h MDT, respectively. The radar is located at the origin of the plots. The scale of individual storm cells is approximately 4 km–10 km, with an average value near 8 km. The rainfall data from the 27 radar scans were processed to determine the correlation length. Fitting the covariance data with one- and two-parameter exponential models, the correlation length, L_S, was determined to be 2.3 km by both covariance models.

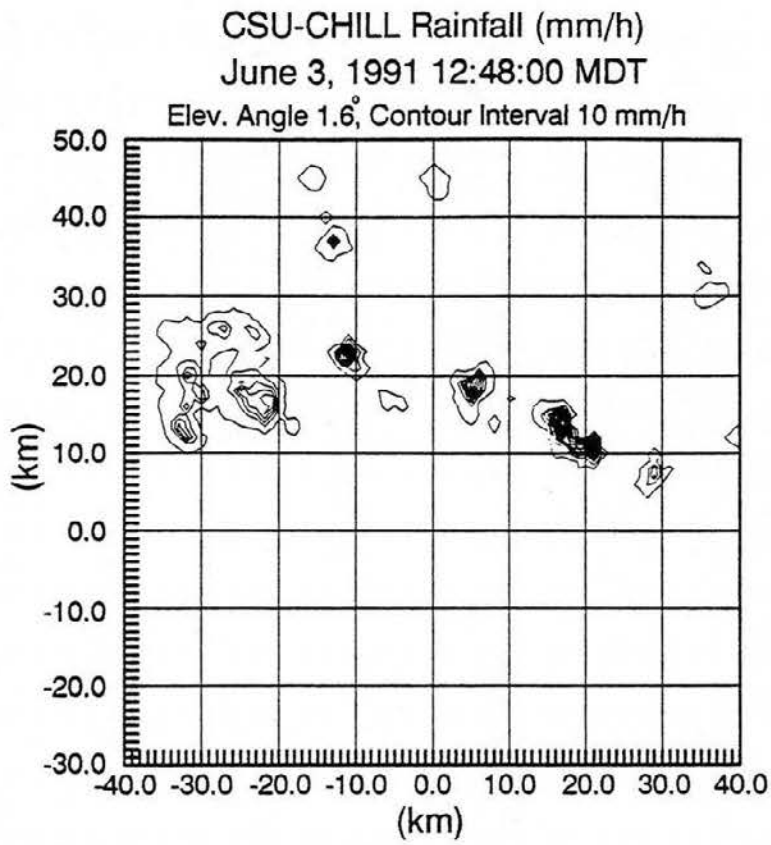

Fig. 2. Multi-parameter estimated rainfall at 12:48:00 MDT.

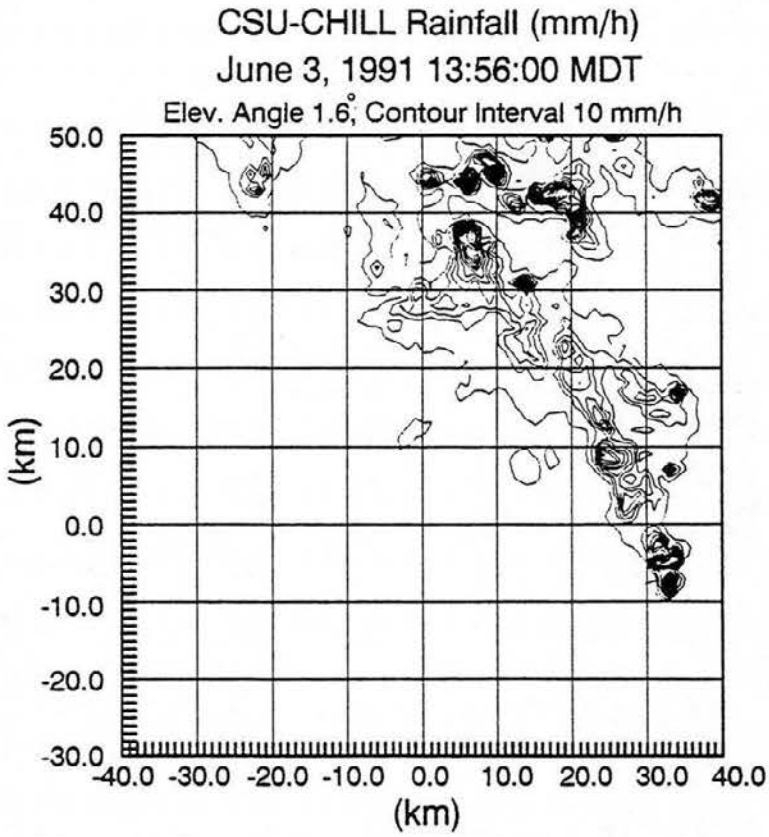

Fig. 3. Multi-parameter estimated rainfall at 13:56:00 MDT.

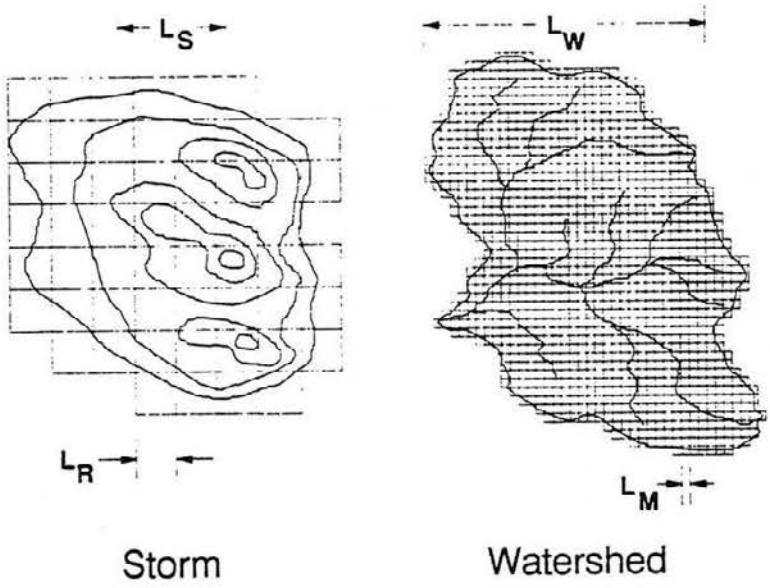

Fig. 4. Definition sketch of relevant length parameters—L_S, L_R, L_W and L_M.

6. Radar data resolution and length scales

Several studies presented in the literature review examined the effect of radar-rainfall data resolution on distributed hydrologic models, without general consideration of length scales. The discussion of length scales presented here represents a new development on this topic. Consider a convective rainstorm passing over a small (less than 150 km^2) watershed as shown in Fig. 4. There are five length parameters associated with this situation in the context of raster-based hydrologic models: the correlation length of the rainfall, L_S; the grid size of the rainfall data, L_R; the characteristic length of the watershed, L_W; the runoff model grid size, L_M; the correlation length of watershed characteristics. The radar and model resolution parameters L_R and L_M are defined by the modeler, whereas the basin and storm size parameters L_W and L_S are determined solely by the site and storm under study. In addition, it is important to note that the correlation length for watershed characteristics is of the order of tens to hundreds of meters, whereas the spatial correlation length for rainfall, L_S, is hundreds to thousands of meters.

There are three conditions which conceptually result in ideal physically based distributed hydrologic modeling. The first is $L_M \ll L_W$, so the basin is subdivided into sufficiently small grid elements to describe the spatial variability of basin characteristics. The second condition is $L_R \ll L_S$, which insures preservation of the spatial gradients of rainfall, particularly for smaller, convective rainstorms. The third requirement is that $L_R \leqslant L_M$, such that rainfall is placed in the correct watershed grid cell. The third strict requirement is most difficult to satisfy, as the practical minimum spatial resolution (approximately 1 km) of radar rainfall estimates cannot satisfy the third condition given the first.

The following analysis considers an ideal physically based hydrologic model, from which the deviations from ideal storm resolution and model input can be examined. Deviations from ideal modeling conditions are typically caused by input smearing,

which occurs as a result of spatial averaging over increasingly large areas. In this study, we focus on two distinct types of input smearing—storm smearing and watershed smearing.

Accepting that the third condition noted above must be relaxed, two surrogate parameters are used in substitution. The first parameter, L_R/L_S, describes storm smearing, and the second parameter, L_R/L_W, describes watershed smearing. Storm smearing occurs when the rainfall data length scale approaches or exceeds the rainfall correlation length, $L_R \rightarrow L_S$, which tends to decrease rain rates in high-intensity regions and increase rain rates adjacent in low-intensity regions, effectively reducing rain rate gradients. The reduction in rainfall intensity gradients owing to storm smearing is independent of basin size. Watershed smearing occurs when $L_R \rightarrow L_W$, and increases the uncertainty of the location of rainfall, which can result in the transfer of rainfall across basin boundaries. Watershed smearing is more likely to occur for smaller basins such as Macks Creek, at smaller values of L_R, than for larger basins such as Taylor Arroyo.

7. Radar resolution analysis

The effects of radar rainfall data grid size on surface runoff modeling for convective rainstorms on small watersheds (less than 150 km^2) are expected to result from storm smearing and watershed smearing. It is hypothesized that watershed smearing can be analyzed as a function of L_R/L_W describing the ratio of rainfall to basin length scales. As $L_R > L_S$ and $L_R \rightarrow L_W$, model error will have sources in both storm and watershed smearing.

The simulation method employed involves the transposition of radar rainfall data recorded in northern Colorado over two basins—one in southeastern Colorado, and one in southwestern Idaho. Given the large extent of the radar coverage (6400 km^2) compared with the areas of the two watersheds (e.g. 121 km^2 for the larger Taylor Arroyo), the precipitation field was subdivided into 50 independent subsets for Macks Creek and 40 independent subsets for Taylor Arroyo. Conceptually, a subset is a location for each basin within the large radar data domain as the storm evolves and passes over. Fig. 5 shows the locations within the 80 km × 80 km radar data domain where Macks Creek was positioned. Each location of Macks Creek in Fig. 5 is separated by a minimum distance of 4 km, which is greater than the correlation length L_S of the rainstorm, insuring reasonable independence between adjacent simulations. The rainfall fields are aggregated from the finest resolution by arithmetically averaging the data into larger grid cells.

The results from simulations with the finest resolution ($L_R = 1$ km) are the best available outflow calculations, and are used as reference outflow hydrographs. First, the results from all simulations with the tested input data resolutions: $L_R = 2, 3, 4, 6,$ and 8 km, at one particular watershed location j, are normalized by the corresponding outflow variable obtained with rainfall data for the smallest grid size (1 km). The normalized peak discharge for any rainfall data grid size L_R and simulation j is denoted as $Q_p^*(L_R, j)$, and is calculated using the equation

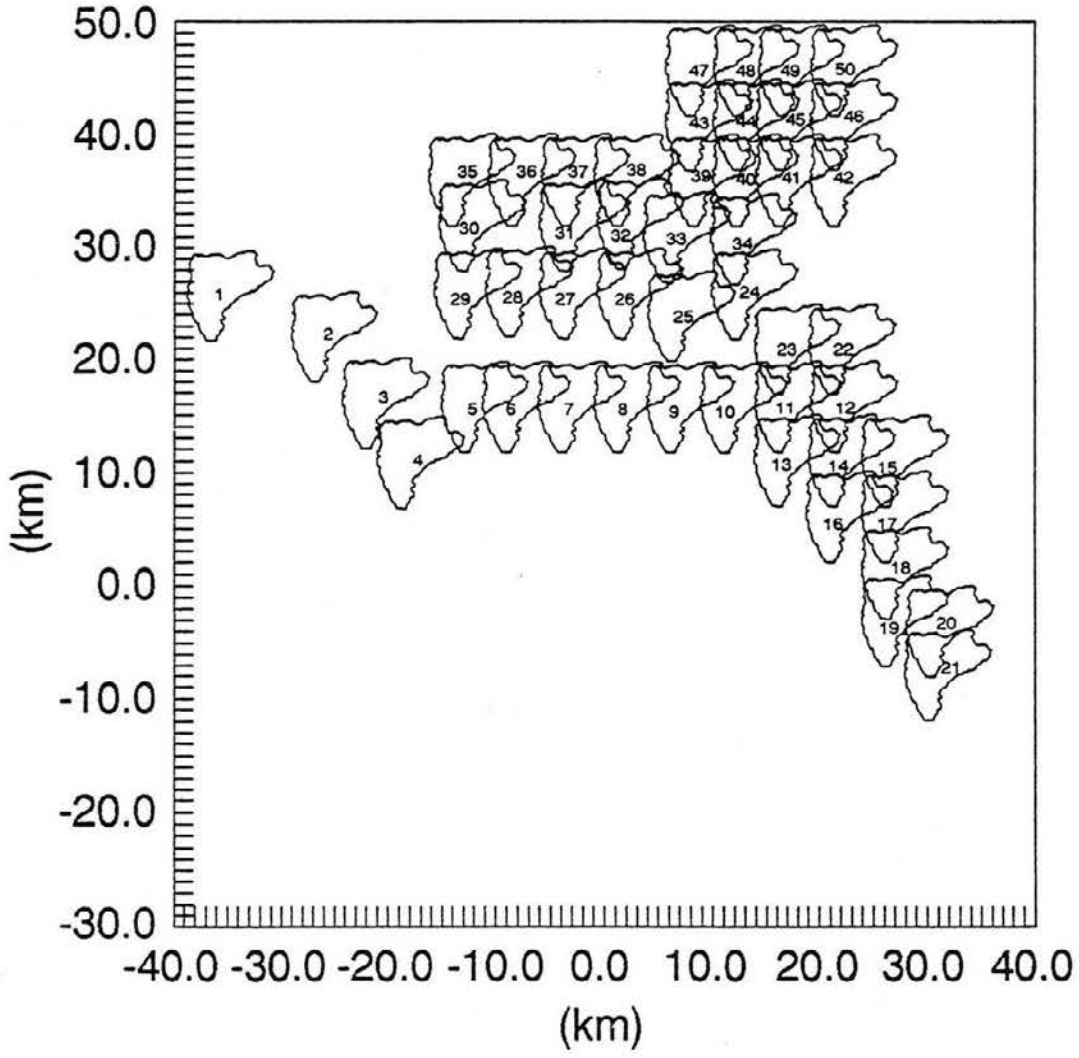

Fig. 5. Macks Creek test locations within the radar data domain.

$$Q_p^*(L_R,j) = \frac{Q_p(L_R,j)}{Q_p(1,j)} \tag{1}$$

Similarly, the normalized outflow and rainfall volumes for the jth simulation are calculated with

$$V_o^*(L_R,j) = \frac{V_o(L_R,j)}{V_o(1,j)} \tag{2}$$

and

$$V_r^*(L_R,j) = \frac{V_r(L_R,j)}{V_r(1,j)} \tag{3}$$

The mean normalized peak discharge, runoff volume, and rainfall volume over N simulations, where N is 50 for Macks Creek and 40 for Taylor Arroyo, are calculated

using

$$\bar{Q}_p(L_R) = \frac{1}{N}\sum_{j=1}^{N} Q_p^*(L_R,j) \tag{4}$$

$$\bar{V}_o(L_R) = \frac{1}{N}\sum_{j=1}^{N} V_o^*(L_R,j) \tag{5}$$

and

$$\bar{V}_r(L_R) = \frac{1}{N}\sum_{j=1}^{N} V_r^*(L_R,j) \tag{6}$$

The standard deviation of the normalized outflow variables for each tested L_R are determined using the following equations for the peak discharge, runoff volume and rainfall volume, respectively:

$$S_{Q_p}(L_R) = \left\{\frac{1}{N-1}\sum_{j=1}^{N}[\bar{Q}_p(L_R) - Q_p^*(L_R,j)]^2\right\}^{1/2} \tag{7}$$

$$S_{V_o}(L_R) = \left\{\frac{1}{N-1}\sum_{j=1}^{N}[\bar{V}_o(L_R) - V_o^*(L_R,j)]^2\right\}^{1/2} \tag{8}$$

$$S_{V_r}(L_R) = \left\{\frac{1}{N-1}\sum_{j=1}^{N}[\bar{V}_r(L_R) - V_r^*(L_R,j)]^2\right\}^{1/2} \tag{9}$$

This analysis technique produces one mean normalized outflow variable on Macks Creek and Taylor Arroyo, respectively, for each L_R tested over N simulations. The mean and standard deviation of these normalized outflow variables are used to identify trends and variability in the normalized outflow characteristics as a function of radar data resolution.

The effect of rainfall rate changes on surface runoff are examined for two types of simulations: (1) impervious basins for which the surface runoff volume will be maintained despite rain rate reductions in high-intensity regions; (2) pervious basins for which the surface runoff volume will decrease as a result of increased infiltration volume from reduced high-intensity rainfall regions.

8. Results without infiltration

The CASC2D outflow summary data for simulations without infiltration are used in the analysis. The rainfall volume is the primary indicator of watershed smearing. The mean $\bar{V}_r$ and standard deviation S_{V_r} of the normalized rainfall volume vs. the watershed smearing parameter L_R/L_W for both Macks Creek and Taylor Arroyo, are plotted in Fig. 6. There is little change in the storm total rainfall volume for

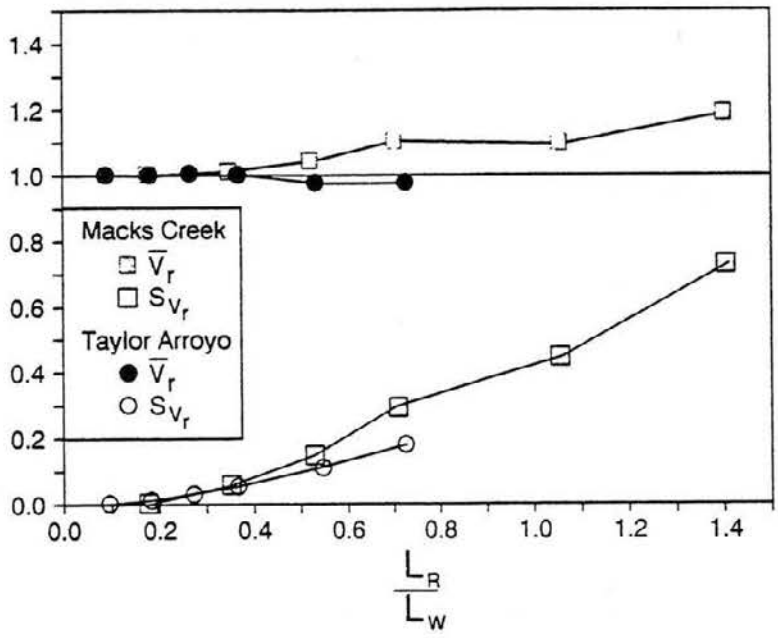

Fig. 6. Watershed smearing effect on rainfall volume for 50 storms on Macks Creek and 40 storms on Taylor Arroyo, without infiltration.

$L_R/L_W < 0.4$ for both basins. As L_R/L_W increases beyond 0.4, there is an increase in rainfall volume, V_r, for the smaller Macks Creek, and a decrease in V_r for Taylor Arroyo. The increase in the mean storm rainfall is larger for Macks Creek than the decrease observed for Taylor Arroyo. The standard deviation of normalized rainfall volume is also appreciably higher for the smaller Macks Creek basin.

It is impossible to separate the effects of watershed smearing and storm smearing in this analysis of the outflow variables because as $L_R \rightarrow L_S$ (storm smearing), L_R also approaches L_W (watershed smearing) for these small basins. However, storm smearing should occur first because $L_S < L_W$ for both basins. The relative magnitudes of the separate effects of input and storm smearing can be judged by comparing the deviation of the normalized outflow variables with decreasing resolution to the corresponding changes in rainfall volume. The mean, $\overline{Q}_p$, and standard deviation, S_{Q_p}, of the normalized peak discharge vs. the storm smearing parameter L_R/L_S for both watersheds are plotted in Fig. 7. The mean and standard deviation of the normalized outflow volume, $\overline{V}_o$, is similarly plotted in Fig. 8. Figs. 7 and 8 show a deviation in the normalized outflow variables $\overline{Q}_p$ and $\overline{V}_o$ from the simulations with the finest resolution, at the first level of aggregation, $L_R = 2$ km. The deviation of the normalized $\overline{Q}_p$ and $\overline{V}_o$ values from those in the simulations with the finest resolution is initially small. The rate of deviation increases is more substantial for both $\overline{Q}_p$ and $\overline{V}_o$ at values of L_R/L_S greater than 0.8 and 1.7 on Macks Creek and Taylor Arroyo, respectively. These L_R/L_S values correspond to $L_R/L_W = 0.4$ on both watersheds, indicating that watershed smearing is beginning to occur. The initial slight deviation of the normalized $\overline{Q}_p$ and $\overline{V}_o$ variables are caused by storm smearing as $L_R \rightarrow L_S$. However, as $L_R \rightarrow L_W$, watershed smearing begins, causing a substantial deviation of both $\overline{Q}_p$ and $\overline{V}_o$ with rainfall data aggregation.

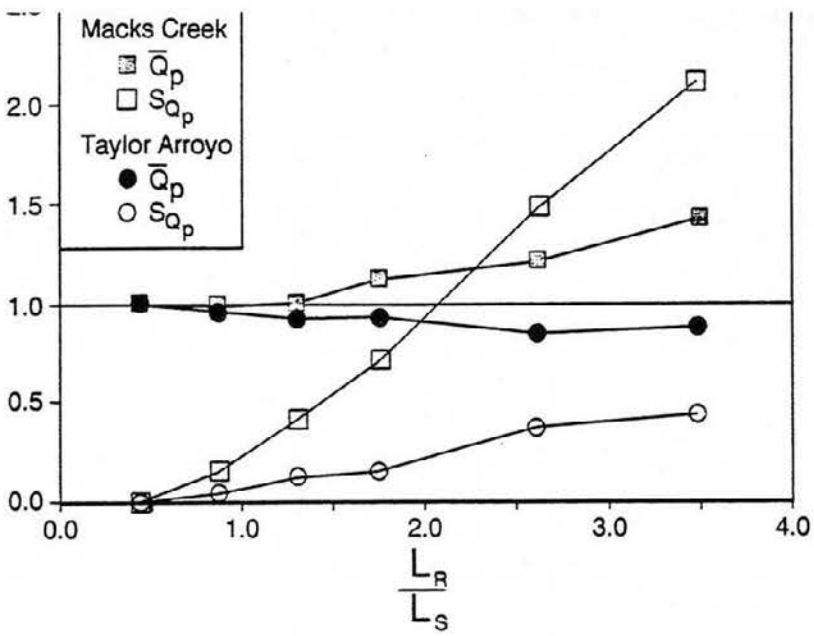

Fig. 7. Combined watershed and storm smearing effects on peak discharge for 50 storms on Macks Creek and 40 storms on Taylor Arroyo, without infiltration.

9. Results with infiltration

The procedures without infiltration detailed in the previous section are duplicated in these simulations. The only additional consideration is the effect of infiltration. The same rainfall data subsets as described previously are used in these simulations. Values of soil moisture deficit, M_d, tested on both watersheds, are 0.3, 0.1, and 0.0,

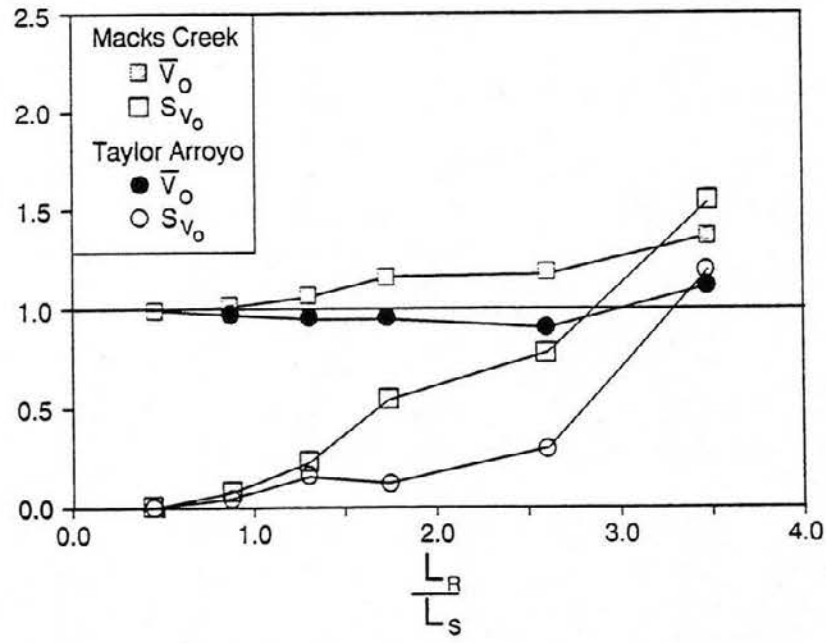

Fig. 8. Combined watershed and storm smearing effects on runoff volume for 50 storms on Macks Creek and 40 storms on Taylor Arroyo, without infiltration.

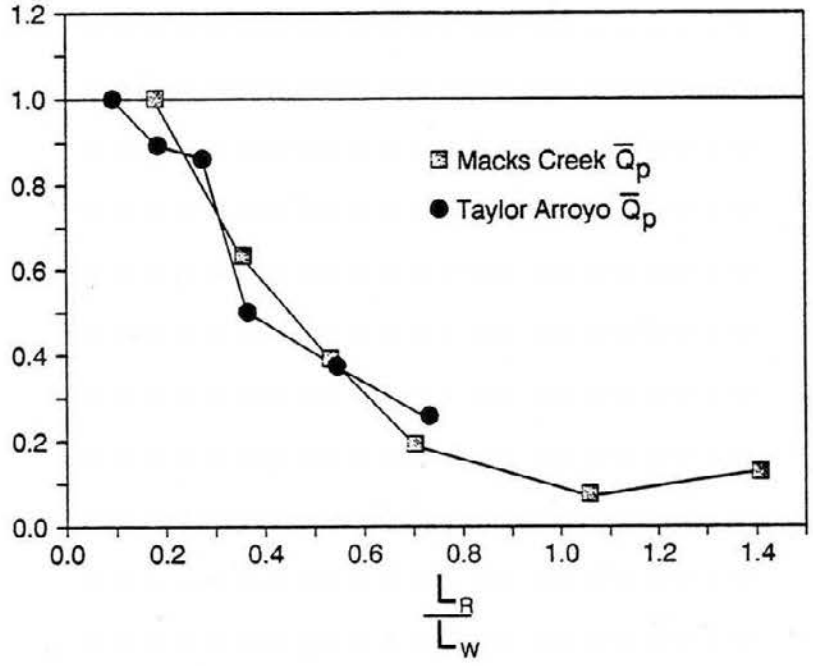

Fig. 9. Combined watershed and storm smearing effects on peak discharge for 11 storms on Macks Creek and 18 storms on Taylor Arroyo, with infiltration and $M_d = 0.3$.

corresponding to dry, wet, and saturated soil initial conditions, respectively. The selected M_d value is applied over the entire basin on all soil types.

The probability of a given storm producing runoff is less than 100% with infiltration, as opposed to the impervious case where every storm produces runoff. With the initial soil moisture deficit of 0.3 (dry conditions), only 11 and 18 rainfall data subsets generate runoff on Macks Creek and Taylor Arroyo watersheds, respectively. The analysis is performed only for rainfall data subsets which produce runoff. The peak discharge data vs. L_R/L_W for these simulations with runoff are plotted in Fig. 9. The mean normalized peak discharge for both watersheds decreases considerably as the rainfall data grid size increases. The watershed smearing parameter L_R/L_W produces reasonable agreement between the behavior of the two pervious basins to rainfall spatial aggregation.

The extreme reduction in peak discharge observed on both watersheds with increasing L_R/L_W indicates a decrease in the volume of excess rainfall, owing solely to rainfall data aggregation. The mean percentage of rainfall infiltrating for storms which produce runoff, versus L_R/L_W at initial soil moisture deficits of 0.3, 0.1, and 0.0 on both watersheds, is plotted in Fig. 10.

10. Conclusions

Two dimensionless similarity parameters which describe different aspects of the relationship between rainfall data spatial aggregation and distributed hydrologic model response are identified. The storm smearing parameter. L_R/L_S, describes a reduction in rain rate gradients. The watershed smearing parameter, L_R/L_W,

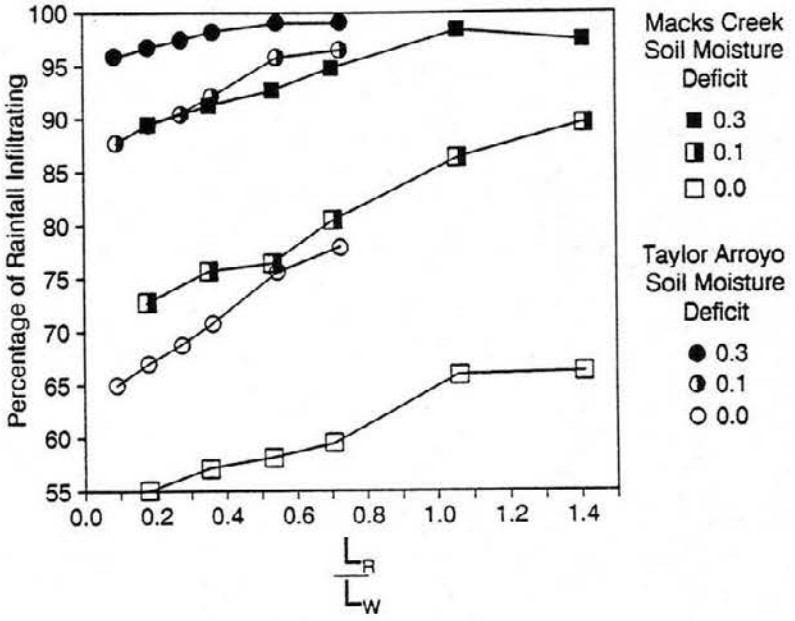

Fig. 10. Combined watershed and storm smearing effects on the percentage of rainfall infiltrating on Macks Creek and Taylor Arroyo for three values of M_d.

describes the uncertainty of rainfall location with respect to the watershed boundary. Simulations without infiltration reveal that watershed smearing is an important source of hydrologic model error when $L_R/L_W > 0.4$, owing to the change in basin-wide storm total rainfall volume, as shown in Fig. 6. The influences of storm smearing and watershed smearing are combined in the outflow variables Q_p and V_o for $L_R/L_W > 0.4$. Deviations of hydrologic model response from the finest-resolution results for $L_R/L_W < 0.4$ are caused primarily by storm smearing. The data in Figs. 7 and 8 indicate that watershed smearing is the main source of hydrologic model error on small catchments (less than 150 km^2).

Simulations with Green and Ampt infiltration reveal that the watershed smearing parameter L_R/L_W adequately describes the reduction of peak outflow owing to rainfall data aggregation as shown in Fig. 9. Significant reductions in $\overline{Q}_p$ with increasing L_R/L_W are caused by reduced excess rainfall rates as shown in Fig. 10. There is no evidence that the percentage of rainfall volume infiltrating converges as the rainfall data grid size is decreased. If the radar data are gridded at an artificially fine resolution ($L_R \leqslant L_M$), convergence must be observed. However, practical radar resolutions provide no convergence. These findings have several ramifications for the practical coupling of weather radar estimated rainfall rates and two-dimensional distributed parameter runoff models.

11. Acknowledgments

This work was performed at Colorado State University and funded by the US Army Research Office (Grant ARO/DAAL 03-86-0175). We acknowledge the

assistance of Dr. Bahram Saghafian and Dr. William Doe III with the watershed model and watershed data. Professor V.N. Bringi of the Department of Electrical Engineering, and Professor Steven Rutledge of the Department of Atmospheric Science, both at Colorado State University, provided access to the CSU-CHILL weather radar data. Special thanks are due to Dr. Walter Bach for his support of this effort. The constructive comments of three anonymous reviewers are also acknowledged and appreciated.

12. References

Austin, P.M., 1987. Relation between measured radar reflectivity and surface rainfall. Mon. Weather Rev., 115: 1053–1070.

Cabral, M.C., Bras, R.L., Tarboton, D. and Entekhabi, D., 1990. A distributed, physically based rainfall–runoff model incorporating topography for real-time flood forecasting. Ralph M. Parsons Laboratory, Rep. 332, Massachusetts Institute of Technology, Cambridge, MA, 220 pp.

Chandrasekar, V., Bringi, V.N., Balakrishnan, N. and Zrnic, D.S., 1990. Error structure of multiparameter radar and surface measurements of rainfall. Part III: Specific differential phase. J. Atmos. Oceanic Technol., 7(5): 621–629.

Chandrasekar, V., Gorgucci, E. and Scarchilli, G., 1993. Optimization of multiparameter radar estimates of rainfall. J. Appl. Meteorol., 32(7): 1288–1293.

Doe, III, W.W., 1992. Simulation of the spatial and temporal effects of Army maneuvers on watershed response. Ph.D. Dissertation, Department of Civil Engineering, Colorado State University, Fort Collins, 301 pp.

Green, W.H. and Ampt, G.A., 1911. Studies on soil physics, 1. The flow of air and water through soils. J. Agric. Sci., 4: 1–24.

Jameson, A.R., 1991. A comparison of microwave techniques for measuring rainfall. J. Appl. Meteorol., 30: 32–54.

Julien, P.Y. and Saghafian, B., 1991. CASC2D users manual—a two-dimensional watershed rainfall–runoff model. Civil Engineering Rep. CER90-91PYJ-BS-12, Colorado State University, Fort Collins, 66 pp.

Klazura, G.E. and Imy, D.A., 1993. A description of the initial set of analysis products available from the NEXRAD WSR-88D system. Bull. Am. Meteorol. Soc., 74(7): 1293–1311.

Kouwen, N., 1986. SIMPLE—a watershed model for flood forecasting. Users Manual. Department of Civil Engineering, University of Waterloo, Waterloo, Ont., 130 pp.

Kouwen, N. and Garland, G., 1989. Resolution considerations in using radar rainfall data for flood forecasting. Can. J. Civ. Eng., 16: 279–289.

Krajewski, W.F., Lakshmi, V., Georgakakos, K.P. and Jain, S.C., 1991. A Monte Carlo study of rainfall sampling effect on a distributed catchment model. Water Resour. Res., 27(1): 119–128.

National Research Council, 1991. Opportunities in the Hydrologic Sciences. Committee on Opportunities in the Hydrologic Sciences, Water Science and Technology Board, Commission on Geosciences, Environment, and Resources, National Research Council, National Academy Press, Washington, DC, 337 pp.

Ogden, F.L. and Julien, P.Y., 1993. Runoff sensitivity to temporal and spatial rainfall variability at runoff plane and small basin scales. Water Resour. Res., 29(8): 2589–2597.

Ogden, F.L. and Turk, F.J., 1991. The applicability of weather radar to hydrologic modeling: radar resolution requirements and comparison with dense raingauge network data. Proc. 11th Annual AGU Hydrology Days, 2–4 April 1991, Colorado State University, Fort Collins, CO, Hydrology Days Publications, Fort Collins, CO, pp. 11–22.

Pessoa, M.L., Bras, R.L. and Williams, E.R., 1993. Use of weather radar for flood forecasting in the Sieve River basin: a sensitivity analysis. J. Appl. Meteorol., 32(3): 462–475.

Rawls, W.J., Brakensiek, D.L. and Miller, N., 1983. Green–Ampt infiltration parameters from soils data. J. Hydraul. Eng. Am. Soc. Civ. Eng., 109(1): 62–70.

Sachidananda, M. and Zrnic, D.S., 1986. Differential propagation phase shift and rainfall rate estimation. Radio Sci., 21: 235–247.

Saghafian, B., 1992. Hydrologic analysis of watershed response to spatially varied infiltration. Ph.D. Dissertation, Department of Civil Engineering, Colorado State University, Fort Collins, 215 pp.

Seliga, T.A. and Bringi, V.N., 1976. Potential use of radar differential reflectivity measurements at orthogonal polarizations for measuring precipitation. J. Appl. Meteorol., 15: 69–76.

Seliga, T.A., Aron, G., Aydin, K. and White, E., 1991. Storm runoff simulation using radar-estimated rainfall rates and a unit hydrograph model (Syn-Hyd) applied to the Greve watershed. Proc. 25th Conf. on Radar Meteorol., Am. Meteorol. Soc., Paris, 1991, Am. Meteor. Soc., Boston, MA, pp. 587–590.

WATER RESOURCES BULLETIN
VOL. 25, NO. 3 AMERICAN WATER RESOURCES ASSOCIATION JUNE 1989

AN AUTO-CAD-BASED WATERSHED INFORMATION SYSTEM FOR THE HYDROLOGIC MODEL HEC-1[1]

T. J. Cline, A. Molinas, and P. Y. Julien[2]

ABSTRACT: A micro computer based Watershed Information System (W.I.S.) is developed to assist in the preparation of input files for the hydrologic simulation model HEC-1. This system consists of three phases. Phase I utilizes the capabilities of AutoCAD version 9 and three programs, BASINS, PLANES, and CHANNELS, to extract, organize, and display watershed data. Phase II uses the program CN to calculate some HEC-1 parameter values. Phase II utilizes the program HECUPDATE to create HEC-1 input files. The system input includes topographic, soils, land use, watershed geometry data, and a skeletal HEC-1 input file. Output from the system includes a summary User Reference File, a Soils File, a Land Use File, a Watershed Geometry File, a Curve Number File, and a HEC-1 input file, which is ready to run. The W.I.S. has been applied to Macks Creek Watershed in southwest Idaho.
(KEY TERMS: hydrologic modeling; watershed information system; AutoCAD; surface runoff; Model HEC-1; input data files; watershed digitization.)

INTRODUCTION

Hydrologic models are very complex nonlinear systems and can simulate rainfall induced runoff on watersheds with characteristics varying both in space and in time. A major problem confronting watershed modelers is the difficulty in obtaining and handling the quantity of spatially and temporally varying data required to successfully use hydrologic models. Computer and Geographic Information System (G.I.S.) technology have been rapidly evolving in recent years and systems have been developed to facilitate data storage, organization, manipulation, access, and display.

The purpose of this work is to examine the potential of using a commercially available computer-aided drafting package AutoCAD as a micro-computer tool for a three phase Watershed Information System (W.I.S.). The system is developed to obtain, organize, and display watershed data; calculate some model parameter values; and create model input files. The watershed model HEC-1 has been selected for the rainfall-runoff simulation and an example application to Macks Creek Watershed in Idaho is also presented.

The proposed W.I.S. uses a PC's Limited 286 machine, a True Grid 8017 digitizing tablet, AutoCAD version 9 as well as FORTRAN and PASCAL compilers. The model HEC-1 (Hydrologic Engineering Center, 1985; Hydrologic Engineering Center, 1979; Feldman and Goldman, 1982) was selected because it is a widely used model providing a number of options useful to the watershed modeler. The options for which the W.I.S. was developed include the S.C.S. curve number technique for determining excess rainfall and the kinematic wave approximation technique for routing both overland and open channel flow. It is assumed that the reader is familiar with the model HEC-1, as this paper is intended for HEC-1 users who seek computerized ways to prepare input data files.

REVIEW OF AUTOCAD CAPABILITIES AND DATA REQUIREMENTS FOR HEC-1

AutoCAD has several attractive features for the development of a W.I.S. dedicated to hydrologic modeling using HEC-1. These features will be reviewed and the basic data requirements of HEC-1 presented.

Review of AutoCAD Capabilities

AutoCAD is a comprehensive micro computer graphics software package (Raker and Rice, 1987). Although first intended for design and drafting purposes, it seems appealing to examine its capability as

[1]Paper No. 88117 of the *Water Resources Bulletin*. **Discussions are open until February 1, 1990.**
[2]Respectively, Graduate Student and Assistant Professors of Civil Engineering, Engineering Research Center, Colorado State University, Fort Collins, Colorado 80523.

81

a micro computer W.I.S. tool. The program has two and three dimensional capabilities that are both useful for watershed data display. Drawing entities are stored in a vector format.

AutoCAD has a number of features that make it useful for obtaining, organizing, formatting, and displaying watershed data.

- First data may be entered manually by digitizing directly from maps. As digitizing proceeds, the data is displayed on the computer screen and can be stored in AutoCAD drawing files.
- Second, AutoCAD has the ability to store data on different layers. The different layers can be distinguished by varying colors or line types and can be turned on and off to emphasize the relationship between a selected number of layers. Layering can greatly enhance the effectiveness of data display and analysis.
- Third, AutoCAD has some analytic capability. It has a very accurate area calculation algorithm which can be used on any irregularly shaped polygon on an AutoCAD drawing. Also, AutoCAD has the ability to calculate lengths.
- Fourth, AutoCAD has the ability to "zoom" into an area of interest on an AutoCAD drawing in order to increase resolution of specific features.
- Fifth, the quality of graphics on the computer screen and output to a plotting device is excellent.
- A sixth feature of AutoCAD which makes it especially useful as a W.I.S. tool is the fact that AutoCAD allows the user to create new commands specific to a particular application using the AutoLISP programming language. These new commands can be invoked from a pull down menu within AutoCAD. These programs can utilize AutoCAD features to extract data from digitized maps of watershed data and prompt the user for other data, organize the data, and then format it into various output files for subsequent analysis.

Data Requirements for the Model HEC-1

HEC-1 simulates rainfall-runoff on a complex watershed that is represented as an interconnected system of terminal basin units, "open book" units, and channel units. Terminal basin units are simulated as single planes and are located at the upstream ends of the watershed. "Open book" units consist of two adjacent planes linked by a channel unit. Figure 1 shows each of these types of units schematically. Spatial uniformity is assumed on planes and channel units. The parameters required include those describing: temporal variation in rainfall; SCS curve number method for determining excess rainfall; overland flow routing using the kinematic wave method; and open channel flow routing with the kinematic wave method. Table 1 summarizes these data requirements needed for *each* overland flow plane and *each* channel unit being simulated in order to run HEC-1 with these options.

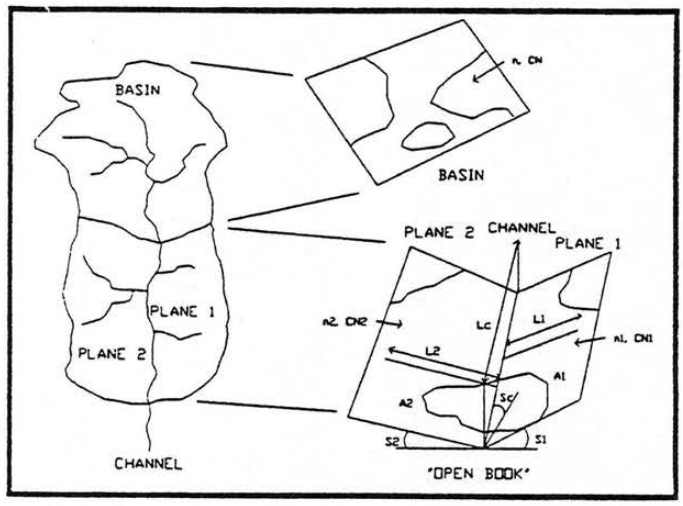

Figure 1. Schematic Representation of Subwatershed Units for the Model HEC-1.

TABLE 1. HEC-1 Data Requirements for This Study.

I. Rainfall depths over time and space

II. Excess rainfall determination
  A. Curve Number (CN)
  B. Initial Abstraction (STRTL)

III. Routing
  A. Overland flow routing (kinematic wave)
    1. Flow length (L)
    2. Slope (S)
    3. Roughness (N)
    4. Area (A)

  B. Channel routing (kinematic wave)
    1. Flow length (L)
    2. Slope (S)
    3. Roughness (n)
    4. Shape (SH)
    5. Bottom width (BW)
    6. Side slope (Z)

DEVELOPMENT OF A WATERSHED INFORMATION SYSTEM FOR HEC-1

A Water Information System (W.I.S.) has been developed for hydrologic simulation using HEC-1 on micro computers. The W.I.S. requires input including soils, vegetation, land use, and topographic data from maps, tables, and other sources. The system is divided into three phases utilizing five programs: BASINS, PLANES, CHANNELS, CN, and HECUPDATE. Final output from the system are HEC-1 input files ready to be run on the computer. Figure 2 shows a schematic flow chart of the system. In the following, the phase-by-phase description of the system is illustrated with fictitious example.

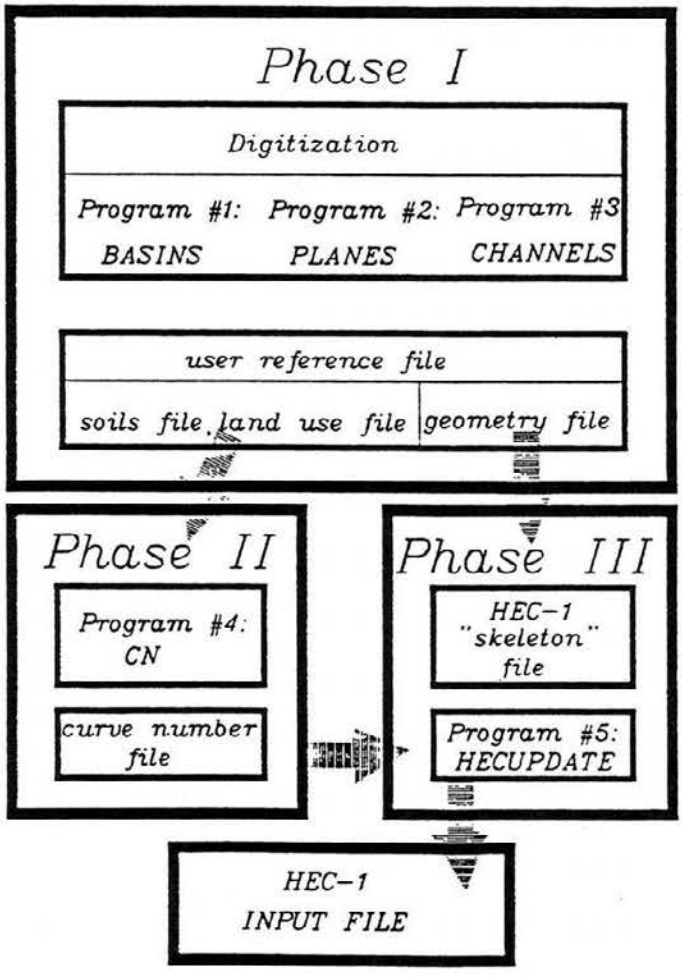

Figure 2. Watershed Information System Structure.

Development of Phase I

Phase I utilizes the capabilities of AutoCAD detailed above to convert watershed data into computer drawing and ASCII data files which are used for display and analysis (Cline, *et al.*, 1988; Cline, 1988]. Phase I starts with the digitization of watershed data into AutoCAD drawing files. This data includes SCS hydrologic soil group zones, land use zones, hydrologic features, and topography. Additional information such as vegetation zones and geologic units may also be digitized. Each data type should be digitized onto a separate layer and may be distinguished by line type, line thickness, and color or fill design of the zones. Topographic data can be displayed by digitizing the subwatershed unit delineations and by digitizing contours. The three dimensional capabilities of AutoCAD can be utilized with the topographic data. Figure 3 shows the superposition of topographic, soils, and channel data layers that have been digitized for an example watershed.

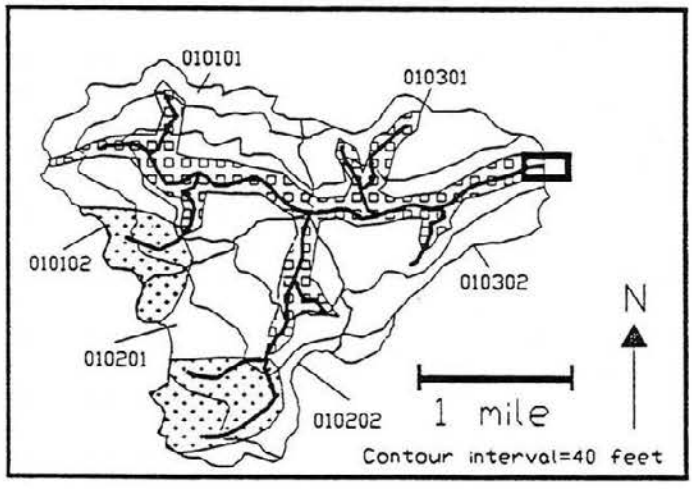

Figure 3. Superposition of Topographic, Channel, and Soil Data Layers for an Example Watershed.

Next, three AutoLISP programs are invoked sequentially from a pull down menu from within AutoCAD. The program BASINS obtains, organizes, and formats data from all of the terminal basin units within the watershed. PLANES and CHANNELS do the same for all "open book" plane and channel units, respectively. The programs BASINS, PLANES, and CHANNELS interact with the user by prompts and are used as follows.

Programs BASINS and PLANES.

1. From within AutoCAD with the digitized, layered drawing on the screen invoke BASINS (or PLANES) from the pull down menu.
2. Digitize a measured mile (used for scaling).
3. Enter number of basins (or planes) to analyze.

BASINS and PLANES sequentially "zoom" into each basin (or plane) designated by the user. For each basin (or plane):

4. Enter unit identification code.
5. Enter representative overland flow roughness coefficient (N) value referring to Hydrologic Engineering Center (1985). A value of 0.055, for example, is typical for open range. Three digit accuracy is desirable (peak flow is moderately sensitive to the value of N used).
6. Enter number of soil zones within the unit.
7. Enter the land use code for each unit referring to Table 2.
8. Digitize a representative average flow length for the unit. Two digit accuracy is desirable (peak flow is moderately sensitive to this value). Using this length and contour data, determine the slope of this flow length and enter the value at the prompt.

For each soil zone within a basin (or plane):

9. Enter name of soil group.
10. Enter the S.C.S. hydrologic soil grouping (A, B, C, D) or the combination of soil groupings within the soil group. (These soil designations are used to determine the S.C.S. curve number for a subwatershed unit. Hydrograph shape, peak, and time to peak are very sensitive to the curve number value.)
11. Digitize the soil group area.
12. For soil zones composed of more than one S.C.S. hydrologic soil grouping (e.g., "B/C"), enter the number of SCS groupings with the soil zone and the proportion of the total area represented by the soil zone (as a decimal, usually assumed to be 50 percent of each type).
13. Enter the soil code identification number for the particular soil referring to designations such as shown in Table 3).

Program CHANNELS.

1. From within AutoCAD, with the digitized layered drawing on the screen invoke CHANNELS from the pull down menu.
2. Digitize a measured mile (used for scaling).
3. Enter the number of channels to analyze

CHANNELS successfully "zooms" into each channel unit designated by the user. For each channel unit:

4. Enter unit identification number.
5. Enter channel Manning's n value. Three digit accuracy will suffice (time to peak is sensitive to the value of n used).
6. Enter channel shape referring to cross section shapes recognized by HEC-1 (Hydrologic Engineering Center, 1985).
7. Enter channel bottom width in feet.
8. Digitize along the channel length. Using the calculated length and contour data determine slope of channel and enter the value at the prompt.

TABLE 2. Land Use Code Numbers and a Land Use File from Phase I of the W.I.S. for an Example Watershed.

Unit ID Number	Land Use Code	Area (acres)	Legend
010101	5	531.12	1. rock land
010102	3	461.30	2. agricultural
010201	1	494.38	3. cleared basins and flats
010202	8	355.98	4. wooded and/or shrubed swamps
010301	6	491.82	5. urban development
010302	2	483.09	6. bottom land hardwood
			7. wooded basins and flats
			8. open range
			9. fish farm

TABLE 3. Soil Code Numbers for This Study and a Soils File from Phase I of the W.I.S. for an Example Watershed.

			Legend		
Unit ID Number	Soil Code	Area (acres)	Soil Code No.	Series	SCS Grouping
010101	4	72.77	1	Rucklick	C
010101	12	72.77	2	Babbington	B
010101	5	385.58	3	Castlevale	D
010102	4	47.51	4	Reywat	D
010102	12	47.51	5	Bakeoven	D
010102	5	283.74	6	Nannyton	B
010102	2	127.54	7	Larimer	B
010201	2	45.76	8	Lassen	D
010201	4	19.34	9	Glasgow	C
010201	12	19.34	10	Ackman	B
010201	5	14.19	11	Gemson	C
010201	2	95.77	12	Lickskillet	C

Phase I produces four output files. First, a Land Use File contains unit identification numbers, land use code number, and the area for the particular land

use in acres. An example is shown in Table 2. Second, a Soils File contains the unit identification number, soil type identification number, and the soil's area in acres. An example is shown in Table 3. Third, a Geometry File contains unit identification numbers, area in acres of the unit, representative average flow length in feet, and representative average slope of the unit in feet per foot. An example for the watershed shown in Figure 3 is given in Table 4. The Soils, Land Use, and Geometry Files are used as input to the Phase II and III programs. Fourth a User Reference File is a summary file containing all the information needed in Phase I. A portion of a User Reference File for one "open book" unit of the demonstration watershed shown in Figure 3 is shown in Table 5.

Phase I is the most time-consuming phase of the W.I.S. Digitization and the operation of the Phase I programs are very simple to use but labor intensive. Once the work is done, a data base is created and can be used for multiple simulations under various possible situations.

TABLE 4. Phase I Output: A Geometry File.

Unit ID Number	Area (acres)	Flow Length (feet)	Slope (foot/foot)
010100	992.42	10323.82	0.0105
010101	531.12	3255.39	0.0369
010102	461.30	3548.16	0.0282
010200	850.32	11246.93	0.0130
010201	494.34	4248.41	0.0235
010202	355.98	2409.07	0.0122
010300	974.91	9984.63	0.0100
010301	491.82	3275.44	0.0122
010302	483.09	2746.10	0.0219

Development of Phase II

Phase II utilizes the FORTRAN program CN to determine a representative S.C.S. curve number for each subwatershed unit. The program was developed by Molinas (1986) and used by Molinas, *et al.* (1988), Cline, *et al.* (1988), Cline (1988). The program was modified to apply to the soils and the number of soil types found in Macks Creek. The Soils File and the Land Use File created in Phase I (Tables 2 and 3) are input to Phase II. The program CN prompts for the names of these files as well as for the name of the output file. Representative curve numbers are obtained by determining an area weighted average S.C.S. hydrologic zone for each subwatershed unit. Using this, the land use designation and a polynomial interpolation scheme, an area weighted average curve number is obtained from the "runoff curve numbers for hydrologic soil-cover complexes" (Soil Conservation Service, 1972) which has been coded, in part, into the program. A representative Manning's n and laminar friction coefficient (not used in this application) are assigned to each subwatershed unit according to the land use designation.

TABLE 5. Phase I Output: Part of a Users Reference File.

USER REFERENCE FILE

010101

mannings n: 0.02500
landuse code: 8
slope (ft/ft): 0.036900
flow length (ft): 3255.388000
number of soil zones: 2
the soil types and their areas:
soil type: R-LK (C) area (acres): 145.539200
soil type: BK (D) area (acres): 385.576700
total area: 0.826820 (sq. miles) 531.115900 (acres)

010100

mannings n: 0.020000
slope (ft/ft): 0.010500
flow length (ft): 10323.820000
channel shape: TRAP
channel side slopes: 2.000000
channel bottom width: 10.000000

The Phase II output file contains unit identification numbers, the representative curve number calculated for each unit, the Manning's n and laminar friction coefficient assigned for each unit, and the area in acres of each subwatershed unit. A Phase II output Curve Number File for the demonstration watershed shown in Figure 3 is shown in Table 6. The land use types and the soil types the program CN recognizes are shown in Tables 2 and 3. The program may be easily modified to recognize different land uses and soil types if the curve numbers, Manning's n and laminar friction coefficients are known for the new land uses and if the S.C.S. hydrologic soil group designations are known for the new soil types.

Development of Phase III

Phase III utilizes the PASCAL program, HECUPDATE, to create HEC-1 input files that are ready to be run. This program was developed by Molinas (1986) and used by Molinas, *et al.* (1988), Cline, *et al.* (1988), and Cline (1988). The geometry file from

TABLE 6. PHASE II Output: A Curve Number File.

Count	Unit ID Number	Curve Number	Manning's n	Laminar Friction Coefficient	Area (acres)
1	010101	83.61	055	1060.00	531.1
2	010102	81.28	055	1060.00	461.3
3	010201	82.27	055	1060.00	494.4
4	010202	80.74	055	1060.00	56.0
5	010301	83.49	055	1060.00	491.8
6	010302	83.77	055	1060.00	483.1

Phase I (Table 4) and the curve number file from Phase II (Table 6) are input to Phase III. In Phase III, the user must generate a HEC-1 "skeleton" file. A HEC-1 "skeleton" file must contain all the card identification codes, the precipitation gage data, output control cards, computational interval cards, comment cards, and portions of routing cards in correct HEC-1 input file structure. These portions of the files should be resident on the computer so that they can be readily accessed and copied by a text editor to quickly and simply generate "skeleton" files for a given HEC-1 application. An example HEC-1 "skeleton" file is shown in Table 7 generated for the demonstration watershed shown in Figure 3. The program HECUPDATE prompts for the names of the geometry file, the "skeleton" file, and for output file. HECUPDATE compiles basin areas, infiltration data (curve number), and routing data (flow lengths, slopes, Manning's n, and areas).

The output from Phase III, and from the entire three phase system, is a HEC-1 input file ready to be run with a minimum of calibration. Table 8 shows a HEC-1 input file for the demonstration watershed shown in Figure 3, which was output from Phase III with all fields filled in. Table 9 shows a summary of the files used in the three phases and their formats.

TABLE 7. Phase III: A HEC-1 "Skeleton" File.

```
ID      AN EXAMPLE SMALL WATERSHED
ID      KINEMATIC WAVE ROUTING
ID      PRECIPITATION DEPTHS IN INCHES, FLOWS IN CFS
*DIAGRAM
IT     6  1MAY79     1200     200
IO     5
PG GAGE1
IN     5  1MAY79     1200
PI 0.800   0.900   0.200   0.800   0.100   0.050   0.050
KK010100
KO     4        2
KM   KINEMATIC ROUTING OVERLAND AND OPEN CHANNEL
PT GAGE1
PW   1.0
PR GAGE1
PW   1.0
BA
LS
UK
UK
RK                                    TRAP      20       2
KK010200
KO     4        2
KM   KINEMATIC ROUTING OVERLAND AND OPEN CHANNEL
BA
LS
UK
UK
RK                                    TRAP      20       2
KKCJ0001
KM     COMBINE FLOWS FROM 010100 AND 010200
HC     2
KK010300
KO     4        2                     21
KM   KINEMATIC ROUTING OVERLAND AND OPEN CHANNEL
BA
LS
UK
UK
RK                                    TRAP      30       2     YES
ZZ
```

APPLICATION TO MACKS CREEK WATERSHED

Macks Creek is a subwatershed of Reynolds Creek Experimental Watershed monitored by the Agricultural Research Service since the early 1960's and is considered representative of arid, mountainous watersheds in the Pacific Northwest (Robbins, *et al.*, 1965). Rainfall-runoff data was available from Agricultural Research Service (1963-1968, 1973-1975, 1977) as well as unpublished data directly from the A.R.S. in Boise, Idaho, and presented by Cline (1988). Topographic, vegetative, geologic, and soils data were available from Stephenson (1977).

Macks Creek Watershed is a small, arid, mountainous watershed in southwest Idaho. The three phase W.I.S. was used to obtain and organize watershed data and to create HEC-1 input files for the study. Macks Creek drains a 12.26 square mile area in the north and west part of Reynolds Creek. Elevations range from about 6000 feet in the mountainous areas in the west to about 3700 feet at the outlet, which is in the flats of Reynolds Valley. Terrain is generally steep with overland flow slope up to about 30 percent in the west and as low as 7 percent near the confluence with Reynolds Creek. Channel slopes can be up to about 8.0 percent but average about 5 percent. Channels are well incised with two principal channels approximately six miles each. One drains the

southern part of the watershed (Macks Creek) and flows north and east. The other (Cottle Creek) drains the northern part of the watershed and flows to the east. The other (Cottle Creek) drains the northern part of the watershed and flows to the east. The Soil Conservation Service (1966) describes surface drainage as good and classifies the character of flow as being "perennial interrupted." Precipitation, baseflow, and a few springs in the area keep the main drainages flowing except in very dry periods. Figure 4 shows the drainage network of Macks Creek watershed.

TABLE 8. Phase III Output: A HEC-1 Input File Ready to Run.

```
ID      AN EXAMPLE SMALL WATERSHED
ID      KINEMATIC WAVE ROUTING
ID      PRECIPITATION DEPTHS IN INCHES, FLOWS IN CFS
*DIAGRAM
IT     6  1MAY79     1200     200
IO     5
PG GAGE1
IN     5  1MAY79     1200
PI 0.800   0.900   0.200   0.800   0.100   0.050   0.050
KK010100
KO     4       2
KM   KINEMATIC ROUTING OVERLAND AND OPEN CHANNEL
PT GAGE1
PW   1.0
PR GAGE1
PW   1.0
BA  1.55
LS          83.61                    81.28
UK  3255 0.03690   0.055   53.52
UK  3548 0.02820   0.055   46.48
RK 10324 0.01050   0.035            TRAP      20       2
KK010200
KO     4       2
KM   KINEMATIC ROUTING OVERLAND AND OPEN CHANNEL
BA  1.33
LS          82.27                    80.74
UK  4248 0.02350   0.055    58.14
UK  2409 0.01220   0.055    41.86
RK 11247 0.01300   0.035            TRAP      20       2
KKCJ0001
KM      COMBINE FLOWS FROM 010100 AND 010200
HC     2
KK010300
KO     4       2                      21
KM   KINEMATIC ROUTING OVERLAND AND OPEN CHANNEL
BA  1.52
LS          83.4                     83.77
UK  3275 0.01220   0.055   50.45
UK  2746 0.02190   0.055   49.55
RK  9985 0.01000   0.035            TRAP      30       2     YES
ZZ
```

Soil types in the area are closely associated with underlying geologic material. Soils are dominantly gravelly, rocky, and stony loams with soil depths ranging from 7 to 55 inches. Permeabilities range from very slow/none to moderately rapid. The soil types in the area have been mapped and described in some detail and are presented in Stephenson (1977). S.C.S. hydrologic soil classifications are typically B, C, and D's and average between C and D due to high clay contents. Table 3 lists the soil types and their S.C.S. soil classifications. Detailed descriptions of the soils can be found in Agricultural Research Service (1966), Stephenson (1977), and S.C.S. soil maps of the area.

Vegetation on Macks Creek Watershed is dominantly sage brush. A more detailed description of the vegetation and its distribution is available in Stephenson (1977) and Agricultural Research Service (1966).

TABLE 9. Summary of the Files Used in the Three Phase System and Their Formats.

	Field
1. Users Reference File	
2. Land Use File (Phase I output)	
unit identification number	1-6
land use code*	7-9
area of land use (acres)	10-19
3. Soils File (Phase I output)	
unit identification number	1-6
soil identification number **	7-9
area of soil (acres)	10-19
4. Geometry File (Phase I output)	
unit identification number	1-6
area (acres)***	7-16
representative flow length (feet)	17-26
representative slope (foot/foot)	27-36
5. Curve Number File (Phase II output)	
count	1-10
unit identification number	11-20
curve number	21-30
Manning's n	31-40
laminar friction coefficient	41-50
area (acres)	51-60
6. HEC-1 Skeleton File (User created)	
7. HEC-1 Input File (Phase III output)	

*See Table 2.
**See Table 3.
***For channel units (ending in '00'), this is the drainage area. For other units, this is the unit area.

In 1966, when Macks Creek watershed was officially delineated as a separate experimental subwatershed of Reynolds Creek Watershed , a precalibrated, 3,500 cfs capacity drop-box weir and 11 Belfort recording rain gages were monitoring Macks Creek Watershed. In 1966, mean monthly runoff ranged from 2.1 cfs (March) to 0.02 cfs (September). Mean daily discharges in 1966 ranged from 7.8 cfs (March 13) to 0.01 cfs (October). Flood events of up to 100 cfs have been recorded for rain-on-snow winter storms.

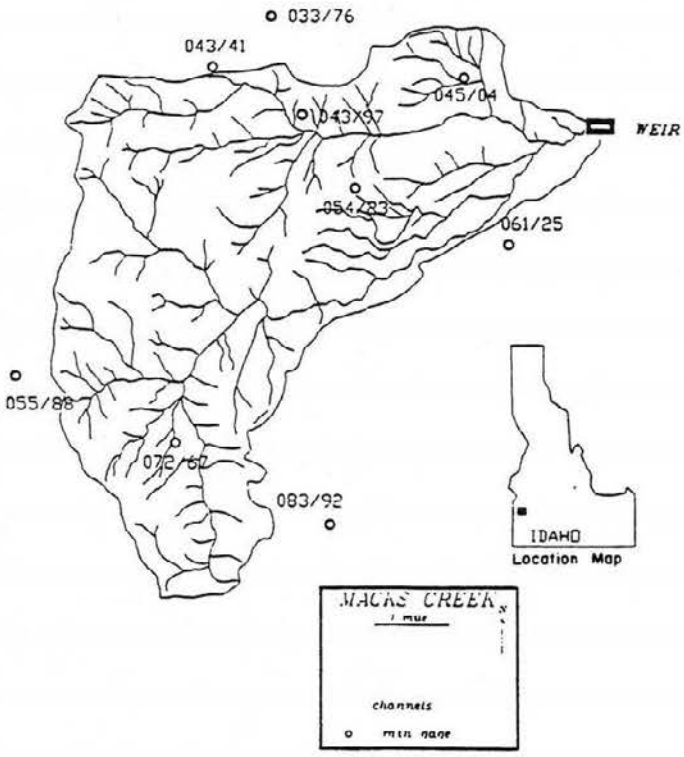

Figure 4. Channel Delineations on Macks Creek Watershed with the Locations of the Rain Gages and the Weir.

numbers) to upstream (largest numbers). For example, 090301 and 090302 represent either plane in an "open book" unit in third unit within the ninth subbasin. The number 090300 would represent the channel unit linking them.

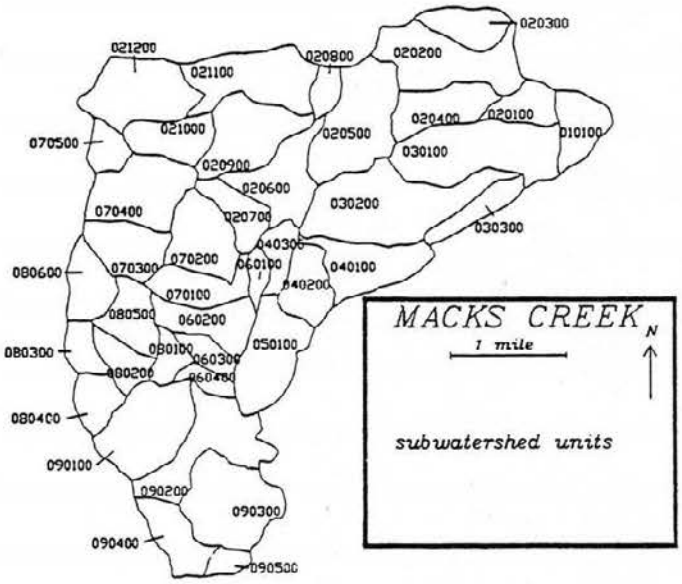

Figure 5. Subwatershed Delineations on Macks Creek Watershed.

APPLICATION OF PHASE I

Before invoking Phase I, the watershed is broken up into a system of terminal basin units, "open book" plane units, and channel units as described earlier. The number of units depends on the spatial variability and resolution of the topography, S.C.S. hydrologic soil zones, and rainfall data. As shown in Figure 5, Macks Creek Watershed is first divided into 14 terminal basin units, 26 "open book" units (averaging 0.2 square miles in area), and 26 channel units. Overland flow units are selected for relative uniformity in topography soils, and vegetation. Hydrologic and topographic information is used to delineate the channel units.

The overland flow units are grouped into nine subbasins and numbered according to the subbasin number, the relative upstream position within the subbasin, and the type of unit such as terminal basins (single plane denoted with '00') or "open books" (double planes denoted with '01' and '02') or channel units (denoted with '00'). One HEC-1 input file was made for each of the nine subbasins. Numbering for the subbasins, as well as for the overland flow units within them, proceeded from downstream (smallest

Computational ordering of the subareas of Macks Creek Watershed proceeds from the terminal basin unit furthest upstream within the furthest upstream subbasin (090500) to the "open book" unit furthest downstream within the furthest downstream subbasin (010100). When computations reached the confluence with another channel, the upstream portion of the other channel was analyzed first prior to computations downstream of the confluence. The calculated hydrographs from each of the nine subbasins are saved in an output file accessible to HEC-1. A tree diagram in Figure 6 shows the computational ordering and numbering of terminal basin units and "open book" plane units in the Macks Creek Watershed.

Rainfall data over space and time was needed for the simulations. HEC-1 can be run assuming uniform precipitation over the entire watershed. Data permitting, HEC-1 can also be run accounting for spatial variability of rainfall. In this case, the user must determine the exact spatial distribution of rainfall varies on the watershed.

Phase I starts with the digitization of watershed data into layered AutoCAD drawing files. Channel

data was digitized first and is shown with the rain gage and weir locations in Figure 4. Main channels and smaller ephemeral channels are also displayed. Terminal basin units and "open book" plane unit delineations were then digitized onto a second layer, which is shown in Figure 5. Identification numbers of overland flow units are also shown in this figure. S.C.S. hydrologic soil zones were digitized onto a third layer, which is shown in Figure 7. The channel, subwatershed, and hydrologic soil zone delineations were superimposed and distinguished by color. The Phase I programs BASINS, PLANES, and CHANNELS are invoked sequentially to produce the User Reference Files, the Soils Files, the Land Use Files, and the Geometry Files for Macks Creek Watershed.

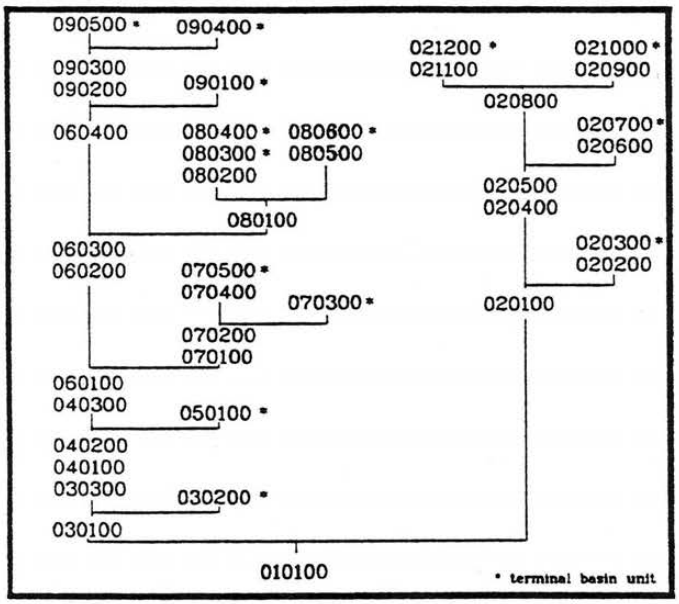

Figure 6. Computational Ordering and Numbering of Terminal Basin Units and "Open Book" Plane Units on Macks Creek Watershed.

Application of Phase II

Phase II commences with the delineation of the S.C.S. hydrologic soil grouping zones on Macks Creek Watershed. An overlay to a soils map presented in Stephenson (1977) showing these zones was created for digitization. The Phase II program CN takes the Soils Files from the Land Use Files produced in Phase I and generates Curve Number Files using the Phase II program CN. The program assigns Manning's and laminar friction coefficients (not used in this study) to each unit. Land use is predominantly open range land with some portions of exposed rock; therefore, typical Manning's n are 0.055 and typical laminar friction coefficients are 1060. Curve numbers calculated by the program ranged from 70 to 80.

Application of Phase III

The spatial distribution of rainfall must be determined to run HEC-1 successfully. For this application, enough rainfall data was available to resolve this distribution. Hyetographs were determined for the centroid of each terminal basin unit and for the centroid of each "open book" unit. This was accomplished by using the contouring software package SURFER. Rainfall intensities for each gage were determined at two-minute time intervals by calculating the slope of the break point accumulated rainfall curves presented in Cline (1988). Contour plots using SURFER were generated for every six minutes during the event using the kriging, octant search method, and smoothing options of the software. These plots were used to determine the rainfall intensities at the centroids of each terminal basin and "open book" unit at six-minute intervals. Similar plots are also available for the accumulated rainfall depth as shown in Figure 8.

Phase III commences with the generation of HEC-1 "skeleton" files. Portions of "skeleton" files stored on the computer in a separate subdirectory are copied into a file for each of the nine subbasins. Comments, computational controls, output controls, rainfall data, unit labels, and channel geometry parameters are entered or modified as appropriate. The Phase III program HECUPDATE assembles HEC-1 input files from the Geometry Fioles and the Curve Number Files produced in Phase I and II and the HEC-1 "skeleton" files produced in Phase III. One HEC-1 input file is produced for each of the nine subbasins on Macks Creek Watershed.

MODELING

The model was calibrated using data from one rainfall-runoff event in June 1967 (Agricultural Research Service, 1967; Cline, 1988) and verified with data from a more intense rainfall-runoff event in August 1965 (Cline, 1988). Figure 9 shows specifically the location of all rain gages, which recorded for the calibration and validation simulations. Measured hyetographs and the measured hydrograph for the August 1965 event are also shown on this figure. Base flow was measured to be between 0.4 and 0.8 cfs at the weir prior to the event. Measured peak flow from this event was 85.14 cfs occurring approximately one

89

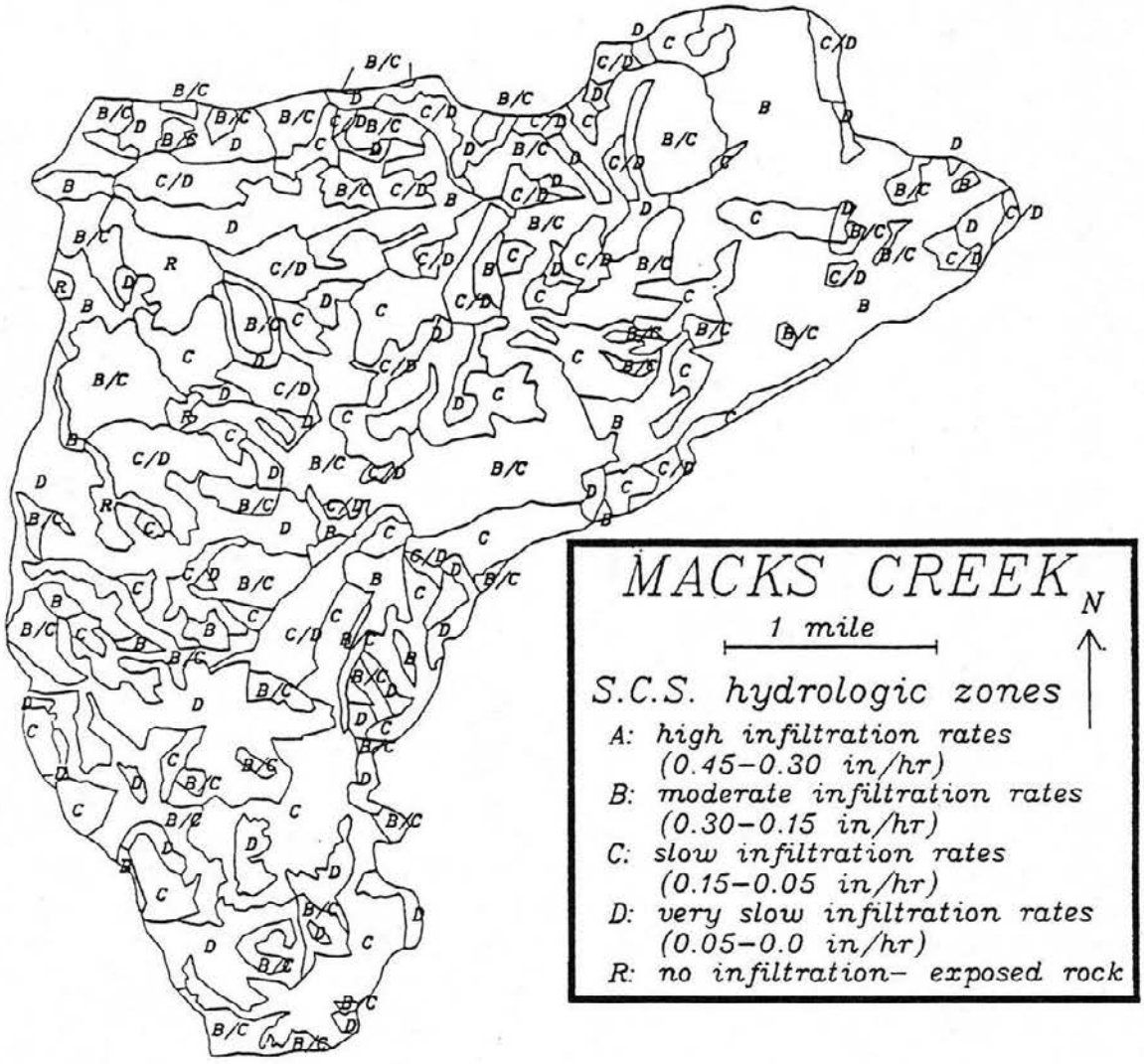

Figure 7. SCS Hydrologic Soil Zone Delineations on Macks Creek Watershed.

hour after the onset of rainfall. This was a phenomenal summer event for Macks Creek Watershed.

The validation was done using a six-minute computational time interval with the rainfall data distribution obtained as explained above. It was necessary to modify the value of the initial abstraction calculated by HEC-1. The initial abstraction was considerably lower than that calculated by HEC-1 because of very wet antecedent conditions.

Cline (1988) performed a sensitivity analysis of important HEC-1 parameters. Results of this analysis were useful in the W.I.S. development and application, as well as in model calibration. The results of this analysis show that HEC-1 is less sensitive to values of curve number (CN) and initial abstraction (STRTL). The model is moderately sensitive to values of the overland flow roughness coefficient (N) and the overland flow length (L). HEC-1 is slightly sensitive to values of the open channel flow roughness coefficient (n) and the computational time interval (NMIN).

SUMMARY AND CONCLUSIONS

The Watershed Information System (W.I.S.) developed, applied, and described in this paper is shown to greatly facilitate watershed data extraction and organization, data display, parameter calculation, and the creation of HEC-1 input files. This three-phase W.I.S. is a systematic integrated method of obtaining and managing watershed data. The system converts map

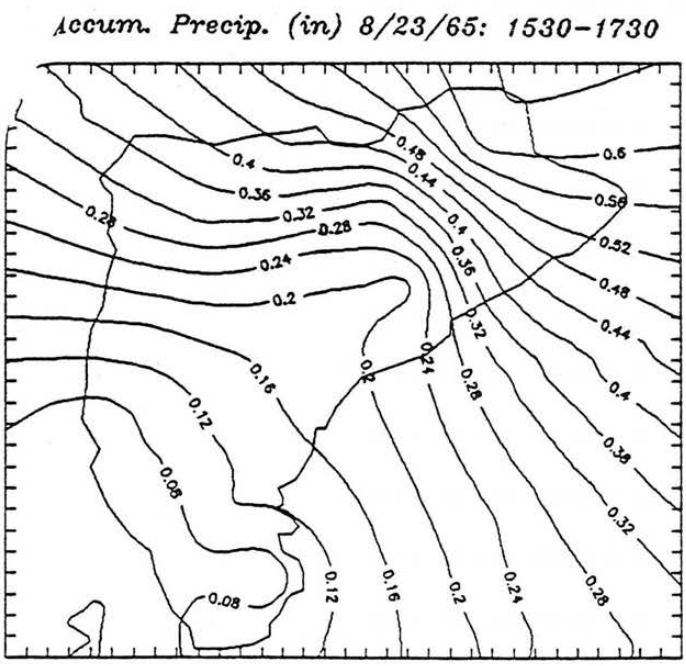

Figure 8. Contoured Accumulated Rainfall Depths for the Event of August 23, 1965.

and other data into computer ASCII and AutoCAD drawing files. It organizes large quantities of data into data files for subsequent analysis. The system has some analytic abilities and is able to calculate areas, lengths, and curve numbers. It facilitates the creation of HEC-1 input files and displays data effectively on layered drawings.

The W.I.S. was applied to a HEC-1 modeling study of Macks Creek Watershed in southwest Idaho. A fairly high resolution of soils, land use, vegetation, watershed geometry, and rainfall data exists for Macks Creek. After generating HEC-1 input files, the model was calibrated using an event on June 5-6, 1967. The calibrated model was then used to simulate a heavier rainfall event which was monitored by eight rain gages in and around Macks Creek Watershed on August 23, 1965. The W.I.S. produces HEC-1 input files which yield good results with a minimum of calibration and establishes a data base for future HEC-1 simulations. Sensitivity analysis results show that HEC-1 is very sensitive to values of curve number and initial abstraction, moderately sensitive to values of overland flow roughness coefficient and overland flow length and slightly sensitive to open channel flow

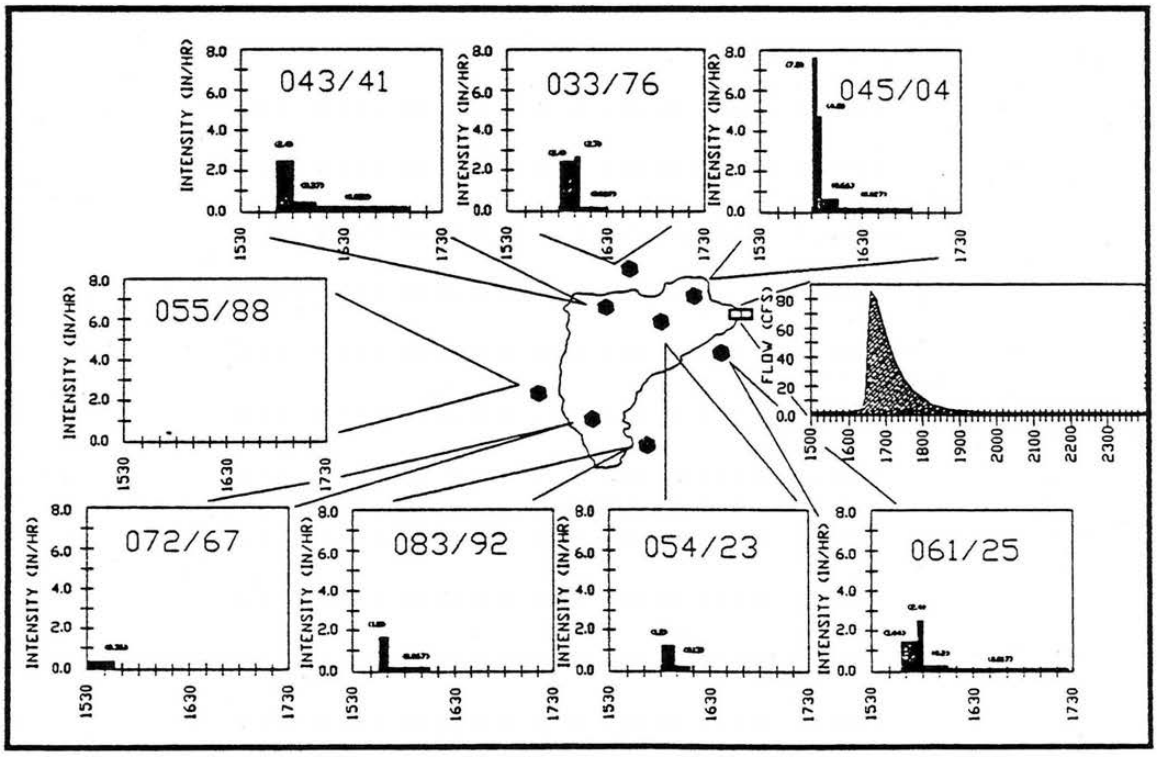

Figure 9. Measured Hyetographs and Outflow Hydrograph for Macks Creek Watershed (August 23, 1967).

91

roughness coefficient and computational time interval.

ACKNOWLEDGMENTS

This study has been conducted with the Hydrologic Modeling Group of the Center for Geosciences at Colorado State University. Funding under the U.S. Army Research Grant No. ARO/DAAL 03-86-K-0175 is greatly appreciated.

LITERATURE CITED

Agricultural Research Service, 1963, 1965, 1966, 1967, 1968, 1973, 1974, 1975, 1977. Hydrologic Data for Experimental Agricultural Watershed in the United States. Misc. Publication, U.S. Department of Agriculture, Agricultural Research Service.

Autodesk, AutoLISP, Release 9.0 Programmers Reference, 1987. Publication TD111-003. Autodesk Inc.

Cline, Thaddeus, J., 1988. Development of a Watershed Information System for HEC-1 With Application to Macks Creek Watershed, Idaho. M.S. Thesis, Department of Civil Engineering, Colorado State University, Fort Collins, Colorado.

Cline, Thaddeus J., Albert Molinas, and Pierre Y. Julien, 1988. A Geographic Information System for Obtaining and Organizing Watershed Data and for Preparing HEC-1 Input Files. Proceedings of the Eighth Annual A.G.U. Front Range Branch Hydrology Days, April 19-21, 1988, Colorado State University, Fort Collins, Colorado, pp. 81-90.

Feldman, A. D. and D. M. Goldman, 1982. The New HEC-1 Flood Hydrograph Package. *In:* Applied Modeling in Catchment Hydrology, V. P. Singh (Editor). Water Resources Publications, Littleton, Colorado, pp. 121-144.

Hydrologic Engineering Center, 1979. Introduction and Application of Kinematic Wave Routing Techniques Using HEC-1. Training Document No. 10, U.S. Army Corps of Engineers, Davis, California.

Hydrologic Engineering Center, 1985. HEC-1: Flood Hydrograph Package, Users Manual. U.S. Army Corps of Engineers, Davis, California.

Molinas, A., 1986. Application of Watershed Sediment routing Model HEC1WS to Yazoo River Basin Bottomland Hardwoods Project. Report prepared for the U.S. Fish and Wildlife SErvice, Rept. No. CER85-86AM19, January, Dept. of Civil Engineering, Colorado State University, Fort Collins, Colorado.

Molinas, A., G. T. Auble, and L. S. Ischinger, 1988. Assessment of the Role of Bottomland Hardwoods in Sediment and Erosion Control. Rept. No. NERC-88/11, February, U.S. Department of the Interior, Fish and Wildlife Service.

Raker, D. and H. Rice, 1987. Inside Autocad. New Riders Publishing, Thousand Oaks, California.

Robins, J. S., L. L. Kelly, and W. R. Hamon, 1965. Reynolds Creek in Southwest Idaho: An Outdoor Hydrologic Laboratory. Water Resources Research 1(3):407-413.

Soil Conservation Service, 1972. National Engineering Handbook, Section 4. U.S. Department of Agriculture, Washington, D.C.

Stephenson, G. R. (Editor), 1977. Soil-Geology-Vegetation Inventories for Reynolds Creek Watershed. Agricultural Experiment Station, University of Idaho College for Agriculture, University of Idaho Miscellaneous Series No. 42.

Reprinted from Nature, Vol. 316, No. 6022, pp. 746-747, 27 June 1985
© Macmillan Journals Ltd., 1985

Direct measurements of secondary currents in a meandering sand-bed river

C. R. Thorne*, L. W. Zevenbergen*, J. C. Pitlick†, S. Rais†, J. B. Bradley† & P. Y. Julien†

* Department of Geography and Earth Science, Queen Mary College, University of London, Mile End Road, London E1 4NS, UK
† Colorado State University, Fort Collins, Colorado 80523, USA

Natural channels often adopt a meandering course. Water flow in meander bends is three-dimensional, consisting of primary velocities which are tangential to the bend, and secondary velocities, which are in the radial plane. The pattern of secondary flow strongly affects the distribution of primary velocities. This in turn affects the distribution of erosion and deposition in the bend and the way in which the channel shifts and changes shape. Measurements of primary and secondary flows in a meandering gravel-bed river[1,2] show that, in addition to the widely recognized main secondary circulation driving surface water outwards and bed water inwards, there can be a small cell of reverse rotation at the outer bank. Further data have been collected in a sand-bedded river at low, intermediate and high discharges. The results confirm the existence of the main and outer bank cells but also indicate that in some bends the main cell does not extend to the inner bank. In fact, secondary flow at the inner bank of wide, shallow bends is directed radially outwards over the whole flow depth at all in-channel flows. This indicates that some models of bend flow and channel development may be significantly in error.

Secondary currents are defined as currents that occur in a plane normal to the axis of primary flow[3]. In meander bends, they develop by skewing of cross-stream vorticity into a long-stream direction[3,4]. The resulting skew-induced secondary circulation carries fast surface water towards the outer bank and slower bed water towards the inner bank.

At the outer bank, the primary flow, secondary circulation, and bank interact to produce a small cell of reverse rotation to the skew-induced cell. This cell occupies the channel to a distance one or two times the bank height away from the bank. Although this is a small proportion of the cross-section in most rivers, the outer bank cell is still important because it strongly affects the distribution of boundary shear stress, thereby influencing bank erosion processes[5,6].

In the central part of the channel, helical skew-induced flow produces inward velocities near the bed, which sweep bedload towards the inner bank. Sediment accumulation as a point bar at the inner bank gives the channel an asymmetrical cross-section. The balance between the transverse, upslope component of fluid drag on a bedload particle, and the transverse, downslope component of particle weight has been used as the basis for models of bed topography in bends[7,8]. This view of secondary flow-point bar interaction has been challenged recently[9]. Dietrich and Smith suggest that secondary flow above the point bar is directed radially outwards over the whole flow depth and that the helical skew-induced cell is confined to the deepest, or thalweg, portion of the cross-section. Sediment accumulation is then concentrated on a steep transverse slope called the point bar face, between the upper point bar (point bar platform) and the thalweg, where near bed flow converges and there is strong upwelling. Bridge[10] suggests that this pattern of flow and point bar building is a characteristic of point bar emergence at flows below about two-thirds bankfull. He suggests that at such low stages the point bar topography causes flow convergence at the bend entrance, but that such patterns are replaced by helical flow at formative (that is, bankfull) discharge.

To help to resolve this discussion, data were collected in this study over a range of discharges in meander bends of the Fall River in Rocky Mountain National Park, Colorado. The reach studied has a bankfull capacity of about $4\,m^3\,s^{-1}$ and well developed meanders with a sinuosity of 2.2. The annual hydrograph is dominated by snowmelt runoff, resulting in long periods of almost steady bankfull flow in May, June and July. The gradient is ~0.1%. The bed material is sand, $D_{50} = 1.0$ mm, moving in dunes, ripples and as suspended load. Sediment availability has been greatly increased by erosion associated with the failure of Lawn Lake Dam on the Roaring River (an upstream tributary) on 15 July 1982. As a result, the bed is mobile at all discharges and point bars in the bends respond quickly to changes in flow stage.

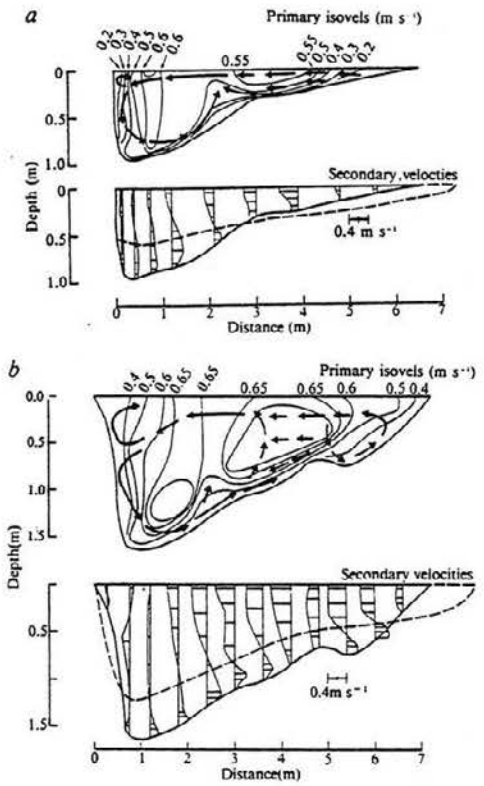

Fig. 1 Upstream bend apex, discharge: *a*, $1.7\,m^3\,s^{-1}$; *b*, $4.0\,m^3\,s^{-1}$. Dashed channel section represents that at the previous measurement section, ~6 m upstream.

Measurements were made at low, intermediate and bankfull stages, corresponding to discharges of 1.7, 2.8, and $4.0\,m^3\,s^{-1}$. Long and cross-stream velocities were measured using an electromagnetic current meter capable of measuring two mutually perpendicular velocity components with an accuracy of $\pm 3\,mm\,s^{-1}$. All measurements were made from temporary bridges aligned at right angles to the outer bank, and care was taken to work only over dune crests, avoiding separation zones on the lee side of dunes. Data were collected at 18 sections evenly spaced along the channel through two consecutive bends. The complete data set is available[11,12] but because of limitations of space, only data for the intermediate and high flow at the bend apices are reported here. However, these sections do typify the different patterns found in the two bends. The long and cross-stream velocities were resolved into primary and secondary components using the method based on three-dimensional continuity recommended by Dietrich and Smith[9]. The results are shown in Figs 1, 2.

At both sections and flows the salient feature of the secondary circulation is the helical, skew-induced cell. However, close to the outer bank, a small cell of reverse rotation is clearly present, especially at bankfull flow. These cells are associated with distortion of the primary isovels and depression of the maximum primary velocity below the free surface in the outer bank region.

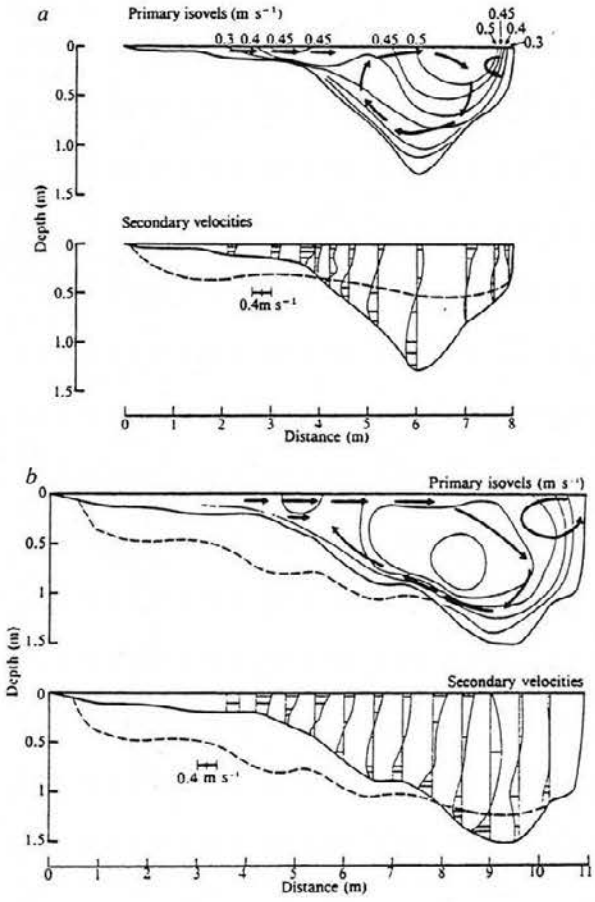

Fig. 2 Downstream bend apex, discharge: *a*, 1.7 $m^3 s^{-1}$; *b*, 4.0 $m^3 s^{-1}$. Dashed channel section represents that at the previous measurement section, ~4 m upstream.

The outer bank cell occupies the channel to a distance 1–2 times the bank height away from the outer bank, as observed elsewhere[5,9,10] and predicted theoretically[13].

The pattern of primary and secondary flows in the outer half of the channel changes little with stage at a bend, and is similar at both apices. This robustness is not present in the flow pattern in the inner half of the channel, where the two bends react differently to changing stage.

At intermediate flow, secondary flow over the point bar is directed radially outwards over the whole depth, as predicted and observed by Dietrich and Smith and by Bridge[9,10]. The reason for this is the dominance of the centrifugal force acting outwards over the hydrostatic pressure gradient, acting inwards. Also, the flow is shelving and narrowing in the longstream direction at the inner bank, as indicated in Figs 1*a* and 2*a* by the dashed lines showing the cross-section just upstream from the bend apex. Consequently, water is driven radially outwards to maintain continuity, leading to outward secondary flow. These arguments agree with the explanation put forward by the previous researchers[9,10].

At bankfull stage, the two bends show different flow patterns in the inner half of the channel. At the upstream bend, outward flow has been replaced by helical flow over most of the width, as predicted by Bridge[10]. The point bar has been scoured and reprofiled by the high flow and this, combined with the increased stage at almost constant width, has significantly increased the importance of the cross stream hydrostatic pressure gradient, which is now able to drive bed flow inwards. This is not the case at the downstream bend. Here, outward flow over the point bar persists up to bankfull discharge. The reason for this is that the width increases markedly with stage at the downstream bend, so that both the depth and the hydrostatic pressure gradient over the point bar remain small (Fig. 2*b*). Also, the point bar is more prominent in the downstream bend, so that shelving in the downstream direction is maintained at bankfull flow (Fig. 2*b*). This is not the case at the upstream bend, where high flow scouring produces deepening downstream at the inner bank (Fig. 1*b*).

We conclude that both patterns of flow in the inner half of the channel are possible and do occur in nature, depending on the morphology of the channel cross-section. Of particular importance is the stage-width relationship. Where there is marked widening with stage, outward flow persists to bankfull flow, but where width is almost constant with stage, helical flow expands almost to the inner bank. A quick survey of the Fall River bends revealed about equal numbers of bends falling into each category. As all the bends have the same bankfull discharge, sediment load, and bed and bank materials, there seems to be no obvious reason for the different morphologies, raising the possibility of there being two stable bend sections for a given set of independent controls. Clearly, point bar-flow interaction is a topic deserving further consideration and study.

This research was supported by the US National Parks Service, US Bureau of Reclamation, and Colorado State University.

Received 26 February; accepted 19 April 1985.

1. Bathurst, J. C., Thorne, C. R. & Hey, R. D. *Nature* 269, 504–506 (1977).
2. Thorne, C. R. & Hey, R. D. *Nature* 280, 226–228 (1979).
3. Prandtl, L. *Essentials of Fluid Dynamics* (Blackie, London, 1952).
4. Perkins, H. J. *J. Fluid Mech.* 44, 721–740 (1970).
5. Bathurst, J. C., Thorne, C. R. & Hey, R. D. *J. Hydraul. Div. Am. Soc. Civ. Engnrs.* 105, 1277–1295 (1979).
6. Thorne, C. R. & Lewin, J. *Adjustments of the Fluvial System* (George Allen and Unwin, London, 1979).
7. Allen, J. R. L. *Physical Processes in Sedimentation* (George Allen and Unwin, London, 1970).
8. Bridge, J. S. *Earth Surf. Process.* 2, 401–416 (1977).
9. Dietrich, W. E. & Smith, J. D. *Wat. Resour. Res.* 19, 1173–1192 (1983).
10. Bridge, J. S. *River Meandering* (American Society of Civil Engineers Spec. Publ. 1984).
11. Thorne, C. R., Rais, S., Zevenbergen, L. W., Bradley, J. B. & Julien, P. Y. *Wat. Resour. Field Support Lab. Rep. 83-9P* (Colorado State University, 1983).
12. Thorne, C. R., Zevenbergen, L. W., Bradley, J. B. & Pitlick, J. C. *Wat. Resour. Field Support Lab. Rep.* No 85-9P (Colorado State University, 1985).
13. Rais, S. Thesis Colorado State Univ. (1984).

Printed in Great Britain by Macmillan Production Ltd., Basingstoke, Hampshire

International Conference on
RIVER REGIME
18-20 May, 1988

PAPER A2

DOWNSTREAM HYDRAULIC GEOMETRY OF NONCOHESIVE ALLUVIAL CHANNELS

Pierre Y. Julien
Engineering Research Center, Colorado State University
Fort Collins, Colorado 80523 U.S.A.

SUMMARY: Four fundamental relationships are combined to theoretically define the downstream hydraulic geometry of noncohesive alluvial channels. The flow depth, channel width, velocity and slope of similar channels depend primarily on discharge and sediment size.

1. INTRODUCTION

Alluvial channels are known to self adjust their slope, width, depth, and velocity. The shape of alluvial channels is modified during extreme events depending on the magnitude of water and sediment discharges. Downstream hydraulic geometry relationships describe the shape of alluvial channels as it progresses in the downstream direction. Early investigations on downstream hydraulic geometry relationships by Leopold and Maddock (Ref. 6) showed that the channel width, the flow depth, the mean flow velocity and the slope can be written as power functions of discharge. Similar relationships have been derived by Li et al. (Ref. 8).

2. FUNDAMENTAL RELATIONSHIPS

In this paper, hydraulic geometry relationships for the channel width W, mean flow depth h, mean flow velocity $\bar{U}$ and channel slope S are theoretically derived after considering the similarities between noncohesive alluvial streams. The following four fundamental concepts are considered: (1) continuity; (2) flow resistance; (3) longitudinal mobility; and (4) radial mobility. The first three concepts are briefly summarized whereas the radial mobility is discussed more thoroughly.

2.1 Continuity

The continuity equation describes conservation of mass flux or discharge Q in steady open-channels:

$$Q = Wh\bar{U} \tag{1}$$

The cross section area, Wh, is measured normal to the mean velocity vector.

International Conference on River Regime, edited by W.R.White.
© Hydraulics Research Limited, 1988. Published by John Wiley & Sons. Ltd.

2.2 Flow Resistance

The resistance relationship proposed by Einstein and Chien (Ref. 2) for turbulent flows over an hydraulically rough boundary reads:

$$\bar{U} \sim \sqrt{g}\,\left(\frac{h}{d_s}\right)^{a} h^{1/2} S^{1/2} \tag{2}$$

in which g is the gravitational acceleration, d_s is the sediment size, and a is an exponent proportional to the relative roughness. For very small relative roughness, $a = 0$, and Eq. 2 reduces to the Chezy equation. The well-known Manning-Strickler relationship corresponds to $a = 1/6$. In gravel and cobble bed streams, the exponent a becomes larger. For example, Kellerhals (Ref. 5) suggested $a = 0.25$; Leopold and Wolman (Ref. 7) found $a = 0.5$ when $0.7 < h/d_s < 10$; and Church (Ref. 1) showed that $0.43 < a < 3.35$.

2.3 Longitudinal Mobility

For steady uniform flow conditions in open channels, the longitudinal boundary shear stress τ_θ is

$$\tau_\theta = \rho g\, h\, S \tag{3}$$

in which ρ is the mass density of water. The stability of straight alluvial channels is described by the relative magnitude of the shear forces exerted on the boundary and the resistance to motion of individual noncohesive particles. The ratio of these two forces defines the longitudinal mobility factor or Shields number τ_θ^*:

$$\tau_\theta^* = \frac{\tau_\theta}{(\rho_s - \rho) g\, d_s} \tag{4}$$

in which ρ_s is the density of particles. The Shields diagram defines the threshold conditions for sediment motion, and τ_θ^* remains constant for turbulent flows over a rough boundary. It must also be recognized that the sediment load increases with τ_θ^* beyond the critical value.

Considering constant values of ρ_s, ρ and g in Eqs. 3 and 4, the longitudinal mobility of sediments reduces to

$$\tau_\theta^*\, d_s \sim h\, S \tag{5}$$

In straight channels without secondary circulation, this relationship describes the cross-sectional geometry of an alluvial channel. Indeed, Lane (Ref. 3) analyzed the stability of particles on channel banks after considering the shear stress in the downstream direction and the weight of the particles. The ideal cross-sectional geometry of noncohesive alluvial channels has been theoretically defined (Refs. 9, 13) when the threshold condition for all sediment particles on the banks and the bed is satisfied.

2.4 Radial Mobility

In curved channels, the concept of radial mobility is introduced to describe the lateral stability of alluvial channel bends subjected to secondary flows. Secondary circulation is generated through a change in channel orientation in the downstream direction. The streamlines near the surface are deviated toward the outer bank whereas those near the boundary are deviated toward the inner bank. As a result, the velocity near the bed, the tangential bed shear stress and the drag on the bed particles are deviated toward the inner bank.

Flow in bends is analyzed in a cylindrical system of coordinates. The relative magnitude of the radial acceleration terms shows that the centrifugal acceleration is counterbalanced by a pressure gradient and radial shear stress, as suggested by Rozovskii (Ref. 10)

$$\frac{\bar{u}^2}{r} = g S_r - \frac{1}{\rho} \frac{\partial \tau_r}{\partial z} \tag{6}$$

in which $\bar{u}$ is the local downstream velocity, r is the radius of curvature, S_r is the radial water surface slope, τ_r is the radial boundary shear stress, and z is the vertical coordinate. With reference to Fig. 1, the transverse boundary shear stress τ_{rR} at point R and the transverse water surface slope S_{rA} at point A serve as scaling factors. These scaling factors are used to define the following dimensionless parameters for the channel width $w' = w/W$; the flow depth, $z' = z/h$; the radius of curvature, $r' = r/W$; the velocity $u' = \bar{u}/\bar{U}$; the radial shear stress, $\tau_r' = \tau_r/\tau_{rR}$; and the radial surface slope, $S_r' = S_r/S_{rA}$. The element of volume $d\forall = rd\phi dzdw$ of a given reach of length $rd\phi$ is reduced to a dimensionless volume $d\forall' = d\forall/W^2h$.

The equation of motion (Eq. 6) is multiplied by ρ and $d\forall$, reduced to a dimensionless form, then integrated over the dimensionless volume $\forall'$ of the reach. The resulting dimensionless momentum equation in the radial direction is

$$Wh\rho\bar{U}^2 \int_{\forall'} \frac{u'^2}{r'} d\forall' = \rho g W^2 h S_{rA} \int_{\forall'} S_r' d\forall' - W^2 \tau_{rR} \int_{\forall'} \frac{\partial \tau_r'}{\partial z'} d\forall' \tag{7}$$

The corresponding force diagram is sketched in Fig. 1 after denoting the centrifugal force on the left-hand side of the equation by F_c, the pressure force on the right-hand side by F_p and the shear force exerted on the fluid by F_s. The pressure force balances the sum of the centrifugal force exerted at a distance c above point A and the shear force exerted at a distance d below point A. Moment equilibrium around point A gives:

$$\pi_r = \rho \frac{h\bar{U}^2}{W \tau_{rR}} = \frac{d}{c} \frac{\int_{\forall'} \frac{\partial \tau_r'}{\partial z'} d\forall'}{\int_{\forall'} \frac{u'^2}{r'} d\forall'} \tag{8}$$

The dimensionless parameter π_r denotes the ratio of the centrifugal force generating motion to the shear force abating the motion and dissipating energy. Owing to the similarities in velocity profiles and shear stress distributions in dimensionless form, the ratio d/c in Eq. 8 and the volume integrals remain constant. It is therefore assumed as a first approximation that a constant value of π_r represents flow conditions in bends.

The mobility of sediment particles in a curved channel is now considered. In dimensionless form, the radial mobility factor or radial Shields parameter τ_r^* describes the ratio of the radial shear force to the submerged weight of a single particle.

$$\tau_r^* = \frac{\tau_{rR}}{(\rho_s - \rho) g d_s} \tag{9}$$

The stability of bed particles on sloping planes when the drag force deviates from the downstream direction has been analyzed by Stevens and Simons (Ref. 14). It is shown from this method that a downward shear stress component mobilizes the particles near the outer bank. On the other hand, a slight upward shear stress component stabilizes the particles and induces deposition. When this upward component becomes large, however, the particles are mobilized and scour occurs near the inner bank. Removal of bed material at the toe of the outer bank is initiated and at low values of the radial Shields parameter, deposition occurs near the river bank. At larger values of the radial Shields parameter, however, particles are eroded along the full width of the channel, which results in channel widening. The result of combining Eq. 8 with Eq. 9 while keeping π_r, ρ_s, ρ and g constant is:

$$\tau_r^* \sim \frac{h\bar{U}^2}{Wd_s} \tag{10}$$

Equation 10 relates radial mobility to hydraulic geometry and bed sediment size, the radial mobility factor being inversely proportional to the width-depth ratio at a given flow velocity. Therefore, widening of a narrow channel through bank erosion is expected to occur until τ_r^* is reduced sufficiently to stabilize the bed and bank material.

3. DOWNSTREAM HYDRAULIC GEOMETRY OF NONCOHESIVE ALLUVIAL CHANNELS

The above cited relationships are combined to algebraically derive the downstream hydraulic geometry of alluvial channels: continuity (Eq. 1); resistance to flow (Eq. 2); longitudinal mobility (Eq. 5); and radial mobility (Eq. 10). As a result of a similar derivation presented by Julien and Simons (Ref. 4), flow depth h, channel width W, velocity $\bar{U}$, and slope S can be written as power functions of discharge Q, bed sediment size d_s, longitudinal and radial mobility factors τ_θ^* and τ_r^*:

$$h \sim Q^{\frac{1}{2+3a}} d_s^{\frac{6a-1}{4+6a}} \tau_\theta^{*\frac{-3}{4+6a}} \tau_r^{*\frac{1}{2+3a}} \tag{11}$$

$$W \sim Q^{\frac{1+2a}{2+3a}} d_s^{-\frac{1+4a}{4+6a}} \tau_\theta^{*\frac{1}{4+6a}} \tau_r^{*-\frac{1+a}{2+3a}} \tag{12}$$

$$\bar{U} \sim Q^{\frac{a}{2+3a}} d_s^{\frac{1-a}{2+3a}} \tau_\theta^{*\frac{1}{2+3a}} \tau_r^{*\frac{a}{2+3a}} \tag{13}$$

$$S \sim Q^{-\frac{1}{2+3a}} d_s^{\frac{5}{4+6a}} \tau_\theta^{*\frac{7+6a}{4+6a}} \tau_r^{*\frac{-1}{2+3a}} \tag{14}$$

These equations are essentially valid for similar channels in noncohesive alluvial material. Typical values of the exponent a range from 0 to more than 0.4 depending on the relative roughness. For constant values of τ_θ^* and τ_r^*, the resulting relationships describing flow depth, channel width, velocity and slope reduce to simple power functions of discharge Q and sediment size d_s.

4. DISCUSSION

4.1 Flow Depth, h (Eq. 11)

The exponent of water discharge varies slightly around 0.4 and the exponent of sediment size can be either positive or negative depending on the relative roughness. Interestingly, the flow depth becomes independent of sediment size when Manning's equation is applicable (a = 1/6). The negative values of the exponent of τ_θ^* indicate that flow depth is inversely proportional to sediment mobility. Thus, flow depth is proportional to discharge and inversely proportional to sediment transport. These results are in agreement with the well-known (Refs. 11, 12) qualitative geomorphic principles for fluvial systems: $Q^+ \sim h^+$; $Q_s^+ \sim h^-$ (the signs + and - denote respectively an increase or decrease of the variable considered).

4.2 Channel Width, W (Eq. 12)

Channel width is proportional to discharge and sediment transport and inversely proportional to sediment size. The exponent of discharge remains close to 0.5 regardless of the relative roughness. This is in perfect agreement with Lacey's regime equation. Sediment mobility appears to have a slight influence on the channel width since the exponent of τ_θ^* remains relatively small. An increase in sediment load results in a small increase in channel width. Here again, the qualitative concepts ($Q^+ \cong W^+$; $Q_s^+ \cong W^+$) proposed by Schumm (Ref. 11) find theoretical support in Eq. 12.

4.3 Average Velocity, $\bar{U}$ (Eq. 13)

The average velocity is proportional to discharge, sediment size, and sediment mobility. A significant reduction of the exponent of d_s and a slight increase in the exponent of discharge result from increasing relative roughness.

4.4 Slope, S (Eq. 14)

The slope is proportional to sediment size and sediment mobility and inversely proportional to discharge. The discharge exponent increases while the sediment size exponent decreases with increasing relative roughness. Equation 14 supports qualitative geomorphic principles ($Q^+ \sim S^-$; $d_s^+ \sim S^+$; $Q_s^+ \sim S^+$) found by Simons et al. (Ref. 12) and Schumm (Ref. 11).

5. SUMMARY AND CONCLUSION

The downstream hydraulic geometry of alluvial channels described by flow depth, channel width, velocity, and slope is examined. Four fundamental relationships (continuity, flow resistance, longitudinal mobility, and radial mobility) are combined to derive theoretical hydraulic geometry relationships for turbulent flows over a rough boundary.

As a result, the hydraulic geometry can be written as a power function of discharge, bed sediment size, and two mobility factors. The theoretical results support very well the qualitative relationships of Simons and Schumm. For constant values of the mobility factors, the hydraulic geometry is then reduced to a power function of sediment size and discharge.

6. ACKNOWLEDGEMENTS

This study has been undertaken with the support of a NATO post-doctoral fellowship from the Natural Sciences and Engineering Research Council of Canada. The writer is indebted to Prof. D. B. Simons for his guidance during the course of this study.

7. REFERENCES

1. Church, M.: "Baffin Island sanders: A study of arctic fluvial process". Geological Survey of Canada Bulletin, 216, 1972, 208 pp.

2. Einstein, H. A. and Chien, N.: "Similarity of distorted river models with unstable bed". Proceedings of the ASCE, Vol. 80, No. 566, 1954, 21 pp.

3. Lane, E. W.: "Design of stable channels". Transactions of the ASCE, Vol. 120, Proc. Paper 2776, 1955, pp. 1234-1279.

4. Julien, P. Y. and Simons, D. B.: "Analysis of hydraulic geometry relationships in alluvial channels". Report No. CER83-84PYJ-DBS45, Civil Engineering Department, Colorado State University, Fort Collins, Colo., 1984, 47 pp.

5. Kellerhals, R.: "Stable channels with gravel-paved beds". Journal of the Waterways and Harbors Division, ASCE, Vol. 93, No. WW1, Proc. Paper 5091, Feb. 1967, pp. 63-84.

6. Leopold, L. B. and Maddock, T.: "The hydraulic geometry of stream channels and some physiographic implications". USGS Prof. Paper 252, 1953.

7. Leopold, L. B. and Wolman, M. G.: "River channel patterns: braided, meandering and straight". USGS Prof. Paper 282-B, 1957, pp. 38-85.

8. Li, R. M., Simons, D. B. and Stevens, M. A.: "Morphology of cobble streams in small watersheds". Journal of the Hydraulics Division, ASCE, Vol. 102, No. HY8, Aug. 1976, pp. 1101-1117.

9. Raudkivi, A. J.: "Loose Boundary Hydraulics" Pergamon Press, 2nd Ed., 1976, pp. 250-254.

10. Rozovskii, I. L.: "Flow of water in bends of open channels". Academy of Science of the Ukrainian SSR, Kiev, Translation by Y. Prushansky, Israel Program for Scientific Translations, S. Monson, Jerusalem, PST Cat. No. 363, 1957.

11. Schumm, S. A.: "The Fluvial System" Wiley Interscience, 1977, 338 pp.

12. Simons, D. B., Richardson, E. V. and Mahmood, K.: "One-dimensional modeling of alluvial rivers". Chapter 19 in Unsteady Flow in Open Channels, Water Resources Publications, Fort Collins, Colo., 1975, pp. 813-877.

13. Simons, D. B. and Senturk, F.: "Sediment transport technology" Water Resources Publications, Fort Collins, Colo., 1977, 807 pp.

14. Stevens, M. A. and Simons, D. B.: "Stability analysis for coarse granular material on slopes" Chapter 17 in River Mechanics," H. W. Shen, Ed., Water Resources Publications, Fort Collins, Colo., 1971, 27 pp.

8. NOTATION

The following symbols are used in this paper:

a exponent of the resistance equation

c distance between F_c and F_p

d distance between F_p and F_s

d_s	sediment size of bed material
F_c	centrifugal force
F_p	pressure force
F_s	shear force
g	gravitational acceleration
h	average depth
Q	discharge
r	radius of curvature
r'	dimensionless radius of curvature
S	longitudinal slope
S_r	radial water surface slope
S_{rA}	radial water surface slope at point A
S'_r	dimensionless radial water surface slope
$\bar{u}$	local longitudinal velocity
u'	dimensionless longitudinal velocity
$\bar{U}$	average longitudinal velocity
$\forall$	volume of fluid within a given reach
$\forall'$	dimensionless volume of fluid
w	channel width at the elevation z
w'	dimensionless width
W	channel width
z	vertical coordinate
z'	dimensionless depth
γ	specific weight of water
ϕ	angle between the downstream direction and the down-valley direction
π_r	dimensionless ratio of centrifugal to radial shear forces in bends
ρ	mass density of water
ρ_s	density of particles
τ_o	longitudinal boundary shear stress

τ_r radial boundary shear stress

τ_{rR} radial boundary shear stress at point R

τ'_r dimensionless radial boundary shear stress

τ^*_θ longitudinal mobility factor

τ^*_r radial mobility factor

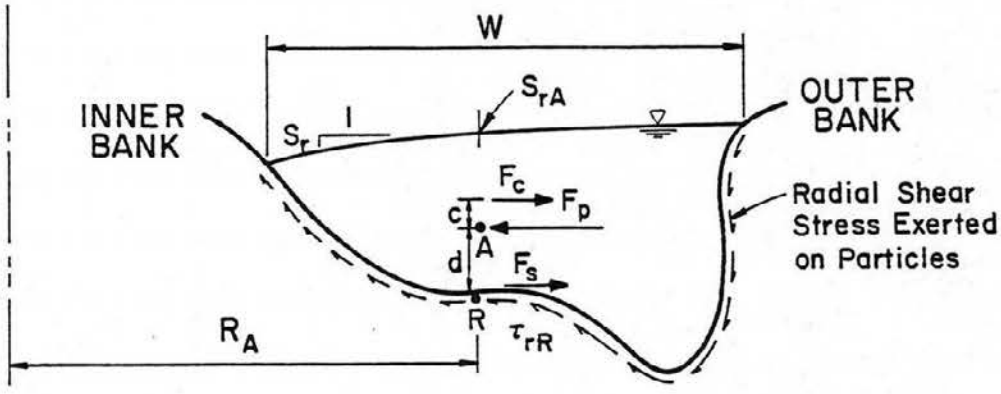

Figure 1. Force diagram in the radial direction.

Sediment Transport Capacity of Overland Flow

P. Y. Julien, D. B. Simons

This article is reprinted from the TRANSACTIONS of the ASAE (Vol. 28, No. 3, pp. 755–762, 1985)
Published by the American Society of Agricultural Engineers, St. Joseph, Michigan

ABSTRACT

OVERLAND flow runoff can be either laminar or turbulent depending on the Reynolds number. The rate of soil erosion may be limited by the sediment transport capacity which depends on the type of flow. Sediment transport equations based on velocity were found to give different results than those based on shear stress. Most of the sediment transport equations developed for turbulent streams should not be applied to soil erosion by overland flow. A general relationship supported by dimensional analysis was derived. The recommended sediment transport capacity relationship can be written as a power function of slope and discharge and the range of exponents was defined from empirical relationships.

INTRODUCTION

Soil erosion by rainfall is one of the major hazards threatening the productivity of farmlands. The physical processes governing the movement of sediments by rainfall are very complex. The rate of soil erosion depends mainly on the detachment of soil particles and on the transporting capacity of overland runoff. Several sediment transport equations and soil loss relationships have been developed both from experimental studies in laboratories under simulated rainfall (Kilinc, 1972) and from statistical and regression analysis using field data (Wischmeier and Smith, 1978). Recently, some researchers have recommended the use of well-known bed-load equations to predict soil erosion losses from overland flow. For example, Komura (1976) used the Kalinske-Brown relationship and obtained fair agreement with observed data though his data set was relatively limited. The Meyer-Peter and Muller equation has also been suggested by Li (1979) for overland flow. Several sediment transport equations have been examined by Alonso, Neibling and Foster (1981) to determine how well they fit observed data on concave slopes.

Fundamental relationships for sediment transport in turbulent stream flows have been used as a basis for the analysis of sediment transport capacity by overland flow. However, since sheet flows are generally classified as laminar a theoretical analysis is required in order to determine if a sediment transport formula derived for turbulent streamflow is also applicable to laminar sheet flow.

Article was submitted for publication in July, 1984; reviewed and approved for publication by the Soil and Water Div. of ASAE in December, 1984.

The contribution of the first author was supported by the Natural Sciences and Engineering Research Council of Canada.

The authors are: P. Y. JULIEN, Fac. Affiliate, Dept. of Civil Engineering, and D. B. SIMONS, Professor, Dept. of Civil Engineering, Colorado State University, Fort Collins.

Therefore, the purpose of this study was to investigate the applicability of several sediment transport equations under various hydraulic conditions, including laminar sheet flow. In the first part of this paper, the hydraulic characteristics relevant to sediment transport are summarized to clearly point out the differences between turbulent and laminar flows. Then several sediment transport formulas valid for turbulent streamflow are examined under laminar sheet flow conditions. These transformed relationships are compared with regression equations obtained from experimental studies of soil erosion.

OVERLAND FLOW CHARACTERISTICS

In natural fields, overland flow occurs when the rainfall intensity is in excess of the infiltration rate of the soil. A very thin film of water covers the soil surface and it is referred to as the laminar sheet flow. As the runoff rate increases downslope, the flow converges into micro-scale channels called rills which gradually develop until they form large-scale channels called gullies. In a recent study, Thorne (1984) also defined ephemeral gullies in arable fields. These gullies are formed by the concentraiton of surface runoff and are obliterated each year by normal tillage.

Gully, rill and sheet runoff have different hydraulic properties depending on the relative magnitude of inertia and viscous forces. The ratio of these two types of forces defines the Reynolds number Re. When the inertia forces largely overcome the viscous forces, such as flows in rivers and gullies, the Reynolds number is large and the flow is turbulent. In the case of thin overland runoff, the viscous forces overcome the inertia forces and the flow is called laminar. In sheet flows, perturbations induced by raindrop impact and surface roughness are greatly attenuated due to the large magnitude of viscous forces at low Reynolds numbers. These forces damp out the velocity fluctuations caused by these disturbances and sheet flows over rough boundaries remain laminar until a critical value of the Reynolds number is exceeded.

Another major difference between stream flow and sheet flow is related to the flow depth. For a given particle size, the transport of sediments by saltation and suspension in overland flow is very limited due to the reduced flow depth. The bed load movement, however, may predominate and the most accurate sediment transport rates might be given by bed-load equations, the validity of this statement being precisely the purpose of this investigation.

The principal variables describing overland flow are shown in Fig. 1. The main geometric variables are slope length L and gradient S. The hydraulic variables are rainfall intensity i, flow depth h, mean velocity $\bar{u}$, unit water discharge q and thickness of the laminar sublayer δ'. The parameter generally associated with the sediment discharge q_s is bed shear stress τ_o; the other properties

 © 1985 American Society of Agricultural Engineers 0001-2351/85/2803-0755$02.00

103

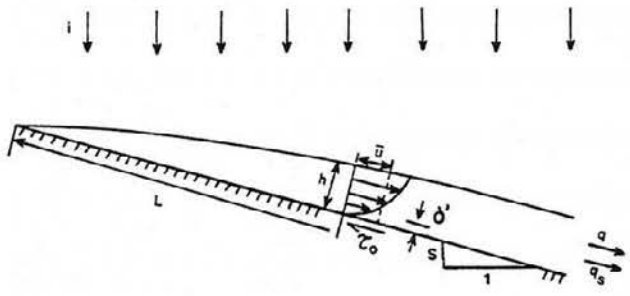

Fig. 1—Overland flow variables.

being gravitational acceleration g, kinematic viscosity ν and specific mass of water ρ.

Fundamental Equations

Two nonlinear partial differential equations derived by de Saint-Venant are generally used to solve the problem of gradually varied unsteady flows. These are the continuity relationship describing the conservation of mass and the momentum equation which is a force equilibrium relationship. In the case of steady overland flow, the continuity equation reduces to:

$$q = \bar{u}\,h \quad \ldots\ldots [1]$$

Considering the principal terms of the momentum equation, the kinematic wave approximation has been recommended by Wooding (1965) and Woolhiser (1975). This approximation states that the slope of the energy line is equal to the soil surface slope, or:

$$S = S_f \quad \ldots\ldots [2]$$

in which S_f is the slope of the energy line or friction slope.

The slope of the energy line can be defined by the Darcy-Weisbach relationship:

$$S_f = \frac{f}{8}\frac{\bar{u}^2}{gh} \quad \ldots\ldots [3]$$

where f is the Darcy-Weisbach friction factor.

The friction factor f is a function of the Reynolds number and the relative roughness for turbulent flows. The Reynolds number is defined as:

$$Re = \frac{\bar{u}\,h}{\nu} \quad \ldots\ldots [4]$$

As the Reynolds number increases, the flow becomes turbulent and the friction factor is then a function of the roughness of the surface. The roughness of the boundary depends on the sediment size d_s and the thickness of the laminar sublayer δ'. Two important variables are associated with the thickness of the boundary sublayer δ'. These are bed shear stress τ_o and shear velocity U_*. These variables are defined as:

$$\tau_o = \rho g h S_f \quad \ldots\ldots [5]$$

$$U_* = \sqrt{\frac{\tau_o}{\rho}} \quad \ldots\ldots [6]$$

$$\delta' = \frac{11.6\,\nu}{U_*} \quad \ldots\ldots [7]$$

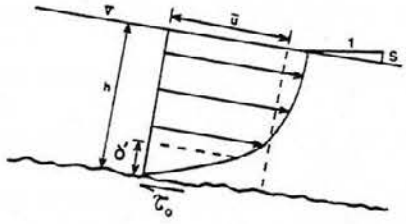

Fig. 2—Turbulent flow over a smooth surface.

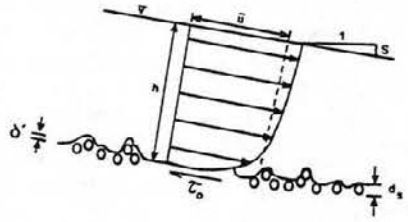

Fig. 3—Turbulent flow over a rough surface.

The ratio of sediment size d_s to the thickness of the laminar sublayer δ' delineates two types of turbulent flow conditions shown in Figs. 2 and 3 for smooth and rough boundaries respectively.

From combining equations [5], [6], and [7], the ratio δ'/d_s is:

$$\frac{\delta'}{d_s} = \frac{11.6\,\nu}{d_s\sqrt{ghS_f}} \quad \ldots\ldots [8]$$

This parameter and the Reynolds number are used to define the type of overland flow.

Overland Flow Types

The four principal types of flow relevant to this investigation on soil erosion by overland flow are: (a) laminar sheet flow; (b) turbulent smooth flow governed by the Blasius equation; (c) turbulent rough flow (Manning equation); and (d) turbulent rough flow with very small relative roughness (Chezy equation). This last flow type is not very likely to occur in overland flow. However, it has been included in this analysis since it represents a limiting case for which the Darcy-Weisbach friction factor remains constant. For steady flow conditions, the principal variables related to soil erosion ($\bar{u}$, h and τ_o) are defined as a function of slope and water discharge.

Laminar Flow

In laminar flows with raindrop impact the Darcy-Weisbach friction factor f is related to: (a) the Reynolds number Re, (b) the surface friction coefficient k_o without raindrop impact, and (c) two empirical coefficients A and b for raindrop impact. The following relationship is generally used:

$$f = \frac{K}{Re} = \frac{k_o + Ai^b}{Re} \quad \ldots\ldots [9]$$

The values of k_o have been tabulated by Woolhiser (1975) for various surface types and the value $k_o = 24$ is representative of the smooth surface condition. Experimental coefficients A and b have been obtained by Izzard (1944), Li (1972), and Fawkes (1972), and these

TABLE 1. RESISTANCE COEFFICIENTS A AND b FOR RAINFALL.

Reference	A†	b
Izzard (1944)	750	1.33
Li (1972)	118	0.4
Fawkes (1972)	393	1.0

†For i in m per hour.

values are indicated in Table 1. The experimental values of the friction coefficient f obtained by Shen and Li (1973) indicate that for a bare smooth surface, the flow is laminar for Re < 900 and the Blasius law is valid for turbulent smooth flows when Re > 2000. Chen's data (1976) show that k_o can be as large as 50,000 for vegetated surfaces and laminar flow conditions were observed for Reynolds numbers as large as 10^5.

At low Reynolds numbers, the friction parameter K for sheet flows is constant, and the Darcy-Weisbach equation is given by:

$$S_f = \left(\frac{K\nu}{\bar{u}\,h}\right)\frac{\bar{u}^2}{8gh} \quad \ldots\ldots\ldots\ldots\ldots\ldots\ldots\ldots [10]$$

The variables $\bar{u}$, h, and τ_o for laminar sheet flows derived from equations [1], [2], [5], and [10] are summarized in Table 2 for comparison with similar relationships valid under turbulent conditions.

Turbulent Flow over a Smooth Surface

For bare soil surfaces the flow becomes turbulent when Re > 2000 and the flow is called hydraulically smooth when the thickness of the laminar sublayer given by equation [7] is much in excess of the size of soil particles

TABLE 2. SUMMARY OF FLOW CHARACTERISTICS (VELOCITY, DEPTH, AND SHEAR STRESS).

Velocity	$\bar{u} = c\,S^a\,q^d$			
Type of flow	c		a	d
Laminar (K = constant)	$\left(\frac{8g}{K\nu}\right)^{0.333}$		0.333	0.667
Turbulent, smooth boundary	$\left(\frac{8g}{0.316}\right)^{0.333}$	$\nu^{-0.083}$	0.333	0.417
Turbulent (n = constant)	$\left(\frac{1}{n}\right)^{0.6}$		0.3	0.4
Turbulent (f = constant)	$\left(\frac{8g}{f}\right)^{0.333}$		0.333	0.333
Depth	$h = c\,S^a\,q^d$			
Type of flow	c		a	d
Laminar (K = constant)	$\left(\frac{K\nu}{8g}\right)^{0.333}$		-0.333	0.333
Turbulent, smooth boundary	$\left(\frac{0.316}{8g}\right)^{0.333}$	$\nu^{0.083}$	-0.333	0.583
Turbulent (n = constant)	$n^{0.6}$		-0.3	0.6
Turbulent (f = constant)	$\left(\frac{f}{8g}\right)^{0.333}$		-0.333	0.667
Shear stress	$\tau_o = c\,S^a\,q^d$			
Type of flow	c		a	d
Laminar (K = constant)	$\rho g\left(\frac{K\nu}{8g}\right)^{0.333}$		0.667	0.333
Turbulent, smooth boundary	$\rho g\left(\frac{0.316}{8g}\right)^{0.333}$	$\nu^{0.083}$	0.667	0.583
Turbulent (n = constant)	$\rho g\, n^{0.6}$		0.7	0.6
Turbulent (f = constant)	$\rho g\left(\frac{f}{8g}\right)^{0.333}$		0.667	0.667

($\delta' > 3\,d_s$). In this case, Keulegan (1938) derived an equation similar to the von Karman-Prandtl logarithmic equation. When the Reynolds number is not too large, this equation can be approximated by the Blasius equation for which the Darcy-Weisbach friction factor becomes:

$$f = \frac{0.316}{Re^{0.25}} \quad \ldots\ldots\ldots\ldots\ldots\ldots\ldots\ldots [11]$$

For turbulent flows over a smooth surface, the variables $\bar{u}$, h and τ_o given in Table 2 are derived from equations [1], [2], [3], [5], and [11]. The exponents of S for these three variables are identical to those obtained for laminar sheet flows.

Turbulent Flow over a Rough Surface

For turbulent flows an increase of the Reynolds number (or water discharge) raises the water level, and decreases the relative roughness and the friction factor. When the thickness of the laminar sublayer is small compared to sediment size ($\delta' < 5\,d_s$), the flow is hydraulically rough and the logarithmic equation given by Keulegan (1938) applies. The friction coefficient is defined as:

$$\sqrt{\frac{8g}{f}} = C = c_1 \log c_2 \frac{h}{d_s} \quad \ldots\ldots\ldots\ldots\ldots\ldots [12]$$

Approximate power relationships such as the Manning equation, however, are frequently used by hydraulic engineers. Since both equations give similar results for open channel flows without bedforms when the relative roughness ranges between 10 and 10000, the Manning equation (SI units) is used in this study. The equivalent Darcy-Weisbach f is then:

$$\sqrt{\frac{8g}{f}} = \frac{h^{1/6}}{n} \quad \ldots\ldots\ldots\ldots\ldots\ldots\ldots [13]$$

in which n is the Manning roughness coefficient. The well-known Manning-Strickler relationship gives the proportionality between the median size of the sediment particles (in mm) at the boundary and the Manning roughness coefficient:

$$n = 0.0132\,d_s^{1/6} \quad \ldots\ldots\ldots\ldots\ldots\ldots\ldots [14]$$

The combination of equations [1], [2], [3], [5], and [13] gives the relationships for $\bar{u}$, h, and τ_o shown in Table 2 for turbulent rough conditions (n = constant).

When the relative roughness becomes extremely small, the Darcy-Weisbach equation is equivalent to the Chezy equation ($f = 8g/C^2$). Both coefficients f and C are constant and after combining equations [1], [2], [3], and [5], the variables $\bar{u}$, h, and τ_o are written as a function of S and q. The resulting expressions are listed in Table 2. The relationship $\tau_o \propto \bar{u}^2$ is valid for the Chezy equation and the exponents are slightly different from those derived for the Manning relationship. The exponents of q and S of the velocity relationship are identical and equal to 0.333.

Discussion

The results of this analysis of the hydraulic characteristics are summarized in Table 2. The velocity, the flow depth, and the bed shear stress are written in

terms of discharge and slope. The exponent of the slope does not vary significantly for different flow conditions ranging from laminar to turbulent. The exponents of the slope for velocity, flow depth, and bed shear stress are respectively 0.33, −0.33, and 0.67. On the other hand, the exponents of the water discharge vary gradually and differ by a factor 2 between the extreme conditions. The exponents of discharge for velocity and shear stress vary in opposite directions. Indeed, for flow conditions changing from laminar to turbulent flows, the exponent of velocity varies gradually from 0.67 to 0.33 while the exponent of shear stress varies from 0.33 to 0.67. This effect is extremely important if we consider the rate of sediment transport.

SEDIMENT TRANSPORT EQUATIONS

The sediment transport capacity of overland flow under rainfall was investigated to obtain a theoretically sound relationship supported by empirical equations. The method of dimensional analysis was applied to the principal variables related to soil erosion.

Variables and Dimensional Analysis

Sheet erosion is the result of the detachment of soil particles by raindrop impact and transport by overland flow. The eroded soil particles are transported downstream by runoff and the unit sediment discharge is a function of the following variables:

$$q_s = f(L, S, i, \bar{u}, h, q, \tau_o, \tau_c, d_s, \rho_s, \rho, \nu, g) \quad \ldots\ldots [15]$$

in which τ_c is critical shear stress and d_s is size of soil particles, and the other variables are as defined previously. Among these variables, the first two (L, S) describe the geometry and the next five (i, $\bar{u}$, h, q, τ_o) are flow characteristics including rainfall intensity. The last six (τ_c, d_s, ρ_s, ρ, ν, g) are associated with soil and water properties and the gravitational acceleration. Shear stress is difficult to measure in the field and is usually computed from other variables. In a river, the variables S, $\bar{u}$, h, and q are used to describe stream flows because the velocity and depth are generally more easily measured than rainfall intensity i and runoff length L. For this reason, Laursen (1956) suggested the reduction of some sediment transport equations to a function of the variables $\bar{u}$ and h. In the case of soil erosion, however, the variables i and L have important physical significance. The slope and unit water discharge may be more easily measured than the velocity and depth. Therefore, the variables S and q may be more convenient than $\bar{u}$ and h as components of a sediment transport relationship for overland flow under steady-state condition; elimination of the variables $\bar{u}$ and h from the Darcy-Weisbach and the continuity equation $q = \bar{u}h$ is possible.

The critical shear stress value τ_c corresponds to the beginning of motion of the sediment particles. Its evaluation remains a complex problem requiring further investigation, but the fundamental relationship defining the incipient motion of sediments indicates that the critical shear stress is a function of the particle size and the specific masses of water and sediment. Therefore, the sediment size can be replaced by the critical shear stress in a sediment transport equation. The specific masses of water and sediment are nearly constant for particle sizes ranging from clays to gravels. In the case of aggregates, equivalent conditions of shear stress can be defined, for example, using an equivalent diameter, while keeping the same specific mass of sediment in the analysis.

Using these relationships and assuming ρ_s constant, equation [15] reduces to:

$$f(q_s, q, i, L, \rho, \nu, \tau_c/\tau_o, S) = 0 \quad \ldots\ldots [16]$$

The following Π-terms are obtained from dimensional analysis after L, ρ, and ν are selected as repeating variables:

$$f\left(\frac{q_s}{\rho\nu}, \frac{q}{\nu}, \frac{iL}{\nu}, \frac{\tau_c}{\tau_o}, S\right) = 0 \quad \ldots\ldots [17]$$

The sediment transport term can be written as a function of the product of the other Π-terms in the form:

$$\left(\frac{q_s}{\rho\nu}\right) = \bar{\alpha}\ S^{\beta}\left(\frac{q}{\nu}\right)^{\gamma}\left(\frac{iL}{\nu}\right)^{\delta}\left(1 - \frac{\tau_c}{\tau_o}\right)^{\epsilon}\ ;\ \text{for } \tau_o > \tau_c \quad \ldots\ldots [18]$$

In this equation, $\bar{\alpha}$, β, γ, δ, and ε are experimental coefficients and the sediment equations based on tractive force and stream power concepts are represents by the term $1 - (\tau_c/\tau_o)$.

Under dimensional form, this equation is transformed to:

$$q_s = \alpha\, S^{\beta}\, q^{\gamma}\, i^{\delta}\, (1 - \frac{\tau_c}{\tau_o})^{\epsilon} \quad \ldots\ldots [19]$$

in which,

$$\alpha = \frac{\bar{\alpha}\rho L^{\delta}}{\nu^{\gamma+\delta-1}} \quad \ldots\ldots [20]$$

The derivation by Julien (1982) gives a general relationship between the sediment discharge and the dominant geometry and flow variables. The first three factors (S, q, i) represent the potential erosion or transport capacity by overland flow, which is reduced by the last factor reflecting the soil resistance to erosion. When τ_c remains small compared to τ_o, the equation for sediment transport capacity is:

$$q_s = \alpha\, S^{\beta}\, q^{\gamma}\, i^{\delta} \quad \ldots\ldots [21]$$

The sediment transport capacity by turbulent flows in deep channels is not a function of the rainfall intensity, and therefore, $\delta = 0$ in this case.

Empirical Equations

Several empirical equations can be transformed to evaluate the coefficients α, β, γ, δ, and ε. Among the equations analyzed those proposed by Musgrave (1957), Li, Shen and Simons (1973), and Kilinc (1972) include tractive force, stream power, velocity, and discharge relationships. When the variables differ from those of equation [19], the relationships in Table 2 are used for the transformation of $\bar{u}$, h, and τ_o for laminar flows, while the Reynolds number is replaced by $Re = \bar{u}h/\nu$. The results summarized in Table 3 suggest that none of the actual equations is complete since some coefficients are still zero. Consequently, for each particular equation, the number of variables is reduced owing to

TABLE 3. TRANSFORMATION OF EMPIRICAL EROSION EQUATIONS FOR LAMINAR FLOW

$$q_s \sim s^{\beta} q^{\gamma} i^{\delta} \left(1 - \frac{\tau_c}{\tau_o}\right)^{\epsilon}$$

Eq. No.	Reference	Equation	α†	β	γ	δ	ϵ
22	Musgrave (1947)	$q_s = \alpha' S^m L^n i^p$	α'	m	n	p-n	0
23	Zingg (1940)	$q_s \sim L^{1.66} S^{1.37}$	--	1.37	1.66	-1.66	--
24	Wischmeier and Smith (1978) (S>5%)	$q_s \sim L^{1.5}$ (.00076S² + .0053S + .0076)	--	≅1.7	1.5	-1.5	--
25	Meyer and Monke (1965)	$q_s \sim L^{1.9} S_o^{3.5}$	--	3.5	1.9	-1.9	--
26	Young and Mutchler (1969)	$q_s \sim L^{2.24} S^{0.74}$	--	0.74	2.24	-2.24	--
27	Li et al. (1973)	$q_s = \alpha' \int_o^L \tau_o^2 \, dx$	$3\alpha' \frac{\gamma^2}{5}\left(\frac{K\nu}{8g}\right)^{2/3}$	1.33	1.67	-1	0
28	Komura (1983)	$q_s \sim q^{11/8} i^{1/2} S^{1.5}$	--	1.5	1.38	0.5	0
29	Kilinc (1972)	$q_s = e^{2.05}(\tau_o - \tau_c)^{2.78}$	$e^{2.05} \gamma^{2.78} \left(\frac{K\nu}{8g}\right)^{0.93}$	1.86	0.93	0	2.78
30	Kilinc (1972)	$q_s = e^{0.122}((\tau_o - \tau_c)\bar{u})^{1.67}$	$e^{0.122} \gamma^{1.67}$	1.67	1.67	0	1.67
31	Kilinc (1972)	$q_s = e^{-3.17} \bar{u}^{3.625}$	$e^{-3.17} (\frac{8g}{K\nu})^{1.21}$	1.21	2.42	0	0
32	Kilinc (1972)	$q_s = e^{1.24} \bar{u}^{4.67} Re^{-0.878}$	$e^{1.24} \nu^{0.878} (\frac{8g}{K\nu})^{1.56}$	1.56	2.24	0	0
33	Kilinc (1972)	$q_s = e^{-11.6} Re^{2.05} S^{1.46}$	$e^{-11.6} \nu^{-2.05}$	1.46	2.05	0	0
34	Kilinc (1972)	$q_s = e^{11.7} q^{2.035} S^{1.66}$	$e^{11.7}$	1.66	2.03	0	0

†Sediment discharge in pounds per ft-s; multiply by 1.64×10^{-3} for q_s in tons/m·s.

these zero values. The most significant parameters pointed out in this analysis are the slope S and the discharge q. The numerical values of the coefficient β vary from 1.2 to 1.9, and γ, varies from 1.4 to 2.4. The variability of these exponents indicates the complexity of the sediment transport processes since only two major parameters are considered in this analysis. These relationships are in most cases particular to a study area or to the laboratory conditions under which the data were collected. Most equations include rill erosion which also influences the rate of soil erosion.

The well-known Universal Soil Loss Equation cannot be transformed directly into the general equation since the slope factor is written in a quadratic form. The equivalent exponent, however, is expected to vary between 1 and 2, and Julien (1982) found an equivalent exponent value near 1.7 while the discharge exponent 1.5 is an approximate value mostly valid when $S > 0.05$. The Kilinc and Richardson equations cannot define the parameters δ and ϵ since in their experiments, the soil surface was nearly impervious and also the bed tractive force was much in excess of the critical shear stress value. Throughout these transformations, the number of independent parameters remains the same. For example, equations [23], [25], and [26] based on slope and length have only two independent parameters because $\delta = -\gamma$. This remark is also valid for equations having one independent parameter since for equation [29] $\epsilon = 3\gamma$ and $\beta = 2\gamma$; for equation [30] $\beta = \gamma = \epsilon$; and for equation [31] $\beta = \gamma/2$.

Further fundamental research is required to better define the exponents δ and ϵ. The coefficients of the general equation obtained by dimensional analysis are kept variable for the purpose of this study and equation [19] is recommended for watershed modeling. The prediction from each equation will be possible, provided the proper set of coefficients is selected from Table 3. Fair estimates can be obtained from a regression

TABLE 4. TRANSFORMED SEDIMENT TRANSPORT EQUATIONS FOR OVERLAND FLOW

$$q_s \sim s^{\beta} q^{\gamma} \left(1 - \frac{\tau_c}{\tau_o}\right)^{\epsilon}$$

Eq. No.	Investigator	Equation	Laminar				Turbulent: Smooth Boundary				Turbulent: Manning Equation				Turbulent: Chezy Equation			
			β	γ	ε	Index*	β	γ	ε	Index*	β	γ	ε	Index*	β	γ	ε	Index*
36	Du Boys	$q_s \sim \tau_o(\tau_o-\tau_c)$	1.33	0.66	1	1	1.33	1.17	1	1	1.4	1.2	1	1	1.33	1.33	1	1
37	WES	$q_s \sim (\tau_o-\tau_c)^{m=1.5}$	1	0.5	1.5	0	1	0.88	1.5	0	1.05	0.90	1.5	0	1	1	1.5	0
38	Shields	$q_s \sim Sq(\tau_o-\tau_c)$	1.67	1.33	1	1	1.67	1.58	1	2	1.7	1.6	1	2	1.67	1.67	1	2
39	Schoklitsch	$q_s \sim S^{1.5}(q-q_c)$	1.5	1	--	1	1.5	1	--	1	1.5	1	--	1	1.5	1	--	1
40	Kalinske-Brown	$q_s \sim \tau_o^{2.5}$	1.67	0.83	0	1	1.67	1.46	0	2	1.75	1.5	0	2	1.67	1.67	0	2
41	Meyer-Peter et al.	$q_s \sim (\tau_o-\tau_c)^{1.5}$	1	0.5	1.5	0	1	0.88	1.5	0	1.05	0.9	1.5	0	1	1	1.5	0
42	Bagnold	$q_s \sim \tau_o^{0.5}(\tau_o-\tau_c)$	1	0.5	1	0	1	0.88	1	0	1.05	0.9	1	0	1	1	1	0
43	Engelund-Hansen	$q_s \sim \tau_o^{1.5}\bar{u}^2$	1.67	1.83	0	2	1.67	1.71	0	2	1.65	1.7	0	2	1.67	1.67	0	2
44	Inglis-Lacey	$q_s \sim \bar{u}^5 h^{-1}$	2	3	0	0	2	2.5	0	0	1.8	1.4	0	2	2	1	0	0
45	Yalin ($\tau_o \cong \tau_c$)	$q_s \sim \tau_o^{0.5}(\tau_o-\tau_c)^2$	1.67	0.83	2	1	1.67	1.46	2	2	1.75	1.5	2	2	1.67	1.67	2	2
46	Yalin ($\tau_o >> \tau_c$)	$q_s \sim \tau_o^{0.5}(\tau_o-\tau_c)$	1	0.5	1	0	1	0.88	1	0	1.05	0.9	1	0	1	1	1	0
47	Chang et al.	$q_s \sim \tau_o\bar{u}$	1	1	0	0	1	1	0	0	1	1	0	0	1	1	0	0
48	Barekyan	$q_s \sim Sq\bar{u}$	1.33	1.67	0	2	1.33	1.42	0	2	1.3	1.4	0	2	1.33	1.33	0	1
49	Pedroli	$q_s \sim \tau_o^{1.6} h^{0.2}$	1	0.6	0	0	1	1.05	0	0	1.06	1.08	0	0	1	1.2	0	0

*The index represents the number of exponents within the ranges: $1.2 < \beta < 1.9$; and $1.4 < \gamma < 2.4$.

equation such as given by Kilinc (1972). For example, excellent results were obtained by Julien (1982) with the use of the discharge and slope formula (equation 34).

The formation of rills locally increases the unit water discharge q and the resulting erosion rate is expected to be larger than for uniform flow conditions. The rill erosion data collected by Kilinc were analyzed by Julien and Simons (1984) and once the volume of rill erosion was subtracted from the total erosion, the following regression equation was obtained:

$$q_s \sim S^{1.31}\, q^{1.93}\ ;(R^2 = 0.96) \ldots\ldots\ldots\ldots [35]$$

Both exponents for S and q are smaller than those for soil erosion including rills (equation [34]). This equation can be used for comparison with sediments transport equations for laminar sheet flow.

Applicability of Sediment Transport Equations for Turbulent Flows

Most of the well-known sediment transport equations originally derived for turbulent stream flows can be transformed to determine their applicability to natural conditions in overland flows.

This analysis included the transformation of the sediment transport equations suggested by Du Boys (1879), O'Brien-Rindlaub (1934), WES (1935), Shields (1936), Schoklitsch (1934), Kalinske-Brown (1949), Meyer-Peter and Müller (1948), Bagnold (1956), Engelund-Hansen (1967), Inglis-Lacey (1968), Yalin (1977), Chang et al. (1967), Barekyan (1962), and Pedroli (1963). The Einstein bedload equation has not been treated separately since it agreed very well with the Yalin and the Meyer-Peter and Müller equations.

The sediment transport capacity was investigated assuming that sediment size, fluid properties and gravitational acceleration were constant. Particular attention was focused at the values of β and γ which are the exponents of the slope and water discharge in equation 19. For each of the four types of flow described previously, the transformed relationships are summarized in Table 4 as follows: (a) laminar sheet flow; (b) turbulent flow over smooth surface as given by the Blasius equation; (c) turbulent flow described by the Manning equation; and (d) turbulent flow with constant Darcy-Weisbach friction factor f or Che'zy coefficient.

The last column for each type of flow represents an index of fitness of these basic equations with the observed value of exponents. This index is equal to the number of parameters (β, γ) enclosed within the ranges of empirical coefficients as determined in the previous section ($1.2 < \beta < 1.9$ and $1.4 < \gamma < 2.4$). The higher the index, the better this equation should compare with observed data. Conversely, when the index is equal to zero, the given equation is expected to be a poor relationship to predict the sediment transport capacity of overland flow.

The results in this table show that the exponents β of most relationships are within the range of observed values while the exponents γ are usually too small to fall within the range of empirical coefficients. These results were anticipated since it was demonstrated in the analysis of flow characteristics summarized in Table 2 that the exponent of slope remains constant while the exponent of discharge varies for different flow conditions.

CONCLUSIONS

This study points at the relationship existing between the mechanics of overland flow and soil erosion by rainfall. The authors address the problem of estimating the sediment transport capacity for rainfall erosion based on the mechanics of overland flow. The results of this study are of particular interest to:

1. soil scientists concerned with the decrease of productivity of agricultural land caused by rainfall erosion;
2. watershed modelers looking for a better sediment transport capacity relationship for mathematical simulation of erosion processes;
3. sedimentologists interested in the mechanics of sediment transport for both laminar and turbulent flows.

A general sediment transport relationship supported by dimensional analysis ($q_s \sim s^{\beta} q^{\gamma} i^{\phi} [1 - \tau_c/\tau_o]^{\epsilon}$) is recommended and the major conclusions of the study are summarized as follows: the analysis of overland flow characteristics encompasses a wide variety of flow conditions varying from laminar sheet flows on uniform soil surfaces to turbulent flows in rills and gullies. When the principal hydraulic variables of flow depth, velocity, and bed shear stress are written in terms of slope and discharge, the exponent of slope remains constant for these various types of flow. For different types of flow the exponents of discharge for the velocity and shear stress were shown to vary in opposite directions. Therefore, for predicting soil erosion the applicability of sediment transport relationships derived for turbulent flows depends on whether the sediment transport capacity is a function of velocity or shear stress.

Most of the sediment transport equations used for turbulent flow in streams should not be applied to rainfall erosion in laminar sheet flows. Among the equations examined, only those proposed by Engelund-Hansen and Barekyan seem relevant for predicting soil erosion losses by overland runoff. The formulas suggested by Shields, Kalinske-Brown and Yalin might also be considered though the exponent of discharge is clearly too small in the case of laminar sheet flow. The other equations generally underestimate the parameters β and γ and are irrelevant to predict rainfall erosion.

The range of values of the exponents of slope β and discharge γ were well-defined in this analysis of empirical relationships. The transformation of several sediment transport equations for overland flow can be summarized as follows: the empirical exponent β varies between 1.2 and 1.9 while the exponent γ ranges from 1.4 to 2.4. The variation of these exponents indicates the complexity of soil erosion processes and the specificity of each relationship for the site-specific conditions under which they were derived. Moreover, these exponents are function of the formation of rills and this study shows that both exponents β and γ of the sediment transport capacity relationship increase when the rills develop.

References

1. Alonso, C.V., W.H. Neibling and G.R. Foster. 1981. Estimating sediment transport capacity in watershed modeling. TRANSACTIONS OF THE ASAE 24(5):1211-1220.
2. Bagnold, R.A. 1956. The flow of cohesionless grains in fluids. Phil. Trans. of the Royal Society of London 249(964):235-297.
3. Barekyan, A.S. 1962. Discharge of channel forming sediments and elements of sand waves. Soviet Hydrol. Selected Papers (Transactions of AGU No. 2), pp. 128-130.
4. Brown, C.B. 1949. Sediment transportation. In: Engineering

hydraulics, (ed.) H. Rouse, chapter XII, pp. 769-857.

5. Chang, F.M., D.B. Simons, and E.V. Richardson. 1967. Total bed-material discharge in alluvial channels. Proceedings of the Twelfth Congress of the IAHR, Fort Collins, CO, pp. 132-140.

6. Chen, C. L. 1976. Flow resistance in borad shallow grassed channels. Journal of the Hydraulics Division, ASCE, 102(HY3):307-322.

7. Du Boys, D. 1879. Le Rhône et les rivieres a lit affouillable. Annales des Ponts et Chausseés, Serie 5, Vol. 18, 1879, pp. 141-195.

8. Engelund, F. and E. Hansen. 1967. A monograph on sediment transport in alluvial streams. Teknisk Forlag, Copenhagen, Denmark, 65 p.

9. Fawkes, P. E. 1972. Roughness in a model of overland flow. M.Sc. Thesis, Colorado State University, 109 p.

10. Inglis, C.C. 1968. Discussion of systematic evaluation of river regime. Journal of Waterways and Harbor Division, ASCE, 94(WW1):109-114.

11. Izzard, C. F. 1944. The surface profile of overland flow. Trans. AGU (6):959-968.

12. Julien, P. 1982. Prediction d'apport solide pluvial et nival dans les cours d'eau nordiques a partir du ruissellement superficiel, These de doctorat, Universite´Laval, Quebec, 240 p.

13. Julien, P. Y. and D. B. Simons. 1984. Analysis of sediment transport equations for rainfall erosion. Report CER83-84 PYJ-DB552, Civil Eng. Dept. Colorado State University, 46 p.

14. Keulegan, G.H. 1938. Laws of turbulent flow in open channels. Research paper 1151, Journal of Research, U.S. Nat. Bureau of Standards, Vol. 21, pp. 707-741.

15. Kilinc, M.Y. 1972. Mechanics of soil erosion from overland flow generated by simulated rainfall. Ph.D. dissertation, Colorado State University, Fort Collins, 183 p.

16. Komura, S. 1976. Hydraulics of slope erosion by overland flow. Journal of the Hydraulics Division, ASCE 102(HY10):1573-1585.

17. Komura, S. 1983. A method of predicting sediment yields from watersheds. Proceedings of the D. B. Simons Symposium on Erosion and Sedimentation, Section 9, pp. 23-41.

18. Laursen, E.H. 1956. The application of sediment transport mechanics to stable channel design. Journal of the Hydraulics Division, ASCE 82(HY4), 11 p.

19. Li, R. M. 1972. Sheet flow under simulated rainfall. M.Sc. thesis, Department of Civil Engineering, Colorado State University, Fort Collins, 111 p.

20. Li, R.M. 1979. Water and sediment routing from watersheds. In: Modeling of rivers, (ed.) H.W. Shen, J. Wiley & Sons, chapter 9, 88 p.

21. Li, R. M., H. W. Shen and D. B. Simons. 1973. Mechanics of soil erosion by overland flow. Paper presented at 15th Congress IAHR, Istanbul, Turkey. Proc. Paper A-54, pp. 437-446.

22. Meyer, L.D. and E.J. Monke. 1965. Mechanics of soil erosion by rainfall and overland flow. TRANSACTIONS OF THE ASAE 8(4):572-580.

23. Meyer-Peter, E. and R. Müller. Formulas for bed-load transport. Proceedings of the Second Meeting of IAHR, Stockholm, pp. 39-64.

24. Musgrave, G.W. 1947. The qualitative evaluation of factors in water erosion: a first approximation. Journal of Soil and Water Conservation, 2(3):1331-138.

25. O'Brien, M.P. and B.D. Rindlaub. 1934. The transportation of bed-load in streams. Transactions of the AGU:573-603.

26. Pedroli, R. 1963. Transporto di materiale solido in canali a fondo fisso e liscio. Communicazione de'l Ufficio federale dell'economia della acque, No. 63.

27. Schoklitsch, A. 1934. Geschiebetrieb und die geschiebefracht. Wasser Kraft und Wasser Wirtschaft, Jgg. 39, Heft 4.

28. Shen, H. W. and R. M. Li. 1973. Rainfall effect on sheet flow over smooth surface. Journal of the Hydraulics Division, ASCE:771-792.

29. Shields, A. 1936. Anwendung der Ähnlichkeitsmechanik und turbulenz forschung auf die geschiebebewegung. Mitteil Preuss, Versuchsanst Wasser und Schiffsbau, Berlin No. 26. Translated to English by W.P. Ott and J.C. van Uchelen, Calif. Inst. of Tech.

30. Thorne, C. R. 1984. Prediction of soil loss due to ephemeral gullies in arable fields. Report CER 83-84 CRT, Dept. of Civ. Eng., Colorado State University, 79 p.

31. U.S. Waterways Experiment Station. 1935. Studies of river bed materials and their movement with special reference to the lower Mississippi River. USWES, Vicksburg, Paper No. 17.

32. Wischmeier, W.H. and D.D. Smith. 1978. predicting rainfall erosion losses — a guide to conservation planning. USDA Agriculture Handbook No. 537, 58 p.

33. Wooding, R. A. 1965. A hydraulic model for the catchment stream, problem 1 — Kinematic wave theory. Journal of Hydrology, Vol 3.

34. Woolhiser, D. A. 1975. Simulation of unsteady overland flow. Chapter 12 in Unsteady flow in open channels. Edited by K. Mahmood and V. Yevjevich, WRP, pp. 485-508.

35. Yalin, M.S. 1977. Mechanics of sediment transport. Pergamon Press. Second Ed., pp. 112-165.

36. Young, R.A. and C.K. Mutchler. 1969. Soil movement on irregular slopes. Water Resources Research 5(5):1084-1085.

37. Zingg, A.W. 1940. Degree and length of land slope as it affects soil loss by runoff. Agricultural Engineering 21(2):59-64.

LIST OF SYMBOLS

A	coefficient for raindrop impact
a, b, c, d	coefficients
r, r_1, r_2	constants
C	Chezy coefficient
d_s	size of sediment
f	Darcy-Weisbach friction factor
g	gravitational acceleration
h	flow depth
i	rainfall intensity
k_o	surface friction coefficient
K	friction parameter for laminar sheet flow
L	slope length
n	Manning coefficient
q	unit water discharge
q_c	critical unit water discharge
q_s	unit sediment discharge
R^2	coefficient of determination
S	slope
S_f	slope of the energy line
u	velocity at a distance y from the water surface
$\bar{u}$	mean velocity
U_*	shear velocity
$\alpha,\beta,\gamma,\delta,\varepsilon$	coefficients of the sediment transport equation
δ'	thickness of the laminar sublayer
γ	dynamic viscosity
ν	kinematic viscosity
ρ	specific mass of water
ρ_s	specific mass of sediments
τ_o	bed shear stress
τ_c	critical bed shear stress

Modeling of Rainfall Erosion

By Pierre Y. Julien[1] and Marcel Frenette[2]

Abstract: A combined stochastic and deterministic method has been developed to evaluate soil erosion from overland flow. The exponential distributions for rainfall duration and intensity are combined with rainfall-runoff relationships for discrete storms. A general equation for sediment discharge is suggested from dimensional analysis with different sets of coefficients representing several existing equations. The expected value of soil erosion during one rainfall event is theoretically derived using hypergeometric series. When applied to the Chaudière watershed near Québec, this equation converges very rapidly, and the first term of the series is recommended. Utilizing sediment-delivery ratios, the sediment yield computed from the total soil erosion is in good agreement with the suspended load measured in the Chaudière River.

Introduction

Soil detachment and transport from upland areas is related to surface runoff, rainfall impact, and vegetation. For bare soils under rainfall, many empirical equations have been proposed to evaluate soil losses from overland flow. However, a general relationship between flow and sediment discharge has not been found yet. The complexity of physical processes between rainfall, overland flow and soil erosion, and also the several man-induced activities, such as land management and agricultural practices, contribute to make the problem of soil erosion a very difficult one to deal with.

Among the first relationships in soil erosion studies, the Musgrave Equation (15) was modified leading to the well-known Universal Soil-Loss Equation (24). Previous investigations by Zingg (29), Meyer and Monke (14), and Young and Mutchler (28) also provided basic understanding of the soil erosion process. For overland flow under simulated rainfall, Kilinc and Richardson (10,11) suggested several sediment transport equations based on regression analysis of experimental data. Li, Shen, and Simons (13) suggested a qualitative equation from analytical considerations. The work of Foster, Smith, Moss, Walker, and others could also be referenced.

Simulation models based on physical processes have been developed more recently by Simons et al. (18,19) and applied to small watersheds. These models use numerical methods to route water and sediment from a watershed for a given rainfall hyetograph. Besides deterministic models, Shen and Li (17) stated that the knowledge for stochastic modeling is rather limited.

The main purpose of this paper is to derive an equation for the expected value of soil erosion and to demonstrate its applicability to wa-

[1]Asst. Prof., Dept. of Civ. Engrg., Colorado State Univ., Fort Collins, Colo.; formerly, Grad. Student at Laval Univ., Québec, Canada.

[2]Prof., Dept. of Civ. Engrg., Laval Univ., Québec, Canada.

Note.—Discussion open until March 1, 1986. To extend the closing date one month, a written request must be filed with the ASCE Manager of Journals. The manuscript for this paper was submitted for review and possible publication on May 8, 1984. This paper is part of the *Journal of Hydraulic Engineering*, Vol. 111, No. 10, October, 1985. ©ASCE, ISSN 0733-9429/85/0010-1344/$01.00. Paper No. 20080.

tershed modeling. First, the fundamental characteristics of rainfall, runoff and sediment discharge are briefly summarized; then, the equation for the expected value of soil erosion by one rainfall event is derived. The last section considers practical applications of the theoretically derived relationship.

Fundamental Characteristics

Rainfall Precipitation.—Point-rainfall precipitation can be described as a random time series of discrete storm events; each event having finite duration and constant intensity. Several stochastic models have been developed by Todorovic, Woolhiser, and Eagleson (3,20,21,22). In these models, the principal variables of rainfall precipitation are: (1) The elapsed time between successive storms; (2) the storm duration; and (3) the storm intensity.

The time of arrival of successive storms has often been described as a Poisson process with intensity λ_0, defined by

$$p(\nu|t) = \frac{(\bar{\nu})^{\nu}}{\nu!} e^{-\bar{\nu}} \quad \ldots\ldots (1)$$

with $$\bar{\nu} = \lambda_0 t \quad \ldots\ldots (2)$$

in which $p(\nu|t)$ is the probability to observe ν storms during the time t; $\nu = 0, 1, 2, \ldots$ is the number of storm events; $\bar{\nu}$ is the mean number of storms during the period of time t; and λ_0 is the average arrival rate of storm events during the period t.

The storm duration, t_r, has been found to be distributed exponentially (5). In a general form, if we allow for the variation with time of the duration parameter $\lambda_1(t)$, the probability density function of storm duration $p(t_r)$ is given by

$$p(t_r) = \lambda_1(t)\, e^{-\lambda_1(t) t_r} \quad \ldots\ldots (3)$$

If we now consider a period of time that is short enough to assume a constant value of the duration parameter λ_1, we can write in dimensionless form

$$p(\lambda_1 t_r) = e^{-\lambda_1 t_r} \quad \ldots\ldots (4)$$

in which $$\lambda_1 = \frac{1}{\bar{t}_r} \quad \ldots\ldots (5)$$

in which λ_1 is the reciprocal of the average storm duration, $\bar{t}_r$, during the period, t, considered. Data collected at the Agronomy Station at Laval University from 1966–1970 were available for this study. The observed and fitted distribution functions of rainfall duration $F(t_r)$ corresponding to the integral of Eq. 4 are shown in Fig. 1, for the month of June. Similar graphs were obtained during the rainy season from June–November; these results support those obtained by Eagleson (3) with data from Boston and Santa Paula.

The storm intensity, i, has also been shown to be exponentially distributed with a probability density function, $p(i)$, and an intensity parameter, $\lambda_2(t)$, written as

112

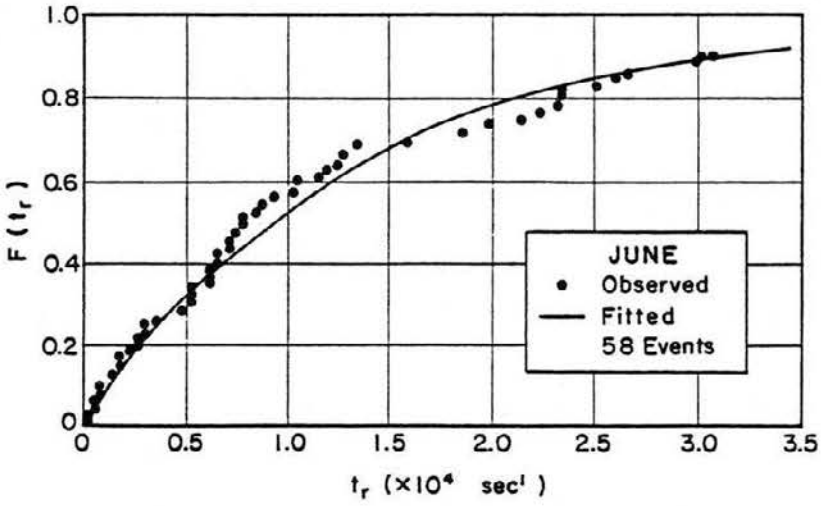

FIG. 1.—Exponential Distribution Function of Rainfall Duration

$$p(i) = \lambda_2(t)e^{-\lambda_2(t)i} \quad \ldots\ldots (6)$$

which, for short time intervals, reduces to

$$p(\lambda_2 i) = e^{-\lambda_2 i} \quad \ldots\ldots (7)$$

$$\text{in which} \quad \lambda_2 = \frac{1}{\bar{i}} \quad \ldots\ldots (8)$$

and λ_2 is the reciprocal of the average rainstorm intensity, $\bar{i}$. The observed and fitted exponential distribution functions of the rainstorm intensity, $F(i)$, at the same meteorological station are shown in Fig. 2. Similar agreement between observed and fitted exponential distributions was obtained from June to November (8).

In Table 1, the values of the rainfall duration parameters, λ_1, show a gradual decrease through the fall months. Conversely, an increase of the rainfall intensity parameter, λ_2, is observed from September–November. The monthly period selected for evaluating the precipitation parameters,

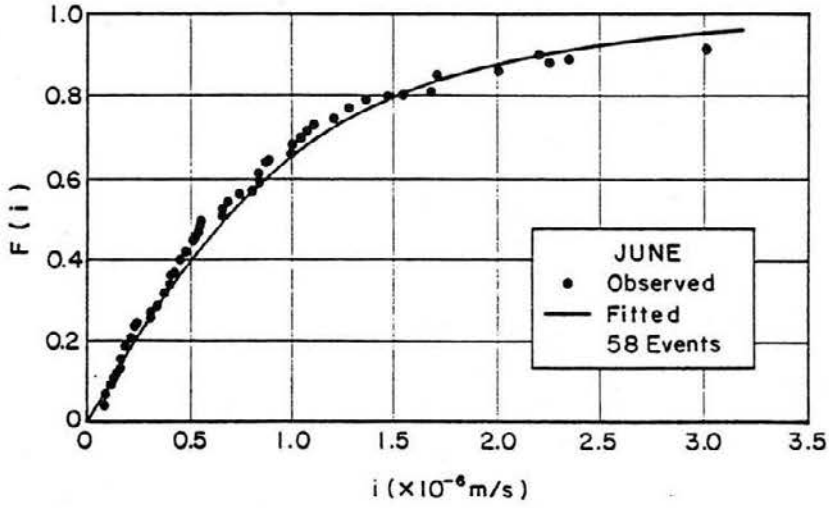

FIG. 2.—Exponential Distribution Function of Rainfall Intensity

TABLE 1.—Monthly Values of Rainfall Duration and Intensity Parameters

Month (1)	$\lambda_1 \times 10^6$, in units per second (2)	$\lambda_2 \times 10^{-5}$, in second per feet (3)
June	42.6	9.15
July	52.4	7.32
August	36.8	9.76
September	36.3	9.15
October	29.4	13.7
November	21.1	15.2

λ_1 and λ_2, seems adequate to allow for the variation of coefficients throughout summer and fall and is also short enough to assume constant values of λ_1 and λ_2 during each month.

Two tests suggested by Yevjevich (27) have been applied to the data to verify the independence between rainfall duration and intensity. The first test is based on the standard deviation of the correlation coefficient and the second uses the standardized variable t. Both tests give identical results and the independence hypothesis has been accepted for all months except October.

Overland Flow and Runoff Hydrographs.—Overland flow refers to the thin surface runoff over upland areas. Sheet runoff over a smooth surface is usually classified as an unsteady nonuniform flow perturbed by raindrop impacts. From experimental data, several authors (2,11,16) have observed overland flow to be laminar.

The two nonlinear partial differential equations derived by Saint-Venant are basically used to solve gradually varied unsteady flow. Considering the relative magnitude of the terms in these equations, the kinematic wave approximation has been most widely recommended (25,26) to define the hydraulics of overland flow.

Laminar flows with raindrop impact can be described by the Darcy-Weisbach equation in which the friction factor, f, is related to: (1) The Reynolds number, R; (2) the friction coefficient, K_o; and (3) the empirical coefficients A and b for raindrop impact. The friction coefficient K includes both effects due to surface roughness and rainfall intensity. The following relationship is generally used

$$f = \frac{K}{R} = \frac{K_o + Ai^b}{R} \quad \ldots\ldots (9)$$

The values of K_o have been tabulated by Woolhiser (26) for various surface characteristics, and the value $K_o = 24$ is representative of a smooth surface. Various sets of coefficients A and b have been obtained experimentally (4,6,12). For rainfall intensity given in ft/sec, $A = 4.32 \times 10^5$ sec/ft ($A = 1.42 \times 10^6$ s/m for i in m/s); and $b = 1$.

For steady and uniform rainfall intensity over an impervious surface, the time t_e elapsed before the runoff hydrograph reaches an equilibrium state (26) is given by

$$t_e = \left(\frac{K\nu_e L}{8gSi^2}\right)^{1/3} \quad \ldots\ldots (10)$$

in which, ν_e is the kinematic viscosity of water; g is the gravitational acceleration; S is the slope; and L is the runoff length. Taking λ (defined as the ratio of the storm duration, t_r to the equilibrium time, t_e), the resulting hydrograph is classified in two distinct types: (1) The complete hydrograph ($\lambda = t_r/t_e > 1$); and (2) the partial equilibrium hydrograph ($\lambda \leqq 1$). These two types of hydrographs are shown in Figs. 3(*a–c*) after the following dimensionless variables for flow discharge ψ and time θ are introduced:

$$\psi = \frac{q}{iL} \quad \text{(11)}$$

$$\text{and} \quad \theta = \frac{t - t_r}{t_e} \quad \text{(12)}$$

in which q is the unit water discharge.

For steady flow conditions in the equilibrium part of the complete hydrograph the average velocity $\bar{u}$, flow depth h, and bottom shear stress τ_o are related to the geometry and to flow characteristics as

$$\bar{u} = \left(\frac{8g}{K\nu_e}\right)^{1/3} S^{1/3} q^{2/3} \quad \text{(13)}$$

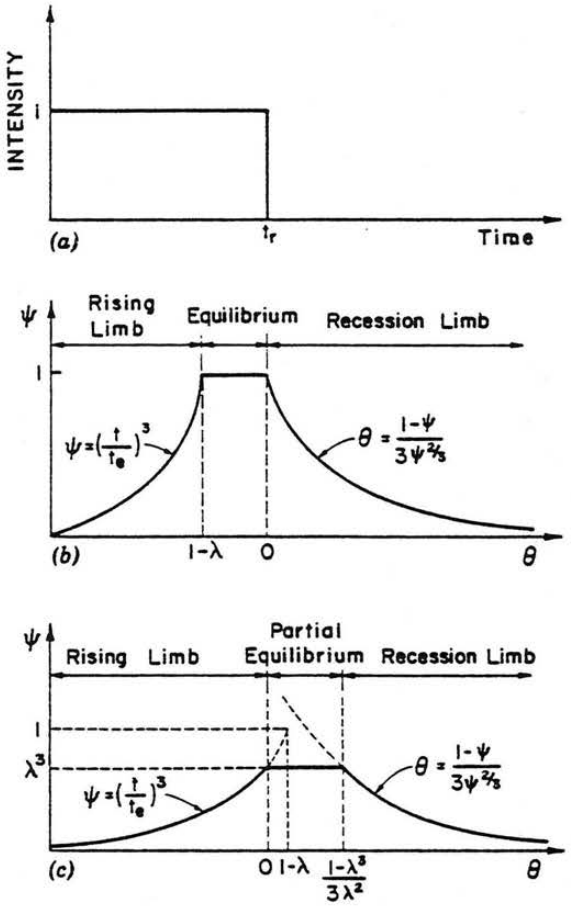

FIG. 3.—Hyetographs and Hydrographs for One Rainfall Event: (*a*) Hyetograph; (*b*) Complete Hydrograph; (*c*) Partial Equilibrium Hydrograph

$$h = \left(\frac{K\nu_e}{8g}\right)^{1/3} S^{-1/3} q^{1/3} \quad \ldots\ldots (14)$$

$$\tau_o = \gamma_e \left(\frac{K\nu_e}{8g}\right)^{1/3} S^{2/3} q^{1/3} \quad \ldots\ldots (15)$$

in which γ_e is the specific weight of water. It is important to note that soil erosion is often described in terms of these three variables.

Sediment Transport Equations.—Sheet erosion is the result of soil particle detachment and transport from raindrop impact and overland flow. Most eroded soil particles are transported downstream by runoff and the unit sediment discharge is a function of the following variables (8)

$$q_s = f(h, \bar{u}, i, q, L, \tau_o, \tau_c, S, \rho_e, \nu_e, d_s, \rho_s) \quad \ldots\ldots (16)$$

in which τ_c is the critical bed shear stress value for the beginning of motion; ρ_e and ρ_s are the density values of water and sediments; and d_s is the size of sediment particles. Elimination of the variables $\bar{u}$ and h is possible from two relationships: the Darcy-Weisbach equation and the continuity equation, $q = \bar{u}h$. The influence of sediment size on sediment transport is considered through the corresponding critical shear stress. Therefore, the sediment size d_s can be eliminated from Eq. 16 using a relationship between τ_c and d_s for laminar flow (23). Eq. 16 thus reduces to

$$f\left(q_s, q, i, L, \rho_e, \nu_e, \frac{\tau_c}{\tau_o}, S, \rho_s\right) = 0 \quad \ldots\ldots (17)$$

The following dimensionless groups are obtained from dimensional analysis after L, ρ_s, and q are selected as repeating variables

$$f\left(\frac{q_s}{\rho_s q}, \frac{q}{\nu_e}, \frac{q}{iL}, \frac{\tau_c}{\tau_o}, S, \frac{\rho_s}{\rho_e}\right) = 0 \quad \ldots\ldots (18)$$

The first group represents the dimensionless concentration of sediments, the second is the Reynolds number, the third is the flow discharge variable, ψ, defined previously and shown in Figs. 3(*a*–*c*). The last three groups represent the ratio of critical to bed shear stresses, the slope and the specific gravity of solid particles. After these nondimensional groups are multiplied or divided by other groups to separate the variables q_s, S, q, i, τ_c, and ρ_s, the modified set of dimensionless groups is presented in the following product form:

$$\left(\frac{q_s}{\rho_e \nu_e}\right) = \bar{\alpha} S^{\beta} \left(\frac{q}{\nu_e}\right)^{\gamma} \left(\frac{iL}{\nu_e}\right)^{\delta} \left(1 - \frac{\tau_c}{\tau_o}\right)^{\epsilon} \left(\frac{\rho_s}{\rho_e}\right)^{\eta}; \quad \text{for} \quad \tau_o > \tau_c \quad \ldots\ldots (19)$$

In this equation, $\bar{\alpha}$, β, γ, δ, ϵ, and η are experimental coefficients, and the sediment transport equations based on excess tractive force and stream power concepts are best represented by the term $[1 - (\tau_c/\tau_o)]$.

Under dimensional form, this equation is transformed to

$$q_s = \alpha S^{\beta} q^{\gamma} i^{\delta} \left(1 - \frac{\tau_c}{\tau_o}\right)^{\epsilon} \quad \ldots\ldots (20)$$

in which, for constant values of the specific gravity, the last group in Eq. 19 is combined with the coefficient α as follows:

$$\alpha = \frac{\bar{\alpha}\rho_e L^{\delta}}{\nu_e^{\gamma+\delta-1}}\left(\frac{\rho_s}{\rho_e}\right)^{\eta} \quad \ldots\ldots (21)$$

Eq. 20 describes a general relationship between sediment discharge, slope, and flow variables. The first three factors (S,q,i) represent the potential erosion (or transport capacity) by overland flow, which is reduced by the last factor describing the soil resistance to erosion. It is also seen that when τ_c is small compared to τ_o, the equation for sediment transport capacity is

$$q_s = \alpha S^{\beta} q^{\gamma} i^{\delta} \quad \ldots\ldots (22)$$

Quantitative evaluation of the coefficients α, β, γ, δ, and ϵ has been done (8) for several types of equations based on different variables. The equations analyzed are those proposed by Musgrave (15); Li, Shen, and Simons (13); and several regression equations obtained by Kilinc and Richardson (11), including tractive force, stream power, velocity, and discharge equations. When the sediment transport equations in Table 2 are expressed in terms of the variables $\bar{u}$, h, τ_o, and R, the Reynolds number is replaced by $R = \bar{u}h/\nu_e$, and Eqs. 13–15 are used to transform the variables $\bar{u}$, h, and τ_o into a function of slope and discharge. From the results shown in Table 2, it is found that none of these eight equations is complete since some coefficients are not defined, which reduces the number of variables. The numerical values of the coefficient β vary from 1.21–1.86, and γ varies from 2.03–2.42, except for Eqs. 20*b*–*d* based on tractive force and stream power concepts. The exponents of Eq. 20 are kept variable in the following analysis. Accordingly, evaluation based on each equation in Table 2 will be possible provided the proper set of coefficients is selected.

TABLE 2.—Evaluation of Empirical Coefficients α, β, γ, δ, and ϵ for Several Erosion Equations

Equation number (1)	Equation (2)	Reference (3)	α[a] (4)	β (5)	γ (6)	δ (7)	ϵ (8)
20*a*	$q_s = \alpha' S^m L^n i^p$	15	α'	m	n	p-n	—
20*b*	$q_s = \alpha' \int_0^L \tau_o^2\, dx$	13	$3\alpha' \frac{\gamma_e^2}{5}\left(\frac{K\nu_e}{8g}\right)^{2/3}$	1.33	1.67	−1	—
20*c*	$q_s = e^{2.05}(\tau_o - \tau_c)^{2.78}$	10	$e^{2.05}\gamma_e^{2.78}\left(\frac{K\nu_e}{8g}\right)^{0.93}$	1.86	0.93	—	2.78
20*d*	$q_s = e^{0.122}[(\tau_o - \tau_c)\bar{u}]^{1.67}$	10	$e^{0.122}\gamma_e^{1.67}$	1.67	1.67	—	1.67
20*e*	$q_s = e^{-3.17}\bar{u}^{3.625}$	10	$e^{-3.17}\left(\frac{8g}{K\nu_e}\right)^{1.21}$	1.21	2.42	—	—
20*f*	$q_s = e^{1.24}\bar{u}^{4.67}R^{-0.878}$	10	$e^{1.24}\nu_e^{0.878}\left(\frac{8g}{K\nu_e}\right)^{1.56}$	1.56	2.24	—	—
20*g*	$q_s = e^{-11.6}R^{2.05}S^{1.46}$	10	$e^{-11.6}\nu_e^{-2.05}$	1.46	2.05	—	—
20*h*	$q_s = e^{11.7}q^{2.035}S^{1.66}$	10	$e^{11.7}$	1.66	2.03	—	—

[a]Sediment discharge in pounds per ft-sec.

PREDICTING MEAN SOIL EROSION LOSSES DURING GIVEN PERIOD OF TIME

Before deriving an expression for the expected soil erosion during a given period of time, the erosion for a single event of given intensity, i, and duration, t_r, must be considered.

Single Event.—Soil erosion by overland flow during a single event, shown in Figs. 4(*a–c*), is obtained by combining Eq. 19 with the flow characteristics corresponding to the runoff hydrograph [Figs. 3(*a–c*)]. In a dimensionless form, the total erosion or mass eroded per unit width, ϕ, is obtained by integrating the sediment discharge, $q_s/\rho_e v_e$, over the dimensionless runoff period, $\lambda_1 t$:

$$\phi = \int_0^\infty \frac{q_s}{\rho_e v_e} d(\lambda_1 t) = \frac{\lambda_1}{\rho_e v_e} \int_0^\infty q_s dt \quad \ldots\ldots\ldots\

$$\phi_c = \frac{\lambda_1}{\rho_e \nu_e} \alpha S^{\beta} L^{\gamma} i^{\gamma+\delta} t_r \left[1 - \frac{9}{\lambda} \left(\frac{\gamma^2 - \gamma}{9\gamma^2 - 3\gamma - 2} \right) \right], \quad \lambda > 1 \quad \ldots\ldots\ldots\ldots \quad (25)$$

$$\phi_p = \frac{\lambda_1}{\rho_e \nu_e} \alpha S^{\beta} L^{\gamma} i^{\gamma+\delta} t_r \left[\left(\frac{1 - \gamma}{3\gamma + 1} \right) \lambda^{3\gamma} + \left(\frac{\gamma}{3\gamma - 2} \right) \lambda^{3\gamma-3} \right], \quad \lambda < 1 \ldots\ldots \quad (26)$$

From Table 2, γ normally varies between 1 and 3. When $t_r >> t_e$ (or $\lambda \rightarrow \infty$), the term in brackets of Eq. 25 (valid for $\lambda > 1$) reduces to unity. In Eq. 26 (for $\lambda \leqq 1$), the soil erosion ϕ_p remains generally small since for partial duration hydrograph, λ is raised to the power 3γ.

Expected Value of Soil Erosion for One Rainfall Event.—The expected value of soil erosion is determined using the probability density functions of rainfall duration and intensity. These independent exponential distributions were previously described and the expected value of soil erosion by one storm Φ is given by

$$\Phi = \int_0^{\infty} \int_0^{\infty} \phi p(\lambda_1 t_r)\, p(\lambda_2 i)\, d(\lambda_1 t_r) d(\lambda_2 i) \ldots\ldots\ldots\ldots\ldots\ldots\ldots\ldots \quad (27)$$

From Eqs. 4 and 7, Eq. 27 becomes

$$\Phi = \int_0^{\infty} \int_0^{\infty} \phi e^{-\lambda_1 t_r} e^{-\lambda_2 i}\, d(\lambda_1 t_r)\, d(\lambda_2 i) \ldots\ldots\ldots\ldots\ldots\ldots\ldots\ldots \quad (28)$$

This integral must be divided in two parts, as indicated by Eqs. 25 and 26, which are valid when $t_r > t_e$ and $t_r \leqq t_e$, respectively. One thus obtains

$$\Phi = \int_0^{\infty} \int_0^{\lambda_1 t_e} \phi_p e^{-\lambda_1 t_r} e^{-\lambda_2 i} d(\lambda_1 t_r)\, d(\lambda_2 i)$$

$$+ \int_0^{\infty} \int_{\lambda_1 t_e}^{\infty} \phi_c e^{-\lambda_1 t_r} e^{-\lambda_2 i}\, d(\lambda_1 t_r)\, d(\lambda_2 i) \ldots\ldots\ldots\ldots\ldots\ldots\ldots\ldots \quad (29)$$

The boundary value, $\lambda_1 t_e$, is a function of i (Eq. 10), while ϕ_p and ϕ_c are given by Eqs. 25 and 26. The exact analytical solution to Eq. 29 including the variation of the friction factor K with rainfall intensity (Eq. 9) has been obtained using hypergeometric series. The complete solution is written in terms of a series of incomplete gamma functions, which converges very rapidly, and the reader is referred to Julien (8) for the derivation. Experience with field data showed that a constant value of the friction coefficient can be assumed for the evaluation of soil erosion. The representative value of the friction coefficient, K_m, can be computed by substituting $\bar{i}$ for i in Eq. 9 ($K_m = K_o + A\bar{i}^b$). This simplification gives the following approximate solution of Eq. 29.

$$\Phi \cong \frac{\pi_1 \Gamma(\gamma + \delta + 1)}{\lambda_1^2 \lambda_2^{\gamma+\delta+1}} - \left[\frac{\pi_1}{\lambda_1} \pi_c \left(\frac{K_m \nu_e L}{8gS} \right)^{1/3} \frac{\Gamma\left(\gamma + \delta + \frac{1}{3} \right)}{\lambda_2^{\gamma+\delta+1/3}} \right] + \ldots \quad \ldots. \quad (30)$$

in which $\pi_1 = \frac{\lambda_1^2 \lambda_2}{\rho_e \nu_e} \alpha S^\beta L^\gamma$ ..... (31)

$$\pi_c = \frac{9\gamma^2 - 9\gamma}{9\gamma^2 - 3\gamma - 2} \quad \text{..... (32)}$$

$$\Gamma(\chi) = \int_0^\infty \xi^{\chi-1} e^{-\xi} d\xi: \quad \text{gamma function} \quad \text{..... (33)}$$

Expected Soil Erosion during Given Period of Time.—The average amount of soil eroded during a given period of time is equal to the product of the expected value of soil erosion for one rainfall event, Φ, and the mean number of events, $\bar{\nu}$, during that period.

$$\bar{\Phi} = \bar{\nu}\Phi \quad \text{..... (34)}$$

Practical Applications

This development has been applied to predict rainfall erosion and sediment yield from the Chaudière Watershed near Québec City, Canada. A detailed description of the methodology including data collection and analysis, discretization of the watershed and computer programs is beyond the scope of this paper. However, the interested reader might refer to previous work (7–9). The writers wish to outline the approach used to cope with practical applications of this theoretical derivation and to provide some of the results obtained.

The significant parameters used to describe the watershed and the monthly rainfall parameters are listed in Table 1. The basin geometry is simplified, and the following parameters are considered: $A_t = 6.27 \times 10^{10}$ ft^2 (5.83×10^9 m^2); $S = 0.0156$; and $L = 300$ ft (91.5 m). The expected value of soil erosion during one rainfall event is computed using numerical integration of the exact formulation (Eq. 29) and the results are compared with the series approximation given by Eq. 30. The exact formulation has been integrated numerically in two different ways: (1) Simple first-order open Newton-Cotes formula (two-dimensional) with 2,500 points; and (2) Gauss quadrature formula (two-dimensional) with 25 points. The results in columns 2 and 3 of Table 3 show that the numerical methods used to solve Eq. 29 give nearly identical results, as one might expect. The results of the series approximation (Eq. 30) are presented in columns 4 and 5 in Table 3 and indicate a very rapid convergence. In this example, the first term of the series can be used to estimate the rate of soil erosion if a 5% error is acceptable. Otherwise, better accuracy is achieved when both terms are considered. Higher order terms in the series were shown to be negligible for the cases investigated. In this example, the expected value of soil erosion after $\bar{\nu}$ storms can be estimated from:

$$\bar{\Phi} = \bar{\nu}\Phi \cong \bar{\nu} \frac{\pi_1 \, \Gamma(\gamma+\delta+1)}{\lambda_1^2 \lambda_2^{\gamma+\delta+1}} \quad \text{..... (35)}$$

A preliminary sensitivity analysis was conducted to account for water losses due to interception, evapotranspiration, and infiltration. Three cases

TABLE 3.—Expected Value of Soil Erosion by One Rainfall on Chaudière Watershed

Month (1)	SOIL EROSION IN METRIC TONS			
	Numerical Methods (Eq. 29)		Series Expansion (Eq. 30)	
	Newton-Cotes (2)	Gauss (3)	1 term (4)	2 terms (5)
June	48.59	48.15	51.01	48.81
July	62.11	61.54	65.30	62.38
August	49.56	49.12	51.78	49.80
September	57.33	56.32	59.87	57.60
October	30.88	30.60	32.39	31.02
November	34.98	34.67	36.43	35.15

have been studied: (1) No water losses (hyp. A); (2) the water losses reduce the rainfall duration such that the equivalent rainfall duration parameter is $\lambda_{1b} = \lambda_1/C_r$, in which C_r is the runoff coefficient (hyp. B); and (3) the water losses reduce the rainfall intensity and the equivalent rainfall intensity parameter is given by $\lambda_{2c} = \lambda_2/C_r$ (hyp. C). The specific erosion rates based on Eq. 20*b* in Table 2 have been computed as a function of surface slope for these three hypotheses and the results are shown in Fig. 5. These curves represent the potential erosion losses for bare soil. The curve obtained by the empirical Universal Soil-Loss Equation (USLE) under the same conditions (7) is also shown on the same figure. The shape of the quadratic expression for slope in the USLE is very similar to power formulas with an exponent value near 1.7.

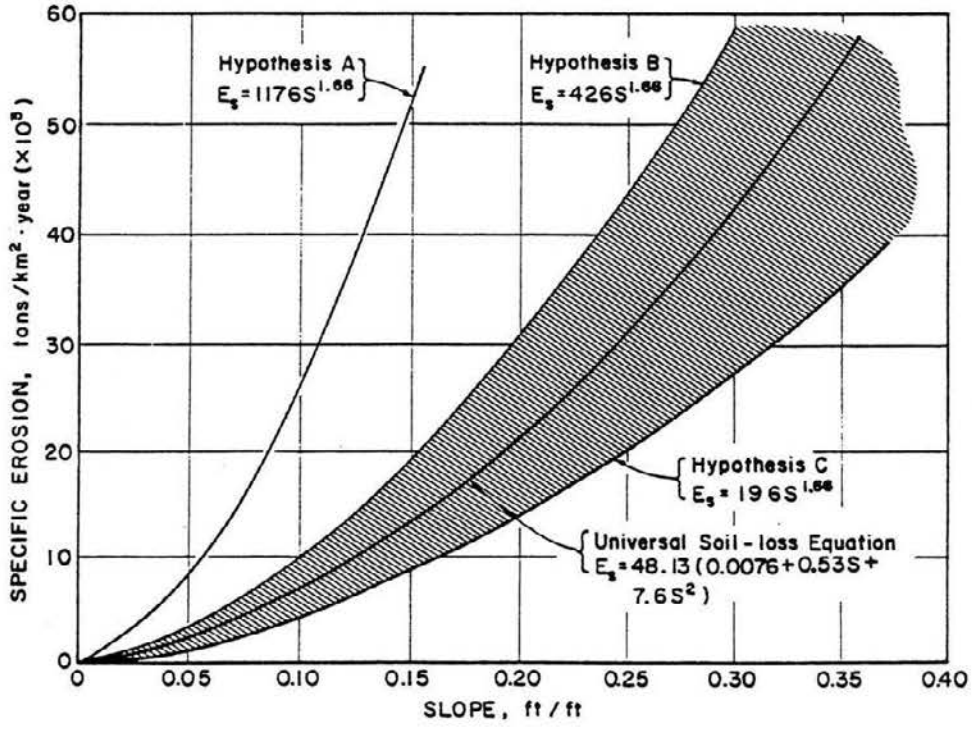

FIG. 5.—Specific Erosion versus Slope on Chaudière Watershed

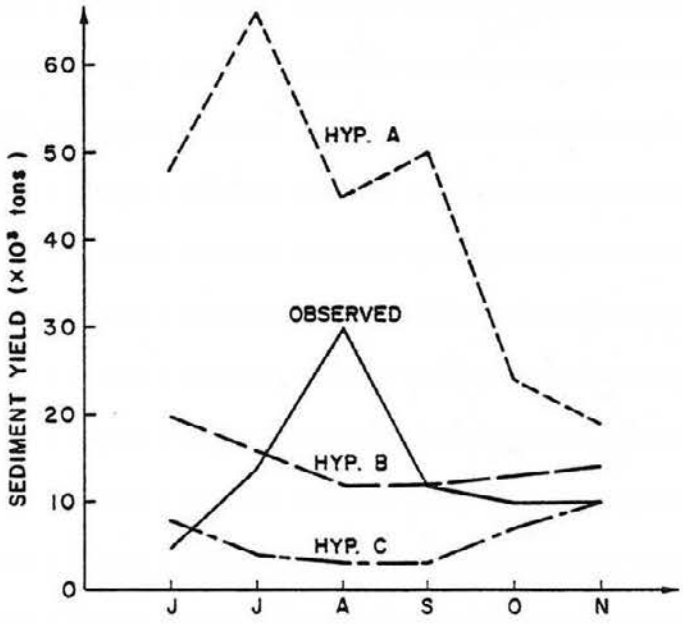

FIG. 6.—Observed and Computed Sediment Yields from Chaudière Watershed

The theoretically derived method has been applied to the Chaudière watershed during the rainfall period (June–November). The cropping management factor of the USLE and the monthly values of the runoff coefficient, C_r, were evaluated to account for vegetation and water losses on the watershed. An average sediment-delivery ratio was estimated from Boyce's data (1,7) to compute monthly sediment yield. These results during the rainfall period are shown in Fig. 6 and compared to the observed suspended load, which is mainly wash load, from 1968–1976 at St-Lambert-de-Lévis near the mouth of the river.

Though the observed values fluctuate, the observed load is in good agreement with the computed sediment yield (hyp. B). The peak in the observed sediment yield for the month of August is related to the occurrence of a severe flood in 1971. The question as to whether hyp. B can be consistently assumed has not yet been fully clarified. However, three other watersheds in Canada were investigated by the writers (9) and the analysis showed that hyp. B gives the best results. In a more detailed analysis of soil erosion and wash load on four northern watersheds (8), this approach to rainfall erosion was extended to soil erosion during snowmelt with excellent results.

Summary and Conclusions

This paper describes a theoretical development in soil erosion modeling based on: (1) The exponential distribution of rainfall duration and intensity; (2) the hydrographs obtained by solving the kinematic wave approximation for the case of a rainfall of constant intensity over an impervious surface; and (3) a general sediment discharge equation for overland flow suggested from dimensional analysis. Two equations for the total soil erosion losses during one rainfall event were derived, respectively, for the complete hydrograph and the partial equilibrium hydro-

graph. The expected value of the quantity of sediment eroded by a storm has been derived using hypergeometric series and a particular solution (Eq. 30) is determined for the case where the friction factor, K, does not dependent on the rainfall intensity.

It can be concluded that although the general equation (Eq. 29) can be solved analytically in terms of a series of incomplete gamma functions, a very simple first-order approximation (Eq. 35) has been derived from hypergeometric series. This equation has been applied on the Chaudière watershed and gives less than 5% difference with an elaborate numerical evaluation of Eq. 29. Better accuracy can also be obtained by taking the first two terms of the series as shown in Table 3. With the use of the runoff coefficient (hyp. B) and the sediment-delivery ratio, the computed sediment yield compares very well with the observed suspended load in the Chaudière River. The method demonstrated herein has been used to analyze complex watershed configurations and appears to be efficient for studying rainfall erosion and sediment yield from large watersheds.

Acknowledgments

This paper is based on studies carried out at the Department of Civil Engineering at Laval University. The writers wish to thank Dr. P. Todorovic from Ecole Polytechnique, Montréal, for his constructive comments and criticism regarding the rainfall characteristics. The writers are also indebted to Dr. D. B. Simons, G. O. Brown, and J. S. O'Brien from Colorado State University for their kind and helpful suggestions in the revision of this paper.

Appendix I.—References

1. Boyce, R., "Sediment Routing with Sediment-Delivery Ratios. Present and Prospective Technology for Predicting Sediment Yields and Sources," U.S. Department of Agriculture, ARS-S-40, 1975, pp. 61–65.
2. Chen, C. L., "Flow Resistance in Broad Shallow Grassed Channels," *Journal of the Hydraulics Division*, ASCE, Vol. 102, No. HY3, Mar., 1976. pp 307-322
3. Eagleson, P. S., "Climate, Soil and Vegetation, 2. The Distribution of Annual Precipitation Derived from Observed Storm Sequences," *Water Resources Research*, Vol. 14, No. 5, Oct., 1978, pp. 713–721.
4. Fawkes, P. E., "Roughness in a Model of Overland Flow," thesis presented to Colorado State University, at Boulder, Colo., in 1972, in partial fulfillment of the requirements for the degree of Master of Science.
5. Grayman, W. M., and Eagleson, P. S., "Streamflow Record Length for Modelling Catchment Dynamics," *Hydrodynamics Laboratory Report 114*, Department of Civil Engineering, M.I.T., Cambridge, Mass., 1969.
6. Izzard, C. F., "The Surface Profile of Overland Flow," *Transactions of the American Geophysical Union*, Vol. 6, 1944, pp. 959–968.
7. Julien, P., "Erosion de Bassin et Apport Solide en Suspension Dans les Cours d'eau Nordiques," thesis presented to Laval University, at Québec, Canada, in 1979, in partial fulfillment of the requirements for the degree of Master of Science.
8. Julien, P., "Prédiction d'apport Solide Pluvial et Nival Dans les Cours d'eau Nordiques à partir du Ruissellement Superficiel," thesis presented to Laval University, at Quebec, Canada, in 1982, in partial fulfillment of the requirements for the degree of Doctor of Philosophy.
9. Julien, P. Y., and Frenette, M., "A Model for Predicting Suspended Load in

Northern Streams," *Proceedings*, Annual Conference of the Canadian Society for Civil Engineering, CSCE, Halifax, May 23–25, 1984, pp. 565–585.
10. Kilinc, M. Y., "Mechanics of Soil Erosion from Overland Flow Generated by Simulated Rainfall," thesis presented to Colorado State University, at Fort Collins, Colo., in 1972, in partial fulfillment of the requirements for the degree of Doctor of Philosophy.
11. Kilinc, M. Y., and Richardson, E. V., "Mechanics of Soil Erosion from Overland Flow Generated by Simulated Rainfall," Hydrology Paper No. 63, Colorado State University, Fort Collins, Colo., 1973, 54 pp.
12. Li, R. M., "Sheet Flow under Simulated Rainfall," thesis presented to Colorado State University, at Fort Collins, Colo., in 1972, in partial fulfillment of the requirements for the degree of Master of Science.
13. Li, R. M., Shen, H. W., and Simons, D. B., "Mechanics of Soil Erosion by Overland Flow," presented at the 15th Congress, International Association for Hydraulic Research, Istanbul, Turkey, Proc. Paper A54, 1973, pp. 437–446.
14. Meyer, L. D., and Monke, E. J., "Mechanics of Soil Erosion by Rainfall and Overland Flow," *Transactions of ASAE*, Vol. 8, No. 4, 1965, pp. 572–580.
15. Musgrave, G. W., "The Quantitative Evaluation of Factors in Water Erosion: A First Approximation," *Journal of Soil and Water Conservation*, Vol. 2, No. 3, 1947, pp. 133–138.
16. Shen, H. W., and Li, R. M., "Rainfall Effect on Sheet Flow Over Smooth Surface," *Journal of the Hydraulics Division*, ASCE, Vol. 99, No. HY5, Proc. Paper 9733, May, 1973.
17. Shen, H. W., and Li, R. M., "Watershed Sediment Yield Model," *Stochastic Application to Water Resources*, Chapter 21, H. W. Shen, Ed., Water Resource Publication, Fort Collins, Colo., 1976, 68 pp.
18. Simons, D. B., Li, R. M., and Eggert, K. G., "Simple Water Routing and Yield Model Using a Small Programmable Calculator," Colorado State University, *Report for USDA Forest Service*, Rocky Mountain Forest and Range Experiment Station, Flagstaff, Ariz., CER76-77DBS-RML-KGE52, 1977.
19. Simons, D. B., Li, R. M., and Stevens, M. A., "Development of Models for Predicting Water and Sediment Routing and Yield from Storms on Small Watersheds," USDA FOREST Service, Rocky Mountain Forest and Range Experiment Station, Flagstaff, Ariz., CER74-75DBS-RML-MAS24, 1974, 130 pp.
20. Todorovic, P., "A Mathematical Study of Precipitation Phenomena," *Report CER67-68PT65*, Engineering Research Center, Colorado State University, Fort Collins, Colo., 1968.
21. Todorovic, P., and Dawdy, D. R., "Stochastic Point-Rainfall Simulation," *Mathematical Models in Hydrology*, Proceedings of Warsaw Symposium, IAHS-AISH, Publ. No. 100, July, 1971.
22. Todorovic, P., and Woolhiser, D., "Stochastic Model of Daily Rainfall," *Proceedings*, Symposium on Statistical Hydrology, Tucson, Ariz., Misc. Pub. No. 1275, ARS, USDA, June, 1974, pp. 232–246.
23. White, C. M., "The Equilibrium of Grains on the Bed of a Stream," *Proceedings of the Royal Society of London*, Series A, Vol. 174, 1940.
24. Wischmeier, W. H., and Smith, D. D., "Predicting Rainfall Erosion Losses—A Guide to Conservation Planning," *USDA Agriculture Handbook No. 537*, 1978, 58 pp.
25. Wooding, R. A., "A Hydraulic Model for the Catchment Stream Problem, II-Numerical Solutions," *Journal of Hydrology*, Vol. 3, Nos. 3/4, 1965, pp. 268–282.
26. Woolhiser, D. A., "Simulation of Unsteady Overland Flow," *Unsteady Flow in Open Channels*, Chapter 12, K. Mahmood and V. Yevjevich, Eds., Water Resources Publications, Fort Collins, Colo., 1975, pp. 485–508.
27. Yevjevich, V. H., "Statistical and Probability Analysis of Hydrologic Data. Part II. Regression and Correlation Analysis," Section B-II, *Handbook of Applied Hydrology*, V. T. Chow, Ed., McGraw-Hill, New York, N.Y., 1965, 55 pp.

124

28. Young, R. A., and Mutchler, C. K., "Soil Movement on Irregular Slopes," *Water Resources Research*, Vol. 5, 1969, pp. 184–1089.
29. Zingg, A. W., "Degree and Length of Land Slope as It Affects Soil Loss in Runoff," *Agricultural Engineering*, Vol. 21, No. 2, 1940, pp. 59–64.

APPENDIX II.—NOTATION

The following symbols are used in this paper:

A, b = friction coefficients of rainfall intensity;
C_r = runoff coefficient;
d_s = sediment size;
E_s = specific erosion;
$F(i), F(t_r)$ = distribution function of rainfall intensity and duration;
f = Darcy-Weisbach friction factor;
g = gravitational acceleration;
h = flow depth;
i = rainfall intensity;
$\bar{i}$ = average storm intensity;
K = friction coefficient including rainfall effect;
K_o = friction coefficient without rainfall effect;
K_m = representative constant friction coefficient;
L = runoff length;
m, n, p = coefficients of existing sediment discharge equations;
$p(i), p(t_r)$ = probability density function of rainfall intensity and duration;
$p(\nu/t)$ = probability to observe ν storms during the time t;
q = unit water discharge;
q_s^*, q_s = unit sediment discharge by weight and by mass;
R = Reynolds number;
S = land surface slope;
t = time;
t_e = equilibrium time;
t_r = storm duration;
$\bar{t}_r$ = average storm duration;
$\bar{u}$ = depth-integrated flow velocity;
$\alpha, \bar{\alpha}, \beta, \gamma, \delta, \epsilon, \eta$ = coefficients of the general sediment discharge equation;
$\Gamma(\chi)$ = gamma function;
γ_e = specific weight of water and sediment;
θ = dimensionless time variable;
λ = ratio of rainfall duration time to equilibrium time;
λ_0 = average arrival rate of storm events;
λ_1, λ_2 = rainfall duration and intensity parameters;
$\lambda_{1b}, \lambda_{2c}$ = equivalent rainfall duration and intensity parameters;
ν = number of rainfall events;
$\bar{\nu}$ = average number of rainfall events;
ν_e = kinematic viscosity of water;
ξ = dummy variable;
π_1, π_c = group of variables;
ρ_e, ρ_e = density of water and sediments;

τ_o = bed shear stress;
τ_c = critical bed shear stress;
Φ = expected value of soil erosion for one storm;
$\bar{\Phi}$ = expected value of soil erosion during a given period of time;
ϕ = total soil erosion for one storm;
ϕ_c, ϕ_p = total soil erosion during complete and partial equilibrium hydrographs; and
ψ = dimensionless flow discharge.

12

Stochastic Hydrol. Hydraul. 1 (1987) 127–134

Stochastic Hydrology and Hydraulics

© Springer-Verlag 1987

On predicting upland erosion losses from rainfall depth

Part 1: Probabilistic approach

P. Y. Julien and **A. M. Dawod**

Civil Engineering Dept., Engineering Research Center, Colorado State University, Fort Collins, CO 80523, USA

Abstract: Point rainfall triggers the complex processes of overland flow and surface erosion. The probability density functions of rainfall duration and intensity are coupled with a physically based dynamic formulation of rainfall-runoff-sediment transport relationships for upland areas. When considering a single storm, rainfall depth alone is a poor predictor of sediment transport because of the dispersion introduced by the effect of rainfall intensity. On a long terms basis, however, the total amount of rainfall can be used to predict total erosion losses.

Key words: Upland erosion, annual erosion losses

1 Introduction

It has long been recognized that rainfall induced runoff has the ability to detach and transport considerable amounts of sediments from upland areas. Raindrop impact on the earth surface loosens soil particles for downslope transport into the fluvial system. Soil erosion deteriorates soil structure and increase nutrient loss, which decreases the potential productivity of agricultural land. The amount of material transported is a function of the soil erodibility and the sediment transport capacity of surface runoff. Upland erosion losses depend on the size of sediment particles, infiltration rate, surface sealing, vegetation cover, resistance to flow and soil conservation practices.

Earlier investigations have been undertaken to quantify upland erosion losses. Musgrave's (1947) contribution has been cast into the well-known Universal Soil-Loss Equation (Wischmeier and Smith 1978). Mathematical models have been developed with increasing interest since the early sixties with contributions of Meyer and Wischmeier (1969), Foster and Meyer (1972), Simons et al. (1975), and Knisel (1980). In these computer models, the complex physical processes of precipitation over soil surface for a single storm are replaced by idealized deterministic configurations of physical elements that preserve the essential characteristics of a drainage area. The relationships derived from the realm of physics are used to simulate the response of watershed systems to the input variables.

When considering the variability of rainfall-runoff relationships, Eagleson (1978) showed that the probability distributions of input variables such as rainfall could be transformed into probability distributions of the output variables using deterministic physical processes. This approach has been extended to the analysis of soil

erosion from upland areas by Julien and Frenette (1985). The probability density functions (pdf) of both rainfall duration and intensity serve as inputs to calculate the expected value of rainfall erosion losses from upland areas. This method has been applied to several large watersheds in Canada (Julien and Frenette 1985). This approach, however, requires detailed knowledge of both rainfall duration and intensity which limits its applicability to locations where sufficient meteorological data are available. The purpose of the present investigation is to combine the effects of both duration and intensity into a single variable, namely rainfall depth, and then examine the relationship between erosion losses and rainfall depth. Previous studies of the probability distribution of rainfall duration and intensity serve as a basis for this theoretical investigation. The relationship between erosion losses and rainfall depth is first examined for a single storm and then for a large number of storms.

2 Problem Formulation

2.1 Rainfall precipitation

Point rainfall precipitation has been treated successfully as a random process by Todorovic (1968) and by Eagleson (1978). A dimensionless rainfall depth parameter ϕ_D has been defined after dividing the rainfall depth of a single storm by the average rainfall depth of a large number of storms. The exponential probability density function (pdf) of the dimensionless rainfall depth can be written:

$$f(\phi_D) = e^{-\phi_D}. \tag{1}$$

Similarly, Grayman and Eagleson (1969), Eagleson (1978) and Julien (1982) showed that both the rainfall duration and intensity can be represented by exponential pdf's that are independent of each other. After normalizing rainfall duration and intensity of a single event with average values, the pdf of the dimensionless rainfall duration ϕ_t and that of intensity ϕ_i can be written:

$$f(\phi_t) = e^{-\phi_t}, \quad \text{and} \quad f(\phi_i) = e^{-\phi_i}. \tag{2a,b}$$

The rainfall depth being equal to the product of storm duration and intensity, the following relation also holds true in dimensionless form:

$$\phi_D = \phi_t \phi_i. \tag{3}$$

As the rainfall intensity exceeds the rate of infiltration in the soil, the excess rainfall intensity generates surface runoff.

2.2 Soil erosion losses

The principal variables involved in the unit sediment transport q_s are the surface slope S, the rainfall intensity i, the runoff length L, the mass density ρ, and the kinematic viscosity ν of the fluid. The method of dimensional analysis reduces the number of parameters. The dimensionless sediment transport rate per unit width ϕ_{q_s} can be written (Julien 1982) as:

$$\phi_{q_s} = \bar{\alpha}\left(\frac{L\bar{i}}{\nu}\right)^{\gamma} S^{\beta} \phi_i^{\gamma} \tag{4}$$

in which $\phi_{q_s} = q_s/\nu$; $\bar{i}$ is the long term average rainfall intensity; and the empirical parameters $\bar{\alpha}$, β, and γ have been determined by Julien and Simons (1985) for: (1) several empirical equations derived from field data; (2) theoretical relationships; and (3) several bed-load formulas describing sediment transport in laboratory flumes and streams. The analysis showed that the exponent β varied between 1.2

and 1.9 whereas the exponent of the sediment rating curve, γ, typically ranged from 1.4 to 2.4 for upland erosion losses.

A single storm of given duration and uniform rainfall intensity, over an impervious rectangular plane of width W, and runoff length L yields the following dimensionless soil loss, ϕ_s, after using Eqs. (3) and (4):

$$\phi_s = \phi_W \phi_{q_s} \phi_t = \pi \phi_D \phi_i^{\gamma - 1} \tag{5}$$

where $\pi = \bar{\alpha} S^{\beta} (\frac{L\bar{i}}{\nu})^{\gamma} \frac{W}{L}$ and $\phi_W = \frac{W}{L}$.

It is noted that Eq. (5) neglects the effects of the rising and falling limbs of the runoff hydrographs. Julien and Frenette (1985) demonstrated that this is a sufficiently good first-order approximation for field applications.

For a given field site the dimensionless group of constants π remains invariant, thus the dimensionless soil loss ϕ_s is proportional to the dimensionless amount of rainfall ϕ_D and the dimensionless rainfall intensity ϕ_i whenever $\gamma > 1$. The issue to be clarified relates to the influence of ϕ_i on ϕ_s in Eq. (5). If ϕ_s could be demonstrated to be insensitive to changes in ϕ_i, then Eq. (5) would indicate a linear relationship between ϕ_s and ϕ_D.

3 Soil erosion losses during single storms given the rainfall depth

The influence of rainfall intersity ϕ_i on soil loss ϕ_s given a constant rainfall depth ϕ_D is examined through the concept of conditional probability schematized in Fig. 1. The expected value, $E(\phi_s \mid \phi_D)$, and the variability of ϕ_s around the expected value are calculated after the joint probability density function is defined. Considering the independence of rainfall duration and rainfall intensity, the joint probability density function equals the product of the individual exponential distributions from Eqs. (2a) and (2b). The conditional probability density function (cpdf) of rainfall intensity ϕ_i for a given rainfall depth (ϕ_D constant) is obtained from $\phi_t = \phi_D / \phi_i$. Thus the cpdf is:

$$f(\phi_i \mid \phi_D) = \frac{e^{-\phi_i} e^{-\phi_D/\phi_i}}{\int_0^{\infty} e^{-\phi_i} e^{-\phi_D/\phi_i} \, d\phi_i} . \tag{6}$$

The denominator in Eq. (6) is a constant normalizing the distribution. The result of integrating Eq. (6) is the conditional cumulative distribution function (ccdf) denoted by $F(\phi_i \mid \phi_D)$ and written as:

$$F(\phi_i \mid \phi_D) = \int_0^{\phi_i} f(\phi_i \mid \phi_D) \, d\phi_i . \tag{7}$$

Interestingly, the function $F(\phi_i \mid \phi_D)$ also serves to describe the ccdf of ϕ_s because from Eq. (5), with π and ϕ_D constant, ϕ_i is directly related to ϕ_s as

$$\phi_i = [\frac{\phi_s}{\pi \phi_D}]^{\frac{1}{\gamma - 1}} . \tag{8}$$

Figure 2 shows the ccdf of soil erosion for different values of ϕ_D ranging from 0.1 to 10 as calculated from numerical integration of Eq. (7). It is seen from this figure that for a given ϕ_i, $F(\phi_i \mid \phi_D)$ decreases with increasing ϕ_D.

The first two moments of the ccdf are calculated to yield insight on the variability of ϕ_s around the expected value of ϕ_s as a function of γ.

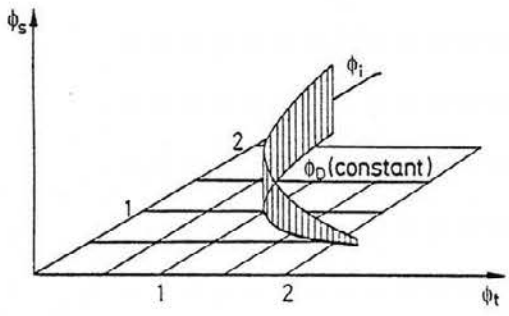

Figure 1

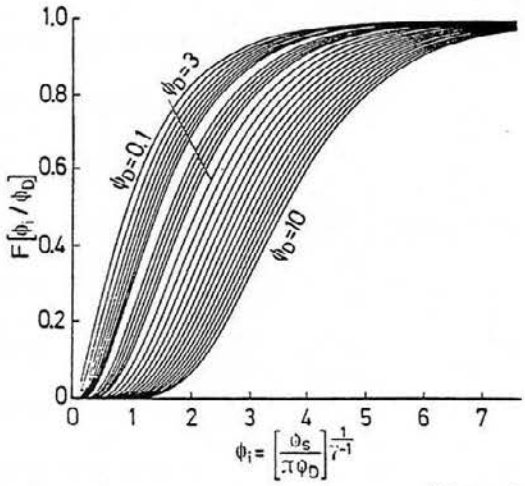

Figure 2

Figure 1. Soil loss ϕ_s given constant values of ϕ_D

Figure 2. Conditional cumulative distribution function of ϕ_i given ϕ_D constant

3.1 Expected value of soil erosion

The first moment of the distribution corresponds to the expected value $E(\phi_s \mid \phi_D)$ of the soil loss for one rainstorm event, given the rainfall depth ϕ_D. This is expressed mathematically by the following integral:

$$E(\phi_s \mid \phi_D) = \int_0^\infty \phi_s f(\phi_i \mid \phi_D)\, d\phi_i \,. \tag{9}$$

From Eq. (5), ϕ_s can be replaced by a function of ϕ_i, thus:

$$E(\phi_s \mid \phi_D) = \frac{\pi\phi_D \int_0^\infty \phi_i^{\gamma-1} e^{-\phi_i} e^{-\phi_D/\phi_i}\, d\phi_i}{\int_0^\infty e^{-\phi_i} e^{-\phi_D/\phi_i}\, d\phi_i} \tag{10}$$

in which the denominator and ϕ_D are constant. Both integrals in Eq. (10) can be expressed in terms of modified Bessel functions, $K_\gamma(2\sqrt{\phi_D})$, of order γ defined in Gradshteyn and Ryzhik (1965):

$$K_\gamma(2\sqrt{\phi_D}) = \frac{1}{2(\phi_D)^{\gamma/2}} \int_0^\infty \phi_i^{\gamma-1} e^{-\phi_i} e^{-\phi_D/\phi_i}\, d\phi_i \,. \tag{11}$$

After substituting Bessel functions of order γ (numerator) and of order 1 (denominator), the expected value of soil erosion losses from Eq. (10) can be written as:

$$\frac{E(\phi_s \mid \phi_D)}{\pi\phi_D} = \phi_D^{\frac{(\gamma-1)}{2}} \frac{K_\gamma(2\sqrt{\phi_D})}{K_1(2\sqrt{\phi_D})} \,. \tag{12}$$

Solution of the Modified Bessel functions is possible with the aid of mathematical tables (Abramowitz and Stegun 1972) for integer values of γ. Asymptotic series expansions or numerical integrations of Eq. (12) can also be used for non-integer values of γ. Dawod (1986) verified numerical solutions with mathematical tables for integer values of γ. The numerical method was then used for non-integer values

of γ. The results for the expected value of soil losses conditional to a given ϕ_D are shown in Fig. 3 as a function of γ ($1.5<\gamma<3.5$) for ϕ_D held fixed between 0.1 and 10. The expected value $E(\phi_s \mid \phi_D)$ is found to increase both with ϕ_D and γ.

3.2 Second moment and coefficient of variation

The second central moment M_2 or variance has been determined from:

$$M_2(\phi_D) = \int_0^\infty [\phi_s - E(\phi_s \mid \phi_D)]^2 f(\phi_i \mid \phi_D)\, d\phi_i \tag{13}$$

with ϕ_s given from Eq. (5). It is noted that $M_2(\phi_D)$ is a random variable. This integral has been solved numerically (Dawod 1986) and is shown to increase with γ and ϕ_D. The results are presented in the form of a coefficient of variation.

$$\eta(\phi_D) = \sqrt{M_2(\phi_D)}/E(\phi_s \mid \phi_D)\,. \tag{14}$$

The coefficient of variation is shown in Fig. 4 to decrease with increasing ϕ_D. For example, the standard deviation reaches twice the expected value of soil losses when $\gamma = 3$ and $\phi_D = 0.1$. This indicates that for a single storm, if calculations of soil erosion are to be based on rainfall depth only, the influence of rainfall intensity cannot be neglected because the variability introduced by the rainfall intensity is excessive. The results shown in Fig. 4 reveal that the influence of rainfall intensity decreases as ϕ_D increases and as γ decreases.

4 Expected soil erosion losses from single storms of unknown rainfall depth

When the amount of rainfall from a given storm is unknown, the expected value of soil erosion $E(\phi_s)$ can still be determined after considering the pdf of rainfall depth (Eq. (1)), thus:

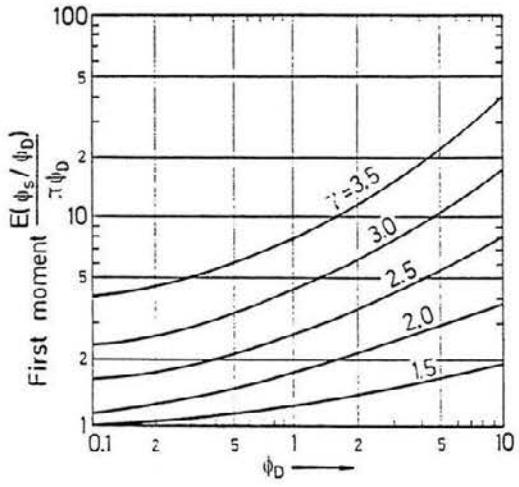

Figure 3

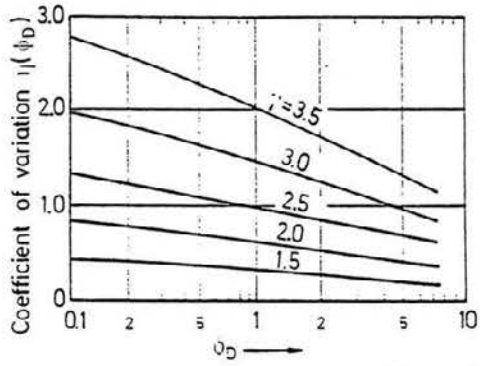

Figure 4

Figure 3. Expected value of soil loss ϕ_s as a function of ϕ_D and γ

Figure 4. Coefficient of variation $\eta(\phi_D)$ as a function of ϕ_D and γ

Table 1. Expected values of first moment $E(\phi_s)$, second moment $E\{M_2(\phi_D)\}$, and coefficient of variation $\eta\{M_2(\phi_D)\}$, for different γ values

γ	$E(\phi_s)$	$E\{M_2(\phi_D)\}$	$\eta\{M_2(\phi_D)\}$
1.5	1.14	0.14	0.33
2.0	1.61	1.19	0.68
2.5	2.50	7.18	1.07
3.0	4.21	42.78	1.55
3.5	7.64	272.96	2.16

$$E(\phi_s) = \int_0^\infty E(\phi_s \mid \phi_D) e^{-\phi_D} \, d\phi_D \, . \tag{15}$$

Simirlarly, the expected values of the variance, $E\{M_2(\phi_D)\}$, and coefficient of variation $\eta\{M_2(\phi_D)\}$ when the rainfall volume is unknown are:

$$E\{M_2(\phi_D)\} = \int_0^\infty M_2(\phi_D) e^{-\phi_D} d\phi_D \, , \text{ and } \eta\{M_2(\phi_D)\} = \frac{\sqrt{E\{M_2(\phi_D)\}}}{E(\phi_s)} . \tag{16a,b}$$

The results of the evaluation of Eqs. (15), (16a), and (16b) are summarized in Table 1. As γ increases beyond unity, $E(\phi_s)$ increases while the second moment increases rapidly when $\gamma > 2.5$. The coefficient of variation $\eta\{M_2(\phi_D)\}$, however, increases steadily from 0 (when $\gamma = 1$) to about 2.2 (when $\gamma = 3.5$). This demonstrates the greater sensitivity of soil erosion calculations based on the rainfall intensity as γ becomes larger. It can be concluded that soil erosion losses from individual storms cannot be estimated accurately from rainfall depth only, except when the exponent γ approaches unity.

5 Soil erosion losses from a large number of storms

A different perspective arises when the sum of individual erosion losses from a large number of storms is considered. The central limit theorem states that the distribution of sums of random variables tends toward a normal distribution when the number of storms becomes large.

The expected value of the sum of n erosion losses resulting from the occurrence of n storms, $E(\sum^n \phi_s)$, equals the sum of expected values from individual storms, $\sum^n E(\phi_s)$. The coefficient of variation of this sum, however, decreases with the number of storms as follows:

$$[1 - \frac{\eta\{M_2(\phi_D)\}}{\sqrt{n}} t_{1-\alpha;n-1}] < \frac{E(\sum^n \phi_s)}{\sum^n E(\phi_s)} < [1 + \frac{\eta\{M_2(\phi_D)\}}{\sqrt{n}} t_{1-\alpha;n-1}] \tag{17}$$

where n = number of storms, t = student's t-distribution, α = specified probability level, and $n-1$ = degrees of freedom.

Hence, the expected value of the sum of n storms remains bounded at a probability level α. For example, the expected value of the sum of 100 storms at a 95% probability level is calculated from Eq. (19) with the aid of Fig. 5 ($t_{0.05;99} = 1.66$) given $\eta\{M_2(\phi_D)\} = 0.68$ when $\gamma = 2$ as obtained from Table 1:

$$0.89 < [\frac{E(\sum^n \phi_s)}{\sum^n E(\phi_s)}] < 1.11 \tag{18}$$

Consequently, as opposed to the previous conclusion regarding single storm events,

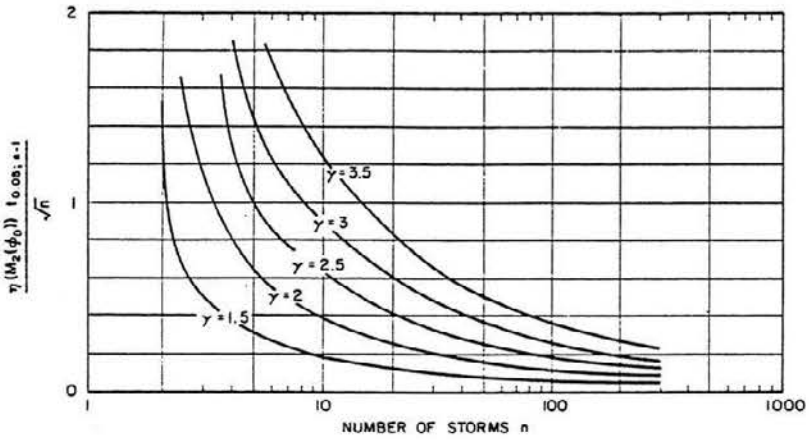

Figure 5. Coefficient of variation of the expected value of erosion losses for n storms

long term erosion losses can be related to the total amount of rainfall provided the number of storms is sufficiently large.

6 Conclusion

On a single storm basis, soil erosion losses cannot be predicted accurately from the rainfall depth only because of the dispersion induced by rainfall intensity. The coefficient of variation increases rapidly with the exponent γ as shown in Table 1.

Total erosion losses from a large number of storms can be calculated from the sum of individual erosion losses. The variance of the expected value of the total erosion losses is shown to decrease as the number of rainstorms increases.

The importance of this conclusion can be seen as it enables the prediction of long term upland erosion losses from long term rainfall amounts. The question as to whether the number of storms is sufficiently large for monthly or annual predictions can be answered from Eq. (17) with the aid of the results shown in Table 1, and Fig. 5.

7 References

Abramowitz, M.; Stegun, I.A. 1972: Handbook of mathematical functions with formulas, graphs and mathematical tables. New York: Dover

Dawod, A.M. 1986: Modeling of soil erosion using rainfall volume. Ph.D. dissertation, Dept. of Civil Engr., Colorado State Univ., Fort Collins

Eagleson, P.S. 1978: Climate, soil and vegetation. 2. The distribution of annual precipitation derived from observed storm sequences. Water Resour. Res. 14, 713-721

Foster, G.R.; Meyer, L.D. 1972: Transport of soil particles by shallow flow. Trans. Amer. Soc. Agric. Engr. 15, 99-102

Gradshteyn, I.S.; Ryzhik, I.M. 1965: Table of integrals, series and products. New York: Academic Press

Grayman, W.M.; Eagleson, P.S. 1969: Streamflow record length for modeling catchment dynamics. Hydrodynamic Lab. report 114, Dept. of Civil Engr., Mass. Inst. Tech., Cambridge, Mass.

Julien, P.Y. 1982: Prédiction d'apport solide pluvial et nival dans les cours d'eau nordiques à partir du ruissellemena superficiel. Ph.D. dissertation, Civil Engr. Dept., Laval Univ.

Julien, P.Y.; Frenette, M. 1985: Modeling of rainfall erosion. J. of Hydrau. Engr. ASCE 111, 1344-1359

Julien, P.Y.; Simons, D.B. 1985: Sediment transport capacity of overland flow. Trans. Amer. Soc. Agric. Engr. 28, 755-762

Knisel, G.W. 1980: Creams. A field scale model for chemicals runoff and erosion from agriculture and management system. U.S. Dept. of Agric. Science and Education Admin. Report 20, 1980

Meyer, L.D.; Wischmeier, W.H. 1969: Mathematical simulation of the process of soil erosion by water. Trans. Amer. Soc. Agric. Engr. 12, 756-762

Musgrave, G.W. 1947: The quantitative evaluation of factors in water erosion: a first approximation. J. of Soil and Water Cons. 2, 133-138

Simons, D.B.; Li, R.M.; Stevens, M.A. 1975: Development of models for predicting water and sediment rounting and yield from storms on small watersheds. USDA Forest Service, Rocky Mountain Forest and Range Exp. Station

Todorovic, P. 1968: A mathematical study of precipitation phenomena. Report CER67-68PT65, Engr. Res. Center, Colorado State Univ., Fort Collins

Wischmeier, W.H.; Smith, D.D. 1978: Predicting rainfall erosion losses from cropland east of the Rocky Mountains. US Dept. of Agric., Handbook 537

Appendix A Notations

$\bar{i}$	average rainfall intensity of a large number of storms
K_γ	Modified Bessel function of order γ
L	length of overland flow
$M_2(\phi_D)$	second central moment conditional on given ϕ_D
n	number of rainstorm events
q_s	unit sediment discharge
S	surface slope
$t_{1-\alpha;n-1}$	student's t-distribution at a probability level α and $n-1$ degrees of freedom
W	width of a rectangular plane
α	probability level
$\bar{\alpha}, \beta, \gamma$	empirical coefficients of the sediment transport relationship
π	group of variables which remain constant at a given field state
ν	kinematic viscosity of the fluid
$\eta(\phi_D)$	coefficient of variation conditional on given ϕ_D
ϕ_D	dimensionless rainfall depth during one storm
ϕ_i	dimensionless average rainfall intensity during one storm
ϕ_{q_s}	dimensionless sediment transport rate per unit width
ϕ_s	dimensionless soil loss
ϕ_t	dimensionless rainfall duration of one storm
ϕ_W	ratio of plane width W to runoff length L

Accepted March 24, 1987.

Stochastic Hydrol. Hydraul. 1 (1987) 135–140

Stochastic Hydrology and Hydraulics
© Springer-Verlag 1987

On predicting upland erosion losses from rainfall depth

Part 2: Field applications in Iraq

A. M. Dawod and **P. Y. Julien**

Civil Engineering Dept., Engineering Research Center, Colorado State University, Fort Collins, CO 80523, USA

Abstract: Annual erosion losses from 135 experimental plots under a variety of soil types, vegetation cover densities and conservation practices in Iraq have been measured over a period of four years. The first three years of this data set demonstrate that annual erosion losses can be predicted from annual rainfall depths. The results obtained from regression analysis were then validated with the fourth year of soil erosion data. These results corroborate the theoretical findings of the companion paper in that long term erosion losses can be predicted from the total amount of rainfall.

Key words: Upland erosion, annual soil losses

1 Introduction

Since the turn of this century, quantitative information on soil erosion rates has been collected on a large number of instrumented field plots under a variety of climatic, physiographic, land use and soil management situations. Previous studies on small experimental plots located across the United States led conclusively to the well known Universal Soil-Loss Equation (USLE). This prediction model developed by Wischmeier and Smith (1960, 1978) expresses the average annual soil-loss as a function of six factors: (1) a rainfall erosion index, (2) a soil erodibility factor, (3) the land gradient, (4) the length of slope, (5) a cropping management factor, and (6) a conservation practice factor.

In a study to determine the best rainfall erosivity index (Wischmeier and Smith 1960), several expressions representing rainfall depth, intensity, and energy were correlated with soil-loss. The product of kinetic energy of rainfall and the maximum 30-minute rainfall intensity (the R factor) explained a larger percentage of soil-loss variation than any other rainfall-derived parameter.

To support these findings, Dragoun (1962) found very poor correlation between sediment yield and rainfall depth on a single storm basis at two field-size watersheds in Nebraska. In the latest version of the USLE (Wischmeier and Smith 1978), the erosivity index was determined empirically for all significant storms to be the summation on an annual basis of the individual storm product of the kinetic energy of rainfall in hundreds of foot-tons per acre, and the maximum 30-minute rainfall intensity in inches per hour.

The objective of this work is to examine the relationship between soil losses and rainfall depth on an annual basis through a detailed analysis of instrumented field

plot data from Iraq. In contrast to the empirically derived USLE which requires detailed knowledge of the kinetic energy of rainfall, it is hypothesized that annual soil erosion losses can be predicted from rainfall depth and without knowledge of the kinetic energy of rainfall.

Field studies related to rainfall, surface runoff and soil erosion losses were conducted at the Zawita Experimental Station within the Dohuk Governate in Iraq. The station is located 480 km north of Baghdad and lies between 42E and 43E longitude and between 36N and 37N latitude.

2 Rainfall

Daily rainfall at 14 stations in the northern part of Iraq has been investigated over a period of 16 to 30 years to determine its temporal and spatial distribution. Three models describing the distribution of rainfall depths were tested against the measurements: (1) the one-parameter exponential distribution, (2) the two-parameter gamma distribution, and (3) the three-parameter mixed-exponential distribution.

The probability density function $f(x)$ of rainfall depth for the exponential, gamma and mixed-exponential models are detailed in Dawod and Julien (1986). The goodness-of-fit based on the Smirnov-Kolmogorov test demonstrated that the exponential distribution can best represent the distribution of rainfall depth in the northern part of Iraq. As an example, the distribution of daily rainfall depth for the months of December and January at Zawita Station is shown in Fig. 1. On a monthly basis, the average rainfall depth per storm at the 14 stations is presented in Table 1. It is observed that rainfall occurs mainly from October until May and that the average rainfall depth per storm at a given station remains fairly constant except for the first and last months of the rainy season. The mean annual rainfall depth per storm is given in the last column of Table 1. When these mean annual values are plotted on a map of Iraq (Fig. 2), a four-fold increase in average rainfall precipitation per storm is noticeable in the northeastern part of the country.

3 Overland runoff

A series of 135 rectangular experimental plots, each covering an area of 100 m^2 (5 m wide and 20 m long) was constructed at five different slopes to measure overland runoff and surface erosion under a set of three different soil conditions, three vegetation types and three conservation practices. Each plot was surrounded with a metal border (30 cm high). Ten holes were drilled into a plate fixed at the lower end of each plot. One of the ten holes was connected to a 4 cm rubber pipe leading to two large barrels used for collecting overland flow and trapping sediments. Surface runoff and erosion losses were measured after each storm and compiled each year for a period of four years from 1976 to 1980. Details on this field investigation are available in Dawod (1981, 1983).

Overland runoff and soil erosion losses from Zawita Experimental Station have been compiled by Dawod (1986) and include fifteen tables similar to Table 2 (presented as an example) with overland flow and soil erosion data for five different slopes (1%, 5%, 10%, 15%, and 20%) and three types of soil texture.

Similar natural precipitation conditions prevailed for each of the 135 plots allowing comparison of the relative erodibility of soil surface to various combinations of slope, soil texture, vegetation cover and conservation practices.

Regression analysis between the measured variables indicates a significant correlation between the surface slope, S, and the annual runoff depth, V_r in mm and the annual rainfall depth r:

Table 1. Monthly and annual variation of rainfall depth per storm (mm) at 14 stations in northern Iraq

	Station	Oct.	Nov.	Dec.	Jan.	Feb.	Mar.	Apr.	May	Annual * Mean
A	Sarsink	18.9	15.6	15.4	17.9	17.2	16.7	14.5	16.1	16.2
B	Amidia	14.1	22.7	20.8	20.4	17.2	16.4	19.2	15.2	19.5
C	Shaqlaw	6.8	13.2	17.9	13.5	22.7	12.7	15.2	12.2	15.9
D	Rawanduz	40.0	23.3	19.6	25.0	23.8	20.0	20.0	19.2	22.0
E	Dokan	5.2	14.3	14.3	14.5	15.9	15.6	14.5	13.5	14.9
F	Mosul	3.0	5.6	6.8	6.1	6.3	6.8	4.9	4.7	6.1
G	Sinjar	4.8	6.7	8.0	8.3	8.1	8.3	7.9	10.5	7.8
H	Kirkuk	3.4	5.1	6.7	7.0	7.1	8.1	6.6	4.3	6.8
I	Khanaqin	4.3	6.4	9.8	7.9	7.1	8.7	6.3	4.0	7.7
J	Sulaimoniya	6.4	11.6	11.4	9.8	14.1	11.8	11.1	11.1	11.6
K	Arbil	17.9	9.1	12.2	12.2	13.2	10.6	16.1	20.4	12.2
L	Salahddin	4.1	17.9	14.5	10.8	10.5	10.6	11.0	13.5	12.6
M	Duhok	19.2	12.2	10.2	15.9	12.7	12.8	11.2	18.2	12.5
N	Zawita	11.5	13.9	13.2	16.9	15.6	13.9	12.7	15.2	14.4

* Average values during the wet season (November through April).

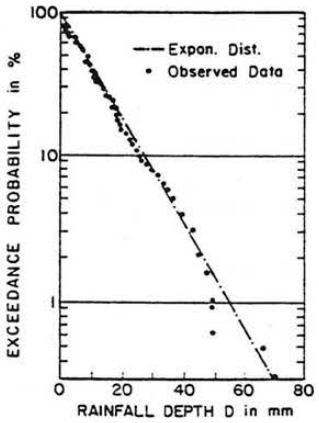

Figure 1

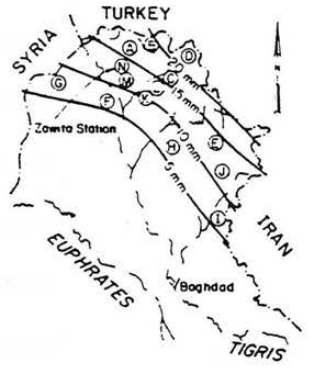

Figure 2

Figure 1. Exceedance probability for rainfall depth at Zawita Station

Figure 2. Average rainfall depth per storm in the northern part of Iraq

Table 2. Annual surface runoff and erosion losses from field plots at Zawita Station for 20% slope gradient and fine soil texture

Conservation practice		NP	NP	NP	CO	CO	CO	WF	WF	WF
Soil texture		NC	MC	FC	NC	MC	FC	NC	MC	FC
Annual	1976-77	127	104	63	98	80	50	120	99	59
Surface	1977-78	111	95	57	90	72	45	109	93	53
Runoff	1978-79	84	73	41	70	66	35	82	69	40
ha.mm/ha	1979-80	135	112	68	102	89	56	133	109	67
Annual	1976-77	192	63	20	130	45	13	149	47	16
Erosion	1977-78	170	60	16	125	43	13	135	49	17
Losses	1978-79	130	47	13	101	32	10	96	36	13
m^3/ha	1979-80	170	62	17	127	44	14	134	47	16

NP = No conservation practice, CO = Contouring, WF = Wattle fences
NC = No vegetation cover, MC = Medium vegetation cover, FC = Full vegetation cover

Table 3. Runoff coefficients for conservation practice P_r, vegetation C_r and soil texture T_r

A.	Conservation practice	P_r	P_s	P
	No conservation practice	1.00	1.00	1.00
	Contouring	0.78	0.89	0.62
	Wattle fences	0.96	0.82	0.77
B.	Vegetation cover density	C_r	C_s	C
	No cover (bare soils)	1.00	1.00	1.00
	Medium vegetation cover	0.77	0.52	0.36
	Full cover	0.54	0.23	0.10
C.	Soil texture	K_r	K_s	K
	Coarse texture	0.81	0.72	0.53
	Medium texture	1.00	1.00	1.00
	Fine texture	1.23	0.54	0.73

$$V_r = 0.23 S^{0.357} r \; ; \quad (R^2 = 82\%). \tag{1}$$

All other conditions being similar, the increase in runoff with slope is likely caused by the increased effects of surface depression storage and higher infiltration losses at low slopes. The variability of runoff volume under various conditions of conservation practice, vegetation cover density, and soil texture was determined from comparison with a reference value. Bare soils with no conservation practice and medium soil texture were selected as the reference conditions. Relative runoff volumes were defined as the ratio of the runoff volume under any condition of vegetation, soil type and conservation to the runoff volume for bare soils used as reference conditions. After averaging the values of the relative runoff volumes, three sets of correction factors were determined as shown in Table 3 for conservation practice P_r, vegetation C_r and soil texture K_r.

Table 3 indicates that the effects of contouring and wattle fences reduce the runoff from experimental plots slightly in comparison with no conservation practice conditions ($P_r = 1$). The coefficient C_r quantifies the influence of vegetation; runoff and hence C_r are shown to decrease gradually as the vegetation density increases. Soils with a coarse texture and larger grain sizes have larger infiltration rates than fine silt soils, thus the soil texture parameter K_r decreases with increasing texture or size of soil particles.

As derived from these experiments at Zawita station, the runoff depth can be expressed as:

$$V_r = 0.23 P_r C_r K_r S^{0.357} r \tag{2}$$

in which the rainfall depth r and the runoff depth V_r are in mm.

4 Soil erosion losses

Multiple non-linear regression analysis was applied to the first three years of the Zawita Station soil erosion loss data and the fourth year of data was used for validation. Annual erosion losses V_s in m^3/ha were regressed against the surface slope S in m/m and runoff depth V_r in mm in the following power form:

$$V_s = 0.743 S^{0.72} V_r^{1.44} P_s C_s K_s \; ; \quad (R^2 = 0.95). \tag{3}$$

The conservation practice coefficient P_s in Table 3 takes a reference value equal to unity for experimental plots with no conservation practice. The relative influence of wattle fences and contouring is shown to reduce soil erosion losses by as much as 20%. The vegetation factor C_s decreases with vegetation cover density.

The soil losses calculated from Eq. (3) are in excellent agreement with the

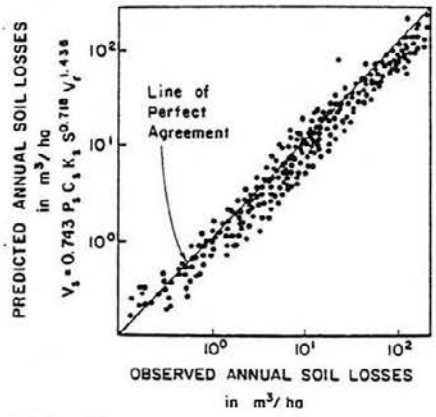

Figure 3

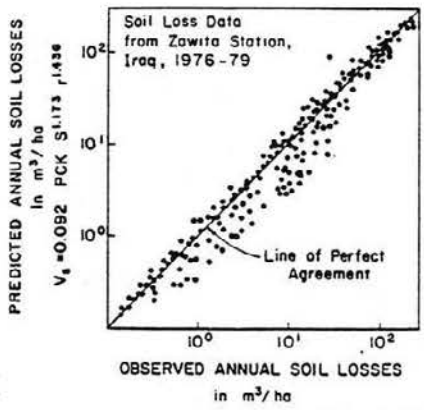

Figure 4

Figure 3. Predicted and observed annual soil losses at Zawita Station 1976-1979 (From Eq. (3))

Figure 4. Predicted and observed annual soil losses at Zawita Station 1976-1979 (From Eq. (4))

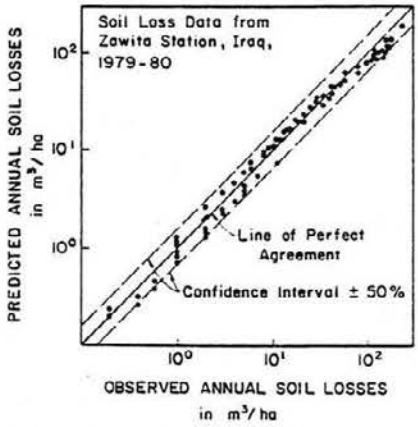

Figure 5. Predicted and observed annual soil losses at Zawita Station 1979-1980 (From Eq. (4))

observed soil losses shown in Fig. 3. Few data points lie outside of a relatively narrow band around the expected value.

The soil loss V_s was also regressed against the slope S and annual rainfall depth r after the coefficients for vegatation C, conservation P and soil texture K were combined as shown in Table 3. The soil loss equation reads:

$$V_s = 0.092 PCK S^{1.17} r^{1.44}, \tag{4}$$

with V_s = annual soil loss in m^3/ha/year, S = slope in m/m, P = conservation practice parameter, C = vegetation parameter, K = soil texture parameter, r = annual rainfall depth in mm.

The field observations from the Zawita Station under a large variety of vegetation, soil types and conservation practices are compared with erosion losses calculated from Eq. (4) in Fig. 4. The analysis demonstrates the feasibility of modeling soil erosion losses from annual rainfall r and the soil surface parameters P, C, K and S.

5 Validation

The data collected during the fourth year (1979-1980) of investigation at Zawita Station were used for validation of the method. As shown in Fig. 5 the observed values of the annual soil erosion losses are in excellent agreement with the calculations from Eq. (4). As could be assessed from the theoretical investigation in the

companion paper, the variability around the mean value can be calculated as follows, with $\gamma = 1.44$, $\alpha = 95\%$ and $n = 46$ on an annual basis,

$$0.90 < \frac{E(\sum_{46}^{46}\phi_s)}{\sum_{46}E(\phi_s)} < 1.10 \tag{5}$$

where ϕ_s is the dimensionless soil loss. It can be concluded that this dispersion is relatively small. Thus, the sum of erosion losses from n storms on an annual basis can be substituted by the sum of expected values which depends on rainfall depth.

6 Summary

The hypothesis that the annual rainfall depth can be used for predicting annual soil erosion losses from upland areas has been tested with field data from 135 experimental plots in Iraq. The 100 m^2 plots were monitored over a period of four years under a broad variety of soil types, vegetation cover and conservation practices. The first three years of data were used in a regression analysis which relates soil losses to rainfall depth and also to runoff depth.

Under similar conditions of rainfall, soil type, vegetation and conservation practices runoff volumes are shown to increase with the slope of the experimental plot. This indicates that infiltration losses increase on flatter surfaces.

The runoff depth and the soil erosion losses were regressed (Eqs. 2, 3 and 4) against surface slope S, rainfall depth r and relative correction factors for the soil type K, vegetation C and conservation practice P. The results shown in Figs. 3 and 4 are excellent. The fourth year of data validates the empirical regression equation and the small dispersion predicted from the theoretical analysis in the companion paper is confirmed with the experiments. It can be concluded that on an annual basis, soil erosion losses can be predicted either as a function of runoff and slope (Eq. (3)) or as a function of rainfall depth and slope (Eq. (4)).

This method for predicting annual soil erosion losses is preferred to the USLE when annual rainfall amounts are known and the rainfall precipitation data are insufficient to calculate the kinetic energy factor of the USLE.

7 References

Dawod, A.M. 1981: Runoff and water yield prediction equations in North Iraq using hydrologic factors. M.S. thesis, Univ. of Nebraska, Lincoln

Dawod, A.M. 1983: The effect of land treatment and structural measures on sediment yield for Dohuk watershed. M.S. thesis, Univ. of Nebraska, Lincoln

Dawod, A.M. 1986: Modeling of soil erosion using rainfall volume. Ph.D. dissertation, Dept. of Civil Engr., Colorado State University, Fort Collins

Dawod, A.M.; Julien, P.Y. 1986: Analysis of daily rainfall precipitation in North Iraq. Proc. of the Sixth Annual AGU Front Range Branch Hydrology Days, pp. 189-197. Colorado, Fort Collins

Dragoun, F.J. 1962: Rainfall energy as related to sediment yield. J. of Geophysical Research 67, 1495-1501

Wischmeier, W.H.; Smith, D.D. 1960: A universal soil loss equation to guide conservation farm planning. 7th Int. Congress of Soil Science. Wisconsin, Madison, 418-425

Wischmeier, W.H.; Smith, D.D. 1978: Predicting rainfall erosion losses from cropland east of the Rocky Mountains. US Dept. of Agric., Handbook 537

Accepted March 24, 1987.

Hydrological Sciences – Journal – des Sciences Hydrologiques, 32, 3, 9/1987

Macroscale analysis of upland erosion

PIERRE Y. JULIEN
Department of Civil Engineering, Colorado State University, Fort Collins, Colorado 80523, USA
MARCEL FRENETTE
Department of Civil Engineering, Laval University, Quebec, Canada G1K 7P4

ABSTRACT Scale effects in computing sheet and rill erosion losses from large basins have been studied for grid sizes ranging from 0.03 to 4 km^2 over drainage areas up to 3000 km^2. As a result of the analysis conducted on the Chaudière basin (5830 km^2), the mean characteristics of the basin can be used to estimate the mean annual upland erosion losses after a correction factor for the influence of grid size is introduced into the calculation. The use of fine-meshed grids can be justified when information on the areal distribution of soil erosion is desired.

Analyse macroscopique de l'érosion superficielles
RESUME Une méthode de prédétermination d'érosion superficielle sur les grands bassins versants a été mise au point à partir d'une étude détaillée du bassin de la rivière Chaudière (A = 5830 km^2). Plusieurs grilles dont la taille varie de 0.03 à 4 km^2 ont été superposées au bassin pour calculer l'érosion pluviale sur des superficies atteignant 3000 km^2. Un facteur de correction fonction de la superficie drainée est introduit dans les équations. Il en résulte que l'érosion totale des grands bassins est estimée à partir des caractéristiques moyennes du bassin. L'utilisation de quadrillages devient justifiable pour définir la distribution spatiale de l'érosion superficielle.

NOTATION

A_o	drainage area of cells
A	drainage area
C	area-weighted value of the crop management factor
C_o	crop management factor
C_v	coefficient of variation for the sum of erosion losses from N independent units
e	estimate of the annual soil erosion loss per unit area
e_o	annual soil erosion loss per unit area
h_1	minimum elevation on an infinitesimal unit
h_2	maximum elevation on an infinitesimal unit
h_{max}	maximum elevation on one unit

Open for discussion until 1 March 1988.

h_{min}	minimum elevation on one unit
ℓ	size of a grid
N	number of units
Q_e	correction factor for the grid size
$\bar{Q}_e$	mean value of the correction factor
Q_e^*	relative correction factor
$\bar{Q}_{es}$	expected value of the correction factor for small grid sizes
$\bar{Q}_e^*$	mean value of the relative correction factor
Q_{e95}	confidence interval at 95 percent of the correction factor
S_o	slope on infinitesimal grids
S	slope estimator
β	exponent of slope in the soil loss equation
θ	angle between contour lines and the side of infinitesimal grid sizes
σ	standard deviation of log-transformed correction factors
σ_s	standard deviation of the sum of N independent log-transformed correction factors

INTRODUCTION

Rainfall-induced overland flow has the ability to detach and transport large amounts of sediment from upland areas. Sheet and rill erosion losses are complex processes related to landform geometry, surface slope, overland runoff length, rainfall intensity, soil infiltration rate, interception, storage, ground cover, canopy cover, evaporation, evapotranspiration, land use and conservation practices. The fundamentals of soil erosion and conservation are detailed in Hudson (1981), Zachar (1982), Jansson (1981), and Schwab *et al.* (1981). Methodologies to quantify erosion losses include the widely used Universal Soil-Loss Equation (USLE) which has been derived for data from small experimental plots.

Because soil-loss equations were developed for small upland areas (about one hectare), small basins are preferably discretized into small homogeneous areas to evaluate soil erosion losses from the drainage area. Square grids can be superimposed onto drainage basins with the mesh size conditioned by the applicability of the soil-loss equation. This method has been successfully applied to drainage areas up to 50 km^2 and soil erosion maps can be plotted with the aid of computers. The inherent limitations of this method are the data requirements which become prohibitive as the size of the drainage area increases beyond 100 km^2.

It seems interesting to examine whether larger grid sizes beyond the limit of applicability of soil-loss equations could provide sufficient accuracy in predicting upland erosion losses. The investigation reported here discusses the applicability of upland erosion equations to large drainage areas. Detailed information from the Chaudière basin in Canada is scrutinized to determine the scale effects associated with various grid sizes in the calculation of soil erosion losses. The development of simple methodologies to estimate on-site erosion losses over large basins with minimum data requirements also figures among the research objectives of foremost

importance.

FIELD SITE AND DATA SOURCES

The Chaudière basin shown in Fig.1 was selected for this study. This Appalachian basin covers an area of 5830 km^2 to St-Lambert-de-Lévis where the downstream gauging station is located.

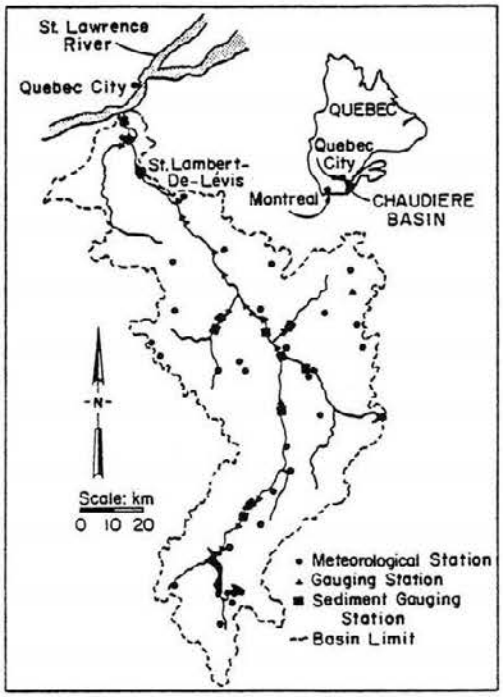

Fig. 1 Location of the Chaudière basin.

The basin geometry, vegetation and land use were accurately determined from topographical maps (1:50 000), land use and soil classification maps (1:200 000), forest maps (1:125 000), aerial photographs and Landsat imagery. Data from a network of 22 meteorological stations, 16 gauging stations and nine sediment gauging stations were available on a daily basis. Approximately 65% of the basin is still forested whereas 35% is used for agriculture and pasture lands. All the parameters related to soil erosion have been carefully documented (Julien, 1979, 1982; Frenette & Julien, 1986). Data analysis shows a relative uniformity of rainfall erosivity, soil erodibility and conservation practice on the drainage basin.

The annual soil erosion loss per unit area, e_o, in kt km^{-2} is a function of the slope, S_o, in m m^{-1} and the crop-management factor, C_o, of the USLE. For the Chaudière basin the following relationship is applicable for predicting rainfall erosion losses:

$$e_o = 226\ S_o^{\beta}\ C_o \qquad (1)$$

Detailed investigations (Julien, 1979; Julien & Frenette, 1986a) showed that the results obtained with Kilinc and Richardson's method ($\beta = 1.46$) are in close agreement with those of the USLE. Julien & Simons (1985) showed similarities between several sediment transport relationships for overland flow, including the USLE, and the values of the exponent, β, using different methods are given.

GRID SIZE ANALYSIS

When an infinitesimal square grid is superimposed onto the drainage basin, the slope and crop-management factors become uniform for each unit. The actual slope, S_o, in m m^{-1} on the unit is calculated from the minimum and maximum elevations h_1 and h_2, located on opposite corners of a square unit of size, ℓ, and angle, θ, sketched in Fig.2:

$$S_o = \frac{h_2 - h_1}{\ell(\cos\theta + \sin\theta)} \qquad (2)$$

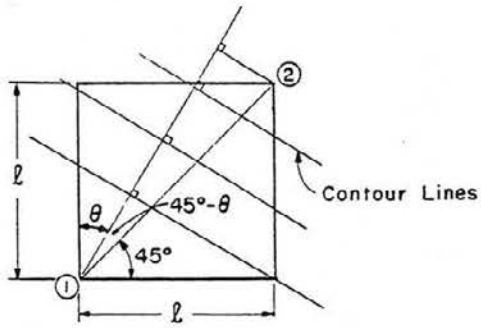

Fig. 2 Infinitesimal grid.

With increasing grid size, the slope varies within each unit and the extreme elevations are not found on opposite corners. The following estimate of slope, S, in m m^{-1} is defined as a function of the maximum elevation h_{max}, in m, the minimum elevation, h_{min}, in m, and the drainage area, A, in m^2:

$$S = \frac{h_{max} - h_{min}}{\sqrt{A}} \qquad (3)$$

Similarly, the area-weighted value of the crop management factor, C, is employed for large areas. Substituting S and C for S_o and C_o in equation (1) yields the soil loss estimator, e. The ratio, e/e_o, defines the correction factor, Q_e, which is to be used with the soil loss estimator, e, to determine the actual erosion losses, e_o.

For infinitesimal grids, equations (1), (2) and (3) yield the following relationship for Q_e as a function of θ and β, given that $C = C_o$, and $A = \ell^2$:

$$Q_e = (\cos\theta + \sin\theta)^{\beta} \qquad (4)$$

The gradual increase in Q_e with θ and β is illustrated in Fig.3(a). Obviously Q_e reduces to unity when $\beta = 0$, or when $\theta = 0$.

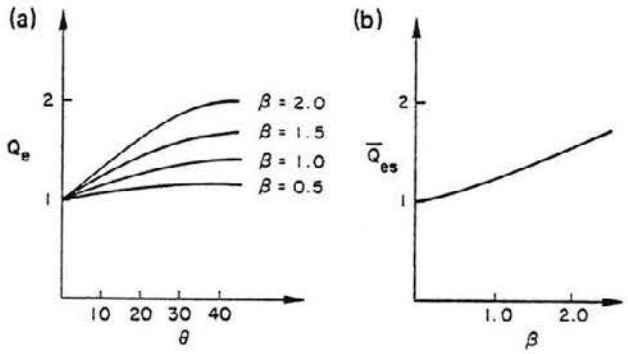

Fig. 3 (a) Variation of Q_e with θ and β for infinitesimal grids; (b) expected value of the correction factor, $\bar{Q}_{es}$, for infinitesimal grids.

When the angle, θ, is unknown, the following procedure has been developed. Considering the random variability of the angle θ, the analytical expression of the expected value of the correction factor, $\bar{Q}_{es}$, is:

$$\frac{1}{\bar{Q}_{es}} = \frac{4}{\pi} \int_0^{\pi/4} \frac{d\theta}{(\cos\theta + \sin\theta)^{\beta}} \qquad (5)$$

The results of the numerical integration of equation (5), plotted in Fig.3(b), indicate a gradual increase in $\bar{Q}_{es}$ with β.

For larger drainage areas, the following grid size analysis has been conducted. Square areas were randomly selected from the Chaudière basin as shown in Fig.4. The square areas were subdivided into matrices of 12 x 12 cells and classified in Table 1 into three sets according to the area of the cells. The surface area of cells in Data Sets A, B and C is respectively 2.8 ha, 25 ha and 4 km^2. In addition, Data Set D combines 4 km^2 cells into large square matrices with surface areas ranging from 4 to 3000 km^2 over the entire basin.

For each of the areas of the four Data Sets, a relative correction factor, Q_e^* (an asterisk is used to denote relative correction factors), has been defined as the ratio of soil erosion from the total area, A, over the sum of individual losses from each cell; this is schematized in Fig.5 for a small 2 x 2 matrix. The calculation procedure is repeated for larger matrices (3 x 3; 4 x 4; 6 x 6...) and details of the computerized data analysis are presented in Julien (1979).

Several thousand values of the relative correction factor were computed; Q_e^* depends on the number of cells, N, and the size A_o, of the cells. For given values of A_o and N, the first three moments

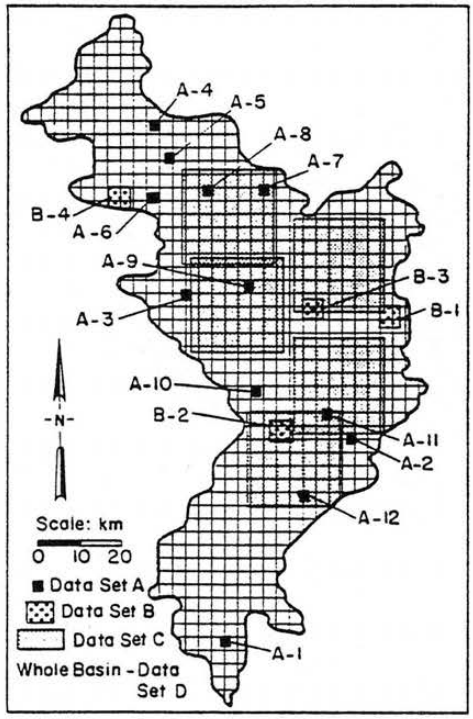

Fig. 4 Random selection of square areas for the grid size analysis.

Table 1 Scope of grid size analysis

Data Set	Cell area (km^2)	Matrix size	Matrix area (km^2)	Number of matrices
A	0.028	144 (12 x 12)	4	12
B	0.25	144 (12 x 12)	36	4
C	4.0	144 (12 x 12)	576	5
D	4.0	up to 1600	3000	N/A

N/A Not Applicable.

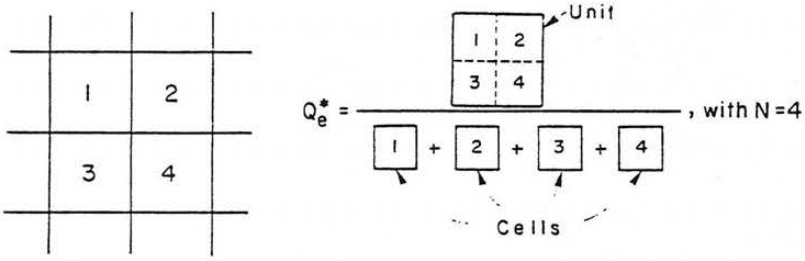

Fig. 5 Definition sketch for the relative correction factor, Q_e^*.

of the distribution of log Q_e^* give very low values of the skewness coefficient. Therefore, it was hypothesized and verified that Q_e^* is lognormally distributed; the results of the analysis for Data Set B are shown in Fig.6 as an example. The mean value and the confidence intervals at 95% are obtained from the following analysis of the first two moments.

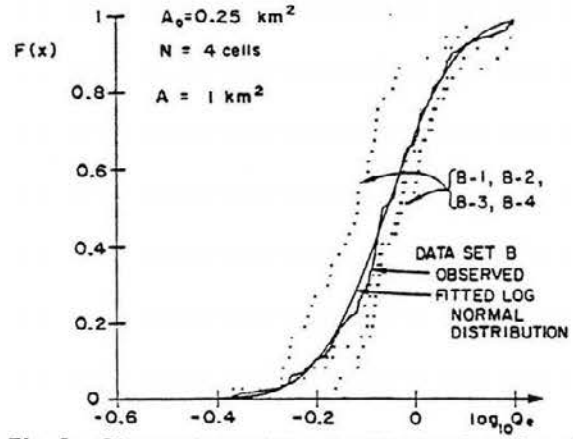

Fig. 6 Observed and fitted distribution function of Q_e for the Data Set B.

Mean value of the correction factor

The mean value of the log-transformed relative correction factor, $\bar{Q}_e^*$, shown in Fig.7 gradually decreases as N increases for all sets. The only exception to this general trend is that values of $\bar{Q}_e^*$ remain constant for N < 9 on the smallest drainage areas (Data Set A). Interestingly, this corresponds to the expected correction factor, $\bar{Q}_{es}$, discussed previously (Fig.3(b)). The value of $\bar{Q}_{es}$ = 1.13 has been obtained for drainage areas smaller than 0.125 km² on the Chaudière basin when the USLE was used for the calculation of soil erosion. For larger areas, regression analysis gives the following relative correction factor, $\bar{Q}_e^*$, as a function of $\bar{Q}_{es}$, A and A_o:

$$\log \bar{Q}_e^* = +0.0061 - 0.137 \log A + 0.083 \log A_o \quad (6)$$

A correction factor, $\bar{Q}_e$, is defined by the following change of variables:

$$\log \bar{Q}_e = \log \bar{Q}_e^* - 0.083 \log A_o - 0.129 + \log \bar{Q}_{es} \quad (7)$$

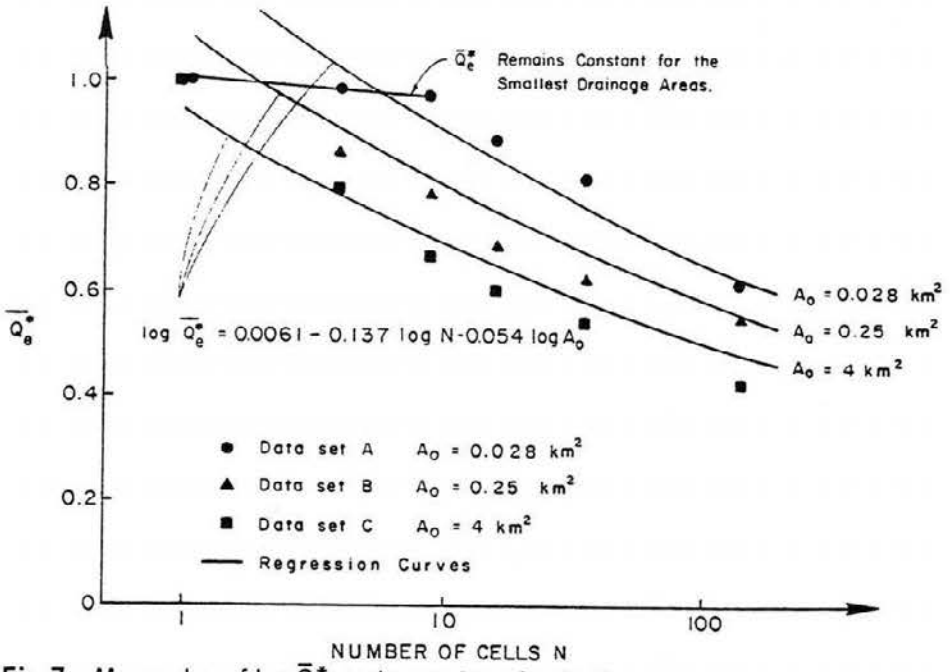

Fig. 7 Mean value of log $\bar{Q}_e^*$ *vs.* the number of cells, N.

Thus substituting equation (7) into equation (6), the correction factor, $\bar{Q}_e$, becomes independent of A_o with the following relationship:

$$\bar{Q}_e = 0.75\ \bar{Q}_{es} A^{-0.137} \qquad A > 0.125\ km^2 \tag{8}$$

As a result, with $\bar{Q}_{es} = 1.13$, a correction factor, $\bar{Q}_e$, which is a function of the drainage area only is obtained and all the data from Fig.6 collapse onto a single curve shown in Fig.8. Two governing laws for the correction factor, $\bar{Q}_e$, are identified. First, for $A < 0.125\ km^2$, the correction factor, $\bar{Q}_e$, remains constant ($\bar{Q}_e = \bar{Q}_{es}$) which indicates that the soil loss equation can be applied to these areas without bias. As the drainage area increases beyond the threshold value $A > 0.125\ km^2$, the correction factor, $\bar{Q}_e$, decreases gradually as shown in Fig.8.

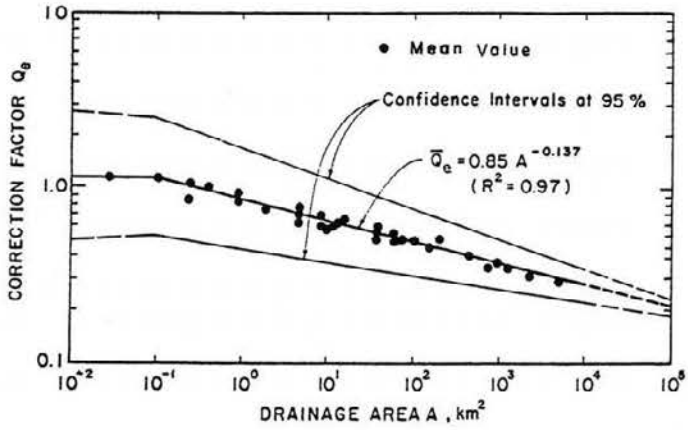

Fig. 8 Mean value and confidence intervals at 95% of the correction factor, Q_e, *vs.* drainage area, A.

Confidence intervals of the correction factor

The standard deviations, σ, of the log-transformed relative correction factor, Q_e^*, for Data Sets A, B and C are shown in Fig.9. All three Data Sets have similar shapes with an increase in σ for $N < 9$, a peak around $9 < N < 36$ and then a gradual decrease for $N > 36$. As a second interesting feature, the magnitude of the peak decreases as A_o increases. Regression analysis provides a quantitative relationship for the standard deviation, σ. After substituting A_o with A/N, the following regression relationship has been obtained.

$$\sigma = 0.00235 + \left[\frac{N - 1}{N}\right] (0.148 - 0.0226 \log A) \tag{9}$$

Note that under this form the standard deviation, σ, depends on the drainage area, A, and the number of cells, N. The standard deviation decreases to zero as N approaches unity. As N increases, the term in brackets reduces to unity and σ becomes solely a function of A.

The confidence intervals of the correction factor, Q_e, are

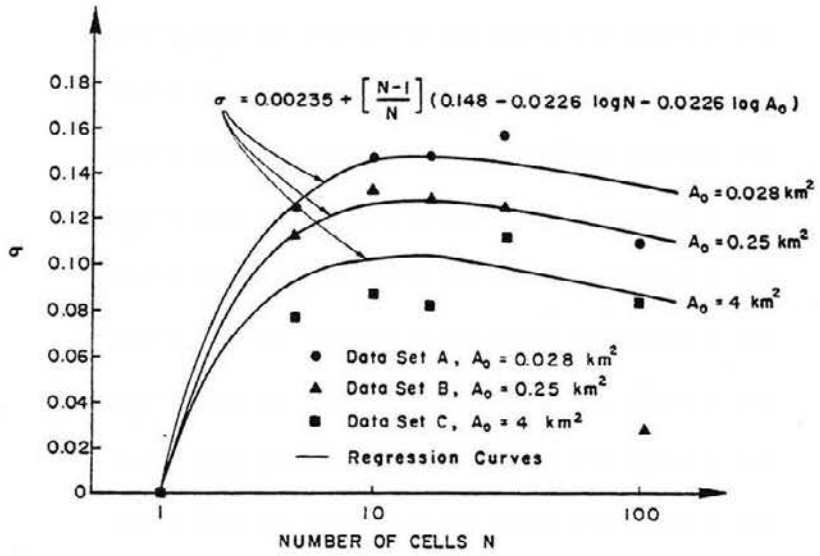

Fig. 9 Standard deviation, σ, of log $\bar{Q}_e^*$ *vs.* the number of cells, N.

obtained after combining equations (8) and (9) using the properties of lognormal distributions for Q_e. The confidence interval at 95% can be written:

$$Q_{e95} = \bar{Q}_e \times 10^{\pm 1.96\sigma} \qquad (10)$$

Agreement between equation (10) and the Data Set D is shown in Fig.10. Confidence intervals at 66% are given after replacing 1.96 in equation (10) with unity. As N becomes large, the expression for the confidence intervals reduces to a function of Q_e and A which has been plotted in Fig.8. These results can be used for design purposes as discussed below.

The foremost conclusion of this analysis is drawn from the

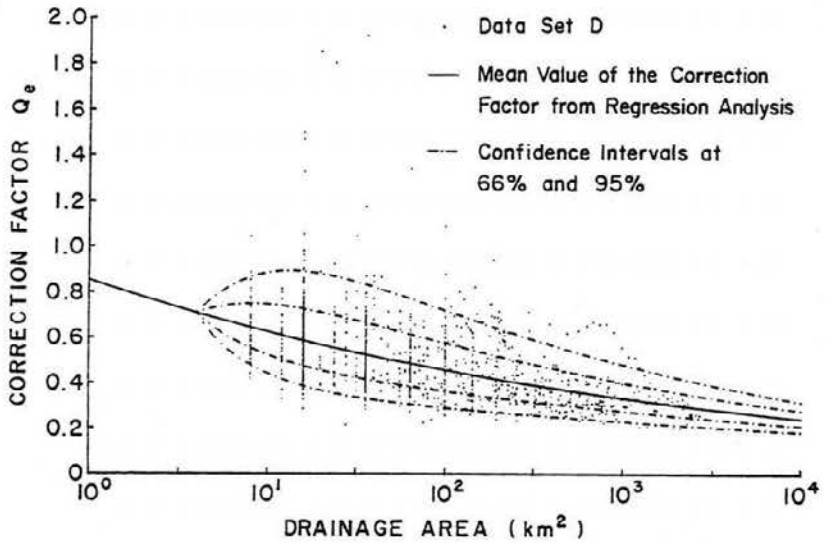

Fig. 10 Mean value and confidence intervals at 66% and 95% of the correction factor, Q_e, for Data Set D.

gradual decrease of the standard deviation with increase in drainage area. This property enables the development of a reasonably accurate method to estimate the total upland erosion losses for large drainage basins. Indeed the results shown in Fig.8 indicate that for drainage basins as large as 1000 km^2, the variability of the correction factor ranged from 0.17 to 0.49 (from equation (10)) with a mean value of 0.33 (from equation (8)). Therefore, a first estimate of the total annual upland erosion losses can be obtained from the soil loss estimator, e, and the average correction factor, $\bar{Q}_e$. Examples are given in Frenette & Julien (1980) and Julien & Frenette (1986b).

When the erosion loss from a large basin is calculated from the sum of N independent calculation units, the standard deviation of the sum, σ_s, is obtained after considering the lognormal distribution of the log-transformed correction factors, thus:

$$\sigma_s = \frac{\sigma}{\sqrt{N}} \tag{11}$$

As could be expected, σ_s decreases as the number of calculation units, N, increases. The coefficient of variation, C_v, of the sum is therefore given by:

$$C_v = 10^{\sigma_s} - 1 \tag{12}$$

After combining equations (9), (11), and (12), the coefficient of variation is illustrated in Fig.11 as a function of A and N. For example, when a drainage basin covering an area of 1000 km^2 is subdivided into N = 1000 units for the calculation of soil erosion, the coefficient of variation of the sum (Fig.11) is less than 1%, as compared to C_v = 6% when the same drainage area is subdivided into N = 10 units.

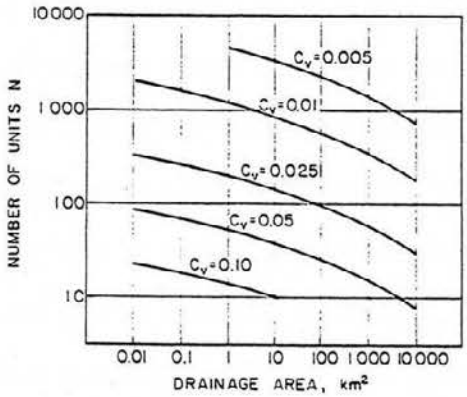

Fig. 11 Coefficient of variation of the sum of N independent upland erosion losses.

This conclusion remains valid when a large number of independent units from the same population is considered. The validity of the

method depends mostly on the applicability of the sediment transport relationship, equation (1). The method should preferably be used on morphologically homogeneous basins since the same soil loss equation is applied to the entire watershed.

CONCLUSION

A substantial analysis of the influence of grid size in calculating sheet and rill erosion losses from upland areas has been presented. Using grid sizes ranging from 0.03 to 3000 km^2 in the Chaudière basin, a correction factor, Q_e, which is a function of the grid size, has been defined and shown in Fig.8. The mean value of Q_e and the confidence intervals at 95% decrease gradually when $A > 0.125$ km^2. A simplified method has been developed to provide estimates of the total soil erosion losses from the mean characteristics of a large drainage basin. Fine-meshed grids are best used to define the spatial distribution of soil erosion, and for better accuracy in predicting the total upland erosion losses from large basins. Quantitative evaluation can be made from Fig.11 as a function of drainage area and number of units.

ACKNOWLEDGEMENTS This study has been carried out at Laval University, Canada. The support from the Civil Engineering Department and the CTI at Laval University for conducting computerized research is gratefully acknowledged.

REFERENCES

Frenette, M. & Julien, P.Y. (1980) Méthode simplifiée de prédiction d'érosion de bassin versant et d'apport solide en suspension dans les cours d'eau nordiques. *Proc. Second Hydrotechnical Conference* (CSCE-Quebec, Sherbrooke, Canada).

Frenette, M. & Julien, P.Y. (1986) LAVSED I - Un modèle pour prédire l'érosion des bassins et le transfert des sédiments fins dans les cours d'eau nordiques. *Can. J. Civ. Engng,* CSCE 13(2), 150-161.

Hudson, N. (1981) *Soil Conservation.* Cornell Univ., Ithaca, New York, USA.

Jansson, M. (1981) Land erosion by water in different climates. *UNGI Report 57, Uppsala Univ.*

Julien, P. (1979) Erosion de bassin et apport solide en suspension dans les cours d'eau nordiques. MS Thesis, Laval Univ., Québec, Canada.

Julien, P. (1982) Prédiction d'apport solide pluvial et nival dans les cours d'eau nordiques à partir du ruissellement superficiel. PhD Dissertation, Laval Univ., Québec, Canada.

Julien, P.Y. & Frenette, M. (1986a) LAVSEDII - A model for predicting soil erosion and washload in streams. *Can. J. Civ. Engng,* CSCE 13(2), 162-170.

Julien, P.Y. & Frenette, M. (1986b) Scale effects in predicting soil erosion. In: *Drainage Basin Sediment Delivery* (Proc.

Albuquerque Symp., August 1986), 253-259. IAHS Publ.no.159.

Julien, P.Y. & Simons, D.B. (1985) Sediment transport capacity of overland flow. *Trans Am. Soc. Agric. Engrs* 28(3), 755-762.

Kilinc, M. & Richardson, E.V. (1973) Mechanics of Soil Erosion from Overland Flow Generated by Simulated Rainfall. *Hydrol. Pap. 63, Colorado State University, Fort Collins, Colorado.*

Schwab, G.O., Frevert, R.K., Edminster, T.W. & Barnes, K.K. (1981) *Soil and Water Conservation Engineering.* Wiley, Chichester, UK.

Zachar, D. (1982) *Soil Erosion.* Developments in Soil Science 10, Elsevier.

Received 1 October 1986; accepted 25 February 1987.

Hydrological Sciences - Journal - des Sciences Hydrologiques, 36, 6, 12/1991

Spatially varied soil erosion under different climates

PIERRE Y. JULIEN

Engineering Research Center, Colorado State University, Foothills Campus, Fort Collins, Colorado 80523, USA

MARTA GONZALEZ DEL TANAGO

Laboratorio de Hidraulica e Hidrologia, E.T.S. de Ingenieros de Montes, Universidad Politecnica de Madrid, 28040 Madrid, Spain

Abstract The spatial variability of the factors of the universal soil loss equation is examined on the mediterranean basin of Conca de Tremp covering 43.1 km^2 in Spain. The evaluation of the rainfall erosivity R and the soil erodibility K is relatively straightforward and spatially-averaged values of these parameters can be applied to the entire basin. Conversely, the spatial variability of annual soil erosion losses on large basins depends primarily on the factors L, S, and C describing topographic, vegetation and land use parameters. A grid size analysis of soil erosion losses from the Conca de Tremp basin under mediterranean climatic conditions in Spain shows excellent agreement with the earlier results on the Chaudière basin in Canada. It is concluded for both basins that unbiassed estimates of soil erosion losses are obtained for grid sizes less than about 0.125 km^2. The analysis of the Conca de Tremp basin validates the use of the grid size factor proposed by Julien & Frenette (1987). It is also found that the grid size factor primarily depends on the average slope gradient which decreases with increasing grid size or drainage area. On the other hand, the grid size factor does not depend on the spatial variability of the factors R, K, L and C.

Variabilité spatiale de l'erosion des sols sous différents climats

Résumé Les variations spatiales des facteurs de l'équation universelle de pertes de sol est examinée sur un bassin méditerranéen en Espagne. Sur le bassin de la Conca de Tremp, couvrant 43.1 km^2, on démontre que la variation spatiale des paramètres d'agressivité des pluies R et d'érosivité des sols K justifie l'utilisation de valeurs moyennes sur les bassins versants. Par contre, la distribution spatiale des pertes de sol annuelles dépend essentiellement du relief, de la végétation et de l'utilisation des sols. Ainsi, les parametres L, S et C doivent être évalués soigneusement bien que les méthodes actuelles soient plutôt subjectives. Une analyse de l'influence de la dimension des mailles sur les calculs d'érosion superficielle du bassin de la Conca de Tremp en climat

méditerranéen, en Espagne, corrobore les résultats antérieurs obtenus sur le bassin de la rivière de la Chaudière, Canada. L'analyse des deux bassins démontre que les calculs non-biasés de de pertes de sol sont obtenus pour des mailles de taille inferieure à environ 0.125 km^2. L'analyse du bassin de la Conca de Tremp confirme la validité du facteur de maillage de Julien & Frenette (1987). Ce facteur de maillage dépend principalement de la réduction de pente moyenne des bassins en fonction de la superficie draînée. Par contre, le facteur de maillage ne dépend pas de la distribution spatiale des facteurs R, K, L et C.

INTRODUCTION

The extent of erosion, specific degradation and sediment yield from drainage basins relates to a complex interaction between topography, geology, climate, soil vegetation, land use and manmade developments. Sheet and rill erosion induced by raindrop impact and surface runoff constitute major components of erosion losses and sediment yield from large basins. The well-known universal soil loss equation (USLE) revised by Wischmeier & Smith (1978) computes long term average soil losses from surface runoff. Eventually, the USLE is intended to be replaced by the revised USLE (Renard & Simanton, 1990), or the water erosion prediction project (WEPP) (Lane *et al.*, 1988; Lane & Nearing, 1989), in an attempt to incorporate recent advances in surface hydrology, soil erosion and computer technology. The USLE proposed by Wischmeier & Smith (1978) remains widely used on small areas. The USLE is also likely to remain the simplest method available to undertake soil erosion studies on large basins. Extensive use at a larger scale has been reported by Williams & Berndt (1972), Boyce (1975), Renfro (1975), Frenette & Julien (1986) and Lee & Camacho (1986). Applications to large areas involve lumping of several parameters describing vegetation, soil types and topography. Discretization of drainage basins under a small grid usually satisfies the conditions of homogeneity over a grid area. On the other hand, it introduces additional complexities in the calculation of slope and runoff length, and the approach requires large data bases not commonly available.

An extensive grid size analysis on the Chaudière Basin in Canada by Julien & Frenette (1987) showed that grid sizes up to 0.125 km^2 can be applied to large basins without introducing biassed estimates of soil erosion losses when compared with smaller grid sizes. For larger grid sizes, they defined a correction factor which is essentially a function of the grid size area for the calculation of erosion losses from large basins. The following two limitations deserve further consideration: (a) since the analysis was carried out on a single basin in Canada, are the results applicable under different climatic conditions? and (b) because only two parameters, namely slope S and vegetation C were considered, should the spatial variability of the other parameters R, K and L be considered in further investigations?

This study has been undertaken in an effort to answer those two questions. The objective is to provide additional insight into the effects of spatial variability of the governing soil erosion parameters for the calculation

annual soil erosion losses under mediterranean climatic conditions. The fects of the spatial variability of the factors of the USLE on the calculation of annual soil erosion losses are critically reviewed through applications of the SLE in the Conca de Tremp area in Spain. A grid size analysis is also resented to either validate or modify the grid size factor proposed by Julien & Frenette (1987).

ESCRIPTION OF THE STUDY AREA

The Conca de Tremp area shown in Fig. 1 is located in the Lerida province, the northeast of Spain. The total area, covering 43.1 km^2 is subdivided into our sub-basins corresponding to the Arroyo de la Columera (14.2 km^2), the Arroyo del Chuli (2.3 km^2), the Barranco de Francoli (19.6 km^2), and the Barrancos de las Moreras y del Molino (6 km^2). These sub-basins are ributaries of the Conques River flowing westerly into the Noguera Pallaresa River, in the pre-Pyrennean area of the Ebro basin.

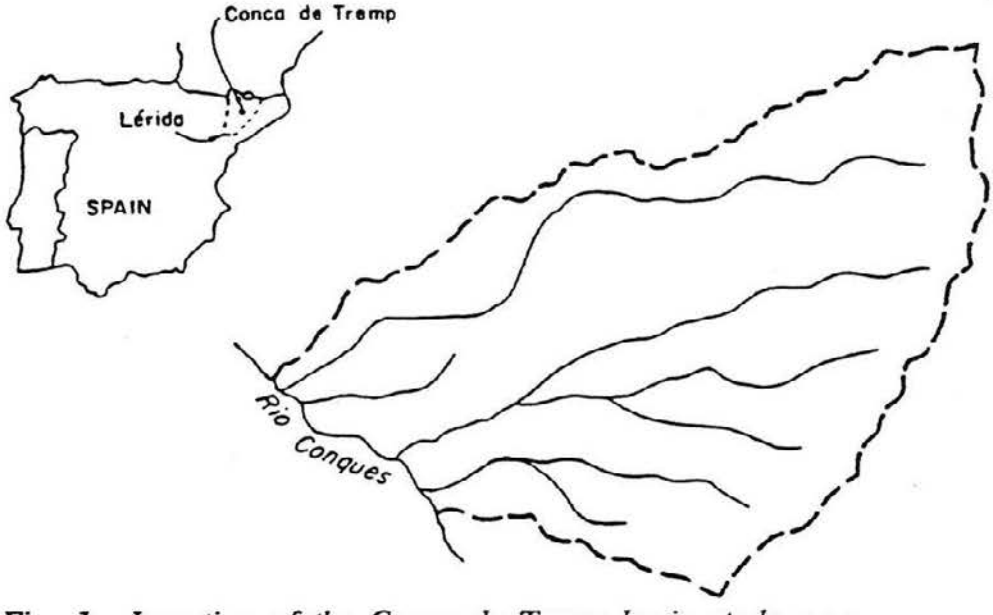

Fig. 1 Location of the Conca de Tremp basin study area.

The highest elevations in this rugged area reach 1460 m a.m.s.l. while the lowest elevations of the sub-basins vary from 530 to 550 m a.m.s.l. with a maximum total relief of 937 m. Detailed information for this study area is available in Redondo (1988). Typical mediterranean climatic conditions prevail in the area, with intense storms at the end of spring and beginning of autumn and dry spells in January–February and early summer. The mean annual precipitation is 690 mm and the mean annual temperature is 12.5°C.

The geology is rather complex, being affected by the orogenic and sedimentation processes in the pre-Pyrennean area. Previous studies (Steering Committee AUW, 1988) recognized four functional soil types corresponding to: piedmonts and conglomerates; colluvial sediments; sandstone and lime-

stone areas; and alluvial sediments. Those soil types are closely related to the vegetation found in the area. The region has been intensively farmed for centuries and only the steepest areas remain forested. Cereals, such as wheat and barley, and almond trees are most common, alternating with vegetables and olive trees in the productive and warmer locations. Natural vegetation constitutes part of the typical mediterranean forest, with several species of oaks (*Quercus faginea, Q. ilex* and *Q. coccifera*) and patches of small mediterranean bushes around and between pine forests (*Pinus sylvestris, P. nigra*).

As a consequence of climate, vegetation and soil conditions, the area shows good examples of all types of erosion, including sheet and rill erosion, frequent landslides and numerous gullies. Detailed information on the Conca de Tremp is available in Redondo (1988) and in Gonzalez del Tanago & Redondo (1989). This mediterranean basin is strikingly different from the Chaudière basin documented by Julien (1979) and Frenette & Julien (1986). The Chaudière basin covering 5830 km^2 in Canada is under a continental humid climate with severe winters, precambrian geology and relatively sparse and recent agriculture. Approximately two-thirds of the basin is covered with dense coniferous and deciduous forests.

EVALUATION OF THE PARAMETERS

The Conca de Tremp basin has been discretized using a square grid of 250 m side oriented NS–EW. Each square element (pixel) covers 6.25 ha resulting in 701 elements for the entire area. Soil erosion losses from each pixel are calculated from the well-known universal soil loss equation, $A = R\,K\,L\,S\,C\,P$.

The rainfall erosivity factor R of the USLE is evaluated using the regression equation developed for the mediterranean area by the Spanish Forest Service (ICONA, 1981) as follows:

$$R = 2.37\,P_{d2} + 0.51\,P_{max} - 57.4 \qquad (1)$$

where R is the erosivity index of the USLE; P_{d2} is the maximum daily precipitation in mm with a period of return of two years; and P_{max} is the average maximum monthly precipitation in mm. Taking into consideration the elevation differences within the study area, the hypsometric method is applied to obtain spatially varied values of the rainfall erosivity factor R which depend on altitude and precipitation, as recommended for small and medium size basins by Shaw (1983).

The soil erodibility factor K of the USLE is evaluated according to soil texture classification using the values from Stewart *et al.* (1975) considering that the organic matter content is less than 4%.

The topographic factors L and S are difficult to evaluate on large areas. They are commonly analysed together and referred to as the joint factor LS. The detailed results of applying the method of Williams & Berndt (1976) and comparisons with field data have been presented by Gonzalez del Tanago & Redondo (1989). Two methods of evaluating the joint factor LS are considered here: (a) average values for each sub-basin; and (b) values calculate

for each grid cell. The first method is based on the contour-extreme-point technique to evaluate the average basin runoff length while the contour-line method estimates the average basin relief. In the second method, the runoff lengths are evaluated from the drainage density method proposed by Horton (1945) and the grid slope gradients are calculated from the grid slope method.

The cropping management factor C is also somewhat cumbersome to evaluate on large areas. Vegetation and land use maps are used to define five different cover types: agriculture, coniferous trees, deciduous trees, range lands and unproductive (urban areas and rock outcrops). Taking into account the values presented by Wischmeier & Smith (1978) for range and idle lands, C values of 0.7 for agriculture and 0.15 for open forest and range land are considered as representative of the study area.

No particular soil conservation practices are observed at the present time, and the conservation practice factor P equals unity. Some decades ago, many "bancales" and terraces were constructed, but field mechanization forced the farmers to remove them in order to improve motor tillage on small and mostly steep field properties.

SPATIAL VARIABILITY OF THE PARAMETERS

A rainfall erosivity map for the Conca de Tremp basin is presented in Fig. 2. The values of R reported in Fig. 2 correspond to average conditions for mediterranean countries as reported by Masson (1971) and ICONA (1981). The spatial variability of the factor R is not significant and average values for

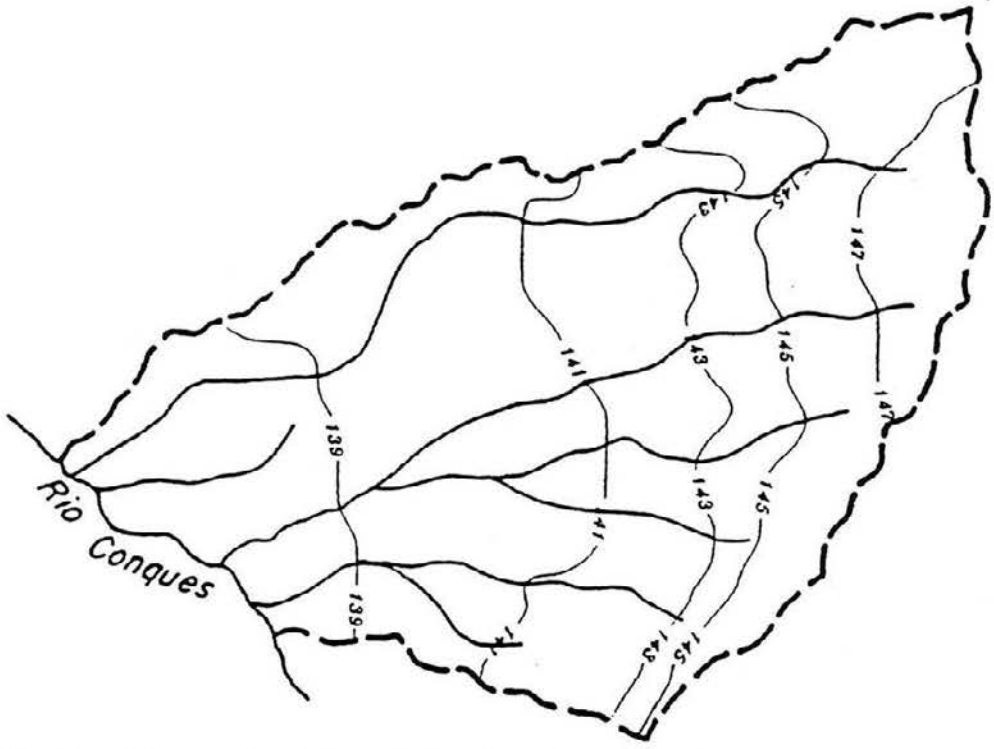

Fig. 2 Map of the factor R for the Conca de Tremp basin.

the entire basin can be assumed. Similar results for the soil erodibility factor K are shown in Fig. 3, where the spatial distribution of this factor is once again relatively uniform. Both the rainfall erosivity and the soil erodibility factors are relatively constant at a regional scale because similar climatic and geological conditions prevail over many large areas. For instance, it is well known from the iso-erodent map (Wischmeier & Smith, 1978) that the factor R varies very gradually over the United States east of the Rocky Mountains. Similarly, soil erodibility is closely related to the texture and soil formation processes (Romkens, 1985), which in turn depend on geological and climatic conditions. The methodologies to evaluate the R and K factors proposed by Wischmeier & Smith (1978) and later revised by Romkens (1985) and Weltz *et al.* (1987) are relatively easy to apply and sufficiently accurate provided enough raingauges and soil samples are available for the study area.

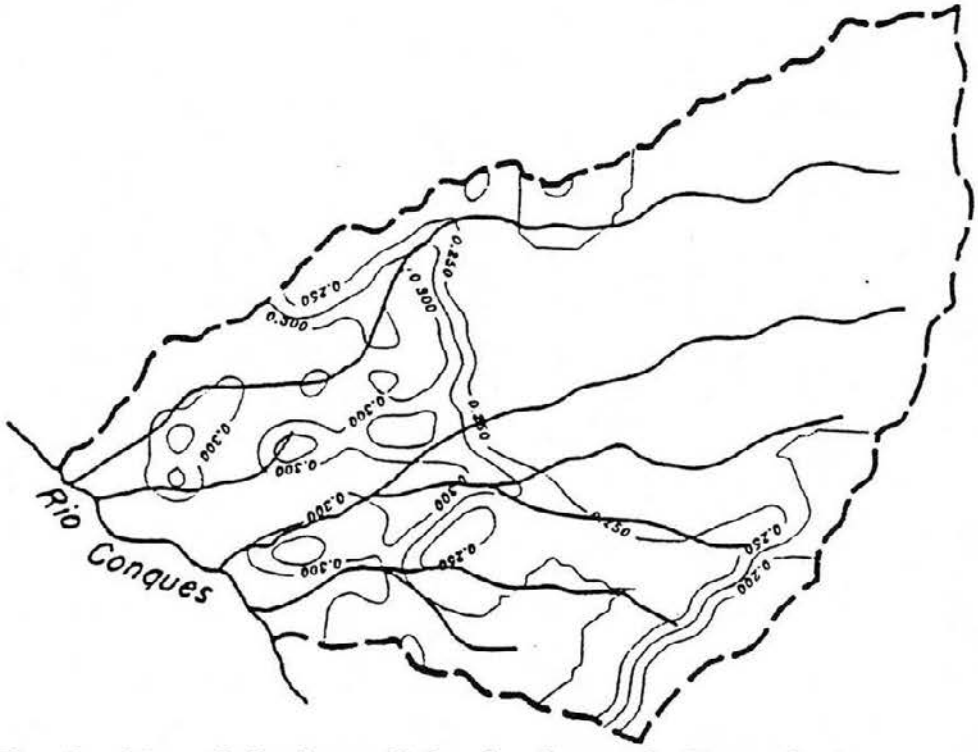

Fig. 3 Map of the factor K for the Conca de Tremp basin.

On the contrary, irregular relief and slope gradient cause significant spatial variability in the topographic factors L and S. The topographic factors are among the most difficult to evaluate outside plot size fields. Williams & Berndt (1976) proposed methods to estimate average values of the slope gradient and slope length of a basin. The slope steepness factor S of the USLE has been recently revised by McCool *et al.* (1987), who proposed a linear relationship between soil losses and slope gradient. Average values of slope gradient and runoff length for sub-basins and grid cells are required and accurate evaluations deserve further investigations. The use of geographic information systems may warrant further advances in this field, and telescopic grid size investigations similar to Julien & Frenette (1987) may also provide

biassed soil erosion estimates at various grid sizes.

Accurate evaluations of average runoff lengths used for the runoff ngth factor L of the USLE remain very difficult and time-consuming, esenting one of the most subjective factors of the USLE (Simanton *et al.*, ...). Although the influence of the runoff length on rill formation and soil sses from rill-susceptible lands has been clearly recognized (Meyer *et al.*, ; Foster *et al.*, 1977), the methodologies for its quantitative evaluation ve not been significantly improved.

Gonzalez del Tanago & Redondo (1989) applied three methods to ulate the runoff length and three other methods to calculate the slope adient on the Conca de Tremp area. They found that none of the three ff length methods gives significant correlation when compared with field urements. Similarly, the three slope gradient methods provide calculated pe values generally smaller than the field measurements, particularly in areas. They concluded that the estimation of the L and S factors on ns with irregular topography remains tedious and imprecise. The uncer- es in evaluating the combined LS factor of the USLE are well illustrated sub-basin scale in Fig. 4 compared to the grid scale in Fig. 5. It is cluded that grid size evaluation of the topographic parameters is essential scribe the spatial variability of surface erosion.

Finally, the evaluation of the factor C shown in Fig. 6 also remains very ective for non-agricultural fields. Dissmeyer & Foster (1984) proposed a d to evaluate the C factor for forested lands and, more recently, Weltz (1987) revised previous procedures, considering conditions of vegetation root biomass and soil roughness. Those methods tend to become elming when applied to large basins.

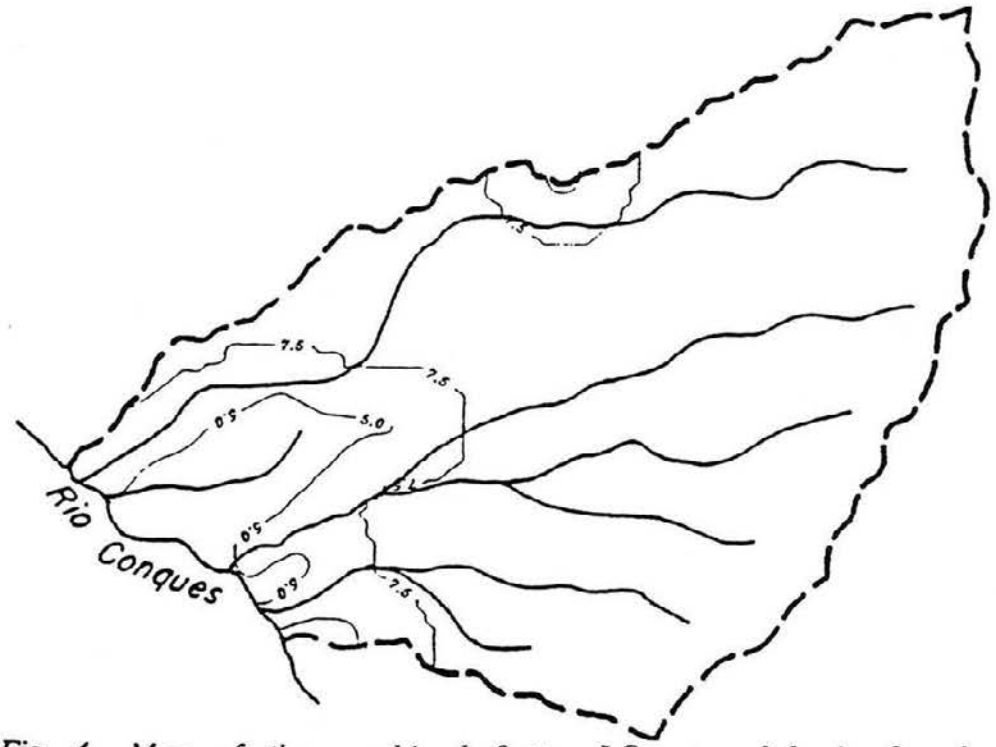

Fig. 4 Map of the combined factor LS per sub-basin for the Conca de Tremp basin.

159

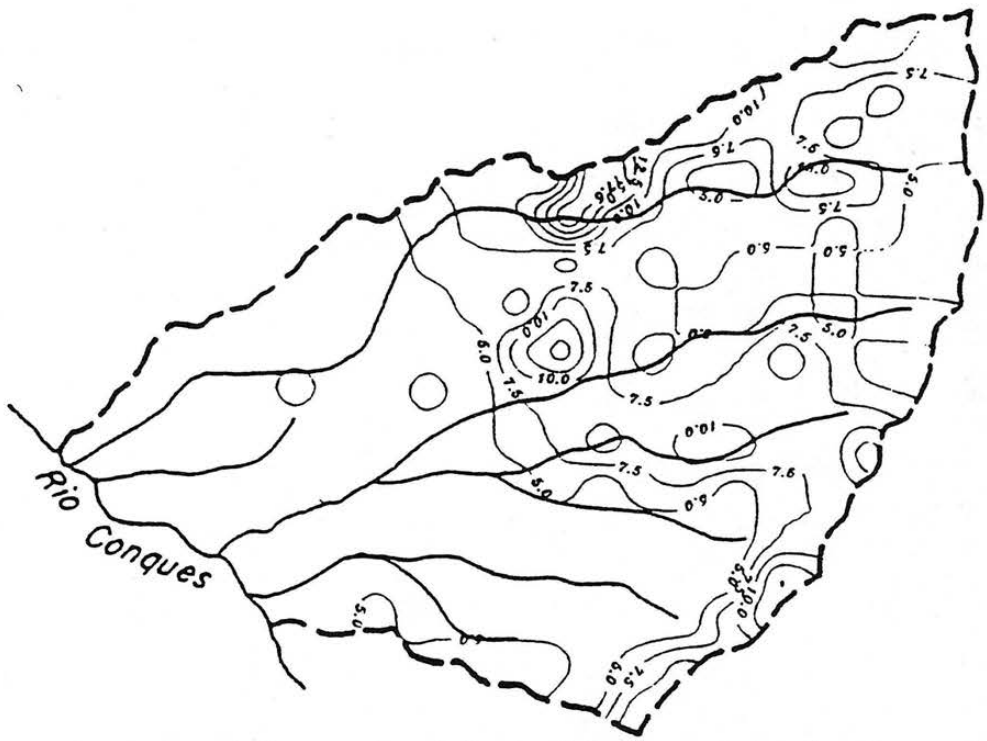

Fig. 5 Map of the combined factor LS per grid for the Conca de Tremp basin.

Average annual soil erosion losses are calculated from the topographic factors plotted in Fig. 5 and the final soil erosion map is presented in Fig. 7. It is found that the topographic factors L and S and the vegetation and land use factor C determine most of the spatial variability in soil erosion losses from large basins. Comparatively, the rainfall erodibility and the soil erosivity parameters remain relatively uniform at the basin scale. These findings corroborate those of Julien (1979) on the Chaudière basin in Canada under different climatic conditions. The spatial variability of the factors S and C requires particular attention in investigations of soil erosion mapping.

GRID SIZE EFFECTS

The influence of the grid size on the computation of soil erosion rates in the Conca de Tremp basin is considered. The total drainage area has been discretized into 701 square elements each covering a surface area A_0 = 0.0625 km^2. The USLE is applied to successive square matrices formed by 1 × 1 element, (0.0625 km^2), 2 × 2 elements (0.25 km^2), 3 × 3 elements (0.56 km^2), up to 39 × 39 elements. This procedure proposed by Julien & Frenette (1987) leads to the definition of a relative grid size factor Q_e^* calculated for each matrix from the following expression:

$$Q_e^* = n\, S \left[\sum_{i=1}^{n} \frac{R_i}{n} \sum_{i=1}^{n} \frac{K_i}{n} \sum_{i=1}^{n} \frac{L_i}{n} \sum_{i=1}^{n} \frac{C_i}{n} \sum_{i=1}^{n} \frac{P_i}{n} \right] / \sum_{i=1}^{n} R_i K_i L_i S_i C_i P_i \qquad (2)$$

where n is the number of elements within each matrix of area $A = n A_o$, and R_i, K_i, L_i, S_i, C_i and P_i are the values of the USLE factors for each element i.

Similarities between the results of the Conca de Tremp basin and those

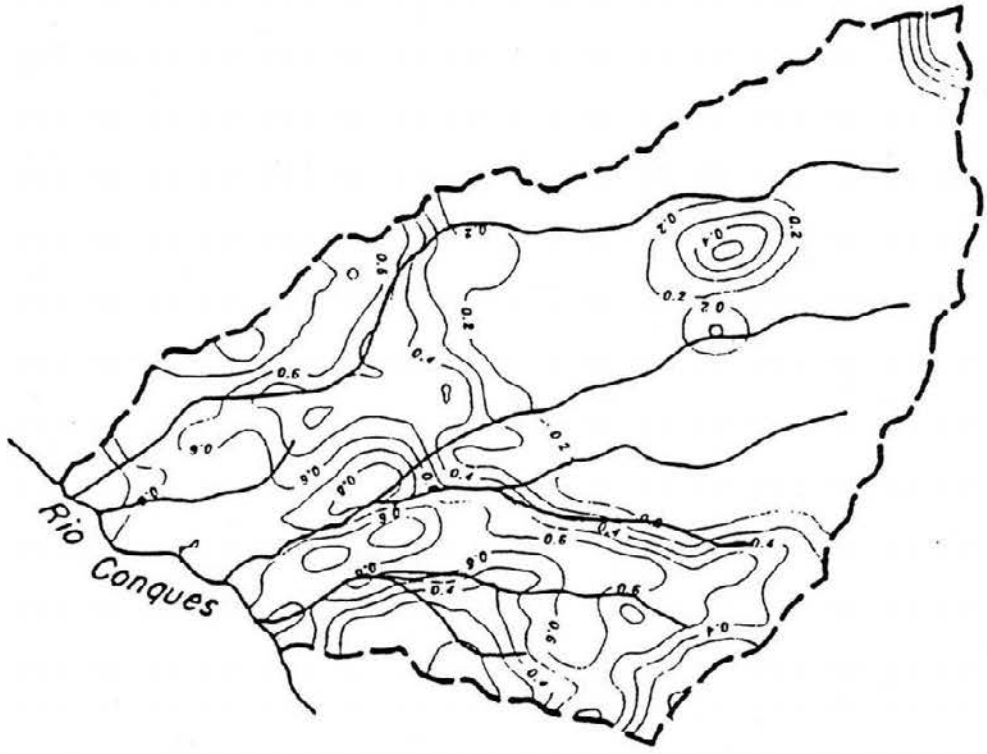

Fig. 6 Map of the factor C for the Conca de Tremp basin.

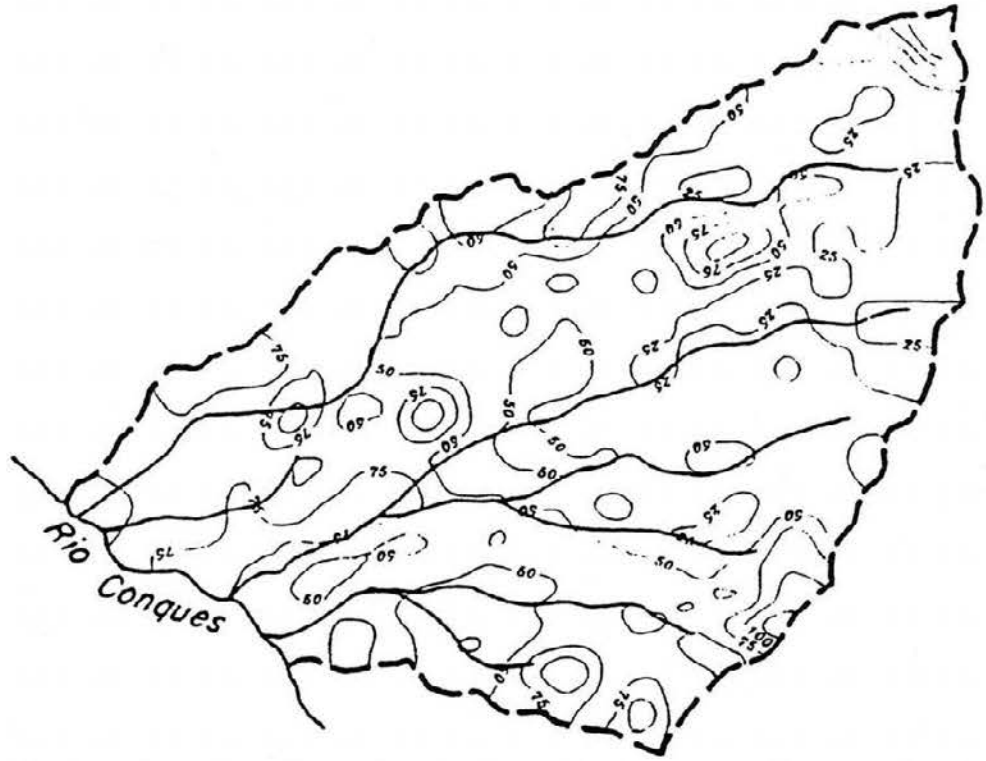

Fig. 7 Annual soil erosion losses E in tons per hectare for the Conca de Tremp basin.

161

from the Chaudière basin are shown in Fig. 8 where the data from both basins are superposed. The relative grid size factor Q_e^* defined in equation (2) is corrected for the bias induced at infinitesimal grids according to the procedure detailed in Julien & Frenette (1987). Accordingly, the grid size factor Q_e is calculated from the relative grid size factor Q_e^* as follows: $Q_e = 1.13 Q_e^*$. At a given grid size area, the analysis of the fluctuating values of Q_e shows that the average value $\overline{Q}_e$ is essentially constant for grid sizes smaller than 0.4 km^2. This means that slight differences exist between calculations at grid sizes of 1 × 1 (0.0625 km^2), 2 × 2 (0.25 km^2) or 3 × 3 (0.56 km^2). At larger grid sizes, the average value of the grid size factor gradually decreases and the results are almost identical to those of the Chaudière basin. The dispersion around the mean also varies with the grid size as shown in Fig. 8. Maximum dispersion is identified for grid sizes between 0.2 and 10 km^2. Overall, the data points of the Conca de Tremp basin are mostly confined within the confidence intervals at 95% defined from the Chaudière data set.

It is concluded from these observations that the grid size factor proposed by Julien & Frenette (1987) is equally applicable to both the Chaudière and Conca de Tremp basins under different climatic, geological and land use conditions. The soil loss equation can be applied to areas up to 0.125 km^2 without introducing bias. The grid size factor from Fig. 8 should be considered when applying soil loss equations to larger grid sizes or drainage areas.

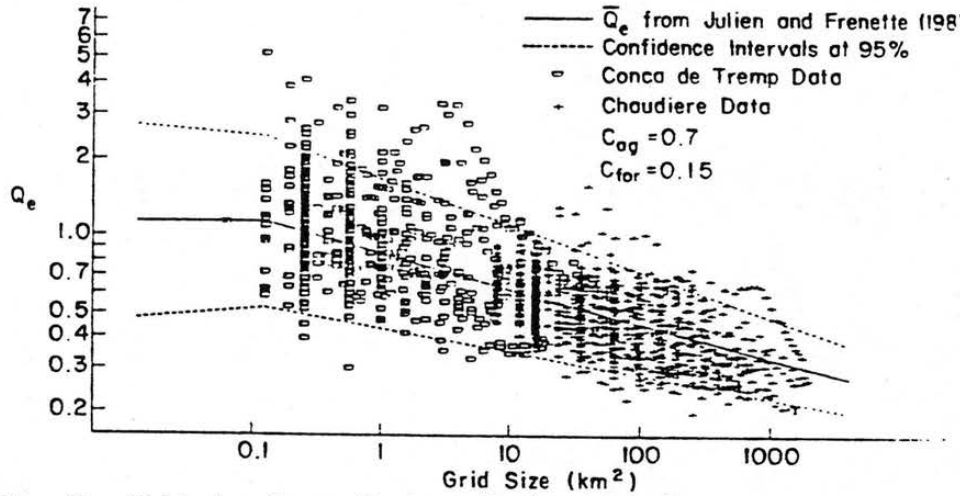

Fig. 8 Grid size factor Q_e vs grid size or drainage area.

PARTIAL CORRECTION FACTORS

The following investigation was carried out in order to determine which of the different factors of the USLE primarily affects the relative grid size factor Q_e^*. Partial correction factors are defined with reference to the spatially varied factors of the USLE. For instance, the partial correction factor Q^*_{RKL} describes the effect of the spatial variability of the factors R, K and L. The

partial correction factor Q^*_{RKL} describes the ratio between the product of spatially-averaged values of the individual factors R, K and L, divided by the sum of products of R_i, K_i and L_i for each element of the grid:

$$Q^*_{RKL} = n \left[\Sigma_{i=1}^n \frac{R_i}{n} \Sigma_{i=1}^n \frac{K_i}{n} \Sigma_{i=1}^n \frac{L_i}{n} \right] / \Sigma_{i=1}^n R_i K_i L_i \qquad (3)$$

Similarly, the modified correction factor Q^*_{RKLC} describes spatial variability in the factors R, K, L and C, and finally the factor Q^*_s describes only the variability in the slope factor S:

$$Q^*_{RKLC} = n \left[\Sigma_{i=1}^n \frac{R_i}{n} \Sigma_{i=1}^n \frac{K_i}{n} \Sigma_{i=1}^n \frac{L_i}{n} \Sigma_{i=1}^n \frac{C_i}{n} \right] / \Sigma_{i=1}^n R_i K_i L_i C_i \qquad (4)$$

$$Q^*_s = \frac{n\, S}{\Sigma_{i=1}^n S_i} \qquad (5)$$

The partial correction factors Q^*_{RKL} and Q^*_{RKLC} in Figs 9 and 10 show very similar results in which both factors are nearly equal to unity regardless of the drainage area. It is interesting to note that, although R and K are relatively uniformly distributed, the parameters L and C are largely varied on the basin. The influence of the spatial variability of these four factors does not significantly contribute to the decrease in Q^*_e with drainage area. On the other hand, the analysis of the slope factor yields different results as shown in Fig. 11. A gradual decrease in the correction factor Q^*_s is found as the drainage area increases. The effect of the slope overshadows the influence of all other factors, resulting in the general trend for Q_e previously discussed.

This analysis demonstrates that the random variability in the factors R,

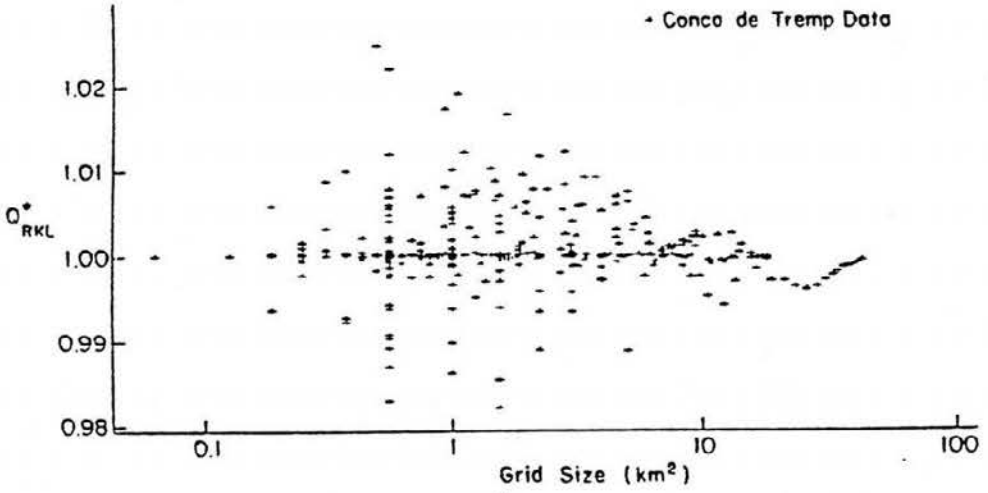

Fig. 9 Partial correction factor Q^*_{RKL} vs grid size or drainage area, Conca de Tremp basin.

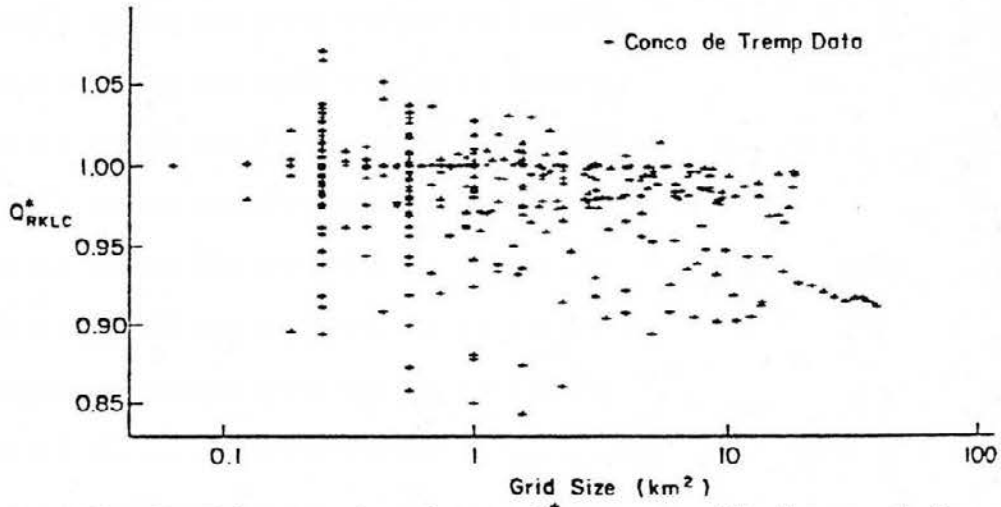

Fig. 10 Partial correction factor Q^*_{RKLC} vs grid size or drainage area, Conca de Tremp basin.

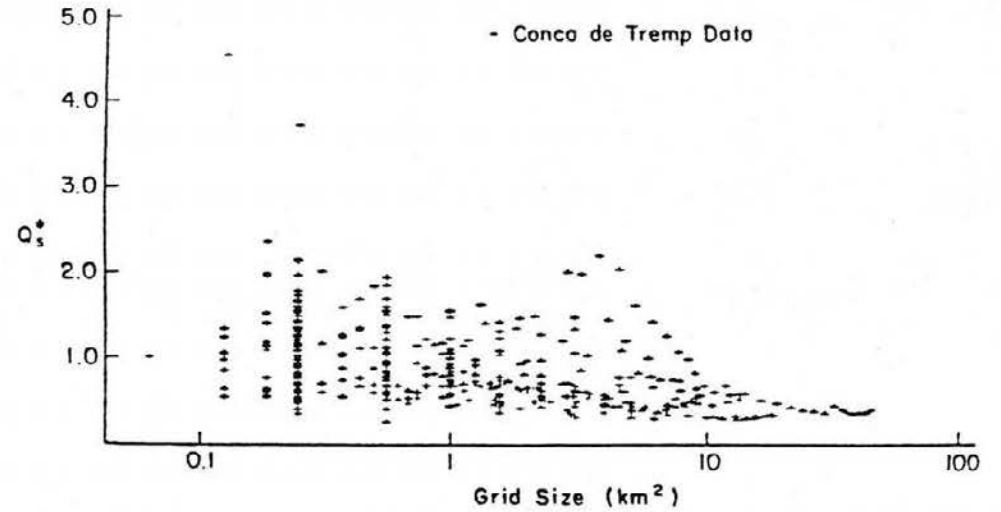

Fig. 11 Partial correction factor Q^*_s vs grid size or drainage area, Conca de Tremp basin.

K, *L* and *C* exerts little influence on the calculated erosion rates at all scales. This is however not the case for the slope factor which decreases with drainage area (Leopold & Maddock, 1953). It is therefore concluded that the decrease in slope with increasing drainage area is reflected in soil erosion calculations using square grids via the correction factor shown in Fig. 8.

SUMMARY AND CONCLUSIONS

The universal soil loss equation is applied to the Conca de Tremp basin in Spain under mediterranean climatic conditions. The investigation of the spatial variability of the parameters of the USLE supports the following conclusions:

(a) the results show relatively uniform distribution of the rainfall erosivity *R* and soil erodibility *K* over the entire area. These two factors remain fairly constant at a regional scale and can be accurately evaluated from

existing methods; and

(b) on the contrary, the spatial variability in topography, vegetation and land use conditions greatly contributes to the large spatial variability in soil erosion losses. The evaluation of the factors *L, S* and *C* remains imprecise and somewhat subjective, introducing potential sources of error when attempting to define the accurate soil erosion losses from each grid cell.

This grid size analysis of soil erosion from the Conca de Tremp basin in Spain demonstrates that previous results from the Chaudière basin in Canada can be applied under different climatic, geological, topographic, vegetative and land use conditions. This analysis corroborates the previous findings that the calculation of erosion losses does not depend on grid size at grid sizes smaller than about 0.125 km^2. At larger scales, the decrease in slope with increasing grid size or drainage area causes an underestimation of erosion rates at large grid sizes. Spatial variability in the other factors of the USLE such as rainfall erosivity, soil erodibility, runoff length, vegetation and land use does not significantly affect calculated erosion rates on large grid sizes. Therefore, the grid size factor proposed by Julien & Frenette (1987) can be used in calculating erosion losses on large basins from spatially-averaged values of each factor of the USLE.

Acknowledgements The authors wish to thank Dr Leo Eppink from Wageningen Agricultural University, The Netherlands, who organized the erosion project on the Conca de Tremp basin and provided assistance in gathering information from the area. Support from the Hydrologic Modelling Group (ARO/DAAL 03-86-K-0175) of the Center for Geosciences at Colorado State University for the computer and technical assistance necessary to the completion of this study is gratefully acknowledged.

REFERENCES

Boyce, R. C. (1975) Sediment routing with sediment delivery ratios. In: *Present and Prospective Technology for Predicting Sediment Yields and Sources.* USDA, ARS-S-40: 61-65.

Dissmeyer, G. E. & Foster, G. R. (1984) A guide for predicting sheet and rill erosion on forest land. USDA Technical Pub. R8-TP6.

Foster, G. R., Meyer, L. D. & Onstad, C. A. (1977) A runoff erosivity factor and variable slope length exponents for soil loss estimates. *Trans. Am. Soc. Agric. Engrs* 20(4), 683-687.

Frenette, M. & Julien, P. Y. (1986) LAVSED I: un modèle pour prédire l'érosion des bassins et le transfert des sédiments fins dans les cours d'eau nordiques. *Can. J. Civil Eng. CSCE* 13(2), 150-161.

Gonzalez del Tanago, M. & Redondo, J. (1989) Evaluation of the topographic factors L, S of the universal soil-loss equation in the "Conca de Tremp" (Spain). Proc. 9th Annual AGU Front Range Branch Hydrology Days, Colorado State University, edited by H. J. Morel-Seytoux & J. C. Loftis, 169-180.

Horton, R. E. (1945) Erosional development of streams and their drainage basins: hydrophysical approach to quantitative morphology. *Bull. Geol. Soc. Am.* 56, 275-350.

ICONA (1981) Mapa de Iso-R para la vertiente mediterranea. ICONA, Madrid (unpublished).

Julien, P. Y. (1979) Erosion de bassin et apport solide dans les cours d'eau nordiques. MSc thesis, Department of Civil Engineering, Laval Univ., Québec, Canada.

Julien, P. Y. & Frenette, M. (1987) Macroscale analysis of upland erosion. *Hydrol. Sci. J.* 32(3), 347-358.

Lane, L. J. & Nearing, M. A. (1989) USDA water erosion prediction project: hillslope profile model documentation, USDA-ARS National Soil Erosion Research Laboratory Report No.

2.
Lane, L. J., Schertz, E. E., Alberts, E. E., Laflen, J. M. & Lopes, V.L. (1988) The US national project to develop improved erosion prediction technology to replace the USLE. In: *Sediment Budgets,* Proc. Porto Allegre Symp., IAHS Publ. no. 174, 473-481.

Lee, M. T. & Camacho, R. (1986) Sediment source and yield assessment: Applications of the hydrologic model and geographic information system. *Proc. 3rd International Symp. on River Sedimentation,* Univ. of Missouri, Missouri, USA, 1213-1221.

Leopold, L. B. & Maddock, T. (1953) The hydraulic geometry of stream channels and some physiographic implications. *USGS Prof. Pap.* 252.

Masson, J. M. (1971) L'érosion des sols par l'eau en climat mediterranéen. Methodes experimentales pour l'étude des quantites de terres erodées a l'échelle du champ. PhD Thesis Ing. Univ. Sciences et Techniques du Languedoc.

McCool, D. K., Brown, L. C., Foster, G. R., Mutchler, C. K. & Meyer, L. D. (1987) Revised slope steepness factor for the universal soil loss equation. *Trans. Am. Soc. Agric. Engrs* 30(5), 1387-1396.

Meyer, L. D., Foster, G. R. & Romkens, M. J. M. (1975) Source of soil eroded by water from upland slopes. In: *Present and Prospective Technology for Predicting Sediment Yield and Sources,* ARS-S-40, 177-189.

Redondo, J. (1988) Hidrologia y factores de erosion potencial en la Conca de Tremp, Lerida. Graduate Thesis. ETSI Montes, Univ. Politecnica de Madrid, Spain.

Renard, K. G. & Simanton, J. R. (1990) Application of RUSLE to Rangelands. *Proc. Symp. on Watershed Planning and Analysis in Action,* ASCE, Durango, Colorado, USA, 164-173.

Renfro, G. W. (1975) Use of erosion equations and sediment-delivery ratios for predicting sediment yield. In: *Present and Prospective Technology for Predicting Sediment Yield and Sources,* ARS-S-40, 33-45.

Romkens, M. J. M. (1985) The soil erodibility factor: a perspective. In: *Soil Erosion and Conservation,* edited by S. A. El-Swaify, W. C. Moldenhauer & A. Lo, Soil Conservation Society of America, Ankeny, 445-461.

Shaw, E. M. (1983) *Hydrology in Practice.* Van Nostrand Reinhold, Wokingham, UK.

Simanton, J. R., Osborn, H. B. & Renard, K. G. (1980) Application of the USLE to southwestern rangelands. In: *Hydrology and Water Resources in Arizona and the Southwest,* Vol. 10, 213-220.

Steering Committee AUW (1988) Een op erosie inventerisatie in en substroomgeied in de Conca de Tremp, Spajne. Agricultural University, Wageningen, The Netherlands.

Stewart, B. A., Woolhiser, D. A., Wischmeier, W. H., Caro, J. H. & Freere, M. H. (1975) Control of water pollution from cropland. Vol. I, Report EPA-600. US Environmental Protection Agency, Washington DC, USA.

Weltz, M. A., Renard, K. G. & Simanton, J. R. (1987) Revised universal soil loss equation for western rangelands. In: *Strategies for Classification and Management of Native Vegetation for Food Production in Arid Zones.* USDA Forest Service, GTR RM-150, 104-111.

Williams, J. R. & Berndt, H. D. (1972) Sediment yield computed with universal equation. *J. Hydraul. Div. ASCE* 98 (HY12), 2087-2098.

Williams, J. R. & Berndt, H. D. (1976) Determining the universal soil loss equation's length-slope factor for watersheds. In: *Soil Erosion Predicting and Control.* Proc. National Conf. on Soil Erosion, Indiana, USA, 217-225.

Wischmeier, W. H. & Smith, D. D. (1978) Predicting rainfall erosion losses. A guide for conservation planning. USDA Agric. Handbook no. 537, Washington, DC, USA.

Received 17 December 1990; accepted 15 April 1991

LAVSED-I — Un modèle pour prédire l'érosion des bassins et le transfert de sédiments fins dans les cours d'eau nordiques

M. Frenette et P. Y. Julien[1]

Département de génie civil, Université Laval, Québec (Qué.), Canada G1K 7P4

Reçu le 5 novembre 1984

Révision acceptée le 14 novembre 1985

L'ordinateur est un outil de premier ordre pour prédire, au niveau d'un bassin versant, les pertes de sol associées à l'action érosive de l'eau et les charges sédimentaires en suspension subséquentes transférées aux cours d'eau. Le déroulement de cette étude a conduit au développement du modèle LAVSED-I (le modèle LAVal-I de prédiction SEDimentologique) lequel inclut quatre composantes: précipitation, caractéristiques du bassin, érosion/sédimentation et utilisation du territoire. Basé sur l'équation universelle de perte de sol de Wischmeier et Smith et l'équation de Kilinc et Richardson, le modèle peut accommoder une combinaison de diverses unités de taille et de forme de bassins divisés selon une grille spatiale variant de 0,03 à 3000 km^2. Le présent article décrit le développement opérationnel et l'application du modèle à l'échelle d'un prototype, soit le bassin de la rivière Chaudière (B.V. = 5830 km^2). Les résultats montrent la cartographie de l'érosion des bassins ainsi que la charge sédimentaire observée dans le cours d'eau.

Computer modeling techniques are used for predicting soil losses from overland flow and subsequent suspended sediment yield from large watersheds. The model LAVSED-I (LAVal SEDidentological model No. I) is based on the universal soil-loss equation of Wischmeier and Smith and the equation of Kilinc and Richardson. The model subdivides the watershed into square units varying in size from 0.3 to 3000 km^2 and the computational procedure is subdivided in four components: precipitation, physical characteristics of watersheds, erosion/sedimentation, and land use. This paper describes the operational development and the application of the model to a prototype-scale watershed. A map for the annual soil loss is presented for the Chaudière watershed (area = 5830 km^2). Results of mapping compared with the sediment yield observed are shown in the paper.

Can. J. Civ. Eng. 13, 150–161 (1986)

Introduction

Chaque bassin hydrographique est lié à une ou plusieurs activités qui gouvernent l'érosion des bassins et l'apport solide dans les cours d'eau. Ainsi, parvenir à estimer la dégradation d'un bassin et la rattacher aux activités humaines, c'est aussi parvenir à se donner des outils de prédiction et partant des outils de gestion. Tel est le but du présent article de présenter les grandes lignes d'une simulation mathématique réalisée à l'Université Laval visant à prédire l'érosion des bassins et l'apport solide dans les cours d'eau, en relation avec les activités du territoire.

Sur les bassins versants, on distingue généralement six types d'érosion: érosion en nappe (dite superficielle), érosion en rigoles, ravinement, érosion de lit et des berges des cours d'eau et glissements de terrain. De nombreuses recherches (Meyer 1971; Wischmeier 1959, 1973; Piest et Miller 1977) soulignent cependant, qu'au niveau des bassins soumis aux activités humaines (ex.: par le déboisement et l'agriculture) l'érosion superficielle constitue la majeure partie des sédiments transportés dans les cours d'eau.

Il existe actuellement plusieurs méthodes permettant de quantifier l'érosion superficielle à l'échelle de petites parcelles, parmi lesquelles on retrouve l'équation universelle de perte de sol (Wischmeier et Smith 1965) basée principalement sur l'intensité des pluies et l'équation de Kilinc et Richardson (1973) reliant l'érosion aux caractéristiques hydrauliques de ruissellement.

Les principales causes de l'érosion superficielle et la prédiction du taux d'érosion est suffisamment précise pour résoudre les problèmes sur une petite échelle. Par contre, à l'échelle de grands bassins versants, l'évaluation du taux d'érosion ainsi que les apports sédimentaires dans les cours d'eau constitue un défi majeur. En effet, il faut composer avec de grandes superficies fort diversifiées, une gamme de données subissant des variations spatio-temporelles et des paramètres qui interfèrent les uns sur les autres. La variété des paramètres et l'interaction simultanée de plusieurs processus reliés à l'eau, aux sols et aux plantes limitent les efforts de recherche en vue d'établir des cartes d'erosion superficielle sur de grandes superficies.

Grâce à l'ordinateur et aux techniques d'analyse moderne, la physique du phénomène basé sur la simulation mathématique permet désormais d'identifier une variété de conditions relatives au processus d'érosion des bassins et à la charge sédimentaire fine transférée aux cours d'eau. Ainsi il devient possible d'analyser une grande quantité de données afin de produire des cartes d'érosion utiles et fiables à un coût minimal basées sur l'utilisation maximale des données disponibles tant au niveau du terrain que d'analyse de relevés. Par analyse de relevés on entend cartes topographiques, cartes géologiques, cartes pédologiques, cartes pluviométriques, cartes forestières et agricoles, photos aériennes, etc. Les observations sur le terrain sont d'autre part de grande utilité pour arriver à calibrer les modèles de simulation. Ces données étant, tout au moins pour les cartes des bassins, relativement facile à obtenir, même dans les régions les plus déshéritées, il devient impérieux d'en tirer le meilleur parti possible. Dans le cadre de la présente recherche, le modèle LAVSED-I a été appliqué sur le bassin de la rivière Chaudière, tributaire du Saint-Laurent (voir fig. 1) situé dans la partie sud–est de la province de Québec (Canada).

Approche fondamentale

À l'échelle d'une parcelle expérimentale, l'approche la plus connue pour estimer l'érosion superficielle à partir de l'intensité des pluies est l'équation universelle de perte de sol (USLE) développée par Wischmeier et Smith (1965). Plus

NOTE: Les commentaires sur le contenu du cet article doivent être envoyés par écrit au directeur de la revue avant le 31 juillet 1986 (voir l'adresse au verso de la page du couverture).

[1] L'adresse courante: Department of Civil Engineering, Colorado State University, Fort Collins, CO, U.S.A.

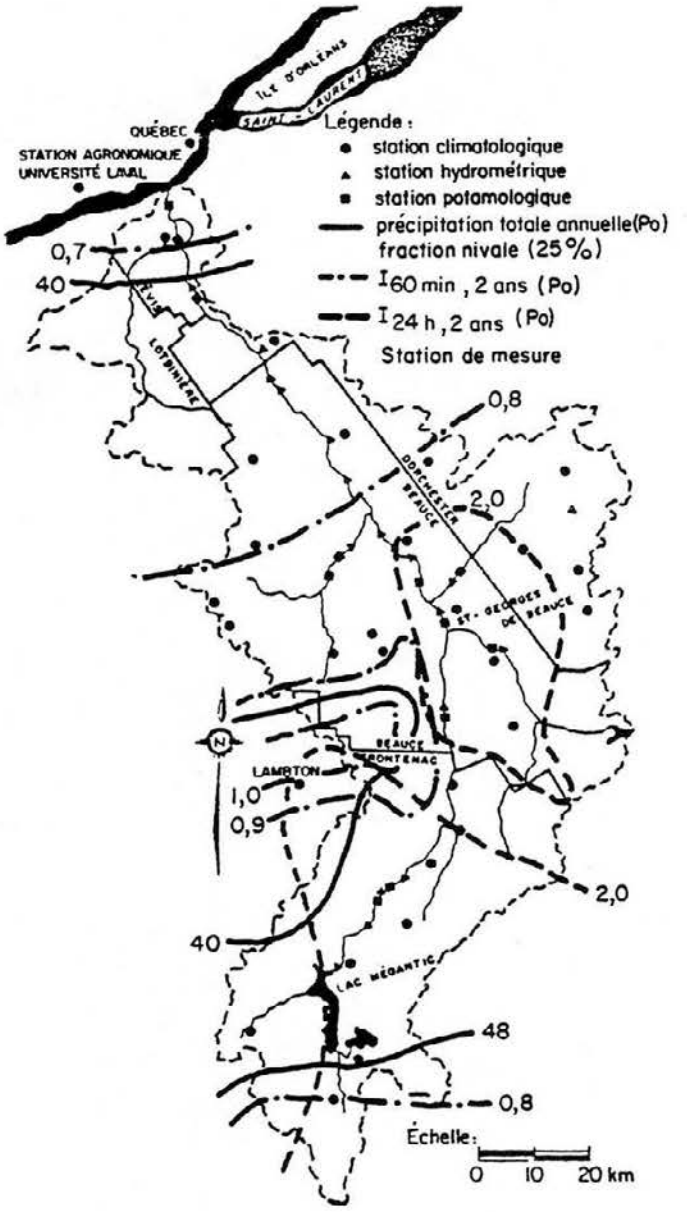

FIG. 1. Plan de localisation du bassin de la rivière Chaudière et courbes de précipitations.

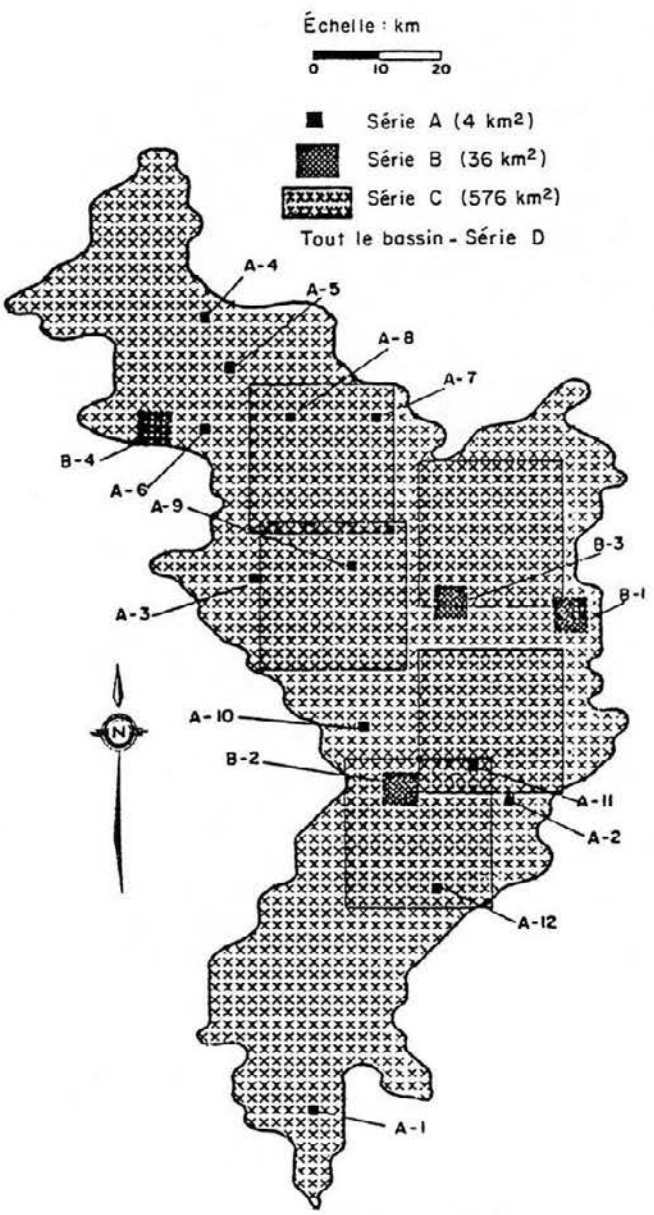

FIG. 2. Bassin de la rivière Chaudière, carte de localisation des series de superficies analysées.

récemment Kilinc et Richardson (1973) ont abordé le problème du détachement des particules solides à partir des caractéristiques hydrauliques de ruissellement. Depuis, des efforts ont été orientés non seulement sur l'estimation potentielle de l'érosion ou des apports solides aux cours d'eau mais aussi sur la cartographie des aires d'érosion. L'ordinateur a ainsi joué tout récemment un rôle important dans la description de l'erosion et du transport solide. Citons en exemple le modèle ANSWERS (Beasley *et al.* 1980), CREAMS (Knisel 1980) et GAMES (Dickinson et Pall 1983). Bien que de tels modèles peuvent être appliqués à une grande variété de conditions, ils ne permettent pas de cartographier les sources d'érosion sur de grandes étendues de bassin, et de plus, ils sont adaptés à des conditions régionales ne prenant pas en compte les effets climatiques saisonniers: pluie, neige, gel, dégel, etc.

Le modèle LAVSED-I vise à développer une approche simple en vue de prédire l'érosion des bassins et l'apport solide dans les cours d'eau nordiques, particulièrement les grands bassins, compte tenu des effets climatiques nordiques tels qu'observés dans le Québec septentrional.

LAVSED-I requiert une grande quantité de données descriptives au niveau des bassins ou des cours d'eau (actuelles ou hypothétiques) tels: (1) pluviométrie: intensité et lame d'eau de ruissellement (pluie, neige); (2) physiographie du territoire; (3) type de sol; (4) couverture végétale (arbustive, herbacée); (5) utilisation du territoire (secteurs boisés, agricoles, urbains); (6) description individuelle du grillage de base; (7) information générale.

Le modèle utilise le concept de subdivision des bassins sous forme d'une grille élémentaire, carrée, de dimension variable dont les maillons sont indépendants sur le plan hydrologique et sédimentologique. Chaque élément est cependant assujetti aux conditions hydro-pluviométriques et autres tel que cités ci-dessus. Au niveau du transfert le concept change puisque à la fois la dimension du quadrillage et la dimension du bassin interviennent dans les coefficients de transfert (voir fig. 2).

168

Équation universelle de perte de sol

Cette formule propose une quantification de l'érosion en nappe sur une parcelle de terre de dimension standard, faisant un hectare de superficie (pente normale 9%), basée exclusivement sur les pluies, comme agent érosif. Elle prend la forme suivante:

$$[1] \quad E = \alpha RKLSCP$$

où E = perte de sol (kt/km^2), R = agressivité des pluies, K = erosivité du sol, L = facteur lié à la longueur de la parcelle, S = facteur lié à la pente de la parcelle, C = facteur lié au couvert végétal, P = facteur lié aux pratiques agricoles ou pratiques anti-érosives et α = coefficient de transformation d'unités (t/acre vs. kt/km^2), égal à 0,247.

Le facteur moyen d'agressivité des pluies R s'obtient pour une région donnée au moyen d'un abaque établi par Wischmeier et Smith (1965), basé sur les statistiques de précipitation. L'équation équivalente est

$$[2] \quad R \simeq 25 + 0{,}75(h_{1/2} \times h_{24/2} \times h_m)$$

où $h_{1/2}$ = hauteur de pluie horaire ayant une période de retour de 2 ans (en pouces), $h_{24/2}$ = hauteur de pluie journalière ayant une période de retour de 2 ans (en pouces) et h_m = précipitation totale annuelle moyenne (en pouces).

Ces données apparaissent sous forme graphique dans la figure 1. Le pourcentage des chutes de neige annuelles correspond à 25% de la précipitation totale.

Le facteur d'érosivité des sols K est évalué à l'aide d'un abaque établi par Wischmeier *et al.* (1971) à partir de la granulométrie, du pourcentage de la matière organique, de la structure et de la perméabilité du sol érodé.

Le facteur lié à la longueur de la parcelle L est moins sensible dans le calcul de l'érosion et s'obtient par la relation suivante:

$$[3] \quad L = \sqrt{l_o}$$

Où l_o est la longueur de la parcelle en pieds.

Le facteur lié à la pente de la parcelle S tient compte de l'accroissement du potentiel érosif des pluies et du ruissellement rattaché à une accentuation de pente. L'équation proposée par Smith et Wischmeier (1957) s'écrit

$$[4] \quad S = 0{,}00076s^2 + 0{,}0053s + 0{,}0076$$

où s est la pente de la parcelle en pour-cent tel que montré à la figure 3.

Le facteur de couvert végétal C représente le degré de protection contre l'érosion des sols assuré par la végétation herbacée, arbustive et arborescente pour laquelle le facteur C se rapproche de 0. À l'opposé, un sol dénudé constitue l'état le plus vulnérable à l'érosion et le facteur C devient alors égal à 1. Le facteur de pratique agricole P diffère du facteur C en tenant compte d'effets additionnels de pratique agricole et de mesures de conservation des sols.

Les résultats que l'on obtient par l'application de l'équation universelle ne reflètent pas le processus d'érosion dû au ruissellement proprement dit. Il est à noter toutefois qu'une amélioration très sensible a été proposée par Williams et Berndt (1976) remplaçant le facteur R par un facteur d'écoulement égal à la puissance 0,56 du produit du volume écoulé par le débit de pointe.

Équation de Kilinc et Richardson

L'équation de régression obtenue par Kilinc et Richardson (1973) relie l'érosion d'une parcelle soumise à des pluies simulées aux caractéristiques hydrauliques du ruissellement. L'impossibilité d'obtenir une solution analytique aux problèmes d'érosion et de ruissellement sur des parcelles soumises à des pluies oblige le chercheur à recourir aux méthodes expérimentales pour déterminer la valeur des coefficients.

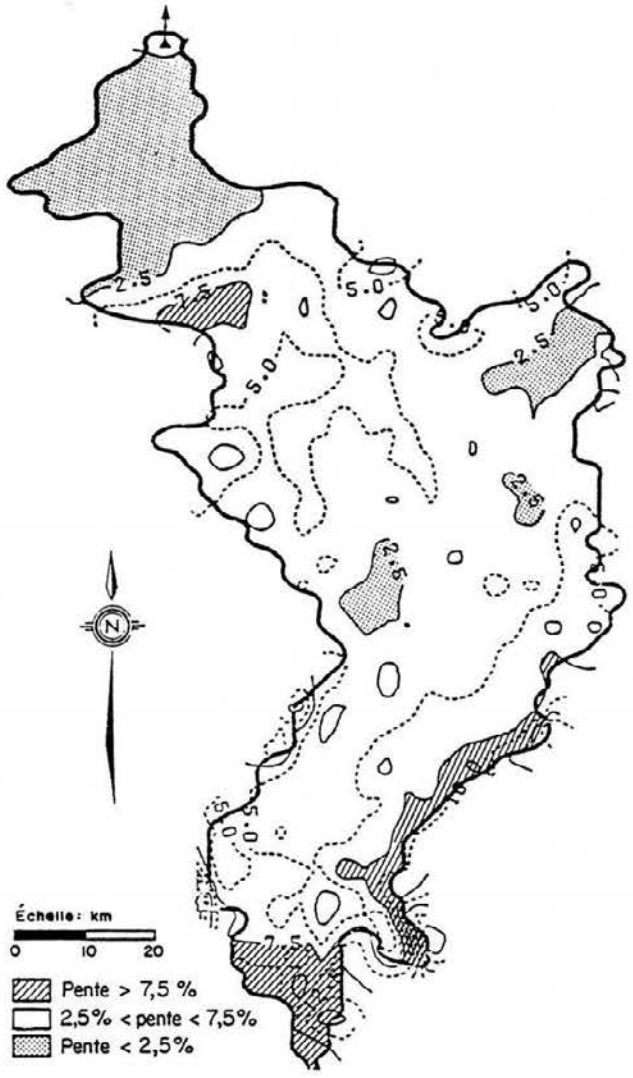

FIG. 3. Bassin de la rivière Chaudière, carte de la pente moyenne du terrain en pourcentage.

Généralement, les modèles de débit solide basés sur le concept de force tractrice prennent la forme suivante:

$$[5] \quad q_s = K_n(\tau_o - \tau_c)^n$$

Et les modèles basés sur la puissance d'érosion s'écrivent:

$$[6] \quad q_s = K_m[(\tau_o - \tau_c)\bar{u}]^m$$

où q_s = débit solide par unité de largeur, K_n et K_m = constantes représentant les propriétés physiques et la rugosité des sols, n et m = coefficients déterminés expérimentalement, $\bar{u}$ = vitesse locale moyenne, τ_c = contrainte critique de cisaillement et τ_o = force tractrice.

La détermination expérimentale des coefficients a été effectuée pour des sols sableux soumis à des pluies simulées d'intensité variant de 1,25 à 4,5 po/h (32 à 114 mm/h) ruissellant sur de courtes pentes. L'analyse des variables par régression multiple a permis à Kilinc et Richardson d'obtenir plusieurs

équations dont les principales sont

$$[7] \quad q_s = e^{0.744}[(\tau_o - \tau_c)\bar{u}]^{1.5836}$$

$$[8] \quad q_s = e^{-9.181}\,\bar{u}^{3.284}\,S^{0.4276}$$

$$[9] \quad q_s = e^{-11.645}\,\mathrm{Re}^{2.054}\,S^{1.46}$$

Les unités étant q_s, lb/(s·pi) (la largeur en pied); τ, lb/pi^2; $\bar{u}$, pi/s; S, pi/pi; e, base naturelle des logarithmes; et Re, nombre de Reynolds.

Ces auteurs suggèrent l'utilisation de [9] comme première approximation de l'érosion du sol résultant du ruissellement d'une seule pluie. Leur jugement est basé sur le fait que les variables indépendantes peuvent être déterminées sans trop d'erreurs, et que l'équation est simple d'utilisation, rapide et, par conséquent, économique.

Bien que cette équation soit fondée sur les caractéristiques hydrauliques du ruissellement, elle ne tient ni compte du couvert végétal, ni du facteur de pratique agricole, et n'est valable que pour les sols sablonneux pour lesquels le facteur d'érosivité K est environ égal à 0,15.

Pour considérer l'influence des facteurs d'érosivité des sols, de la végétation et des pratiques agricoles, il nous a fallu modifier l'équation de Kilinc et Richardson de la façon suivante afin de pouvoir l'adapter au modèle de prédiction:

$$[10] \quad q_s = e^{-11.65}\,\mathrm{Re}^{2.054}\,S^{1.46}\,\frac{K}{0{,}15}\,CP$$

où les paramètres K, C et P correspondent aux facteurs introduits dans l'équation universelle.

Modélisation mathématique

Le modèle considère un système hydro-sédimentologique basé sur l'utilisation d'une grille élémentaire à l'intérieur d'un bassin de grande dimension dont les entrées ont déjà été citées. Les sorties sont l'érosion brute, à l'échelle d'un maillon, l'érosion actuelle sur l'ensemble d'un bassin, l'érosion potentielle associée à l'utilisation du territoire et l'apport solide aux cours d'eau en sédiments fins. Un tel modèle regroupe ainsi l'essentiel des données de base généralement utilisées pour prédire le taux ou la susceptibilité à l'érosion et le transfert de la masse solide des bassins vers les cours d'eau.

L'emploi du modèle comporte quatre phases:
—l'analyse de l'ensemble des données physiques et climatiques d'un bassin à l'échelle des élements du grillage;
—la caractérisation physique du système de grille et sa discrétisation (influence de la dimension de la grille);
—la simulation des mécanismes de transferts;
—la prédiction de l'érosion actuelle et potentielle au niveau d'un bassin et des apports solides dans les cours d'eau.

Analyse des données—bassin expérimental

Comme bassin expérimental nous avons choisi celui de la rivière Chaudière situé dans la partie sud–est de la province de Québec (Canada) en raison de la quantité et de la qualité des données disponibles: son bassin de drainage, montré à la figure 1, couvre une superficie de 6684 km^2 à l'embouchure entre les méridiens de longitude 70°15′O et 71°40′O et les parallèles 45°15′N et 46°45′N. Par rapport à la station d'observation à Saint-Lambert-de-Lévis le bassin présente une superficie de 5830 km^2. La rivière Chaudière qui en consitute le principal cours d'eau, prend sa source dans la chaîne montagneuse des Appalaches à la frontière canado-américaine. Elle s'écoule vers le nord, traversant successivement les Appalaches puis la plaine du Saint-Laurent pour se déverser dans le fleuve à proximité de la ville de Québec.

TABLEAU 1. Calcul du facteur d'érosivité des sols pour les principaux profils pédologiques, bassin de la rivière Chaudière

Série	Type	% superficie	K
Beaurivage	Loam sableux	12,7	0,10
Kamouraska	Loam	9,5	0,15
Mawcook	Loam sablo-pierreux	16,5	0,17
Platon	Argile	2,2	0,15
Saint-André	Loam sablo-graveleux	11,8	0,20
Saint-Jude	Sable loameux	12,3	0,18
Saint-Nicolas	Loam sablo-schisteux	5,2	0,04
Saint-Samuel	Sable fin	6,6	0,15
	Tourbe grossière	3,8	0
	Marécages	7,0	0
	Affleurements rocheux	3,1	0
Arago	Loam pierreux	13,8	0,25
Beaurivage	Loam sablo-graveleux	1,8	0,10
Brompton	Loam argileux-pierreux	3,7	0,30
Le bras	Loam sableux	0,9	0,10
Chabot	Loam pierreux	1,1	0,10
Chapais	Loam pierreux	8,5	0,15
Dessaint	Loam pierreux	2,3	0,10
Fourchette	Loam sablo-graveleux	1,2	0,20
Garneau	Loam pierreux	11,9	0,10
Lafontaine	Loam argileux-pierreux	4,4	0,10
Leeds	Loam graveleux	15,6	0,15
Mont-Carmel	Loam pierreux	1,0	0,10
Neubois	Loam sableux	1,2	0,10
Painchaud	Loam pierreux	3,3	0,10
Rivière-du-Loup	Loam sablo-graveleux	2,4	0,20
Saint-Bruno	Loam sablo-graveleux	4,6	0,17
Sainte-Marie	Loam graveleux	11,9	0,10
Saint-Anésime	Loam pierreux	2,2	0,10
	Total	91,8%	$\bar{K}$ = 0,155

Parmi les données disponibles sur ce bassin, on retrouve la topographie, la climatologie, l'hydrométrie, la sédimentologie, la pédologie, la foresterie et l'agriculture, de même que des observations sur la charge solide en suspension effectuées à Saint-Lambert-de-Lévis depuis 1968.

Les caractéristiques physiques du bassin de la rivière Chaudière (pente, couvert forestier, emploi des terres, etc.) introduites dans le modèle et analysées, sont présentées aux figures 4*a*–4*d*. On notera en particulier que la pente moyenne du terrain (fig. 3) varie entre 2,5% et 7,5% sur près de 90% du bassin, sauf aux limites périphériques amont où la pente excède parfois 7,5%. Les figures 4*a* et 4*b* montrent aussi l'importance de l'agriculture combinée à l'utilisation des sols par les boisés mixtes sur une grande proportion du territoire. Quant au type de sol, le tableau 1 indique un loam (argileux, sableux, graveleux ou pierreux) sur près de 75% du territoire.

Dimensionnement de la grille et intégration des données

L'érosion à la surface de petits bassins versant peut être obtenue facilement en découpant la superficie considérée en entités physiographiques homogènes, dont la superficie unitaire standard est d'un hectare, sur lesquelles on calcule l'érosion à partir d'une des deux équations précitées.

Une telle subdivision dans le cas de grand bassin tel celui de la rivière Chaudière aurait entraîné un découpage trop serré, soit près de 600 000 unités de calcul. Or, étant donné la difficulté de lier le prélèvement d'un très grand nombre de points

170

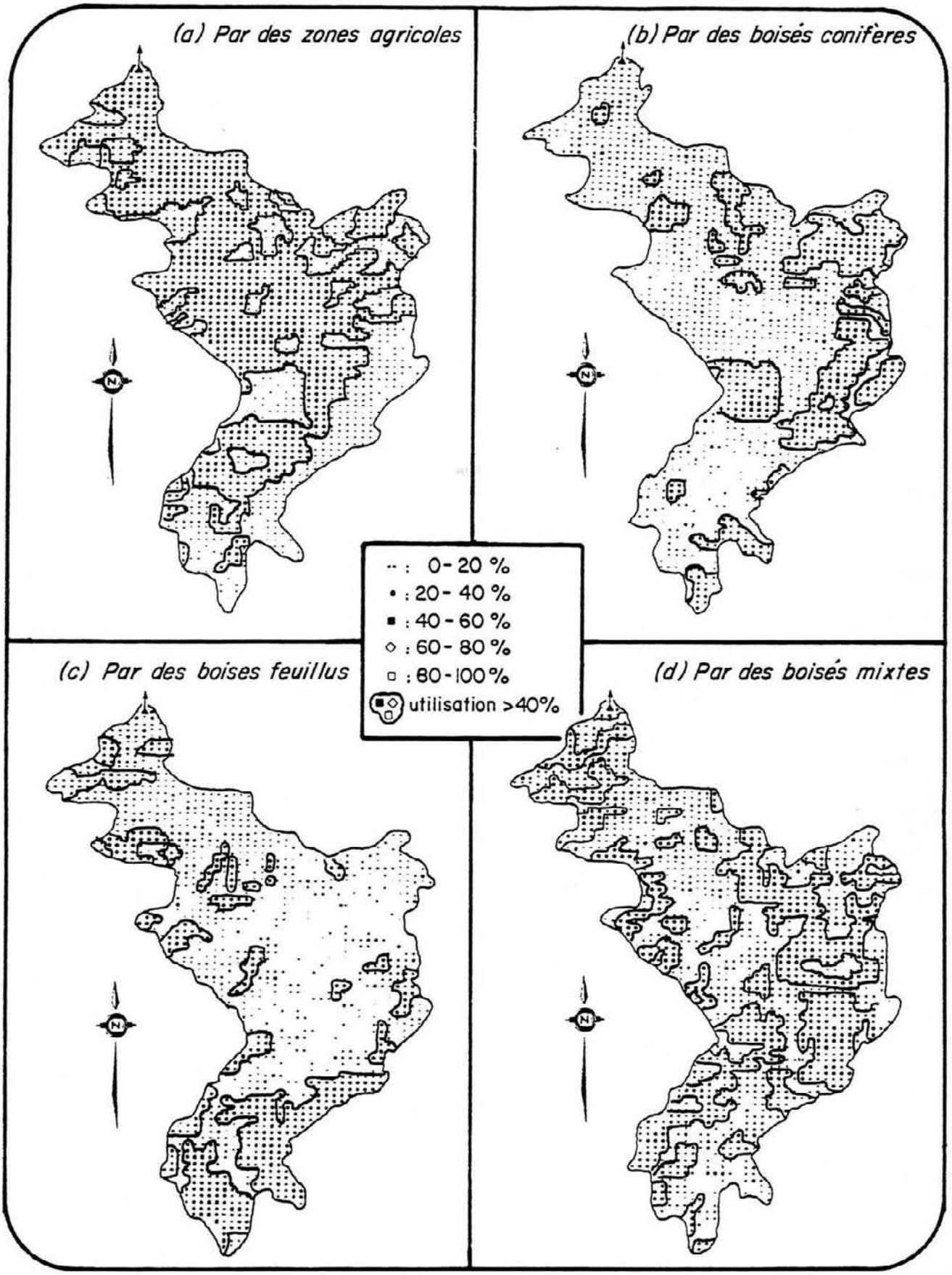

FIG. 4. Bassin de la rivière Chaudière, cartes du pourcentage d'utilisation du sol: (*a*) par des zones agricoles, (*b*) par des boisés conifères, (*c*) par des boisés feuillus, (*d*) par des boisés mixtes.

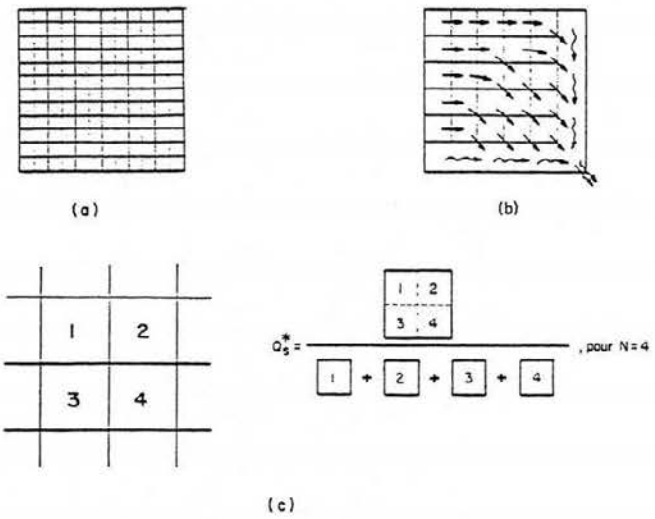

FIG. 5. (*a*) Schéma de regroupement des superficies de 144 éléments pour 36 sous-groupes de 4 éléments; (*b*) schema d'érosion et de transport au niveau d'un grillage; (*c*) schéma du calcul du quotient d'érosion Q_s^*.

de calcul à la précision des données disponibles à cette échelle, une méthode différente a été envisagée. Cette méthode se divise en deux étapes. La première consiste à découper le bassin versant en éléments carrés de superficie supérieure à celle des parcelles unitaires standard, et à prédire l'érosion sur ces éléments de calcul. La seconde étape vise à déterminer l'influence de la dimension des éléments du quadrillage sur la prédiction d'érosion et à introduire un facteur de correction au processus de calcul, tenant compte de la dimension de la grille.

Dans un premier temps donc le bassin expérimental a été découpé en 1671 éléments de 4 km^2, suivi dans un deuxième temps d'une subdivision partielle de la grille avec des maillons variant de 0.03 à 3000 km^2 (voir fig. 2, 5*a*–5*c*).

Cette approche peut être considérée comme faisant partie d'un ensemble que si l'information est reportée à chaque élément en supposant qu'une des deux équations ou les deux s'appliquent à l'élément. Dans la présente étude, les données ont été schématisées au moyen de l'ordinateur en faisant ressortir les aspects dominants intervenant au niveau de chaque maille.

Facteur de correction associé au système de grille

La discrétisation spatiale autorise l'utilisation systématique et indépendante des paramètres qui conditionnent l'érosion. Au départ nous avons proposé un découpage de l'espace en mailles carrées sur lesquelles ont été discrétisées les caractéristiques physiques du milieu. Or dans le calcul de l'érosion, la pente moyenne définie par Wischmeier et Smith (1965) et par Kilinc et Richardson (1973) et intervenant dans les équations de base est un des paramètres les plus significatifs se rattachant à l'érosion. Puisque le facteur pente est fonction de la longueur de l'élément, il est raisonnable de croire que la dimension et l'orientation du quadrillage influencent directement le calcul d'érosion, à plus forte raison lorsque la superficie des éléments est très grande par rapport à celle des parcelles expérimentales.

La pente d'un élément de calcul infinitésimal doit être considérée uniforme, tel que montré à la figure 6. Les élévations extrêmes sont alors situées sur la diagonale et non sur le côté de l'élément tel que prescrit dans le calcul du facteur de pente de l'équation universelle, exprimée par [4]:

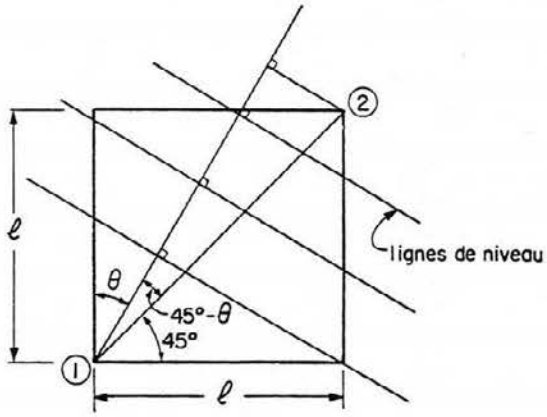

FIG. 6. Elément infinitésimal de calcul d'érosion.

$$[11] \quad S = 0{,}00076s^2 + 0{,}0053s + 0{,}0076$$

avec

$$[12] \quad s = \frac{E_{max} - E_{min}}{l} \times 100$$

où s = pente d'un élément de la grille, E_{max} = élévation maximale sur un élément de la grille et E_{min} = élévation minimale sur un élément de la grille (longueur unitaire de la grille).

Or, eu égard à un élément infinitésimal (fig. 6) la pente s'écrit

$$[13] \quad s_i = \frac{100\,(E_{max} - E_{min})}{l(\cos\theta + \sin\theta)} = \frac{s}{\cos\theta + \sin\theta}$$

La modification entraînée dans le calcul d'érosion s'évalue pour un élément de calcul en connaissant la valeur de l'angle θ. Sachant que l'intensité et l'orientation de la pente est équiprobable dans toutes les directions, pour un grand nombre d'éléments, les propriétés de symétrie de la variable θ peuvent alors être numériquement évaluées en utilisant la règle de Simpson ce qui permet d'obtenir

$$[14] \quad S_i = (0{,}93 \times 0{,}00076s^2) + (0{,}79 \times 0{,}0053s) + 0{,}0076$$

où

$$[15] \quad S_i = S/k$$

où k est la constante de calcul pour un élément infinitésimal.

Pour la discrétisation du bassin versant quatre séries de mailles possédant une grande variation de pente et diverses caractéristiques physiques ont été choisies arbitrairement: série *a*: 12 mailles de 4 km^2 divisées en 144 unités de 0,028 km^2; série *b*: 4 mailles de 36 km^2 divisées en 144 unités de 0,25 km^2; série *c*: 5 mailles de 575 km^2 divisées en 144 unités de 4 km^2; série *d*: la totalité du bassin subdivisé selon le grillage de base (4 km^2).

À partir des données de ces quatre séries, l'analyse a porté sur l'évaluation de l'érosion sur une superficie quelconque A, selon les calculs effectués sur de plus petites superficies A_o; $A > A_o$. Pour chacune des superficies des séries *a*, *b* et *c*, chaque élément couvrant 1/144 de la superficie a d'abord été considéré individuellement puis en groupe selon les arrangements suivants: 36 groupes de 4 éléments; 16 groupes de 9 éléments; 9 groupes de 16 éléments; 4 groupes de 36 éléments; 1 groupe de 144 éléments. En ce qui concerne la série *d*, les éléments de 4 km^2 ont été regroupés pour former des sous-groupes successifs de 4, 9, 16, ..., 1600 éléments.

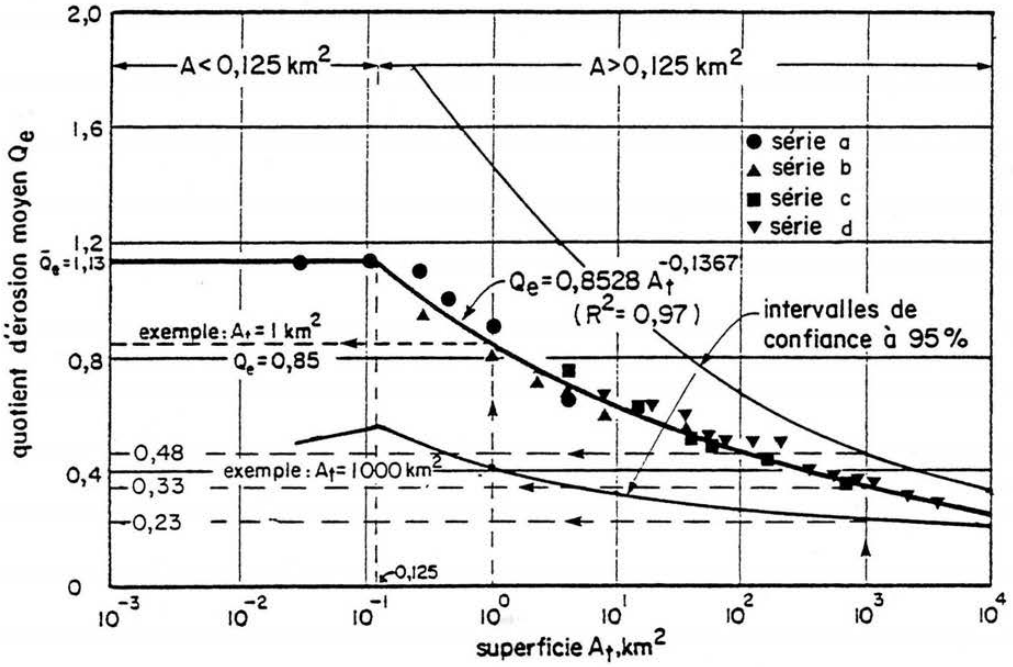

FIG. 7. Valeur moyenne du quotient d'érosion et intervalles de confiance (95%) en fonction de la superficie drainée.

La méthode consiste donc à analyser pour chacun des groupes un très grand nombre de valuers et de définir un *quotient d'érosion* Q_e, exprimant le rapport de l'érosion calculée sur un ensemble à la sommation de l'érosion sur chacun des éléments formant cet ensemble, tel que schématisé à la figure 5*c*.

Étant donné le très grand nombre de points de calculs, la moyenne $\bar{Q}_e$ et l'écart-type σ ont été relevés pour chacun des groupes et sous-groupes.

Valeur moyenne du quotient d'érosion

À partir des résultats obtenus pour chacune des séries individuelles exprimant la valeur moyenne du quotient $\bar{Q}_e$ en fonction du nombre d'éléments par sous-groupe, il devient possible d'obtenir une expression reliant la valeur de $\bar{Q}_e$ à la superficie des éléments. L'analyse par régression multiple donne (Julien 1979)

$$[16] \quad \bar{Q}_e = \text{Cte} = 1{,}13 \qquad \text{pour } A < 0{,}125 \text{ km}^2$$

$$[17] \quad \bar{Q}_e = 0{,}85AA^{-0.137} \qquad \text{pour } A > 1{,}25 \text{ km}^2 \ (R^2 = 0{,}97)$$

où $\bar{Q}_e$ = valeur moyenne du quotient d'érosion de chaque série individuelle d'éléments et A = superficie de chaque sous-groupe d'éléments (km^2). La constante 1,13 a été obtenue en prenant la valeur moyenne de 1728 valeurs individuelles de la série *a*.

Ces deux dernières équations sont illustrées à la figure 7 et comparées aux valeurs moyennes obtenues de chacune des séries du groupe *a*, *b*, *c* ou *d*. L'excellent ajustement obtenu pour des superficies variant de 0,03 à 3000 km^2, revêt une grande importance pratique. En effet, les résultats montrés à la figure 7 signifient qu'un calcul d'érosion à partir d'éléments de 1 km^2, par exemple, représente en moyenne 85% de l'érosion calculée en découpant la superficie selon les parcelles expérimentales standard (1 ha). Il est intéressant de constater que pour une superficie inférieure à 0,125 km^2, le calcul d'érosion peut être effectué sans modification majeure de l'équation universelle tandis que la valeur de $\bar{Q}_e$ diminue avec l'accroissement de la superficie du grillage lorsque $A > 0{,}125$ km^2.

Intervalles de confiance du quotient d'érosion

Une seconde analyse par régression multiple linéaire a été effectuée avec les valeurs de l'écart-type σ et l'équation finalement obtenue s'écrit sous la forme

$$[18] \quad \sigma = 0{,}00235 + \left(\frac{1 - A_o}{A}\right)(0{,}148 - 0{,}0226 \log_{10} A) \qquad (R^2 = 0{,}71)$$

où σ = écart-type logarithmique du quotient d'érosion Q_e obtenu par régression; A = superficie des sous-groupes d'éléments (km^2); A_o = superficie des éléments de base (km^2).

Cette équation est uniquement valable lorsque $A \geq A_o$. Les valeurs calculées ont été comparées aux valeurs obtenues par régression. Les fonctions de répartition du quotient d'érosion sont symétriques et obéissent à une loi de type log-normal (Julien 1979).

Si on considère maintenant les intervalles de confiance à 95% calculés à partir des équations de régression, lorsque A_o tend vers zéro, on obtient les deux courbes enveloppes ($\bar{Q}_e \pm 1{,}960$) montrées à la figure 7 qui tendent asymptotiquement vers la valeur moyenne pour de grande superficie.

Établissement des cartes d'érosion

Selon l'équation universelle

Puisque l'équation universelle a d'abord été dérivée en système anglais et que les élévations relevée sur les cartes topographiques sont en pieds, nous avons effectué les calculs dans ce système puis transformé le résultat dans le système international (SI). L'équation transformée dans le cas du bassin de la rivière Chaudière est

$$[19] \quad E_i = \alpha R_c K_c L_c S C_i P$$

ou

$$[20] \quad E_i = 48{,}13(0{,}0076 + 0{,}0053 s_i + 0{,}00076 s_i^2) \times C_i$$

avec E_i = érosion moyenne annuelle sur l'élément i (kt/(km^2 · a)); R_c = 75 (selon les précipitations régionales de

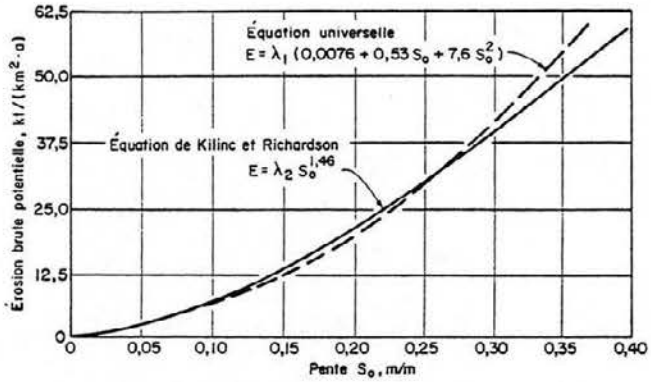

FIG. 8. Comparaison des deux équations fondamentales de calcul d'érosion.

la rivière Chaudière; $K_c = 0,15$ (en moyenne), le tableau 1 fournit la valeur des sous-régions; $L_c = \sqrt{300}$; S_i = facteur de pente ajusté d'un élément de calcul i; s_i = pente effective de l'élément de calcul i; $C_i = (F_a + 0,01 \times F_b)$, où F_a = fraction agricole et F_b = fraction boisée; P = facteur de pratique agricole ($P = 1$).

Selon l'équation de Kilinc et Richardson

L'équation de Kilinc et Richardson a été obtenue pour un sol sableux dont le facteur d'érosivité $K \approx 0,15$. Or, ce facteur s'apparente à celui du bassin de la rivière Chaudière. L'équation est fondée sur les caractéristiques du ruissellement et ne tient pas compte de la couverture végétale ni du facteur de pratique agricole. Selon les auteurs, la pluie significative pour représenter l'érosion totale annuelle est celle d'une durée de 30 min avec une période de retour de 2 ans. En supposant cette intensité de pluie et en modifiant l'équation pour tenir compte des facteurs d'érosivité des sols, de végétation et de pratique agricole telle l'équation universelle, la relation suivante a été obtenue:

$$[21] \quad E_i = 32,3e^{-11.645}\, \mathrm{Re}^{2.054}\, S^{1.46}\, \frac{K}{0,15}\, C_i P$$

ou

$$[22] \quad \mathrm{Re} = \frac{q l_o}{\nu} = \frac{1,4 \times 300 \times 10^5}{12 \times 3600 \times 1,3} = 747,8$$

et après simplification,

$$[23] \quad E_i = 226,2\, S^{1.46} C_i$$

où S_i = pente en m/m de l'élément i et C_i = facteur de couvert végétal de l'élément i.

Comparaison des deux approches

Pour un bassin donné les facteurs R, K, L, C et P, apparaissant dans l'équation universelle ont leur équivalence dans l'équation de Kilinc et Richardson, si bien que c'est le facteur pente qui gouverne chacune des équations. En rendant les unités comparables ($E \rightarrow$ kt/(km^2 · a)) [20] et [23] peuvent facilement être comparées.

La comparaison des deux approches de calcul de l'érosion apparaît à la figure 8. Les courbes démontrent une nette ressemblance: il appert donc que l'une ou l'autre des équations peut être utilisée dans l'établissement des cartes d'érosion.

Les résultats simulés par chaque méthode sont présentés aux figures 9*a* et 9*b*. Ils sont très cohérents et les courbes diffèrent peu l'une de l'autre.

Apports solides aux cours d'eau

Coefficient de transfert

À partir de la discrétisation précédente le modèle d'érosion doit considérer deux facteurs en vue de déterminer l'apport solide dans les cours d'eau:

(a) Un facteur de transformation de la parcelle élémentaire de 1 ha à la superficie des mailles de la grille découpant le bassin. Ce coefficient est connu et défini par le quotient d'érosion $\bar{Q}_e$.

(b) Un coefficient de transfert associé aux pourcentages effectifs de sédiments érodés pouvant atteindre le cours d'eau lors d'une même averse (ou séquence d'averses) ou lors de la fonte printanière.

En effet, une grande quantité de matériaux érodés sur un bassin peut se déposer par la suite à l'intérieur du territoire sans atteindre le réseau hydrographique. Cette déposition diminue d'autant la quantité de solides susceptible d'être observée dans un cours d'eau. Le pourcentage d'érosion brute observé, sous forme de débit solide à une section quelconque d'un cours d'eau est représenté par un coefficient empirique d'apport solide ("sediment-delivery ratio"). Ce coefficient est relié de façon significative à la superficie même du bassin de drainage, à la pente du bassin, aux dépressions internes, à la densité de drainage, aux précipitations et à l'écoulement dans le cours d'eau. Les recherches à ce jour n'ont pas permis de structurer et de quantifier la relation complète entre tous ces facteurs mais certains sont particulièrement mis en évidence. Le plus important d'après Boyce (1975) est la superficie du bassin de drainage comme l'indique la figure 10.

En prenant en considération les coefficients de transfert, il devient alors possible de prédire la charge solide à une section quelconque d'un cours d'eau à partir de l'érosion brute des bassins versants. La relation obtenue se définit comme suit:

$$[24] \quad Q_{sp} = C_s \sum_{i=1}^{N} \frac{A_i E_i}{(\bar{Q}_e)_i}$$

où Q_{sp} = charge solide moyenne annuelle par les pluies en kt/a; C_s = coefficient d'apport solide; A_i = superficie de l'élément de calcul i en km^2; E_i = érosion brute annuelle en kt/(km^2 · a) sur l'élément de calcul i; N = nombre d'éléments de calcul sur le bassin; $(\bar{Q}_e)_i$ = quotient d'érosion moyen de l'élément de calcul i.

Par comparaison, pour une superficie de 5830 km^2, la valeur moyenne du coefficient d'apport solide tirée de la figure 10 est environ égale à 0,03 (comprise entre 0,01 et 0,07), ce qui indique que seulement 3% en moyenne, de la quantité de solides érodés sur le bassin de la rivière Chaudière serait transportée jusqu'à Saint-Lambert-de-Lévis par le cours d'eau.

Les valeurs calculées par une des deux équations de base ([20] et [23]) qui sont présentées au tableau 2 sont pratiquement identiques, en dépit du très grand nombre de variables et d'hypothèses formulées. Par rapport aux valeurs mesurées, les résultats sont cependant variables et certes influencés par des effets climatiques nordiques (fonte de neige, effets de gels et de dégels, etc.).

Influence des saisons

La station d'observation, en opération depuis 1968, à Saint-Lambert-de-Lévis, a permis d'évaluer le débit solide de la rivière Chaudière et également d'établir la relation entre le débit liquide et la concentration des sédiments en suspension. Un modèle de régression entre ces paramètres journaliers a été établi par Frenette *et al.* (1974) permettant de définir la charge sédimentaire moyenne durant la crue printanière à

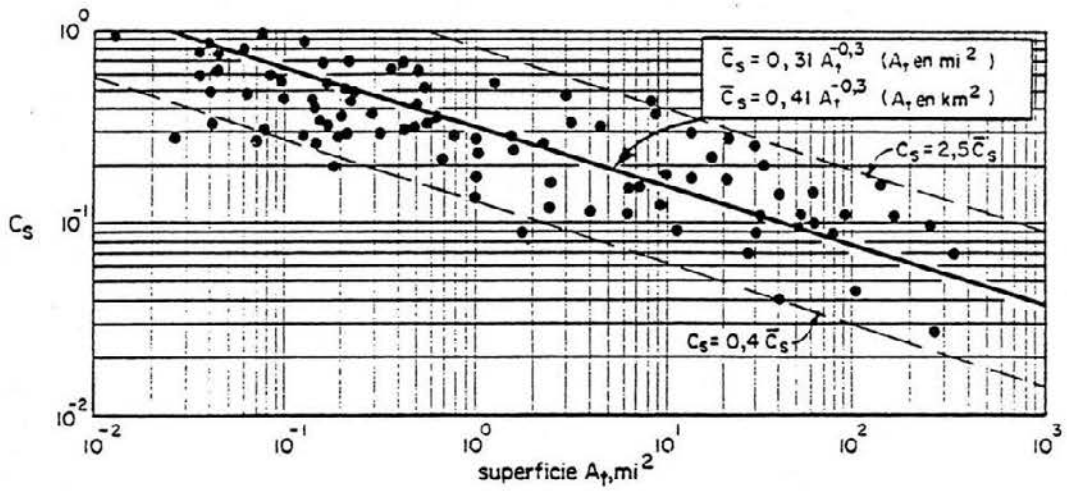

FIG. 9. Coefficient d'apport solide en fonction de la superficie drainée (d'après Boyce 1975).

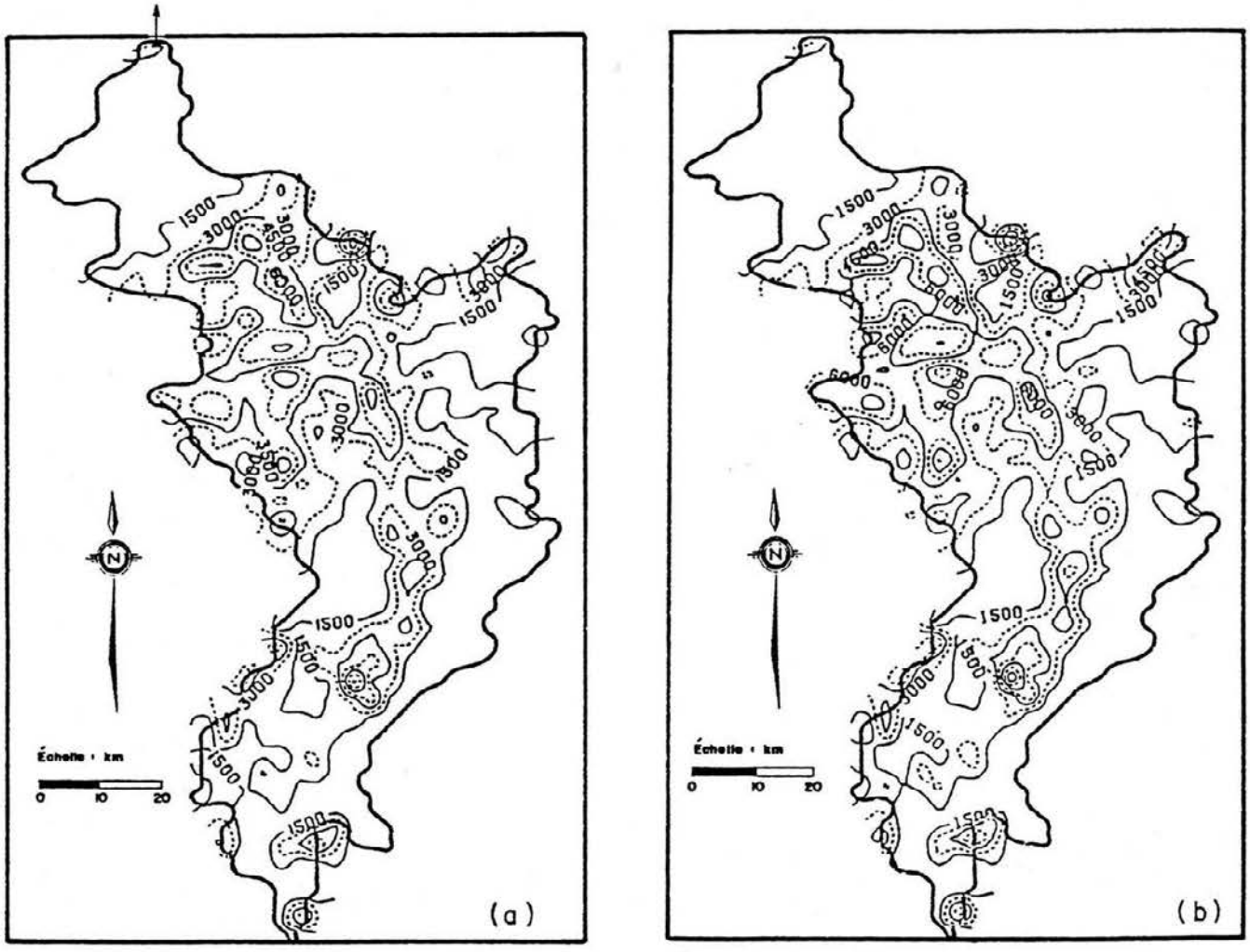

FIG. 10. Bassin de la rivière Chaudière—carte de l'érosion brute corrigé ($\bar{t}$/(km^2·a)) calculée par (*a*) l'équation de Kilinc et Richardson et (*b*) l'équation universelle.

273 kt (métrique)/a. Par contre, pour l'ensemble de l'année la valeur moyenne mensuelle est présentée à la figure 11.

Selon ce sédimentogramme mensuel, il appert que le régime sédimentologique est fortement influencé par les saisons, ce qui a conduit à regrouper les données selon les périodes suivantes: période pluviale: juin à novembre; période nivale: décembre, janvier et février; période printanière: mars, avril et mai.

La comparaison des calculs, théoriques et observés en tenant compte des précipitations respectives à chaque saison, apparaît dans le tableau 3. Les résultats de ce tableau indiquent que le modèle mathématique représente assez fidèlement l'éro-

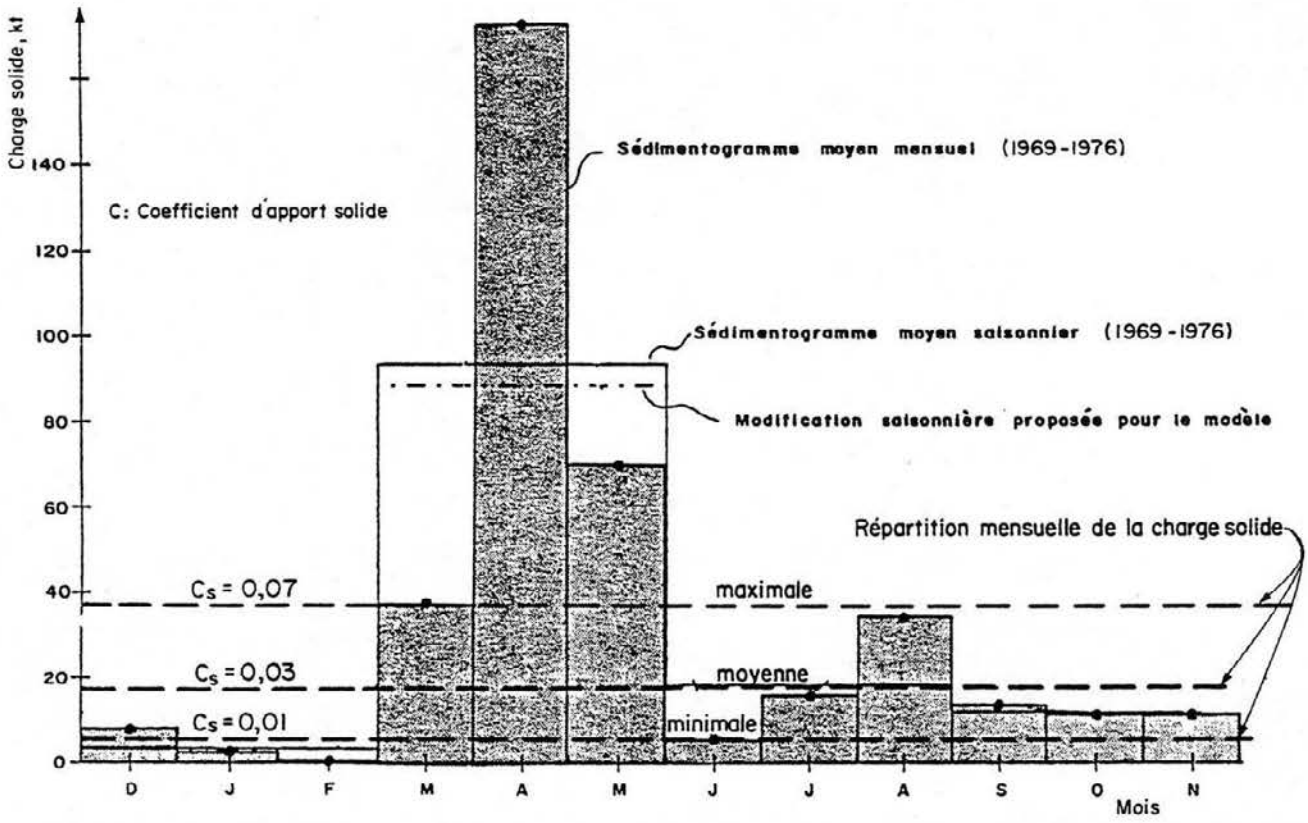

FIG. 11. Rivière Chaudière à St-Lambert-de-Lévis—sédimentogrammes moyen mensuel et saisonnier observés (1969–1976) et répartition mensuelle de la charge solide estimée.

TABLEAU 2. Bassin de la rivière Chaudière à Saint-Lambert-de-Lévis—comparaison de la charge solide moyenne annuelle théorique et observée

Équation de prédiction	Érosion brute sur tout le bassin (Mt/a)	Coefficient d'apport solide	Charge solide moyenne annuelle (kt/a)	Charge solide moyenne mensuelle (kt/a)
Équation universelle	6,44	0.01	64 (min.)	5,1
		0.03	193 (moy.)	16,1
		0.07	450 (max.)	37,5
Équation de Kilinc et Richardson	6,70	0.01	66 (min.)	5,1
		0.03	197 (moy.)	16,4
		0.07	460 (max.)	38,3
Valeurs observees:			364	

sion pluviale ayant lieu de juin à novembre pour une valeur moyenne de $C_s = 0.03$, mais sous-estiment les apports printaniers, même avec $C_s = 0,07$, et surestiment les apports d'hiver, même avec $C_s = 0,01$. Il appert ainsi que pour l'ensemble de l'année, la prédiction mathématique équivaut en moyenne ($C_s = 0,03$) à environ 54% des apports solides totaux. Plusieurs hypothèses peuvent expliquer ce résultat:

(a) En milieu nordique, le manteau nival et le phénomène de gel et de dégel ont pour effet d'augmenter la résistance des sols à l'érosion et, partant, de diminuer le facteur d'érosivité K (C_s = faible à très faible).

(b) Le phénomène de dégel entraîne le craquement, la fissuration, ou le soulèvement (par formation de lentille) des sols fins et (ou) le relâchement de contrainte intergranulaire, ce qui a pour effet de diminuer la résistance des sols à l'érosion et, partant, d'accroître le facteur d'érosivité K.

(c) À l'augmentation du facteur d'érosivité s'ajoutent l'effet du ruissellement accéléré associé à la fonte printanière et de la température de fonte (±0°C) affectant directement la viscosité de l'eau, donc l'action érosive. Le coefficient d'apport solide devient alors plus élevé. Notons, par exemple, qu'aux États-Unis on a observé que le transport solide augmentait par un facteur de 2,5 lorsque la température de l'eau diminuait d'une vintaine de degrés Fahrenheit (±11°C).

Étant donné la bonne concordance des résultats en période pluviale (6 mois) avec un rapport de 0,82 entre les valeurs prédites et observées, il faut en déduire que les coefficients de transfert, $\bar{Q}_c$ et C_s moyens ($C_s \approx 0,03$), s'ajustent bien aux conditions estivales et automnales régies par les pluies. En saison froide, il va de soi que le coefficient d'érosivité et d'apport solide diminue, même en-dessous de la cote $C_s \approx 0,01$, tandis qu'au printemps, au contraire, la valeur de

TABLEAU 3. Charge solide saisonnière de la rivière Chaudière

Période	Tonnage théorique selon l'équation universelle Q_s^t (kt)	Tonnage observé Q_s (kt)	Q_s/Q_s^t
Moyenne annuelle (1968–1976)	197 (C_s = 0,03)	364	1,85
	462 (C_s = 0,07)		0,78
Saison pluviale (juin–novembre)	98,5 (C_s = 0,03)*	81*	0,82*
Saison nivale (décembre–février)	49,2 (C_s = 0,03)	10	0,20
	16,4 (C_s = 0,01)*		0,63*
Saison printanière (mars–mai)	49,2 (C_s = 0,03)	273	5,55
	114,8 (C_s = 0,07)		2,40
	278 (C_s = 0,17)*		0,99*

*Valeur représentative.

C_s dépasse largement la limite moyenne maximale de 0,07 (C_s = 0,17). Ce double phénomène de dépassement des limites usuelles, inférieures et supérieures, est aussi associé au phénomène d'accumulation de la neige en hiver, qui constitue un indice d'érosion en puissance dont les effets ne se font sentir qu'au printemps. Il y a donc là un transfert saisonnier entre les causes de l'érosion et les effets observés.

L'état actuel de la recherche ne permet pas cependant de discerner laquelle des hypothèses citées plus haut explique le mieux l'accroissement printanier. De toutes les façons cependant, le phénomène se rattache aux conditions nordiques et à prime abord a un effet combiné des trois hypothèses. Cela permet d'expliquer d'après les observations que, règle générale, plus de 70% de la charge solide dans les cours d'eau nordiques survient durant la crue printanière.

Afin de tenir compte de ce phénomène et d'apporter une amélioration sensible du modèle, il convient d'introduire un coefficient d'ajustement associé aux effets saisonniers. Ce facteur de correction moyen annuel peut être obtenu facilement en calculant la moyenne des coefficients saisonniers par rapport à la valeur moyenne du coefficient (C_s = 0,03), soit dans le cas de la rivière Chaudière.

$$[25] \quad \bar{c} = \frac{0{,}20 + (2 \times 0{,}82) + 5{,}6}{4} = 1{,}85$$

Cela démontre, toute proportion gardée, une plus grande sensibilité à l'érosion des bassins nordiques situés en milieu agricole par rapport aux bassins localisés en milieu plus tempéré. Le taux d'apport solide est alors deux fois supérieur à la normale. Rappelons, comme le montre la figure 4*a*, que le bassin de la rivière Chaudière est essentiellement agricole (près de 70% du territoire) alors que le reste du bassin est caractérisé par la forêt. L'hypothèse d'une érosion pelliculaire dominante est alors bien confirmée par le modèle.

Impact de l'utilisation du territoire sur le processus d'érosion

A priori, l'érosion des sols en valeur absolue est difficile à estimer, mais en terme relatif l'impact de l'utilisation du territoire sur le processus d'érosion est facile à prédire. Il s'agit en effet de rechercher un taux d'évolution en valeur relative en utilisant une des formules d'érosion. Par exemple, pour l'équation universelle, le taux d'évolution peut s'écrire

$$[26] \quad \lambda = \frac{K'}{K} \cdot \frac{L'}{L} \cdot \frac{S'}{S} \cdot \frac{C'}{C} \cdot \frac{P'}{P}$$

où K, L, S, C et P sont les facteurs tels que définis par l'USLE et K', L', S', C' et P' sont les facteurs prévisibles après modification du bassin.

Il suffit alors d'introduire dans le modèle les nouvelles valeurs primées au lieu des valeurs d'érosion brute pour obtenir les effets des travaux planifiés au niveau d'un bassin.

Conclusions

Le problème posé par l'érosion hydrique des sols est complexe et, dans l'état actuel des choses, la détermination quantitative de la susceptibilité à l'érosion est possible seulement par une modélisation mathématique.

Cette approche met l'accent sur l'importance primordiale des certains facteurs qui dominent l'érosion, à savoir: la pluviométrie ou les caractéristiques de ruissellement printanier, la pente, la couverture végétale, la superficie des bassins, la discrétisation des bassins, l'importance des coefficients de transfer, etc.

En admettant des hypothèses vraisemblables, le modèle LAVSED-I considère que l'érosion en nappe constitue la majeure partie de l'érosion. En sélectionnant deux types d'équations de pente de sol (équations universelle et de Kilinc et Richardson), modifiées et adaptées aux caractéristiques du modèle il a été possible d'obtenir des résultats significatifs en regard de la charge sédimentaire transportée par la rivière Chaudière, tributaire du Saint-Laurent. Les résultats démontrent en particulier l'influence du gel et dégel, et, de la présence de la neige au sol en milieu nordique.

Au niveau de la gestion d'un bassin, il importe par ailleurs d'apprécier l'impact des travaux sur le territoire (ex.: influence du déboisement ou mise en valeur agricole). À cet égard, avec la modélisation proposée, il est possible d'effectuer deux types de calculs: détermination de l'érosion actuelle et potentielle, c'est-à-dire avant et après exploitation (ou aménagement proposé) et distinguer ainsi les zones les plus susceptibles à l'érosion.

L'application de la simulation démontre comment il convient d'être prudent dans la prédiction du taux d'érosion. Par contre, le modèle conduit à conclure qu'il est possible d'utiliser une des deux équations de base, même en milieu nordique, moyennant certains coefficients d'ajustement, pour prédire le taux d'érosion et l'apport solide dans les cours d'eau en milieu nordique.

BEASLEY, D. B., HUGGINS, L. F. et MONKE, E. J. 1980. ANSWERS. A model for watershed planning. Transactions of the ASAE, pp. 938–944.

BOYCE, R. 1975. Sediment routing with sediment-delivery ratios. Present and prospective technology for predicting sediment yields and sources. United States. Department of Agriculture. Agricultural Research Service, ARS-S-40.

DICKINSON, T. et PALL, P. 1982. GAMES: identification and control of soil erosion and fluvial sedimentation agricultural areas of the Canadian Great Lakes basin. Rapport soumis à Approvisionnements et Services série 0S081-00223.

EINSTEIN, H. A. 1950. The bed-load function for sediment transportation in open channel flows. United States. Department of Agriculture, Technical Bulletin, n° 1026.

FRENETTE, M., LLAMAS, J. et LARINIER, M. 1974. Modèle de simulation du transport solide en suspension des rivières Châteauguay et Chaudière. Rapport du Centre de Recherches sur l'Eau, Université Laval, Québec (Qué.)

JULIEN, P. 1979. Érosion de bassin et apport solide en suspension dans les cours d'eau nordiques. Thèse de maîtrise. Département de génie civil, Université Laval, Québec (Qué.), 186 p.

KILINC, M. et RICHARDSON, E. V. 1973. Mechanics of soil erosion from overland flow generated by simulated rainfall. Colorado State University (Fort Collins), Hydrology Papers, n° 63.

KNISEL, G. W. 1980. CREAMS. A field scale model for chemicals runoff and erosion from agriculture land management system. United States Department of Agriculture, Science and Education Administration, rapport n° 20.

LI, R. M. 1972. Sheet flow under simulated rainfall. Thèse de maîtrise, Colorado State University, Fort Collins, CO.

MEYER, L. D. 1971. Soil erosion by water on upland areas. *Dans* River mechanics. *Edité par* H. W. Shen. *Publié par* H. W. Shen, Fort Collins, CO.

PIEST, R. F. et MILLER, C. R. 1977. Sediment sources and sediment yields. *Dans* Sedimentation engineering. ASCE Manuals and Reports on Engineering Practice, Chap. IV, n° 54.

SMITH, D. A. et WISCHMEIER, W. H. 1957. Factors affecting sheet and rill erosion. Transactions American Geophysical Union, **38**(6).

WILLIAMS, J. R. et BERNDT, H. D. 1976. Sediment yield prediction based on watershed hydrology. Transactions of the ASAE, **20**(6).

WISCHMEIER, W. H. 1959. A rainfall erosion index for a universal soil-loss equation. Soil Society of America Proceedings, **23**(3).

——— 1973. Upslope erosion analysis. *Dans* Environmental impact on rivers. *Edité par* H. W. Shen. *Publié par* H. W. Shen, Fort Collins, CO.

WISCHMEIER, W. H. et SMITH, D. D. 1965. Predicting rainfall-erosion losses from cropland east of the Rocky Mountains. United States, Department of Agriculture, Agriculture Handbook, n° 282.

WISCHMEIER, W. H., JOHNSON, C. B. et CROSS, B. V. 1971. A soil erodibility monograph for farm land and construction sites. Journal of Soil and Water Conservation, **26**(5).

Liste des symboles

α	coefficient de transformation d'unités (t/acre vs. kt/km^2) = 0,247
τ	lb/pi^2
τ_c	contrainte critique de cisaillement
τ_o	force tractrice
A	superficie de chaque sous-groupe d'éléments (km^2)
A_i	superficie de l'élément de calcul i (km^2)
A_o	superficie des éléments de base (km^2)
C	facteur lié au couvert végétal
C_i	facteur de couvert végétal de l'élément i
C_s	coefficient d'apport solide
E	perte de sol (kt/km^2)
E_i	érosion brute annuelle en kt/(km^2 · a) sur l'élément de calcul i
E_{max}	élévation maximale sur un élément de la grille
E_{min}	élévation minimale sur un élément de la grille
e	base naturelle des logarithmes
F_a	fraction agricole
F_b	fraction boisée
$h_{1/2}$	hauteur de pluie horaire ayant une période de retour de 2 ans (po)
$h_{24/2}$	hauteur de pluie journalière ayant une période de retour de 2 ans (po)
h_m	précipitation totale annuelle moyenne (po)
K	érosivité du sol
K_c	érosivité moyenne des sols du bassin de la rivière Chaudière
K_n, K_m	constantes représentant les propriétés physiques et la rugosité des sols
k	constante de calcul pour un élément infinitésimal
L	facteur lié à longueur de la parcelle
L_c	longueur normale d'une parcelle standard
l	longueur unitaire de la grille
l_o	longueur de la parcelle en pieds
N	nombre d'éléments de calcul sur le bassin
n, m	coefficients déterminés expérimentalement
P	facteur lié aux pratiques agricoles ou pratiques anti-érosives
$\bar{Q}_e$	valeur moyenne du quotient d'érosion de chaque série individuelle d'éléments
$(\bar{Q}_e)_i$	quotient d'érosion moyen de l'élément de calcul i
Q_{sp}	charge solide moyenne annuelle par les pluies (kt/a)
q_s	débit solide par unité de largeur
R	agressivité des pluies
R_c	facteur d'agressivité des pluies du bassin de la rivière Chaudière
Re	nombre de Reynolds
S	facteur ilé à la pente de la parcelle
S_i	facteur de pente ajusté d'un élément de calcul i
s	pente de la parcelle (%)
s_i	pente effective de l'élément de calcul i
$\bar{u}$	vitesse locale moyenne

LAVSED-II—A model for predicting suspended load in northern streams

P. Y. JULIEN[1] AND M. FRENETTE
Department of Civil Engineering, Laval University, Quebec, P.Q., Canada G1K 7P4

Received November 5, 1984
Revised manuscript accepted October 24, 1985

The model LAVSED-II (LAVal SEDimentological model number II) has been developed to evaluate the suspended load in northern streams that results from rainfall and snowmelt erosion on upslope areas. The most important parameters are (1) the physical characteristics involved in soil erosion processes and (2) the climatic parameters on a month-to-month basis. Two fundamental relationships are obtained from the governing physical processes and empirical relationships describing snowmelt and sediment transport. The model has been applied to four large watersheds, tributaries of the St. Lawrence River. The computed sediment yield compares very well with the measured suspended load (mostly wash load) in the rivers. The magnitude of the peak during spring is particularly well predicted. The computed sediment yield is shown to be very sensitive to meteorological data. In the case of ungaged watersheds, the model can be applied to estimate the sediment yield.

Le modèle LAVSED-II (second modèle SEDimentologique de l'Université LAVal) a été développé pour évaluer la charge solide en suspension dans les cours d'eau nordiques à partir de l'érosion superficielle pluviale et nivale à l'échelle de grands bassins versants. Deux relations fondamentales sont obtenues en considérant les principales caractéristiques physiques rattachées à l'érosion des sols ainsi que la variabilité des paramètres climatiques sur une base mensuelle. Le modèle a été appliqué sur quatre bassins versants, tributaires du fleuve St-Laurent, dont la charge solide provient essentiellement de l'érosion superficielle. L'apport solide calculé par le modele est comparable à celui observé. La pointe sédimentologique lors de la crue printanière est particulièrement bien définie et l'analyse démontre l'importance des données météorologiques régionales. Pour les bassins non jaugés, la charge solide peut également être estimée par le modèle.

Can. J. Civ. Eng. 13, 162–170 (1986)

Introduction

Sediment transport in streams can be classified in different ways according to the mode of transport and the origin of sediments. The part of the total sediment load composed of particles finer than the sediment bed mixture is commonly referred to as the wash load. The total number of particles transported as suspended load or wash load depends mostly on the upslope supply rate of particles from sheet and rill erosion on the watershed.

Two mathematical models (LAVSED-I and LAVSED-II) have been developed at Laval University for predicting sediment yield from large watersheds. The model LAVSED-I (Frenette and Julien 1986) is based on the universal soil loss equation and an empirical sediment transport equation. Whereas the model LAVSED-I is intended for mapping soil erosion on a mean annual basis, the model LAVSED-II is used to obtain monthly predictions of the sediment yield. This paper briefly describes the principal components of the model LAVSED-II and illustrates its predictive capabilities as applied to large northern watersheds.

First the physical processes are summarized; then the equations are presented for sediment yield due to rainfall and snowmelt. The equations are used in a quasi-stochastic model that calculates the mean monthly sediment yield from stochastic rainfall and deterministic physical characteristics. Finally, the computed yields are compared with the observed sediment load in the four rivers shown in Fig. 1.

Physical processes

Most of the suspended sediment load in northern streams under investigation originates from soil erosion by overland flow. There is snow accumulation on the frozen ground from December to March. The snow cover usually melts over a relatively short period of time, generally in March, and the sediment load peaks during spring floods. From May to November, the sediment load in streams is limited by the rainfall erosion supply.

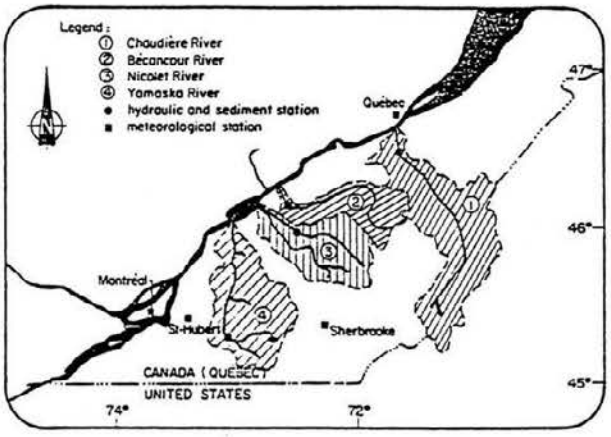

FIG. 1. Location of watersheds.

As shown in Fig. 2, soil erosion through the action of raindrop impact and runoff is a complex process of detachment and transport of soil particles. In most cases, soil detachment by raindrop impact does not control the supply of sediment to overland flow. Most soil particles are moved downslope by surface runoff. For this reason, runoff is a better variable than rainfall to describe soil erosion.

Early in spring, the snowmelt water percolates through the unsaturated zone of the snowpack. As the percolating meltwater reaches the ground, the water in excess of the infiltration rate flows downslope in the saturated layer. Early in the season, the flow in the saturated layer is similar to flow in porous media. As the melting season progresses, however, micro-

NOTE: Written discussion of this paper is welcomed and will be received by the Editor until July 31, 1986 (address inside front cover).

[1]Present address: Department of Civil Engineering, Colorado State University, Fort Collins, U.S.A.

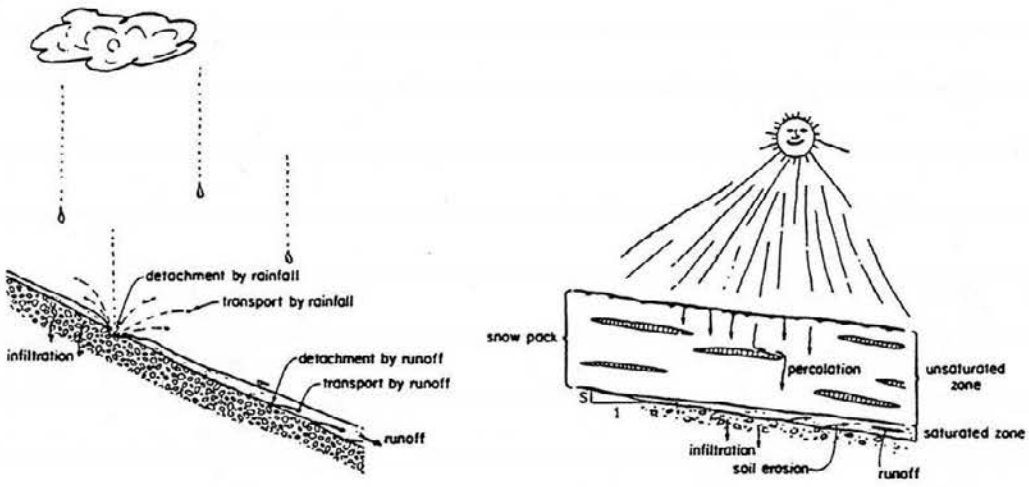

FIG. 2. Soil erosion processes during rainfall and snowmelt.

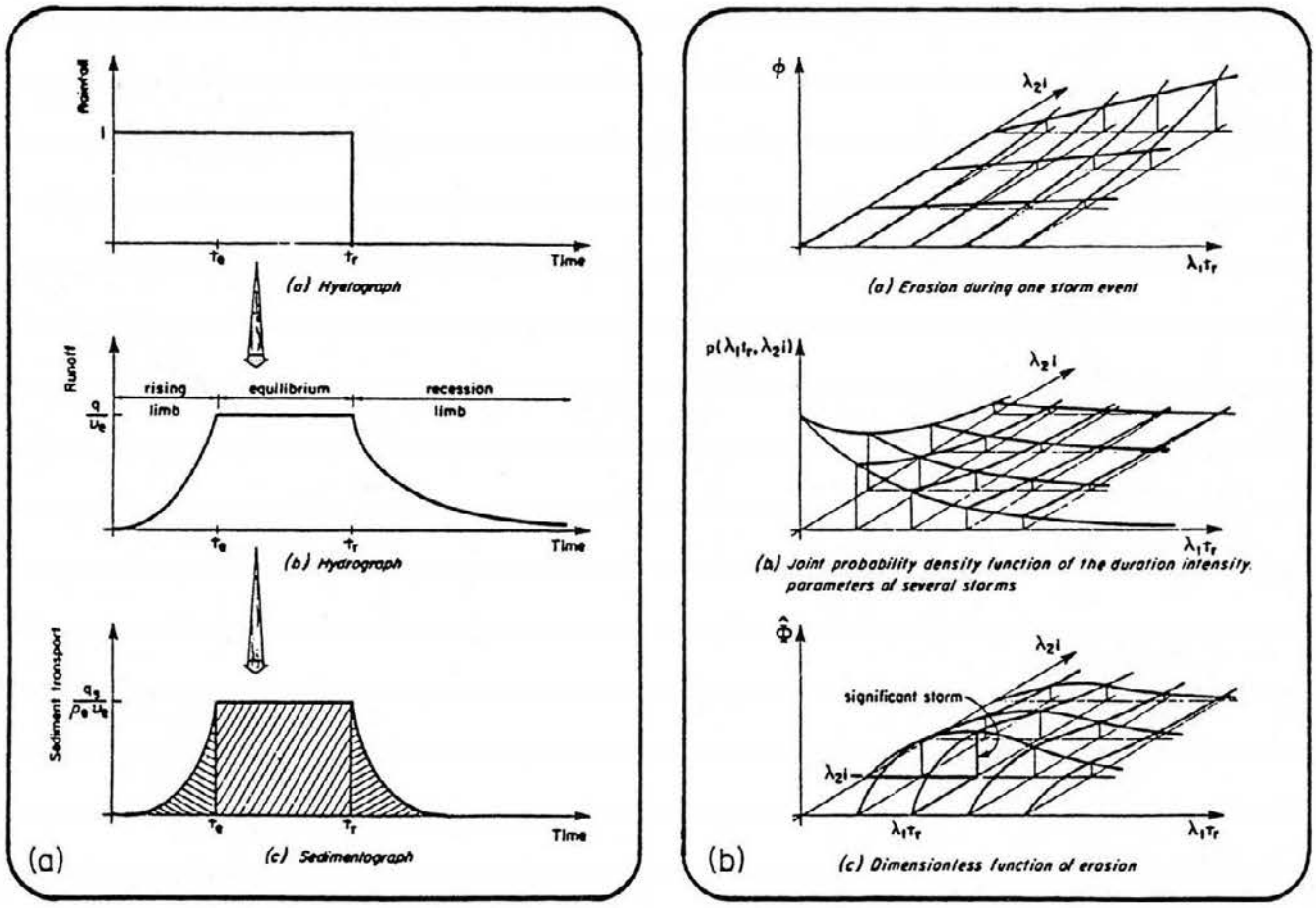

FIG. 3 (*a*). Rainfall erosion analysis. (*b*) Computation of the dimensionless function of erosion.

channels develop in the snowpack and flow conditions gradually degenerate into open channel flows.

Sediment yield during rainfall

As suggested by Todorovic (1968) and Eagleson (1978), point rainfall can be described as a random series of discrete storm events of finite duration and constant intensity. The two principal variables are the storm duration t_r and intensity i. These two variables have been shown by Eagleson (1978) and Julien (1982) to be nearly independent and distributed exponentially, with probability density functions $p(t_r)$ and $p(i)$ written as

$$[1] \quad p(t_r) = \lambda_1 e^{-\lambda_1 t_r}$$

and

$$[2] \quad p(i) = \lambda_2 e^{-\lambda_2 i}$$

The parameters for rainfall duration λ_1 and intensity λ_2 are evaluated for each month.

The problem of rainfall erosion on a small plot is then con-

sidered. Surface runoff is a complex phenomenon involving sheet flow and rills depending on geometry and soil conditions. For modeling purposes, it is assumed that the runoff occurs in a thin-sheet layer over an impervious surface area A_e of given length L and slope S. The resulting hydrograph is subdivided into three parts: the rising limb, the equilibrium, and the falling limb. A detailed evaluation of soil erosion for complete and partial equilibrium hydrographs schematized in Fig. 3 has been conducted at Laval University. A series expansion solution was theoretically derived (Julien 1982) and a first-order approximation is obtained when the first term of the series is considered. When applied to field problems, the authors found that the first-order approximation generally gives less than 5% discrepancy between the two computed results. Hence, the specific discharge q to calculate soil erosion is given in terms of the length L and intensity i by

$$[3] \quad q = iL$$

Dimensional analysis supports the following sediment transport capacity relationship q_s as a power function of slope S, discharge q, rainfall intensity i, and four coefficients (α, β, γ, δ):

$$[4] \quad q_s = \alpha S^\beta q^\gamma i^\delta$$

Julien and Simons (1985) discussed the evaluation of the coefficients α, β, γ, and δ using different approaches. From experimental data, Kilinc and Richardson (1973) obtained a regression-type equation and the following coefficients are recommended: $\alpha = 25\,500$, $\beta = 1.66$, $\gamma = 2.035$, and $\delta = 0$ (note q_s in t/(m·s) and q in m^2/s). The total soil erosion by a single rainfall event $\bar{m}$ is obtained by the following equation:

$$[5] \quad \bar{m} = \frac{A_e}{L} q_s t_r$$

In this equation, the soil erosion $\bar{m}$ is a function of the surface area A_e and the duration of rainfall t_r. After substitution of [3] and [4], [5] gives

$$[6] \quad \bar{m} = A_e \alpha S^\beta L^{\gamma-1} i^{\gamma+\delta} t_r$$

This equation estimates the mass of potential soil erosion provided the rainfall duration and intensity are known.

For any rainfall event, the expected value of soil erosion is determined with regard to the variability of the rainfall intensity and duration:

$$[7] \quad M = \int_0^\infty \int_0^\infty \bar{m} p(t_r) p(i)\, dt_r di$$

After substitution of [1], [2], and [6], the integration of [7] leads to

$$[8] \quad M = A_e \frac{\alpha S^\beta L^{\gamma-1}}{\lambda_1 \lambda_2^{\gamma+\delta}} \Gamma(\gamma + \delta + 1)$$

where $\Gamma(\gamma + \delta + 1)$ is the gamma function.

The expected value of potential soil erosion for one rainfall event is a function of the distributions of rainfall duration and intensity respectively through the parameters λ_1 and λ_2. When compared with the complete series expansion solution, [8] has been shown by Julien (1982) to give accurate evaluation of soil erosion when the following criterion between physical and rainfall characteristics is verified:

$$[9] \quad \left(\frac{8gS}{K\nu_e L}\right)^{1/3} \gg \lambda_1 \lambda_2^{2/3}$$

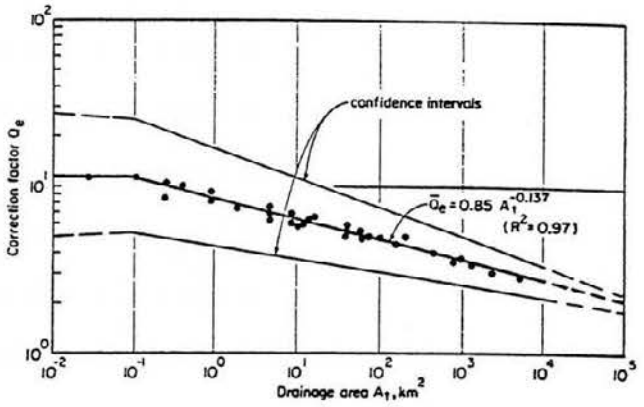

FIG. 4. Mean value and confidence limits (95%) of the correction factor Q_e vs. drainage area.

where g = gravitational acceleration, K = friction coefficient, and ν_e = kinematic viscosity of water. This criterion is largely satisfied for most conditions encountered in the field. For a given month, the expected value of the potential soil erosion $M_{\bar{\nu}}$ is proportional to the mean number of storms $\bar{\nu}$ during that period:

$$[10] \quad M_{\bar{\nu}} = M\bar{\nu}$$

The cropping management factor C of the well-known universal soil-loss equation (Wischmeier and Smith 1978) is used to reduce the potential erosion given by [10] to account for the effects of vegetation. The runoff coefficient C_r, computed from the ratio of runoff to rainfall for a given period of time allows for water losses due to interception, evapotranspiration, and infiltration. A sensitivity analysis involving the following three hypotheses has been undertaken: (1) no infiltration; (2) the runoff coefficient reduces the effective duration of rainfall; and (3) the runoff coefficient reduces the effective intensity of rainfall (or discharge). From application on four watersheds, it was concluded that the best results were obtained with the second hypothesis, and therefore the soil erosion is proportional to the runoff coefficient.

When dealing with large watersheds ($A > 500$ km^2), Julien (1979) introduced the concept of characteristic values for slope length $\bar{L}$, slope $\bar{S}$, and cropping factor $\bar{C}$. A correction factor Q_e was defined as the ratio of soil erosion computed with the characteristic parameters, to the soil erosion computed using the tedious process of subdividing the watershed into small units. Several thousand values of the correction factor were determined and the relationship shown in Fig. 4 ($Q_e = 0.85 A_t^{-0.137}$ is recommended (Julien 1979; Frenette and Julien 1986).

The sediment yield is, by definition, equal to the product of total erosion and the sediment–delivery ratio C_s. Further discussion on the evaluation of the parameters $\bar{L}$, $\bar{S}$, $\bar{C}$, and C_s is given in the section on Applications. The monthly sediment yield Q_{sp} in kt is

$$[11] \quad Q_{sp} \simeq 994 C_s \bar{C} C_r A_t \frac{\bar{\nu} \alpha \bar{S}^\beta \bar{L}^{\gamma-1}}{Q_e \lambda_1 \lambda_2^{\gamma+\delta}} \Gamma(\gamma + \delta + 1)$$

This equation is used in the model LAVSED-II for predicting the sediment yield from large watersheds during the rainfall season.

Sediment yield during snowmelt

The relationship of sediment yield to runoff was investigated

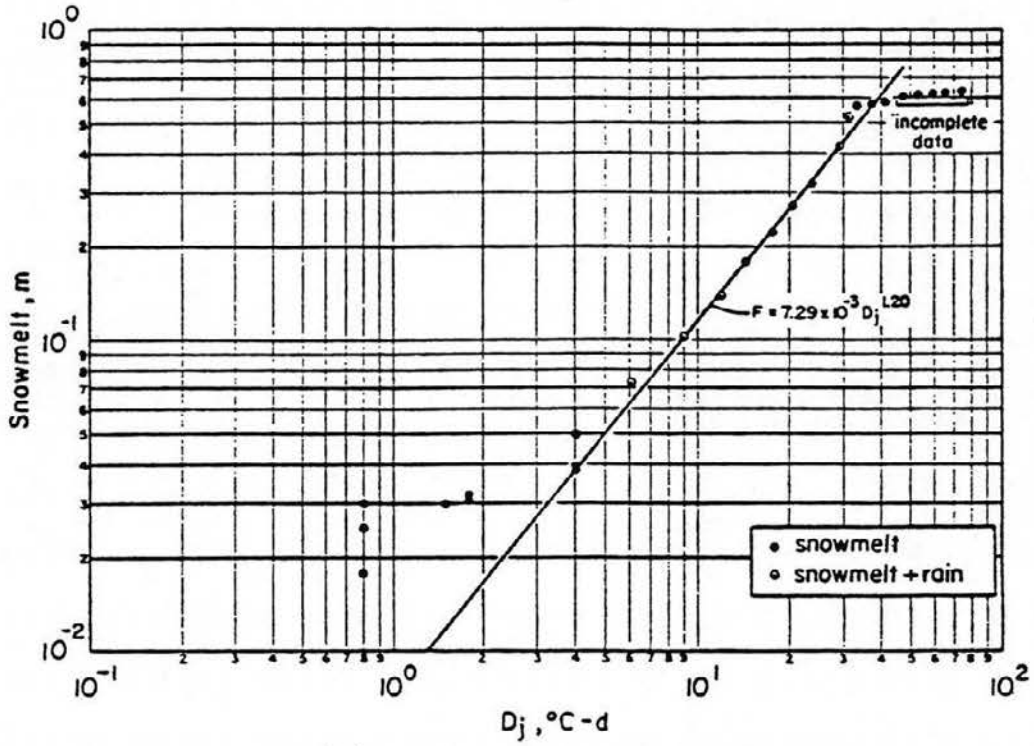

(a) Number of degree-days, Dj

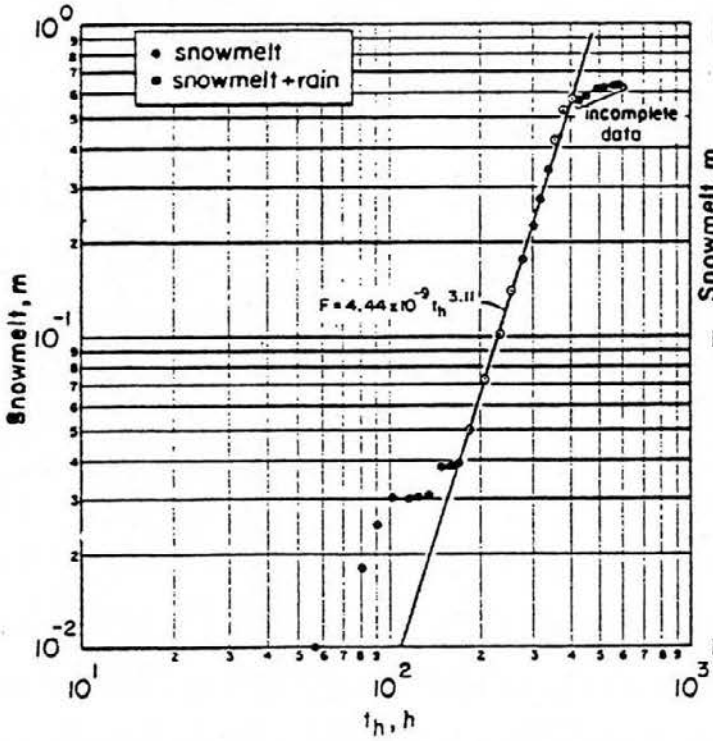

(b) Cumulative time when the temperature is above 0 °C, t_h

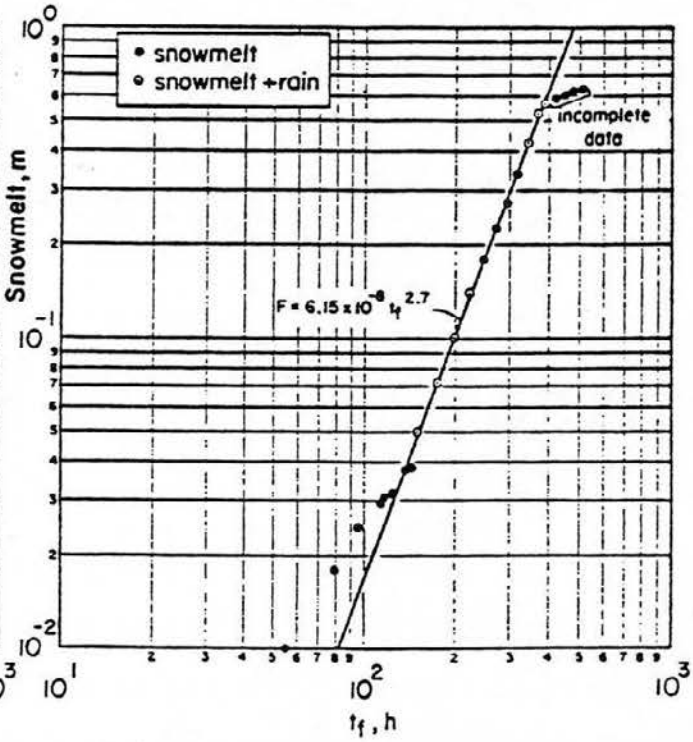

(c) Cumulative time of snowmelt, t_f

FIG. 5. Cumulative snowmelt as a function of three parameters.

for large watersheds during the snowmelt period. Snowmelt data from a small experimental plot were available for the analysis. Hourly data of runoff intensity were scrutinized, and the cumulative snowmelt F was successfully correlated to three factors (see Fig. 5): (1) the cumulative number of degree-days D_j in °C · d; (2) cumulative time when the temperature is above 0°C, t_h in h; and (3) cumulative time of snowmelt t_f in s:

[12] $$F = 7.29 \times 10^{-3} D_j^{1.2}$$

[13] $$F = 4.44 \times 10^{-9} t_h^{3.11}$$

182

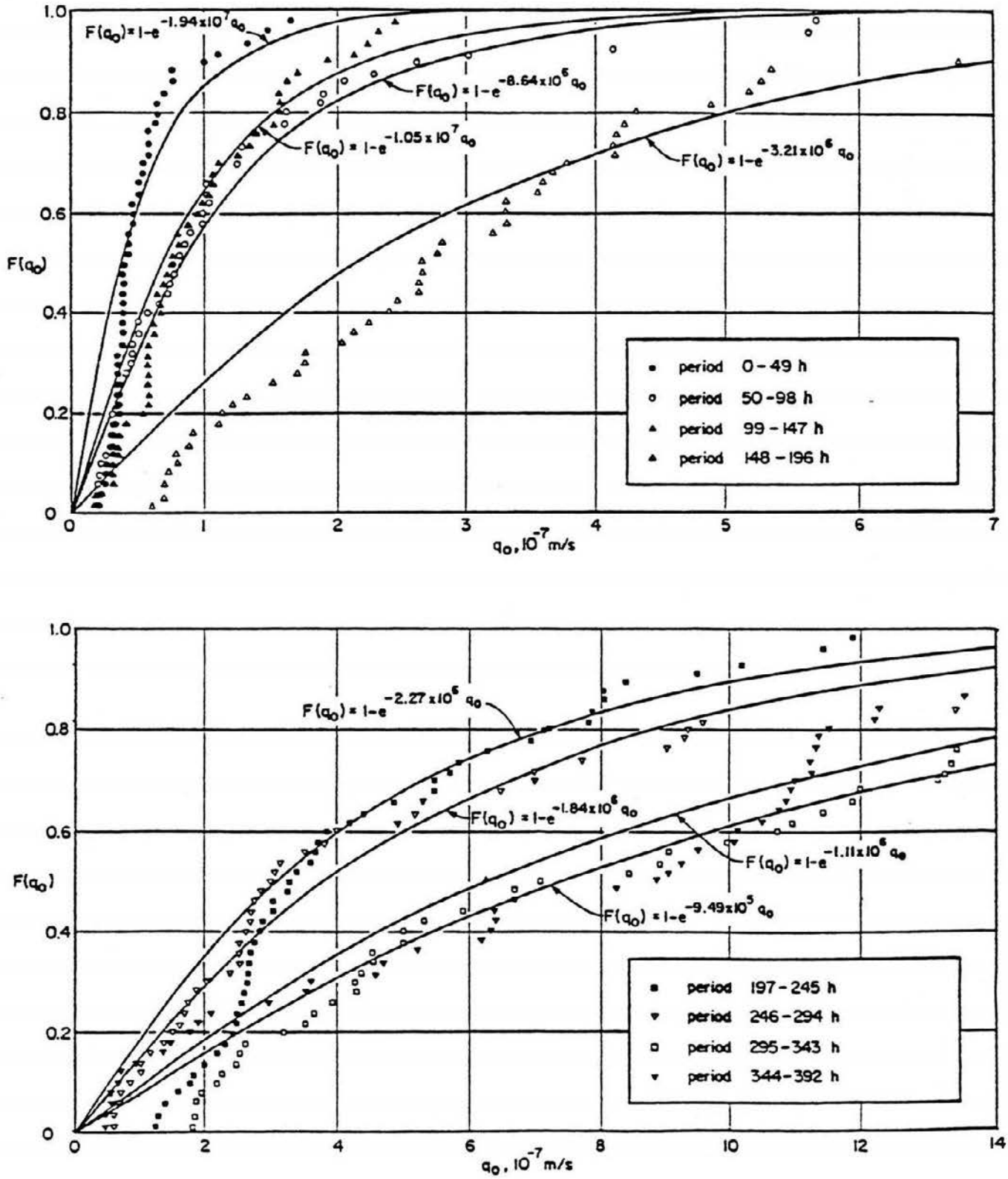

FIG. 6. Runoff distribution during snowmelt.

[14] $F = \alpha_f t_f^{\beta_f} = 1.54 \times 10^{-17} t_f^{2.7}$

where α_f, β_f are the snowmelt parameters.

Equation [14] should be given preference since it is physically sound. Either [12] or [13] is best suited to obtain F when data for t_f is not available. The first derivative of [14] gives the mean runoff intensity, which is also a function of t_f. Consequently, the two variables are not independent. The distribution functions $F(q_0)$ of the hourly runoff intensity q_0 are shown in Fig. 6. The observed data fit an exponential probability density function reasonably well, which can be written as

[15] $F(q_0) = \int_0^{q_0} p(q_0)\, dq_0 = \int_0^{q_0} \lambda_{2f}\, e^{-\lambda_{2f} q_0}\, dq_0$

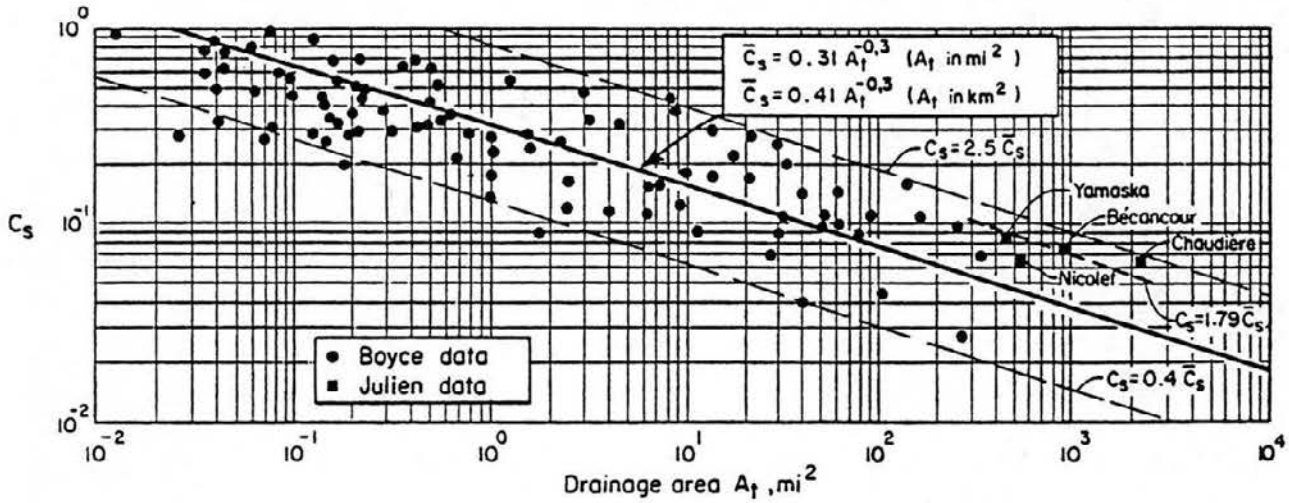

FIG. 7. Sediment–delivery ratio versus drainage area (modified after Boyce 1975).

TABLE 1. Principal characteristics of watersheds

Watershed	Area A_t (km^2)	Cropping factor $\bar{C}$	Characteristic slope $\bar{S}$	Runoff length $\bar{L}$ (m)
Chaudière	5830	0.35	0.0156	91.5
Bécancour	2340	0.40	0.0134	91.5
Nicolet	1530	0.65	0.0164	91.5
Yamaska	1260	0.15	0.0216	91.5

and

$$[16] \quad \lambda_{2f} = \frac{dt_f}{dF}$$

When [14] is substituted into [16], the snowmelt parameter λ_{2f} decreases as the melting period progresses. The influence of thawing of the frozen ground has been included in the equations. The effective surface on which soil erosion occurs is assumed to be proportional to the relative time of melting defined as follows:

$$[17] \quad A_f = A_e \left(\frac{t_f}{T_f}\right)^{\gamma_f}$$

in which t_f = time of melting, T_f = total time of melting, and γ_f = thawing parameter (assumed equal to unity). Sensitivity analysis showed that soil erosion is not very sensitive to γ_f. The cumulative soil erosion during snowmelt M_f is

$$[18] \quad M_f = \int_0^{t_f} \int_0^{\infty} \frac{A_f}{L} \alpha S^{\beta} q_0^{\gamma} L^{\gamma} \lambda_{2f}\, e^{-\lambda_{2f} q_0}\, dq_0\, dt_f$$

After integration, this equation transforms to

$$[19] \quad M_f = \frac{A_e \alpha S^{\beta} L^{\gamma-1} (\alpha_f \beta_f)^{\gamma}}{\gamma_f + \gamma\beta_f - \gamma + 1} \left(\frac{F}{\alpha_f}\right)^{(\gamma\beta_f - \gamma + 1)/\beta_f} \times \left(\frac{F}{F_t}\right)^{\gamma_f/\beta_f} \Gamma(\gamma + 1)$$

in which F_t is the total snowmelt.

Analysis of erosion on large watersheds indicates that the cumulative erosion E_f can be estimated when the vegetation $\bar{C}$ and the parameters $\bar{S}$, $\bar{L}$, and Q_e are considered:

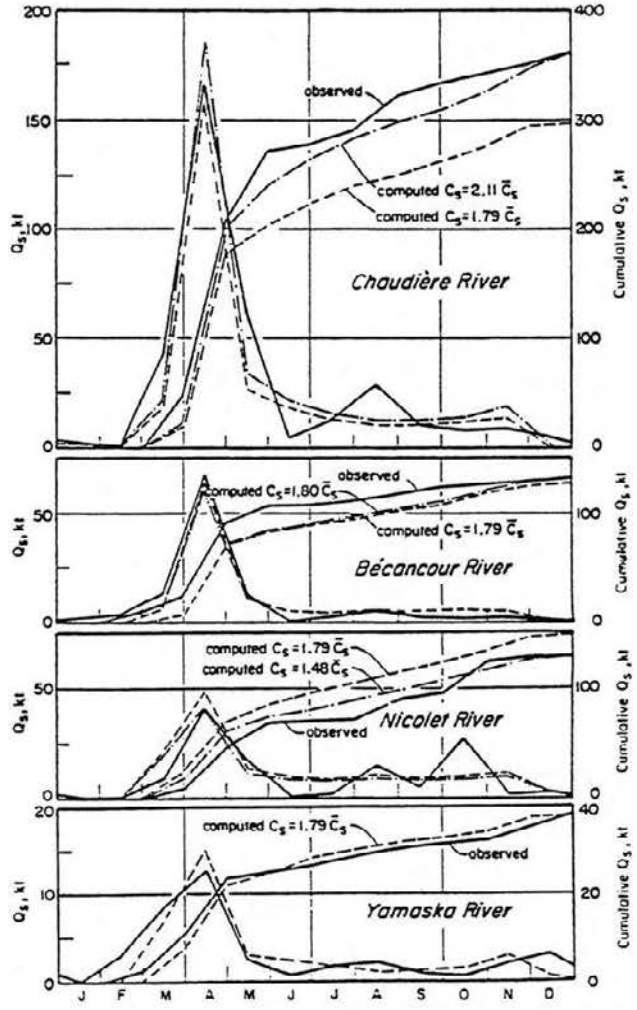

FIG. 8. Computed sediment yield and observed suspended load.

$$[20] \quad E_f = 1000\, \frac{\bar{C}}{Q_e} \frac{A_t \alpha \bar{S}^{\beta} \bar{L}^{\gamma-1} (\alpha_f \beta_f)^{\gamma}}{\gamma_f + \gamma\beta_f - \gamma + 1} \times \left(\frac{F}{\alpha_f}\right)^{(\gamma\beta_f - \gamma + 1)/\beta_f} \left(\frac{F}{F_t}\right)^{\gamma_f/\beta_f} \Gamma(\gamma + 1)$$

After substitution of the parameters α, β, γ, α_f, β_f, γ_f, and

TABLE 2. Data required for the model LAVSED-II

Item	Jan.	Feb.	Mar.	Apr.	May	June	July	Aug.	Sept.	Oct.	Nov.	Dec.
	Month											
(*a*) Meteorological data at Québec												
Rainfall (mm)	12.4	9.2	22.4	57.6	80	101.8	107.8	102.6	105.6	78.2	66.6	25.4
Percent time of rainfall	0.9	1	2.2	10.5	11.5	11.8	9.8	12.1	12.1	13.1	12.9	3.3
Snowfall (mm of water)	75.2	70.2	48	16.8	1	0	0	0	0	4.4	33.2	78
Percent time with temperature above 0°C	2.9	3	24.8	77.1	98	100	100	100	99.4	91.2	52.5	10.9
(*b*) Runoff and sediment yield from the Chaudière River												
Runoff (mm)	20.4	13.6	48.7	184.6	112.5	42.3	26.2	27.2	25.5	42.5	49	42.9
Sediment yield* (kt)	2.6	0.2	42	167	63	4.9	14	30	12	10	10	6.9

*The sediment yield data were used for the validation of the model LAVSED-II but are not required for simulation of the sediment yield.

TABLE 3. Comparison of precipitation data between Montréal and Québec

Location	Jan.	Feb.	Mar.	Apr.	May	June	July	Aug.	Sept.	Oct.	Nov.	Dec.
	Month											
(*a*) Rainfall (mm)												
Montréal	22.8	14.8	34.2	64.0	65.6	83.0	85.0	86.6	79.8	73.6	65.8	31.8
Québec	12.4	9.2	22.4	57.6	80.0	101.8	107.8	102.6	105.6	78.6	66.6	25.4
(*b*) Snowfall (cm)												
Montréal	54.8	58.2	35.0	8.6	1.6	—	—	—	0.2	1.6	22.2	57.4
Québec	75.2	70.2	48.0	16.8	1.0	—	—	—	—	4.4	33.2	78.0

Q_e, one thus obtains

$$[21] \quad E_t \simeq 30.7 A_t^{1.137}\, \bar{C}\, \bar{S}^{1.66}\, \bar{L}^{1.035} F^{1.65} \left(\frac{F}{F_t}\right)^{0.37}$$

Finally, the cumulative sediment yield during snowmelt Q_{sf} is obtained from the total erosion E_t and the sediment–delivery ratio C_s as:

$$[22] \quad Q_{sf} \simeq 30.7 C_s A_t^{1.137}\, \bar{C}\, \bar{S}^{1.66}\, \bar{L}^{1.035} F^{1.65} \left(\frac{F}{F_t}\right)^{0.37}$$

Equations [22] and [11] are used in the model LAVSED-II to estimate the average sediment yield in northern streams from the main physical characteristics of the watersheds and the variable parameters of rainfall and snowmelt.

Applications

Four watersheds, tributaries of the St. Lawrence River, were analyzed for validation. The principal characteristics of these watersheds are shown in Table 1. The drainage area was obtained from topographic maps (1:250 000). The cropping factor $\bar{C}$ was determined from topographic maps (1:50 000) and from forest and agricultural maps (1:250 000). The characteristic slope was computed from the relationship $\bar{S} = \Delta H/1000\sqrt{A_t}$, in which ΔH is the difference of level between extreme elevations obtained from topographic maps. The runoff length $\bar{L}$ is the length of sheet and rill flow on upland areas. Based on topographical maps and field observations, this length was estimated to be ~300 ft (the value $\bar{L}$ = 91.5 m was used for the computations), and was assumed constant for these watersheds. The determination of these parameters ($\bar{C}$, $\bar{L}$, $\bar{S}$) is straightforward and they were not optimized.

The data from 22 meteorological stations on the Chaudière watershed were analyzed to conclude that the data at Quebec Airport shown in Table 2 were representative of the average meteorological conditions on the Chaudière watershed. These data are obtained from the hourly data summaries for the period 1943–1970. The runoff and sediment yield data for the Chaudière watershed are also given in the same table. The runoff data extend from the period 1915–1978 while the sediment data are obtained from the measured suspended load from 1968–1976.

The computer model LAVSED-II based on [11] and [22] predicts monthly sediment yield. The sediment–delivery ratios are computed from the total soil erosion and the observed sediment yield in the river. In Fig. 7, the sediment–delivery ratios are plotted as a function of the drainage area. These results are in good agreement with those from smaller watersheds and a regional trend $C_s = 1.79\bar{C}_s$ is expected to provide a better estimate than $\bar{C}_s$ for these watersheds.

The computed and observed sediment yields are shown in Fig. 8. The data from the nearest meteorological station (namely Québec for Chaudière and Bécancour, and Sherbrooke for Nicolet and Yamaska) were considered. Two values of the sediment-delivery ratio were used: (1) the individual value of C_s for each watershed and (2) the mean regional value given by $C_s = 1.79\bar{C}_s$. Except for the value of C_s, which is calibrated from observed data, the other parameters were not optimized. The model LAVSED-II gives very good prediction of the peak sediment yield during spring. The predicted values during the rainfall season remain within the fluctuation range; and during winter, the sediment loads are shown to be negligible.

Two watersheds were selected (Nicolet and Yamaska) for a sensitivity analysis focused on different meteorological condi-

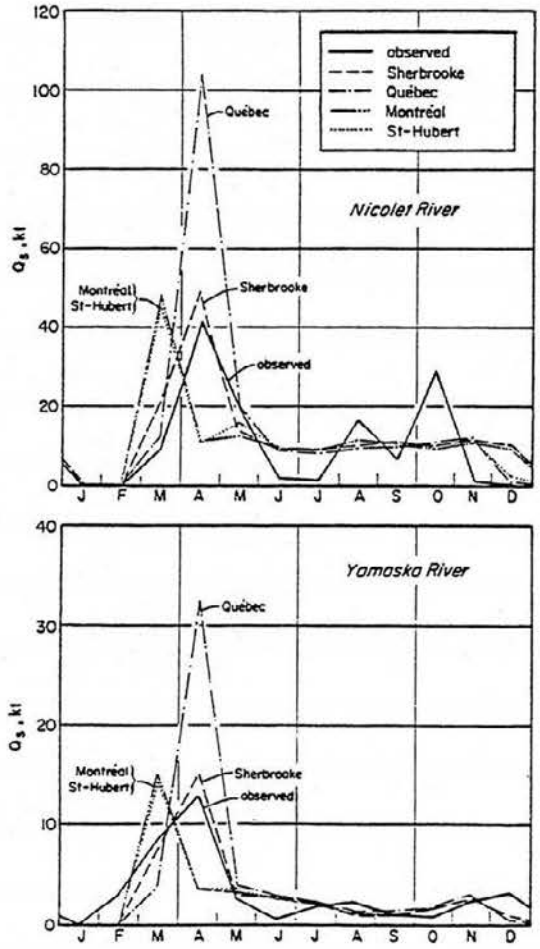

FIG. 9. Sensitivity analysis with different meteorological conditions.

tions summarized in Table 3. The regional value of C_s was used, and from the results shown in Fig. 9, the data of the nearest station give the best results for simulation, namely, the magnitude and the time of occurrence of the peak. Simulations with meteorological data from a warmer statio n (Montréal) produce an earlier peak in sediment yield while the data from a colder region (Québec) give a much higher peak in sediment yield due to the larger accumulation of snow during winter.

Conclusion

The model LAVSED-II described in this paper is well-suited for month-to-month prediction of sediment yield from northern watersheds. The model is based on the most significant physical processes of rainfall, overland flow, snowmelt runoff, soil erosion, and sediment yield. The model LAVSED-II has been successfully applied to several watersheds and the results are shown in Figs. 8 and 9. The model is also applicable to watersheds for which no suspended data are available. In this case the order of magnitude of the sediment yield can be predicted from physical parameters and meteorological and runoff data. Further developments on watershed modeling of snowmelt erosion and sediment yield are currently under preparation at Laval University.

Acknowledgments

This paper is based on studies carried out at the Department of Civil Engineering at Laval University. The authors wish to thank D. M. Hartley, Dr. D. B. Simons, Dr. R. M. Li, G. O. Brown, and J. S. O'Brien from Colorado State University for their helpful and constructive comments in the revision of this paper.

EAGLESON, P. S. 1978. Climate, soil and vegetation. 2. The distribution of annual precipitation derived from observed storm sequences. Water Resources Research, **14**(5), pp. 713–721.

BOYCE, R. 1975. Sediment routing with sediment–delivery ratios. Present and prospective technology for predicting sediment yields and sources, U.S. Department of Agriculture, ARS-S-40, pp. 61–65.

FRENETTE, M., and JULIEN, P. Y. 1986. LAVSED-I — Un modèle pour prédire l'érosion des bassins et le transfert de sédiments fins dans les cours d'eau nordiques. Canadian Journal of Civil Engineering, **13**, this issue.

JULIEN, P. 1979. Érosion de bassin et apport solide en suspension dans les cours d'eau nordiques. Thèse de maîtrise, Département de génie civil, Université Laval, Québec, P.Q., 186 p.

——— 1982. Prédiction d'apport solide pluvial et nival dans les cours d'eau nordiques à partir du ruissellement superficiel. Thèse de doctorat, Département de génie civil, Université Laval, Québec, P.Q., 240 p.

JULIEN, P. Y., and SIMONS, D. B. 1985. Sediment transport capacity of overland flow. Transactions of the ASAE, **28**(3), pp. 755–762.

KILINC, M., and RICHARDSON, E. V. 1973. Mechanics of soil erosion from overland flow generated by simulated rainfall. Hydrology paper No. 63, Colorado State University, Fort Collins, CO, 54 p.

TODOROVIC, P. 1968. A mathematical study of precipitation phenomena. Report CER67-68PT65, Engineering Research Center, Colorado State University, Fort Collins, CO, 123 p.

WISCHMEIER, W. H., and SMITH, D. D. 1978. Predicting rainfall-erosion losses from cropland east of the Rocky Mountains. U.S. Department of Agriculture Handbook No. 537, 58 p.

List of symbols

A_e	surface area of a plot
A_f	effective surface area during snowmelt
A_t	drainage area of a watershed
C	cropping management factor
$\bar{C}$	characteristic cropping factor of a watershed
C_r	runoff coefficient
C_s	sediment–delivery ratio
D_j	cumulative degree-days, °C·d
E_f	cumulative erosion over a large surface
F	cumulative snowmelt
F_t	total snowmelt
$F(q_0)$	distribution function of snowmelt runoff
g	gravitational acceleration
i	rainfall intensity
K	friction coefficient
L	plot length
$\bar{L}$	characteristic slope length of a watershed
$\bar{m}$	soil erosion during a single rainfall event of intensity i and duration t_r
M	expected value of soil erosion by a rainfall event
M_f	cumulative soil erosion during snowmelt
$M_{\bar{v}}$	expected value of soil erosion during a given period
$p(i)$	probability density function of rainfall intensity
$p(q_0)$	probability density function of hourly snowmelt intensity
$p(t_r)$	probability density function of rainfall duration
q	overland flow discharge
q_0	hourly snowmelt intensity

q_s	potential sediment discharge
Q_e	correction factor for grid size
Q_{sf}	cumulative sediment yield during snowmelt
Q_{sp}	monthly rainfall sediment yield
S	slope of a plot
$\bar{S}$	characteristic slope of a watershed
t	time
t_f	cumulative time of snowmelt
t_h	cumulative time when the temperature is above 0°C
t_r	rainfall duration
T_f	total time of snowmelt
α, β, γ, δ	coefficients of the erosion equation
α_f, β_f, γ_f	snowmelt parameters
λ_1	rainfall duration parameter
λ_2	rainfall intensity parameter
λ_{2f}	snowmelt intensity parameter
ν_e	kinematic viscosity of water
$\bar{\nu}$	average number of storms during a period

International Journal of Sediment Research
No. 1, November, 1987

COMPUTER MODELING OF SOIL EROSION AND SEDIMENT YIELD FROM LARGE WATERSHEDS

Frenette, M.[1] Julien, P.Y.[2]

ABSTRACT

Mathematical modeling techniques for predicting soil losses by overland flow and sediment yield from large watersheds are reviewed and three models are presented.

1) A daily simulation model is first discussed. The regression analysis of suspended load and discharge data gives the best results when the analysis of residuals is included.

Mathematical models based on physical characteristics of watersheds figure among the most powerful tools because the rate of sediment transport can be predicted for alternative watershed conditions. Two mathematical models, LAVSED-I and LAVSED-II (LAVal SEDimentological model), were developed for a long-term simulation of sedi-

---

1. Professor, Dept. of Civil Engineering, Laval Univ., Quebec, Canada.
2. Fac. Affil., Dept. of Civil Engineering, Colorado State Univ., Fort Collins, Colorado and former graduate student at Laval University.

Received August 16, 1985
Note: Discussion open until December 31, 1988

ment sources and yields based on topography, precipitation, soil and vegetation.

2) The model LAVSED-I uses the well-known Universal Soil Loss Equation. Maps of the mean annual soil-loss are plotted and a case study is discussed.

3) The model LAVSED-II predicts the wash load in streams as a function of the rate of sediment transport from upland areas. A stochastic component for precipitation and snowmelt runoff is combined with deterministic relationships for overland flow and sediment transport. The average sediment yield is predicted for each month. Validation of the model on several large watersheds in Canada shows excellent agreement between the computed sediment yield and the measured suspended load.

These computer models offer various complementary results which prove to be extremely useful, for instance in management of large watersheds, reservoir sedimentation, long-term changes in land use, soil conservation practices, effect of deforestation and reforestation.

INTRODUCTION

A large fraction of the sediments transported to rivers and reservoirs is eroded from upland areas. Soil erosion is one of the major hazards threatening the productivity of farmlands. The amount of sediment carried in the fluvial system is usually governed by the availability of the upstream supply from watersheds rather than the transport capacity of rivers. Upland erosion pollutes surface waters and often causes serious problems when deposition occurs. The physical processes governing the movement of sediments by

rainfall and snowmelt are very complex. In addition to rainfall erosion, sediment transport during snowmelt may significantly increase the sediment load in streams located in mountainous areas or in northern countries. The snow cover protects the frozen ground from soil erosion and usually melts during a relatively short period of time. In some countries, like Canada, the sediment load in rivers peaks during the spring flood while rainfall erosion controls the sediment load in streams only during summer.

This paper reviews the current techniques for predicting soil losses by overland flow and sediment yield from large watersheds. The physical processes are briefly summarized with constitutive relationships and mathematical modeling techniques for overland runoff and sediment transport are presented.

PHYSICAL PROCESSES

The rate of erosion on a particular land area can be determined from the complex interrelations of several factors. These factors include the erosive forces of rainfall and runoff, and the soil resistance to detachment and transport. The detachment and transport of soil particles under the action of raindrop impact and runoff is schematized in Fig. 1. Loose sediment particles are carried downslope by surface runoff and the sediment transport capacity is controlled by the overland flow variables. The snowmelt water percolates through the snow cover until the saturated layer is reached. As the water flows through the snowpack, micro channels develop to gradually yield free surface flow conditions.

Rainfall Characteristics

As suggested by Eagleson (1978) and Todorovic (1968), point rain-

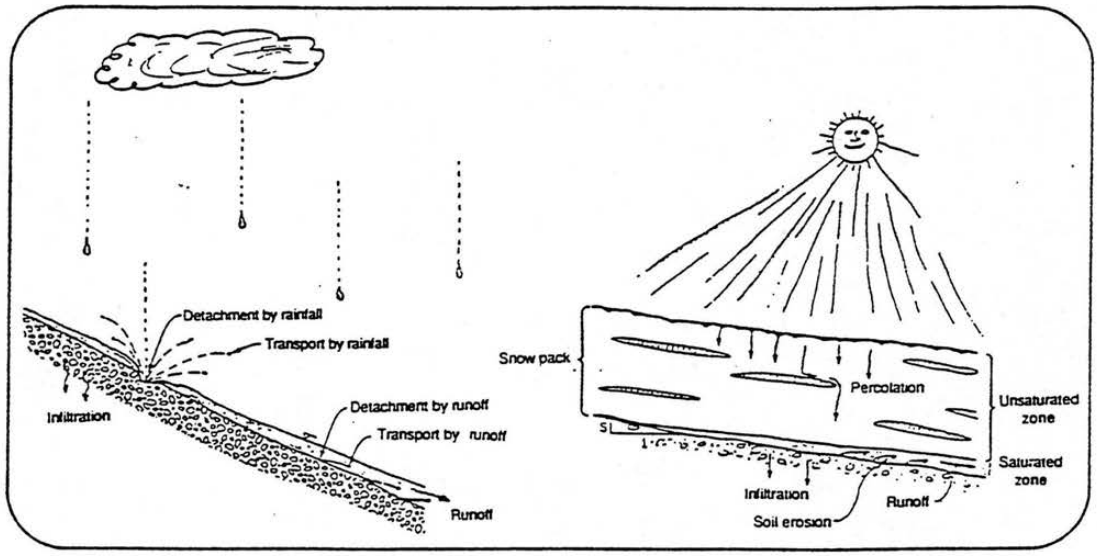

Fig. 1 Soil erosion processes during rainfall and snowmelt

fall can be described as a random series of discrete storm events of finite duration and constant intensity. The two principal variables are the storm duration t_r and intensity i. These two variables have been shown by Julien and Frenette (1985) to be nearly independent and distributed exponentially with probability density functions $p(t_r)$ and $p(i)$ written as:

$$p(t_r) = \lambda_1 e^{-\lambda_1 t_r} \quad (1)$$

and

$$p(i) = \lambda_2 e^{-\lambda_2 i} \quad (2)$$

The parameters for rainfall duration λ_1 and intensity λ_2 are evaluated for each month. Examples of distribution of rainfall duration and intensity near Québec City, Canada, are shown in Figure 2.

Overland Flow Characteristics

The rainfall-runoff relationship is then considered. After the

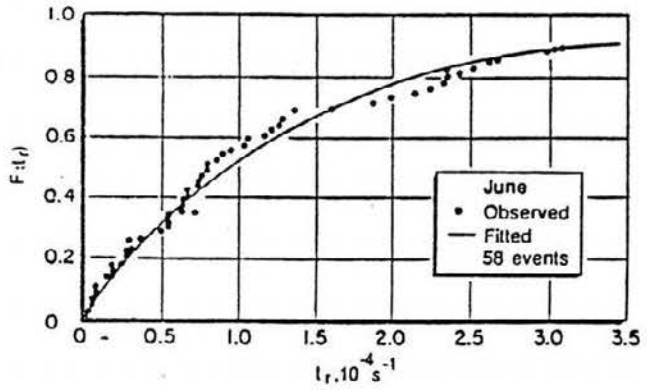

a) Duration

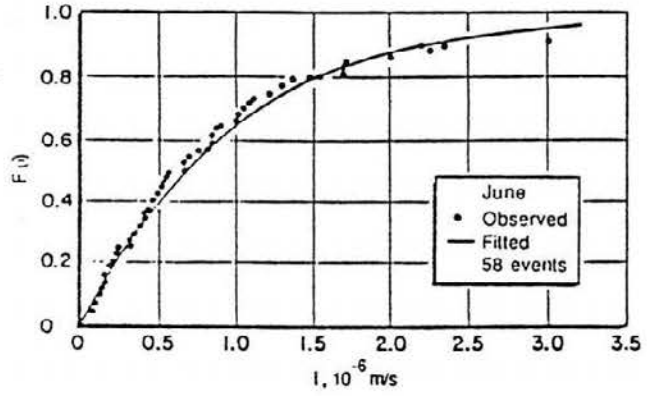

b) Intensity

Fig. 2 Exponential distribution function of rainfall characteristics

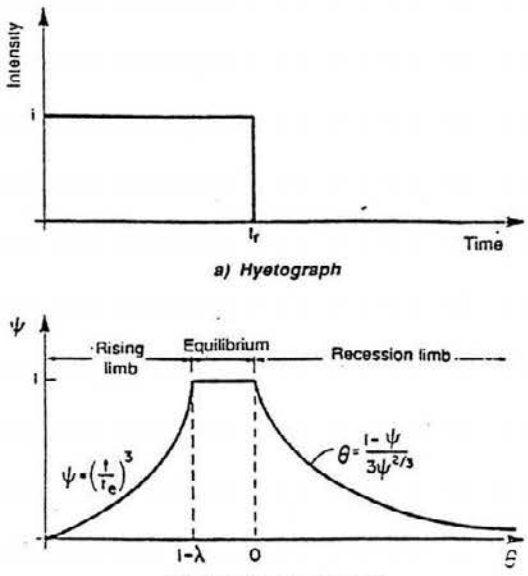

a) Hyetograph

b) Complete hydrograph

c) Partial equilibrium hydrograph

Fig. 3 Rainfall-runoff relationship

infiltration rate is subtracted from the rainfall intensity, the excess rainfall initiates surface runoff. Though the formation of rills over irregular land surface is generally observed, mathematical modeling techniques are based on the properties of sheet flows. The resulting hydrograph is subdivided into three parts: the rising limb, the equilibrium and the falling limb. A detailed analysis of soil erosion including both complete hydrographs and partial equilibrium hydrographs, schematized in Fig. 3, has been

conducted at Laval University and a theoretical solution in terms of series expansion was derived by Julien and Frenette (1985). They concluded that in most cases the first term in the series is equivalent to the complete solution. This first term representing the equilibrium flow conditions has therefore been recommended for practical use. The equilibrium flow conditions in terms of velocity $\bar{u}$, flow depth h and bed shear stress τ_o can be written as power functions of slope s and discharge q:

$$\bar{u} = \left(\frac{8g}{k\nu}\right)^{1/3} s^{1/3} q^{2/3} \tag{3}$$

$$h = \left(\frac{k\nu}{8g}\right)^{1/3} s^{-1/3} q^{1/3} \tag{4}$$

$$\tau_o = \gamma \left(\frac{k\nu}{8g}\right)^{1/3} s^{2/3} q^{1/3} \tag{5}$$

in which γ is the specific weight of the fluid; k is the friction coefficient; ν is the kinematic viscosity of the fluid; and g is the gravitational acceleration.

Snowmelt Runoff

Snowmelt runoff from an experimental plot under natural conditions was investigated at Laval University. The cumulative snowmelt F computed from hourly runoff data was correlated to three factors: 1) the cumulative number of degree-days D_j in ^oC-d; 2) the cumulative time when temperature is above 0^oC, t_h in h; and 3)the cumulative time of snowmelt t_f in sec. The following empirical relationships shown in Fig. 4 were obtained:

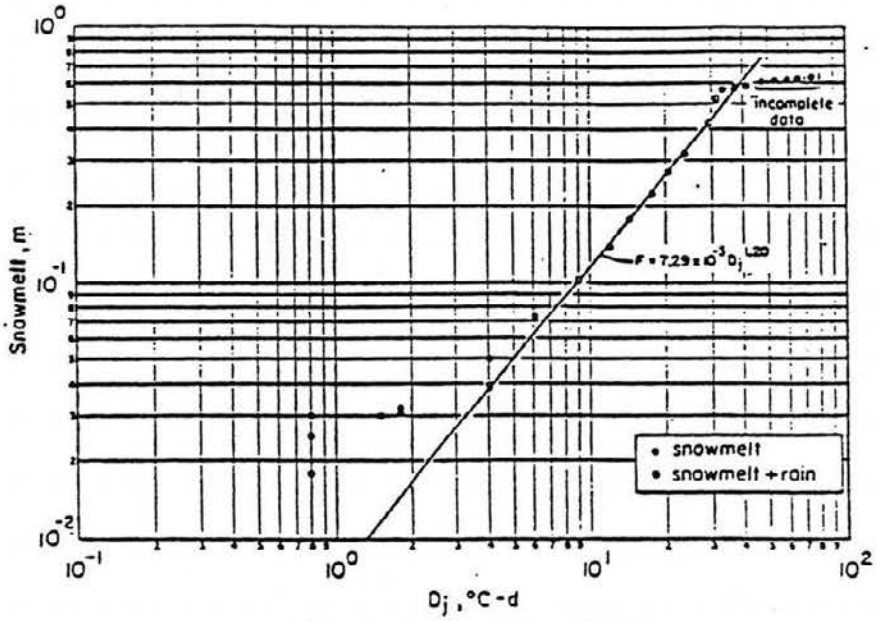

a) Number of degree-days, Dj

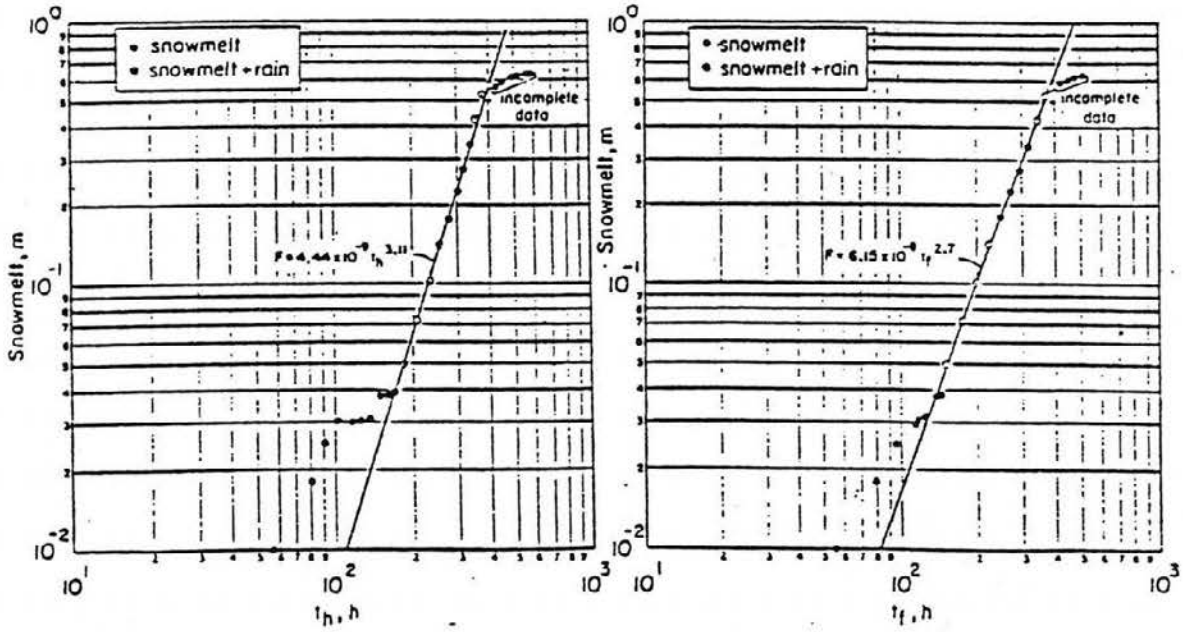

b) Cumulative time when the temperature is above 0 °C, t_h

c) Cumulative time of snowmelt, t_f

Fig. 4 Cumulative snowmelt as a function of three parameters

$$F = 7.29 \times 10^{-3} D_j^{1.2} \quad (6)$$

$$F = 4.44 \times 10^{-9} t_h^{3.11} \quad (7)$$

$$F = \alpha_f t_f^{\beta_f} = 1.54 \times 10^{-17} t_f^{2.7}; \; t_f \text{ in sec} \quad (8)$$

in which α_f and β_f are the snowmelt parameters.

Sediment Transport by Overland Flow

The erosion rate can be estimated from empirical equations such as the well-known USLE, an acronym for the Universal Soil Loss Equation (Wischmeier and Smith, 1978). The USLE gives the mean annual soil loss by rainfall erosion from sheet flow and rill erosion. This equation is a function of several factors and can be written as:

$$E = \alpha \, RKLSCP \quad (9)$$

E = annual soil loss kt/km^2
R = rainfall and runoff factor
K = soil erodibility factor
L,S = topographic factors
C = cover and management factor
p = support practice factor
α = 0.247 coefficient to transform units t/acre into kt/km^2.

These factors are evaluated from nomographs (Wischmeier and Smith, 1978). The USLE has been modified by Williams and Berndt (1975) to include the runoff variables. The modified variable R is a function of the product of the total runoff volume and the peak discharge raised to the 0.56 power.

The sediment transport capacity of overland flow depends on the

flow characteristics. The method of dimensional analysis was used to reduce the number of significant variables related to sheet erosion. As a result the sediment discharge written in a dimensional form is:

$$q_s = \alpha\, s^{\beta}\, q^{\gamma}\, i^{\delta}\, (1 - \frac{\tau_c}{\tau_o})^{\varepsilon} \qquad (10)$$

in which the coefficients, $\alpha, \beta, \gamma, \delta$ and ε can be determined experimentally. Several sediment transport equations have been transformed into the form of Eq. 10 to define the coefficients shown in Table 1. Julien (1982) and Julien and Simons (1984) found that the coefficient β varies from 1.2 to 1.9 while γ varies from 1.4 to 2.4. In the case of the Universal Soil Loss Equation the approximate values of the coefficient $\beta \cong 1.7$ and $\gamma = 1.5$ compare very well with sediment transport relationships from Table 1. The following coefficients from Kilinc and Richardson (1973) were used in the model LAVSED II for predicting the rate of sediment transport q_s in t/m.s from q in m^2/s; $\alpha = 25500$, $\beta = 1.66$, $\gamma = 2.03$ and $\delta = 0$. In the model LAVSED I, the regression equation from Kilinc and Richardson (1973) has been modified to account for vegetation, soil erodibility and the crop and management factor. The modified relationship can be written as:

$$q_s = e^{-11.65} Re^{2.05} s^{1.46} \frac{K}{0.15} CP \qquad (11)$$

in which Re is the Reynolds number and s is the slope. This relationship combines runoff and topographical factors (Re, s) with three empirical factors from the USLE (K, C, and P).

Sediment-Delivery Ratio

The rate at which eroded material is delivered to river systems and oceans is often much less than the rate at which it is eroded from

Table 1. Transformation of several erosion equations.

Eq. No.	Reference	Equation	α^a	β	γ	δ	ε
22	Musgrave (1947)	$q_s = \alpha' S^m L^n i^p$	α'	m	n	p-n	0
23	Zingg (1940)	$q_s \alpha L^{1.66} S^{1.37}$	--	1.37	1.66	-1.66	--
24	Wischmeier and Smith (1978)	$q_s \alpha L^{1.5} (.00076S^2 + .0053S + .0076)$	--	≅1.7	1.5	-1.5	--
25	Meyer and Monke (1965)	$q_s \alpha L^{1.9} S_o^{3.5}$	--	3.5	1.9	-1.9	--
26	Young and Mutchler (1969)	$q_s \alpha L^{2.24} S^{0.74}$	--	0.74	2.24	-2.24	--
27	Li et al. (1973)	$q_s = \alpha' \int_o^L \tau_o^2 dx$	$3\alpha' \frac{\gamma^2}{5}\left(\frac{K\nu}{8g}\right)^{2/3}$	1.33	1.67	-1	0
28	Komura (1983)	$q_s \alpha q^{11/8} i^{1/2} S^{1.5}$	--	1.5	1.38	0.5	0
29	Kilinc (1972)	$q_s = e^{2.05}(\tau_o - \tau_c)^{2.78}$	$e^{2.05} \frac{\gamma^{2.78}}{} \left(\frac{K\nu^2}{8g}\right)^{0.93}$	1.86	0.93	0	2.78
30	Kilinc (1972)	$q_s = e^{0.122}((\tau_o - \tau_c)\bar{u})^{1.67}$	$e^{0.122} \gamma^{1.67}$	1.67	1.67	0	1.67
31	Kilinc (1972)	$q_s = e^{-3.17} \bar{u}^{3.625}$	$e^{-3.17} (\frac{8g}{K\nu_e})^{1.21}$	1.21	2.42	0	0
32	Kilinc (1972)	$q_s = e^{1.24} \bar{u}^{4.67} Re^{-0.878}$	$e^{1.24} \nu^{0.878} (\frac{8g}{K\nu})^{1.56}$	1.56	2.24	0	0
33	Kilinc (1972)	$q_s = e^{-11.6} Re^{2.05} S^{1.46}$	$e^{-11.6} \nu^{-2.05}$	1.46	2.05	0	0
34	Kilinc (1972)	$q_s = e^{11.7} q^{2.035} S^{1.66}$	$e^{11.7}$	1.66	2.03	0	0

[a]Sediment discharge in pounds per ft-sec.

the land surface. The bulk of sediment is deposited at intermediate locations wherever the runoff waters are insufficinet to sustain transport. The percentage of sediment delivered from the erosion source, including gully erosion and streambank erosion, to any specified downslope location defines the sediment-delivery ratio. There are no generalized delivery relationships applicable to every situation. The decrease in sediment-delivery ratio with increasing drainage area was observed for most locations by several researchers.

COMPUTER MODELING TECHNIQUES

To simulate the combined processes of rainfall-runoff and sediment runoff, Negev (1967) developed a sediment model coupled with the Stanford Watershed Model IV. The Negev Model can be considered as an extension of the sediment-rating curve approach. More recently, Simons et al. (1982) developed a computer program based on physical processes to route water and sediments from relatively small watersheds. The model MULTSED simulates single storm events and works best when base flow is relatively small. Sediment is routed by size fractions and several alternatives can be quickly evaluated by altering the appropriate physical parameters. The model CREAMS (Knisel, 1980) has been developed by the Staff of the Science and Education Administration-Agricultural Research to evaluate nonpoint source pollution for field-scale areas.

Stochastic models for predicting sediment yield have been extended by Woolhiser and Todorovic (1974) without extensive testing against field data. The mathematical modeling techniques developed at Laval University can be classified as follows:

a) Regression models based on measured sediment load and discharge

on a daily basis,

b) Empirical techniques based on the principal characteristics of watersheds,

c) Modeling techniques combining stochastic rainfall processes and deterministic runoff and sediment transport.

These models have been used extensively on several large watersheds in the province of Quebec, Canada (see Fig. 5).

Models Based on Sediment Load and Discharge Data

Sediment discharge in a stream is commonly evaluated by integration of the product of depth-integrated concentration and unit discharge along the channel width. The daily sediment load is then estimated from the product of the average sediment concentration by the total daily volume of water. If the sediment discharge or the concentration is plotted against the water discharge, a power relationship can be fitted through the data:

$$Q_s = \alpha Q_l^{\beta} \tag{12}$$

in which α and β are obtained by regression analysis. Hysteresis effects between discharge and concentration, seasonal variation, inaccuracies in flow and sediment measurements and variability in the wash load may explain the scatter of points on the sediment transport graph. Better results may sometimes be achieved when sufficient data is available and a regression analysis is made for each month. Rising and falling parts of each hydrograph can also be analyzed separately. For a given discharge, higher sediment discharge rates are generally observed during the rising limb of the hydrograph. Streambank erosion effects can sometimes be separated from upland sediment sources. Snowmelt erosion rates can be compared to rainfall erosion rates. Examples are given in

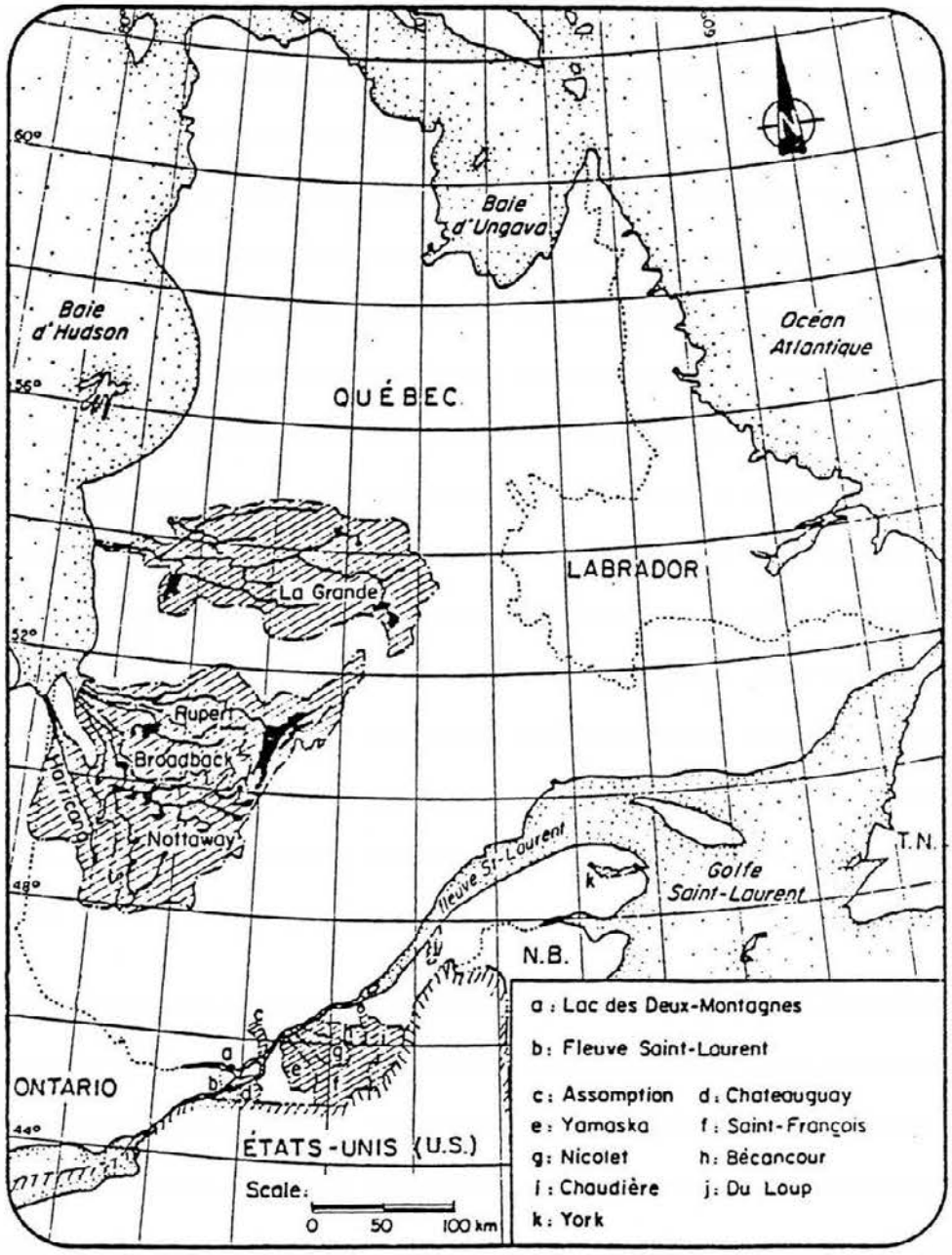

Fig. 5 Location of watersheds

Figures 6, 7, and 8.

The analysis of measured sediment load also gives the sediment yields of watersheds for consecutive years and extreme sediment loads can be assessed. However, short-term predictions of the

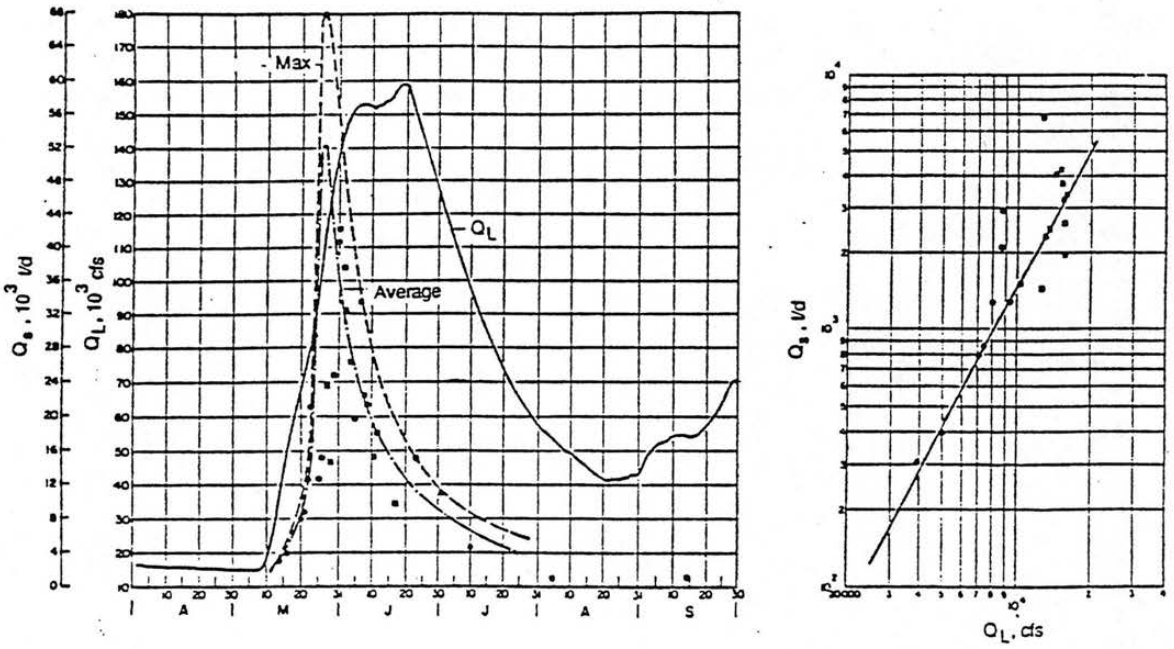

Fig. 6 Suspended load in La Grande River, 1974

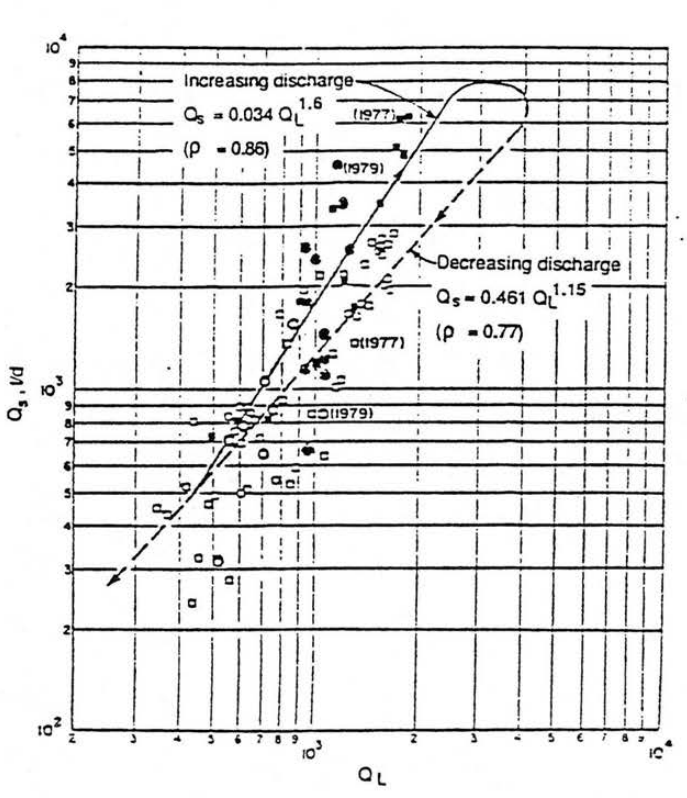

Fig. 7 Sediment rating curves, Bell River, 1977-1979

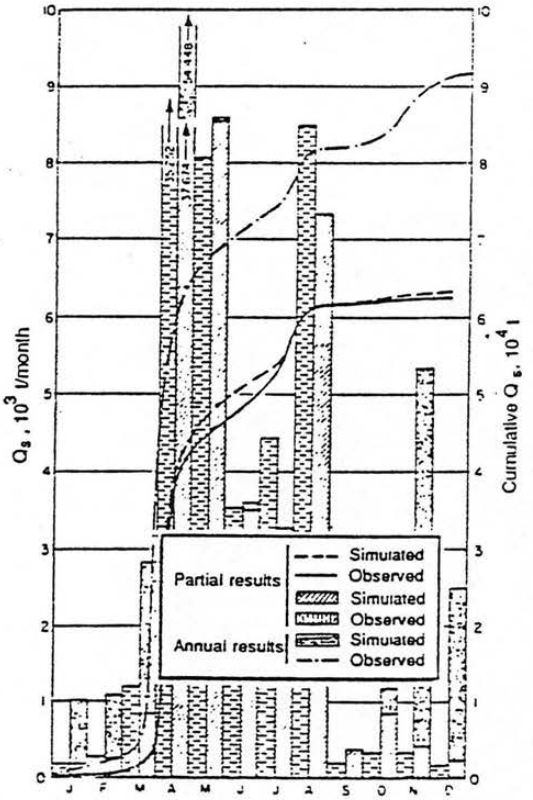

Fig. 8 Sediment loads in the Chateauguay River, 1972

sediment load lack accuracy unless the residuals are considered in the analysis. Daily sediment load can be predicted from one of the following two methods: a linear model and a nonlinear model.

a) Linear modeling of daily sediment load

The sediment load is assumed to have a linear relationship with water discharge. The best relationship (Frenette et al.,1974; Frenette and Nzakimuena, 1976) found for several rivers in Canada is:

$$C_{i+1} = \alpha_0 + \alpha_1 C_i + \alpha_2 Q_{i+1} + \alpha_3 Q_i + \bar{S}_k A^* \qquad (13)$$

in which

C_{i+1}	sediment concentration of day i+1 in mg/L
C_i	sediment concentration of day i in mg/L
Q_i	water discharge of day i in ft^3/s
Q_{i+1}	water discharge of day i+1 in ft^3/s
$\alpha_{0,1,2,3}$	multiple linear regression coefficients
A^*	random numbers following a normal distribution N (0,1)
$\bar{S}_k$	standard deviation of residuals in class k
k	class to which the discharge Q_{i+1} belongs

For simulation purposes the variance was modified for different classes of water discharge since for this linear model, the third and fourth moments of the distribution of residuals are significantly high.

b) Nonlinear modeling of daily sediment load

This nonlinear modeling technique can be written in the general form with unknown exponents as:

$$C_{i+1} = C_i^{\alpha_1} \left(\frac{Q_{i+1}}{Q_i}\right)^{\alpha_2} e^{\alpha_0 + \bar{S}_k A^* + \bar{E}_k} \qquad (14)$$

in which $\bar{E}_k + \bar{S}_k A^*$ is the logarithm of the residual simulated. The variables $\bar{E}_k$ and $\bar{S}_k$ represent the mean value and the standard variation of the residual for the class k.

The daily sediment load is computed from the following relationship:

$$Q_{s_{i+1}} = 0.0027\, Q_{i+1} C_{i+1} \qquad (15)$$

The agreement between computed and observed sediment load is shown in Figure 9 for two rivers in Canada: Chaudière River, 1969-74 and York River, 1973-74.

These two models reflect the importance of peak discharge in sediment transport. The nonlinear model has been shown to be better suited for predicting suspended load. The main advantage of this model lies in its direct relationship with observed sediment data. Homogeneity of water and sediment data are assumed and the sediment transport rate is not related to the physical characteristics of watersheds. This methodology is therefore not appropriate for watersheds and river systems under significant modifications in land use.

Model LAVSED-I Based on the Characteristics of Watersheds

In this model (Frenette and Julien, 1984) the sediment yield from watersheds is predicted as a function of the sediment sources from upland areas. Such models are applicable when upland erosion is the major source of sediments in the river system. A watershed is subdivided in small homogeneous unit areas of the order of one hectare. Each parameter influencing the rate of soil erosion must be considered and the evaluation of each unit cell is required. The following variables must be determined: climate (rainfall, snow),

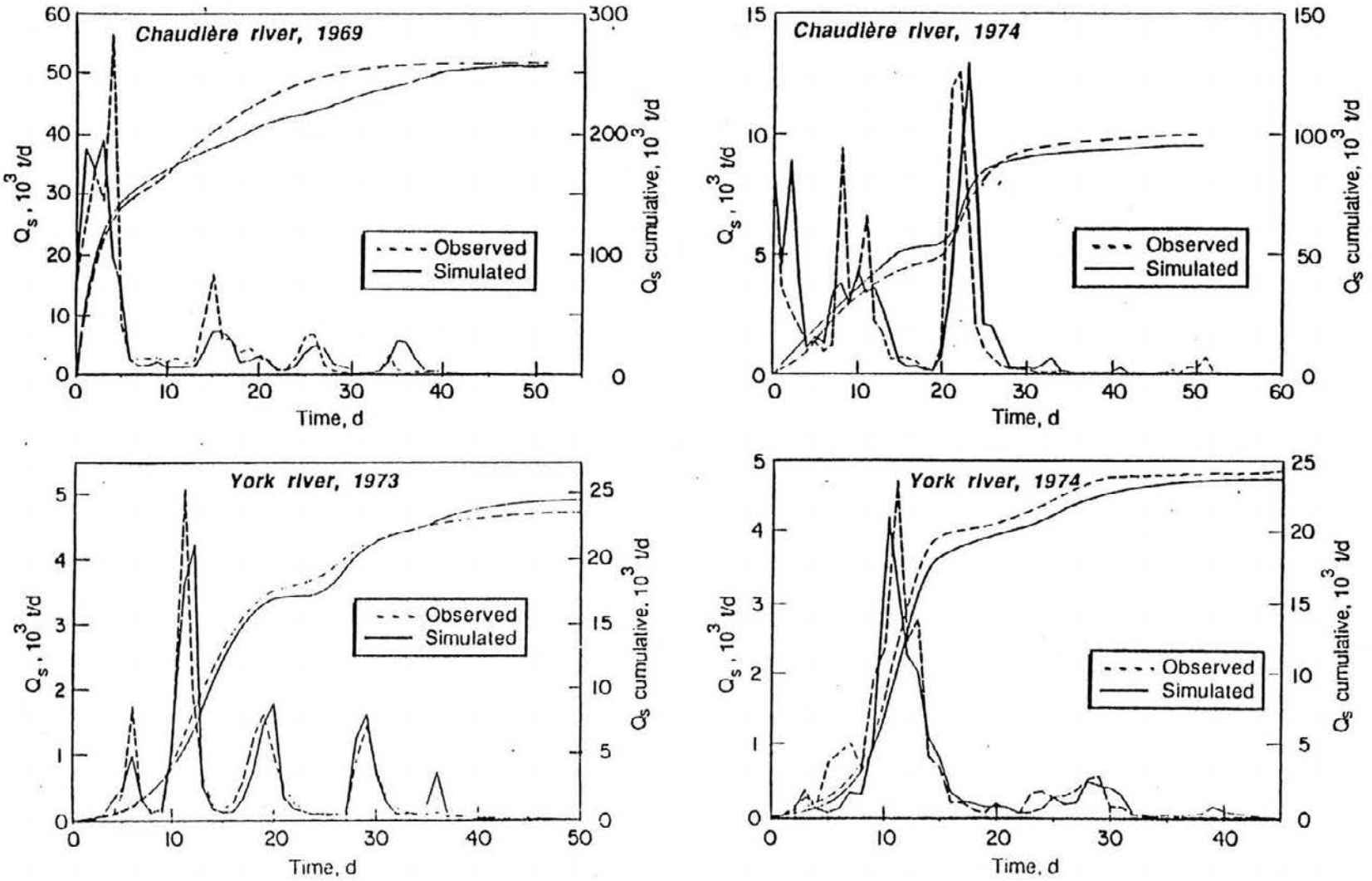

Fig. 9 Daily simulation of the sediment loads in the Chaudière and York Rivers, Canada

topography, soil type, vegetation (trees, shrubs and grass), land use, and runoff characteristics. In many instances these data are available in reports, maps and raw data on meteorology, geology, soil science, topography, forestry, and hydraulics. This information may be completed with LANDSAT, aerial photographs and field trips.

The computation of soil erosion from large watersheds can be handled easily with computers. A fixed square grid system is superimposed on the watershed to define the plan geometry of each unit cell. Appropriate data in terms of meteorology, runoff, topography, soil type, vegetation management practice must be coded for the computerized evaluation of the mean annual soil erosion under natural conditions. Potential erosion rates can be simulated with the sediment yield from the watershed. The basic information on the rate of soil erosion and sensitivity to soil erosion under various hypothetical land use practices are computed with the sediment yield in the river system. The example of the Chaudiere River in Canada (Fig. 10) has been selected to illustrate the use of this model. The total drainage area of the watershed is 6684 km^2, and a sediment gauging station is located near the mouth of the river (A= 5830 km^2). The following four phases are considered for modeling:

a) Analysis of physical and meteorological data for each unit cell of the watershed,
b) Influence of the grid size on soil erosion calculations,
c) Sediment transfer on the watershed,
d) Prediction of actual and potential erosion rates and sediment yield from the watershed.

a) The use of small unit areas of one hectare would require nearly a miliion cells to cover the entire watershed. Obviously, even with

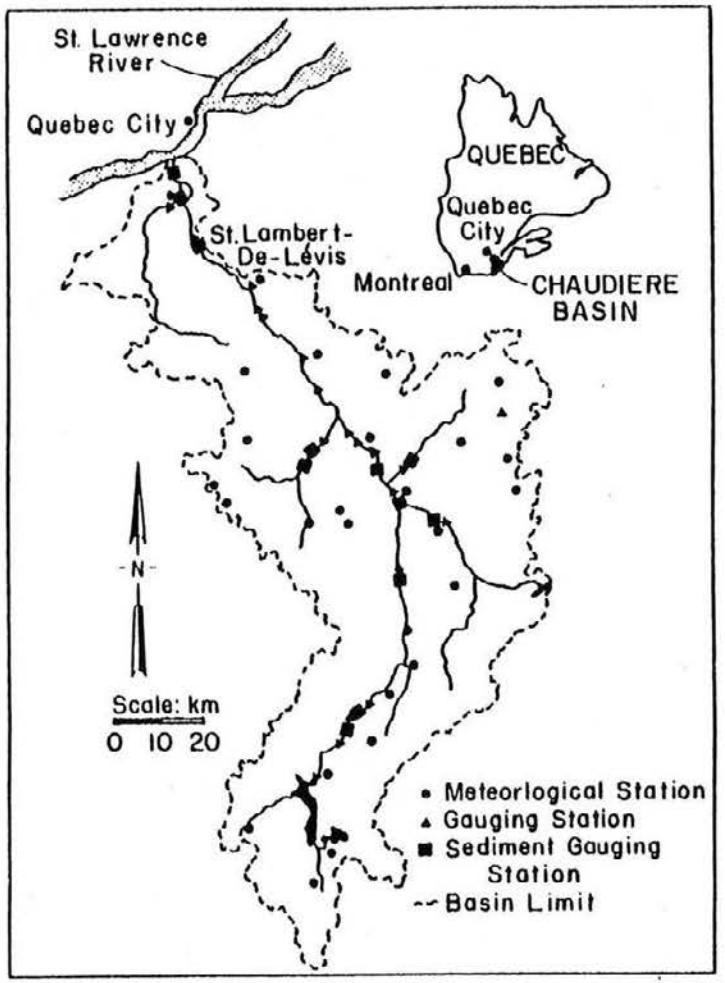

Fig. 10 Chaudière basin

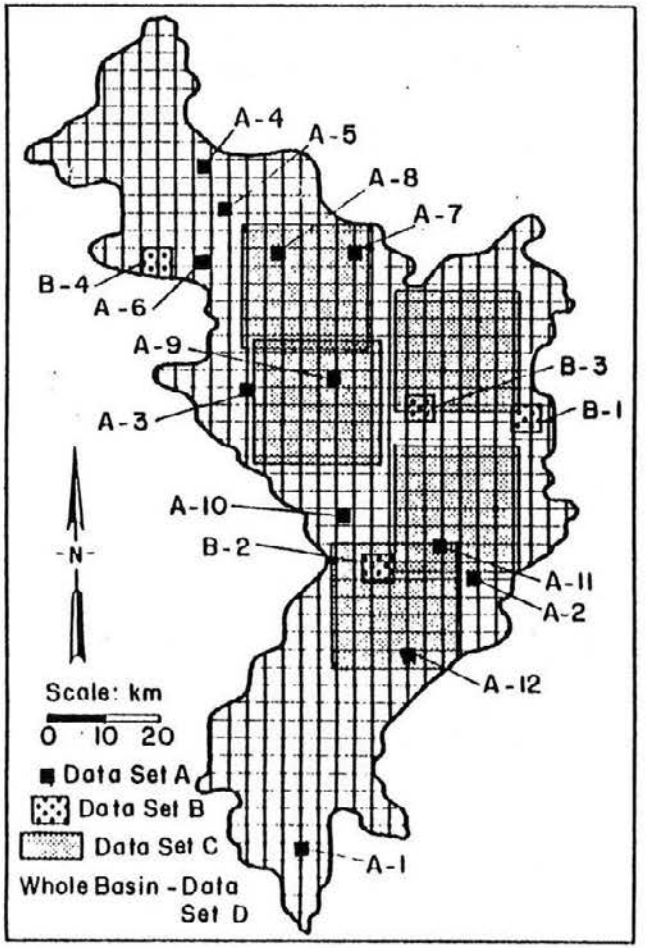

Fig. 11 General scales of the grids

the aid of computers, such a small grid size is not desirable because of the labor involved in collecting the data. The watershed was therefore subdivided in 1671 square cells covering 4 km^2 each as shown in Fig. 11. The factors used in the soil erosion computations were digitized and stored in data files. The relative importance of two variables is illustrated in Fig. 12.

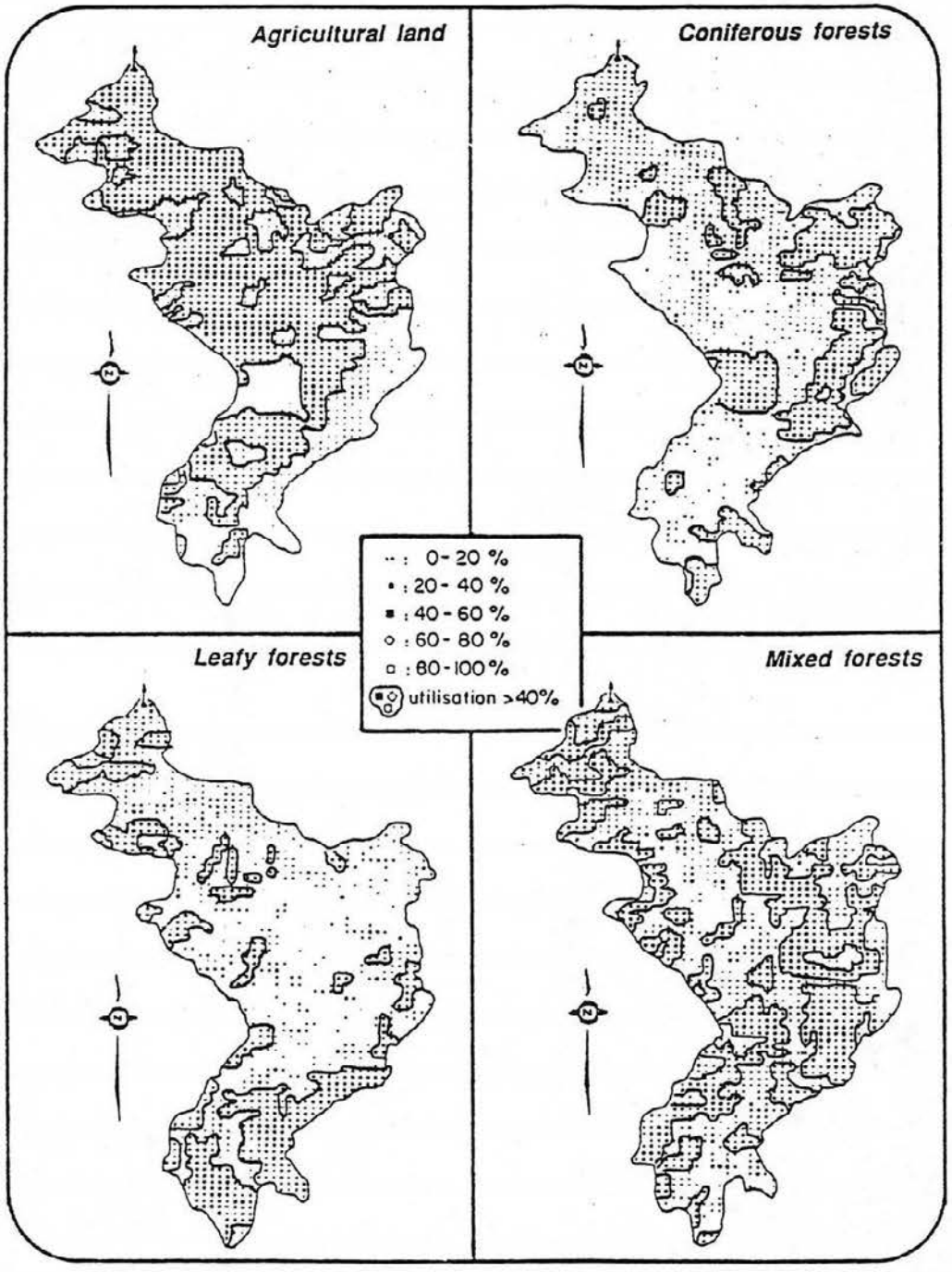

Fig. 12 Chaudière basin, percentage of land uses

b) A correction factor Q_e taking into consideration the influence of the grid size on the evaluation of soil erosion was defined from various grid sizes as shown in Fig. 11. Soil erosion was evaluated on surface areas ranging from 0.03 to 3000 km^2. The mean value of the correction factor Q_e and the confidence intervals at 95% were found to decrease with the size of the cell as illustrated in Fig.13.

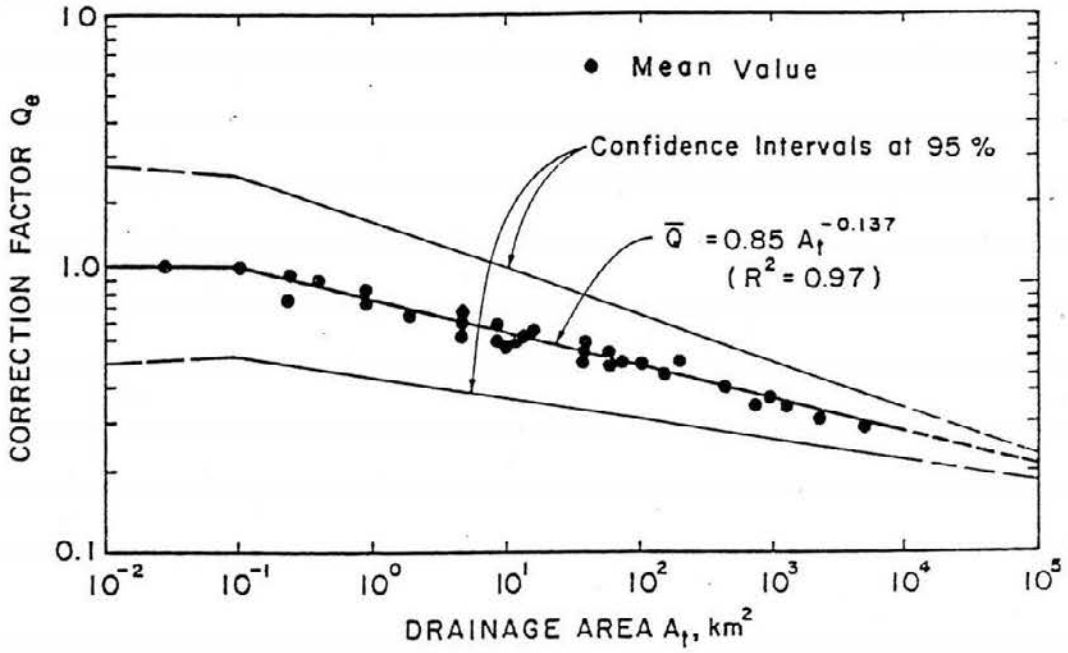

Fig. 13 Correction factor Q_e versus drainage area

c) The sediment yield is estimated from the product of the total soil erosion on the watershed and the mean value of the sediment delivery ratio C_s plotted in Fig. 14. The variability of the delivery ratio ranges between 0.4 and 2.5 times the mean value C_s.

d) The estimated sediment yield simulated by the model LAVSED-I is compared in Fig.15 with the observed sediment load measured in the river. Maps of the mean annual soil losses on the watershed are presented in Fig. 16. It is concluded from this analysis that soil losses and sediment yield computed from the USLE are only valid during rainfall. On this particular watershed, Fig. 15 shows that

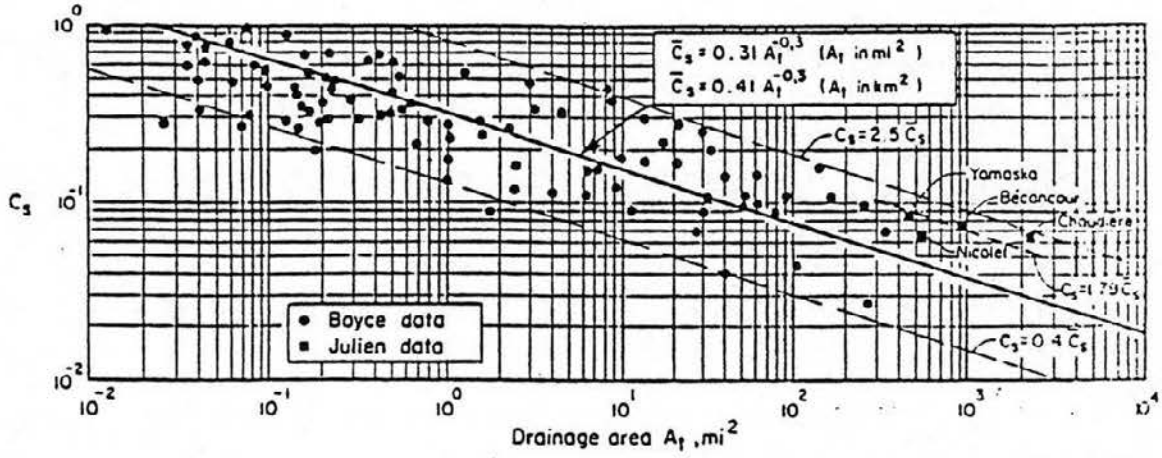

Fig. 14 Sediment-delivery ratio versus drainage area

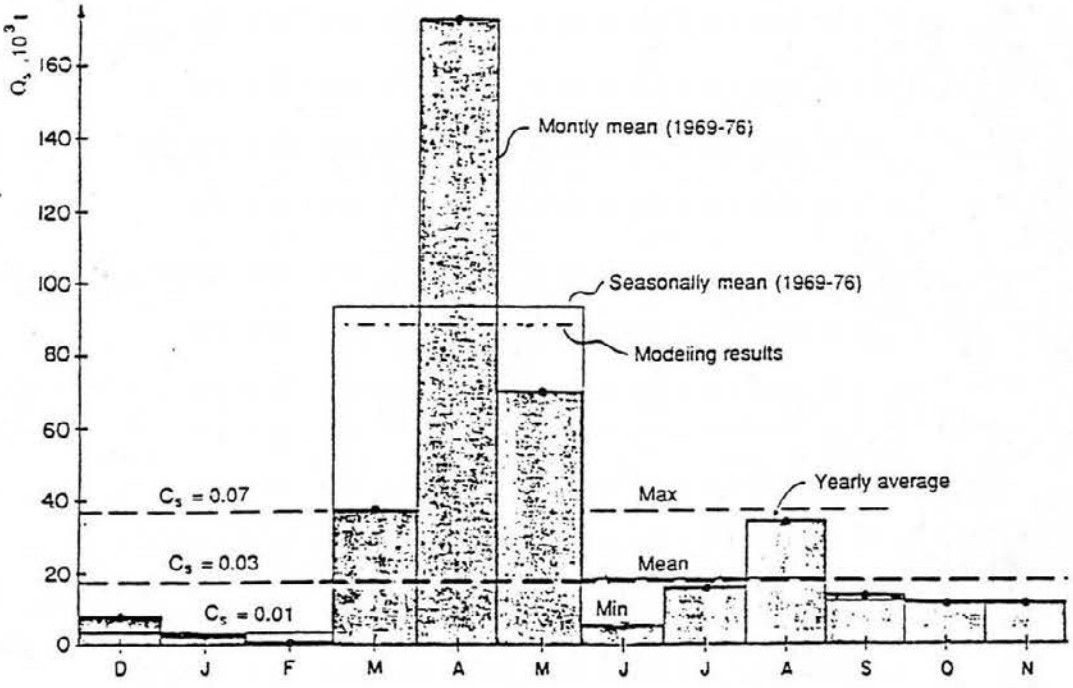

Fig. 15 Observed and computed sediment load of the Chaudière River

nearly 70 percent of the annual sediment load is observed during spring (March, April and May) when snowmelt occurs.

Model LAVSED-II Based on Runoff Characteristics

The model LAVSED-II(Julien and Frenette, 1984) has been developed to

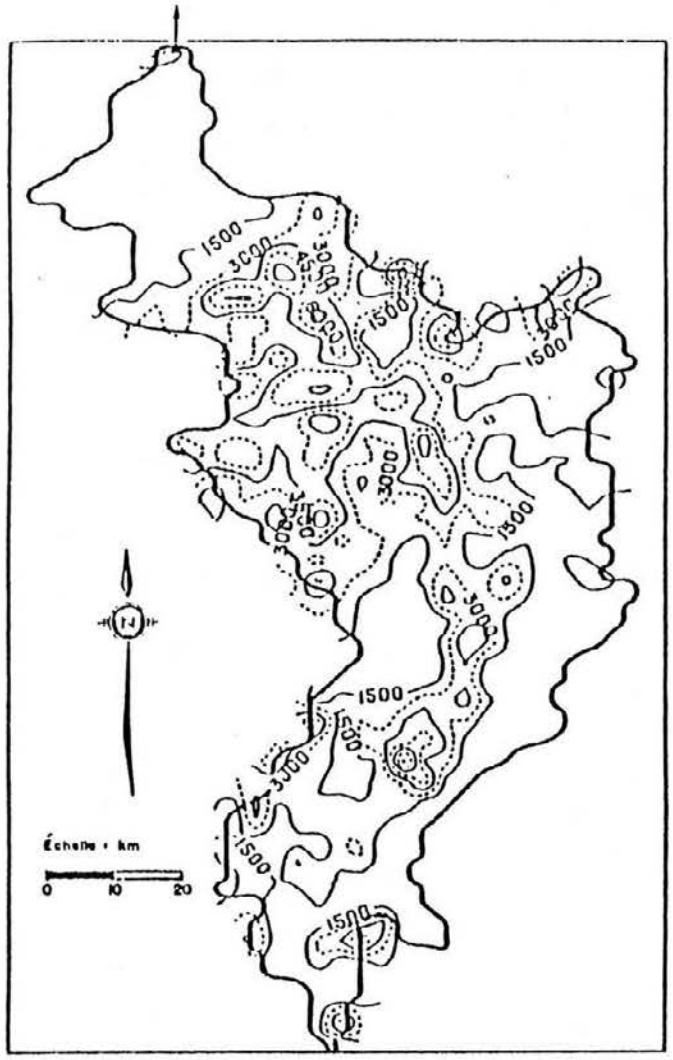

Fig. 16a Soil erosion map (t/km^2.year) of the Chaudière River using Kilinc and Richardson equation

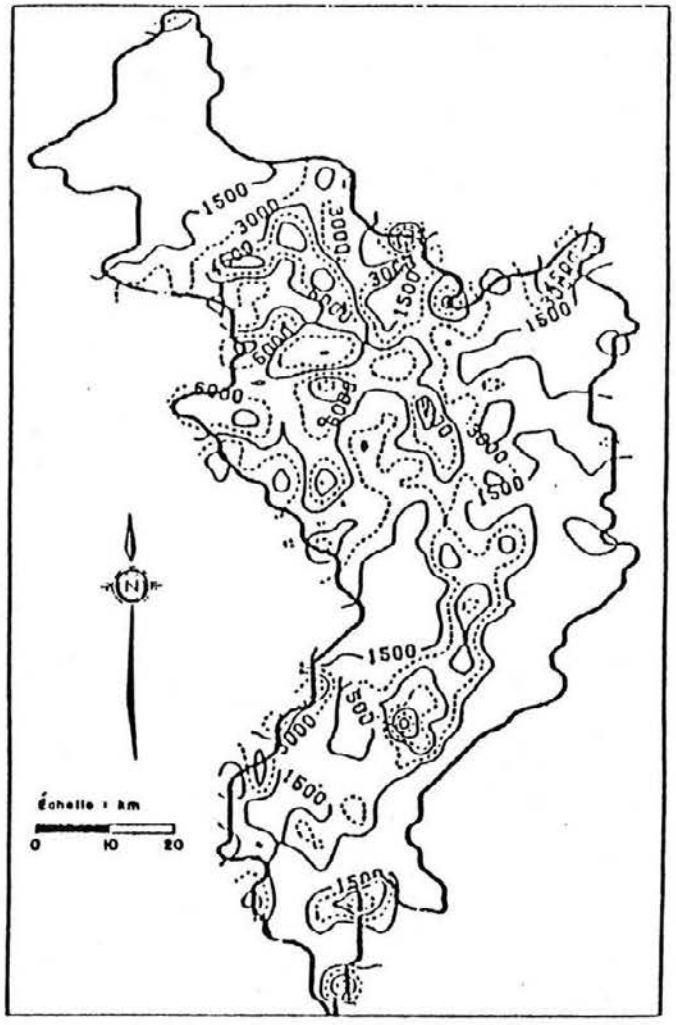

Fig. 16b Soil erosion map (t/km^2.a) of the Chaudière River using the Universal Soil Loss Equation

better describe the changes in sediment yield associated with rainfall and snowmelt. This model is principally based on the runoff characteristics and is a function of the physical characteristics of the watershed. On upland areas, rainfall-runoff-sediment relationship is treated as deterministic as shown in Fig. 17 while the rainfall duration and intensity are treated as random variables (Fig. 18). The expected value of soil loss on upland areas is obtained by integrating the sediment discharge over the complete range of rainfall duration and intensities shown in Fig. 18 as described by their respective probability density functions from Eqs. 1 and 2. The influence of vegetation and water losses due to infiltration are accounted for during the rainfall period. During snow-melt, the probability density function of runoff follows an exponential function and the mean runoff rate increases gradually during the season. After consideration of the probability density functions of rainfall duration, intensity and snowmelt runoff, the sediment yield from watersheds can be computed from the total erosion and the sediment-delivery ratio. The monthly sediment yield during rainfall Q_{sp} and snowmelt Q_{sf} in kt are respectively:

$$Q_{sp} \simeq 2417\, C_s\, \bar{C}\, C_r\, A_t^{1.137}\, \frac{\bar{\nu}\, \alpha\, \bar{S}^{1.66}\, \bar{L}^{1.035}}{\lambda_1\, \lambda_2^{2.035}} \qquad (16)$$

and

$$Q_{sf} \simeq 30.7\, C_s\, \bar{C}\, A_t^{1.137}\, \bar{S}^{1.66}\, \bar{L}^{1.035}\, F^{1.65}\, \left(\frac{F}{F_T}\right)^{0.37} \qquad (17)$$

in which

C_s = sediment-delivery ratio

$\bar{C}$ = mean cropping fator

C_r = runoff coefficient

A_t = drainage area in km^2

$\bar{\nu}$ = number of rainstorms

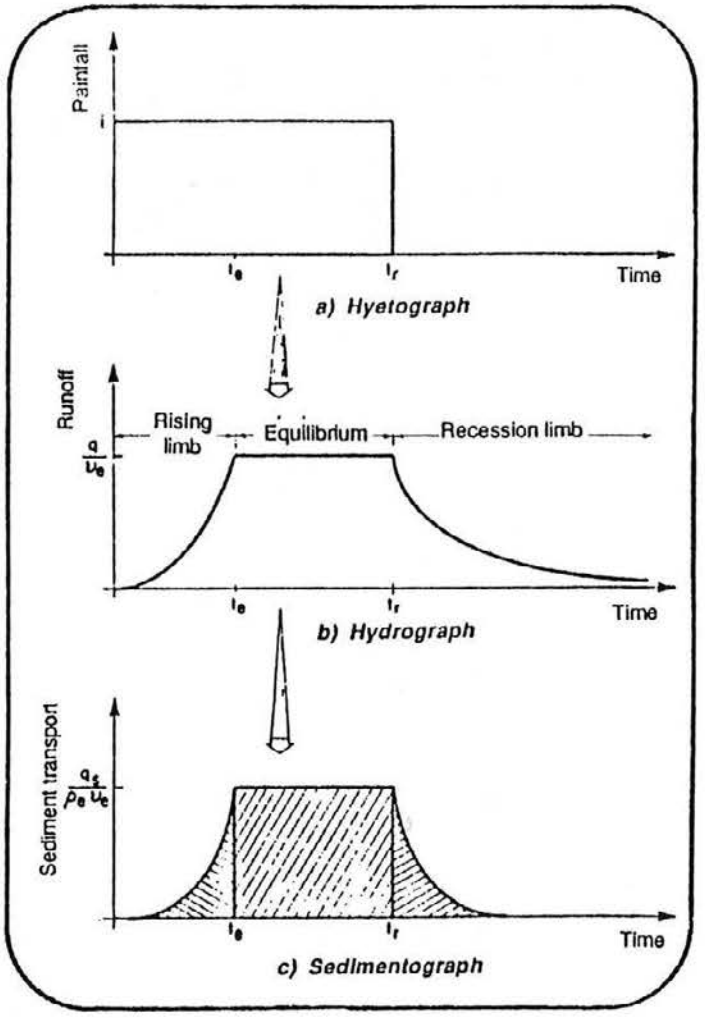

Fig. 17 Soil erosion for single event

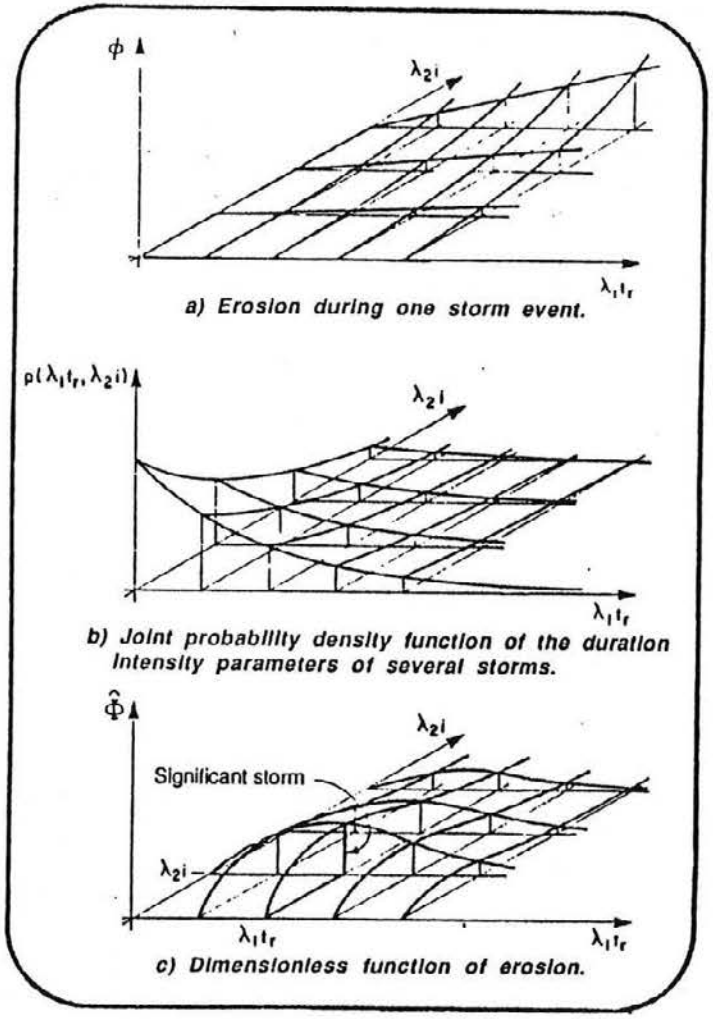

Fig. 18 Expected value of soil erosion for several events

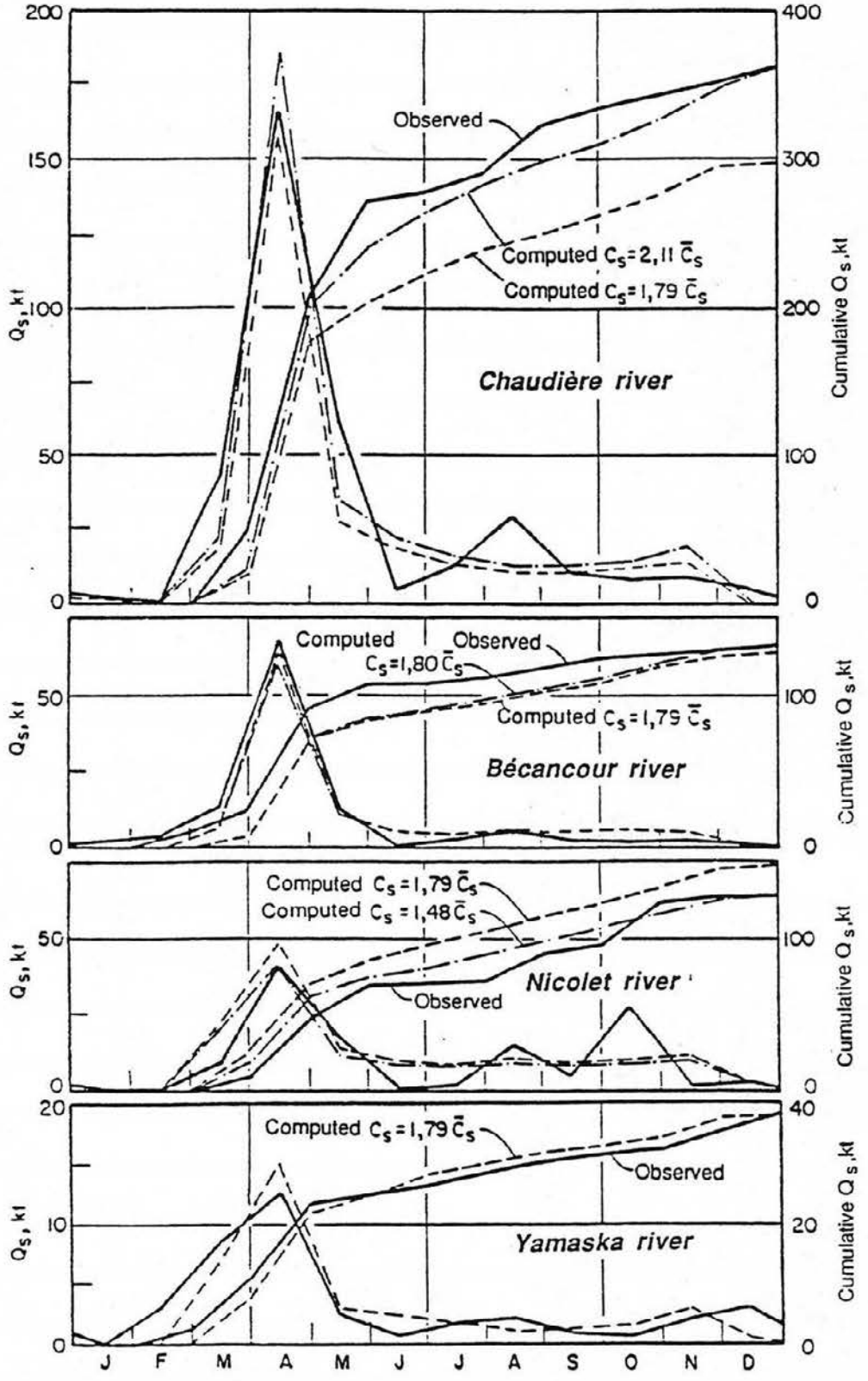

Fig. 19 Observed and calculated sediment loads

α = coefficient of the sediment discharge equation

$\bar{S}$ = average slope of the watershed

$\bar{L}$ = average runoff length

λ_1 = storm duration parameter

λ_2 = storm intensity parameter

F = cumulative snowmelt in m of water

F_T = total snowpack in m of water.

These two equations were used in the model LAVSED-II for predicting the average sediment yield from large watersheds in Canada for each month. The results are shown in Fig. 19 and compared with the measured sediment load in the streams. The model LAVSED-II requires detailed climatological data and several variables defining the overland flow characteristics.

DISCUSSION

Each computer model requires measured data of sediments for validation. These models offer various complementary results which prove to be extremely useful, for instance, in management of large watersheds, reservoir sedimentation, long-term changes in land-use, soil conservation, clear-cutting and reforestation. Research efforts are pursued at Laval University for developing better technologies in the analysis of erosion, transport and sedimentation problems on large watersheds. Though the research developments were primarily oriented toward modeling northern watersheds, the models are flexible so that specific needs in other countries can be met easily.

ACKNOWLEDGMENTS

This paper has been prepared under partial support from the

National Sciences and Engineering Research Council of Canada. The NATO postdoctoral fellowship to the second author is gratefully acknowledged.

REFERENCES

Eagleson, P. S. 1978, Climate, soil and vegetation, Water Resources Research, Vol. 14, No. 5, pp. 705-721.

Frenette, M., Llamas, J. et Larinier, M. 1974, Modèle de simulation du transport solide en suspension des rivières Châteauguay et Chaudière. CENTREAU Report, Laval University, Québec. 34p. (In French)

Frenette, M. et Nzakimuena, T., 1976, Modèle de prédiction des apports solides des rivières Chaudière, York, Châteauguay et Eaton, First Hydrotechnical Conference CSCE-QUEBEC, Montreal. (In French)

Frenette, M. et Julien P., 1984, Etablissement de cartes d'érosion par modélisation mathématique, Proceedings of the Annual Conference of the Canadian Society for Civil Engineering, CSCE, Halifax, May 23-25, pp. 543-564.(In French)

Julien, P., 1982, Prédiction d' apport solide pluvial et nival dans les cours d'eau nordiques a partir du ruissellement superficiel, Ph.D. Dissertation, Department of Civil Engineering, Laval University, Québec, Canada, 240 p. (In French)

Julien, P. and Frenette, M., 1984, A model for predicting suspended load in northern streams, Proceedings of the Annual Conference of the Canadian Society for Civil Engineering, CSCE, pp. 565-585.

Julien, P. and Frenette, M., 1985, Modeling of rainfall erosion, Paper accepted for publication in the Journal of Hydraulic Engineering ASCE.

Julien, P. Y. and D. B. Simons, 1984, Analysis of sediment transport equations for rainfall erosion, Report CER 83-84 PYJ-DBS52, Engineering Research Center, Colorado State University, Colorado, 46 p.

Kilinc, M. and Richardson, E. V., 1973, Mechanics of soil erosion from overland flow generated by simulated rainfall, Hydrology Paper No. 63, Colorado State University, Fort Collins, Colorado, 54 p.

Knisel, W. G., 1980, Editor, A field-scale model for chemical, runoff, and erosion from agricultural management systems, USDA, Conservation Research Report No. 26, 640 p.

Negev, M., 1967, A sediment model on digital computer, Tech. Report No. 76, Department of Civil Engineering, Stanford University, California.

Simons et al., 1982, Engineering analysis of fluvial systems, SLA, P.O. Box 1816, Fort Collins, Colorado.

Todorovic, P., 1968, A mathematical study of precipitation phenomena, Report CER 67-68PT65, Engineering Resrarch Center, Colorado State University, Colorado. 123 p.

Williams, J. R. and H. D. Berndt, 1972, Sediment yield computed with the universal equation, Journal of the Hydraulics Division, ASCE, Vol. 98, No. HY22, Proc. Paper 9426, pp. 2087-2098.

Wischmeier, W. H. and Smith, D. D., 1978, Predicting rainfall-erosion losses - A guide to conservation planning, U. S. Dept. Agriculture, Handbook, No. 537, 48 p.

Woolhiser, D.A. and P. Todorovic, 1974, A stochastic model for sediment yield for ephemeral streams, USDA Misc. Pub. 1275, pp. 295-308.

C[illegible] — R[illegible] WORK[illegible] . . . 95
6.[illegible] Control Works on River . . . 95
6.1.a Rill and gully erosion control measures . . . 95
6.1.b Practices to minimize sediment yield in rural and urban areas . . . 96
6.1.c Design criteria for debris basins (gravel traps) . . . 96
6.1.d Avalanche protection measures . . . 97
6.1.e Water works for landslide control . . . 97
6.2 Control Works in Stream Channels . . . 98
6.2.a Closure of secondary channels . . . 98
6.2.b Guidelines for cutoff design . . . 99
6.2.c Channel alignment criteria . . . 99
6.2.d Layout of river training structures . . . 100
6.2.e River diversion structures . . . 101
6.2.f Design criteria for navigation channels and structures . . . 101
6.2.g Dredging operation in rivers . . . 102
6.2.h Design criteria for channel bank and bed protection . . . 103
6.2.i River confluences and branches design improvement . . . 104
6.2.j Design criteria for groynes . . . 105
6.2.k Medium and long term impacts for river training works . . . 105
6.3 Flood Control Works . . . 106
6.3.a Practices to improve floodways . . . 106
6.3.b Design criteria for flood water diversions . . . 106
6.3.c Design of floodwater detention dams . . . 107
6.3.d Design criteria for flood control levees . . . 108
6.3.e Criteria for selection of flood control works . . . 109
6.4 Sediment Control Works . . . 109
6.4.a Design criteria for sediment excluders and ejectors . . . 109
6.4.b Local scour protection . . . 110
6.4.c Design criteria for debris flow control works . . . 111
6.4.d Design criteria for settling basins . . . 111
Chapter 7 — RIVER RELATED IMPACTS . . . 113
7.1 Hydrologic Impacts . . . 113
7.1.a Land use changes . . . 113
7.1.b Sedimentation in reservoirs . . . 114
7.1.c Navigation . . . 115
7.1.d Dredging . . . 116
7.1.e Channel erosion . . . 116
7.2Biological and Chemical Impacts . . . 117
7.2.a Efects of sediments on the eutrophication processes . . . 117
7.2.b Effects of river works on wildlife and habitat . . . 118
7.2.c Biological response to exceptional floods and rare droughts . . . 118
7.2.d Biological aspects of thermal pollution . . . 119
7.2.e Effects of reservoirs on the environment . . . 120
7.2.f Influence of sediment on water quality . . . 120
7.3 Socio-Economic Impacts . . . 121
7.3.a Public response to flood warning systems . . . 121
7.3.b Flood warning systems . . . 122
7.3.c Implementation of flood control strategies . . . 122
7.3.d Economic assessment of flood damages and benefits . . . 123
7.3.e Economic assessment of stram flows . . . 123
APPENDIX . . . 125
IAHR Task Group . . . 125
Portuguese Organizing Committee . . . 125
Participants . . . 126
Contributing Institutions . . . 129
INDEX . . . 131

RESEARCH TRENDS IN SEDIMENTATION

by
E.V. Richardson, Professor
Department of Civil Engineering
Colorado State University
Fort Collins, Colorado

and
H.S. Woo, Graduate Student
Department of Civil Engineering
Colorado State University
Fort Collins, Colorado

and
P.Y. Julien, Assistant Professor
Department of Civil Engineering
Colorado State University
Fort Collins, Colorado

ABSTRACT

Recent research trends in the field of sedimentation are reviewed. Three topics of major interest in sedimentation are discussed: bed forms; total sediment discharge; and hyperconcentrated flow. The fundamental problem of predicting bed forms and sediment discharge is related to the fluid-sediment interaction near the bed. A satisfactory method for predicting bed forms should combine a theoretical analysis verified with laboratory and field data over a wide range of flow depth. Future research topics on the mechanics of bed forms should include the effect of water temperature, seepage, and sediment concentration of fines. Large scale roughness such as alternate bars should also be given further consideration in alluvial channels. The diffusion theory is very sensitive to several factors such as the reference height a, the reference concentration C_a, the exponent Z, the fall velocity W, and the coefficient β. Methods to evaluate these parameters should be reconsidered. The analysis of hyperconcentrated flows is a relatively underdeveloped research field of great importance in semi-arid regions. Theoretical and experimental research is being conducted at Colorado State University on the rheological properties, bed sediment transport, fall velocity, and characteristics of hyperconcentrated flows including mudflows.

INTRODUCTION

Mega projects have been built on most of the major fluvial systems around the world to increase hydropower production, supply water for irrigation and control floods. Past experience demonstrates that very few structures in alluvial streams can be designed without careful consideration of sedimentation. Bank erosion, channel stability, silting in navigable channels and reservoirs are threatening hydraulic structures. Sedimentation should be addressed as an issue of foremost importance at this Hydraulics Specialty Conference.

There is significant historical evidence that ancient civilizations were concerned with hydraulics and sediment transport in large river systems such as the Yellow, Nile, Tigris, and Euphrates Rivers. Although there is no written manuscript on hydraulics, canals and aqueducts were built for water supply and irrigation purposes. The development of the experimental method occurred during the Renaissance with Leonardo Da Vinci. Important contributions to the field of mechanics were made during the 17th and 18th centuries. P. DuBuat (1734-1809), carried out many different hydraulic experiments. During the 19th century, serious considerations to the transport of sediment in open channels were made by Dupuit (1804-1866), DuBoys (1847-1924) and others. Their concepts of sediment transport in suspension and bed-load have been generally accepted.

G.K. Gilbert (1914) conducted sediment transportation experiments in flumes. His keen observations and measurements of sediment movement under controlled conditions greatly advanced research in this field. Several processes have been described through extensive studies during the 20th century and solutions are available for several complex phenomena such as total bed sediment discharge, stage-discharge relationships, scouring and bed armoring processes. However, completely satisfactory solutions to several fundamental problems have not been obtained yet. Vanoni (1984) summarized the past fifty years of research and pointed out that the basic problems of predicting sediment discharge and velocity are intimately related to the fluid-sediment interaction at and near the bed.

This paper reviews recent contributions to the knowledge of the sedimentation processes. Three topics are particularly discussed: 1. bed forms; 2. total sediment discharge; and 3. hyperconcentrated flows. Bed forms in alluvial channels are intimately related to the resistance to flow, the stage-discharge relationship, and the transport of bed sediment. The prediction of total bed sediment discharge plays a key role in river mechanics. Hyperconcentrated flows are rather common in the semi-arid regions of the United States.

BED FORMS

The flow of water over a loose boundary molds the geometry of the channel bed and casts its hydraulic roughness. The importance of bed forms has been brought to attention by Gilbert (1914), Shields (1936), Einstein and Barbarossa (1952), and Liu (1957). The mechanics of bed forms has been investigated by hydraulicians and sedimentologists for predicting the bed configuration and resistance to flow in alluvial channels.

Changes in bed forms during flood periods have been known to be primarily responsible for discontinuous rating curves. Simons and Richardson (1961, 1966) classified bed forms into either a lower or an upper flow regime separated by a transition zone, see Fig. 1. The lower flow regime is characterized by small bed sediment discharge and large resistance to flow as given by the Darcy-Weisbach friction factor, $(0.04 \leq f \leq 0.16)$. The upper flow regime is characterized by large bed sediment discharge and low resistance to flow $(0.02 \leq f \leq 0.07)$ except in chute and pool conditions. In the transition, the bed forms are extremely variable, ranging from dunes to antidunes. From the analysis of flume and field data the bed configuration of shallow streams can be predicted using Simons and Richardson's chart shown in Fig. 1.

Different approaches were presented for the prediction of bed forms in the 1960's and 1970's. Anderson (1953), Kennedy (1963) and other investigators tried to explain and predict theoretically bed forms with the potential flow theory. Kennedy introduced the concept of the lag distance for which the sediment discharge at a point is expressed in terms of the velocity at a distance slightly upstream. Recent theoretical models based on the potential flow theory have focused on the analytical and experimental detemination of the lag distance, and the results remain uncertain. On the other hand, Smith (1970), Engelund (1980) and others pursued models of bed form prediction with real fluid flow. The

model of Engelund is based on the stability analysis of the erodible beds and does not require the lag distance. Another graphical presentation of the bed form predictor was developed by Engelund (1967) using the dimensionless total shear stress vs. the dimensionless grain shear stress. Recently, a bed form predictor has been presented by van Rijn (1984b) for the transition and the lower flow regime using a particle parameter and a transport stage parameter.

The randomness of the bed configurations has prompted statistical and spectral investigations. Nordin and Algert (1966) proposed a second-order Markov model to describe dune profiles. Since then, many researchers have tried to describe the bed elevation as a random function in two and three dimensions. These studies appear to have produced only vague conclusions partly due to the lack of suitable data.

Since the early measurements of temporal mean tractive force and intensity of turbulence over ripples by Raudkivi (1963) recent numerical models include a modified version of the standard k-η turbulence model (Mendoza and Shen, 1984). This model for predicting velocity profiles, distribution of bottom pressure, shear stresses, and the total force acting on a dune shows good agreement with laboratory data. Further investigation including the fluid-particle interaction should be very promising.

Water temperature and presence of fine sediments in the flow are known to affect bed forms and thus the resistance to flow as well as total sediment discharge. It is generally accepted that the decrease in water temperature during winter increases both the viscosity of the fluid and the bed sediment transport, and decreases the resistance to flow. The effect of fine sediments has been studied less than that of water temperature. Simons, et al. (1963) showed experimentally that the concentration of fine sediments changes the bed form configuration. These changes from dunes to flat bed to antidunes are thought to be due to the decrease in the fall velocity of bed sediment particles and the increase in tractive forces. Further investigation on the influence of water temperature and concentration of fines on bed forms should provide insight on the physical processes governing the formation of ripples and dunes.

Inflow seepage affects the bed forms, the hydraulic parameters and the sediment transport. Richardson (1984) showed that the form roughness and subsequently the

resistance to flow in low regime is increased due to the reduced thickness of the layer between the main flow and the bed. The infiltration of fine sediments in the surface layer of the bed affects the bed forms and the transport of bed sediment.

The cross-sectional and plan form geometry of alluvial channels substantially affect the total resistance to flow. An introductory study of the resistance to flow in a sinusoidal channel was done by Leopold, et al. (1960). The knowledge on the cross-sectional bed configurations such as point bars, alternate bars, chute and pools remains limited. Further studies in this field, such as Ikeda's (1983), should prove of great value to the analysis of resistance in sinuous streams and gravel-bed rivers.

In summary, the knowledge on bed form configuration in alluvial channels appears to have greatly advanced in the past twenty years. However, the theoretical and empirical approaches have not given fully satisfactory explanations for the prediction of bed forms in alluvial channels. One encouraging aspect of the comparison between various methods is that the more recently developed predictors are generally more reliable (Vanoni, Ed., 1977, p. 149). It is suggested that one of the urgent needs is the development of a satisfactory bed form predictor that can be used in alluvial channels with a broad range of channel depths. The relationship between bed forms and hydraulic roughness should be further understood. Future research needs in the mechanics of bed forms include numerical modeling of flow over bed forms; the effect of water temperature, seepage, and sediment concentration on bed forms; and the resistance to flow due to large scale roughness such as point bars, alternate bars, and chute and pool sequences in alluvial streams.

TOTAL SEDIMENT DISCHARGE RELATIONS

One of the foremost research objectives in sedimentation is to predict total bed sediment discharge as a function of hydraulic parameters and bed sediment characteristics. In the past fifty years new sediment transport formulas and modifications of existing ones have been presented repeatedly. Although significant progress has been accomplished, to date none of the existing sediment transport formulas has been widely accepted.

Sediment Transport Formulas

The existing sediment transport formulas can be classified into several categories according to their basic approaches. One is the diffusion-advection type of model. This model is composed of: (1) a thin bed-layer where the bed load is transported by rolling, sliding, and saltating; and (2) a suspension zone where sediment particles are suspended by the fluid turbulence. Einstein's bed load function (1950), Chang, et al.'s (1965), Toffaleti's (1968), Karim and Kennedy's (1983), and van Rijn's (1984a) formulas can be included in this category.

A second type of model is the energy approach in which the rate of work done for transporting sediment particles in turbulent flow is related to the rate of energy expenditure. Since Bagnold (1966) first introduced this concept for the prediction of the rate of sediment transport under equilibrium conditions, Engelund and Hansen (1967), Yang (1973, 1979), Ackers and White (1973), and Holtorff (1983) extended the applicability of the energy approach. Recently, Wiuff (1985) treated transport of the suspended matter based on energy efficiency. The energy efficiency is defined as the ratio between the gain in potential energy of the suspended material and the turbulent dissipation.

The third type of model is the empirical approach based on regression techniques and graphical methods. This kind of approach has the merit of its simplicity. Colby's relations (1964), and Shen and Hung's regression equation (1971) can be categorized in this group. Ranga Raju, et al. (1981) presented a simple relation between total bed sediment discharge and other hydraulic parameters, among which the dimensionless grain shear stress is suggested to be dominant.

The last type of model deals with modifications of existing formulas. Bishop, et al. (1965) presented a method for predicting total bed sediment discharge in graphical forms by modifying Einstein's parameters of ϕ and ψ from data analysis. The modified Einstein procedure by Colby and Hembree (1955) and Shen and Hung's (1983) remodified procedure can be included in this category.

This classification, however, is not definite because some of the sediment transport formulas may belong to more than one type of model. For example, Yang obtained all the

coefficients in his sediment transport relation using regression techniques although it is expressed as a function of the so-called unit stream power. The equation proposed by Kikkawa and Ishikawa (1978) is different from the types of models mentioned above since the total bed sediment discharge is given by a stochastic model describing both the bed load and the suspended load.

All the existing sediment transport formulas appear to have at least one empirical factor or coefficient that can only be obtained from experiments. Several comparisons were made between formulas, and flume and field data (Vanoni, Ed., 1977, pp. 221-22; White, et al., 1973; Yang and Molinas, 1982). The sediment transport formulas based on energy concepts seem somewhat superior to other formulas. One merit of these equations is their inherent simplicity comparatively to the equations based on the diffusion theory. For example, the Einstein formula requires more than 20 calculation steps while Yang's formula needs only a few steps. The first approach, however, remains superior when considering the flow properties and sediment concentration at every point along a vertical; whereas the stream power approach represents an integrated form and gives only the mean flow characteristics and sediment concentration at a given vertical.

Diffusion-Advection Model

The concentration distribution of suspended sediment in turbulent flow can be predicted by the diffusion theory. Rouse's solution (1937) of the differential equation for suspension has been experimentally verified and is widely accepted. The equation for the concentration C has been used by Einstein, among others, and is written as

$$C/C_a = [a(d-y)/y(d-a)]^Z;\ Z = W/\beta k U_* \qquad (1)$$

in which a is the reference height; C_a is the reference concentration; Z is the exponent; W is the fall velocity of sediment particles; k is the von Kármán constant; β is a coefficient corresponding to the ratio of the sediment diffusivity to the fluid momentum diffusivity; U_* is the shear velocity; and d is the flow depth. The relative concentration profile given by this equation is shown in Fig. 2. Total bed sediment discharge q_t per unit width is calculated as the sum of the unit bed load rate q_b and the unit suspended load rate as follows

$$q_t = q_b + \int_a^d C\,u\,dy \qquad (2)$$

in which u is the time-averaged local velocity.

In general, it is accepted that the bed sediment discharge can be more reliably estimated from sediment transport relationships than the suspended sediment discharge since the wash load can be highly variable. The accuracy in the evaluation of the total bed sediment discharge relies on the evaluation of the following parameters: (1) the reference height a; (2) the reference concentration C_a; (3) the von Kármán k; (4) the sediment diffusivity and the coefficient β; (5) the fall velocity of the sediment particles W; and (6) the velocity profile. Each of these parameters is discussed as follows.

1) Reference Height "a"

One of the basic difficulties in the use of the diffusion-advection model is the distinction between bed load and suspended load. Many investigators have tried to overcome this problem by disregarding any such distinction. However, there are several good reasons for maintaining this distinction as suggested by Engelund and Fredsøe (1976). Einstein suggested that a is equal to twice the particle diameter. Van Rijn uses the criterion $a = \Delta/2$ or $a = k_s$ (with "a" min = 0.01 d) in which Δ is the dune height and k_s is the characteristic roughness defined by Nikuradse. Karim and Kennedy (1983) suggested that $a = D_{50}\,U_*/U_{*c}$, in which D_{50} is the mean particle diameter and U_{*c} is the critical shear velocity. Brooks (1965) and Willis (1979) suggested various reference heights phenomenologically rather than physically. Therefore, it appears that the value of "a" is rather arbitrary.

2) Reference Concentration C_a

Most equations describing the concentration of suspended sediments are function of the reference concentration C_a at the elevation "a". Studies on the estimation of the reference concentration were initiated by Lane and Kalinske (1939), who related the reference concentration to the ratio of the particle fall velocity to the fluid shear velocity. To estimate the reference concentration many researchers used a simple bed layer model where the concentration in a thin layer near the bed is given from the bed load transport q_b,

the distance a, and the mean transport velocity of the bed load U_a.

$$C_a = q_b/(U_a\,a) \qquad (3)$$

The value of U_a has been obtained experimentally by investigators (Einstein; Chang, et al.; van Rijn, 1984a; Karim and Kennedy; Engelund and Fredsøe, 1976). The inadequacy of Eq. 3 was recently pointed out by Murphy and Aguirre (1985). They suggested that the transport processes of bed load and suspended load are not the same and should not be equated. Instead, the reference concentration for turbulent diffusion was obtained by considering an equilibrium source strength and the diffusion equation. The suspended load is very sensitive to the evaluation of C_a, particularly when C_a is large and the concentration profile is nearly uniform.

According to Einstein and Chien (1955) the value of log C/C_a deviates from the linear relationship with log (d-y)/y and the concentration distribution becomes more uniform when the reference concentration $C_a > 0.038$ by volume. The value of C_a usually exceeds 0.1 by volume and sometimes 0.5 when the Einstein bed load function is applied to flume data with relatively high sediment transport rates. In this respect, more extensive research on sediment transport near the moving bed will be necessary in the bottom boundary condition to clarify.

No reference concentration is required in the stochastic model for turbulent suspension proposed by Kikkawa and Ishikawa (1978). Itakura and Kishi (1980) also suggested an equation for the concentration of suspended sediment in which the reference concentration is calculated by the flow data alone.

3) Von Kármán k

Several investigators have presented a reduction in the von Kármán constant k, with increasing sediment concentration (Einstein and Chien, 1955; and recently Wang, 1981). At least one different suggestion on this topic was presented by Coleman (1981) who disputed previous investigations. Based on the wake flow function, he recommended the invariance of k with the presence of sediment.

4) Sediment Diffusivity and Coefficient β

The evaluation of the momentum diffusivity of turbulent flow is usually made by applying the Boussinesq concept analogous to the laminar flow conditions. The momentum diffusivity of fluid in sediment-laden flow can be analytically evaluated from the force balance under steady uniform conditions for a given velocity in the profile. The parabolic distribution of the momentum diffusivity has been generally accepted (Rouse, 1937; Steffler, et al., 1985). On the other hand, Hinze (1975) showed a linear-constant distribution of the momentum diffusivity in turbulent flow with the wake flow region over the turbulent boundary layer.

Jobson and Sayre (1970b) showed that the velocity distribution is found to have a very minor effect on the predicted concentration distribution when the differential equation for suspension is solved with the Reynolds analogy. With larger concentrations of suspended sediment, however, the exact evaluation of the momentum diffusivity or the sediment diffusivity becomes increasingly important.

The coefficient β represents the ratio of the sediment diffusivity to the momentum diffusivity. The studies of the evaluation of β in sediment-laden flow have led to opposite results. Carstens (1952) showed that β decreases from unity as the inertia of suspended particles increases. His results are based on the assumption that turbulence may be simulated by a simple oscillating motion of fluid. On the other hand, Singamsetti (1966) suggested that turbulence is composed of eddies with circulatory motion. Accordingly, the centrifugal force acting on sediment particles would be greater than that acting on fluid particles thereby causing the sediment to be thrown to the outside of the eddies with a consequent increase in effective mixing length and diffusion rate. Jobson and Sayre (1970a) tried to combine these two distinct effects of turbulence on the sediment diffusivity by the kinematic consideration of eddy motion. Van Rijn (1984a) suggested a quantitative relation between the value of β and the characteristics of flow and suspended sediment particles. His empirical relation is based on the experimental results of Coleman (1970) on the vertical distribution of the sediment diffusivity in the flow.

It is considered that the Reynolds analogy is still useful in evaluating the sediment diffusivity. However, the application of the diffusional theory for turbulent diffusion

of suspended sediment in the flow cannot be complete until the sediment diffusivity is satisfactorily estimated. It appears that the diffusional theory might no longer be applicable when the inertia of sediment particles increases, considering the larger discrepancy between computed and measured exponents Z. In this respect, basic studies on the limitation and the applicability of the diffusional theory in sediment-laden flow has been conducted by Antsyferov and Kos'yan (1980). They show that the diffusional theory is limited by the inertia of particles and it should not be applied to sediments for which $W > 0.27U_*$. Defects of the kinematic consideration on turbulent diffusion of particles had been previously discussed by Bagnold (1966).

5) Fall Velocity of Sediment Particles W

The analysis by Colby and Hembree (1955) gave a practical solution to the evaluation of the exponent Z based on empiricism. The values of the exponent Z are related to the fall velocities of sediment raised to the 0.7 power. This has been recently revised by Shen and Hung (1983).

The fall velocity of sediment particles in sediment-laden flow is an additional important factor governing the concentration distribution of suspended sediment. The fall velocity of a single sediment particle in quiescent water is well known. The effect of turbulence on the fall velocity has been investigated experimentally and theoretically by simulating turbulence in oscillating fluid (Houghton, 1968; Hwang, 1985). According to their results turbulence seems to reduce the fall velocity. A similar conclusion was obtained by Bechteler, et al., (1983) by using high speed camera and digitized particle trajectories. Recently, Bouvard and Petkovic (1985) measured the fall velocity of particles in turbulent open channel flow. The measured fall velocities are nearly 30 percent less than the settling velocities in quiescent water. On the other hand, Jobson and Sayre (1970a) showed that the fall velocity may increase slightly in turbulent flow.

The effect of hindered settling has been studied primarily at lower particle Reynolds numbers (McNown and Lin, 1952). Two effects of sediment concentration are explained by investigators. One is the effect of the hydrodynamic interference of fluid between sediment particles and the other is the effect of the direct inter-particle collision. Investigators in the chemical engineering field have

emphasized the first effect on fluidization-sedimentation processes (Richardson and Zaki, 1954; Maude and Whitmore, 1958). The second effect was suggested by Einstein and Chien (1955) as a function of the product of the concentration gradient and a length scale which indicated the travel distance of particles prior to collision. These effects of sediment concentration are expected to be pronounced especially near the bed.

6) Velocity Profile

A proper description of the velocity profile is important since the total sediment discharge is obtained from the integration of the product of the sediment concentration by the time-averaged velocity of sediment-water mixture over depth as given from Eq. 2.

For turbulent flows in open channels, many equations for the velocity profile have been proposed. These equations may be classified into three categories. One is the group of equations that are based on the logarithmic law (Keulegan, 1938; Hunt, 1954; Einstein and Chien, 1955; Ordonez, 1970; Hino, 1963; Yalin and Finlayson, 1972). The logarithmic velocity profile has been modified by these researchers to account for the effect of concentrations of sediment. A second is the group of equations involving the wake flow function about the turbulent boundary layer (Coleman, 1981; Vedula and Achanta, 1985). Their derivations are based on the fact that the entire flow region in a turbulent open channel flow is composed of the turbulent boundary layer near the bed where the flow is influenced by the boundary, and the outer flow region where the wake flow dominates with negligible boundary effect.

The third is the group of equations purely based on empiricism. The power-law is included in this category. The power-law equation has been frequently used instead of the logarithmic equation (Toffaleti, 1968; Shen, et al., 1981; Karim and Kennedy, 1983). While the two equations fit equally well the velocity distribution in sediment-laden flow, the power-law avoids the singularity at the boundary obtained by the log-law and is more convenient for mathematical treatment. The analytical relation between the exponent of the power-law and the von Kármán constant k in the logarithmic equation has been recommended by Hus and Kennedy (1971) in pipe flow, and Zimmermann and Kennedy (1978) in open channel flow.

Improvement upon the Einstein formulation may be achieved through further investigation of these factors in Eq. 1 to minimize possible errors. For example, results obtained by van Rijn (1984a) showed good agreement with the data of total bed sediment discharge in flumes and in the field. The results seem superior to the equations based on the energy concept. A noteworthy trend in studies of velocity distributions and suspended sediment distributions is the use of the two-layer model for turbulent suspension. These two layers for turbulent suspension may be extended to a three-layer model including the bed layer for bed load transport.

HYPERCONCENTRATED FLOWS

Flows with extremely high sediment concentrations during floods have been observed throughout the world. The Yellow River in China is well known for its tremendous sediment concentrations. The occurrence of extremely high sediment concentrations is also rather common to several streams in the semi-arid southwestern United States. A general classification of sediment-laden flow suggested by Beverage and Culbertson (1964) has been modified after considering the mud floods defined by the National Research Council (1982). Hyperconcentrated flows can be subdivided into four categories: water floods, mud floods, mud flows, and landslides as shown in Fig. 3.

Nordin (1963), and Nordin and Dempster (1963) collected data on the Rio Grande where sediment concentrations have been observed up to 200,000 ppm (parts per million). They measured the velocity profiles and the sediment concentration distributions in the channels, and the fall velocity of sand particles in clay suspensions. They concluded that both the velocity profiles and the sediment concentration distributions may still be described by the conventional logarithmic equation and by the Rouse equation, respectively, if the fall velocity of the sands is corrected for the influence of the fine sediments.

A method for correcting bed sediment discharge due to the presence of fine sediment in suspension was presented by Colby (1964). Colby's method is one of the few known attempts to modify transport relations to consider the effect of the presence of fine sediment. His correction factor for the high concentration of fine sediment up to 50,000 ppm is

based on the changes in the viscosity with water temperature. Using field data he extended the range of fine sediment concentrations up to 200,000 ppm.

Kikkawa and Fukuoka (1969) examined the flow characteristics with wash loads of nearly uniform silica sands. They experimentally found that the concentration of bed sediment load increases with wash load. Egiazaroff (1969) presented some data on the hyperconcentrated flows of fine material as high as 380,000 ppm during floods in the USSR. Since the viscosity increases and the effective weight of sand particles decreases as the concentration of fine sediment increases he reasoned that hyperconcentrated flows have larger transporting capacity. Bradley (1983) reported suspended sediment concentrations as high as 650,000 ppm in the Toutle River downstream of Mount St. Helens.

As the suspended sediment concentration in natural streams increases one can observe that the size distribution of the suspended sediment becomes broader, from the clay-sized particles to the large sized sand particles. The interactions between particles, and between particles and fluids are predictable.

Turbulence Structure in Hyperconcentrated Flow

Turbulence appears to play a major role in suspending and transorting bed material in highly concentrated flow until complete damping of turbulence occurs and the flow becomes laminar. In general, turbulence has been known to be damped by the presence of suspended sediment. Bagnold (1956) suggested that turbulence ceases with higher concentrations such as 30 percent by volume when the dispersive stress is dominant. On the other hand, Hino (1963) indicated that the decrease in the turbulent intensity due to suspension of sediment particles is relatively small whereas a rather rapid decrease in the lifetime of eddies will result. Bondurant (1950) speculated from the data of the hyperconcentrations in the Rio Puerco that even at very high concentration (68 percent by weight) the stream possesses all the characteristics of fully developed turbulence with numerous intermittent sand waves and high velocities. Therefore, it appears that large scale turbulence may still be present in hyperconcentrated flow whereas small scale turbulence may be rapidly damped. The effect of concentrations on turbulence in streams varies for different size distributions of suspended particles.

Velocity distributions in hyperconcentrated flows with less than 10 percent by weight of fines show that the Newtonian structure of turbulence persists and the logarithmic profile is applicable (Gust, 1976; Terwindt, et al., 1965). The thickness of the viscous sublayer increases as compared with the flow of clear water (Gust, 1976).

Rheological Properties of Water-Sediment Mixtures

Several papers presented by Chinese researchers to the International Symposium on River Sedimentation (1980, 1983) dealt with rheology, settling velocity, and resistance to flow in hyperconcentrated flows. In general, they attempted to develop empirical formulas by considering the sediment-water mixture as a whole, while researchers in the United States approach the problem by dividing sediment into two parts: the fine sediments and the bed sediments.

It is recognized that the flow usually becomes more viscous and non-Newtonian as the concentration of suspended sediment increases from a few thousands to several hundred thousands ppm. The difficulties in treating the transitional properties of hyperconcentrated flows are related to the presence of yield, laminar, turbulent and dispersive stresses in non-Newtonian fluids. The presence of large concentrations of sediment induces complex processes of energy dissipation in the fluid matrix. Besides the viscous and turbulent stresses existing in clear water flows, the interaction of water and sediment, the exchange of sediment particles with the channel boundary, and the collisions between suspended particles (dispersive stress) contribute to the dissipation of energy from the fluid matrix. Moreover, the presence of clay particles whose cohesive forces (yield stress) arise from hydrophilic bonding, modifies the physical processes governing the fluid flows.

The rheological properties of sediment-water mixtures vary with the size distribution of sediment as well as the concentration of suspended sediment. As far as the rheological properties of clay suspension are concerned, investigators have agreed that the Bingham model is usually acceptable. The Bingham model is composed of the yield stress and the viscous stress. The concentration of coarse sediment such as sand particles affects the viscosity of the sand-water mixture although its effect is generally less pronounced than that of fine sediment. Since Einstein (1905,

1906) first presented a theoretical equation for the relative viscosity of dilute suspensions, many empirical equations have been presented in the form of series (Thomas, 1965; Ward, 1955; Bradley and McCutcheon, 1985). At very high concentrations of cohesionless particles in the confined flow gravity-free system, Bagnold (1954, 1956) introduced the notion of dispersive stress as a function of the square of the velocity gradient.

Chen (1983), and O'Brien and Julien (1984) recently developed different models that may cover a wide spectrum of fluid rheology including the turbulent and the dispersive stresses. The total shear stress τ in the model suggested by O'Brien and Julien is:

$$\tau = \tau_y + \eta \, du/dy + C_1 \, (du/dy)^2 \qquad (4)$$

in which τ_y is the yield stress due to cohesive properties of the fluid matrix; η is the viscosity of the mixture; and C_1 is a combined function of the turbulent stress and the dispersive stress due to the collision of particles ($C_1 = D_{1T} + C_{1D}$). The turbulent component of C_{1T} is a function ($C_{1T} = \rho_m \, L^2$) of the mass density of the mixture ρ_m and the Prandtl mixing length L. The dispersive component C_{1D} is a function of the linear concentration λ, the particle diameter D_s and a coefficient a_1 ($C_{1D} = a_1 \, \lambda^2 \, D_s^2$). This has been verified experimentally under a limited range of fluid properties. Recent inestigations in progress at Colorado State University show that hyperconcentrated mixtures of bentonite and water are non-Newtonian and the viscosity of the mixture η can be up to five orders of magnitude larger than the viscosity of water.

Dimensionless numbers define the relative magnitude of various stresses. The Bingham Reynolds number Re_B, the Yield number Y, the Hedstrom number H_e and the Plasticity number P, figure among the commonly used dimensionless numbers. The Bingham Reynolds number represents the ratio of inertial to viscous forces. The Yield number, sometimes called Bingham number, represents the ratio of yield to viscous forces. The Hedstrom number corresponds to the product of the Yield number and the Bingham Reynolds number. The Plasticity number represents the ratio of the yield to inertial forces. The Plasticity number is equivalent to the ratio of the Yield number to the Bingham Reynolds number. These four dimensionless numbers are defined as follows:

$Re_B = 4\rho_m R_h V/\eta$; Bingham Reynolds number

$Y = 4R_h \tau_y/V\eta$; Yield number

$H_e = Re_B \, Y = 16\rho_m \, R_h^2 \, \tau_y/\eta^2$; Hedstrom number

$P = Y/Re_B = \tau_y/\rho_m V^2$; Plasticity number

in which V is the average channel velocity; R_h is the hydraulic radius.

Studies of the transition from laminar to turbulent flow in hyperconcentrated flows are briefly discussed. The transition is a function of several parameters including the Reynolds number. Chinese researchers (Quian, et al., 1980; Dia, et al., 1980) experimentally demonstrated that the critical Reynolds number varies with the Hedstrom number as well as the Bingham Reynolds number. Hanks (1963) theoretically evaluated the critical Bingham Reynolds number in terms of the Hedstrom number for smooth boundaries. Hampton (1972) showed experimentally that the transition varies with the Yield number as well as the Bingham Reynolds number. That is in agreement with the above results.

Fall Velocity of Sediment Particles in Hyperconcentrated Flow

The fall velocity of spherical particles is expected to be greatly reduced in hyperconcentrated flow (Simons, et al., 1963; and Wan, 1985). Plessis and Ansley (1967) developed an empirical equation for the drag coefficient C_D of the drag force exerted by a Bingham fluid on particles. Pazwash (1970) treated semi-theoretically the drag force of a Bingham fluid on various geometric solid boundaries. His relation is basically the same as that of Plessis and Ansley and the drag coefficient C_D can be written:

$$C_D = C_{DN} + 2K \, P \qquad (5)$$

in which K is the empirical constant depending upon the geometry of the solid boundary; and C_{DN} is the Newtonian drag coefficient.

Chinese investigators have shown an interest in the settling behavior of particles in hyperconcentration. Zhang, et al. (1980) recognized three regions of settling characteristics in hyperconcentration based on their experimental

results: (1) hindered settling region; (2) selective settling region; and (3) uniform suspension region. A similar classification with the presence of fine flocculated particles less than 0.05 mm was suggested by Quian, et al. (1980). They obtained empirical relations for the relative fall velocity in terms of volume concentration. Their approach appears to be purely empirical without paying much attention to the rheology of fine sediment and its effect on the fall velocity in hyperconcentrations.

In summary interesting studies on the hyperconcentration phenomena have been initiated. Estimation of the rheological properties of hyperconcentrated flows depends entirely upon several empirical formulas for the yield, viscous, and dispersive stresses. The turbulence structure of clay suspensions is shown to be still Newtonian at low concentrations. The fall velocity of sand particles in clay suspension is reduced as compared to the fall velocity in clear water. The frequent occurrences of hyperconcentrated flow in southwestern United States and other countries should stimulate further research in this practically untouched field of study in sedimentation engineering.

CONCLUSIONS

Recent research trends in sedimentation are reviewed and three topics of major interest are discussed: bed forms; total sediment discharge; and hyperconcentrated flows. The study of bed forms in alluvial channels appears to have been greatly advanced considering the relatively short period of research time. There is still, however, no comprehensive method of general validity for predicting bed forms and resistance to flow in alluvial channels. The work by Simons and Richardson, Shen, Kennedy, Engelund, and Van Rijn figure among the best developments achieved so far. Topics of interest for further research should include the influence of temperature, infiltration, and concentration of fines on bed forms. Large scale roughness such as point bars, alternate bars, chute and pools requires additional investigations for predicting the resistance to flow in alluvial channels.

The evaluation of the parameters in the diffusional theory for the suspension of sediments should be carefully reconsidered. Indeed the results of the diffusion models rely heavily on accurate evaluation of the reference height a, the reference concentration C_a, the exponent Z, the coefficient β, and the fall velocity W.

Studies on hyperconcentrated flows in alluvial channels have been greatly reactivated in recent years. Some theoretical and experimental research is currently in progress at Colorado State University on the characteristics of hyperconcentrated flows such as bed sediment transport, rheological properties, fall velocity of bed sediment particles in clay suspensions, and characteristics of mud flows.

NOTATIONS

a	reference height
a_1	coefficient of the Bagnold equation for dispersive stress
C	concentration of sediment
C_1	combined function of turbulent stress and dispersive stress
C_{1T}	function of turbulent stress
C_{1D}	function of dispersive stress
C_a	reference concentration at y=a
C_D	drag coefficient
C_{DN}	drag coefficient of a Newtonian fluid
d	channel depth
D_s	particle diameter
D_{50}	mean particle diameter
f	Darcy-Weisbach friction factor
q_b	unit bed load rate
q_t	total unit bed material discharge
H_e	Hedstrom number
K	empirical constant in Pazwash's equation
k_s	characteristic roughness defined by Nikuradse
k	von Kármán constant
L	Prandtl mixing length
P	Plasticity number
Re_B	Bingham Reynolds number
R_h	hydraulic radius
u	time-averaged local velocity
U_a	mean transport velocity of bed load
U_*	shear velocity
U_{*c}	critical shear velocity
V	average channel velocity
W	particle fall velocity
Y	Yield number
y	vertical coordinate
Z	exponent in the Rouse equation
du/dy	rate of shear
β	coefficient of sediment diffusivity
Δ	dune height
η	viscosity of the mixture
λ	linear concentration
ρ_m	mass density of mixture
τ	shear stress
τ_y	yield stress
ϕ	transport intensity
ψ	shear intensity on particle

REFERENCES

Ackers, P. and W.R. White, 1973, "Sediment Transport: New Approach and Analysis," Journal of the Hydraulics Division, ASCE, Vol. 99, No. HY11, Nov.

Anderson, A.G., 1953, "The Characteristics of Sediment Waves formed by Flow in Open Channels," Proceedings, Third Midwestern Conference on Fluid Mechanics, University of Minnesota, Minneapolis, Minnesota, June.

Antsyferov, S.M. and R.D. Kos'yan, 1980, "Sediments Suspended in Stream Flow," Journal of the Hydraulics Division, ASCE, Vol. 106, No. HY2, Feb.

Bagnold, R.A., 1956, "Flow of Cohesionless Grains in Fluids," Philosophical Transactions of the Royal Society of London, Series A, Vol. 249.

Bagnold, R.A., 1954, "Experiments on a Gravity Free Dispersion of Large Solid Spheres in a Newtonian Fluid Under Shear," Proceedings, Royal Society of London, Series A, Vol. 225, London, England.

Bagnold, R.A., 1966, "An Approach to the Sediment Transport Problem From General Physics," Professional Paper 422-I, USGS, Washington, D.C.

Bechteler, W., K. Farber and W. Schrimpf, 1983, "Settling Velocity Measurements in Quiescent and Turbulent Water," The Second International Symposium on River Sedimentation, Nanjing, China, Oct.

Beverage, J.P. and J.K. Culbertson, 1964, "Hyperconcentrations of Suspended Sediment," Journal of the Hydraulics Division, ASCE, Vol. 90, HY6, Nov.

Bishop, A.A., D.B. Simons and E.V. Richardson, 1965, "Total Bed Material Transport," Journal of the Hydraulics Division, ASCE, Vol. 91, HY2, Mar.

Bondurant, D.C., 1950, Discussion of "Sedimentation Studies at Conchas Reservoir in New Mexico," Trans., ASCE, Paper No. 2466, Aug.

828

Bouvard, M. and S. Petkovic, 1985, "Vertical Dispersion of Spherical Heavy Particles in Turbulent Open Channel Flow," Journal of Hydraulics Research, IAHR, Vol. 23, No. 1.

Bradley, J.B., 1983, "Transition of a Meandering River to a Braided System Due to High Sediment Concentration Flow," Proceedings of the Conference Rivers '83, ASCE, New Orleans, Oct.

Bradley, J.B. and S.C. McCutcheon, 1985 (In Press), "Effects of High Sediment Concentration on Transport Processes and Flow Phenomena," Proceedings International Symposium on Erosion, Debris Flow, and Disaster Prevention, Sept. 3-5, Tsukuba, Japan.

Brooks, N.H., 1963, "Calibration of Suspended Load Discharge From Velocity and Concentration Parameters," Proceedings of the Federal Interagency Sedimentation Conference, 1965, Miscellaneous Publication No. 970, ARS, U.S. Department of Agriculture, Washington, D.C.

Carstens, M.R., 1952, "Accelerated Motion of a Spherical Particle," Transactions of the American Geophysical Union, Vol. 33, No. 5, Oct.

Chang, F.M., D.B. Simons and E.V. Richardson, 1965, "Total Bed Material Discharge in Alluvial Channels," Water-Supply Paper 1498-I, USGS, Washington, D.C.

Chen, C.L., 1983, "On Frontier Between Rheology and Mud Flow Mechanics," Proc. ASCE Hydraulics Division Speciality Conference, Boston, Mass., Aug.

Coleman, N.L., 1970, "Flume Studies of the Sediment Transfer Coefficient," Water Resources Res. 6, No. 3.

Coleman, N.L., 1981, "Velocity Profiles with Suspended Sediment," Journal of Hydraulic Research, 19, No. 3.

Colby, B.R., 1964, "Discharge of Sands and Mean Velocity Relationships in Sand-Bed Streams," Professional Paper 462-A, USGS, Washington, D.C.

Colby, B.R. and C.H. Hembree, 1955, "Computations of Total Sediment Discharge Niobrara River near Cody, Nebraska," Water-Supply Paper 1357, USGS, Washington, D.C.

Dia, J., et al., 1980, "An Experimental Study of Transport in Pipes," Proc. of the International Symposium on River Sedimentation, Beijing, China, Mar.

Egiazaroff, I., 1969, "Polyphase Currents With Nonuniform Sediments and the Physics of River Flow," 13th Congress of IAHR Proceedings, Vol. 2, Tokyo.

Einstein, A., 1905; 1906, Ann. Physik, 17, 459, 1905; 19, 289, 1906.

Einstein, H.A., 1950, "The Bed Load Function for Sediment Transportation in Open Channels," Technical Bulletin 1026, U.S. Department of Agriculture, SCS, Washington, D.C.

Einstein, H.A. and N. Chien, 1955, "Effects of Heavy Sediment Concentration near the Bed on Velocity and Sediment Distribution," MRD Series No. 8, University of California, Institute of Engineering Research and United States Army Engineering Division, Missouri River, Corps of Engineers, Omaha, Nebr.

Einstein, H.A. and N. Barbarossa, 1952, "River Channel Roughness," Trans., ASCE, Vol. 117, Paper No. 2528.

Engelund, F., 1967, "Hydraulic Resistance of Alluvial Streams," Journal of the Hydraulic Division, ASCE, Vol. 93, No. HY4, July.

Engelund, F., 1980, "Instability of Erodible Beds," Journal of Fluid Mechanics, Vol. 42, pp. 225-40.

Engelund, F. and E. Hansen, 1967, "A Monograph on Sediment Transport to Alluvial Streams," Teknish Forlag, Technical Press, Copenhagen, Denmark.

Engelund, F. and J. Fredsøe, 1976, "A Sediment Transport Model for Straight Alluvial Channels," Nordic Hydrology, No. 7.

Gilbert, G.K. 1914, "Transportation of Debris by Running Water," Professional Paper No. 86, USGS.

Gust, G., 1976, "Observations on Turbulent Drag Reduction in a Dilute Suspension of Clay in Sea-Water," Journal of Fluid Mechanics, Vol. 75, Part I.

229

Hanks, R.W., 1963, "The Laminar-Turbulent Transition for Fluids with a Yield Stress," A.I.Ch.E. Journal, Vol. 9, No. 3.

Hampton, M.A., 1972, "The Role of Subaqueous Debris Flow in Generating Turbidity Currents," Journal of Sedimentary Petrology, Vol. 42.

Hino, M., 1963, "Turbulent Flow with Suspended Particles," Journal of the Hydraulics Division, ASCE, Vol. 89, HY4, July.

Hinze, J.D., 1975, Turbulence, 2nd edition, McGraw-Hill Book Company, pp. 729-30.

Holtorff, F., 1983, "Steady Bed Material Transport in Alluvial Channels," Journal of the Hydraulics Division, ASCE, Vol. 109, No. 3, Mar.

Houghton, G., 1968, "Particle Retardation in Vertically Oscillating Fluids," The Canadian Journal of Chemical Engineering, Vol. 46, No. 2.

Hunt, J.N., 1954, "The Turbulent Transport of Suspended Sediment in Open Channels," Proc., Royal Society of London, Series A, Vol. 224, No. 1158.

Hus, S.T. and J.F. Kennedy, 1971, "Turbulent Flow in Wavy Pipes," Journal of Fluid Mechanics, Vol. 47, No. 3, June.

Hwang, P.A., 1985, "Fall Velocity of Particles in Oscillating Flow," Journal of the Hydraulics Division, ASCE, Vol. 111, No. 3, Mar.

Ikeda, S., 1983, "Flow and Bed Topography in Channels With Alternate Bar," River Meandering, Proc. of the Conference Rivers '83, New Orleans, Louisiana, Oct. 24-26.

International Symposium on River Sedimentation, 1980, Beijing, China; 1983, Nanjing, China.

Itakura, T. and T. Kishi, 1980, "Open Channel Flow with Suspended Sediments," Journal of the Hydraulics Division, ASCE, HY8, Aug.

Jobson, H.E. and W.W. Sayre, 1970a, "Vertical Transfer in Open Channel Flow," Journal of the Hydraulics Division, ASCE, Vol. 96, No. HY3, Mar.

Jobson, H.E. and W.W. Sayre, 1970b, "Predicting Concentration Profiles in Open Channels," Journal of the Hydraulics Division, ASCE, Vol. 96, No. HY10, Oct.

Karim, F. and J.F. Kennedy, 1983, "Missouri River Computer-Based Predictors for Sediment Discharges and Friction Factors of Alluvial Streams," MRD Sediment Series, No. 29, U.S. Army Corps of Engineers, Missouri River Division, July.

Kennedy, J.F., 1963, "Mechanics of Dunes and Antidunes in Erodible-Bed Channels," Journal of Fluid Mechanics, Vol. 16, No. 4.

Keulegan, G.H., 1938, "Laws of Turbulent Flow in Open Channels," Journal of Research, U.S. Bureau of Standards, Research Paper, RP1151, Vol. 21, Dec.

Kikkawa, M. and S. Fukuoka, 1969, "The Characteristics of Flow With Wash Load," 13th Congress of IAHR, Tokyo, Vol. 2, pp. 233-40.

Kikkawa, H. and T. Ishikawa, 1978, "Total Load of Bed Materials in Open Channels," Journal of the Hydraulics Division, ASCE, Vol. 104, No. HY7, July.

Lane, E.W. and A.A. Kalinske, 1939, "The Relation of Suspended to Bed Material in Rivers," Trans., American Geophysical Union, Part IV, Washington, D.C.

Leopold, L.B., R.A. Bagnold, M.G. Wolman and L.M. Brush, Jr., 1960, "Flow Resistance in Sinuous or Irregular Channels," USGS Professional Paper 282-D, Washington, D.C.

Liu, H.K., 1957, "Mechanics of Sediment-Ripple Formation," Proc., ASCE, Vol. 83, No. HY2.

Maude, A.D. and R.L. Whitmore, 1958, "A Generalized Theory of Sedimentation," British Journal of Applied Physics, Vol. 9, Dec.

230

McNown, J.S. and P.N. Lin, 1952, "Sediment Concentration and Fall Velocity," Proc., 2nd Midwestern Conference on Fluid Mechanics, Ohio State University, Columbus, Ohio, pp. 401-11.

Mendoza, C. and H.W. Shen, 1985, "Steady Two-Dimensional Flow Over Dunes," Submitted to the 21st Congress of the International Association for Hydraulic Research, Melbourne, Australia, Aug.

Murphy, P.J., 1985, "Equilibrium Boundary Condition for Suspension," Journal of the Hydraulics Division, ASCE, Vol. 111, No. 1, Jan.

Murphy, P.J. and E.J. Aguirre, 1985, "Bed Load or Suspended Load," Journal of the Hydraulics Division, ASCE, Vol. 111, No. 1, Jan.

National Research Council, 1982, "Selecting a Methodology for Delineating Mudslide Hazard Areas for the National Flood Insurance Program," Committee on Methodologies for Predicting Mudflow Areas, National Academy Press, Washington, D.C.

Nordin, C.F., Jr., 1963, "A Preliminary Study of Sediment Transport Parameters, Rio Puerco Near Bernardo, New Mexico," Professional Paper 462-C, USGS, Washington, D.C.

Nordin, C.F., Jr. and G.R. Dempster, Jr., 1963, "Vertical Distribution of Velocity and Suspended Sediment, Middle Rio Grande, New Mexico," Professional Paper 462-B, USGS, Washington, D.C.

Nordin, C.F., Jr. and J.H. Algert, 1966, "Spectral Analysis of Sand Waves," Journal of the Hydraulics Division, ASCE, Vol. 92, HY5.

O'Brien, J.S. and P.Y. Julien, 1984, "Physical Properties and Mechanics of Hyperconcentrated Sediment Flow," Specialty Conference on Delineation of Landslide, Flash Flood and Debris Flow Hazards in Utah, June 14-15.

Ordonez-C, Nelson A., 1970, "The Absolute Concentration Distribution of Suspended Sediment in Turbulent Streams," Ph.D. Thesis, M.I.T., R.M. Parsons Lab. for Water Resources and Hydrodynamics, July.

Pazwash, H., 1970, "Drag Forces on Bodies Moving Through Aqueous Clay Suspensions," Ph.D. Thesis, University of Illinois.

Plessis, M.P. and R.W. Ansley, 1967, "Settling Parameters in Solid Pipelining," Journal of the Pipeline Division, ASCE, Vol. 93, No. PL2, July.

Quian, Y., et al., 1980, "Basic Characteristics of Flow with Hyperconcentration of Sediment," Proceedings of the International Symposium on River Sedimentation, Beijing, China, Mar.

Ranga Raju, K.G., R.J. Garde and R.C. Bhardwaj, 1981, "Total Load Transport in Alluvial Channels," Journal of the Hydraulics Division, ASCE, Vol. 107, No. HY2, Feb.

Raudkivi, A.J., 1963, "Study of Sediment Ripple Formation," Proc., ASCE, Vol. 89, HY6.

Richardson, J.R., 1984, "Inflow Seepage Effects of Straight Alluvial Channels," M.S. Thesis, Colorado State University, Fort Collins, Colorado.

Richardson, J.F. and W.N. Zaki, 1954, "Sedimentation and Fluidization," Part I, Trans. Inst. Chen. Engrs., London, Vol. 32.

Rouse, H., 1937, "Modern Conceptions of the Mechanics of Fluid Turbulence," Trans., ASCE, Vol. 102, Paper No. 1965.

Shen, H.W. and C.S. Hung, 1971, "An Engineering Approach to Total Bed Material Laod by Regression Analysis," Proceedings, Sedimentation Symposium, Berkeley, California.

Shen, H.W. and C.S. Hung, 1983, "Remodified Einstein Procedure for Sediment Load," Journal of the Hydraulics Division, Vol. 109, No. 4, Apr.

Shen, H.W., W.C. Wang and J.Y. Lu, 1981, "Missouri River Vertical Sediment Concentration Distribution for Different Sediment Sizes," MRD Sediment Series, No. 25, U.S. Army Corps of Engineers, Missouri River Division, Nov.

231

Shields, A., 1936, "Anwendung der Aehnlichkeitsmechanik und der Turbulenzforschung auf die Geschiebebewegung," Preussische Versuchsanstalt für Wasserbau und Schiffbau, Berlin.

Simons, D.B. and E.V. Richardson, 1961, "Form of Bed Roughness in Alluvial Channels," Proc., ASCE, Vol. 87, No. HY3.

Simons, D.B. and E.V. Richardson, 1966, "Resistance to Flow in Alluvial Channels," Professional Paper 422-J, USGS, Washington, D.C.

Simons, D.B., E.V. Richardson and W.L. Haushild, 1963, "Some Effects of Fine Sediments on Flow Phenomena," Water-Supply Paper 1498G, USGS, Washington, D.C.

Singamsetti, S.R., 1966, "Diffusion of Sediment in a Submerged Jet," Journal of the Hydraulics Division, ASCE, Vol. 92, No. HY2, Mar.

Smith, J.D., 1970, "Stability of a Sand Bed Subjected to a Shear Flow of Low Froude Number," Journal of Geophysical Research, Vol. 75, pp. 5928-39.

Steffler, P.M., N. Rajaratnam and A.W. Peterson, 1985, "LDA Measurements in Open Channel," Journal of the Hydraulics Division, ASCE, Vol. 111, No. 1, Jan.

Terwindt, J.H.J., H.N.C. Breusers and J.N. Svasek, 1965, "Experimental Investigation on the Erosion Sensitivity of a Sand-Clay Lamination," Sedimentology, Vol. II.

Thomas, D.G., 1965, "Transport Characteristics of Suspension," Journal of Colloid Science, Vol. 20.

Toffaleti, F.B., 1968, "A Procedure for Computation of the Total River Sand Discharge and Detailed Distribution, Bed to Surface," Technical Report No. 5, Committee on Channel Stabilization, Corps of Engineers, U.S. Army, Vicksburg, Mississippi, Nov.

Vanoni, V.A., 1946, "Transportation of Suspended Sediment by Water," Trans., ASCE, Vol. III, Paper No. 2267.

Vanoni, V.A., Editor, 1977, Sedimentation Engineering, ASCE, N.Y.

Vanoni, V.A., 1984, "Fifty Years of Sedimentation," Journal of the Hydraulics Division, ASCE, Vol. 110, No. 8, Aug.

Vedula, S. and R.R. Achanta, 1985, "Bed Shear From Velocity Profiles: A New Approach," Journal of the Hydraulics Division, ASCE, Vol. 111, No. 1, Jan.

van Rijn, L.C., 1984a, "Sediment Transport, Part II: Suspended Load Transport," Journal of the Hydraulics Division, ASCE, Vol. 110, No. 11, Nov.

van Rijn, L.C., 1984b, "Sediment Transport, Part III: Bed Forms and Alluvial Roughness," Journal of the Hydraulics Division, ASCE, Vol. 110, No. 12, Dec.

Wan, Z., 1985, "Bed Material Movement in Hyperconcentrated Flow," Journal of the Hydraulics Division, ASCE, Vol. 111, No. 6, June.

Wang, S., 1981, "Variation of Kármán Constant in Sediment-Laden Flow," Journal of the Hydraulics Division, ASCE, Vol. 107, HY4, Apr.

Ward, S.G., 1955, "Properties of Well-Defined Suspensions of Solids in Liquids," Journal of Oil and Colour Chemists' Association, Vol. 38.

White, W.R., M. Milli and A.D. Crabbe, 1973, "Sediment Transport: An Appraisal of Available Methods," Vol. 2, Report INT 119, Hydraulics Research Station, Wallingford, England.

Willis, J.C., 1979, "Suspended Load From Error-Function Models," Journal of the Hydraulics Division, ASCE, Vol. 105, No. HY7, July.

Wiuff, R., 1985, "Transport of Suspended Material in Open and Submerged Streams," Journal of the Hydraulics Division, ASCE, Vol. 111, No. 5, May.

Yalin, M.S. and G.D. Finlayson, 1972, Sedimentation, Symposium to Honor Professor M.A. Einstein, Edited by H.W. Shen.

Yang, C.T., 1973, "Incipient Motion and Sediment Transport," Journal of the Hydraulics Division, ASCE, Vol. 99, No. HY10, Oct.

Yang, C.T., 1979, "Unit Stream Power Equations for Total Load," Journal of Hydrology, Vol. 40, No. 1/2.

Yang, C.T. and A. Molinas, 1982, "Sediment Transport and Unit Stream Power Function," Journal of the Hydraulics Division, Vol. 108, No. HY6, June.

Zhang, H., et al., 1980, "Settling of Sediment and the Resistance to Flow at Hyperconcentration," Proceedings of the International Symposium on River Sedimentation, Vol. 1, Beijing, China.

Zimmermann, C. and J.F. Kennedy, 1978, "Transverse Bed Slopes in Curved Alluvial Streams," Journal of the Hydraulics Division, ASCE, HY1, Jan.

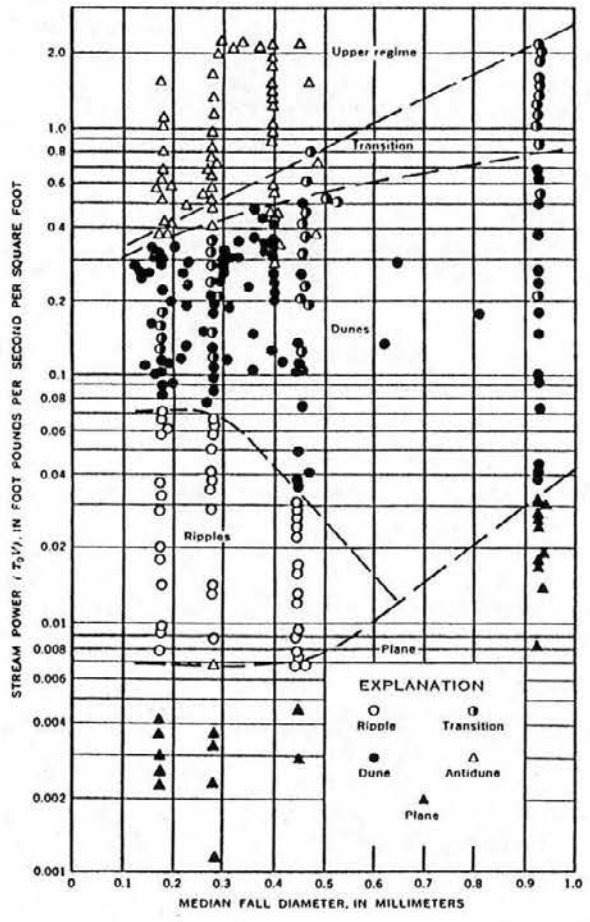

Fig. 1. Diagram for Bed-Form Classification (After Simons and Richardson, 1961)

233

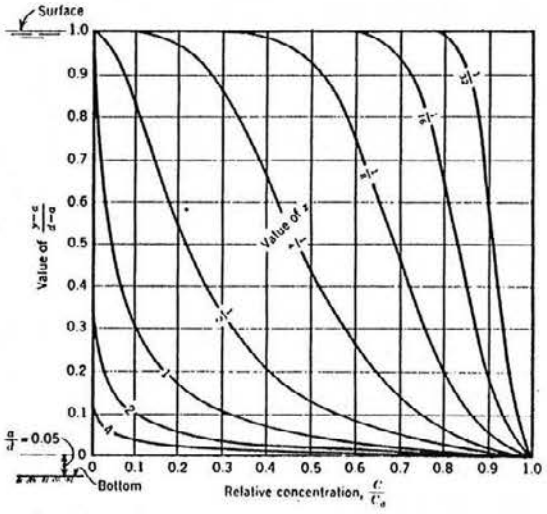

Fig. 2. Relative Concentration of Suspended Sediment (After Rouse, 1937)

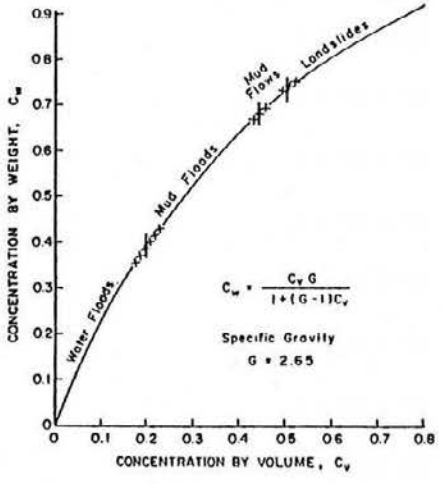

Fig. 3. Classification of Hyperconcentrated Flows.

APPLICATION OF NUMERICAL MODELING TECHNIQUES AT MOUNT ST. HELENS

by
D.B. Simons
Professor
Colorado State University
and Principal Engineer
Simons & Associates, Inc.
Fort Collins, Colorado

and
J.B. Bradley
Research Associate
Colorado State University
Fort Collins, Colorado

ABSTRACT

On 18 May 1980, just before a magmatic blast signaled the onset of the Mount St. Helen's eruption, an earthquake triggered a major slope failure on the north flank of the mountain. As a result, approximately three billion cubic yards of rock and ice avalanched into the North Fork Toutle River Valley. Mud and debris flows were generated and swept down the Toutle and Cowlitz Rivers destroying bridges, inundating buildings, and eventually blocking the navigation channel of the Columbia River. Within twenty-four hours the mud flows deposited some fifty million cubic yards of sediment in the lower twenty-three miles of the Cowlitz River reducing channel capacity by nearly eighty percent. Five years after the initial eruption, large volumes of sediment continue to be delivered to these rivers from the debris avalanche. Continuing sedimentation problems of this magnitude have resulted in utilization of both analytical and numerical techniques to predict future erosion and sedimentation within the river system. This paper assesses the numerical modeling approaches used to date in predicting "normal" sediment transport rates and high concentration flow rates (hyperconcentrated flows and mud flows). The applicability of these techniques and future developments in modeling sediment laden flows such as those experienced at Mount St. Helens and elsewhere will also be addressed.

234

WASHLOAD AND FINE SEDIMENT LOAD

By Hyoseop S. Woo,[1] Pierre Y. Julien,[2] M. ASCE, and Everett V. Richardson,[3] F. ASCE

INTRODUCTION

Einstein (3) does not take credit for designing the washload concept, but he describes it very distinctly. He stated that if the sediment is added to the upstream end of a concrete channel and the channel is swept clean, and the sediment has not left any trace in the channel, its rate of transport need not be related to the flow rate. This kind of sediment load has been called washload because it has just washed through the channel. He further stated that all particle sizes that are not significantly represented in the deposit must be considered as washload. This washload concept, which is generally accepted by professionals working in the field, means that on the high plains of the United States the washload normally consists of silts and clays (1,7). As a result the misconception that washload consists only of the fine sediments, silts and clays is quite common.

Many investigators dislike the term "washload" and often substitute "fine sediment" for "washload." The late Paul Benedict always insisted that his colleagues use the term fine sediment instead of washload. However, the use of the term fine sediment load for washload helps perpetuate the confusion that sometimes occurs.

LOAD AND DISCHARGE

The term "load," which refers to the material that is being transported, has sometimes been used in place of "discharge," which refers to the rate of transport of the material. Therefore, "sediment discharge" refers to the transport rate of sediment load. The term "bed sediment load" should be used instead of bed material load because "material load" is redundant. Similarly, "fine sediment load" should be preferred to "fine material load."

FINE SEDIMENT LOAD

Fine sediment load is defined as the load of silts and clays, which have diameters smaller than 0.0625 mm. The fine sediment load includes the electro-chemically interacting clay particles which affect the fluid properties and settling velocity of larger particles.

[1]Grad. Student, Dept. of Civ. Engrg., Colorado State Univ., Ft. Collins, CO 80523.

[2]Asst. Prof., Dept. of Civ. Engrg., Colorado State Univ., Ft. Collins, CO 80523.

[3]Prof., Dept. of Civ. Engrg., Colorado State Univ., Ft. Collins, CO 80523.

Note.—Discussion open until November 1, 1986. To extend the closing date one month, a written request must be filed with the ASCE Manager of Journals. The manuscript for this paper was submitted for review and possible publication on November 11, 1985. This paper is part of the *Journal of Hydraulic Engineering*, Vol. 112, No. 6, June, 1986. ©ASCE, ISSN 0733-9429/86/0006-0541/$01.00. Paper No. 20768.

235

WASHLOAD

The concept of washload was introduced by Einstein, Anderson and Johnson (2) and defines the size fractions of total sediment load not present in significant amounts in the sediment bed and which is easily washed away by the flow. Washload depends upon the upslope supply of fine sediments and the upstream flow conditions. Einstein (3) suggested that the largest sediment size of washload may be arbitrarily chosen as the grain diameter D_{10} of which 10% of the total bed sediment is finer. The sediment load excluding the washload is termed the bed sediment load. Einstein and Chien (4) experimentally verified that the washload could not be predicted from Einstein's bedload function. The limiting sediment size between washload and bed sediment load corresponds to the point at which the sediment transport capacity equals the sediment supply from upstream (9). Washload does not have any direct relation to the size of the sediment although many engineers assume the limiting size of washload to be approximately 0.0625 mm which corresponds to the fine sediment load defined above.

In summary, three criteria have been recommended to separate the washload from bed sediment load: (1) Grain diameter D_{10}; (2) transport capacity and supply curves; and (3) sediment size finer than 0.0625 mm. Some difficulties in the use of these criteria are analyzed in the following examples.

LARGE CONCENTRATIONS OF FINES

With large concentrations of fine sediments in suspension, the range of particle sizes in the bed broadens to the extent that the sediment size corresponding to D_{10} is arbitrarily defined. Fine sediments are found in large proportions in the bed and the D_{10} can be much smaller than 0.0625 mm as shown in Fig. 1.

The backbone of Einstein's concept based on D_{10} implies continuous exchange between the particles in suspension and those found in the bed. With increasing concentration of fines, the viscosity increases and the settling velocity of sand-sized particles is reduced significantly (11).

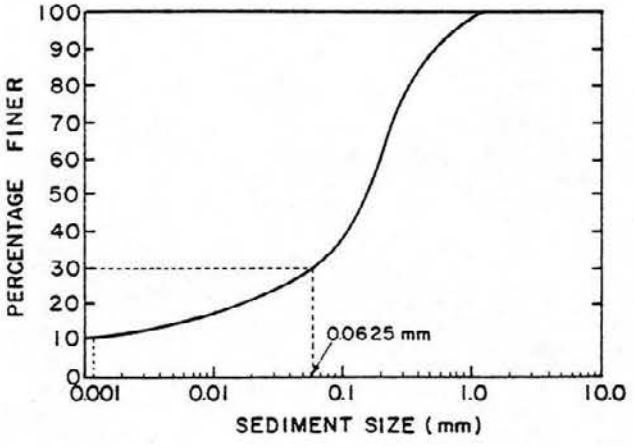

FIG. 1.—Bed Sediment Size Distribution

Once particles larger than D_{10} in the bed are brought to motion, their sedimentation diameter becomes so small that there is virtually no exchange between these particles and those remaining in the bed. In this case, particles larger than D_{10} can be considered as part of the washload.

Changes in viscosity by several orders of magnitude have been observed at very low concentrations of montmorillonite and kaolinite clays (8). In addition to major increases in viscosity, the fluid gradually behaves as a non-Newtonian fluid due to the cohesive properties of the clay particles. The criteria based on sediment supply and transport capacity then proves difficult to apply since large concentrations of fines affect both the fluid properties and the transport capacity.

Experiments by Einstein and Chien (5) with a wide range of sediment sizes showed segregation of bed material which makes the determination of a representative bed sediment size rather difficult. Flume studies by Simons, Richardson and Haushild (10) showed that sand bed channels can be impregnated with clays. Nordin (6) also reported field evidence of clay-cemented channels in which the bed is armored with clays. These additional effects of segregation of bed sediment, impregnation of clays and clay-cemented channels invalidate the definition of washload at large concentrations of fine sediments.

Gravel and Cobble Bed Streams

The concept of washload in coarse bed streams also poses some difficulties. Unlike the previous example, all the material transported is basically non-cohesive. Flow velocities in steep mountain streams are sufficiently large to transport large sediment sizes without significant

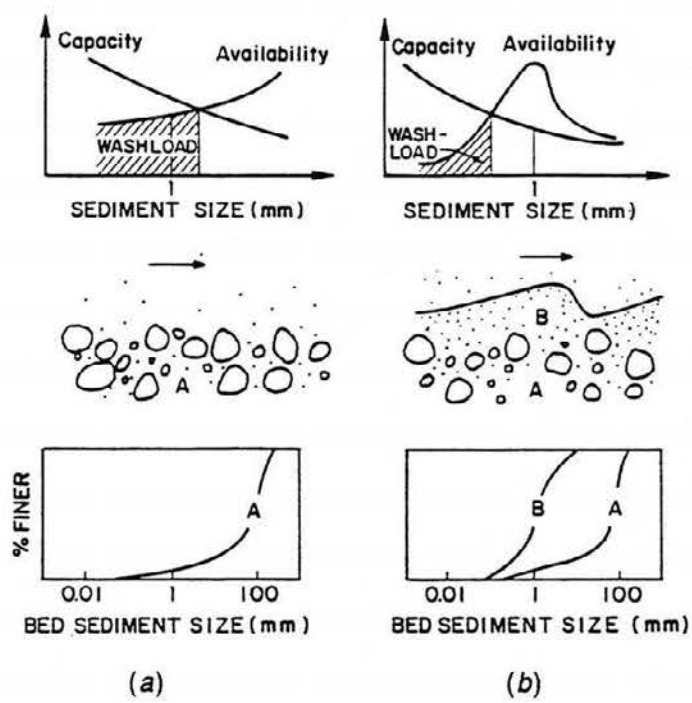

FIG. 2.—Washload versus Bed Sediment Load in Coarse Bed Streams: (*a*) Sand-Free Cobble-Bed Stream; (*b*) Sand-Covered Cobble-Bed Stream

237

deposition on the gravel or cobble bed. As a result, sand-sized particles may be included in the washload.

Two cases are illustrated in Fig. 2. When the sediment transport capacity exceeds the availability of sediments, or supply, the sand particles transported as washload are not found significantly in the armored bed illustrated in Fig. 2(*a*). In some cobble-bed streams the sand supply varies periodically and at times may increase until it exceeds the transport capacity of the flow. Deposition then occurs until the cobble-bed stream is completely covered with sands [Fig. 2(*b*)]. Sand particles can then be treated temporarily as part of the bed sediment load of a sand-covered channel. Schematically, the bed sediment size distribution shifts from Curve A to Curve B when the sediment supply exceeds the transport capacity, and returns to Curve A when the transport capacity exceeds the supply. Consequently, in a given channel the same sediment size can be included either in the washload or the bed sediment load, depending upon the availability and the transport capacity for that size fraction.

Conclusions

"Washload" and "fine sediment load" are not synonymous. Fine sediment load refers to silts and clays and washload refers to the part of the total load that is washed through the channel and not found in significant quantity in the bed. The term sediment load denotes the material that is being transported and the term sediment discharge designates the rate of transport of the sediment load.

In streams with large concentrations of fines, the sediment size D_{10} may be much smaller than 0.0625 mm. The fluid becomes very viscous at low concentrations of clays and the reduced settling velocity inhibits the exchange of sediment particles between the bed and the suspension. The sediment transport capacity under those conditions remains very poorly defined.

In coarse bed streams, sands and fine gravels can be considered as washload as long as the sediment transport capacity remains larger than the availability of sediment. Intermittently, different conditions prevail when the upstream supply exceeds the transport capacity.

Appendix.—References

1. Colby, B. R., "Fluvial Sediments—A Summary of Source, Transportation, Deposition, and Measurement of Sediment Discharge," USGS Bulletin 1181-A, 1963.
2. Einstein, H. A., Anderson, A. G., and Johnson, J. W., "A Distinction Between Bed-Load and Suspended Load in Natural Streams," Trans. American Geophysical Union, Vol. 21, pt. 2, 1940, pp. 628–633.
3. Einstein, H. A., "The Bed Load Function for Sediment Transportation in Open Channels," Technical Bulletin 1026, U.S. Department of Agriculture, Soil Conservation Service, Washington, D.C., 1950.
4. Einstein, H. A., and Chien, N., "Can the Rate of Wash Load be Predicted From the Bed-Load Function?" Trans. American Geophysical Union, Vol. 34, No. 6, 1953, pp. 876–882.

5. Einstein, H. A., and Chien, N., "Transportation of Sediment Mixture With Large Ranges of Grain Sizes," Univ. of California, Institute of Engineering Research, Berkeley, Calif.; The Missouri River Division, Corps of Engineers, U.S. Army, Missouri River Division Sediment Series, No. 2, June, 1953.
6. Nordin, C. F., Jr., "A Preliminary Study of Sediment Transport Parameters, Rio Puerco Near Bernardo, New Mexico," USGS Professional Paper 462-C, Washington, D.C., 1963.
7. Nordin, C. F., Jr., "Aspects of Flow Resistance and Sediment Transport, Rio Grande Near Bernalillo, New Mexico," USGS Water Supply Paper 1498-H, 1964.
8. O'Brien, J. S., and Julien, P. Y., "Physical Properties and Mechanics of Hyperconcentrated Sediment Flows," *Proceedings*, Specialty Conference on Delineation of Landslide, Flashflood and Debris Flow Hazards in Utah, Utah State Univ., Logan, Utah, June 14–15, 1984, pp. 260–279.
9. Shen, H. W., "Wash Load and Bed Load," *River Mechanics*, H. W. Shen, Ed., Fort Collins, Colo., 1971, pp. 11.1–11.4.
10. Simons, D. B., Richardson, E. V., and Haushild, W. L., "Some Effects of Fine Sediments on Flow Phenomena," USGS Water Supply paper 1498-G, Washington, D.C., 1963.
11. Woo, H. S., "Sediment Transport in Hyperconcentrated Flows," thesis presented to Colorado State University at Fort Collins, Colo., in 1985, in partial fulfillment of the requirements for the degree of Doctor of Philosophy.

Morel, T. (1979). "Experimental study of a jet-driven Helmholtz oscillator." *J. Fluid Engrg.*, 101, 383–390.
Rockwell, D., and Naudascher, E. (1979). "Self-sustained oscillations of impinging free shear layers." *Annual Review of Fluid Mech.*, 11, 67–94.
Schachenmann, A., and Rockwell, D. (1980). "Self-sustained oscillations of turbulent pipe flow terminated by an axisymmetric cavity." *J. Sound and Vibration*, 73(1), 61–72.
Ziada, S., and Rockwell, D. (1982). "Oscillations of an unstable mixing layer impinging upon an edge." *J. Fluid Mech.*, 124, 307–334.

TRANSPORT OF BED SEDIMENT IN CLAY SUSPENSIONS

By Hyoseop Woo,[1] A. M. ASCE, Pierre Y. Julien,[2] M. ASCE, and Everett V. Richardson,[3] F. ASCE

INTRODUCTION

The presence of fine sediments is known to increase the bed sediment discharge (2,3). Concentrations of suspended sediments larger than 600,000 ppm (about 40% by volume) have been reported in the United States (2) and in China (11). These hyperconcentrated flows have caused irrigation and flood control problems such as clogging and aggradation (2,6).

Several researchers (3, 7, 9, and 11) documented the effects of large concentrations of sediments on the fluid properties such as the viscosity, the density, and the reduction of fall velocity of bed sediment particles. For example, Simons, et al. (9) measured the fall velocity of sand particles in suspensions of bentonite and kaolinite. Wan (11) suggested that in clay suspensions the contact bed sediment discharge may decrease due to the increased threshold velocity. On the other hand the suspended sediment discharge could increase due to the reduction of sediment fall velocity. Colby (3) pioneered several investigations on highly concentrated flows with both fine sediments and sands. Colby's empirical method for estimating total bed sediment discharge in hyperconcentrated flows accounts for the effect of fine sediment with concentra-

[1]Visiting Scholar, Dept. of Civ. and Envir. Engrg., Univ. of Cincinnati, Cincinnati, OH 45221.
[2]Asst. Prof., Dept. of Civ. Engrg., Colorado State Univ., Fort Collins, CO 80523.
[3]Prof., Dept. of Civ. Engrg., Colorado State Univ., Fort Collins, CO 80523.

Note.—Discussion open until January 1, 1988. To extend the closing date one month, a written request must be filed with the ASCE Manager of Journals. The manuscript for this paper was submitted for review and possible publication on May 1, 1986. This paper is part of the *Journal of Hydraulic Engineering*, Vol. 113, No. 8, August, 1987. ©ASCE, ISSN 0733-9429/87/0008-1061/$01.00. Paper No. 21746.

240

tions up to 200,000 ppm (about 9% by volume).

The purpose of this study is to test the applicability of existing sediment transport formulas for predicting the total bed sediment discharge in flows of clay suspensions. Einstein's sediment transport formula (4) is selected because the parameters are related to the fluid viscosity and density. Colby's graphical method (3) includes the effect of large concentrations of fine sediments. The flume data collected by Simons, Richardson, and Haushild (9) with high concentrations of both fine sediments and sands are used to test the applicability of these two methods.

Einstein's Method

Einstein's sediment transport formula (4) predicts separately the bed sediment discharges in contact with the bed and in suspension, the sum of which gives the total bed sediment discharge. The contact sediment discharge depends on the shear intensity factor obtained after considering the stochastic motion of the sediment particles on the bed. The suspended bed sediment discharge, a portion of the total bed sediment discharge in suspension, is predicted by using the Rouse sediment concentration profile equation and the logarithmic velocity profile. The reference concentration is obtained from the contact bed sediment discharge within the bed layer. The shear velocity related to the grain roughness is calculated using the graphical method suggested by Vanoni and Brooks (10). Pemberton's (8) correction procedure for the hiding factor ξ has been followed with Einstein and Chien's (5) correction factor θ for the laminar flow effects on fine sediment particles.

The sediment transport data for sand particles (0.47 mm and 0.59 mm) in bentonite clay suspensions collected by Simons, et al. (9) has been used. The data set includes a total of 92 runs with uniformly dispersed concentrations of fine sediments C_f less than 59,000 ppm and bed sediment discharge q_T smaller than 182 N/m/s. The 22 runs where C_f exceeds 10,000 ppm and q_T exceeds 1.9 N/m/s were used for this study. The largest apparent kinematic viscosity in the experiment was about 2.8×10^{-6} m^2/s, which is three times larger than that of clear water at 20° C. The bed forms changed from dunes to standing waves as the average channel velocity increased from 0.6 m/s to 1.83 m/s. The channel depth varied from 11.9 cm to 26.5 cm, and the channel slope varied from 0.0018 to 0.019.

Contact Bed Sediment Discharge.—The increase in viscosity and density of the suspension alters the parameters of the Einstein bed load function. These parameters include the hiding factor, the pressure reduction effect, the laminar flow effect, and the shear velocity. As shown in Fig. 1, the ratio q_{bc}/q_{bu} of the calculated contact bed sediment discharges (corrected, q_{bc}; and uncorrected, q_{bu}, for the viscosity and density of the suspension) is not significantly affected by the concentration of fine sediments. This implies that the increase in the total bed sediment discharge at large concentrations of fine sediments is not caused by the contact bed sediment discharge.

Total Bed Sediment Discharge.—The reduction in fall velocity of sand particles in a clay suspension decreases the exponent Z of the Rouse equation. This increases the concentration of suspended bed sediment

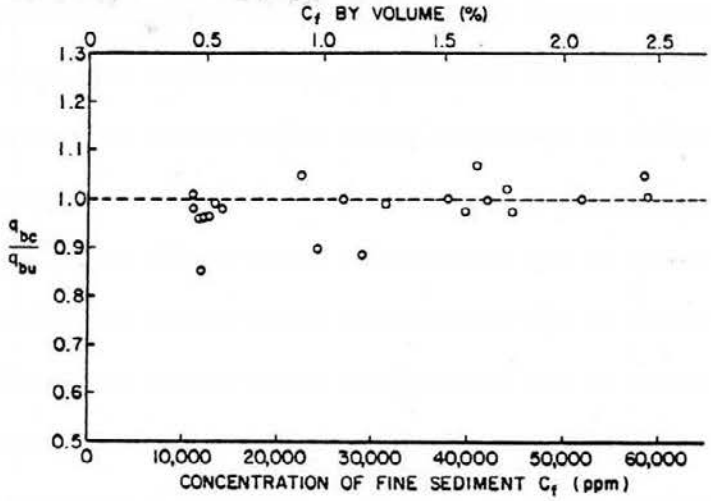

FIG. 1.—Ratio of Contact Bed Sediment Discharges Calculated from Einstein's Formula Corrected, q_{bc}, to Uncorrected, q_{bu}, for Viscosity and Density of Suspension

particles and thus the suspended bed sediment discharge in the flow.

The total bed sediment discharge q_t has been calculated by Einstein's formula both with (q_{tc}) and without (q_{tu}) correction for the viscosity and density of the suspension due to fine sediments. Rubey's equation using the measured apparent viscosity and density gave the fall velocity of sand particles in suspension. In Bingham fluids such as a clay suspension, however, the fall velocity can be best estimated by the method of Ansley and Smith (1) after the viscosity is corrected for the yield stress of the suspension. The results obtained from Einstein's formula are shown in Fig. 2. All the calculated values fall within a factor 0.25 to 4 times the

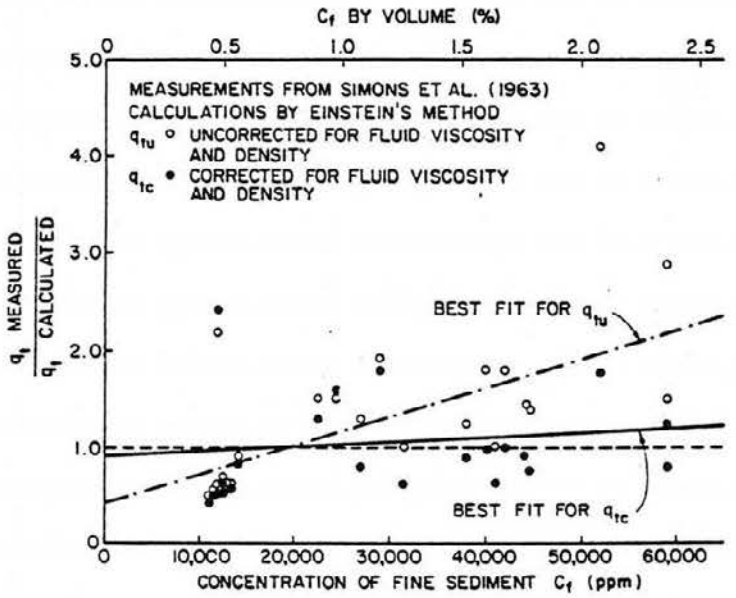

FIG. 2.—Ratio of Total Bed Sediment Discharges Measured and Calculated by Einstein's Formula

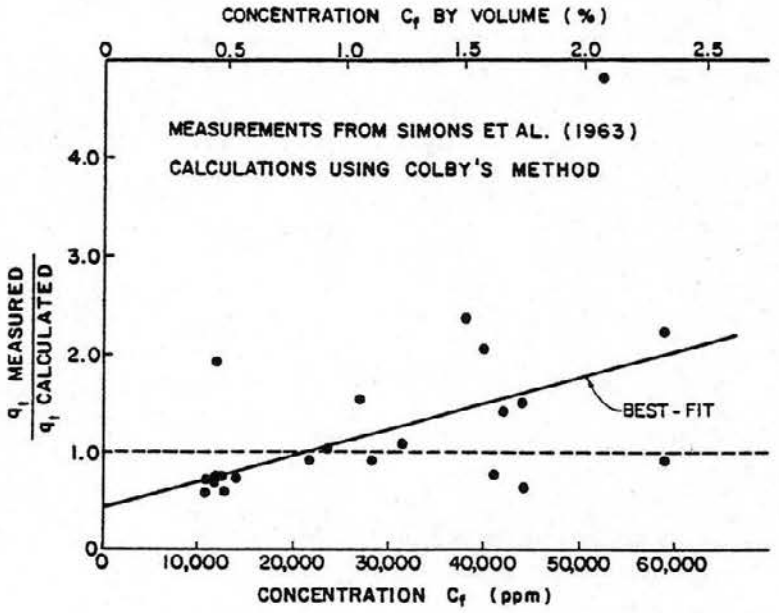

FIG. 3.—Ratio of Total Bed Sediment Discharges Measured and Calculated by Colby's Method

measured values. Nevertheless, the best fit lines show that the correction yields improved results, particularly at large concentrations. It is, therefore, concluded that the viscosity of clay suspensions increases the suspended load through fall velocity reduction while bed load remains basically constant.

Colby's Graphical Relations

The merit of Colby's method for predicting sediment discharge of large concentrations of sand particles lies in its simplicity. The empirical correction factor k_2 at concentrations of fine sediments up to 50,000 ppm was obtained after assuming that both the temperature and concentration of fine sediments affect the relationship between bed sediment discharge and average flow velocity only through changes in fluid viscosity. The non-Newtonian behavior of the fluid and the change in the density of the suspension are neglected in Colby's method. For concentrations of fine sediments ranging from 50,000 ppm up to 200,000 ppm, the correction factor k_2 is based on the limited data from the Rio Puerco, New Mexico.

Colby's method has been applied to the same data set discussed previously. The results shown in Fig. 3 do not provide better agreement than Einstein's uncorrected formula (q_{tu} shown in Fig. 2). Colby's method underestimates sediment transport as the concentration of fine sediment increases.

Summary and Conclusions

Large concentrations of fine sediments increase the viscosity and density of the suspension. Colby's method and Einstein's formulation of sediment discharge have been tested with the flume data of Simons, et

al. (9). The following conclusions are drawn from this analysis: (1) According to calculations based on Einstein's method, the sediment discharge in contact with the bed remains practically unchanged in presence of fine sediments; (2) the increase in total bed sediment discharge is mainly attributable to the increase in suspended sediment discharge; and (3) Colby's graphical relations yield results quite similar to those of Einstein without correction and do not provide better prediction of the total bed sediment discharge than Einstein's formula.

Appendix I.—References

1. Ansley, R. W., and Smith, T. N., "Motion of Spherical Particles in a Bingham Plastic," *AIChE Journal*, Vol. 13, No. 6, Nov., 1967, pp. 1193–1196.
2. Beverage, J. P., and Culbertson, J. K., "Hyperconcentrations of Suspended Sediment," *Journal of the Hydraulics Division*, ASCE, Vol. 90, No. 6, Nov., 1964, pp. 118–128.
3. Colby, B. R., "Discharge of Sands and Mean Velocity Relationships in Sand-Bed Streams," *Professional Paper*, No. 462-A, United States Geological Survey, Washington, D.C., 1964.
4. Einstein, H. A., "The Bed Load Function for Sediment Transportation in Open Channels," *Technical Bulletin*, No. 1026, U.S. Department of Agriculture, Soil Conservation Service, Washington, D.C., 1950.
5. Einstein, H. A., and Chien, N., "Transport of Sediment Mixture with Large Ranges of Grain Sizes," *M.R.D. Sediment Series*, No. 2, University of California, Institute of Engineering Research, and the U.S. Army Corps of Engineers, Missouri River Division, Jun., 1953.
6. Engelund, F., and Wan, Z., "Instability of Hyperconcentrated Flow," *Journal of Hydraulic Engineering*, ASCE, Vol. 110, No. 3, Mar., 1984, pp. 219–233.
7. Nordin, C. F., Jr., "A Preliminary Study of Sediment Transport Parameters, Rio Puerco Near Bernardo, New Mexico," *Professional Paper*, No. 462-C, United States Geological Survey, Washington, D.C., 1963.
8. Pemberton, E. L., "Einstein's Bedload Function Applied to Channel Design and Degradation," *Sedimentation (Einstein)*, H. W. Shen, Ed., Water Resources Publications, Fort Collins, Colo., 1972, pp. 16.1–16.28.
9. Simons, D. B., Richardson, E. V., and Haushild, W. L., "Some Effects of Fine Sediments on Flow Phenomena," *Water-Supply Paper*, No. 1498G, United States Geological Survey, Washington, D.C., 1963.
10. Vanoni, V. A., and Brooks, N. H., "Laboratory Studies of the Roughness and Suspended Load of Alluvial Streams," *Sedimentation Laboratory Report*, No. E68, California Institute of Technology, Pasadena, Calif., Dec., 1957.
11. Wan, Z., "Bed Material Movement in Hyperconcentrated Flow," *Journal of Hydraulic Engineering*, ASCE, Vol. 111, No. 6, Jun., 1985, pp. 987–1002.

Appendix II.—Notation

The following symbols are used in this paper:

C_f = concentration of fine sediments (part per million);
k_2 = Colby's correction factor for concentration of fine sediments;
q_b = contact bed sediment discharge per unit width of channel;
q_{bc} = contact bed sediment discharge per unit width, corrected for viscosity;
q_{bu} = contact bed sediment discharge per unit width, uncorrected for viscosity;
q_t = total bed sediment discharge per unit width of channel;

q_{tc} = total bed sediment discharge per unit width, corrected for viscosity;
q_{tu} = total bed sediment discharge per unit width, uncorrected for viscosity;
Z = Rouse's exponent for sediment concentration distribution;
θ = Einstein and Chien's correction factor for laminar flow effect; and
ξ = Einstein's hiding factor.

Applicability Index for Sand Transport Equations

By David T. Williams[1] and Pierre Y. Julien,[2] Members, ASCE

Methodology

The selection of an appropriate sediment transport equation has puzzled at least a generation of river engineers and computer modelers confronted with the analysis of the alluvial river response to natural and man-induced changes. Although some guidelines were proposed by Shen (1971) and Yang (1987), the complexity of sediment transport process as has been recognized by most investigators warrants further investigation.

This paper describes the results of a preliminary investigation of the condition of applicability and inherent limitation of sediment transport relationships, which should be conducive to an implementation of existing guidelines.

In spite of the complexity of sediment transport due to the large number of variables involved, the dominant processes can be described with fewer dimensionless parameters. Among the key dimensionless parameters selected in this analysis, the relative roughness (or submergence) Z, the mobility number F_{gr}, and the dimensionless grain sizes d_{gr} (defined in the following equations) are common to several transport equations.

$$d_{gr} = d\left[\frac{g(G-1)}{\nu^2}\right]^{1/3} \quad \ldots\ldots (1)$$

$$F_{gr} = \frac{U_*^2}{gd(G-1)} \quad \ldots\ldots (2)$$

$$Z = \frac{D}{d} \quad \ldots\ldots (3)$$

The parameter d_{gr} indicates the ratio of gravitational to viscous forces exerted on sediment particles, and involves the following variables: sediment size d, gravitational acceleration g, specific gravity of sediments G, and kinematic viscosity ν.

The parameter F_{gr} is equivalent to the Shields number, and depends on the shear velocity U_*. The relative submergence Z, describes resistance to flow and varies with flow depth D.

The four sediment transport equations selected in this preliminary analysis are those of Ackers and White (1973), Shen and Hung (1971), Toffaleti (1968), and Yang (1973). The data sets used in the development and cal-

[1]Res. Hydr. Engr., Hydr. Lab., USAE Waterways Experiment Station, Vicksburg, MS 39180.

[2]Asst. Prof., Dept. of Civ. Engrg., Colorado State Univ., Fort Collins, CO 80523.

Note. Discussion open until April 1, 1990. To extend the closing date one month, a written request must be filed with the ASCE Manager of Journals. The manuscript for this paper was submitted for review and possible publication on August 12, 1988. This paper is part of the ***Journal of Hydraulic Engineering***, Vol. 115, No. 11, November, 1989. ©ASCE, ISSN 0733-9429/89/0011-1578/$1.00 + $.15 per page. Paper No. 24057.

246

TABLE 1. Range of Parameters d_{gr}, F_{gr}, and Z

Equation (1)	d_{gr} (2)	F_{gr} (3)	Z (4)
Ackers-White	4–60	<5.7	20–2,500
Shen-Hung	3.3–33.3	<7.2	23–3,000
Toffaleti	2.2–24	<9.5	41–92,500
Yang	2.6–43.8	<5.8	20–19,500

culation of these sediment transport relationships were examined to determine the range of these three dimensionless parameters as shown in Table 1.

For given stream-flow conditions, the three field parameters, d_{gr}, F_{gr}, and Z, are calculated from Eqs. 1–3 and compared with the ranges presented in Table 1. An applicability index is defined as the sum of the number of field parameters within the range of values of Table 1 (high = three parameters, medium = two parameters, and low = one or no parameter). Of course, a sediment transport equation is expected to provide best results for high values of the index because the field conditions are within the sediment and flow conditions used for the calibration of the sediment transport equation. Conversely, low values of the index indicate that sediment transport calculations involve extrapolation beyond the range of applicability of the re-

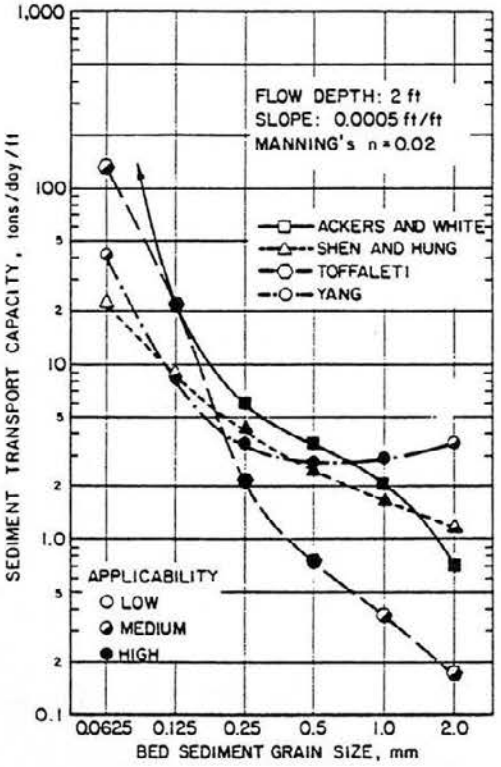

FIG. 1. Sediment Transport Potential versus Bed Sediment Grain Size [Slope = 0.0005, n = 0.02, $T°$ = 70° F (21° C), G = 2.65]

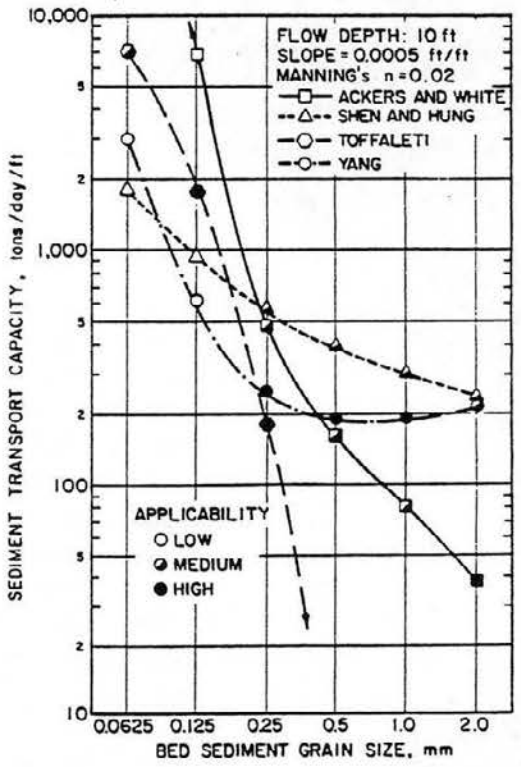

FIG. 2. Sediment Transport Potential versus Bed Sediment Grain Size [Slope = 0.0005, n = 0.02, $T°$ = 70° F (21° C), G = 2.65]

247

lationship that may yield either accurate or incorrect results.

The following example illustrates the usefulness of the applicability index. Steady uniform flow in wide channels was considered with keeping the slope constant at 0.0005, Manning's $n = 0.02$, water temperature at 70° F (21° C), and specific gravity of the sediments at 2.65. Sediment transport capacity was calculated for flow depths of 2 and 10 ft (0.61 and 3.05 m) assuming uniform sand bed with sediment size ranging from 0.0625 to 2 mm. In spite of these flow limitations, the variabilities of the three dimensionless parameters are:

$$1.6 < d_{gr} < 51 \quad (4)$$

$$0.09 < F_{gr} < 14.8 \quad (5)$$

$$304 < Z < 48{,}640 \quad (6)$$

The calculated sediment transport capacities are shown in Figs. 1 and 2 for flow depths of 2 ft and 10 ft (0.61 and 3.05 m). Note that full, half-full, and empty symbols refer respectively to high, medium, and low values of the applicability index. Details on calculations with different flow depths are also available in Williams (1986).

Results

The results obtained from this analysis are rather instructive. Fig. 1 illustrates the variability of sediment transport calculations for sand-size particles at a flow depth of 2 ft (0.61 m). Most equations have a high applicability index and give similar rates of sediment transport, except the Toffaleti method with $d = 0.5$ mm. Results in Fig. 1 get worse, however, when the applicability index is medium or low. This is well illustrated when $d = 0.0625$ mm and none of the equations has high applicability. Interestingly, the Toffaleti method predicts minimum sediment transport rates when $d = 2$ mm and Yang's sediment transport capacity slightly increases with sediment size, which is somewhat unexpected.

At a flow depth of 10 ft (3.05 m), Fig. 2 illustrates that sediment discharge calculations for 0.125 mm $< d <$ 0.5 mm remain comparable as long as the index is high or medium. It is noticeable that the equations of Toffaleti and Ackers and the White equation are very sensitive to sediment size.

The applicability of these four sediment transport equations to these flow conditions has been discussed by Williams and Julien (1987). Extension of this analysis to a wide range of slopes and roughness values is underway.

Acknowledgment

This study has been carried out as part of the first writer's studies at Colorado State University. The findings and opinions of the writers do not necessarily reflect those of the Army Corps of Engineers. Permission to publish this paper was granted by the chief of engineers.

Appendix. References

Ackers, P., and White, W. R. (1973). "Sediment transport: new approach and analysis." *J. Hydr. Div.*, ASCE, 99(11), 2041–2060.

248

Shen, H. W. (1971). "Total Sediment Load." *River mechanics*, H. W. Shen, ed., Fort Collins, Colo., 13-1–13-23.
Shen, H. W., and Hung, C. S. (1971). "An engineering approach to total bed material load by regression analysis." *Proc. Sedimentation Symp.*, H. W. Shen, ed., Fort Collins, Colo., 14-1–14-17.
Toffaleti, F. B. (1968). "A procedure for computation of the total river sand discharge and detailed distribution, bed to surface." *Technical Report No. 5*, Committee on Channel Stabilization, Corps of Engrs., U.S. Army, Vicksburg, Miss., Nov.
Williams, D. T. (1986). "Considerations in the selection of transport equations in sediment modeling." *River Mechanics, Report CER85-86 PYJ-28*, Civ. Engrg. Dept., Colorado State Univ., Fort Collins, Colo., 126–142.
Williams, D. T., and Julien, P. Y. (1987). "On the selection of sediment transport equations." *ASCE Nat. Conf. on Hydr. Engrg.*, ASCE, 925–929.
Yang, C. T. (1973). "Incipient motion and sediment transport." *J. Hydr. Div.*, ASCE, 99(10), 1679–1704.
Yang, C. T. (1987). "Sediment transport and unit stream power." *Civil engineering practice*, vol. 5, Technomic Publishing Co., Lancaster, Pa.

249

Concentration of very fine silts in a steady vortex

Concentration de limons très fins dans un vortex en régime permanent

P. Y. JULIEN
Assistant Professor,
Colorado State University, Fort Collins, Colorado, U.S.A.

SUMMARY
The presence of fine sediment particles in a steady horizontal vortex is examined theoretically and experimentally. Starting from an homogeneous mixture, particles denser than the surrounding fluid are moved outside of the vortex core by centrifugal action. As a sediment concentration gradient gradually builds up across the vortex, a diffusive flux opposite to the centrifugal flux is induced. Equilibrium is reached when the two fluxes are equal. Theoretical relationships describing the suspended sediment concentration profiles in a steady Rankine vortex are verified with experimental data.

RÉSUMÉ
La présence de fines particules solides dans un vortex plan de Rankine est étudiée analytiquement et expérimentalement. Partant d'un mélange homogène, les particules plus denses que le fluide sont projetées à l'extérieur du noyau central par centrifugation. Ceci crée un gradient de concentration dans le vortex et induit un flux diffusif opposé au flux centrifuge. L'équilibre est obtenu lorsque les flux centrifuges et diffusifs sont égaux et opposés. Les équations analytiques décrivant les profils d'équilibre de concentration de sédiments en suspension sont conformes aux mesures expérimentales.

1 Introduction

A Rankine combined vortex is a simple two-dimensional model describing vortices in homogeneous fluids. It combines a rotational vortex core surrounded by an irrotational vortex. The fundamental flow properties in a Rankine combined vortex have been discussed in great detail in the literature: Lamb (1932), Prandtl and Tietjens (1934), Rouse and Hsu (1952), Sedov (1959), Rouse (1966), Batchelor (1967), Fortier (1967), Happel and Brenner (1973) and Daily and Harleman (1973).

As opposed to flow in homogeneous fluids, the flow characteristics of a water-sediment mixture are obscured by the presence of solid particles. It is intuitively recognized that particles in a vortex tend to separate from the fluid by centrifugal action. Full understanding of this problem is as yet incomplete considering the interaction of viscous, gravitational and inertia forces and the unsteady nature of eddies in turbulent flows.

In this paper a steady two-dimensional horizontal vortex is considered. The fluid mixture under investigation is composed of very fine cohesionless sediment particles in distilled water. With very small particles, the analysis is simplified since the viscous forces exerted on the particles are dominant compared to their weight and inertia.

Open for discussion till April 1, 1987.

The forces exerted on the particles in circular motion are first examined in order to define the acceleration components and the limit velocity of small particles in the vortex. Diffusion concepts are then introduced to determine the steady-state sediment concentration profiles.

2 Velocity and pressure distribution in a Rankine combined vortex

The mathematical concept of vorticity is known as a vector quantity ω having three orthogonal components, each of which is expressible in terms of transverse gradients of the velocity vector. The vorticity ω is equal to twice the angular velocity Ω of a fluid element and the product of vorticity by the cross-sectional area defines the circulation Γ which is constant along a vortex filament. As schematized in Fig. 1 the Rankine combined vortex is composed of a forced vortex core of finite radius r_0 and constant vorticity ω surrounded by a free vortex of constant circulation $\Gamma = 2\pi\Omega r_0^2$. In the following analysis, the two-dimensional vortex rotates around a vertical axis for which the fluid motion in a horizontal plane is considered gravity-free.

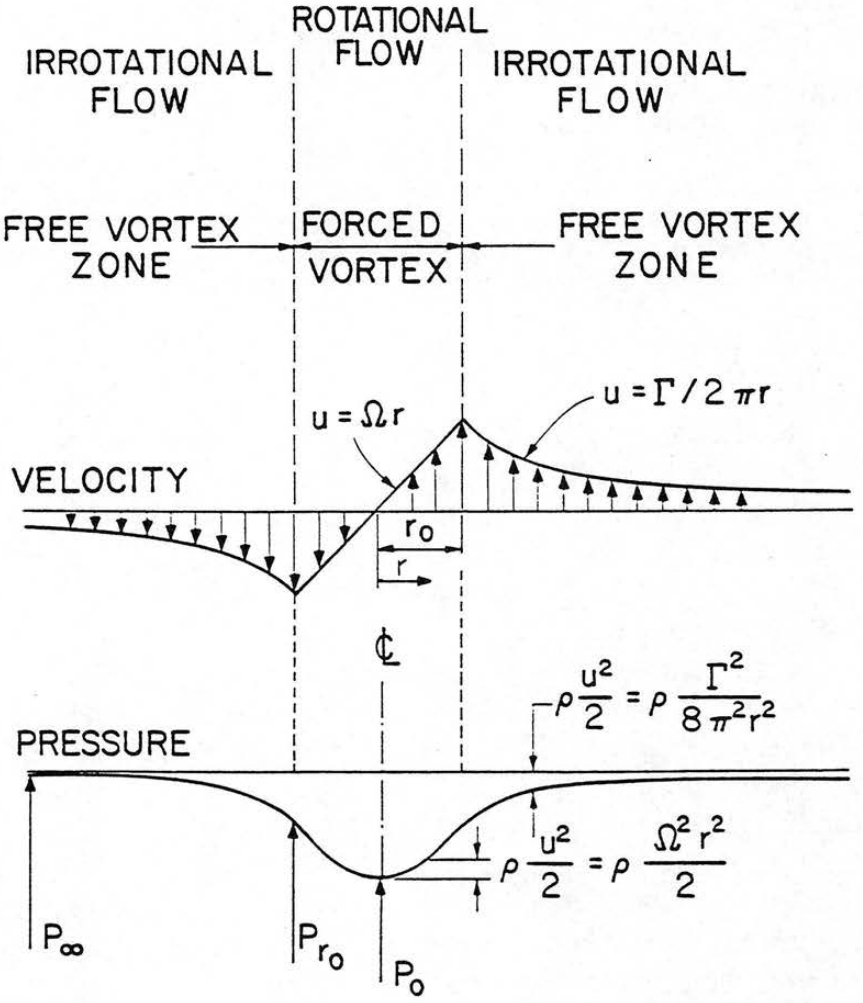

Fig. 1. Velocity and pressure distribution in a two-dimensional Rankine combined vortex.
Répartition de la vitesse et de la pression dans un vortex de Rankine.

2.1 *Free vortex zone*

In the free vortex zone the flow is irrotational with constant circulation. The velocity varies inversely with the radius to satisfy the requirement of constant circulation and the boundary condition of no motion at infinity:

$$u=\frac{\Gamma}{2\pi r} \tag{1}$$

in which u is the tangential velocity at a distance r from the center of the vortex. The Bernoulli theorem for a steady irrotational flow of an inviscid incompressible fluid is:

$$p+\varrho\,\frac{u^2}{2}=\text{constant} \tag{2}$$

in which ϱ is the mass density of fluid and p is the pressure. The pressure distribution in a free vortex is obtained as follows from equations (1) and (2) after taking the constant equal to the pressure p_∞ at $r=\infty$:

$$p_\infty-p=\varrho\,\frac{u^2}{2}=\varrho\,\frac{\Gamma^2}{8\pi^2r^2} \tag{3}$$

The Bernoulli sum along different stream lines remains constant.

2.2 *Forced vortex core*

In a homogeneous fluid, the forced vortex flow is rotational without any viscous energy dissipation though the Bernoulli sum between different streamlines is not constant. The velocity varies linearly with the radius ($u=\Omega r$) and the pressure gradient is balanced by the centrifugal acceleration:

$$\frac{1}{\varrho}\frac{\partial p}{\partial r}=\frac{u^2}{r} \tag{4}$$

The pressure distribution is:

$$p-p_0=\frac{\varrho u^2}{2}=\frac{\varrho\Omega^2r^2}{2} \tag{5}$$

in which p_0 is the pressure at the center of the vortex.

3 Particle motion in a vortex

The following analysis (Julien, 1985b) describes the motion of a small spherical particle of diameter d_s, specific mass ϱ_s and mass $\pi\varrho_s d_s^3/6$ located at distance r from the center of the vortex. Small particles refer to cohesionless particle sizes much smaller than the vortex core radius r_0. The symbol v denotes the velocity of the particle while u designates the fluid velocity. The forces exerted on sediment particles in a vortex can be defined from the velocity and pressure distribution described in Section 2. The relative magnitude of pressure and centrifugal forces defines the acceleration of solid particles in a forced and a free vortex. Viscous forces are exerted on particles in motion relative to the fluid and equilibrium conditions are reached when the sum of all forces reduces to zero.

The pressure force F_p exerted on a small particle toward the center of the vortex is:

$$F_p = \frac{\pi}{6} \varrho d_s^3 \frac{u^2}{r} \tag{6}$$

The centrifugal force F_c depends on the tangential velocity of a sediment particle v_t and the radius of curvature. Assuming that the radius of curvature is equal to the distance r from the center of the vortex, the centrifugal force outward from the center is equal to:

$$F_c = \frac{\pi}{6} \varrho_s d_s^3 \frac{v_t^2}{r} \tag{7}$$

It is considered that for small particles, the velocity of the particle is very close to the velocity of the fluid. The Coriolis acceleration is thus considered negligible compared to the centrifugal acceleration. A radial acceleration a_r is imparted to a sediment particle provided the centrifugal and pressure forces are not equal. In this case, the motion of a sediment particle in a vortex is given when the viscous forces are included in the analysis. The velocity components of a particle in the radial v_r and tangential v_t directions are assumed to differ from the fluid velocity u as sketched in Fig. 2. The velocity of the particle relative to the fluid v' is equal to:

$$v' = \sqrt{v_r^2 + (v_t - u)^2} \tag{8}$$

and the angle $\psi = \tan^{-1} v_r/(v_t - u)$ between the two relative velocity components is indicated in Fig. 2.

The friction force exerted on the particle in the direction opposite to v' is function of the relative velocity v', the Reynolds number of the particle $Re' = v' d_s/\upsilon$, the surface area and the drag coefficient C_D:

$$F_V = C_D \frac{\pi d_s^2 \varrho v'^2}{8} \tag{9}$$

It is assumed that the drag coefficient C_D in the curvilinear vortex flow field is not significantly different from the C_D value in a parallel flow field. The friction forces exerted on small particles are predominantly viscous and the drag coefficient is inversely proportional to the Reynolds number:

$$C_D = \frac{24}{Re'} = \frac{24\upsilon}{v' d_s} \tag{10}$$

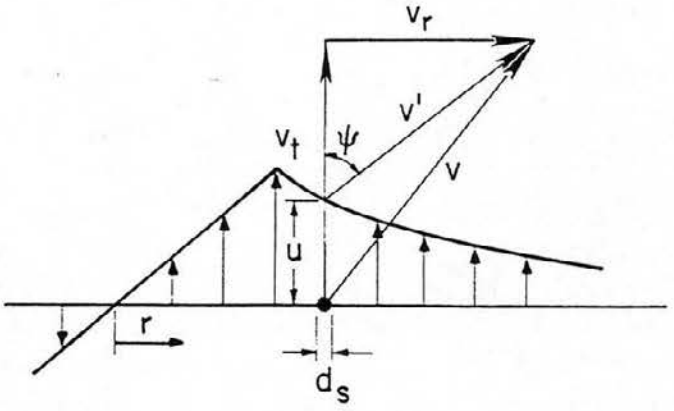

Fig. 2. Relative velocity of a sediment particle in a vortex.
Vitesse relative d'une particule solide dans un vortex.

253

The resulting radial acceleration of the particle is obtained after considering the equilibrium of pressure, viscous ($F_v \sin \psi$) and centrifugal forces divided by the mass of the particle:

$$a_r = \frac{v_t^2}{r} - \frac{\varrho}{\varrho_s}\frac{u^2}{r} - 18\,\frac{\varrho \upsilon}{\varrho_s}\frac{v_r}{d_s^2} \tag{11}$$

The tangential acceleration a_t equals the tangential viscous force, $F_v \cos \psi$, per unit mass of the particle.

$$a_t = -18\,\frac{\varrho \upsilon}{\varrho_s}\frac{(v_t - u)}{d_s^2} \tag{12}$$

Equation (12) indicates that as the ratio υ/d_s^2 becomes very large the tangential acceleration term prevails until the tangential velocity of the particle v_t reaches the velocity of the fluid u. Therefore, the tangential velocity of small particles should always remain close to the fluid velocity. Equilibrium condition in the radial direction for $v_t = u$ occurs when the acceleration component a_r from equation (11) vanishes. The corresponding limit velocity v_e' of the particles in the radial direction is:

$$v_e' = \frac{1}{18}\left(\frac{\varrho_s}{\varrho} - 1\right)\frac{u^2}{r\upsilon}\,d_s^2 \tag{13}$$

Which can be rewritten in a dimensionless form as a function of the Reynolds number, $Re = ud_s/\upsilon$, as:

$$\frac{v_e'}{u} = \left[\frac{1}{18}\left(\frac{\varrho_s}{\varrho} - 1\right)\frac{d_s}{r}\right] Re \tag{14}$$

From these relationships, the limit radial velocity of the particle is proportional to ϱ_s/ϱ, d_s and u and decreases as the viscosity υ and the radius r increase. These equations also verify the previous assumptions regarding the circular motion of small sediment particles.

4 Sediment concentration profile in a vortex

In a viscous fluid, small sediment particles reach the fluid velocity very rapidly and particles heavier than the fluid are moved outside of the vortex core. Therefore the concentration of particles decreases toward the center, thus creating a concentration gradient across the vortex. A diffusion flux proportional to this gradient induces the transport of solid particles toward the regions of lower concentration. Equilibrium conditions are reached when the flux of sediment particles due to centrifugal force is balanced by the diffusion flux in the opposite direction. This equilibrium condition implies that the radius of curvature of the particles is r as assumed previously in the derivation of equation (7). Equilibrium condition can be mathematically described as follows:

$$\frac{dC}{C} = \frac{v_e'}{\varepsilon}\,dr \tag{15}$$

in which C is the sediment concentration by volume and ε is the diffusion coefficient. It is assumed that the diffusion coefficient ε remains independent of r regardless of whether laminar

254

or turbulent diffusion is involved. After substituting equation (13) into equation (15), the concentration profile is described by the following integral:

$$\int \frac{dC}{C} = \frac{1}{18} \int \left(\frac{\varrho_s}{\varrho} - 1 \right) \frac{u^2}{r} \frac{d_s^2}{\upsilon \varepsilon} \, dr \tag{16}$$

With the boundary condition at infinity $C = C_\infty$, the integration of equation (16) yields two expressions for the sediment concentration profile since two velocity relationships are applicable to free and forced vortex.

These two concentration profiles are respectively:

$$\frac{C}{C_\infty} = e^{\alpha \left(\frac{r^2}{r_0^2} - 2 \right)} \quad \text{when} \quad r \leq r_0 \tag{17}$$

and

$$\frac{C}{C_\infty} = e^{-\alpha \frac{r_0^2}{r^2}} \quad \text{when} \quad r > r_0 \tag{18}$$

A dimensionless parameter α describing the distribution of sediments is defined as follows:

$$\alpha = \left(\frac{\varrho_s}{\varrho} - 1 \right) \frac{\Gamma^2}{144 \pi^2 \varepsilon \upsilon} \left(\frac{d_s}{r_0} \right)^2 \tag{19}$$

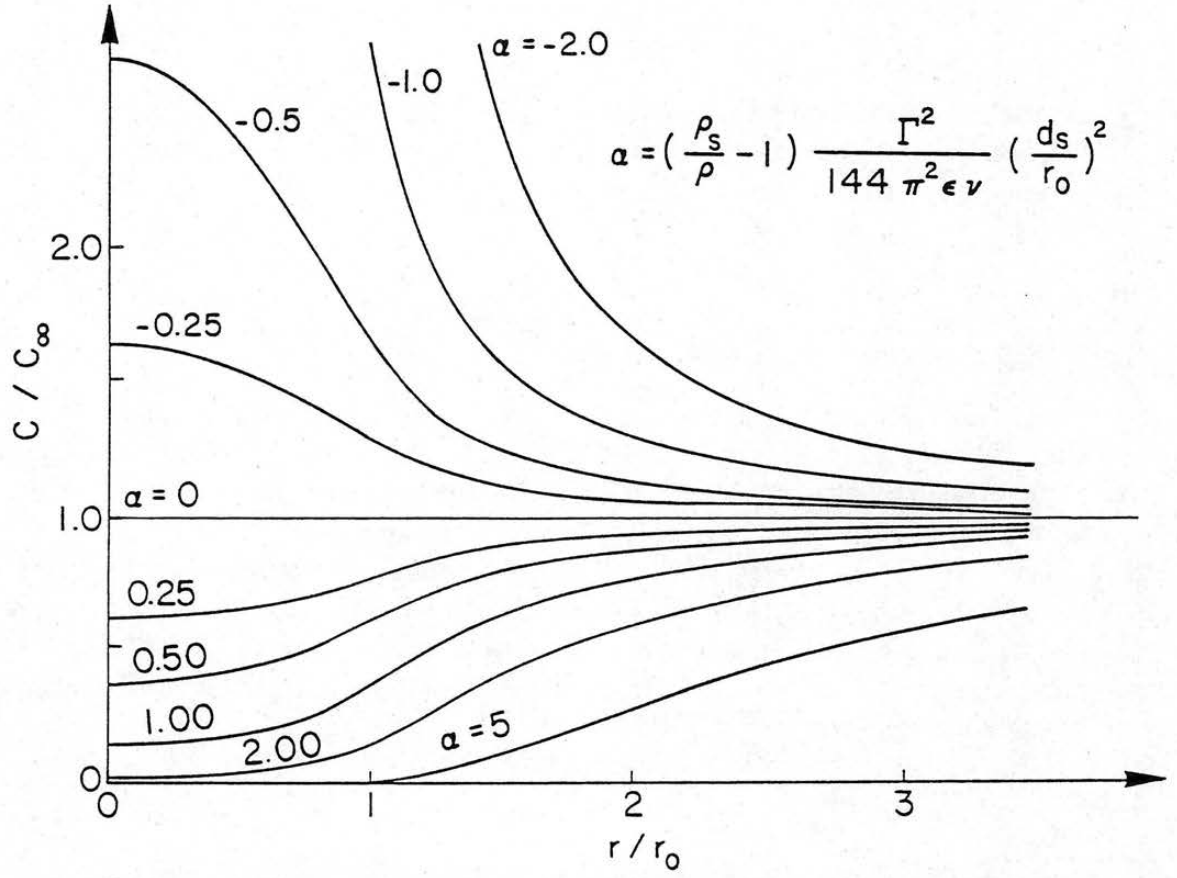

Fig. 3. Steady-state sediment concentration profile in a Rankine combined vortex.
Profil de concentration en régime permanent dans un vortex de Rankine.

The theoretical concentration profiles in a Rankine combined vortex with various α values are shown in Fig. 3 as a function of r/r_0. It is concluded from this analysis that the concentration is constant when $\alpha = 0$ which corresponds to infinitely small particles or neutrally buoyant particles $\varrho_s = \varrho$. The curves for $\alpha > 0$ indicate a decrease in concentration toward the center of the vortex while the concentration increases toward the center when $\varrho_s < \varrho$. The boundary condition at $r = r_0$ and at the center of the vortex are respectively:

$$C_{r_0} = C_\infty e^{-\alpha} \tag{20}$$

$$C_0 = C_\infty e^{-2\alpha} \tag{21}$$

Interestingly the ratio C_{r_0}/C_∞ equals the square root of C_0/C_∞.

5 Experimental investigation

Laboratory experiments were conducted at the Engineering Research Center to determine the sediment concentration profile in a steady vortex for validation of the theoretical profiles when $\alpha > 0$. A water sediment mixture composed of very fine silts (0.0053 mm $< d_s <$ 0.0074 mm) at a concentration of 50 g/l was used for the experiments. A steady vortex was induced in three liters of the mixture by rotating a 76 mm (3 in.) magnetic stirring bar at the bottom of a fixed cylindrical flask. The nearly horizontal motion of sediment particles, as observed through the glassed walls indicates that no significant secondary circulation was present in the vortex. Water surface profiles were measured using a point gage and several 30 ml samples were pipetted, dried and weighed (± 0.1 mg) to measure the sediment concentration profiles across the steady vortex. The data and their analysis are detailed in Julien (1985a). The circulation Γ, the angular velocity Ω and the velocity u_0 at the radius of the core r_0 are obtained from the surface profile data. The parameter u_0 is calculated from $\varrho u_0^2 = p_\infty - p_0$ and r_0 from $\Gamma = 2\pi r_0 u_0$. The coefficients α and C_∞

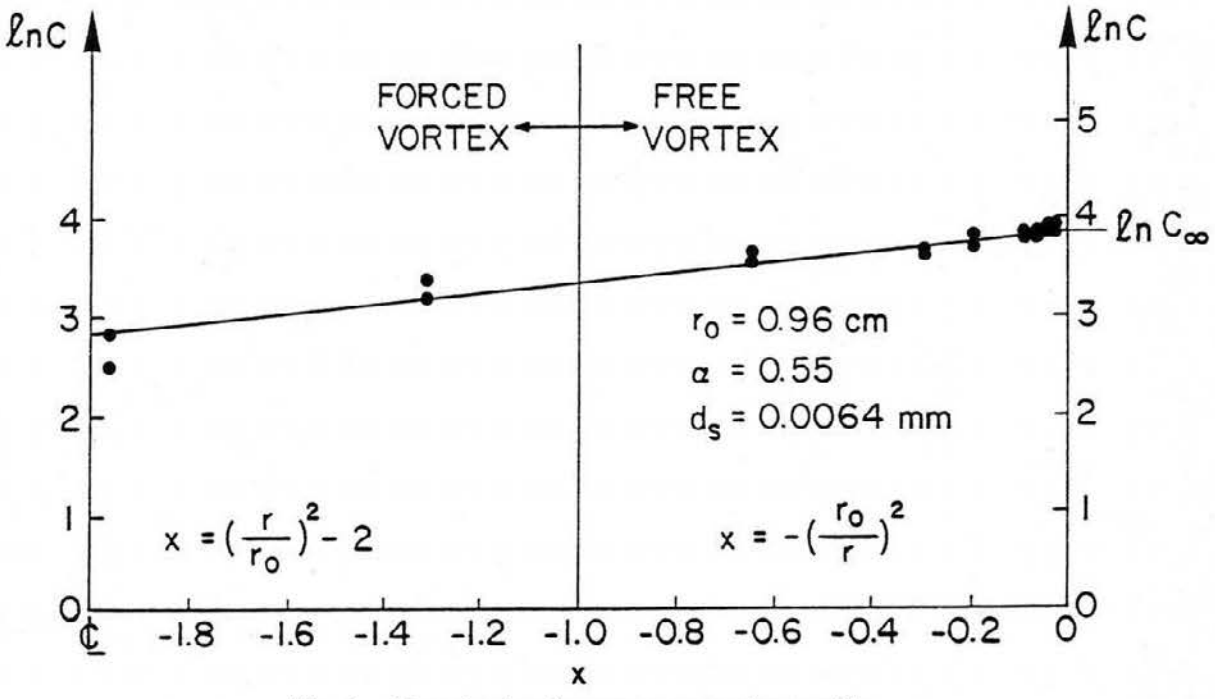

Fig. 4. Linearized sediment concentration profile.
Profil linéarisé de concentration en sédiments.

256

are then evaluated from the sediment concentration data after equations (17) and (18) are linearized as follows:

$$\ln C = \ln C_\infty + \alpha\left[\left(\frac{r}{r_0}\right)^2 - 2\right] \quad \text{when} \quad r \leq r_0 \tag{22}$$

and

$$\ln C = \ln C_\infty - \alpha\left(\frac{r_0}{r}\right)^2 \quad \text{when} \quad r \geq r_0 \tag{23}$$

A linearized sediment concentration profile is presented in Fig. 4 for the evaluation of C_∞ and α. In Fig. 5, two sediment concentration profiles measured in this preliminary experimental study are compared with the theoretically derived relationships. In both cases, the agreement is excellent and it is concluded that when $\varrho_s > \varrho$, the sediment concentration decreases toward the

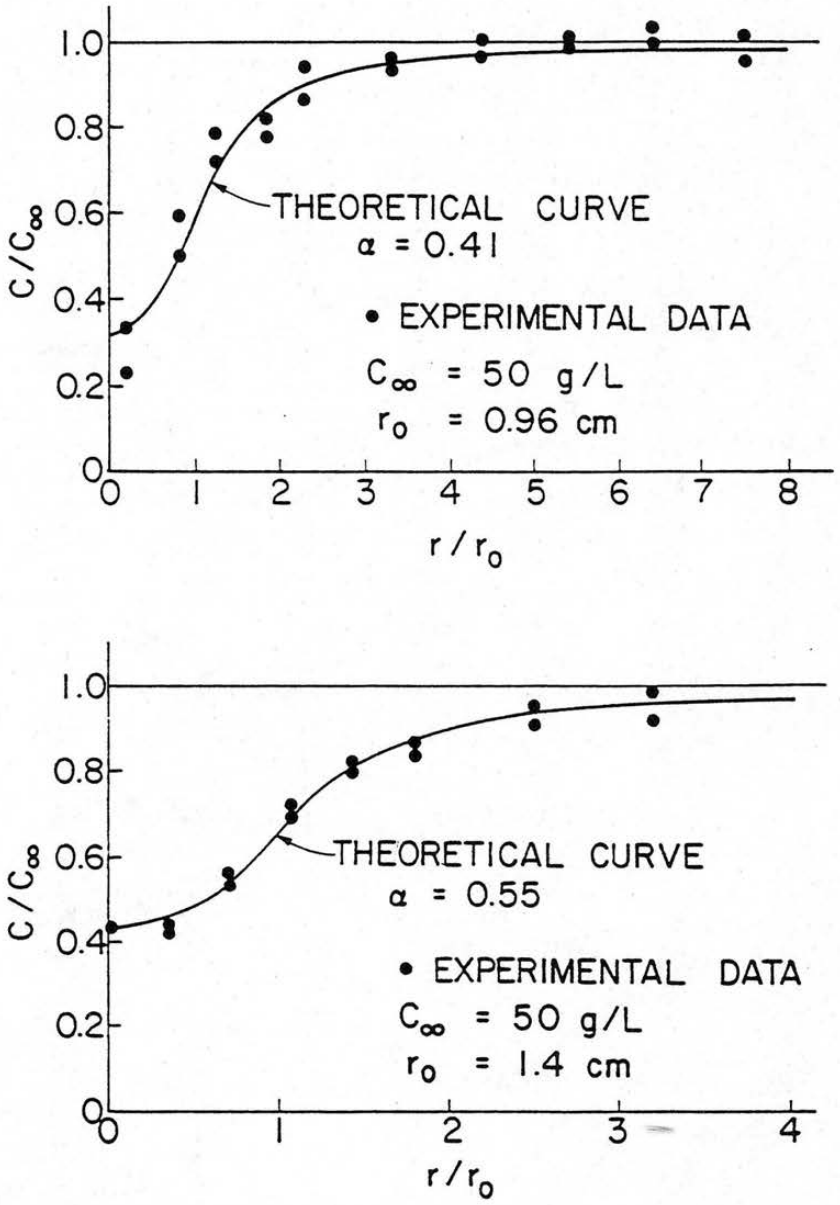

Fig. 5. Sediment concentration profile.
Profil de concentration en sédiments.

257

center of a vortex. The sediment concentration profile depends on three major factors: diffusion, friction and centrifugal force exerted on small particles. The diffusion coefficients for the two experiments shown in Fig. 5 are respectively 1.67 cm^2/s and 9.4 cm^2/s which corresponds very likely to turbulent diffusion. It is recognized that further experiments are required to better define the diffusion coefficient. At this point, however, it seems relevant to emphasize that the experimental data are in good agreement with the theoretical results for which the diffusion coefficient is assumed constant throughout the vortex.

6 Summary and conclusions

The presence of small sediment particles in a steady horizontal Rankine vortex is examined. For small particles, the viscous force is dominant compared to inertia and gravity forces. The similarities of motion in both the forced vortex and the free vortex are apparent. A particle at rest is accelerated toward the center. The tangential velocity of small particles reaches rapidly the velocity of the fluid and particles denser than the fluid move toward the outside of the vortex. The centrifugal flux created by the outward motion of denser particles induces a diffusion flux in the opposite direction. Equilibrium conditions are obtained when the two fluxes are equal and opposite. Under steady state conditions, the sediment concentration profiles of fine particles in suspension are theoretically derived and plotted using dimensionless scales. Preliminary experiments verified the theoretical profiles for $\alpha > 0$. Experimental evidence supports the assumption that the diffusion coefficient remains constant throughout the vortex.

Acknowledgements

This paper has been prepared at the Engineering Research Center during the author's post-doctoral studies at Colorado State University. The support of a NATO fellowship from the Natural Sciences and Engineering Research Council of Canada is gratefully acknowledged. The writer is indebted to his friend J. S. O'Brien for his thoughtful advice and assistance during the course of the experiments.

Notations

a_r radial acceleration of a sediment particle
a_t tangential acceleration of a sediment particle
a_{vr} radial acceleration due to viscous forces
a_{vt} tangential acceleration component due to viscous forces
C sediment concentration
C_0 sediment concentration at $r=0$
C_{r_0} sediment concentration at $r=r_0$
C_∞ sediment concentration at $r=\infty$
C_D drag coefficient
d_s diameter of a sediment particle
F_c centrifugal force on a sediment particle
F_p pressure force on a sediment particle
F_v viscous force on a sediment particle
p pressure

258

p_0 pressure at the center of the vortex
p_{r_0} pressure at $r = r_0$
p_∞ pressure at $r = \infty$
r radial distance from the center of the vortex
r_0 radius of the vortex core
Re' Reynolds number using the relative velocity of the particle
Re Reynolds number of the particle using the fluid velocity
u tangential velocity of the fluid
v total velocity of a sediment particle
v_r radial velocity of a sediment particle
v_t tangential velocity of a sediment particle
v' velocity of the particle relative to the fluid velocity
v'_e limit radial velocity of the particle
α parameter governing the sediment concentration profile
Γ circulation
ε diffusion coefficient
υ kinematic viscosity of the fluid
ϱ mass density of the fluid
ϱ_s mass density of the sediment particles
ψ angle between the radial and tangential components of a particle velocity relative to the fluid
ω vorticity
Ω angular velocity of the forced vortex

References / Bibliographie

BATCHELOR, G. K., An Introduction to Fluid Dynamics. Cambridge University Press, 1967, 615 p.

DAILY, J. W. and HARLEMAN, D. R., Fluid Dynamics. Addison-Wesley, 1973, 454 p.

FORTIER, A., Mécanique des Suspensions, Monographie de Mécanique des Fluides et Thermique, Masson et Cie, 1967, 176 p.

JULIEN, P. Y., Motion of Sediment Particles in a Rankine Combined Vortex. Report CER84-85PYJ6, Colorado State University, Fort Collins, May 1985a, 37 p.

JULIEN, P. Y., Theoretical Analysis of Sediment Particles in a Rankine Combined Vortex. Proceedings of the CSCE Annual Conference, Saskatoon, Canada, May 1985b, pp. 89–105.

HAPPEL, J. and BRENNER, H., Low Reynolds Number Hydrodynamics. Noordhoff International Publishing, 1973, 553 p.

LAMB, H., Hydrodynamics. Dover, 1932, 738 p.

PRANDTL, L. and TIETJENS, O. G., Fundamentals of Hydro and Aeromechanics. Dover, 1934, 270 p.

ROUSE, H. and HSU, H. C., On the Growth and Decay of a Vortex Filament. Proceedings of the First National Congress of Applied Mechanics, ASME, 1951.

ROUSE, H., On the Role of Eddies in Fluid Motion. Science in Progress, Vol. 51, No. 3, Yale University Press, 1966, pp. 263–308.

SEDOV, L. I., Similarity and Dimensional Methods in Mechanics. Academic Press, 1959, pp. 97–99.

259

Turbulent Shear Stress in Heterogeneous Sediment-Laden Flows

By Hyoseop Woo,[1] Associate Member, ASCE, and Pierre Y. Julien,[2] Member, ASCE

Introduction

Current knowledge of the mechanics of alluvial channels depends very largely on calculations of turbulent shear stresses; typical examples are the beginning of motion of sediment particles and sediment transport in alluvial channels. If shear stress can be well defined in clear-water flows, comparatively little is known about shear stresses in sediment-laden flows. Einstein and Chien (1955) proposed a turbulent shear stress relationship that does not depend on the fall velocity of uniform sediment particles. Opposite results were later proposed by Zagustin (1969) and Willis (1972).

This study briefly reviews existing relationships for turbulent shear stress in homogeneous sediment-laden flows, and proposes a derivation of turbulent shear stress in heterogeneous sediment-laden flows. The analysis of turbulent shear stress for steady-uniform flows carrying heterogeneous sediment mixtures provides additional insight on the role played by sediment size gradation and fall velocity by size fraction.

Previous Derivations

Einstein and Chien (1955) first derived the turbulent shear stress relationship for sediment-laden flows. Without providing further clarification they first assumed that

$$\tau = -\rho_f \overline{u'(1-c)v} - \rho_s \overline{u'c(v-\omega)} \quad \ldots\ldots (1)$$

in which the shear stress τ depends on three constants and three variables. The constants are the fall velocity of uniform sediment particles ω, the mass density of the fluid ρ_f, and the mass density of sediment ρ_s; the variables are the instantaneous velocity components u and v, and the volumetric sediment concentration c. These variables fluctuate around their respective time-average values $\bar{u}$, $\bar{v}$, and $\bar{c}$ by the amounts u', v', and c'. The time-average values of the Reynolds stress components are obtained from the Prandtl mixing theory as follows:

$$\overline{-u'v'} = \epsilon_m \frac{d\bar{u}}{dy} \quad \ldots\ldots (2)$$

[1]Res. Fellow, Water Resour. Engrg. Div., Korea Inst. of Constr. Tech., Umyeon-dong 142, Socho-gu, Seoul, Korea 150-010.

[2]Assoc. Prof., Dept. of Civ. Engrg., Engrg. Res. Ctr., Colorado State Univ., Ft. Collins, CO 80523.

Note. Discussion open until April 1, 1991. To extend the closing date one month, a written request must be filed with the ASCE Manager of Journals. The manuscript for this paper was submitted for review and possible publication on May 17, 1990. This paper is part of the *Journal of Hydraulic Engineering*, Vol. 116, No. 11, November, 1990. ©ASCE, ISSN 0733-9429/90/0011-1416/$1.00 + $.15 per page. Paper No. 25213.

2160

TABLE 1. Turbulent Shear Stress in Sediment-Laden Flows

Source (1)	Formula (2)
Einstein and Chien (1955)	$\tau = \rho_f \epsilon_m d\bar{u}/dy(1 + A\bar{c})$
Zagustin (1969)	$\tau = \rho_f \epsilon_m d\bar{u}/dy(1 + A\bar{c}) - \rho_s \omega \bar{u}\bar{c}$
Willis (1972)	$\tau = \rho_f \epsilon_m d\bar{u}/dy(1 + A\bar{c}) + (\rho_s - \rho_f)\bar{u}[\epsilon_m d\bar{c}/dy + \omega\bar{c}]$

$$\overline{-u'(1-c)'} = \epsilon_f \frac{d(1-\bar{c})}{dx} = 0 \quad \ldots\ldots (3)$$

for streamwise uniform concentrations

$$\overline{-u'c'} = \epsilon_s \frac{d\bar{c}}{dx} = 0 \quad \ldots\ldots (4)$$

for streamwise uniform concentrations where ϵ_f, ϵ_m, and ϵ_s denote the diffusion coefficients for fluid, momentum, and sediment, respectively. Using Eqs. 3 and 4, Eq. 1 can be reduced to

$$\tau = -\rho_f \overline{u'v'}\,(1 + A\bar{c}) \quad \ldots\ldots (5)$$

where

$$A = \frac{\rho_s - \rho_f}{\rho_f} \quad \ldots\ldots (6)$$

Zagustin (1969) provided a slightly different derivation in order to explain the reduction of the von Karman constant in sediment-laden flows. His final relationship, given in Table 1, differs from Eq. 5 and involves the fall velocity ω. Based on Taylor series expansion, Willis (1972) derived a third relationship for turbulent shear stress in sediment-laden flows. This relationship given in Table 1 also depends on ω. Woo and Julien (1989) reviewed these formulations and indicated that all three derivations are questionable. For instance, Einstein and Chien used Eq. 1 without justification and erroneously neglected the correlation between c and v. Questionable steps in Zagustin's derivation include the constant value of the sediment concentration and the use of the velocity fluctuation v' instead of v in the vertical direction. Willis' equation would reduce to Einstein and Chien's relationship if ϵ_m were substituted by ϵ_s.

Turbulent Shear Stress for Heterogeneous Sediment-Laden Flows

The following derivation by size fractions (Woo 1985) clarifies the role played by the fall velocity of sediment particles from a graded sediment mixture. Consider the steady and uniform motion of a heterogeneous sediment-laden flow in an open channel. With reference to Fig. 1, the fluxes of water F_f and sediment F_s passing respectively through a horizontal plane of area dA_f and dA_s parallel to the main flow direction are

$$F_f = \rho_f v dA_f \quad \ldots\ldots (7)$$

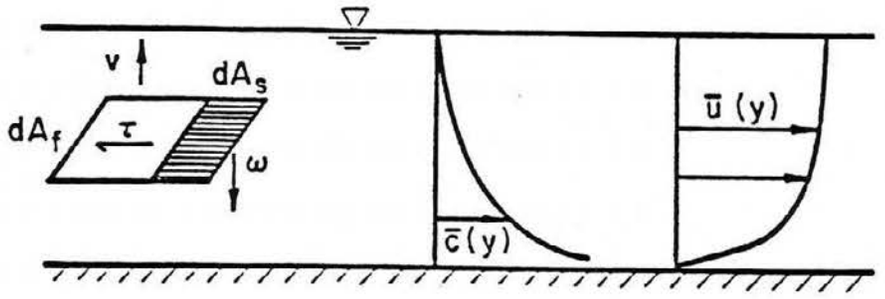

FIG. 1. Two-Dimensional Diagram for Sediment-Laden Flow

and

$$F_s = \sum_{i=1}^{n} \rho_{si}(v - \omega_i) dA_{si} \quad \ldots\ldots (8)$$

respectively. Here the subscript i denotes one of the n sediment size fractions and ω_i refers to the fall velocity of this size fraction.

The turbulent shear stress τ is thus obtained from adding the turbulent momentum fluxes in the x-direction for both the fluid and each fraction of sediments:

$$\tau = -u\left[\rho_f v \frac{dA_f}{dA} + \sum_{i=1}^{n} \rho_{si}(v - \omega_i) \frac{dA_{si}}{dA}\right] \quad \ldots\ldots (9)$$

It is assumed that the inertia of sediment particles is so small that the sediment velocity in the x-direction equals the fluid velocity, u, whereas in the y-direction the sediment velocity differs from the fluid velocity, v, by the settling velocity ω_i of the size fraction i. The following identities are defined:

$$\frac{dA_{si}}{dA} = c_i \quad \ldots\ldots (10)$$

$$c = \sum_{i=1}^{n} c_i \quad \ldots\ldots (11)$$

$$\frac{dA_f}{dA} = \frac{dA}{dA} - \frac{1}{dA}\sum_{i=1}^{n} dA_{si} = 1 - c \quad \ldots\ldots (12)$$

$$\rho_m = \rho_f + (\rho_s - \rho_f)c \quad \ldots\ldots (13)$$

With these four relationships (Eqs. 10–13), and assuming that ρ_s is constant for all size fractions ($\rho_{si} = \rho_s$), Eq. 9 reduces to

$$\tau = -\rho_m uv + \rho_s \sum_{i=1}^{n} \omega_i c_i u \quad \ldots\ldots (14)$$

Instantaneous values of the sediment concentration and the mass density of the mixture are defined as follows:

$$c = \bar{c} + c' = \sum_{i=1}^{n} \bar{c}_i + \sum_{i=1}^{n} c_i' \quad \ldots\ldots (15a)$$

n Flow

..... (8)

nt size fractions

g the turbulent
each fraction of

..... (9)

small that the
u, whereas in
velocity, v, by
g identities are

..... (10)

..... (11)

..... (12)

..... (13)

that ρ_s is con-

..... (14)

mass density

..... (15a)

$$\rho_m = \bar{\rho}_m + \rho'_m \quad \text{..... (15}b\text{)}$$

$$\bar{\rho}_m = \rho_f + (\rho_s - \rho_f)\bar{c} \quad \text{..... (15}c\text{)}$$

$$\rho'_m = (\rho_s - \rho_f)c' \quad \text{..... (15}d\text{)}$$

in which the overbar denotes the time-average value of the parameter and the prime denotes fluctuations of the same parameter. Substitution of Eqs. 15a and 15d into Eq. 14 and the application of the Reynolds averaging process gives

$$\tau = -\overline{(\bar{\rho}_m + \rho'_m)(\bar{v} + v')(\bar{u} + u')} + \rho_s \overline{\sum_{i=1}^{n} \omega_i(\bar{c}_i + c'_i)(\bar{u} + u')} \quad \text{..... (16)}$$

The expression for τ is the time-average value of the shear stress. Under equilibrium conditions, the time-average mass transfer of water in the y-direction can be written as

$$\overline{\left(1 - \sum_{i=1}^{n} c_i\right)v} = 0 \quad \text{..... (17}a\text{)}$$

which can be rewritten as

$$\overline{\sum_{i=1}^{n} c'_i v'} = \bar{v}(1 - \bar{c}) \quad \text{..... (17}b\text{)}$$

For sediments, the time-average mass transfer in the y-direction is given by

$$\overline{\sum_{i=1}^{n} c_i(v - \omega_i)} = 0 \quad \text{..... (18}a\text{)}$$

i.e.

$$\bar{v} = \sum_{i=1}^{n} \omega_i \bar{c}_i \neq 0 \quad \text{..... (18}b\text{)}$$

This relationship (Eq. 18b) demonstrates that the average velocity $\bar{v}$ in the vertical direction is not zero but proportional to the fall velocity of sediment particles and the concentration of each size fraction.

With the aid of Eqs. 3, 4, 17, and 18, the shear stress relationship (Eq. 16) can be expanded (see Appendix I) and simplified to

$$\tau = \overline{-\rho_m u'v'} \quad \text{..... (19)}$$

This relationship is valid without any restriction on the triple correlation. Further simplification of Eq. 19 is possible when neglecting the triple correlation term $\overline{\rho_m u'v'}$ can be justified. This is possible from an order of magnitude analysis of the terms in Eq. 15b. Indeed, when the mass density fluctuation ρ'_m is negligible compared to $\bar{\rho}_m$, Eq. 19 further reduces to

$$\tau = -\rho_f \overline{u'v'}\,(1 + A\bar{c}) \quad \text{..... (20)}$$

which is identical to the relationship derived by Einstein and Chien. This

derivation shows that turbulent shear stress in sediment-laden flows is similar to that of the water flow except that the fluid mass density ρ_f is replaced with the density of the water sediment mixture ρ_m.

Eq. 19 is the chief result of this analysis, which demonstrates that the sediment size distribution and the fall velocity of sediment particles do not affect turbulent shear stress of heterogeneous sediment mixtures under steady-uniform flow conditions.

Acknowledgments

The writers are grateful to Prof. E. V. Richardson for his support of the first author's graduate studies at Colorado State University. We are also thankful to Mr. Y. Lan for his careful review of the manuscript.

Appendix I. Derivation

Applying the Reynolds averaging method to Eq. 16 yields

$$-\tau = \bar{\rho}_m \bar{u}\bar{v} + \bar{\rho}_m \overline{u'v'} + \bar{v}\,\overline{\rho'_m u'} + \bar{u}\,\overline{\rho'_m v'} + \overline{\rho'_m u'v'}$$

$$- \rho_s \bar{u} \sum_{i=1}^{n} \omega_i \bar{c}_i - \rho_s \sum_{i=1}^{n} \omega_i \overline{c'_i u'} \quad \ldots\ldots (21)$$

The last term of Eq. 21 can be dropped due to Eq. 4 because $d\bar{c}/dx = 0$ under steady-uniform flow conditions. Note that Eq. 4, which is critical to this derivation, is also substantiated by the findings of Fischer et al. (1979), who stated that "the total mass transport in the streamwise direction is proportional to the concentration gradient in the streamwise direction." With Eq. 18*b*, the remaining summation reduces to $-\rho_s \bar{u}\bar{v}$. Now expanding ρ'_m from Eq. 15*d* gives

$$-\tau = \bar{\rho}_m \bar{u}\bar{v} + \overline{\rho_m u'v'} + \bar{v}\,\overline{u'(\rho_s - \rho_f)c'} + \bar{u}\,\overline{v'(\rho_s - \rho_f)c'} - \rho_s \bar{u}\bar{v} \quad \ldots\ldots (22)$$

The third term on the right-hand side vanishes due to Eq. 4 and the following term reduces to $\bar{u}\bar{v}(1 - \bar{c})(\rho_s - \rho_f)$ according to Eq. 17*b*. Expanding $\bar{\rho}_m$ from Eq. 15*c* yields the final form of Eq. 22

$$-\tau = \rho_f \bar{u}\bar{v} + \rho_s \bar{u}\bar{v}\bar{c} - \rho_f \bar{u}\bar{v}\bar{c} + \overline{\rho_m u'v'} + \rho_s \bar{u}\bar{v}$$

$$- \rho_s \bar{u}\bar{v}\bar{c} - \rho_f \bar{u}\bar{v} + \rho_f \bar{u}\bar{v}\bar{c} - \rho_s \bar{u}\bar{v} \quad \ldots\ldots (23)$$

which simply reduces to

$$\tau = \overline{-\rho_m u'v'} \quad \ldots\ldots (24)$$

Appendix II. References

Einstein, H. A., and Chien, N. (1955). "Effects of heavy sediment concentration near the beds on velocity and sediment distribution." *MRD Series No. 8*, U.S. Army Engrg. Div., Missouri River, Corps of Engrs., Omaha, Nebr., Aug.

Fischer, H. B., et al. (1979). *Mixing in inland and coastal waters*. Academic Press, New York, N.Y.

Willis, J. C. (1972). "Mathematical models for suspension from a momentum diffusion viewpoint." *Sedimentation* (Einstein), H. W. Shen, ed., Fort Collins, Colo.

Woo, H. (1985). "Sediment transport in hyperconcentrated flows," thesis presented

to Colorado State University, at Fort Collins, Colo., in partial fulfillment of th requirements for the degree of Doctor of Philosophy.
Woo, H. S., and Julien, P. Y. (1989). "Mathematical models for turbulent shea stress in sediment-laden flows." *Proc. Int. Symp. on Sediment Transport Modeling*, Aug., 204–208.
Zagustin, A. (1969). "Mechanics of turbulent flow in sediment-laden streams." *Proc 13th Congress of Int. Association for Hydr. Res.*, Vol. 2.

APPENDIX III. NOTATION

The following symbols are used in this paper:

A = density quotient; $A = (\rho_s - \rho_f)/\rho_f$;
c = volumetric sediment concentration;
dA = area of elementary plane parallel to main flow direction;
dA_s = portion of dA occupied by sediment;
dA_f = portion of dA occupied by water;
F_f = mass flux of fluid;
F_s = mass flux of sediment;
n = number of sediment size fractions;
u = longitudinal fluid velocity;
v = vertical fluid velocity;
x = longitudinal distance in downstream direction;
y = vertical distance from channel bed;
ϵ_f = diffusion coefficient for fluid mass (water);
ϵ_m = diffusion coefficient for fluid momentum;
ϵ_s = diffusion coefficient for sediment;
ρ_f = density of fluid (water);
ρ_m = density of sediment-water mixture;
ρ_s = density of sediment;
τ = shear stress; and
ω = settling velocity of sediment in flow.

Subscripts and Superscripts

$'$ = fluctuating value of parameter;
$\overline{\ }$ = time-average value of parameter; and
i = size fraction of sediment.

Suspension of Large Concentrations of Sands

By H. S. Woo,[1] P. Y. Julien,[2] Member, ASCE, and E. V. Richardson,[3] Fellow, ASCE

Abstract: Existing methods based on the diffusion theory have been extended to determine the sediment concentration distribution for large concentrations of sand. The modifications for volumetric concentrations ranging from 4 to 20% include decreased fall velocity, and increased viscosity and specific weight of the suspension. The sediment concentration profiles are sensitive to the velocity profiles and the fall velocity of sediment particles. In turbulent flows, either a power law or a two-layered logarithmic law can be used to describe the velocity profiles and the sediment diffusivity. The proposed method accurately depicts the deviation from the Rouse equation at large concentrations of sands, and the agreement with sediment concentration profiles measured by Einstein and Chien is excellent. The proposed numerical solution gradually reduces to the relationships of Karim and Kennedy, and Rouse as the volumetric concentration decreases below four percent.

Introduction

Flowing water has the ability to suspend large quantities of sand particles depending on the availability of sediment and the transport capacity of the flow. To describe equilibrium conditions in turbulent flows, Rouse (1937) used Schmidt's (1925) diffusion equation and derived the following equation for the vertical distribution of sediment particles

$$\frac{C}{C_a} = \left[\left(\frac{d-y}{y}\right)\left(\frac{a}{d-a}\right)\right]^Z \quad \ldots\ldots\ldots\ldots\ldots\ldots\ldots\ldots\ldots\ldots\ldots\ldots (1)$$

in which

$$Z = \frac{W_s}{\beta\kappa u_*} \quad \ldots\ldots\ldots\ldots\ldots\ldots\ldots\ldots\ldots\ldots\ldots\ldots\ldots\ldots\ldots\ldots (2)$$

The sediment concentration C at a distance y above the bed depends on the total depth d and the reference concentration C_a at the reference height a. The exponent Z expresses the ratio of the fall velocity W_s of sediment particles to the product $\beta\kappa u_*$ involving the shear velocity u_*, the von Kármán constant κ, and the ratio β of the sediment diffusivity to the fluid momentum diffusivity. For sediment-laden flows with concentrations below a few percent, Rouse's relationship (Eq. 1) has been verified extensively with laboratory and field measurements. Einstein and Chien (1955) experimentally found that in highly concentrated flows, however, the distribution of sands in suspension deviates progressively from what is

[1]Res. Assoc., Dept. of Civ. Engrg., Colorado State Univ., Ft. Collins, CO 80523.
[2]Asst. Prof., Dept. of Civ. Engrg., Colorado State Univ.
[3]Prof., Dept. of Civ. Engrg., Colorado State Univ.

Note. Discussion open until January 1, 1989. To extend the closing date one month, a written request must be filed with the ASCE Manager of Journals. The manuscript for this paper was submitted for review and possible publication on June 15, 1987. This paper is part of the ***Journal of Hydraulic Engineering***, Vol. 114, No. 8, August, 1988. ©ASCE, ISSN 0733-9420/88/0008-0888/$1.00 + $.15 per page. Paper No. 22696.

266

predicted by the Rouse equation. Sediment concentration becomes more uniform as the local sediment concentration exceeds a value of 100 g/l ($C \cong 3.8\%$ by volume).

Chien and Wan (1965) reanalyzed the experimental results of Einstein and Chien for the velocity and sediment concentration profiles. After considering the fall velocity reduction according to Richardson and Zaki's (1954) formula, a modified power form of the velocity profile was used to provide a graphical solution to the Schmidt diffusion equation. More recent contributions by Ordonez (1970), Lavelle and Thacker (1978), and van Rijn (1984) are based on similar concepts with Richardson and Zaki's equation for the fall velocity reduction and Schmidt's formulation of the diffusion equation.

This study examines the vertical distribution of sands in suspension at volumetric concentrations ranging between 4 and 20%. At such high concentrations, Schmidt's approximation of the diffusion equation no longer applies. The properties of the fluid mixture in terms of viscosity and density of the suspension are modified accordingly. Theoretical sediment concentration profiles are determined and compared with Einstein and Chien's data, which is a unique data set at such large concentration of sands in suspension.

Diffusion of Large Concentrations of Sand Particles

After considering the diffusion equations proposed by Schmidt (1925), Halbronn (1949), and Hunt (1954), the relationship best suited to large concentration of sands involves the diffusion coefficient of sand particles ε_s and the representative fall velocity W_p as follows

$$\varepsilon_s \frac{dC}{dy} + C(1 - C)W_p = 0 \quad \ldots\ldots\ldots\ldots\ldots\ldots\ldots\ldots\ldots\ldots\ldots\ldots\ldots\ldots \quad (3)$$

This equation derived by Hunt improves upon Schmidt's formulation ($W_s C + \varepsilon_s \, dC/dy = 0$) for volumetric concentration between 4 and 20% because it satisfies continuity of sediment and water.

The representative fall velocity of the mixture W_p varies with the volumetric concentration C as defined by Richardson and Zaki (1954) or Maude and Whitmore (1958) as

$$W_p = \omega_p(1 - C)^{\alpha} \quad \ldots\ldots\ldots\ldots\ldots\ldots\ldots\ldots\ldots\ldots\ldots\ldots\ldots\ldots\ldots\ldots \quad (4)$$

Although there is no strict rule guiding the selection of the exponent α, it varies with the particle Reynolds number and the particle shape, and decreases from 4.65 to 2.35 as the size of noncohesive particles increases from silts to gravels. The representative fall velocity in clear water ω_p is calculated from the fall velocity ω_i of individual size fractions as:

$$\omega_p = \sum_{i=1}^{N} \frac{\omega_i \bar{C}_i}{\bar{C}} \quad \ldots\ldots\ldots\ldots\ldots\ldots\ldots\ldots\ldots\ldots\ldots\ldots\ldots\ldots\ldots\ldots \quad (5)$$

The subscript i denotes each one of the N-size fractions of sands in suspension, whereas the overbar represents depth-averaged values of the concentration.

The diffusion coefficient ε_s in Eq. 3 is determined from shear stress analysis. At large concentrations of sands, the total shear stress τ is balanced by the sum of the viscous shear stress τ_v and the turbulent shear stress τ_t.

$$\tau = \tau_t + \tau_v \quad \ldots\ldots (6)$$

The reason for adding the viscous shear stress to the commonly used turbulent shear stress is to describe the variability of τ_v due to the increase in sediment concentration. Of course this added term τ_v can be neglected as the concentration becomes vanishingly small in turbulent flows.

The turbulent shear stress relationship derived by Einstein and Chien (1955) considers the turbulent momentum exchange in fluid-particle mixtures

$$\tau_t = \rho_f \varepsilon_m \frac{d\bar{u}}{dy}(1 + AC) \quad \ldots\ldots (7)$$

In clear water ($C = 0$), this equation reduces to Boussinesq's formulation given by the product of the fluid density ρ_f with the fluid momentum diffusivity ε_m and the gradient of the time-averaged velocity $\bar{u}$. The correction factor $A = (\rho_s - \rho_f)/\rho_f$ is a function of the densities of sand particles ρ_s and of the fluid ρ_f.

The viscous shear stress, τ_v, depends on the concentration of sand particles, the dynamic viscosity η of the fluid, and the velocity gradient

$$\tau_v = g(C)\eta \frac{d\bar{u}}{dy} \quad \ldots\ldots (8)$$

The function $g(C) = 1 + 2.5\,C + 10.05\,C^2 + 0.00273 \exp(16.6\,C)$ has been suggested by Thomas (1965) and reduces to Einstein's equation [$g(C) = 1 + 2.5\,C$] at lower concentrations.

The total shear stress component τ depends on the unit weight of the suspension γ_m and the energy gradient S_e of the flow

$$\tau = \int_y^d \gamma_m S_e \, dy \quad \ldots\ldots (9)$$

The bed shear stress is $\tau_0 = \rho_f u_*^2 (1 + A\bar{C})$. Accordingly, the vertical distribution of shear stress τ/τ_0 can be written as a function of the dimensionless depth $\zeta = y/d$

$$\frac{\tau}{\tau_0} = \frac{1 - \zeta + A\int_\zeta^1 C \, d\zeta}{1 + A\bar{C}} \quad \ldots\ldots (10)$$

After substituting Eqs. 7, 8, and 10 into Eq. 6, the diffusion coefficient for suspended sands, ε_s, is obtained from the fluid momentum diffusivity coefficient ε_m according to the Reynolds analogy ($\varepsilon_s = \beta\varepsilon_m$)

$$\varepsilon_s = \beta \left[\frac{u_*^2 \left(1 - \zeta + A \int_\zeta^1 C \, d\zeta \right)}{\frac{d\bar{u}}{dy}(1 + AC)} - \frac{\nu_f g(C)}{(1 + AC)} \right] \quad \ldots\ldots\ldots\ldots\ldots (11)$$

in which ν_f is the kinematic viscosity of the fluid ($\eta = \rho_f \nu_f$). The sediment diffusivity coefficient ε_s can be evaluated from Eq. 11 after the velocity gradient is determined.

Velocity Profiles

Similarities between velocity profiles for clear water and sediment-laden flows suggest the use of the logarithmic velocity profile. The velocity gradient can thus be expressed as

$$\frac{d\bar{u}}{dy} = \frac{u_*}{\kappa y} \quad \ldots\ldots\ldots\ldots\ldots\ldots\ldots\ldots\ldots\ldots\ldots\ldots\ldots\ldots\ldots\ldots (12)$$

Alternatively, the time-averaged velocity $\bar{u}$ can be written as a power function of the dimensionless depth ζ and the depth-averaged velocity V

$$\frac{\bar{u}}{V} = n_1 \zeta^{n_2} \quad \ldots\ldots\ldots\ldots\ldots\ldots\ldots\ldots\ldots\ldots\ldots\ldots\ldots\ldots\ldots\ldots (13)$$

The empirical coefficients n_1 and n_2 depend on the flow characteristics. One can demonstrate that $n_1 = 1 + n_2$ in a two-dimensional flow, and the following analytical relationship between κ and n_2, ($n_2 = u_*/\kappa V$), was derived by Zimmermann and Kennedy (1978) for open-channel flow. Note that Eq. 13 is strictly valid for a power formulation of velocity profiles.

Vertical Distribution of Large Concentrations of Sands

The vertical distribution of sediments in suspension is obtained after substituting the turbulent diffusion coefficient (Eq. 11) and the representative fall velocity (Eq. 4) into the diffusion relationship (Eq. 3).

$$\frac{dC}{dy} = \frac{\omega_p}{\beta} \left[\frac{\frac{d\bar{u}}{dy} f(C)}{\nu_f g(C) \frac{d\bar{u}}{dy} - u_*^2 \left(1 - \zeta + A \int_\zeta^1 C \, d\zeta \right)} \right] \quad \ldots\ldots\ldots\ldots (14)$$

in which $f(C) = C\,(1 - C)^{\alpha+1}\,(1 + AC)$. Eq. 14 is of general applicability and can be solved, provided the velocity profile is accurately depicted. Substituting the velocity gradient from the power-law (first derivative of the velocity profile given by Eq. 13) into Eq. 14 yields

$$\frac{dC}{d\zeta} = \frac{f(C) Z_k}{g(C) H_k - \zeta^{1-n_2} \left(1 - \zeta + A \int_\zeta^1 C \, d\zeta \right)} \quad \ldots\ldots\ldots\ldots\ldots (15)$$

Two dimensionless parameters are defined: $Z_k = n_1 n_2 V \omega_p / \beta u_*^2$; and $H_k = n_1 n_2 \nu_f V / u_*^2 d$. From Eq. 15, concentration decreases with the relative depth

only when the denominator of the right-hand side of the equation is negative, which invalidates its applicability at the bed or near the surface.

Eq. 15 constitutes an integro-differential equation also called "Volterra Integral," which after differentiating with respect to ζ transforms into the following second-order nonlinear ordinary differential equation

$$\frac{d^2C}{d\zeta^2} = \left(\frac{n_2 - 1}{\zeta}\right)\frac{dC}{d\zeta} - h(C)\left(\frac{dC}{d\zeta}\right)^2 - \left\{\left[\frac{H_k}{Z_k}\right]\left[\frac{g'(C)}{f(C)}\right]\right\}\left(\frac{dC}{d\zeta}\right)^3 \quad \ldots\ldots (16)$$

in which

$$h(C) = \left\{\frac{H_k}{Z_k}\left(\frac{n_2 - 1}{\zeta}\right)\frac{g(C)}{f(C)} + \frac{1}{Z_k}\left[\frac{1 + AC}{f(C)}\right]\zeta^{1-n_2} - \frac{f'(C)}{f(C)}\right\} \quad \ldots\ldots\ldots (17)$$

The functions $f'(C)$ and $g'(C)$ denote derivatives of the functions $f(C)$ and $g(C)$ with respect to C. The fifth- and sixth-order Runge-Kutta method detailed in Woo (1985) provides a numerical solution to Eq. 16 after two boundary conditions are satisfied. First, $C = C_a$ at $\zeta = \zeta_a$ taking ζ_a as the dimensionless reference height. The second boundary condition of $\zeta = \zeta_a$ can be obtained from Eq. 15 as

$$\frac{dC}{d\zeta} = \frac{Z_k f(C_a)}{g(C_a)H_k - \zeta_a^{1-n_2}(1 - \zeta_a)(1 + A\bar{C})} \quad \ldots\ldots\ldots\ldots\ldots\ldots (18)$$

An iterative procedure has been used to solve Eq. 18. The first value of $\bar{C}$ is obtained from Rouse's equation. Few iterations are sufficient, since the solution to Eq. 18 is not sensitive to $\bar{C}$.

Logarithmic Velocity Profile

When using logarithmic velocity profiles in turbulent flows, the velocity gradient from Eq. 12 is substituted into Eq. 14. The solution to Eq. 14 is then very similar to the formulation presented with Eqs. 16, 17, and 18, except that: (1) $n_2 = 0$; (2) H_k is negligible; and (3) Z_k is replaced by $Z = \omega_p/\beta\kappa u_*$. Note that this result has not been obtained from Eq. 13 with $n_2 = 0$. Since n_2 does not appear in Eq. 12, it must therefore not appear in the resulting formulation of Eqs. 16, 17, and 18 for logarithmic velocity profiles; hence, $n_2 = 0$.

Approximate Suspended Sediment Distributions at Low Concentrations

Approximate analytical solutions to Eq. 14 are available for low sediment concentrations because several terms in Eqs. 14 and 15 can be simplified or neglected: (1) $f(C) = C(1 - C)^{\alpha+1}(1 + AC) \simeq C$; (2) $A\int_\zeta^1 C\, d\zeta \simeq 0$; and (3) $H_k \simeq 0$. When τ_v is negligible compared to τ_t in Eq. 6, Eq. 15 then reduces to

$$\left(\frac{1}{C}\right)\left(\frac{dC}{d\zeta}\right) + \left[\frac{Z_k}{(1 - \zeta)\zeta^{1-n_2}}\right] = 0 \quad \ldots\ldots\ldots\ldots\ldots\ldots\ldots (19)$$

A graphical solution to this equation was reported by Laursen and Lin (1952), while Karim and Kennedy (1983) suggested the following series expansion formulation

$$\frac{C}{C_a} = \exp Z_k \left(\sum_{j=0}^{\infty} \frac{\zeta_a^{j+n_2} - \zeta^{j+n_2}}{j+n_2} \right) \quad \ldots\ldots\ldots\ldots\ldots\ldots\ldots\ldots\ldots\ldots \quad (20)$$

When logarithmic velocity profiles are considered (with $n_2 = 0$, and Z_k replaced with Z), Eq. 19 simplifies further to

$$\left(\frac{1}{C}\right)\left(\frac{dC}{d\zeta}\right) + \frac{Z}{\zeta(1-\zeta)} = 0 \quad \ldots\ldots\ldots\ldots\ldots\ldots\ldots\ldots\ldots\ldots\ldots\ldots \quad (21)$$

The solution of Eq. 21 gives the well-known Rouse relationship (Eq. 1).

Experimental Verification of the Sediment Concentration Profiles

The theoretical profiles from Eq. 16 have been tested against one of the most comprehensive data sets on velocity and sediment concentration profiles for suspensions of large quantities of sand particles. From a total of 16 runs, the flume data collected by Einstein and Chien (1955) includes seven runs with local volumetric sediment concentrations between 4% and 23%. The flow and sediment characteristics of these runs are summarized in Table 1.

The velocity profiles of the hyperconcentrated flows are shown on both logarithmic (Fig. 1) and semilogarithmic scales (Fig. 2). The velocity measurements above the lowest point of the concentration measurement are used to calculate the slopes of the straight lines in these two figures. The values of n_2 are obtained from Fig. 1, and a two-layer model has been chosen to better describe the logarithmic velocity profiles in Fig. 2. The break in slope is observed near the lower 10% of the flow depth ($\zeta \simeq 0.1$). The slopes of the lower and the upper region define two values of the von Kármán coefficient (e.g., for run *S*-15, $\kappa_l = 0.241$ and $\kappa_u = 0.168$). The corresponding values of the Z factor of the Rouse equation are denoted Z_l and Z_u, respectively and the values are compiled in Table 1.

Figs. 3 and 4 illustrate the comparison between theoretical and measured sediment concentration profiles with the reference concentrations, C_a, taken at the lowest elevation near the bed. Excellent agreement is shown between the solution of Eq. 16 and the measurements of Einstein and Chien. In spite of the breakdown in two layers, both Rouse's linear profiles and Karim and Kennedy's slightly curved profiles remain far from the

TABLE 1. Hyperconcentrated Flow and Sediment Characteristics from Einstein and Chien Data

Run (1)	D (mm) (2)	κ_l (3)	κ_u (4)	n_2 (5)	C_a (6)	α (7)	β (8)	Z_k (9)	Z_l (10)	Z_u (11)
S-5	1.3	0.173	0.173	0.445	0.123	2.7	3.0	14.18	6.01	6.01
S-10	0.99	0.248	0.248	0.311	0.081	3.0	1.7	8.32	4.02	4.02
S-12	0.27	0.330	0.274	0.257	0.077	3.5	1.0	2.80	1.30	1.57
S-13	0.27	0.268	0.237	0.273	0.131	3.5	1.0	3.20	1.61	1.82
S-14	0.27	0.310	0.218	0.300	0.144	3.5	1.0	3.05	1.21	1.72
S-15	0.27	0.241	0.168	0.370	0.232	3.5	1.0	4.21	1.59	2.29
S-16	0.27	0.360	0.182	0.387	0.230	3.5	1.0	3.75	1.01	2.00

. . . . . (20)

= , and Z_k

. . . . . (21)

shi (Eq. 1).

N PROFILES

st ne of the
oncentration
Fr n a total
5 includes
veen 4% and
su marized

own on both
h velocity
ne urement
two figures.
de as been
F . 2. The
th ($\zeta \simeq 0.1$).
s f the von
0 58). The
e denoted Z_l

nd easured
rations. C_a,
er is shown
Ei ein and
near profiles
ar from the

n Einstein and

Z_l	Z_u (11)
	6.01
4.02	4.02
1.30	1.57
	1.82
	1.72
1.59	2.29
1.01	2.00

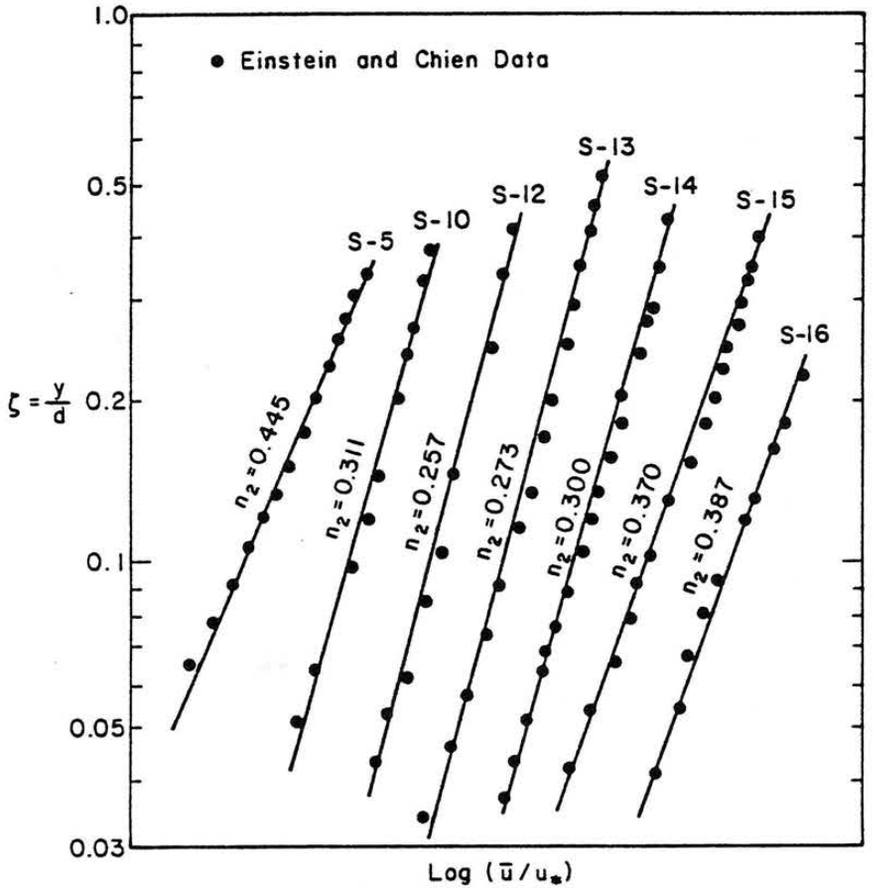

FIG. 1. Velocity Profiles at Large Concentrations of Sands

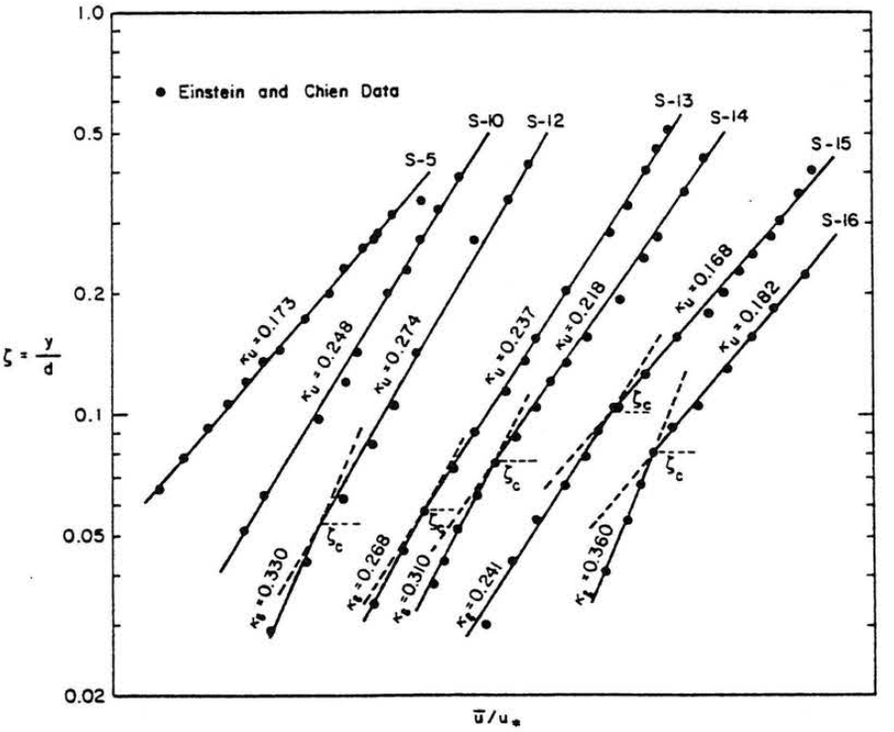

FIG. 2. Two-Layered Logarithmic Velocity Profiles at Large Concentration of Sands

272

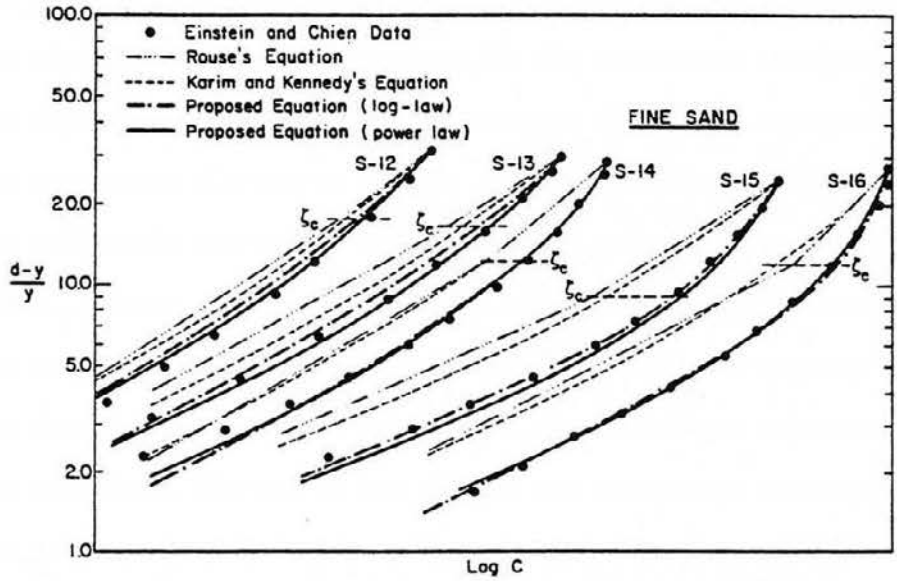

FIG. 3. Concentration Profiles at Large Concentration of Fine Sands

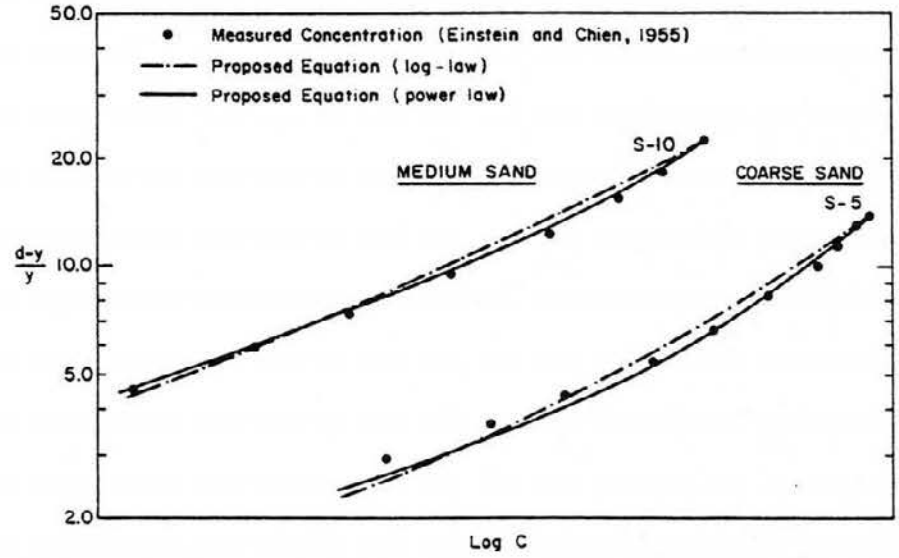

FIG. 4. Concentration Profiles at Large Concentrations of Medium and Coarse Sands

observed profiles. These relationships are best suited to sediment concentrations of less than about four percent volume.

Summary and Conclusions

The applicability of the diffusion approach to determine the vertical distribution of large concentrations of sand particles has been closely examined for concentrations of sands ranging from 4 to 20% by volume. Existing methods have been modified in the following aspects: (1) Hunt's diffusion equation (Eq. 3) is preferred to Schmidt's formulation because it satisfies continuity of fluid and sediments; (2) the fall velocity of sand particles decreases with sediment concentration; and (3) the derivation

includes the effects of increased viscosity and specific weight of the suspension.

The proposed theoretical profiles obtained from solving Eq. 16 depend on the velocity profiles. Solutions using both a power function or a two-layered logarithmic velocity profile demonstrate excellent agreement with the sediment concentration profiles measured by Einstein and Chien. At lower concentrations, Eq. 16 reduces gradually to the equations of Karim and Kennedy, and Rouse. The methodology thus presented extends the applicability of existing methods based on the diffusion equation to large concentrations (up to 20% by volume) of noncohesive particles in suspension. This methodology, however, is not expected to be applicable when substantial fractions of fine cohesive particles are added to the suspension.

Appendix I. References

Chien, N., and Wan, Z. (1965). "The effect of sediment concentration gradient on the characteristics of flow and sediment motion." *J. Hydraul. Eng.*, Beijing, China, 2, 1–20 (in Chinese).

Einstein, H. A., and Chien, N. (1955). "Effects of heavy sediment concentration near the bed on velocity and sediment distribution." *MRD series, no. 8*, Univ. of California, Inst. of Engrg. Res. and U.S. Army Engrg. Div., Missouri River, Corps of Engrs., Omaha, Nebr.

Halbronn, G. (1949). "Remarque sur la théorie de l'Austausch appliquée au transport des matériaux en suspension." *Proc.*, Int. Assoc. of Hydr. Res., 3rd Meeting, 1–6.

Hunt, J. N. (1954). "The turbulent transport of suspended sediment in open channels." *Proc.*, Royal Society of London, Series A., 224(1158), 322–335.

Karim, F., and Kennedy, J. F. (1983). "Missouri River computer-based predictors for sediment discharges and friction factors of alluvial streams." *MRD Sediment Series, No. 29*, U.S. Army Corps of Engrs., Missouri River, Mo.

Laursen, E. M., and Lin, P. N. (1952). Discussion of "Turbulent transfer mechanism and suspended sediment in closed channels," *Trans.*, ASCE, 117(2500), 435–443.

Lavelle, J. W., and Thacker, W. C. (1978). "Effects of hindered settling on sediment concentration profiles." *J. Hydraul. Res.*, 16(4), 347–355.

Maude, A. D., and Whitmore, R. L. (1958). "A generalized theory of sedimentation." *British Journal of Appl. Physics*, Bristol, England, 9, Dec., 477–482.

Ordonez, C. N. A. (1970). "The absolute concentration distribution of suspended sediment in turbulent streams," thesis presented to the Massachusetts Institute of Technology, Cambridge, Mass., in partial fulfillment of the requirements for the degree of Doctor of Philosophy.

Richardson, J. F., and Zaki, W. N. (1954). "Sedimentation and fluidization, part I." *Trans.*, Institute of Chemical Engineers, 32, 35–53.

Rouse, H. (1937). "Modern conceptions of the mechanics of fluid turbulence." *Trans.*, ASCE, 102, 463–543.

Schmidt, W. (1925). "Der Massenaustausch in freier Luft und verwandte Erscheinungen." *Probleme der kosmischen Physik*, 7, Hamburg, Germany, (in German).

Thomas, D. G. (1965). "Transport characteristics of suspension: VIII. A note on the viscosity of Newtonian suspensions of uniform spherical particles." *Journal of Colloid and Interface Sci.*, 20, 267–277.

van Rijn, L. C. (1984). "Sediment transport part II: Suspended load transport." *J. Hydr. Engrg.*, ASCE, 110(11), 1613–1641.

Woo, H. S. (1985). "Sediment transport in hyperconcentrated flows," thesis presented to Colorado State University, at Fort Collins, Colo., in partial fulfillment of the requirements for the degree of Doctor of Philosophy.

Zimmermann, C., and Kennedy, J. F. (1978). "Transverse bed slopes in curved alluvial streams." *J. Hydr. Div.*, ASCE, 104(HY1), 33–48.

APPENDIX II. NOTATION

The following symbols are used in this paper:

A = density quotient; $A = (\rho_s - \rho_f)/\rho_f$;
a = reference height above the bed;
C = volumetric sediment concentration;
$\bar{C}$ = depth-averaged sediment concentration;
C_a = reference concentration;
D = median particle size;
d = channel depth;
$f(C)$ = a function of sediment concentration;
$g(C)$ = a function related to relative viscosity of cohesionless particle-fluid system;
H_k = H-factor for the power-law equation;
$h(C)$ = a coefficient for the differential equation (Eq. 17);
i = one of the N-size fraction of sands;
j = summation index in Karim and Kennedy's equation;
N = number of size fractions;
n_1 = coefficient of power-law equation;
n_2 = exponent of power-law equation;
S_e = energy gradient of channel;
$\bar{u}$ = time-averaged local velocity;
u_* = shear velocity; $u_* = \sqrt{gdS_e}$;
V = depth-averaged velocity;
W_p = representative fall velocity reduced because of the concentration of sands (Eq. 4);
W_s = fall velocity of sands in suspension (low concentration);
y = vertical distance from bed;
Z = exponent in the Rouse equation (Eq. 2);
Z_k = Z-factor for the Karim and Kennedy relationship;
Z_l = Z-factor in the lower portion of the velocity profile;
Z_u = Z-factor in the upper portion of the velocity profile;
α = exponent of the fall velocity reduction equation;
β = ratio of sediment diffusivity, ε_s, to fluid momentum diffusivity, ε_m;
γ_m = unit weight of water-sediment mixture;
ε_m = diffusion coefficient for fluid momentum;
ε_s = diffusion coefficient for sands;
ζ = dimensionless height: $\zeta = y/d$;
ζ_a = dimensionless reference height: $\zeta_a = a/d$;
η = dynamic viscosity of fluid;
κ = von Kármán constant;
κ_l = von Kármán constant for lower flow region;
κ_u = von Kármán constant for upper flow region;
ν_f = kinematic viscosity of fluid;
ρ_f = density of fluid;
ρ_s = density of sand particles;

τ = shear stress;
τ_0 = bed shear stress;
τ_t = turbulent shear stress;
τ_v = viscous shear stress;
ω_i = fall velocity in clear water of a sand particle of the i-th size fraction; and
ω_p = representative fall velocity in clear water (Eq. 5).

DELINEATION OF LANDSLIDE, FLASH FLOOD, AND DEBRIS FLOW HAZARDS IN UTAH

Proceedings of a Specialty Conference
Held At
Utah State University, Logan, Utah
June 14-15, 1984

Edited By

David S. Bowles

GENERAL SERIES
UWRL/G-85/03

Utah Water Research Laboratory
Utah State University
Logan, Utah 84322-8200

August 1985

277

PHYSICAL PROPERTIES AND MECHANICS OF HYPERCONCENTRATED SEDIMENT FLOWS

by J. S. O'Brien and P. Y. Julien

ABSTRACT

The authors advance a better understanding of hyperconcentrated sediment flows, commonly referred to as debris flows or mudflows, with a fundamental investigation of the nature of fluid motion. In these flows of large concentrations of sediment, the predominant processes of energy dissipation are related to the viscous, turbulent, dispersive and yield stresses. The relative magnitude of these components largely depend on the fluid properties and whether the flow matrix consists of cohesive or noncohesive sediment. Based on experimental data, the following relationships are provided: 1) stress versus rate of strain, 2) viscosity versus sediment concentration, and 3) yield strength versus sediment concentration. These results expand our knowledge of the physical properties of hyperconcentrated flows.

The authors also review the application of fluid principles to these flows. The fundamentals of fluid mechanics are outlined for the case of hyperconcentrated flows on steep slopes with emphasis on the physical properties of non-Newtonian fluids. A theoretically sound and simplified methodology prescribe the engineering analysis for these hazard flows.

INTRODUCTION

Hyperconcentrated sediment flows are commonly referred to as mud flows or debris flows. The term hyperconcentrated, however, depicts a broader spectrum of sediment transport ranging from large concentrations of suspended sediment in streams to landslides. Sharp and Nobles (1953) refer to hyperconcentrated flows as debris flows instead of mud flows when fifty percent or more of the sediment in the flow matrix is coarser than sand. Debris flows have also been described as granular flows which are identified by the absence of fine material (silts and clays).

Hyperconcentrated flows originate in basins which can be delineated into three zones. The sediment source area is located in the uppermost region of the watershed and may be in a landslide area. The zone of sediment transport is a steep channel system in which erosion and deposition are generally in equilibrium. Finally, the alluvial fan is a depositional zone often identified by a break in the bed slope of the main channel.

Jim S. O'Brien, P.E., is Research Associate at the Civil Engineering Department, Colorado State University, Fort Collins, Colorado.
Pierre Y. Julien, Ph.D., is faculty Affiliate at the Civil Engineering Department, Colorado State University, Fort Collins, Colorado.

Alluvial fans in the mountain communities of Colorado and Utah have become attractive sites for development; homes, subdivisions and even entire towns are located on the fans of small watersheds. Recent growth and development trends are forcing construction to encroach on apparently inactive fans with devastating results. There has been a dramatic increase in the number of destructive and life threatening encounters with high hazard mud floods and mud flows. The annual cost incurred from these destructive events now exceeds millions of dollars. In 1984 damages in Colorado were estimated at $32 million. There is a critical need to delineate these hazard areas and develop a predictive methodology that will define the level of hazard.

The long-term objective of this research is to develop a predictive mathematical model for hyperconcentrated sediment flows that is manageable and cost effective. The model should be based on a thorough understanding of the physical processes and should predict the following flow properties at desired reach stations: peak discharge, time to peak, average velocity, average flow depth, volume of water and sediment, impact pressure, runout distances, and areas of inundation for a given event frequency.

A steep watershed model for water and sediment routing of overland flow and in open channels using the kinematic wave approximation for the momentum equation has been in use for several years. It remains to link the watershed model with constitutive equations for mud and debris flows, routing them down open channels and across alluvial fans. In addition, a complete model will require description of the mobilization processes of the eroded material which comes off the slope and enters the channels. Such processes may include rill and gully erosion, bank sloughing failure, landslide and overland flow.

The continuing research on hyperconcentrated sediment flows at Colorado State University is directed towards development of a predictive methodology. This requires a thorough understanding of the physical processes of water-sediment mixtures which can only be accomplished through a research program involving theoretical analysis laboratory measurements and field investigation. Initially in this paper, the physical properties of hyperconcentrated sediment flows are defined, followed by a description of the shear stress relationships linked to the mechanics of hyperconcentrated flows. The proposed theoretical developments are supported by laboratory analysis from field samples. A simple methodology has been applied to 16 watersheds to evaluate the relative magnitude of internal to boundary energy losses.

DELINEATION OF HYPERCONCENTRATION SEDIMENT FLOW CATEGORIES

Hyperconcentrated sediment flows encompass a wide range of flow concentration conditions. An attempt to delineate mass wasting processes into several categories with different flow properties was initiated by the National Research Council Committee on Methodologies for Predicting Mud Flows (NRC, 1982). To refine the delineation with some physical properties of the fluid matrix, several experiments were performed at Colorado State University on mud flow samples extracted from undisturbed deposits located in Colorado. The samples were

analyzed for size fraction and silt and clay content, and the properties of the mixture were described for various water and sediment concentrations. The results were incorporated into the definitions promulgated by the NRC committee and are shown in Table 1.

In nature, there exist a continuum of flow conditions and one hydrologic event may consist of several flow processes. Flow deposits, scour characteristics, and fan patterns are helpful tools in identifying the flow regimes and processes. Although the transition between the different types of flow are difficult to distinguish, mass wasting processes can be divided in four main categories: water floods, mud floods, mud flows, and landslides.

Conventional water flooding is defined as water inundation by overbank discharge. Sediment is transported through the mechanisms of suspension and rolling and saltation along the bed which depend largely on water velocity and turbulence. For water floods, standard hydrologic and sediment transport capacity methods and formulas are applicable. Water floods are not a phenomena analyzed in this paper.

Mud floods define a range of concentration from 20 to 45 percent by volume (Table 1). This concentration refers to the fluid matrix and should be assumed to consist of silts, clays and fine sands only. Water floods and mud floods display inherent fluid properties, both are unable to resist shear stress without motion or exhibit any appreciable yield strength. Conventional analysis using momentum, energy and continuity equations are applicable. Sediment transport capacity equations such as Einstein and Meyer-Peter and Müller are inappropriate because higher viscosities of the mixture and lower fall velocities of solid particles invalidate the empirical constants which are based on clear water as the fluid medium. Water floods and mud floods are classified under the National Flood Insurance Program (NFIP) definition of floods by the NCR (see Figure 1).

In mud flows the sediment concentration is sufficient to support large clastic material in a quiescent condition without settling. The flow matrix exhibits a distinct resistance to motion (high yield strength). This resistance to shear stress is a pseudo-plastic flow property corresponding to high viscosities. The National Research Council (NRC, 1982) report states, "The key characteristic in differentiating between mud floods and mud flows is that a mud flow displays a combination of density and strength that will support inclusions of higher density than water, such as boulders, both during transport and when the mass comes to rest". Throughout the flow process the combination of fluid matrix density and small settling velocities keep the boulders near the surface in the absence of turbulence. In steep basins, mud flows are generated under certain conditions of rainfall and sediment availability. When unlimited supplies of sediment become available, the probability of producing a mud flow is very high for intense rainfall events. Debris flows are acknowledged as having more than fifty percent of the sediment sizes coarser than sand. Debris flows without fine materials (silts and clays) are referred to as granular flows.

TABLE 1. DESCRIPTION OF HYPERCONCENTRATED SEDIMENT FLOW AS A FUNCTION OF CONCENTRATION†

Flow Type	Concentration by Volume C_v	Concentration by Weight C_w *	Flow Characteristics
Landslides	.53-.90	.75-.96	Will not flow, failure by block sliding
	.50-.53	.73-.75	Block sliding failure with internal deformation during the slide, slow creep prior to failure
Mud Flows	.48-.50	.72-.73	Flow evident, slow creep sustained mud flow, plastic deformation under its own weight, cohesive, will not spread on level surface
	.45-.48	.69-.72	Begins spreading, cohesive
Mud Flood	.40-.45	.65-.69	Mixes easily, shows fluid properties in deformation; spreads on horizontal surface but maintains a inclined fluid surface, large particle settling, waves appear but dissipate rapidly
	.35-.40	.59-.65	Marked settling, spreading nearly complete on horizontal surface, liquid surface two phases appear, waves travel substantial distance
	.30-.35	.54-.59	Separation of water on surface, two phases, waves travel easily, most sand and gravel has settled out
	.20-.30	.41-.54	Distinct wave action, fluid surface, all particles resting on bottom in quiescent fluid condition
Water Flood	<.20	.41	Water flood with bed and suspended loads

†This information is qualitative guideline in which the concentration refers to the fluid matrix consisting of silts, clays and fine sands.

*The concentration by weight is computed using 2.72 as the specific gravity for the sediment as measured in the laboratory.

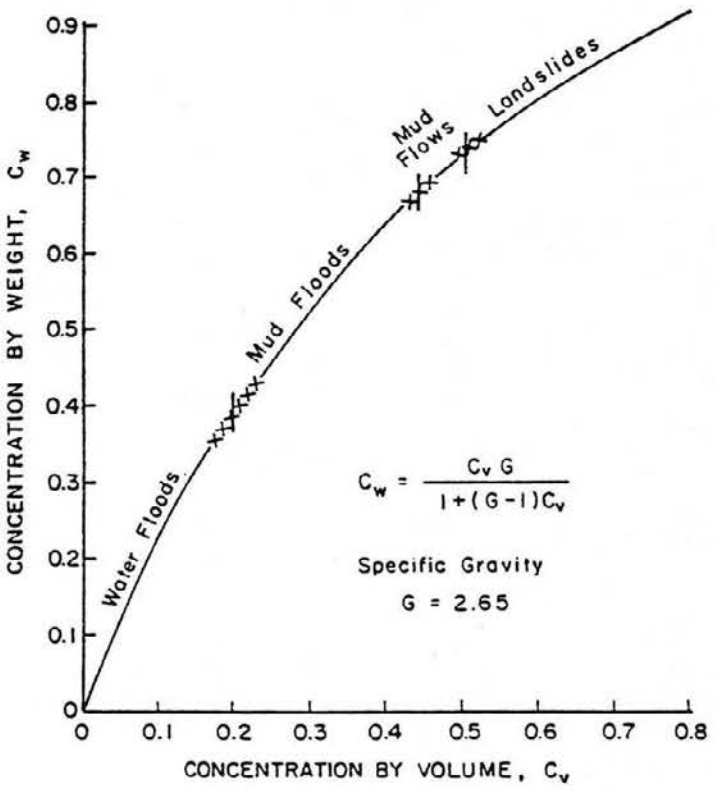

FIGURE I. HYPERCONCENTRATED SEDIMENT FLOWS CLASSIFICATION

Landslides consist of downslope movement of earth by mechanisms of falling, toppling, sliding and spreading. Such earth movements may be either wet or dry. Landslides and bank slumps are an integral part of generating mud flows and mud floods in steep basins. This mechanism delivers source material to channel in brief singular events that often perturbate the channel flow hydraulics.

PHYSICAL PROPERTIES OF THE FLUID MATRIX

The presence of large concentrations of sediment induces complex processes of energy dissipation in the fluid matrix. Besides the viscous and turbulent stresses existing in clear water flows, the interaction of water and sediment, the exchange of sediment particles with the channel boundary, and the collisions of suspended particles (dispersive stress) all contribute to the dissipation of energy from the fluid matrix. Moreover, the presence of clay particles whose cohesive forces arise from hydrophilic bonding, modifies the physical processes governing the fluid flows. Hyperconcentrated sediment flows, therefore, are a function of complex interrelationships between water and sediments which require further investigation.

Conventionally, the force in fluids necessary to produce a given deformation is proportional to the rate of deformation. For a real fluid in motion relative to a rigid boundary, shear stresses develop in proportion to the rate of angular deformation. This definition implies that shear stresses will exist only in moving fluids. Figure 2 shows different relationships between shear stress and the rate of deformation.

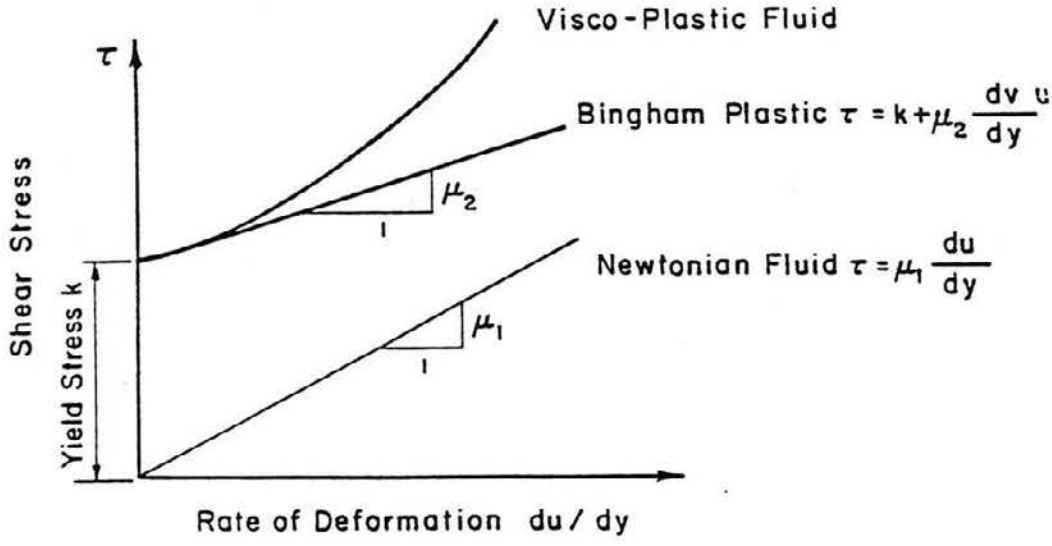

FIGURE 2. BEHAVIOR OF FLUIDS

Newtonian fluids follow a linear relationship between shear stress and rate of strain in which the slope of the line is the viscosity μ of the fluid. The Bingham plastic model combines a yield stress k and a linear stress-strain relationship for shear stresses in excess of the yield value. Hyperconcentrated flows are non-Newtonian, the shear stress exhibited by the flow is not proportional to a linear rate of strain. Bingham plastic and visco-plastic relationships are commonly used to describe hyperconcentrated flows. The property of a yield stress which must be exceeded to initiate motion gives rise to the plastic or Bingham nature of the fluid.

In the analysis of most rivers and streams, the sediment being transported has negligible effect on the Newtonian properties of the fluid (water). In mud flows, however, large concentrations of fine sediment alter the fluid properties, particularly viscosity and turbulence. For the case of mud flows, the 'fluid' consists of the water and fine sediment and is referred to as the fluid matrix. Mud flows generally transport large clastic material, including large boulders. The clastic material is suspended in the fluid matrix, often being rafted on or near the surface of the flow. The large concentration of fine material (silt and clay) have altered the fluid matrix

properties of viscosity and density and, therefore, the lift, drag and buoyancy forces acting on the particle exceed that which would have been exerted by water alone. The fluid matrix consists of the fluid plus the sediment particles which will have a negligible fall velocity in a quiescent condition.

Consider the case of granular flows in which the fluid matrix is water and the sediment is virtually all noncohesive clastic material. Granular flows may be either wet or dry (Passman et al., 1980, Nunziato and Passman, 1980 and Savage, 1979). The fluid medium is water and the fall velocity of the particle is large due to the absence of fines and the corresponding small viscosity of the fluid matrix.

Concentration and flow properties should be expected to change with larger concentrations of silt and clay. Graf (1971) reported that the fall velocity of particles decreases with the addition of fine sediment to water. A small percent concentration by weight of sediment in flowing water dampens turbulent eddies (Vanoni, 1941). Bagnold (1956) further indicated that at high concentrations of sediment, the turbulence may disappear altogether. Increasing the concentration of fines has the effect of increasing both the viscosity and density of the flow. Viscosities of actual debris flow deposits have been measured in the laboratory in excess of 1000 poises (the viscosity of water is about 0.01 poises).

The sediment concentration determines the physical characteristics of hyperconcentrated sediment flows. Concentration can be measured either by weight C_w or by volume C_v with a conversion of

$$C_w = \frac{C_v G}{1 + (G-1)C_v} \qquad (1)$$

where G is the specific gravity of dry sediment. A concentration of 50% by volume corresponds to 73% concentration by weight using 2.65 as the specific gravity for the sediment. Referring to Table 1, 50% concentration by volume represents a perceived limit to a mud flow with some fluid properties as determined through laboratory experiments.

It is noteworthy that Bagnold (1954), in his paper on dispersive stress theory, described flows of uniform grains with a concentration by volume of 57% as a granular paste and 52% concentration by volume as the Newtonian fluid limit. In his calculations he correctly reported that the maximum concentration for spheres is 74% by volume with a lower value of 65% for natural, reasonably rounded uniform grains. Using some data from Lamb and Whitman (1969) and Das (1983) the concentrations in Table 2 were computed. The loosest stable arrangement for uniform spheres is a simple cubic structure with a concentration of 53% by volume. The average minimum volumetric concentration of several soil types shown in this table is 54%. For impending fluid motion of the sediment, the concentrations must decrease from these minimum values given in Table 2; otherwise the sediment would move as a block. This evidence supports the delineation of flow definitions indicated in Table 1.

TABLE 2. CONCENTRATION BY VOLUME OF GRANULAR SOILS
(Modified After Lamb and Whitman, 1969 and Das, 1983)

Description	C_v Minimum	C_v	C_v Maximum
Uniform Spheres	0.53		0.74
simple cubic configuration		0.53	
bodied-centered cubic		0.68	
face-centered cubic		0.74	
hexagonal close-packed structure		0.74	
Uniform Inorganic Silt	0.48		0.61
Standard Ottawa Sand	0.56		0.67
Clean Uniform Sand	0.50		0.61
Silty Sand	0.53		0.78
Fine Sand	0.54		0.71
Coarse Sand	0.57		0.74
Fine to Coarse Sand	0.51		0.83
Micaceous Sand	0.45		0.71
Silty Sand and Gravel	0.54		0.88
Gravelly Sand	0.59		0.83
Gravel	0.63		0.77
Average	0.54		

In the field, higher concentrations may be possible with larger quantities of silt and clay in the flow matrix. Written accounts of mud flows describe a wide range of concentrations with maximum concentrations by weight as high as 79 to 85% (Sharp and Nobles, 1953), 60 to 78% (Pierson, 1981) 59 to 86% (Pierson, 1980), 60 to 90% (Johnson, 1970) and 91% (Curry, 1966). Any loss of water during the sampling process, however, could result in significantly higher concentrations than actually occurred during the flow events. Surges and nonuniformity in the flow concentrations also distort the measured estimates of the flow properties. It is suggested that attempts at reporting mud and debris flow events should focus on a description of the mean flow properties which will assist in developing future predictive methods.

MECHANICS OF HYPERCONCENTRATED SEDIMENT FLOWS

The predominant processes of energy dissipation and resistance to motion are a function of the viscous, turbulent, dispersive and yield shear stresses. The relative magnitude of these stresses largely depend on the fluid properties, the concentration of sediment and whether the flow matrix includes cohesive sediment. Although the initiation of motion through landslides and creeping soil failures are more properly examined through a soil mechanics approach, the hyperconcentrated flows should be analyzed in a continuum approach to describe a wide range of concentrations ranging from clear water to very viscous mud flows.

Newton's second law is applied to describe the one-dimensional motion of an incompressible water-sediment mixture. The force equilibrium per unit mass may be written as

$$\frac{\partial u}{\partial t} + u \frac{\partial u}{\partial x} = g \sin\theta - \frac{1}{\rho_m} \frac{\partial p}{\partial x} + \frac{1}{\rho_m} \frac{\partial \tau}{\partial y} \qquad (2)$$

where ρ_m is the density of the fluid mixture, u is the velocity in the downstream x-direction, p is the internal pressure, τ is the shear stress, g is the gravitational acceleration, $\sin\theta$ is the channel slope and y is the upward distance above the channel bed perpendicular to the flow. The left side of the equation represents the local and convective acceleration of the fluid. These terms depict the unsteadiness and nonuniformity of the flow. The right side of the equation represents the gravity, pressure, and resistive shear stress terms. In the original Navier-Stokes equation valid for Newtonian fluids, the pressure distribution can be assumed to be hydrostatic and the shear stress is a function of the viscosity μ and of the rate of deformation

$$\tau = \mu \frac{\partial u}{\partial y} \qquad (3)$$

In mud flows, however, the shear stress is a complex function of the water and sediment properties comprising the fluid matrix which limits its direct application for predictive modeling. A general equation postulated for the resistive shear stress in a water sediment mixture is

$$\tau = k + \mu_m \frac{\partial u}{\partial y} + C_1 \left(\frac{\partial u}{\partial y} \right)^2 + \ldots \qquad (4)$$

where k is the yield stress, μ_m is the viscosity of the fluid matrix and C_1 may be a variable whose magnitude depends on depth and concentration. The combination of the first two terms is referred to as the Bingham model for mud flows. The Bingham model consists of a yield stress term and a viscous stress term. This model is applicable when the applied shear stress exceeds the yield stress ($\tau > k$) and the resistive stress is linearly proportional to the rate of strain. Both the yield stress k and the viscosity μ_m are functions of concentration as shown in Figures 3 and 4. The Bingham model can be used somewhat successfully to describe the motion of mud flows in smooth prismatic open channels for partially turbulent or transitional flows without energy losses due to roughness.

The $C_1(\frac{\partial u}{\partial y})^2$ term is a composite of the dispersive and turbulent stresses. It is referred to as the inertial term in the shear stress equation. The conventional representation for the turbulence stresses in clear water is

$$\tau_R = \rho \kappa^2 y^2 (\frac{\partial u}{\partial y})^2 \qquad (5)$$

in which ρ is the density of clear water and κ is the von Karman constant. The dispersive stress arising from the collision of sediment particles as defined by Bagnold (1954) is

$$\tau_D = a_i \lambda^2 D_s^2 (\frac{\partial u}{\partial y})^2 \qquad (6)$$

where D_s is a representative grain diameter and a_i is a constant. The linear concentration λ can be written as a function of the concentration by volume C_v and the maximum possible static concentration by volume C_o

$$\lambda = \frac{1}{(C_o/C_v)^{1/3} - 1} \qquad (7)$$

In a water and sediment mixture, these two stresses can be combined in Eq. 4 since both are functions of the second power of the rate of deformation. The turbulent stresses assist in suspending particles into the flow by exchanging momentum from the fluid to the sediment particles. The dispersive stresses meanwhile, impart momentum transfer between the particles. Increasing concentration and the corresponding collisions between the particles dampens turbulence. A characteristic of turbulence is the irregular or random motion of a fluid which generates pseudo-stresses in the sense that they originate from the acceleration terms. The momentum is transferred to the boundary by viscous diffusion (vorticity). The flow is mixed through eddies and the stretching of vortices create smaller eddies and drive the interaction between eddies of different sizes. High sediment concentration dampens

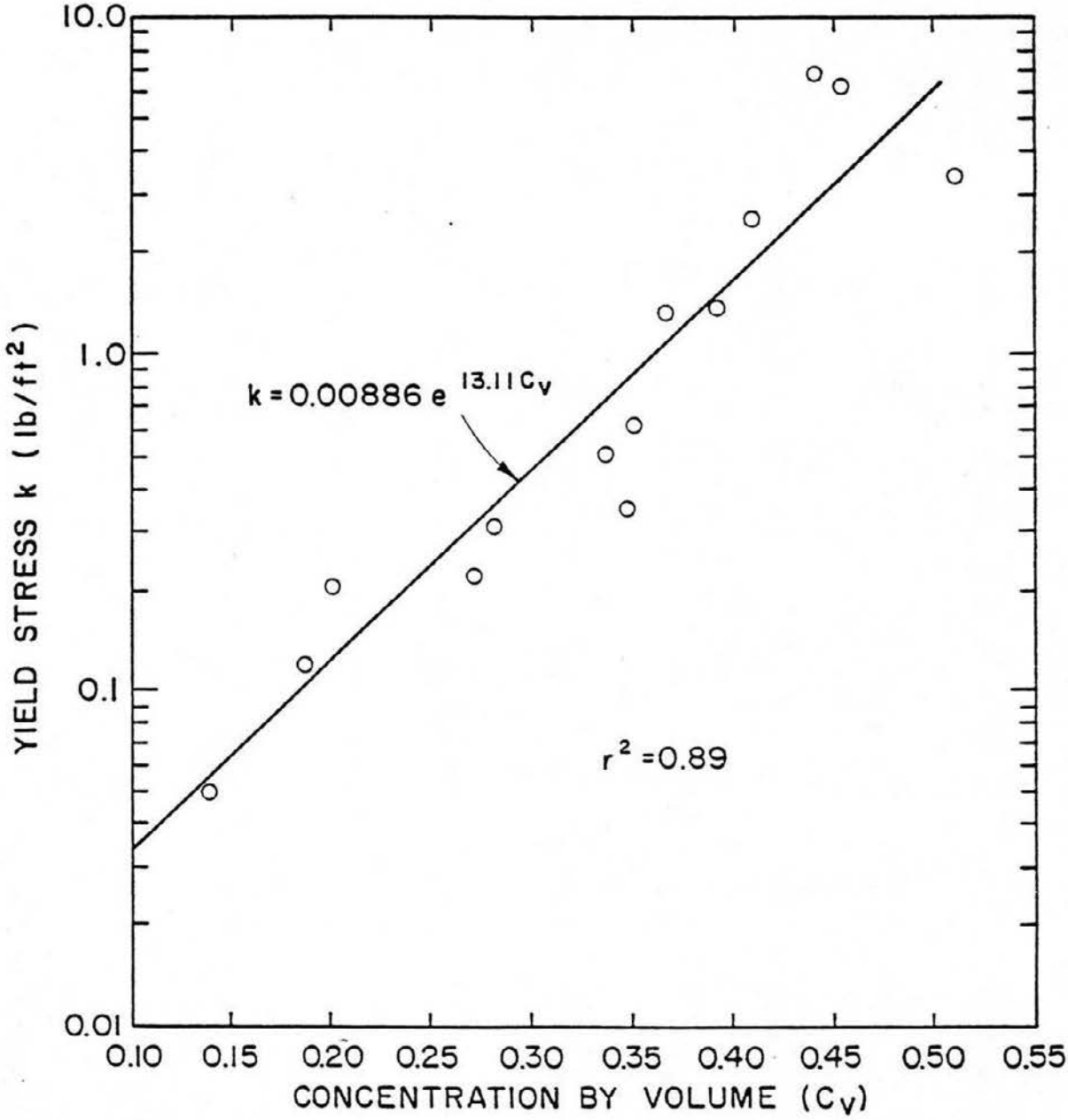

FIGURE 3. YIELD STRESS vs. CONCENTRATION BY VOLUME

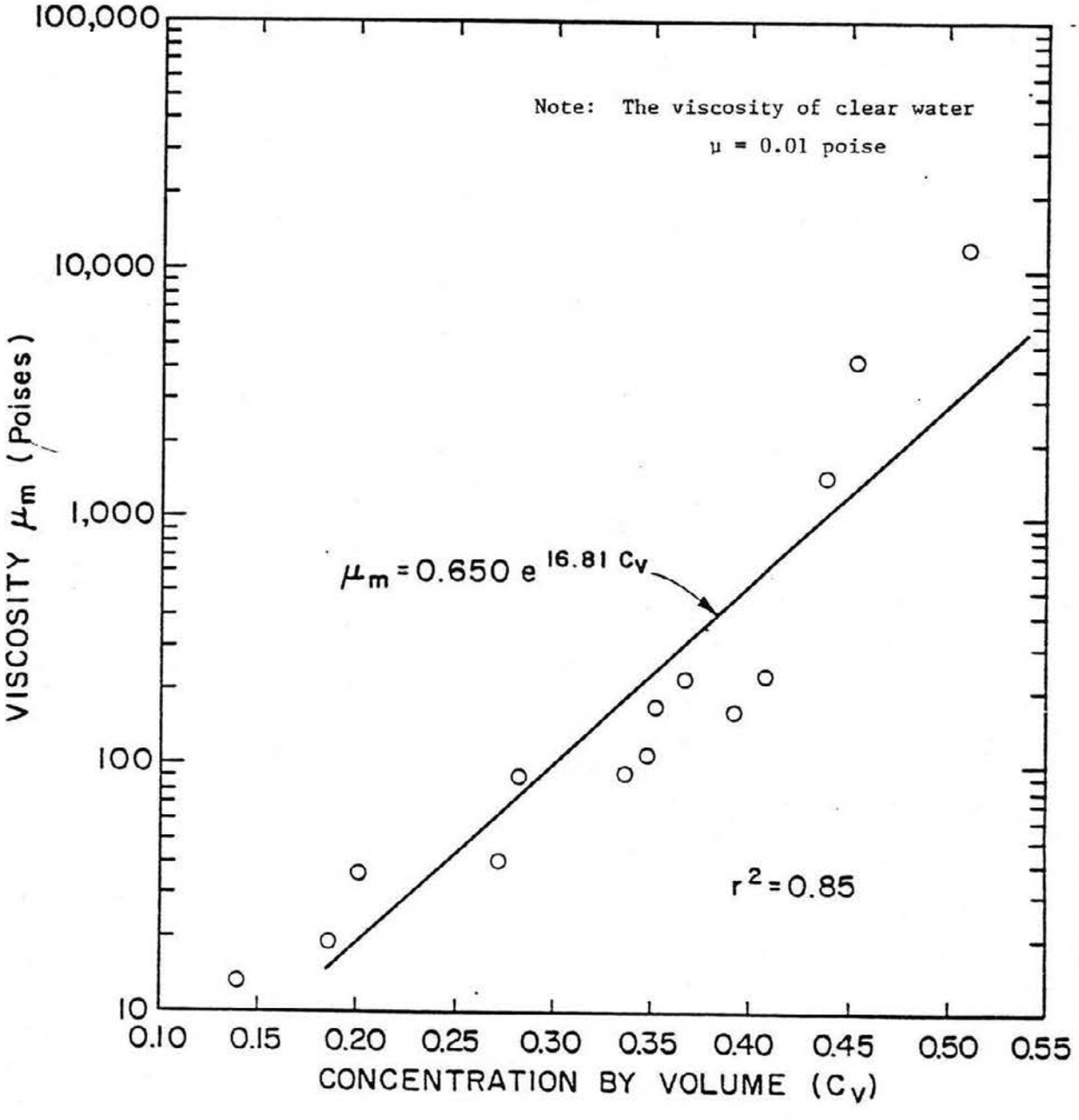

FIGURE 4. VISCOSITY vs. CONCENTRATION BY VOLUME

the eddies in a cumulative manner dissipating the smaller eddies first or hampering their formation altogether. Sharp and Nobles (1953) noted this phenomena in their descriptive paper. In this fashion, the energy is sapped from the main body of the flow and expended to increase the sediment particle velocity and the height of suspension. This energy is distributed throughout the various levels of the flow and is eventually lost in the fluid mixture through viscous heat.

The turbulence and dispersive stresses lose their separate identities in a hyperconcentrated sediment flow and both stresses can be combined in the last term of Eq. 4. The stress-strain relationship given by Eq. 4 is promoted as correctly representing the behaviour of hyperconcentrated sediment mixtures. This relationship is theoretically sound since it is derived from fundamental principles in fluid mechanics, and the parameters of this function represent physical quantities. The relative magnitude of these parameters depends on the composition of the water-sediment mixture which can be described by (the concentration by weight C_w or the concentration by volume C_v and the concentration of fine material C_f.

Equation 4 was tested in laboratory analysis using a rotating viscometer to measure the stress-strain relationship of a fluid matrix from a mud flow deposit. The results are shown in Figure 5. The physical properties defined by the relationship are the yield stress ($k = 0.0108$ lb/ft^2), the viscosity of the fluid matrix ($\mu_m = 0.00065$ lb-s/ft^2 = 0.31 poises) and $C_1 = 0.0065$ lb-s^2/ft^2. The viscosity of the mixture is about thirty times larger than that of clear water. The parabolic relationship defined by regression analysis generates a better fitting curve ($r^2 = 0.98$) than a linear relationship between stress and strain rate ($r^2 = 0.95$). The Bingham model erroneously predicts a viscosity (9.43 poises) thirty times larger than the Eq. 4.

The ratio R of the inertial stress term to the viscous stress, the last two terms on the right side of Eq. 4, is

$$R = \frac{C_1}{\mu_m} \frac{\partial u}{\partial y} \tag{8}$$

This non-dimensional ratio defines the relative magnitude of the inertial to viscous stresses in a form similar to the Rouse number for clear water turbulent flows. This ratio supercedes the use of any critical Reynolds number which is not applicable to delineate non-Newtonian flow regimes. A small value of R indicates the predominance of viscous stresses and suggest the use of a Bingham model rather than the complete solution of Eq. 4. The value of C_1 is determined through laboratory analysis from Figure 3 and is a function of the sediment concentration, particle diameter, flow depth and clay concentration.

Similarly the Bingham number can be written as the ratio of the yield stress to the viscous stress

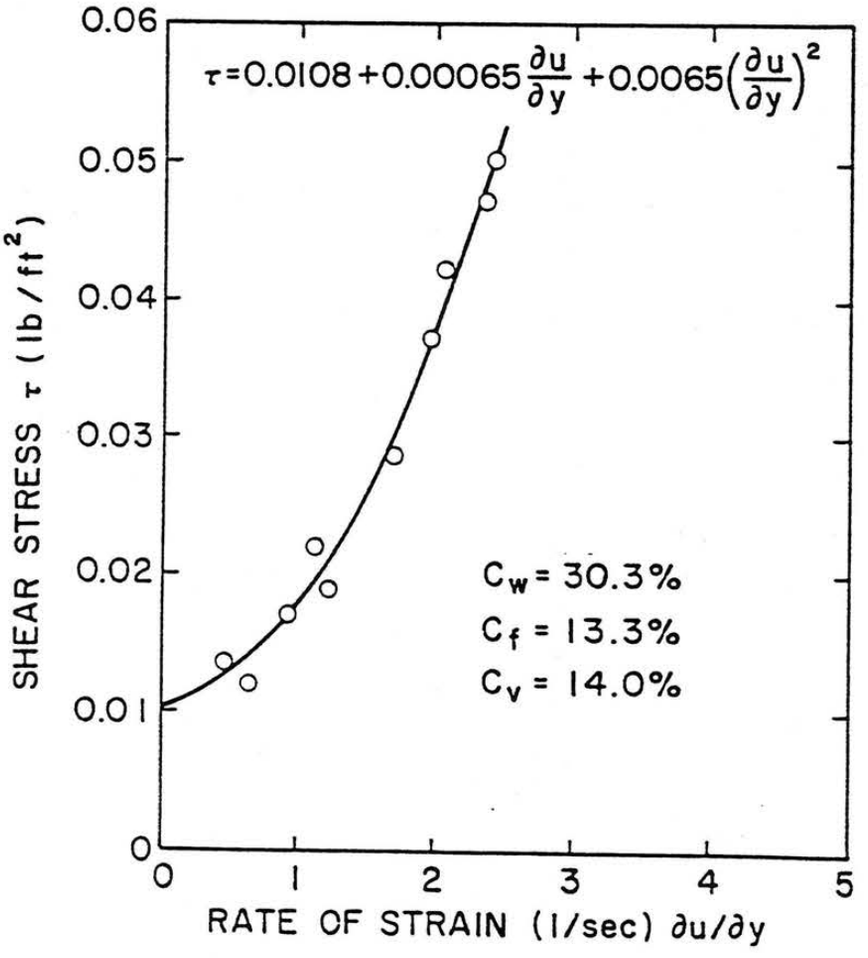

FIGURE 5. SHEAR STRESS vs. RATE OF STRAIN

$$B = \frac{k}{\mu_m} \frac{\partial y}{\partial u} \tag{9}$$

This ratio indicates the relative magnitude of the yield and viscous terms. As R becomes small and B reduces to zero, the fluid will behave as a Newtonian fluid. These two ratios R and B are valid at every point along a velocity profile since they are both a function of $\frac{\partial u}{\partial y}$. In order to describe the mean flow characteristics, however, the partial derivative $\frac{\partial u}{\partial y}$ can be replaced by the ratio of average velocity $\bar{u}$ to the flow depth d in Eqs. 8 and 9. Both ratios must be defined by laboratory investigation.

APPLICATIONS

The physical processes encountered in mud flows are extremely complex. Valuable insight into the real nature of these non-Newtonian flows was gained through theoretical work, laboratory analysis and field investigations. Simplified methodologies based on the dominant physical processes have been applied to 16 small steep watersheds generating mud flows near Glenwood Springs, Colorado. One objective was to determine the relative magnitude of the losses attributed to internal viscous dissipation as compared to the losses due to channel boundary roughness. This analysis is based on the force balance equation (Eq. 2). The pressure term is written as a function of flow depth d and the shear stress τ in the channel is subdivided in two components. The first component τ_b is due to the large boundary roughness elements written as a function of the boundary energy loss gradient S_b and the second accounts for the internal stress τ_i. Assuming an hydrostatic pressure distribution in a one-dimensional flow over rough boundaries, Eq. 2 can be rewritten as

$$\frac{\partial u}{\partial t} + u \frac{\partial u}{\partial x} + g \frac{\partial d}{\partial x} - g \sin\theta + g S_b + \frac{1}{\mu_m} \frac{\partial \tau_i}{\partial y} = 0 \tag{10}$$

The solution to this equation when combined with the continuity equation gives a complete one-dimensional dynamic description of the motion of hyperconcentrated sediment flows. Steady uniform flow conditions can be assumed which eliminates the first three terms of Eq. 10, the internal energy gradient S_i is then defined as

$$S_i = \frac{1}{\rho_m g} \frac{\partial \tau_i}{\partial y} = S_o - S_b \tag{11}$$

where the bed slope ($\sin\theta$) is written as S_o. The boundary friction slope term S_b is important because the large boundary roughness elements force the fluid mixture to flow around boulders, trees and other channel obstacles, thus creating additional losses which enhance the C_1 term in Eq. 4. In this manner, energy is first transformed into turbulence and

then dissipated in viscous heat. These energy losses S_i and S_b are treated separately for the purpose of this discussion. The shear stress can be written, in a first approximation, as a function of the mean flow velocity u, depth d and resistance coefficient c_b

$$\tau_b = \rho_m g\, d\, S_b = c_b\, \rho_m\, \bar{u}^2 \tag{12}$$

This equation leads to a Chézy type of relationship which can be transformed into the more widely used Manning's type of equation

$$S_b = \left(\frac{n\, \bar{u}}{1.49\, d^{2/3}} \right)^2 \tag{13}$$

in which the equivalent Manning n value is derived from Eq. 12

$$n = 1.49 \sqrt{\frac{c_b}{g}}\, d^{1/6} \tag{14}$$

The friction slope given by Eq. 13 is a function of the flow depth and velocity. These two variables were computed by assuming that the internal stress, obtained after integrating Eq. 11, obeys a Bingham plastic model such that

$$\tau_i = \gamma_m\, (S_o - S_b)(d-y) = k + \mu_m \frac{du}{dy} \tag{15}$$

The mean velocity is then obtained by integration along the flow depth d

$$\bar{u} = \frac{1}{d} \int_o^d \int_o^y \frac{du}{dy}\, dy\, dy = \frac{\gamma_m (S_o - S_b) d^2}{3\mu_m} - \frac{kd}{2\mu_m} \tag{16}$$

After substitution of Eq. 13 into Eq. 16, and satisfying the continuity relationship $q = \bar{u}d$, these equations were solved by iteration to obtain $\bar{u}$ and d. The substitution into Eq. 13 then gives the boundary friction slope S_b.

The magnitude of the internal stresses as determined from Eq. 11 can be compared to the magnitude of the boundary roughness stresses expressed as a percentage of the bed slope using the following ratio

$$R_s = \frac{S_i}{S_o} = \frac{S_o - S_b}{S_o} \tag{17}$$

Table 3 represents the mean values of $\bar{R}_s$ as a function of concentration for 16 different basins analyzed in the vicinity of Glenwood Springs, Colorado, for three different return period floods (10 year, 25 year and 100 year). This table shows a very rapid increase of $\bar{R}_s$ at concentrations larger than 0.44 and similar trends are observed for the three flood events. These conclusive results indicate that for concentrations smaller than 0.42 the energy losses are mainly the result of channel roughness. For larger concentrations, however, the internal losses are increasingly important in the role of energy dissipation.

TABLE 3. RATIO OF INTERNAL TO BOUNDARY ROUGHNESS STRESSES R_s

C_v	Flood Event Return Period in Years		
	100	25	10
.36	2.2*	2.3	2.7
.38	3.3	4.0	4.9
.40	5.3	6.6	8.2
.42	9.5	11.9	14.6
.44	17.0	20.8	24.9
.46	30.0	36.4	42.3
.49	48.2	57.0	63.5
.51	71.5	78.1	82.7
.54	88.3	92.3	94.2

*R_s values in percent, Standard Error ranged from 0.3 to 3.9%

This simplified analysis reveals the importance of the physical properties of the fluid matrix and prescribes the need for more fundamental research on mud flows. Ignoring either the viscous or friction slope term in the analysis would result in the overprediction of the velocity of the flow. There are inaccuracies in this analysis. First, the Manning's equation is only applicable for fully developed rough turbulent flows. Second, the Bingham model is not applicable for high velocity, rough turbulent flow. Mud flows and debris are inherently unsteady, nonuniform flows. On steep slopes, using the kinematic wave analogy, equation (15) should be solved using the three terms of Eq. 4 and this requires the use of C_1. More experimental analysis is required for the evaluation of C_1 and its variability with concentration, sediment size and boundary roughness. A stainless steel viscometer has been designed for this purpose.

CONCLUSION

The devastating effects of hyperconcentrated sediment flows in the past demonstrate an urgent need for a predictive methodology to define the hazard levels and to aid in the design of adequate mitigations measures and structures. Such a methodology would rely on an accurate knowledge of the physical properties of the water-sediment mixture. Research efforts must be focused on fundamental investigations involving both theoretical and experimental analysis.

This paper emphasizes the physical properties of hyperconcentrated sediment flows. Flow descriptions have been classified as a function of the concentration of sediments. Various experimental, theoretical and field data show that the maximum concentration by volume for mud flows is unlikely to be in excess of 0.50.

Basic fluid mechanics principles are recommended to describe the broad continuum of hyperconcentrated flows. A simple quadratic model (Eq. 4) is postulated, in which each term represents a well-defined physical property of the fluid. The last term of this equation

represents the inertial losses and requires further investigation. Physical meaning of this term, however, has been demonstrated to be associated with turbulent and dispersive stresses in the fluid matrix and has been verified experimentally. Empirical relationships between yield stress, viscosity and the concentration by volume were obtained from laboratory analysis of mud flow samples.

A simplified methodology, applied on 16 small steep watersheds near Glenwood Springs, Colorado, showed that at low concentrations by volume (C_v < 40%), the energy losses are controlled by boundary roughness. For larger concentration, the internal energy losses rapidly become dominant. For the mathematical routing of open channel flows both a macro- and microscopic fluids approach must be applied. The macroscopic approach is needed for energy dissipation attribued to channel roughness. The real energy losses occur in the form of heat dissipation from the viscous interaction between water and sediment particles. The viscous energy dissipation is enhanced by turbulence which, in turn, is promoted by boundary roughness.

Continuing research at CSU on hyperconcentrated flows will focus on the complex physical processes of hyperconcentrated sediment flows preparing the foundation for the eventual mathematical routing of these flows in open channels.

ACKNOWLEDGEMENTS

The work supporting this paper was sponsored, in part, by the National Park Service, Water Resources Field Support Laboratory located on the campus of Colorado State University in Fort Collins, Colorado. Dr. Ray Herrmann, Director of the Laboratory, is acknowledged in appreciation for that support. The Natural Sciences and Engineering Research Council of Canada contributed to this paper through fellowship support to the second author.

LIST OF SYMBOLS

a_i coefficient of the dispersive stress equation

B Bingham number

c_b resistance coefficient for boundary roughness

C_o maximum possible concentration by volume

C_1 coefficient of the inertial stress term

C_f concentration of fines

C_v concentration by volume

C_w concentration by weight

d flow depth

D_s representative grain diameter

g gravitational acceleration

G	specific gravity of sediments
k	yield stress
p	internal pressure
r^2	coefficient of determination
R	ratio of inertial stress to viscous stress
R_s	ratio of internal stress to boundary roughness stress
S_b	boundary energy gradient
S_i	internal energy gradient
S_o	bed slope
t	time
u	velocity
$\bar{u}$	mean velocity
x	longitudinal coordinate (positive downstream)
y	upward distance above the channel bed
κ	von Karman constant
θ	angle of the channel with the horizontal
λ	linear concentration
μ_m	dynamic viscosity of the mixture
ρ	density of clear water
ρ_m	density of the fluid mixture
τ	shear stress
τ_b	shear stress from the boundary roughness
τ_D	dispersive stress
τ_i	internal stress
τ_R	turbulence stress

REFERENCES

Bagnold, R. A. 1954. Experiments on a gravity-free dispersion of large solid spheres in a Newtonian fluid under shear. Proceedings Royal Society of London, Series A, V. 225, pp. 49-63.

Bagnold, R. A. 1956. Flow of cohension grains in fluids. Philosophical Transactions of the Royal Society of London, Series A, V. 249, pp. 234-297.

Curry, R. R. 1966. Observations of alpine mudflows in the Ten Mile Range, central Colorado. Geol. Soc. Am. Bull., V. 77, pp. 771-776.

Das, B. M. 1983. Advanced Soil Mechanics, McGraw-Hill, New York, 511 p.

Graf, W. H. 1971. Hydraulics of Sediment Transport, McGraw-Hill, New York, 513 p.

Johnson, A. M. 1970. Physical Processes in Geology. San Francisco. Freeman, Cooper & Co., Chapters 12, 13, 14, 15, pp. 432-571.

Lamb, T. W. and C. V. Whitman. 1969. Soil Mechanics, John Wiley and Sons, Inc., New York, p. 31.

National Research Council. 1982. "Selecting a Methodology for Delineating Mudslide Hazard Areas for the National Flood Insurance Program," Committee on Methodologies for Predicting Mudflow Areas, National Academy Press, Washington, D.C.

Nunziato, J. W. and S. L. Passman. 1980. Gravitational flows of granular materials with incompressible grains. Journal of Rheology, Vol. 24, pp. 395-420.

Passman, S. L., J. W. Nunziato, P. B. Bailey, and J. P. Thomas, Jr. 1980. Shearing flows of granular materials. Journal of the Engineering Mechanics Div., ASCE, V. 106, pp. 773-783.

Pierson, T. C. 1980. Erosion and deposition by debris flows at Mt. Thomas, North Canterbury, New Zealand, Earth Surface Processes, V. 5, pp. 227-247.

Pierson, T. C. 1981. Dominant particle support mechanisms in debris flows at Mt. Thomas, New Zealand, and implication for flow mobility. Sedimentology, Vol. 28, pp. 49-60.

Savage, S. B. 1979. Gravity flow of cohesionless granular materials in chutes and channels. Journal of Fluid Mechanics, Vol. 92, Part 1, pp. 53-96.

Sharp, R. P. and Nobles, L. H. 1953. Mudflow of 1941 at Wrightwood, Southern California. Geol. Soc. Am. Bull., V. 64, pp. 547-460.

Vanoni, V. A. 1941. Some experiments on the transportation of suspended load. Transactions of American Geophysical Union, Vol. 22, pp. 608-620.

Laboratory Analysis of Mudflow Properties

By Jim S. O'Brien[1] and Pierre Y. Julien,[2] Member, ASCE

Abstract: A rotational viscometer has been designed for laboratory measurements of the rheological properties of natural mudflow deposits in Colorado. The mudflow matrices comprised of silt and clay particles are sheared under temperature-controlled conditions at volumetric sediment concentrations ranging from 0.10–0.45. This study stresses the importance of conducting rheological measurements at low rates of shear because: 1) Those are the conditions found in natural channels; and 2) they avoid the slippage problems observed at large sediment concentrations. At low rates of shear, the Bingham model is fitted to the measured rheograms, and both the viscosity and yield stress increase exponentially with the sediment concentration of the fluid matrix. Both the yield stress and the viscosity increase by three orders of magnitude as the volumetric concentration of sediments in the fluid matrix changes from 0.10 to 0.40. The addition of sand particles does not significantly alter the rheological properties of the matrix unless the volumetric concentration of sands exceeds 0.20.

Introduction

In the United States, losses from landslides, subsidence, and other ground failures exceed the losses from all other natural hazards combined. Indeed, the Committee on Ground Failure Hazards (NRC 1982) reported that landsliding in the U.S. causes $1–$2 billion in economic losses and 25–50 deaths each year. Individual landslides can be widely scattered in space and time, but a substantial portion of the annual landslide loss is associated with a few major catastrophic events such as the mudflows in the San Francisco Bay area and along the Wasatch Front in Utah. Semiarid alpine mudflows and debris flows are triggered by the slumping or slipping of unconsolidated material on steep slopes (Higgins et al. 1983). Such movement usually occurs following soil saturation due to fairly intense and short-duration rainfall events, or as a consequence of rapid snowmelt. Mud and debris flows originate on steep slopes or landslide areas. The zone of sediment transport typically has a steep channel system, at the end of which a sudden break in slope on the valley floor induces deposition to form a conical debris fan.

Several investigations have promulgated various classifications of mudflows and hyperconcentrated flows [e.g., Blackwelder (1928), Sharp and Nobles (1953), Johnson (1965), and O'Brien and Julien (1985)]. An attempt to delineate hyperconcentrated flows and mass wasting processes was initiated by the National Research Council Committee on Methodologies for Predicting Mud Flows (NRC 1982). The committee proposed four main categories: water floods, mud floods, mudflows, and landslides. The

[1]Res. Assoc., Dept. of Civ. Engrg., Colorado State Univ., Ft. Collins, CO 80523.
[2]Asst. Prof., Dept. of Civ. Engrg., Colorado State Univ., Ft. Collins, CO 80523.

Note. Discussion open until January 1, 1989. To extend the closing date one month, a written request must be filed with the ASCE Manager of Journals. The manuscript for this paper was submitted for review and possible publication on May 6, 1987. This paper is part of the *Journal of Hydraulic Engineering*, Vol. 114, No. 8, August, 1988. ©ASCE, ISSN 0733-9420/88/0008-0877/$1.00 + $.15 per page. Paper No. 22680.

297

sediment-water mixtures in water floods and mud floods are both unable to resist shear stress without motion. The large sediment concentrations in mudflows invalidate the use of existing sediment transport equations such as Einstein's and Meyer-Peter and Muller's because the higher viscosity and shear strength of the mixture reduces the fall velocity of sediment particles. Mudflows were defined as a division of landslides where: "the transporting mechanism is that of a flow having sufficient viscosity to support large boulders within a matrix of smaller sized particles." The divisions among hyperconcentrated flows, mudflows, and debris flows are still subject to disagreement, and a comprehensive classification of hyperconcentrated flows is not yet available (Bradley and McCutcheon 1985).

The objective of this study is to provide a better description of the physical properties of mudflow material. Laboratory measurements of the rheological properties of natural mudflow deposits were conducted on several samples from the central Colorado Rocky Mountains. The mudflow matrix, consisting only of silt and clay particles at volumetric sediment concentrations $0.10 < C_v < 0.45$, was sheared in a rotational viscometer to measure the viscosity and yield stress. The effect of adding sand particles to the fluid matrix was then documented.

Rheological Models

The rheology of fluids and water-sediment mixtures can be analyzed from measurements of shear stress at various rates of angular deformation, du/dy. With a fluid having low sediment concentrations, this stress-strain relationship is linear with intercept at the origin. This water-sediment mixture is called a Newtonian fluid. The viscosity of the mixture, defined as the slope of the stress-strain relationship, increases with sediment concentration (Thomas 1963; Happel and Brenner 1965). At higher concentrations, the fluid matrix can resist shear stress without motion, owing to the shear strength provided by cohesion between sediment particles. A threshold value of shear stress called yield stress τ_y must be exceeded prior to fluid motion. A mixture with a finite yield-stress value is a non-Newtonian fluid. According to the experiments of Fei (1981), the critical volumetric concentration at which the water-sediment mixture turns into a non-Newtonian fluid is closely related to the content of fine sediments (0.01 mm). In this study, the fluid matrix refers to a suspension of fine sediments with sizes smaller than 0.072 mm (silt and clay particles). A mixture can behave as a non-Newtonian fluid at a low concentration, provided the proportion of fine particles is high.

Rheological models for non-Newtonian fluids include the Bingham plastic model and the yield-pseudoplastic model. Bingham fluids exhibit a linear stress-strain relationship at shear stresses in excess of the yield stress. The equation describing Bingham fluids is

$$\tau = \tau_y + \eta \frac{du}{dy} \quad \ldots\ldots\ldots\

shows convexity to the shear stress, and this behavior is referred to as yield-pseudoplastic. There is no theoretically based equation for yield-pseudoplastics, but any empirical equation such as the power-law equation can be used:

$$\tau = \tau_y + a\left(\frac{du}{dy}\right)^n \quad \ldots\ldots\ldots\

moderate shear rates. Isothermal conditions and an absence of secondary flows are required.

After considering existing commercial viscometers, a rotational viscometer was designed especially (O'Brien 1986) to investigate the rheological properties of natural mudflow material. The design of the concentric cylindrical viscometer was constrained by low shear rates, sediment size within the mixture, and stability criteria for laminar flow without secondary flow. The flow annulus is sized by the criteria specified by Van Wazer et al. (1963), and the gap size is at least ten times larger than the coarsest particle size in the fluid matrix. The stability criteria suggested in Schlichting (1968) must be satisfied to prevent the formation of Taylor vortices in the annulus. The shear stress contribution at the end of the rotating cylinder is found to be negligible. Temperature is controlled by inserting the whole apparatus into a water bath. The torque exerted on the viscometer bob is measured with strain gages calibrated to provide a torque versus voltage relationship covering the full range of torque measurements encountered during the test program. The resulting accuracy of the device was checked using glycerol solutions with viscosities ranging from 0.1–10 poises.

Laboratory Analysis of Mudflow Samples

A variety of samples were collected from natural mudflows deposits in the Colorado Rocky Mountains near the towns of Aspen and Glenwood Springs. The properties of the mudflow samples in terms of sediment size distribution and content of clay are given in Table 1. No detailed information on clay mineralogy is available; however, the samples with large clay content were tested to determine the liquid limit and the plasticity index. The plasticity chart indicates inorganic clays with low to medium plasticity. A fluid matrix comprising fine sediments (only silts and clays) was prepared for testing in the new viscometer; 10–15 measurements of shear stress versus shear rates were made for each concentration, as shown in Fig. 1. The volumetric concentration was varied by adding water after each test. In some tests with very large sediment concentrations, slippage was observed around the annulus at rates of shear as low as

TABLE 1. Properties of Mudflow Matrices (Silts and Clays Only)

Sample (1)	Sediment Size Distribution: Clay (%) (2)	D_{16} (mm) (3)	$D_{<0}$ (mm) (4)	D_{84} (mm) (5)	Liquid limit (6)	Plasticity index (7)
Glenwood original	4.8	0.010	0.034	0.062	—	—
Glenwood sample 1	6.8	0.009	0.023	0.050	—	—
Glenwood sample 2	3.0	0.016	0.035	0.061	—	—
Glenwood sample 3	4.8	0.011	0.025	0.053	—	—
Glenwood sample 4	7.6	0.001	0.018	0.032	—	—
Aspen pit 1	31.3	0.001	0.011	0.032	0.32	0.11
Aspen natural soil	27.0	0.001[a]	0.012	0.028	0.25	0.06
Aspen mine fill	27.8	0.001[a]	0.013	0.030	0.24	0.06
Aspen natural soil source	31.6	0.001[a]	0.016	0.039	—	—
Aspen mine fill source	25.2	0.001[a]	0.018	0.061	—	—

[a]These values were extrapolated from sieve analysis graphs.

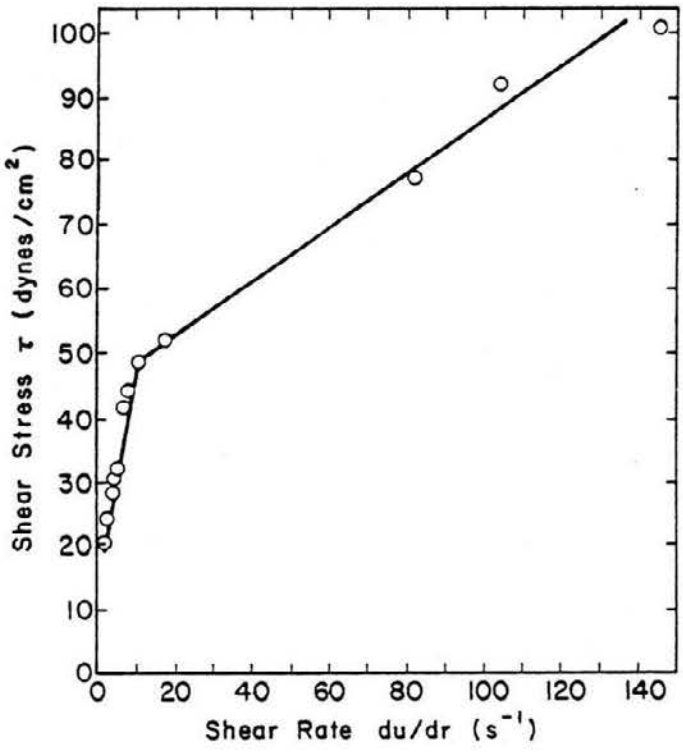

FIG. 1. Aspen Natural Soil Rheogram (C_v = 34.2%; Silts and Clays)

$10\ s^{-1}$, as shown in Fig. 1. For this reason, the evaluation of viscosity and yield stress from the Bingham plastic model was based on the measurements taken at lower shear rates. Of course, when compared to measurements at high rates of shear, this analysis gives slightly lower values of yield stress and larger viscosity measurements.

In hyperconcentrated flows, the Bingham plastic model (Eq. 1) has been used by many researchers, e.g., Cao et al. (1983), Hou and Yang (1983), Higgins et al. (1983), Street (1958), Thomas (1963), Qian et al. (1980), Govier and Aziz (1982), and Dai et al. (1980). It has been generally accepted that both the viscosity η and the yield stress τ_y increase exponentially with the volumetric concentration of fine sediments C_v:

$$\eta = \alpha_1 e^{\beta_1 C_v} \quad \ldots\ldots (3)$$

and

$$\tau_y = \alpha_2 e^{\beta_2 C_v} \quad \ldots\ldots (4)$$

The values of the four empirical coefficients α_1, α_2, β_1, and β_2 obtained by regression analysis for each mudflow sample are presented in Table 2; the results are in reasonable agreement with those found in the literature. Particularly, the experimental values of the yield stress fall within the range of values defined by Fei (1981). The dispersion of the points at a given concentration certainly calls for more fundamental research to examine possible effects of thixotropy and clay mineralogy. Nevertheless, the open points (Glenwood) indicating lower percentages of clay in Fig. 2 have lower values of yield stress when compared with the samples with larger clay contents (Aspen). This trend is not quite apparent when

TABLE 2. Yield Stress and Viscosity of Mudflow Matrices

Source (1)	$\tau_y = \alpha_2 e^{\beta_2 C_v}$		$\eta = \alpha_1 e^{\beta_1 C_v}$	
	α_2 (dynes/cm^2) (2)	β_2 (3)	α_1 (poises) (4)	β_1 (5)
(*a*) Relationships Found in Field				
Aspen pit 1	1.81×10^{-1}	25.7	3.60×10^{-2}	22.1
Aspen pit 4	2.72	10.4	5.38×10^{-2}	14.5
Aspen natural soil	1.52×10^{-1}	18.7	1.36×10^{-3}	28.4
Aspen mine fill	4.73×10^{-2}	21.1	1.28×10^{-1}	12.0
Aspen natural soil source	3.83×10^{-2}	19.6	4.95×10^{-4}	27.1
Aspen mine fill source	2.91×10^{-1}	14.3	2.01×10^{-4}	33.1
Glenwood 1	3.45×10^{-2}	20.1	2.83×10^{-3}	23.0
Glenwood 2	7.65×10^{-2}	16.9	6.48×10^{-1}	6.2
Glenwood 3	7.07×10^{-4}	29.8	6.32×10^{-3}	19.9
Glenwood 4	1.72×10^{-3}	29.5	6.02×10^{-4}	33.1
(*b*) Relationships Found in Literature				
Iida (1938)	—	—	3.73×10^{-5}	36.6
Dai et al. (1980)	2.60	17.48	7.5×10^{-3}	14.39
Kang and Zhang (1980)	1.75	7.82	4.05×10^{-2}	8.29
Qian et al. (1980)	1.36×10^{-3}	21.2	—	—
	$\sim 5.0 \times 10^{-2}$	~15.48	—	—
Chien and Ma (1958)	5.88×10^{-2}	19.1~32.7	—	—
Fei (1981)	1.66×10^{-1}	25.6	—	—
	$\sim 4.7 \times 10^{-3}$	~22.2	—	—

viscosity measurements are considered as shown in Fig. 3. It is clearly shown, however, that both the yield stress and viscosity increase by three orders of magnitude as the volumetric concentration increases from 0.10–0.40.

Since the laboratory analysis of the mudflow deposits dealt primarily with the finer fractions of the mudflow material, additional tests were undertaken (O'Brien and Julien 1986) to determine the influence of adding concentrations of sands to be bentonite clay suspensions. At large concentrations, slippage between particle layers occurred at shear rates exceeding 5 s^{-1}, as shown in Fig. 4. Thus, roughness elements consisting of sand particles ranging from 1–1.6 mm in size were glued to the stainless steel bob cylinder of the viscometer. These elements did not alter the viscosity and yield stress measurements at low rates of shear but prevented slippage at higher shear rates. The results shown in Fig. 5 reveal that with increasing sand concentration, the viscosity remains comparable to that given from the clay content alone until the sand concentration exceeds about 20% by volume. Note that with bentonite clay content of 5–6%, the dynamic viscosity shown in Fig. 5 is two orders of magnitude larger than the viscosity of clear water (η_{water} = 0.01 poise). Further experiments were made with natural mudflow deposits at a larger concentration (shown as dark points on Fig. 5). Similar conclusions were

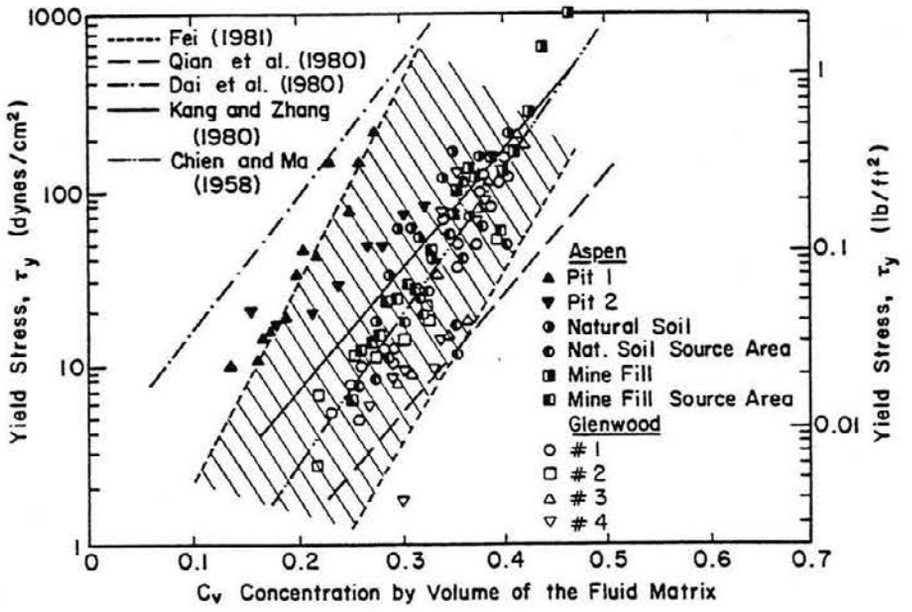

FIG. 2. Yield Stress of Mudflow Samples versus Volumetric Concentration

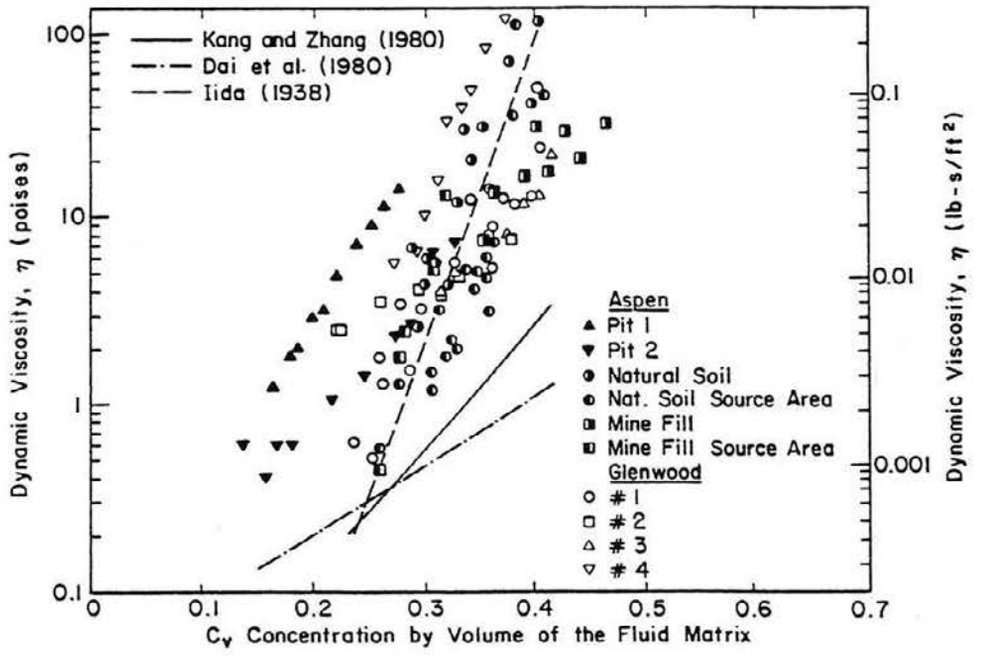

FIG. 3. Dynamic Viscosity of Mudflow Samples versus Volumetric Concentration

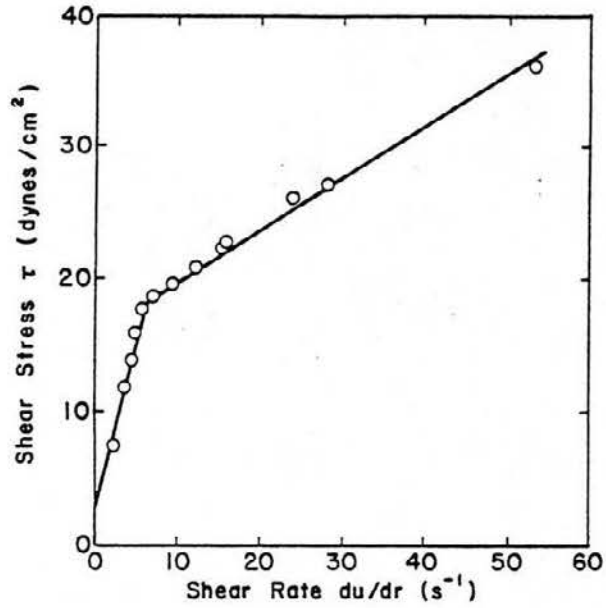

FIG. 4. Rheogram for Aspen Natural Soil (C_v = 30% Silts and Clays) with Added Sand Concentration C_v = 14%; C_{total} = 44%)

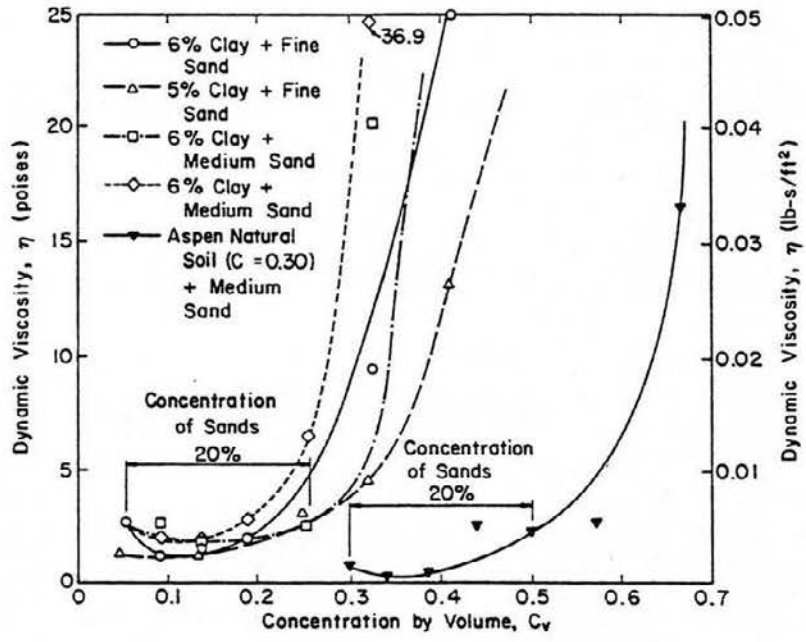

FIG. 5. Dynamic Viscosity of Mixtures with Added Sand Particles versus Total Volumetric Concentration

obtained, which indicates that large concentrations of sand particles are required in order to significantly alter the physical properties of the mudflow matrix. The viscosity of the fluid matrix increases very rapidly at volumetric concentrations of sand in excess of 20%. Further investigation is needed with coarser grained slurries.

Summary and Conclusion

Two physical properties of the fluid matrix of natural mudflow deposits in the central Colorado Rocky Mountains have been investigated at concentrations ranging from 10–45% by volume. The fluid matrix comprised of particles finer than 0.07 mm (silts and clays) was sheared in a special viscometer designed for the analysis of mudflow samples under temperature-controlled conditions. The viscometer gap size was determined to provide laboratory measurements of the fluid matrix properties under laminar flow conditions at low rates of shear without secondary flows. This study stresses the importance of conducting measurements at low rates of shear because: (1) those are the conditions found in natural channels; and (2) they avoid the slippage problems observed at large sediment concentrations. The Bingham rheological model was applied to the measured rheograms at low rates of shear. Both the yield stress and viscosity are shown in Figs. 2 and 3 to increase by three orders of magnitude as the volumetric concentration of sediments in the fluid matrix changes from 10–40%. The effect of adding sand particles to either a bentonite clay suspension or natural mudflow matrix of silts and clays is negligible, provided that the sand concentration remains less than 20% by volume. The viscosity of mudflow material with volumetric sand concentrations less than 20% simply corresponds to the viscosity of the silt-clay mixture. The viscosity of the mixture, however, increases rapidly with volumetric sand concentrations beyond 20%.

Acknowledgments

We are grateful to Y. Lan, Ph.D. candidate at CSU, for his comprehensive review of the Chinese literature.

Appendix I. References

Blackwelder, E. (1928). "Mudflow as a geologic agent in semiarid mountains." *Geologic Soc. Am., Bulletin* 39(1), 465–484.

Bradley, J. B., and McCutcheon, S. C. (1985). "The effects of high sediment concentration on transport processes and flow phenomena." *Proc., Conf. on Erosion, Debris Flow, and Disaster Prevention*, Tsukuba, Japan, 219–225.

Cao, R., et al. (1983). "The Law of hydraulic resistance in density current with hyperconcentration." *Proc., Second Int. Symposium on River Sedimentation*, 65–79.

Chien, N., and Ma, H. (1958). "Properties of slurry flow." *J. Sediment Res.*, 3(3), Beijing, China (in Chinese).

Dai, J., et al. (1980). "An experimental study of slurry transport in pipes." *Proc., Int. Symposium on River Sedimentation*, 195–204 (in Chinese).

Fei, X. J. (1981). "Bingham yield stress of sediment water mixtures with hyperconcentration." *J. Sediment Res.*, 3, Beijing, China, 19–28 (in Chinese).

Govier, G. W., and Aziz, K. (1982). *The flow of complex mixtures in pipes*. Krieger Publishing Co., Melbourne, Fla.

Happel, J., and Brenner, H. (1965). *Low Reynolds number hydrodynamics*. Prentice-Hall, Englewood Cliffs, N.J.
Herschel, W. H., and Bulkley, R. (1926). "Measurement of consistency as applied to rubber-benzene solutions." *A.S.T.M. Proc.*, 26(621).
Higgins, J. D., et al. (1983). "The mechanics of mud flow." *State of Washington Water Research Center Report No. 51*, Pullman, Wash.
Hou, H., and Yang, X. (1983). "Effect of fine sediment on the drag reduction in muddy flow." *Proc., Second Int. Symposium on River Sedimentation*, 67–80 (in Chinese).
Iida, K. (1938). "The mud flow that occurred near the explosion crater of Mt. Bandai on May 9 and 15, 1938," and "Some physical properties of volcanic mud." *Tokyo Imperial University Earthquake Research Institute Bulletin*, 16, 658–681.
Johnson, A. M. (1965). "A model for debris flow," thesis presented to Pennsylvania State University, at University Park, Pa., in partial fulfillment of the requirements for the degree of Doctor of Philosophy.
Johnson, A. M. (1970). *Physical processes in geology*. Freeman, Cooper, and Co., San Francisco, Calif.
Kang, Z., and Zhang, S. (1980). "A preliminary analysis of the characteristics of debris flow." *Proc., Int. Symposium on River Sedimentation*, Beijing, China, 213–220 (in Chinese).
Mills, S. V. (1983). "An experimental study of the rheology of mud flows," thesis presented to Washington State University, at Pullman, Wash., in partial fulfillment of the requirements for the degree of Master of Science.
National Research Council (1982). "Selecting a methodology for delineating mudslide hazard areas for the National Flood Insurance Program." National Academy of Sciences report by the advisory Board on the Built Environment, Washington, D.C.
O'Brien, J. S. (1986). "Physical processes, rheology and modeling of mudflow," thesis presented to the Civil Engineering Department, Colorado State University, at Fort Collins, Colo., in partial fulfillment of the requirements for the degree of Doctor of Philosophy.
O'Brien, J. S., and Julien, P. Y. (1985). "Physical properties and mechanics of hyperconcentrated sediment flows." *Proc., ASCE Specialty Conf. on Delineations of Landslide, Flashflood, and Debris Flow Hazards in Utah*, D. S. Bowles, ed., Logan, Utah, 260–279.
O'Brien, J. S., and Julien, P. Y. (1986). "Rheology of non-Newtonian fine sediment mixtures." *Proc., ASCE Specialty Conference on Aerodynamics, Fluid Mechanics and Hydraulics*, Minneapolis, Minn., 989–996.
du Plessis, M. P., and Ansley, R. W. (1967). "Settling parameter in solids pipelining." *J. Pipeline Engrg. Div.*, ASCE, 93(PL2), 1–17.
Qian, N., and Wan, Z. (1986). *A critical review of the research on the hyperconcentrated flow in China*. International Research and Training Center on Erosion and Sedimentation, Beijing, China.
Qian, Y., et al. (1980). "Basic characteristics of flow with hyperconcentration of sediment." *Proc., Int. Symposium on River Sedimentation*, Beijing, China, Vol. 1, 175–184 (in Chinese).
Schlichting, H. (1968). *Boundary-layer theory*. 6th Ed., McGraw-Hill, New York, N.Y.
Sharp, R. P., and Nobles, L. H. (1953). "Mudflow of 1941 at Wrightwood, Southern California." *Geologic Soc. Am. Bull.*, 64(1), 547–560.
Street, N. (1958). "Viscosity of clay suspensions." *World Oil*, 147(7), 151–156.
Thomas, D. G. (1963). "Non-Newtonian suspensions. Part I: physical properties and laminar transport characteristics." *Ind. Eng. Chem.*, 55(11), 18–29.
Valentik, L., and Whitmore, R. L. (1965). "The terminal velocity of spheres in Bingham plastics." *British J. Appl. Phys.*, 16, 1197–1203.
Van Wazer, J. R., et al. (1963). *Viscosity and flow measurement*. John Wiley and Sons, New York, N.Y.
Yano, K., and Daido, A. (1965). "Fundamental study on mudflow." *Annuals*,

Disaster Prevention Research Institute, Kyoto University, Kyoto, Japan, 7, 340–347.

Appendix II. Notation

The following symbols are used in this paper:

a, n = empirical parameters for pseudo-plastic fluids;
C_v = volumetric concentration of fluid matrix;
D = sediment size;
du/dy = velocity gradient;
α_1, α_2, β_1, β_2 = coefficients;
η = dynamic viscosity of fluid matrix;
τ = total shear stress; and
τ_y = yield stress.

RHEOLOGY OF HYPERCONCENTRATIONS

By Pierre Y. Julien[1] and Yongqiang Lan[2]

ABSTRACT: A physically based quadratic rheological model for hyperconcentrated flows is tested with experimental data sets. The model includes components describing: (1) Cohesion between particles; (2) viscous friction between fluid and sediment particles; (3) impact of particles; and (4) turbulence. The resulting quadratic formulation of the shear stress is shown to be in excellent agreement with the experimental data sets of Bagnold, Savage and McKeown, and Govier et al. When the quadratic model is written in a linearized dimensionless form, the ratio D_v^* of dispersive to viscous stresses is shown to play a dominant role in the rheology of hyperconcentrations. The quadratic model is best suited when ($30 < D_v^* < 400$). At low values of D_v^*, the quadratic model reduces to the simple Bingham plastic model ($D_v^* < 30$), and at large values of D_v^*, a turbulent-dispersive model is indicated ($D_v^* > 400$).

INTRODUCTION

The rheology of highly concentrated sediment mixtures has been studied by various researchers including Bagnold (1954), Jeffrey and Acrivos (1976), Takahashi (1980), and Savage and McKeown (1983). Under high rates of shear, Bagnold proposed that the dominant shear stress can be attributed to interparticle friction and collisions. In this grain inertia region, both the normal and shear stresses depend on the second power of the shear rate. These results contrast with observations under low rates of shear (O'Brien and Julien 1988) because in the viscous region, the shear stress in excess of the yield stress increases linearly with the shear rate.

This study describes the rheological properties of hyperconcentrated sediment mixtures at shear rates ranging from the viscous region to the inertial region. It is proposed to test the quadratic rheological model suggested by O'Brien and Julien (1985) with existing data sets from Govier et al. (1957), Savage and McKeown (1983), and Bagnold (1954). This analysis points at the similarities and differences between these three data sets, which give quite different results when analyzed separately. As a second objective, the relative magnitude of the terms in the quadratic model is examined to define the conditions under which simplified rheological formulations can be applied.

RHEOLOGICAL MODEL FORMULATION

The shear stress encountered in fluids with large concentrations of sediments should include components to describe: (1) Cohesion between particles; (2) viscous interaction between sediment particles and the surrounding fluid; (3) impact of sediment particles; and (4) turbulence. After considering

[1]Assoc. Prof. of Civ. Engrg., Engrg. Res. Ctr., Colorado State Univ., Fort Collins, CO 80523.

[2]Res. Asst., Dept. of Civ. Engrg., Colorado State Univ., Fort Collins, CO.

Note. Discussion open until August 1, 1991. To extend the closing date one month, a written request must be filed with the ASCE Manager of Journals. The manuscript for this paper was submitted for review and possible publication on November 20, 1987. This paper is part of the ***Journal of Hydraulic Engineering***, Vol. 117, No. 3, March, 1991. ©ASCE, ISSN 0733-9429/91/0003-0346/$1.00 + $.15 per page. Paper No. 25612.

that both turbulence and inertial impact of particles increase with the second power of the shear rate, O'Brien and Julien (1985) proposed the following quadratic rheological model:

$$\tau = \tau_y + \eta \frac{du}{dy} + \zeta\left(\frac{du}{dy}\right)^2 \quad \ldots\ldots (1)$$

where τ = the shear stress; τ_y = the yield shear stress, η = the dynamic viscosity, ζ = the turbulent-dispersive parameter; and du/dy = the velocity gradient normal to the flow direction. The physical reasoning behind this quadratic formulation (Eq. 1) is briefly summarized. The first term, τ_y, describes the yield stress due to cohesion between fine sediment particles. The yield strength is assumed to be a property of the material that does not depend on the rate of deformation. The second term describes the viscous stress of the fluid interacting with sediment particles. The third term referred to as the turbulent-dispersive stress combines the effects of turbulence and the effects of dispersive stress induced by the collisions between sediment particles. The conventional expression for the turbulent stress in sediment-laden flows merges with Bagnold's dispersive stress relationship because both stresses are proportional to the second power of the rate of shear. The purpose of combining these two terms stems from the concept that at large concentrations of coarse particles, the dispersive stress will be dominant, whereas at large concentrations of fine particles, the yield strength and the viscous stress will overcome the turbulent stress.

The combined turbulent-dispersive parameter ζ can be written as:

$$\zeta = \rho_m l_m^2 + a_1 \rho_s \lambda^2 d_s^2 \quad \ldots\ldots (2)$$

where ρ_m and l_m = the density and mixing length of the mixture, respectively; d_s = the diameter of sediment particles; a_1 = the empirical constant defined by Bagnold; and ρ_s = the density of sediment particles. The linear concentration λ defined by Bagnold depends on the volumetric sediment concentration C_v and the maximum volumetric sediment concentration C^* ($C^* \sim 0.615$):

$$\lambda = \left[\left(\frac{C^*}{C_v}\right)^{1/3} - 1\right]^{-1} \quad \ldots\ldots (3)$$

The density ρ_m of the mixture in Eq. 2 is calculated as follows from the volumetric sediment concentration C_v and the mass densities of the fluid, ρ, and of the solid particles, ρ_s:

$$\rho_m = \rho(1 - C_v) + \rho_s C_v \quad \ldots\ldots (4)$$

It can be seen from Eq. 2 that both sediment concentration and particle size play an important role in determining the magnitude of the turbulent-dispersive parameter ζ.

Experimental Test of the Quadratic Model

Three data sets from Govier et al. (1957), Savage and McKeown (1983), and Bagnold (1954) are examined to test the validity of the rheological model proposed in Eq. 1.

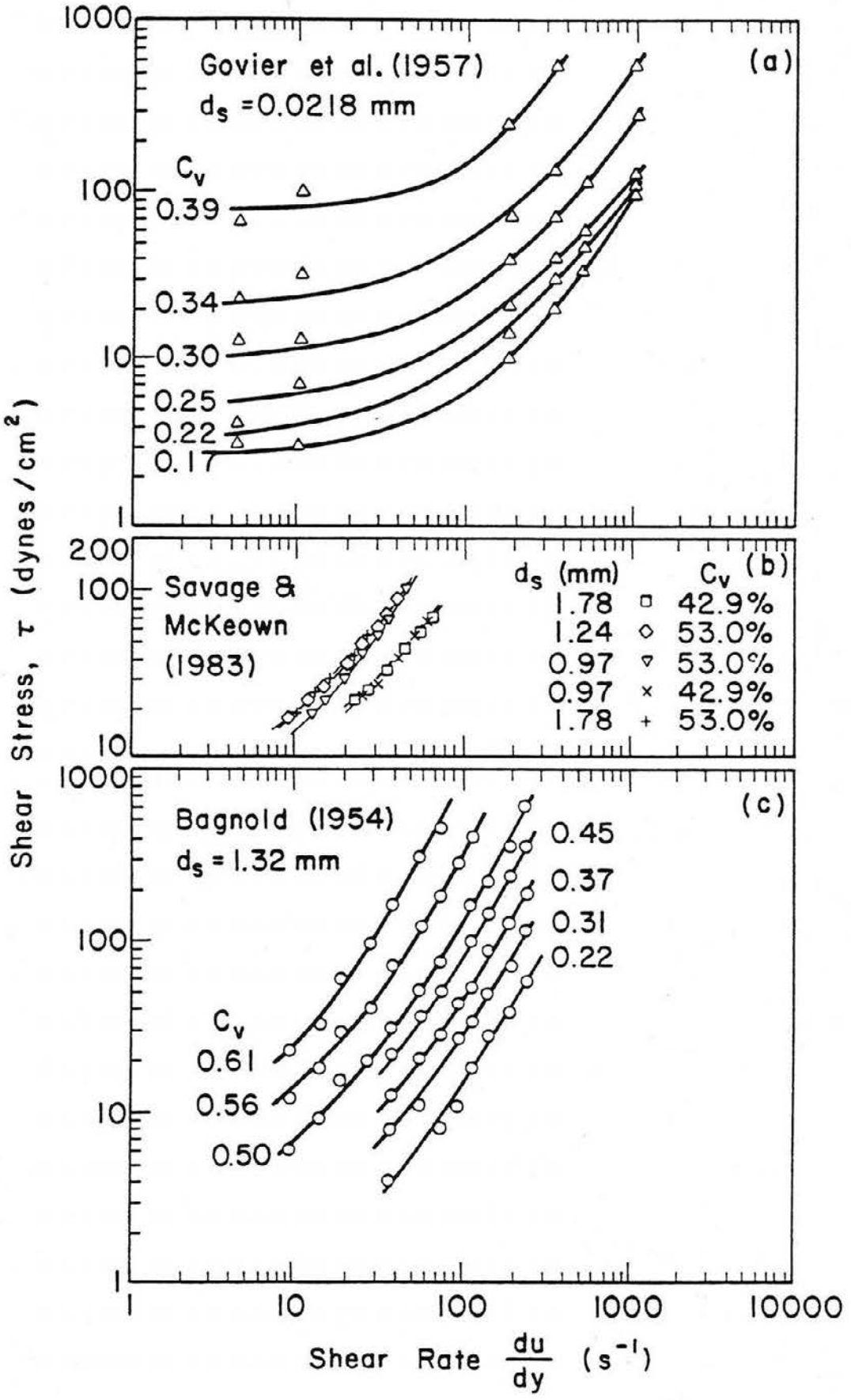

FIG. 1. Rheograms for Three Data Sets: Govier et al. (1957); Savage and McKeown (1983); and Bagnold (1954)

310

TABLE 1. Coefficients τ_y, η, and ζ for Three Data Sets

d_s (mm) (1)	C_v (%) (2)	τ_y (dynes/cm^2) (3)	η poises (4)	ζ (g/cm) (5)
		(*a*) Govier et al. (1957)		
0.0218	39.7	78.4	0.351	3.15×10^{-3}
0.0218	34.1	20.7	0.29	2.4×10^{-4}
0.0218	30.3	9.84	0.137	1.28×10^{-4}
0.0218	24.9	5.0	0.093	3.10×10^{-5}
0.0218	21.8	3.2	0.0670	3.8×10^{-5}
0.0218	16.8	2.61	0.0315	6.34×10^{-5}
		(*b*) Savage and McKeown (1983)		
0.97	42.9	1.96	0.715	5.8×10^{-3}
0.97	53.0	1.75	0.975	2.55×10^{-3}
1.78	53.0	3.59	1.34	1.88×10^{-2}
1.78	42.9	0.14	0.882	2.72×10^{-3}
1.24	53.4	6.61	0.983	2.63×10^{-2}
		(*c*) Bagnold (1954)		
1.32	60.6	8.15	0.75	0.0342
1.32	55.5	6.72	0.485	0.0224
1.32	49.5	3.0	0.3	0.0088
1.32	44.5	4.2	0.185	0.0048
1.32	37.3	2.93	0.126	0.0025
1.32	30.8	2.18	0.083	0.00144
1.32	22.2	0.0	0.067	0.00064

In Govier's experiments, the gap size ΔR of the rotational viscometer was small (ΔR = 1.17 mm), and fine galena particles of medium silt size (d_s = 0.0218 mm) were sheared at rates varying from 5 s^{-1} to 1,000 s^{-1}. In both Bagnold, and Savage and McKeown's experiments, neutrally buoyant particles of coarse sand size (d_s = 0.5 ~ 2 mm) were sheared in rotational viscometers with about the same gap size (ΔR = 1.08 cm and 1.43 cm, respectively). Two types of coaxial rotational viscometers have been used for the rheological measurements: (1) Bagnold and Govier et al. rotated the outer cylinder; and (2) Savage and McKeown rotated the inner cylinder. The shear rates in Bagnold's experiments (5 s^{-1}–250 s^{-1}) were larger than those of Savage and McKeown (10 s^{-1}–60 s^{-1}). Therefore, larger turbulent-dispersive stresses are expected in Bagnold's experiments.

In spite of the similarities in sediment sizes and rates of shear, the experimental measurements from all three data sets (Fig. 1) yield fairly different results. For example, in Govier et al. (1957) data set, the values of shear stress remain relatively constant at rates of shear smaller than about 70 s^{-1}. Beyond this value, shear stress increases by about one order of magnitude as the rate of shear increases from 100 s^{-1} to 1,000 s^{-1}. Under similar rates of shear, the results of Bagnold, and Savage and McKeown are strikingly different. For example, the shear stress increases by about two orders of magnitude in Bagnold's experiment as the rate of shear varies from 10 s^{-1} to 250 s^{-1}.

The best-fitted quadratic curves obtained by regression analysis are com-

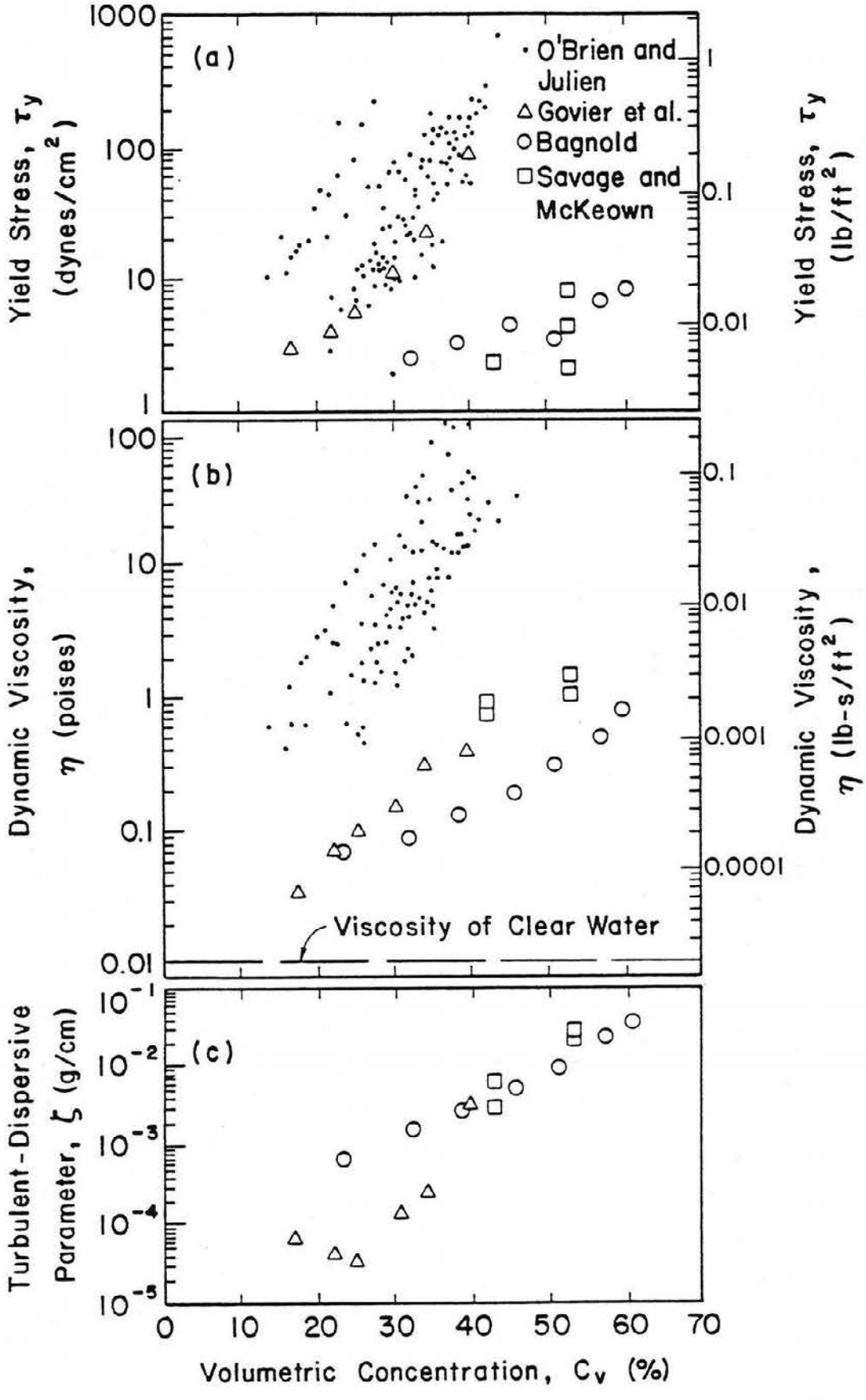

FIG. 2. Yield Stress τ_y, Dynamic Viscosity η, and Turbulent-Dispersive Parameter ζ for Hyperconcentrations

312

pared with the experimental data points in Fig. 1, and the parameters τ_y, η, and ζ for each data set are compiled in Table 1. Yield stress values from Table 1 are plotted against sediment concentration in Fig. 2(*a*) for comparison with measurements for natural mudflow matrices from O'Brien and Julien (1988). It is found that Govier's measurements for silt size galena particles compare with mudflow matrices comprising silt and clay particles, whereas, the neutrally buoyant sand size particles of Bagnold, and Savage and McKeown give lower values of yield stress. For all three data sets, the dynamic viscosity measurements shown in Fig. 2(*b*) range between those of clear water ($\eta = 0.01$ poise) and the mudflow matrices (silt and clay mixtures). The interesting Fig. 2(*c*) shows reasonable agreement among all values of the combined turbulent-dispersive parameter, ζ. For the three data sets, the values of ζ are found to increase very rapidly with volumetric sediment concentration.

Dimensionless Formulation of the Rheological Model

The relative magnitude of the terms in Eq. 1 is examined to seek possible reduction of the three data sets into a dimensionless rheological model, and also to better define the conditions under which simplified models can be applied.

A dimensionless rheological model can be obtained after rewriting Eqs. 1 and 2 in the following form:

$$\tau^* = 1 + (1 + T_d^*)a_1 D_v^* \quad \ldots\ldots (5)$$

in which the three dimensionless parameters are defined as:

1. Dimensionless excess shear stress

$$\tau^* = \frac{\tau - \tau_y}{\eta \dfrac{du}{dy}} \quad \ldots\ldots (6)$$

2. Dimensionless dispersive-viscous ratio

$$D_v^* = \frac{\rho_s \lambda^2 d_s^2}{\eta} \left(\frac{du}{dy}\right) \quad \ldots\ldots (7)$$

3. Dimensionless turbulent-dispersive ratio

$$T_d^* = \frac{\rho_m l_m^2}{a_1 \rho_s \lambda^2 d_s^2} \quad \ldots\ldots (8)$$

This linearized formulation of the rheological model (Eq. 5) for hyperconcentrated water-sediment mixtures has three major advantages over previous formulations:

1. It involves three dimensionless parameters τ^*, D_v^*, and T_d^*.
2. The second term on the right-hand side of Eq. 5 reflects the deviation from the Bingham plastic model.

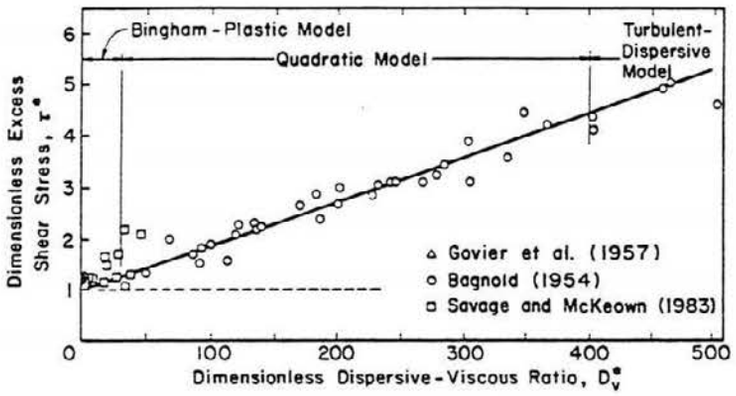

FIG. 3. Comparison of Dimensionless Model with Experimental Data

3. Newtonian and non-Newtonian fluids can be modeled depending on the relative magnitude of the parameters D_v^*, T_d^*, and τ_y.

The usefulness of the dimensionless rheological model is demonstrated in Fig. 3 where τ^* is plotted versus D_v^*. When Eq. 5 is fitted to the experimental data sets of Govier et al. (1957), Savage and McKeown (1983), and Bagnold (1954), it is found that $a_1(1 + T_d^*) = 0.0087$. It has not been possible to evaluate the parameter T_d^* because the mixing length l_m from existing experiments is not available. It is interesting to notice, however, that the value $a_1 = 0.01$ suggested by Bagnold is comparable to the value $a_1 (1 + T_d^*) = 0.0087$ obtained from Eq. 5 when assuming that the turbulent stress is negligible compared to the dispersive stress ($T_d^* << 1$).

It is found in this analysis that not only the linearized dimensionless model (Eq. 5) is applicable to all three data sets, but the parameter D_v^* can be used to delineate particular cases of the quadratic model. The results shown in Fig. 3 indicate that τ^* is sufficiently close to unity when $D_v^* < 30$ to justify the use of a Bingham plastic model. On the other hand, τ^* exceeds 4 when D_v^* is roughly larger than 400, which indicates that in this region the turbulent-dispersive stress is dominant.

Summary and Conclusion

We concur with Savage and McKeown's (1983) conclusion that the rheology of hyperconcentrations is somewhat more complex than originally pictured by Bagnold (1954). The quadratic model describing the rheology of hyperconcentrated sediment flows is well suited to the experimental data sets of Govier et al. (1957), Savage and McKeown (1983), and Bagnold (1954). This analysis illustrates the benefits of combining the turbulent stress with the dispersive stress. When the quadratic model is written in a linearized dimensionless form (Eq. 5), the ratio of dispersive to viscous stresses D_v^* becomes of foremost importance in selecting appropriate rheological models.

It can be concluded that the quadratic model is valid for all values of the parameter D_v^*, and reduces to the Bingham plastic model when $D_v^* < 30$. Turbulent-dispersive formulations may be useful in the inertial region when $D_v^* > 400$.

Acknowledgments

The writers are grateful to E. V. Richardson, who demonstrated great enthusiasm in this work and also supported the second writer during the course of his Ph.D. studies at Colorado State University.

Appendix I. References

Bagnold, R. A. (1954). "Experiments on a gravity-free dispersion of large solid spheres in a Newtonian fluid under shear." *Proc. of the Royal Soc. of London,* 225, 49–63.

Govier, G. W., Shook, C. A., and Lilge, E. O. (1957). "The properties of water suspension of finely subdivided magnetite, galena, and ferrosilicon," *Trans. Can. Inst. Mining and Met.*, 60, 147–154.

Jeffrey, D. J., and Acrivos, A. (1976). "The rheological properties of suspension of rigid particles." *Am. Inst. of Chem. Engrg. J.*, 22, 417–432.

O'Brien, J. S., and Julien, P. Y. (1985). "Physical properties and mechanics of hyperconcentrated sediment flows." *Proc. of the Specialty Conference on Delineation of Landslides, Flash Flood and Debris Flow Hazards in Utah,* Utah Water Research Laboratory, 260–279.

O'Brien, J. S., and Julien, P. Y. (1988), "Laboratory Analysis of Mudflow Properties," *J. Hydr. Engrg.*, ASCE, 114(8), 877–887.

Savage, S. B., and McKeown, S. (1983). "Shear stresses developed during rapid shear of concentrated suspension of large spherical particles between concentric cylinders." *J. Fluid Mech.*, 127, 453–472.

Takahashi, T. (1980). "Debris flow on prismatic open channel." *J. Hydr. Div.*, ASCE, 106(3), 381–396.

Appendix II. Notation

The following symbols are used in this paper:

a_1 = dispersive stress coefficient;
C_v = volumetric sediment concentration;
C^* = maximum volumetric sediment concentration ($C^* \sim 0.615$);
D_v^* = dimensionless dispersive-viscous ratio;
d_s = average diameter of sediment particles;
l_m = mixing length of mixture;
T_d^* = dimensionless turbulent-dispersive ratio;
ΔR = gap size of viscometer;
ζ = turbulent-dispersive parameter;
η = dynamic viscosity of mixture;
λ = linear concentration of sediments;
ρ, ρ_s, ρ_m = densities of fluid, particles, and sediment-water mixture, respectively;
τ = shear stress;
τ_y = yield shear stress; and
τ^* = dimensionless excess shear stress.

Two-Dimensional Water Flood and Mudflow Simulation

By J. S. O'Brien,[1] P. Y. Julien,[2] and W. T. Fullerton,[3] Members, ASCE

Abstract: FLO-2D is a two-dimensional finite difference model that simulates clear-water flood hazards, mudflows, and debris flows on alluvial fans and urban floodplains. Interactive flood or mudflow routing between channel, street, and floodplain flow is performed using a uniform grid system to describe complex floodplain topography. A quadratic rheological model, developed from field and laboratory mudflow data, enables appropriate simulations of flooding conditions ranging from clear water to hyperconcentrated sediment flows. Computer-aided design (CAD) graphics of predicted time-sequenced flood depths automates the delineation of flood hazards. Replication of the 1983 Rudd Creek mudflow in Utah demonstrates the capability of the model.

Introduction

Most flood hazard studies, and particularly those on alluvial fans, are conducted in urban development areas. The extent of urban flooding is generally defined by considering a variety of flow conditions, including flow through subdivisions, street flow, and culvert or flood channel discharge. Conventional one-dimensional hydraulic models, such as the U.S. Army Corps of Engineers HEC-2 model, require the interpretation of overbank flood boundaries between cross sections that may extend through urban areas. Flood elevations and areas of inundation are difficult to interpret for locations where floodplain storage, flood attenuation, flow around buildings, or flow in streets is significant.

Flood hazards on alluvial fans are presently delineated with a simplistic probabilistic model adopted by the Federal Emergency Management Agency (FEMA) (*FAN*, 1990). Since the FEMA method doesn't simulate flood hydrographs, it is inappropriate for the design of flood mitigation structures such as levees, flood containment walls and flood channels. It is also inappropriate for flooding in urban areas, as well as for analyzing mud and debris flow hazards.

Previous attempts to simulate debris flows were accomplished with one-dimensional flow-routing models. DeLeon and Jeppson (1982) modeled laminar water flows with enhanced friction factors. Spatially varied and steady-state Newtonian flow was assumed, and flow stoppage could not be simulated. Schamber and MacArthur (1985) designed a one-dimensional finite element model for mudflows using the Bingham rheological model to evaluate the shear stresses of a nonNewtonian fluid. O'Brien (1986) designed a one-dimensional mudflow model for watershed channels that also utilized the Bingham model.

In 1986, MacArthur and Schamber presented two-dimensional finite element model for application to simplified overland topography. The fluid properties were considered to be those of a Bingham fluid, whose static

[1]Prin., FLO Engrg., Inc., P.O. Box 1659, Breckenridge, CO 80424.
[2]Assoc. Prof., Dept. of Civ. Engrg., Colorado State Univ., Fort Collins, CO 80523.
[3]Pres., FLO Engrg., Inc., P.O. Box 1659, Breckenridge, CO 80424.

Note. Discussion open until July 1, 1993. To extend the closing date one month, a written request must be filed with the ASCE Manager of Journals. The manuscript for this paper was submitted for review and possible publication on August 27, 1992. This paper is part of the ***Journal of Hydraulic Engineering***, Vol. 119, No. 2, February, 1993. ©ASCE, ISSN 0733-9429/93/0002-0244/$1.00 + $.15 per page. Paper No. 1965.

shear stress is a function of the fluid viscosity and yield strength. The model description was published by the U.S. Army Corps of Engineers (*Incorporating* 1986), and included applications for mudflow on simplified, single-plane topography.

Takahashi and Tsujimoto (1985) proposed a two-dimensional finite difference model for debris flows based on a dilatant-fluid model coupled with Coulomb flow resistance. The dilatant-fluid model was derived from Bagnold's dispersive stress theory, which describes the stress resulting from the collision of sediment particles. More recently, Takahashi and Nakagawa (1989) modified the debris flow model to include turbulence.

O'Brien and Julien (1988), Major and Pierson (1990), and Julien and Lan (1991) showed in rheological investigations that mudflow matrices behave as Bingham fluids at high concentrations of fine sediments and low shear rates. At low sediment concentrations, turbulent stresses dominate. High concentrations of coarse particles combined with low concentrations of fine particles are required to generate dispersive stresses. The quadratic shear stress model proposed by O'Brien and Julien (1985) seems most appropriate to describe the continuum of flow regimes from viscous to turbulent/dispersive flow.

The two-dimensional finite difference model FLO-2D was conceived for routing non-Newtonian flood flows on alluvial fans. The objective in designing this model was to estimate the probable range of flow properties (velocity and depth), predict a reasonable area of inundation, and simulate flow cessation. The model has been applied to a variety of flooding problems, including the replication of the 1983 Rudd Creek mudflow.

The advantage of this model is embodied in its versatility to route channel flow using variable area cross sections, predict channel overbank discharge, and simulate floodplain flow over complex topography. Simulation of urban flooding on developed fans and floodplains became plausible when model components were designed to evaluate street flow and account for flow path obstructions, such as buildings.

Governing Equations

The two-dimensional constitutive equations include the continuity equation

$$\frac{\partial h}{\partial t} + \frac{\partial h V_x}{\partial x} + \frac{\partial h V_y}{\partial_y} = i \quad \ldots\ldots\ldots\ldots\ldots\ldots\ldots\ldots\ldots\ldots\ldots\ldots\ldots\ldots\ldots\ldots (1)$$

and the two-dimensional equations of motion

$$S_{fx} = S_{ox} - \frac{\partial h}{\partial x} - \frac{V_x}{g}\frac{\partial V_x}{\partial x} - \frac{V_y}{g}\frac{\partial V_x}{\partial y} - \frac{1}{g}\frac{\partial V_x}{\partial t} \quad \ldots\ldots\ldots\ldots\ldots\ldots\ldots\ldots\ldots\ldots (2)$$

$$S_{fy} = S_{oy} - \frac{\partial h}{\partial y} - \frac{V_y}{g}\frac{\partial V_y}{\partial y} - \frac{V_x}{g}\frac{\partial V_y}{\partial_x} - \frac{1}{g}\frac{\partial V_y}{\partial t} \quad \ldots\ldots\ldots\ldots\ldots\ldots\ldots\ldots\ldots\ldots (3)$$

in which h = flow depth; and V_x and V_y = depth-averaged velocity components along the x and y coordinates. The excess rainfall intensity i may be nonzero on the alluvial fan or the floodplain. The friction slope components S_{fx} and S_{fy} are written in (2) and (3) as a function of bed slope S_{ox} and S_{oy}, pressure gradient, and convective and local acceleration terms. A diffusive wave approximation to the equations of motion is defined by ne-

311

glecting the last three acceleration terms of (2) and (3). Further, by neglecting the pressure term, a kinematic wave representation is derived. These approximations are valid for steep alluvial fans. The option of using either a kinematic wave or diffusive wave equation is available in FLO-2D.

The diffusive wave aproximation has a broader application than the kinematic wave model (Ponce et al. 1978), and very little accuracy is normally sacrificed compared to the full dynamic model (Akan and Yen 1981). Concomitantly, computation time improves when a diffusive wave approximation is used instead of the full dynamic wave (Hromadka and Yen 1987).

The rheological behavior of hyperconcentrated sediment flows involves the interaction of several complex physical processes. The nonNewtonian behavior of the fluid matrix is controlled in part by the cohesion between fine sediment particles. This cohesion contributes to the yield stress τ_y, which must be exceeded by an applied stress in order to initiate fluid motion. By combining the yield stress and viscous stress components, the well-known Bingham plastic model is prescribed. For large rates of fluid matrix shear (as might occur on steep alluvial fans), turbulent stresses may be generated. An additional shear stress component arises in turbulent flow from the collision of sediment particles under large rates of deformation.

The total shear stress in hyperconcentrated sediment flows, including those described as debris flows, mud flows, and mud floods, can be calculated from the summation of five shear stress components

$$\tau = \tau_c + \tau_{mc} + \tau_v + \tau_t + \tau_d \quad \ldots\ldots (4)$$

in which the total shear stress τ depends on the cohesive yield stress τ_c, the Mohr-Coulomb shear τ_{mc}, the viscous shear stress τ_v, the turbulent shear stress τ_t, and the dispersive shear stress τ_d. When written in terms of shear rates (dv/dy), the following quadratic rheological model can be developed (O'Brien and Julien 1985):

$$\tau = \tau_y + \eta \left(\frac{dv}{dy}\right) + C \left(\frac{dv}{dy}\right)^2 \quad \ldots\ldots (5a)$$

where

$$\tau_y = \tau_c + \tau_{mc} \quad \ldots\ldots (5b)$$

and

$$C = \rho_m l^2 + f(\rho_m, C_v)\, d_s^2 \quad \ldots\ldots (5c)$$

in which η = dynamic viscosity; τ_c = cohesive yield strength; the Mohr-Coulomb stress $\tau_{mc} = p_s \tan \phi$ depends on the intergranular pressure p_s and the angle of repose ϕ of the material; and C = inertial shear stress coefficient, which depends on the mass density of the mixture ρ_m, the Prandtl mixing length l, the sediment size d_s, and a function of the volumetric sediment concentration C_v. Bagnold (1954) defined $f(\rho_m, C_v)$ as

$$f(\rho_m, C_v) = a_i \rho_m \left[\left(\frac{C_*}{C_v}\right)^{1/3} - 1\right] \quad \ldots\ldots (5d)$$

in which the empirical coefficient $a_i = 0.01$ and C_* = maximum static volume concentration for the sediment particles. Egashira et al. (1989) challenged this relationship, and posed

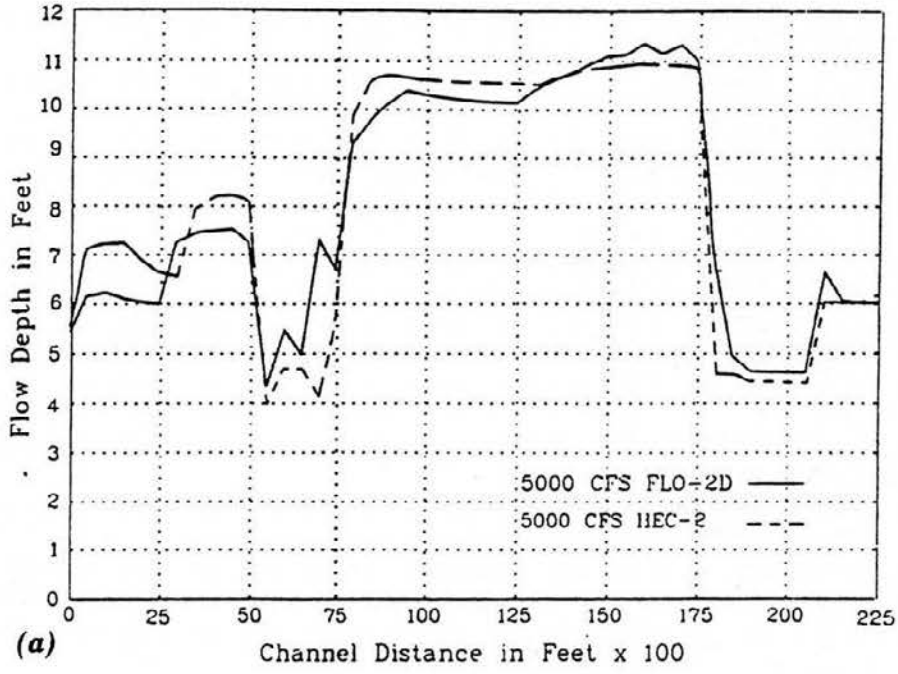

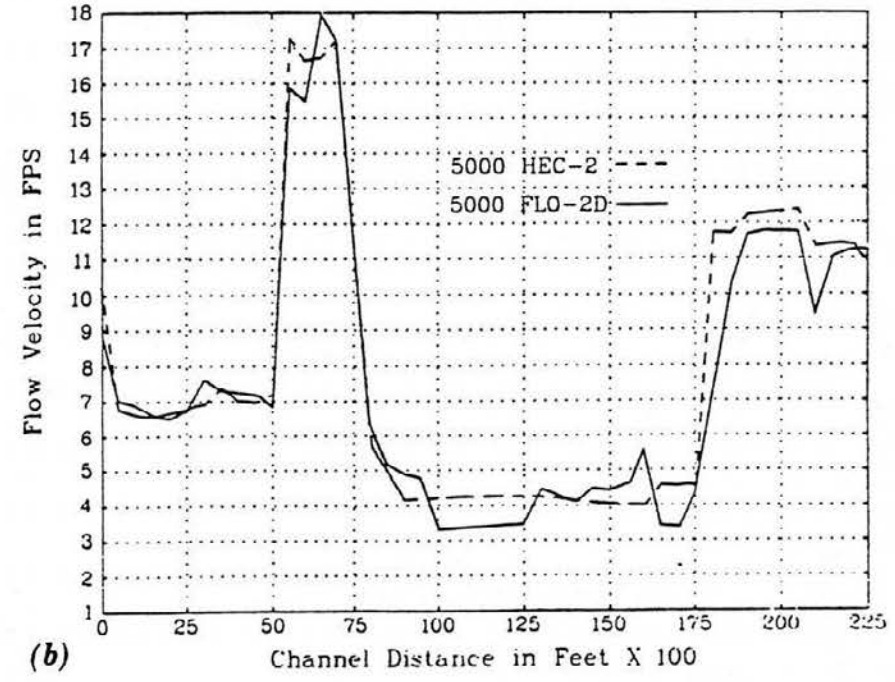

FIG. 1. Comparison of HEC-2 and FLO-2D Results: (a) Flow Depth; and (b) Velocity

$$f(\rho_s, C_v) = \frac{\pi}{12}\left(\frac{6}{\pi}\right)^{1/3} \sin^2\alpha_l \rho_s (1 - e_n^2) C_v^{1/3} \quad \ldots\ldots\ldots\ldots\ldots\ldots\ldots\ldots (5e)$$

in which the energy restitution coefficient e_n after impact ranges within $0.70 < e_n < 0.85$ for sands; α_l = average particle impact angle; and ρ_s = mass density of sediment particles.

The first two terms in (5*a*) are referred to as the Bingham shear stresses,

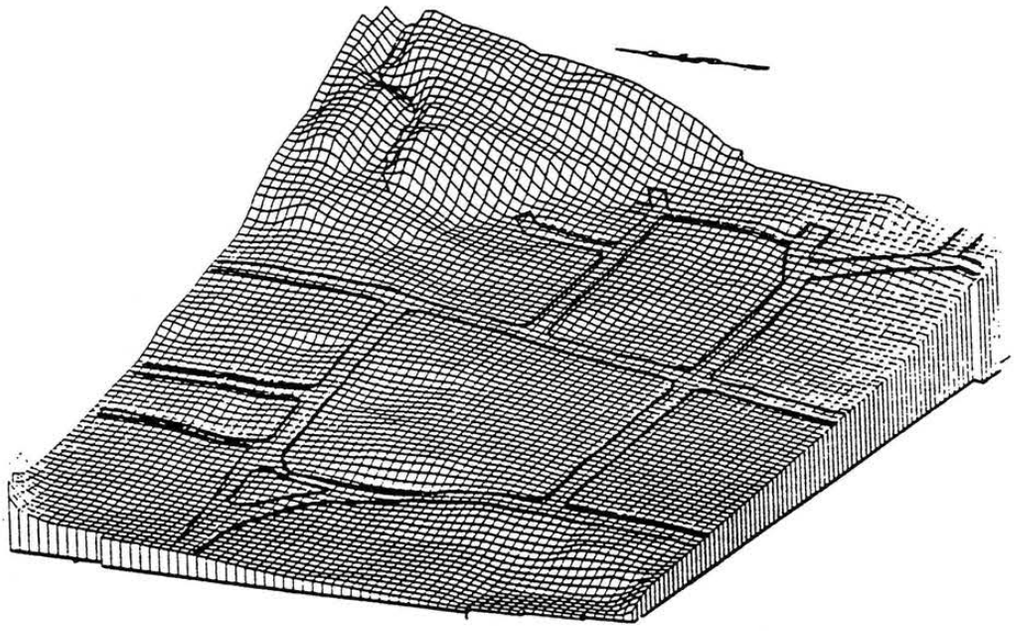

FIG. 2. Rudd Creek Alluvial Fan Topography

and represent the internal resistance stresses of a Bingham fluid. The sum of the yield stress and viscous stress defines the shear stress of a cohesive, hyperconcentrated sediment fluid in a viscous flow regime. The last term represents the sum of the dispersive and turbulent shear stresses, which depends on the square of the vertical velocity gradient. A discussion of these stresses and their role in hyperconcentrated sediment flows can be found in Julien and O'Brien (1987).

A mudflow model that incorporates only the Bingham stresses, and ignores the inertial stresses, assumes that the simulated mudflow is viscous. This assumption is not generally applicable, because all mud floods and some mudflows are turbulent, with velocities as high as 8 m/s (25 fps). Even flows considered as mudflows with concentrations up to 40% by volume can be turbulent (O'Brien 1986). Depending on the fluid matrix properties, viscosity and yield stresses for concentrations up to 40% can still be relatively small compared to the turbulent stresses at high velocities.

To define the terms in (5*a*) for use in the FLO-2D model, the following approach was taken. By analogy with the work of Meyer-Peter and Müller (1948) and Einstein (1950), the shear stress relationship (4) is depth-integrated and rewritten in the following slope form

$$S_f = S_y + S_v + S_{td} \quad \ldots\ldots\ldots\

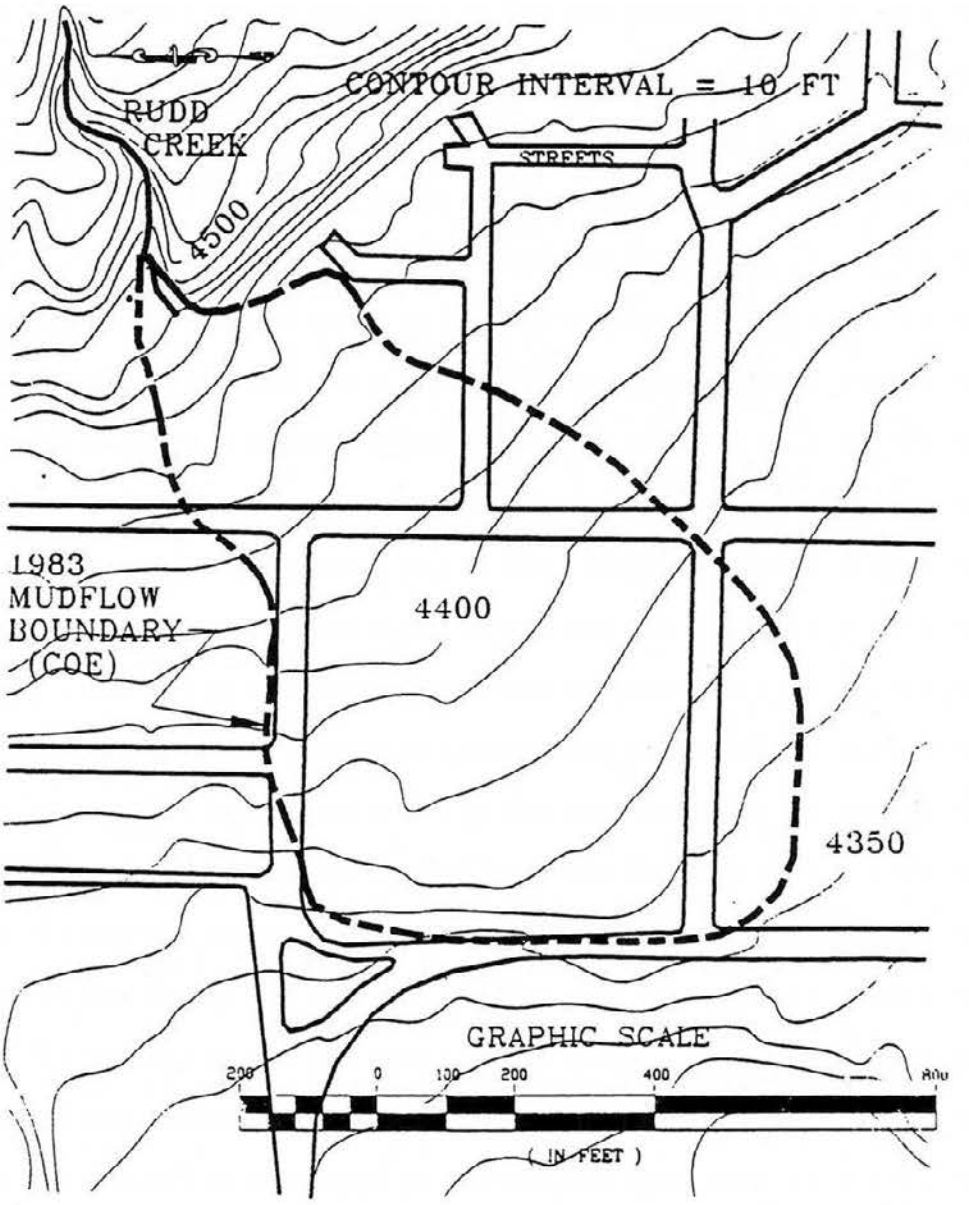

FIG. 3. Rudd Creek 1983 Mudflow Boundary

The flow resistance of the turbulent and dispersive components of (7) are combined into an equivalent Manning n value for the flow

$$S_{td} = \frac{n^2V^2}{h^{4/3}} \quad \ldots\ldots\ldots\

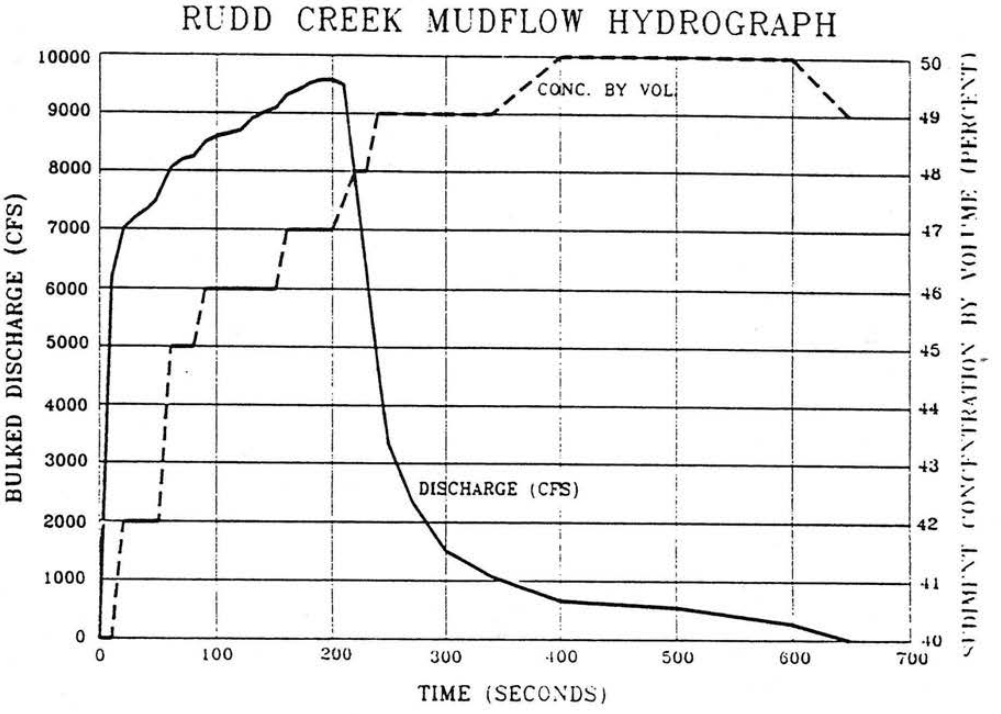

FIG. 4. Rudd Creek Mudflow Hydrograph

FIG. 5. Mudflow Frontal Deposit (Courtesy of USDA Soil Conservation Service, Salt Lake City)

322

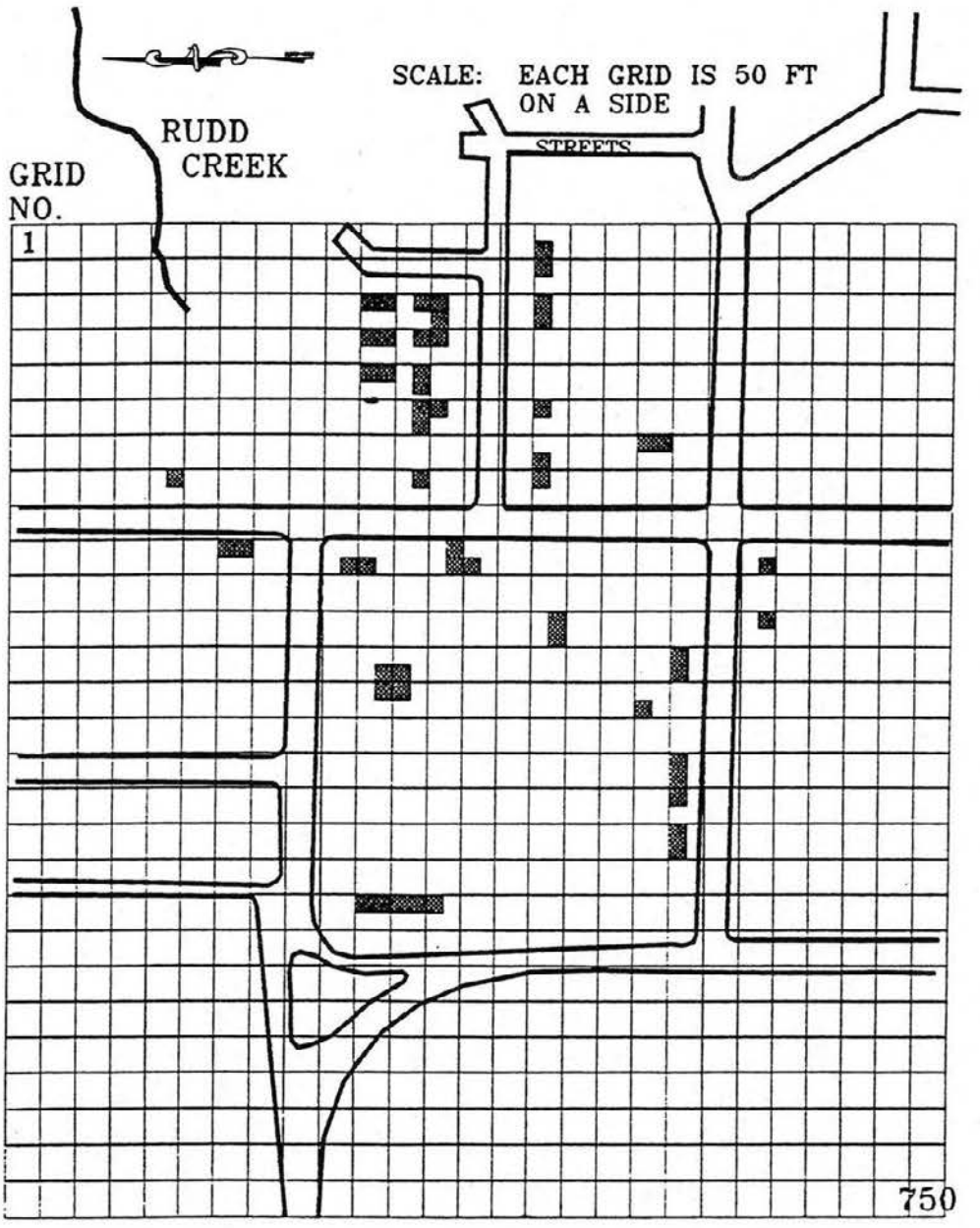

FIG. 6. FLO-2D Grid System and Location of Principal Streets and Buildings

tration. The yield stress τ_y and the viscosity η vary principally with sediment concentration. The following empirical relationships can be selected, unless a rheological analysis of the material is available:

$$\eta = \alpha_1 e^{\beta_1 C_v} \quad \ldots\ldots (10)$$

and

$$\tau_y = \alpha_2 e^{\beta_2 C_v} \quad \ldots\ldots (11)$$

in which α_i and β_i = empirical coefficients defined by laboratory experiment (O'Brien and Julien 1988). The viscosity and yield stress are shown to be functions of the volumetric sediment concentration C_v of silts, clays, and in some cases, fine sands, and do not include larger clastic material rafted along with the flow.

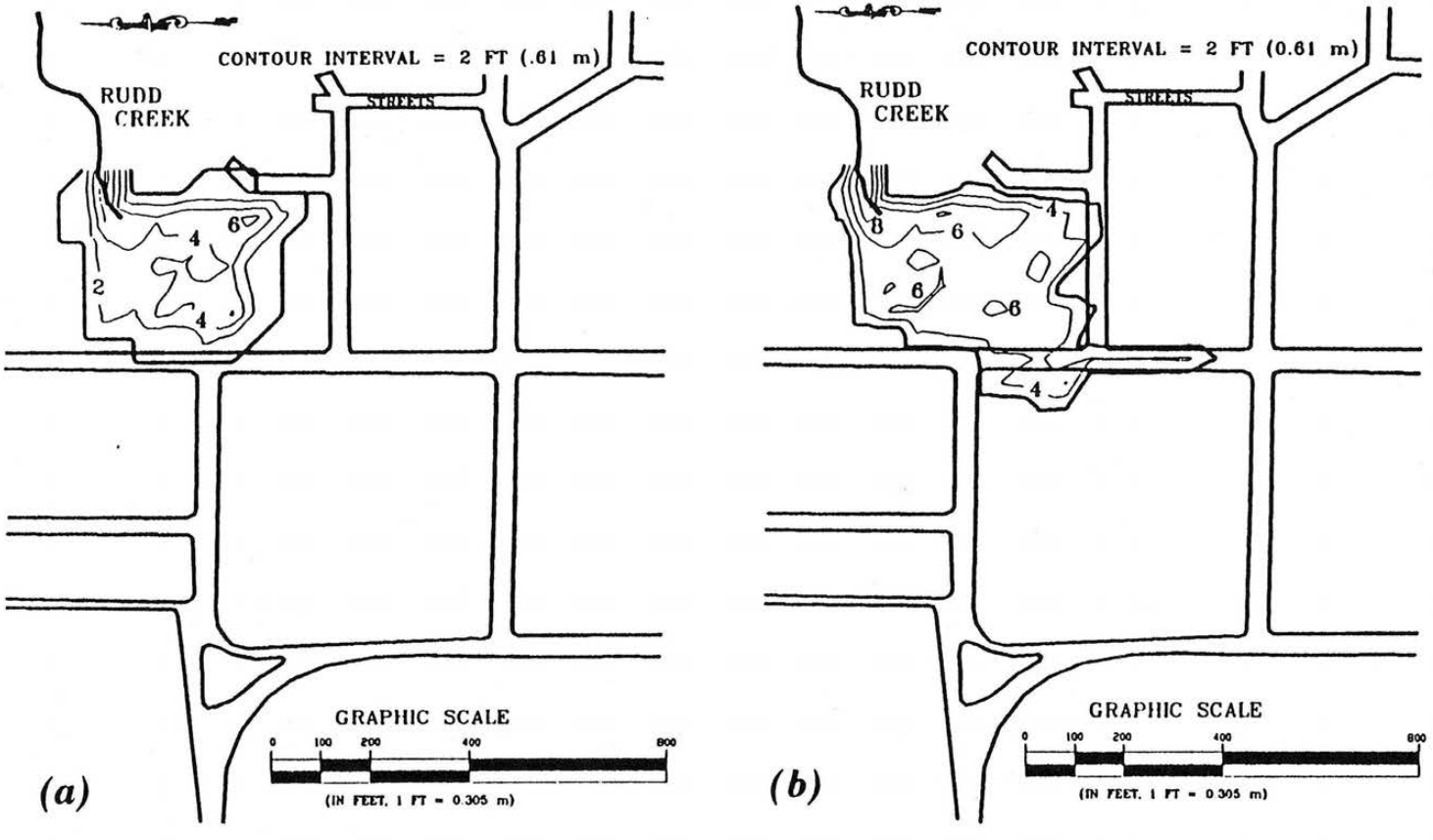

FIG. 7. Time-Lapse Simulation of Rudd Creek Mudflow: (*a*) Flow Depth after 1 Min; (*b*) Flow Depth after 2 Min

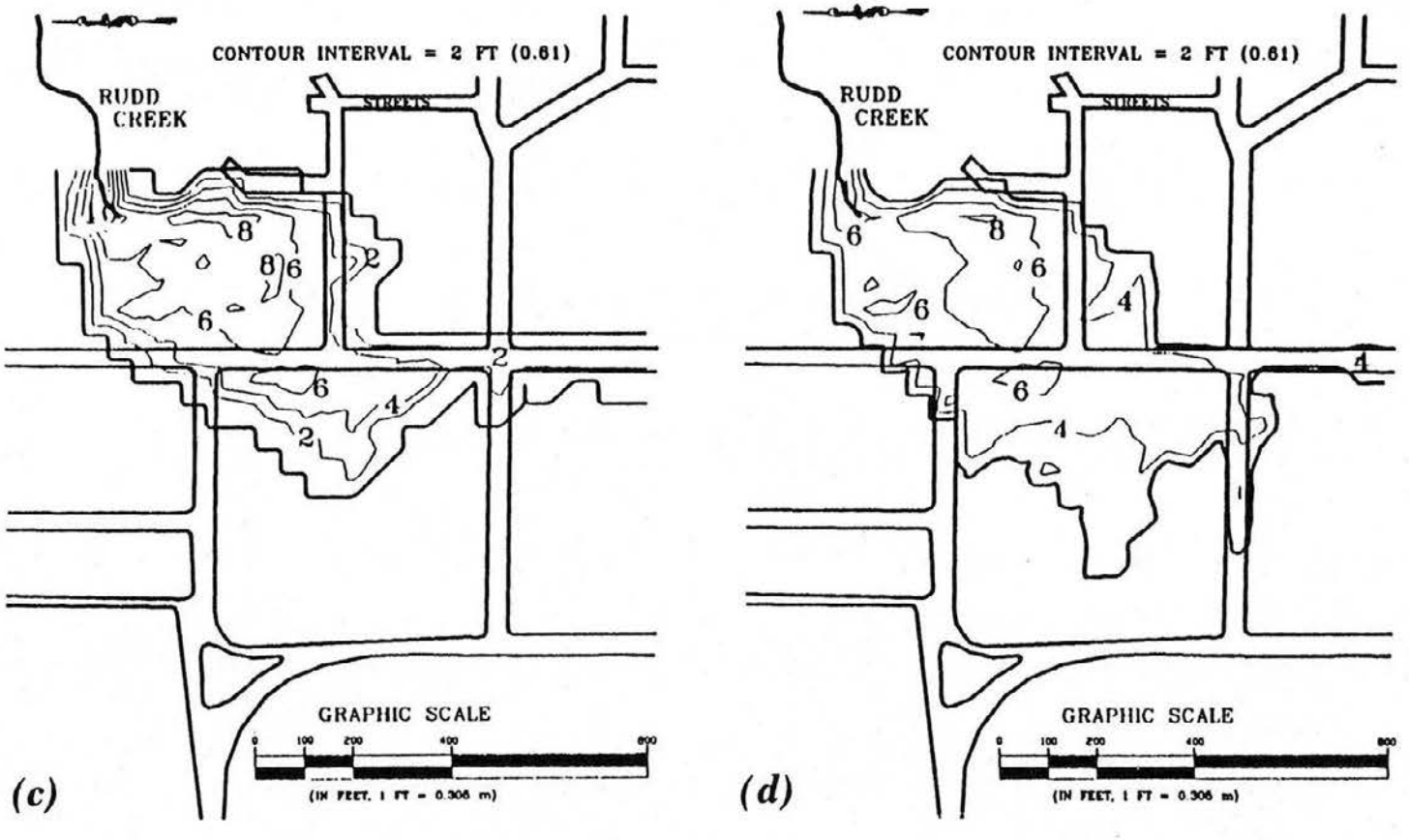

FIG. 7. (*Continued*) Time-Lapse Simulation of Rudd Creek Mudflow: (c) Flow Depth after 3 Min; (*d*) Flow Depth after 5 Min

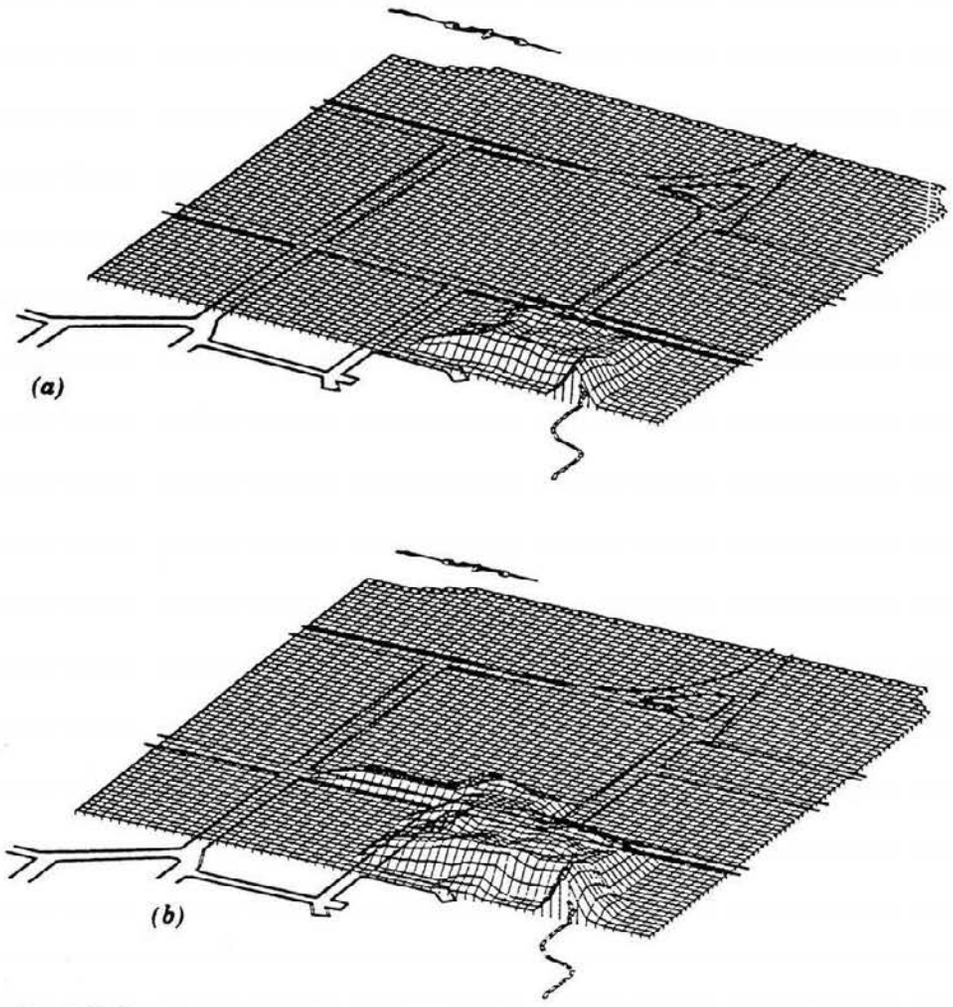

FIG. 8. 3-D Graphic Presentation of Time-Lapse Simulation: (*a*) Flow Depth after 1 Min; (*b*) Flow Depth after 2 Min

FLO-2D Model Description

The FLO-2D model evolved from the diffusive hydrodynamic model (DHM) (Hromadka and Yen 1987). The original DHM routing algorithm was revised and expanded to improve computational stability, decrease computational time, and broaden its application to more diverse flooding conditions. Very little of the original code remains.

The model uses a central finite difference routing scheme (an explicit numerical technique) for the application of the equations of motion. The surface topography is discretized into uniform square-grid elements. Each element is assigned a location on the grid system, an elevation, a roughness factor, and area and flow width reduction factors used to simulate flow blockage.

Flow is routed through the grid system using estimates of the flow depth to compute discharge. For a given element and time step, the discharge across each of the four boundaries is computed and summed. The resultant volume change is uniformly distributed over the available flow area in the element. Time steps vary according to the Courant-Friedrich-Lewy stability condition (Liggett and Cunge 1975), resulting in relatively short time steps (e.g., 1–30 s).

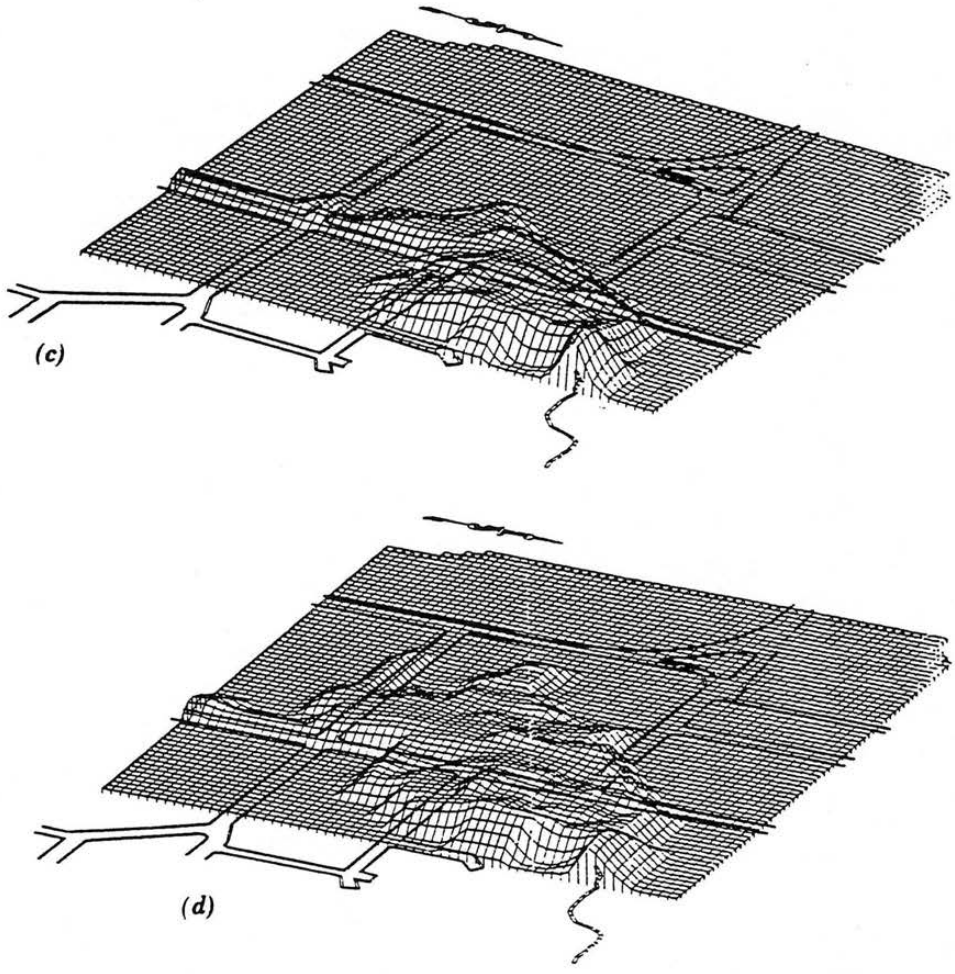

FIG. 8. (*Continued*) 3-D Graphic Presentation of Time-Lapse Simulation: (c) Flow Depth after 3 Min; (*d*) Flow Depth after 5 Min

Mass conservation is maintained for both the water and mudflow sediment volumes as the flow hydrograph is routed over the grid system. When routing mudflows, the sediment continuity is preserved by tallying the sediment volume for each grid element; thus tracking the sediment volume through the grid system. At each time step, the model computes the change in water and sediment volumes, and the corresponding change in sediment concentration.

Flow cessation is simulated with the potential for remobilization. For mudflows, high sediment concentrations result in a very viscous flow, which may halt on mild slopes. When successive discharges of less sediment concentration enter a grid element with a halted flow, the diluted mixture may remobilize.

The accuracy of FLO-2D hydraulic computations for steady flow was verified through a comparison with field data and replication of HEC-2 results for contained channel flow, as shown in Fig. 1. Both water surface and velocity results were compared using similar data files for a variable area channel and alternating subcritical and supercritical slope reaches extending over 6.4 km (4 mi). Separate HEC-2 runs were required for the subcritical and supercritical flow regimes. The HEC-2 predicted water surface was estimated in the flow transition locations. Additional information on model verification is available in O'Brien and Fullerton (1990).

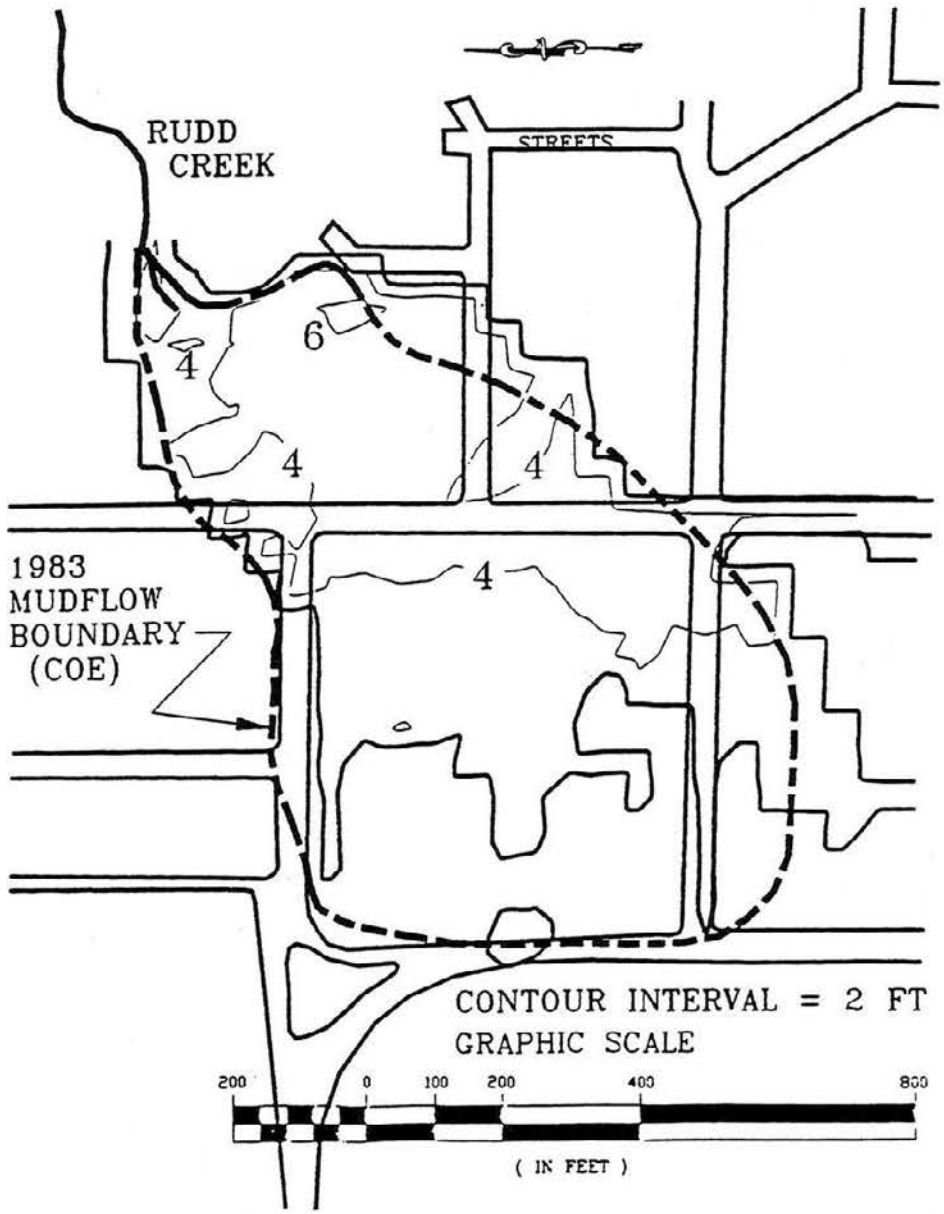

FIG. 9. Rudd Creek Mudflow Simulation after 15 Min

Model Limitations and Assumptions

Wave attenuation in the diffusive model is the result of overbank storage and the interaction of the friction slope and diffusive pressure gradient terms with the bed slope. The present model does not have the ability to simulate shock waves or hydraulic jumps, and tends to smooth out these abrupt changes in the flow profile.

The inherent assumptions in applying the model for flood routing are: (1) Steady flow for the duration of the time step (usually a few seconds); (2) hydrostatic pressure distribution; (3) steady flow resistance equation; (4) sufficiently uniform cross section shape and hydraulic roughness of the channel; and (5) single values of grid-element elevation and roughness.

In addition, FLO-2D is a rigid bed model and does not simulate degradation. This is not a serious limitation for urban floodplain flow (less erodible

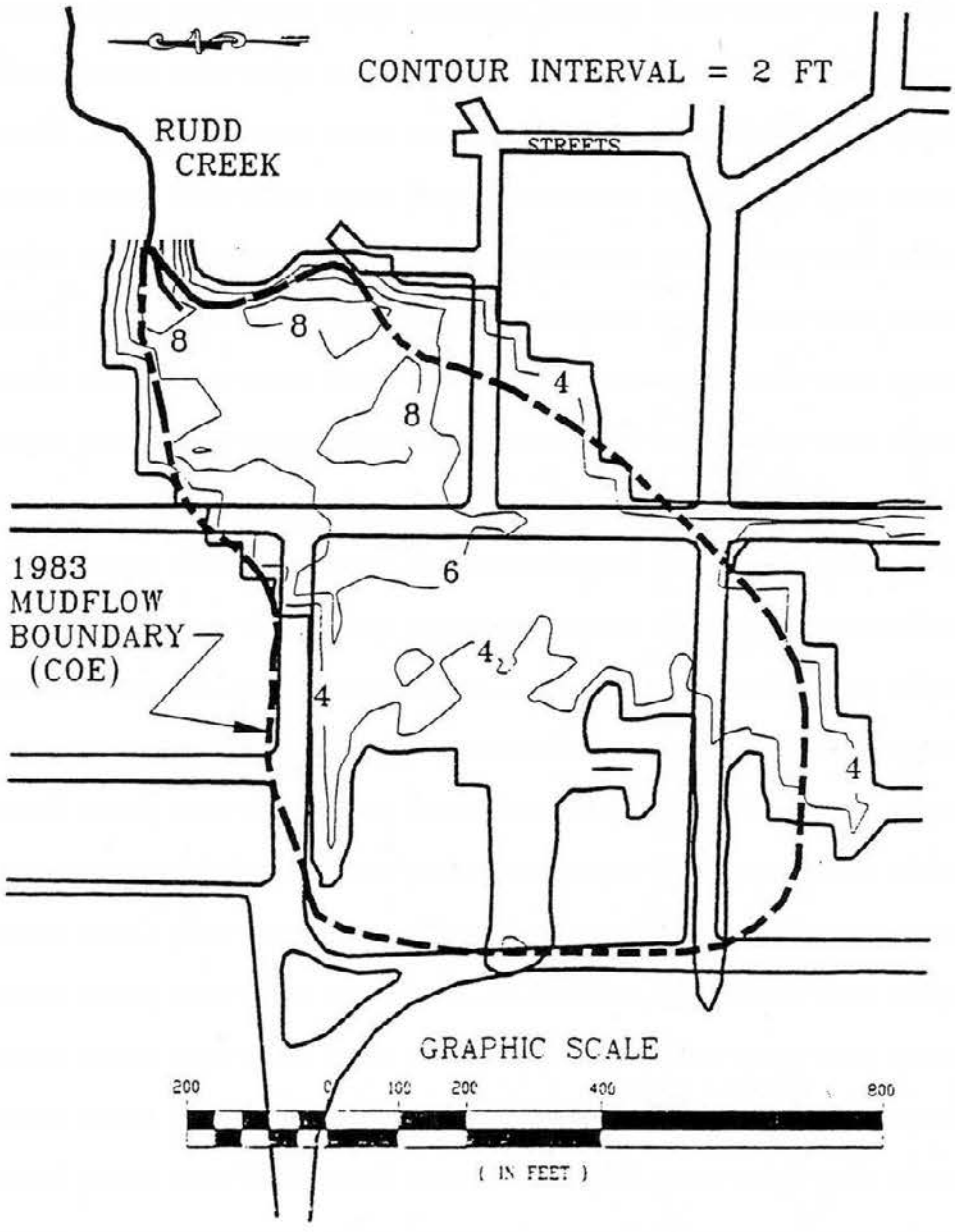

FIG. 10. Rudd Creek Mudflow Simulated Maximum Flow Depth Contours

surfaces) and depositional flows such as mudflows, which may cease flowing when obstacles are encountered.

The detail and accuracy of a flood simulation is related to grid size. A grid size of 30–150 m (100–500 ft) is usually appropriate for detailed simulations. Finer grid resolution requires more computer run time, more extensive data files, and more detailed boundary conditions.

Case Study—1983 Rudd Creek Mudflow

Model simulation of water flooding through urban areas with channels and streets has produced excellent results (O'Brien and Fullerton 1990). The simulation of mud or debris flow requires more engineering judgment. To demonstrate FLO-2D's capability to model mudflows, the 1983 Rudd Creek mudflow in Davis County, Utah, is presented. Figs. 2 and 3 show

the approximate boundary of the mudflow after the flow had ceased, as indicated by the U.S. Army Corps of Engineers (*Incorporating* 1986). Close examination of photos taken after the event shows that the boundaries of the deposit were slightly more irregular than shown in Figs. 2 and 3, but the correlation is reasonable.

The flood hydrograph and other pertinent data used in the simulation were published by the U.S. Army Corps of Engineers (*Incorporating* 1986). The hydrograph is shown in Fig. 4. Available field data from the event included: (1) The area of inundation indicated from photography; (2) a surveyed volume of the mudflow deposit of approximately 64,200 m^3 (84,000 cu yd); (3) mudflow frontal velocity on the alluvial fan of approximately the speed that a man could walk [0.6–1.2 m/s (2–4 fps), eyewitness account]; and (4) observed mudflow depths that ranged from approximately 3.7 m (12 ft) at the apex of the alluvial fan to approximately 0.6–0.9 m (2–3 ft) at the debris front (Fig. 5).

The mudflow was initiated by a landslide, and therefore a relatively uniform sediment concentration was assumed, which increased slightly as the event progressed to simulate dewatering (Fig. 4). Manning n roughness values for each grid element varied from 0.035 to 0.10, depending on vegetation and flow obstruction. Appropriate values from laboratory data were selected for α_i and β_i in (10) and (11) to compute viscous and yield stresses. The buildings that influenced the flow path were modeled, and their location is shown in Fig. 6.

A time-lapse simulation of the progression of the mudflow over the Rudd Creek alluvial fan is illustrated in Fig. 7. Time-sequence flow depths are written to files for a CAD graphics program that plots the depth contours. With the plotting package, the flood hazard delineation is automated. When the viscous flow encounters a street with a favorable slope, it proceeds ahead of the main body of the flow, as shown for the 2 min and 5 min simulation times in Fig. 7. A 3-dimensional graphic display of the time-lapse simulation, as viewed from the upstream direction, is shown in Fig. 8. The 3-D view helps to visualize how the mud piles up near the fan apex. Postevent photos revealed that houses in this vicinity received the most damage.

The hydrograph in Fig. 4 indicates that the flood event was over in less than 7 min. The model predicted that the mudflow continued to creep down the fan for several more minutes before flow cessation. By the end of 15 min, all the flow on the fan had ceased (Fig. 9). There is little difference in the mudflow boundary after 15 min (Fig. 9) and the boundary for the 5 min simulation (Fig. 7).

The maximum computed flow depth of 3.6 m (11.8 ft) downstream of the apex compared well with the 3.7 m (12 ft) observed depth (Fig. 10). Mudflow velocities predicted on the fan ranged from 0.3 to 1.2 m/s (1–4 fps) or approximately walking speed, as was observed. Near the fan apex, maximum predicted velocities were less than 3.0 m/s (10 fps). Just upstream of the apex in the Rudd channel area, predicted velocities exceeded 6.1 m/s (20 fps). Predicted frontal lobe depths ranged from 0.6 to 1.2 m (2–4 ft), depending on the location on the fan, and correlated well with postevent photos.

Conclusions

The two-dimensional model FLO-2D is a flexible tool to augment the capability of the floodplain manager and engineer to predict flood hydraulics, identify areas of inundation, and design options for flood containment.

The model has components to enhance the prediction of floodplain or alluvial fan flooding including flood hydrograph routing, prediction of street flow, and mudflow simulation. Urban flood simulation has been improved by modeling flow-path obstruction and storage loss due to buildings and flood-containment walls.

Simulation of the 1983 Rudd Creek mudflows with FLO-2D correlated well with the observed area of inundation, maximum flow depth at the fan apex, frontal wave flow depths, and velocities and final deposits based on mudflow cessation. Mudflow in streets was predicted to advance in front of the main flow body, while building obstructions caused increased flow depth near the fan apex.

APPENDIX I. REFERENCES

Akan, A. O., and Yen, B. C. (1981). "Diffusion-wave routing in Channel Networks." *J. Hydr. Div.*, ASCE, 107(6), 719–732.

Bagnold, R. A. (1954). "Experiments on a gravity-free dispersion of large solid spheres in a Newtonian fluid under shear." *Proc., Royal Society of London, series A*, 225, 49–63.

DeLeon, A. A., and Jeppson, R. W. (1982). "Hydraulic and numerical solutions of steady-state but spatially varied debris flow." *Hydraulics and hydrology series, UWRL/H-82/03*, Utah State Univ., Logan, Utah.

Egashira, S., Ashida, K., Yajima, H., and Takahama, J. (1989). "Constitutive equations of debris flow." *Ann., disaster prevention res. inst., No. 32B–2*, Kyoto Univ., Kyoto, Japan, 487–501.

Einstein, H. A. (1950). "The bed-load function for sediment transportation in open channel flows." *USDA tech. bull. no. 1026*, U.S. Department of Agriculture, Washington, D.C.

FAN, an alluvial fan flooding computer program, user's manual. (1990). Federal Emergency Management Agency, Office of Risk Assessment, Washington, D.C.

Hromadka, T. V. II, and Yen, C. C. (1987). "Diffusive hydrodynamic model." *Water Resources Investigations Report 87-4137*, USGS, Denver Federal Center, Denver, Colo.

Incorporating the effects of mudflows into flood studies on alluvial fans. (1986). U.S. Army Corps of Engineers, Omaha District, Omaha, Ne.

Julien, P. Y., and Lan, Y. Q. (1991). "On the rheology of hyperconcentration." *J. Hydr. Engr.*, ASCE, 117(3), 346–353.

Julien, P. Y., and O'Brien, J. S. (1987). "Discussion of "Mountain torrent erosion." *Sediment transport in gravel-bed rivers*. John Wiley & Sons, New York, N.Y., 537–539.

Liggett, J. A., and Cunge, J. A. (1975). "Numerical methods of solution of the unsteady flow equations." *Unsteady Flow in Open Channels*, K. Mahmood and V. Yevjevich, eds., Water Resources Publications, Fort Collins, Colo.

MacArthur, R. C., and Schamber, D. R. (1986). "Numerical methods for simulating mudflows." *Proc., 3rd Int. Symp. on River Sedimentation*, Univ. of Mississippi, Oxford, Miss., 1615–1623.

Major, J. J., and Pierson, T. C. (1990). "Rheological analysis of fine-grained natural debris-flow material." *Proc., Int. Symp. on Hydr./Hydro. of Arid Lands*, ASCE, New York, N.Y., 225–231.

Meyer-Peter, E., and Müller, R. (1948). "Formulas for bedload transport." *Proc., IAHRM 2nd Congr.*, Int. Assoc. for Hydr. Res., Stockholm, 39–64.

O'Brien, J. S. (1986). "Physical processes, rheology and modeling of mudflows," PhD thesis, Colorado State University, Fort Collins, Colo.

O'Brien, J. S., and Fullerton, W. T. (1990). "Urban floodplain and alluvial fan stormwater modeling." *Urban Hydro., Proc., 26th Annual AWRA Conf.*, Denver, Colo.

O'Brien, J. S., and Julien, P. Y. (1985). "Physical properties and mechanics of hyperconcentrated sediment flows." *Proc., ASCE Specialty Conf. on the Deline-*

ation of Landslides, Flash Floods and Debris Flow Hazards in Utah, Utah Water Research Lab., Univ. of Utah at Logan, Utah, 260–279.
O'Brien, J. S., and Julien, P. Y. (1988). "Laboratory analysis of mudflow properties." *J. Hydr. Engrg.*, ASCE, 114(8), 877–887.
Ponce, V. M., Li, R. M., and Simons, D. B. (1978). "Applicability of kinematic and diffusion models." *J. of Hydr. Div.*, ASCE, 104(3), 353–360.
Schamber, D. R., and MacArthur, R. C. (1985). "One-dimensional model for mudflows." *Proc., ASCE specialty conference on hydr. and hydro. in the small comp. age.* Vol. 2, ASCE, New York, N.Y., 1334–1339.
Takahashi, T., and Tsujimoto, H. (1985). "Delineation of the debris flow hazardous zone by a numerical simulation method." *Proc., Int. Symp. on Erosion, Debris Flow and Disaster Prevention*, Tsukuba, Japan, 457–462.
Takahashi, T., and Nakagawa, H. (1989). "Debris flow hazard zone mapping." *Proc., Japan-China (Taipei) Joint Seminar on Natural Hazard Mitigation*, Kyoto, Japan, 363–372.

APPENDIX II. NOTATION

The following symbols are used in this paper:

a_i = coefficient defined by Bagnold;
C = inertial shear stress coefficient;
C_v = volumetric sediment concentration;
C_* = maximum static volume concentration for sediment particles;
d_s = representative sediment size;
e_n = particle energy restitution coefficient after impact;
f = Darcy-Weisbach friction coefficient;
g = gravitational acceleration;
h = flow depth;
i = rainfall intensity;
K = resistance parameter for viscous flow;
l = Prandtl mixing length;
n = Manning resistance coefficient;
S_f = friction slope;
S_{fx} = friction slope component along x coordinate axis;
S_{fy} = friction slope component along y coordinate axis;
S_{td} = turbulent-dispersive slope;
S_v = viscous slope;
S_y = yield slope;
S_{ox} = bed slope component along x coordinate axis;
S_{oy} = bed slope component along y coordinate axis;
t = time;
V = depth averaged velocity;
V_x = velocity component along x coordinate axis;
V_y = velocity component along y coordinate axis;
v = velocity;
x = coordinate axis;
y = coordinate axis;
α_I = average particle impact angle;
α_i = coefficients of viscosity and yield stress;
β_i = exponents of viscosity and yield stress;
γ_m = specific weight of mixture;
η = dynamic viscosity;

ρ_m = mass density of mixture;
ρ_s = sediment particle mass density;
τ = total shear stress;
τ_c = cohesive yield strength;
τ_d = dispersive shear stress;
τ_{mc} = Mohr-Coulomb shear stress;
τ_t = turbulent shear stress;
τ_v = viscous shear stress;
τ_y = yield stress; and
ϕ = angle of repose of flow material.

VELOCITY PROFILES AND SCOUR DEPTH MEASUREMENTS AROUND BRIDGE PIERS

by

Vincenza C. Santoro[1], Pierre Y. Julien[2], Everett V. Richardson[3] and Steven R. Abt[4]

ABSTRACT

Local scour around a model of the Schoharie bridge pier was experimentally investigated in the laboratory. The tests simply focused on the effects of the angle of attack and flow velocity on the maximum depth of scour. Clear water scour conditions prevailed, i.e. the shear stress at the bottom in the upstream flow is always less than the critical value for beginning of sediment motion. The experimental results show that the effect of the angle of attack is related to the undisturbed flow Froude number. In particular, the ratio of the measured scour depths for skewed and aligned piers decreases with increasing Froude number. Velocity is found to have an important influence on scour depth.

INTRODUCTION

The 1987 bridge failure on the Schoharie Creek in the State of New York claimed ten lives and required considerable effort to rebuild the structure. The bridge collapse has been attributed to the scouring action of the flow around its piers. The risk of bridge failure due to pier scour and the design of appropriate countermeasures remain serious concerns for thousands of bridges in the United States and abroad. The past 50 years of research provided basic understanding of the physical mechanism of local scour. Nevertheless, the quantitative dependence of the scour depth on the scouring parameters justifies further investigations because existing scour equations are not yet fully reliable.

---

[1] Asst. Prof. of Civil Engineering, Istituto di Idraulica Idrologia e Gestione delle Acque, Universita di Catania, V. le A. Doria 6, 95125 Catania, Italy.

[2] Assoc. Prof. of Civil Engineering, Engineering Research Center, Colorado State University, Fort Collins, CO 80523, 303/491-8450.

[3] Prof. of Civil Engineering, Engineering Research Center, Colorado State University, Fort Collins, CO 80523, 303/491-8582.

[4] Prof. of Civil Engineering & Director of the Hydraulics Laboratory, Engineering Research Center, Colorado State University, Fort Collins, CO 80523, 303/491-8203.

A series of experiments was conducted at Colorado State University using a laboratory model of one of the Schoharie Creek bridge piers. The main objective was to investigate pier scour under the effects of two variables: angle of attack and mean flow velocity. Two sets of runs, one with the pier aligned with the flow and one with the pier angled at 10° with respect to the main flow direction were completed. Within each set of runs the upstream velocity was maintained below the critical conditions of motion of the bed material, thus clear water scour conditions prevailed during the experiments. Scour depth, change in water surface elevation, time-average point velocity and maximum velocity fluctuations were measured along six cross-sections near the pier.

EXPERIMENTAL SETUP AND PROCEDURE

The experiments were conducted in a 61 m x 2.4 m x 1.2 m recirculating laboratory flume at the Engineering Research Center. A large scale model, scale 1:15, of the Schoharie Creek bridge pier is shown in Fig. 1. The footing has a rectangular shape, wider and longer than the pier itself, which is well rounded on both ends. Metal pieces fixed the model pier to the flume sidewalls. Pea-size gravel (D_{50} = 3.3 mm) covered the flume bed up to the top of the foundation footing. Rails on the top of each flume sidewall supported a motorized carriage holding a point gage, a depth measuring device and the current meter probe used for velocity measurements. From a total of six tests, the first three showed the pier aligned with the flow, the remaining three showed the pier skewed at an angle α of 10° between the pier axis and the main flow direction. The discharge and slope were controlled to maintain average velocities of 0.3, 0.6 and 0.9 m/s while keeping the flow depth constant at y_1 = 0.3 m for each run. The test conditions are summarized in Table 1. The downstream conditions were controlled by a tail gate. With the study reach located 30 m upstream of the tailgate, steady uniform flow conditions prevailed in the study reach without the pier. Each run was allowed sufficient time, at least 8 hours, to simulate conditions approaching the maximum expected scour.

Reference nets in Figs. 2 and 3 show the location of each measuring vertical. In the case of the aligned pier, measurements were taken on only half the flow field after checking the symmetry in velocity profiles on each side of the pier. At least five velocity measurements were taken on each vertical, except where deposits significantly reduced the flow depth. When the erosive action would allow it, measurements were also taken below the "zero reference" (the elevation of the undisturbed bed).

Velocity measurements were taken using a Marsh-McBirney 2D electromagnetic current meter. Average values and maximum fluctuations of the two velocity components parallel and perpendicular (in a plane parallel to the bottom of the flume) to the main flow direction were recorded. The current meter was connected to an HP 3468 Multimeter connected to an HP 82162A thermal printer and to an HP 71 calculator in an IL loop. Over a period of 30 seconds, 57 measurements were read, stored and averaged for each probe position and each flow direction. Changes in the bed elevation and water surface elevation profiles were also compiled from these measurements by Santoro (1989).

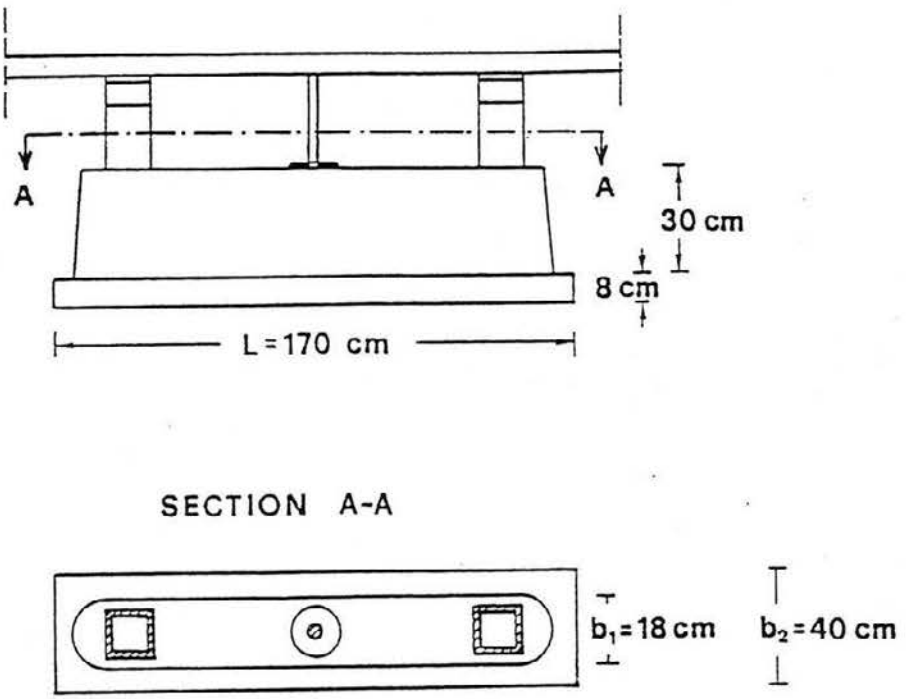

Figure 1. Geometric characteristics of the Schoharie bridge pier model.

Table 1. Summary of tests conditions.

Run number	Upstream flow depth y_1 [m]	Upstream flow velocity V [m/s]	Discharge Q [m^3/s]	Slope S [%]	Froude number Fr	Pier Angle α
1	0.3	0.3	0.223	0.014	0.176	0°
2	0.3	0.6	0.447	0.055	0.352	0°
3	0.3	0.9	0.670	0.123	0.529	0°
4	0.3	0.3	0.223	0.014	0.176	10°
5	0.3	0.6	0.447	0.055	0.352	10°
6	0.3	0.9	0.670	0.123	0.529	10°

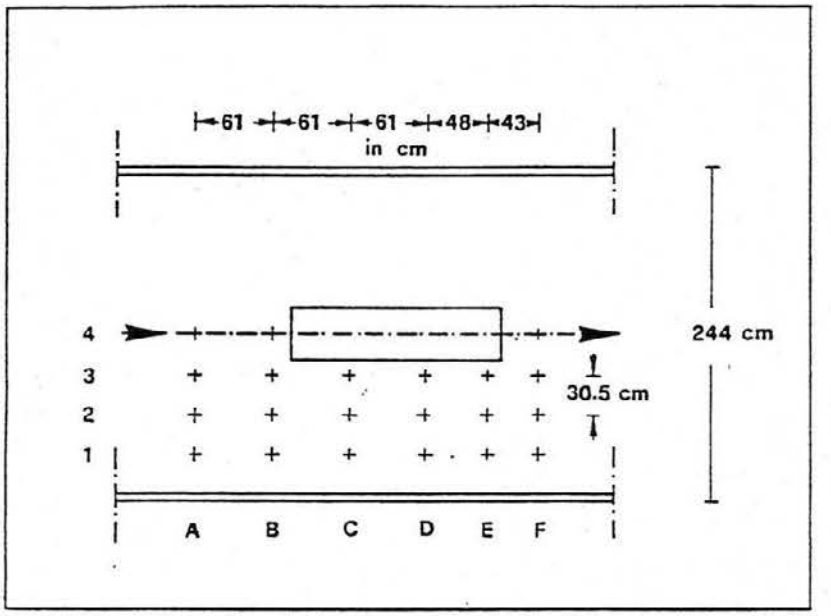

Figure 2. Reference net for aligned pier (α = 0°).

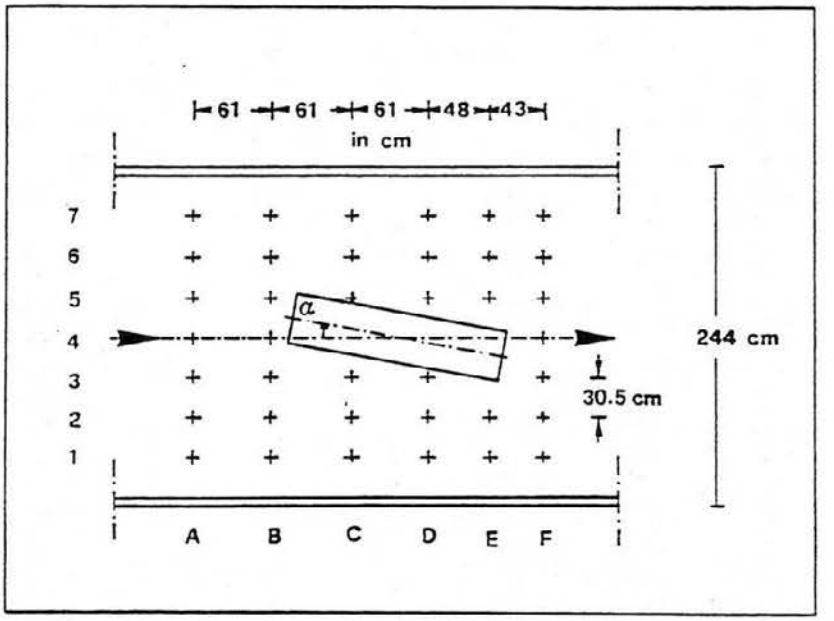

Figure 3. Reference net for angled pier (α = 10°).

RESULTS

Flow Patterns Around the Pier

The downstream velocity distribution was obtained from the measurements at each cross-section and at planes parallel to the flume bed. The flow is slowed down in the central area upstream of the pier, this effect is accentuated for the angled pier. Figure 4 shows the results of the measured velocity distribution at cross-section C from Run 4 for the angled pier. The velocity is maximum on the side the pier is skewed toward, and the maximum velocity is found at an elevation ranging between 0.4 and 0.7 of the undisturbed flow depth y_1. The ratio of the maximum measured velocity to the undisturbed flow velocity is 1.4 for the aligned pier and 1.6 for the angled pier.

Lower velocity is measured in the wake of the pier and asymmetric profiles result for the angled pier. Figure 5 shows a planview of the dimensionless velocity distribution in a section parallel to the bottom of the flume set at an elevation corresponding to 0.4 of the undisturbed flow depth y_1. The overall flow pattern is well described in that maximum velocities are found on the narrow sides of the skewed pier. The number of verticals, however, precludes any detailed analysis of the flow near the pier and along the sidewalls.

Discharge measurements from the orifice inserted in the recirculating pipeline compared favorably with the calculated discharge from the integration of the velocity distribution over the cross-section.

Total Scour Around the Pier

The total scour around the pier combines the effects of two causes: contraction scour due to the higher velocity in the reduced cross-section area near the pier, and local scour due to the horseshoe vortex around the base of the pier. Qualitative and comparative information can be drawn from the photographs and measurements of the flume bed surface at the end of each run.

Under low flow velocities, the extent of scour is relatively limited downstream of the pier. Only the front part of the pier was exposed. At higher velocities (Fig. 6) the scour hole extended alongside the entire pier and a deposition area formed downstream of the pier. The scour pattern of the skewed pier is highly asymmetrical with the maximum scour localized on the side toward which the pier is skewed (Fig. 7). The areas of deposition downstream of the pier were more accentuated. Table 2 summarizes the geometric characteristics of the scour hole in the different runs. It can be noticed that the side slope of the scour hole is steeper for the aligned pier than for the skewed pier.

Contraction Scour

The presence of the pier contracted 7.3% of the channel width at the pier level and 16% at the footing level. The measurements suggest that at least part of the erosion alongside the pier was due to contraction scour. Measured contraction scour depths were

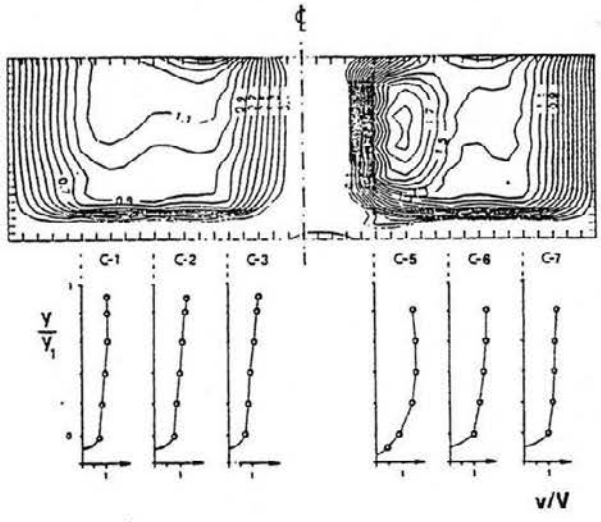

Figure 4. Dimensionless velocity distribution v/V, Run no. 4, sec. C (V = 0.3 m/s, α = 10°).

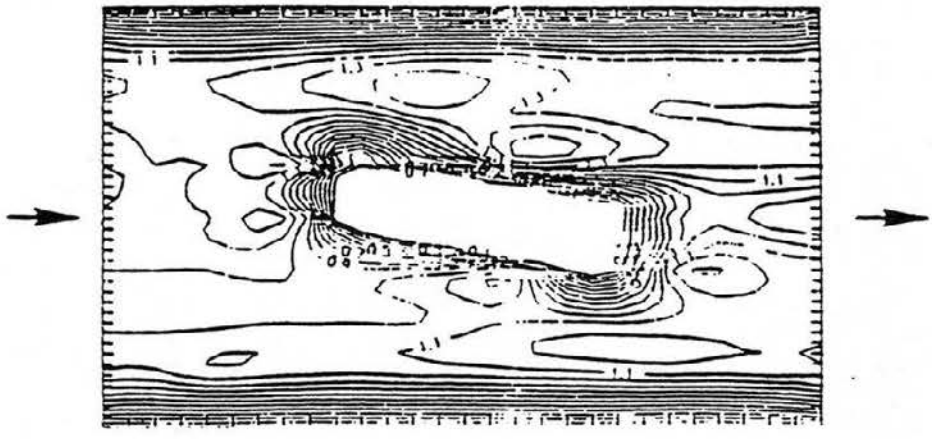

Figure 5. Planview of the dimensionless velocity distribution v/V at a depth y = 0.4 y_1, Run no. 4 (V = 0.3 m/s, α = 10°).

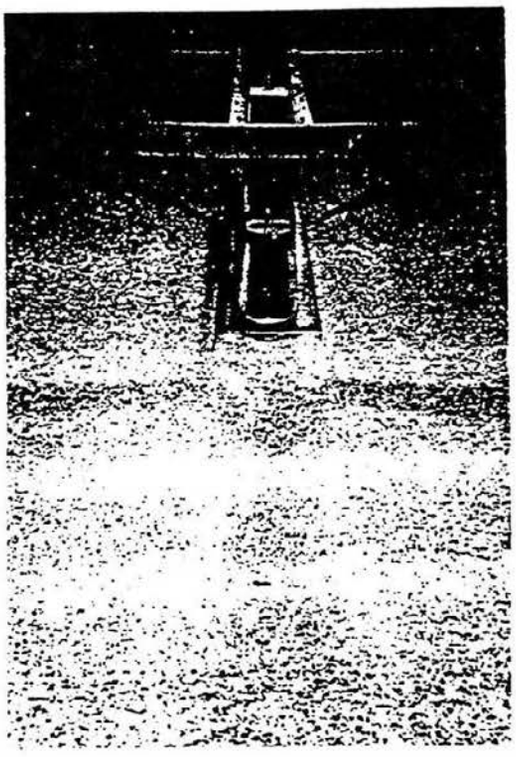

Figure 6. Scour alongside the aligned pier (Run No. 3).

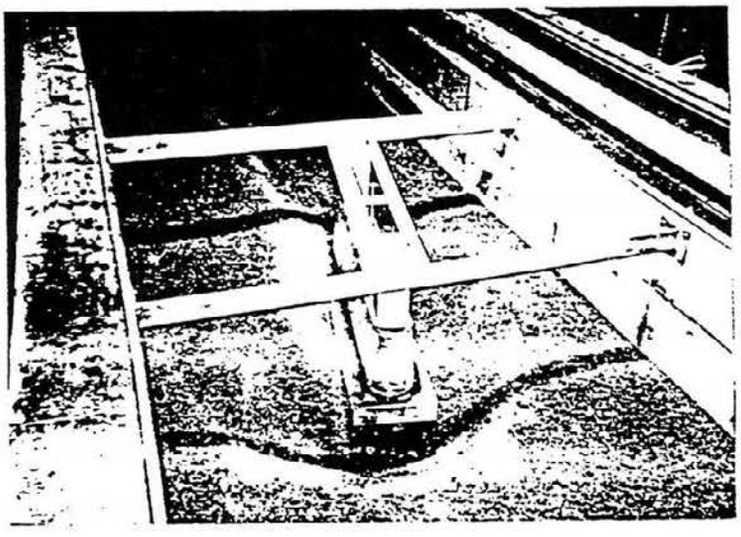

Figure 7. Scour around the skewed pier (Run No. 6).

compared with the depths predicted by Laursen's equation (1980), which computes the contraction scour depth y_c as the difference between the flow depth y_2 in the contracted reach and the upstream flow depth y_1

$$y_c = y_2 - y_1 \tag{1}$$

where y_2 is given by

$$\frac{y_2}{y_1} = \left[\frac{W_1}{W_2}\right]^A \left[\frac{n_2}{n_1}\right]^B \tag{2}$$

in which W is the channel width, n is the Manning's coefficient, A and B are two exponents whose values are tabulated as a function of the mode of transport of the bed material in the contracted reach, and the subscripts 1 and 2, respectively, refer to the undisturbed and contracted reach. Assuming $n_1 = n_2$ while the width ratio is based on the pier width, a constant value of $y_c = 0.035$ m is obtained for all test conditions. This result is compared with the measurements in Figure 8.

Maximum Local Scour Depths

The deepest scour always occurred right in front of the pier where contraction scour is not yet present. This means that the maximum scour depth is not significantly influenced by the contraction scour. It was then possible to compare the measured local scour depths y_{sm} with the maximum calculated scour depth y_{sc} from the following equations:

CSU equation (Richardson et al., 1990):

$$\frac{y_{sc}}{Y_1} = 2.0 \left[\frac{b}{y_1}\right]^{0.65} Fr^{0.43} \tag{3}$$

Laursen (1980) equation:

$$\frac{b}{y_1} = 5.5 \frac{y_{sc}}{y_1} \left[\left[\frac{y_{sc}}{11.5\, y_1} + 1 \right]^{7/6} / \left(\tau_0/\tau_c\right)^{1/2} - 1 \right] \tag{4}$$

and Froehlich (1987) equation:

$$\frac{y_{sc}}{b} = 0.32\, \phi \left[\frac{b'}{b}\right]^{0.62} \left[\frac{y_1}{b}\right]^{0.46} Fr^{0.20} \left[\frac{b}{D_{50}}\right]^{0.08} + 1 \tag{5}$$

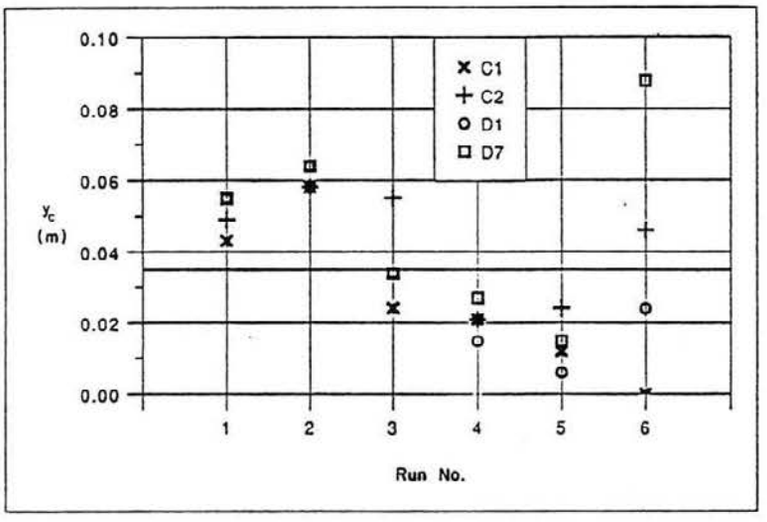

Figure 8. Computed and measured contraction scour depths.

Table 2. Geometric characteristics of the scour hole.

Run number	Upstream flow velocity V [m/s]	Pier angle α	Scour depth y_s [m]	Scour width [m]	Side slope
1	0.3	0°	0.076	0.152	1.00
2	0.6	0°	0.158	0.274	0.87
3	0.9	0°	0.305	0.457	0.75
4	0.3	10°	0.122	0.213	0.88
5	0.6	10°	0.241	0.357	0.75
6	0.9	10°	0.427	0.518	0.61

where, y_1 is the upstream flow depth, b is the pier width, Fr is the Froude number, τ_o is the bed shear stress, τ_c is the critical bed shear stress, b′ is the projected pier width normal to the flow direction, D_{50} is the mean sediment size, and ϕ is a pier-shape factor equal to $\phi=1$ for a round-nosed pier.

Since the complex pier geometry provides both the pier width and the footing as possible values for b, calculations of scour depth using both values are considered separately. Figs. 9 and 10 illustrate the results.

It is concluded from our experimental results on Figures 9 and 10 that the pier width, rather than the foundation width, is more appropriate in calculating local pier scour. In general, these equations tend to overestimate the scour depth, with the exception of Laursen's equation which underestimates the scour depth at low Froude numbers.

Influence of the Pier Angle

These experiments allow direct comparison between the scour depth $y_{s10°}$ when the pier is angled at 10°, and pier scour of an aligned pier $y_{s0°}$, the other parameters being equal. The ratio $y_s^* = y_{s10°}/y_{s0°}$ between corresponding scour depths separates the effect of the pier angle α in the case of these experiments. Figure 11 compares the values of y_s^* from laboratory measurements obtained from the three scour depth equations. From Fig. 11, a trend is noticed in that the effect of pier orientation seems correlated to the Froude number, decreasing when the Froude number increases. The possibility of a dependence of the angle correction coefficient on the flow velocity (or Froude number) is not unreasonable. First of all, the strength of the vortices depends on both the upstream velocity and the projected pier width perpendicular to the flow direction (which is affected by the pier angle). The influence of the angle of attack might be related to the flow average velocity in the sense that as the Froude number increases (here velocity and Froude number are used interchangeably because the depth remains constant) and the inclination of the pier increases the scour depth cannot increase indefinitely, but must approach an ultimate limit.

Maximum Velocities

Some riprap design methods are based on velocity measurements. Typically, a representative riprap size or stone weight can be determined from average velocity, bottom velocity or a reference velocity. For instance, the Isbash formula relates the riprap stone weight to the sixth power of the velocity. It is then clear that riprap design is highly sensitive to velocity measurements.

In the particular case of riprap design around piers, the velocity increases due to both the contraction effect and the turbulence. Maximum and minimum instantaneous velocities were measured at each point to provide an indication of the maximum velocity fluctuations normally expected around bridge piers. The measurements show that the maximum ratio of the maximum point velocity v_{max} to the average undisturbed velocity V decreases with increasing velocity. The maximum measured ratio is as high as 1.8 and it is registered during Run no. 4.

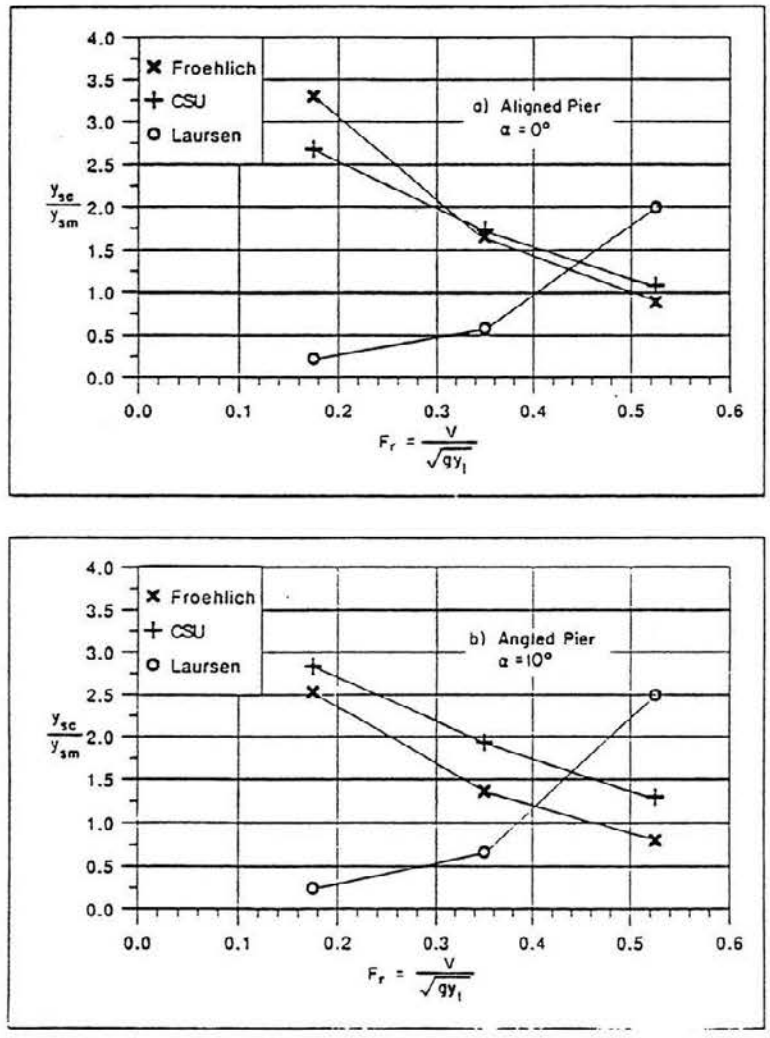

Figure 9. Ratio of computed to measured scour depths using b = pier width.

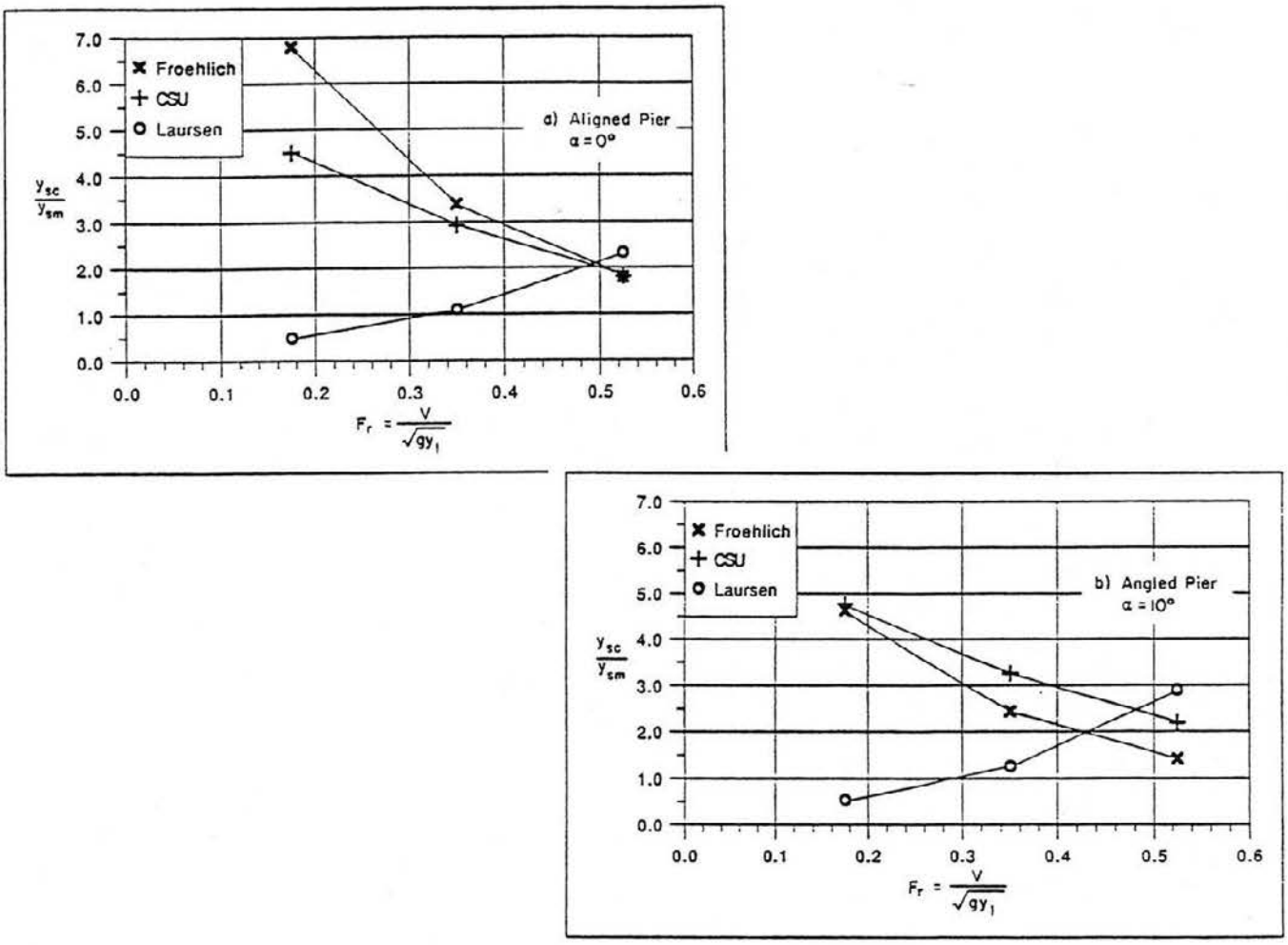

Figure 10. Ratio of computed to measured scour depths using b = footing width.

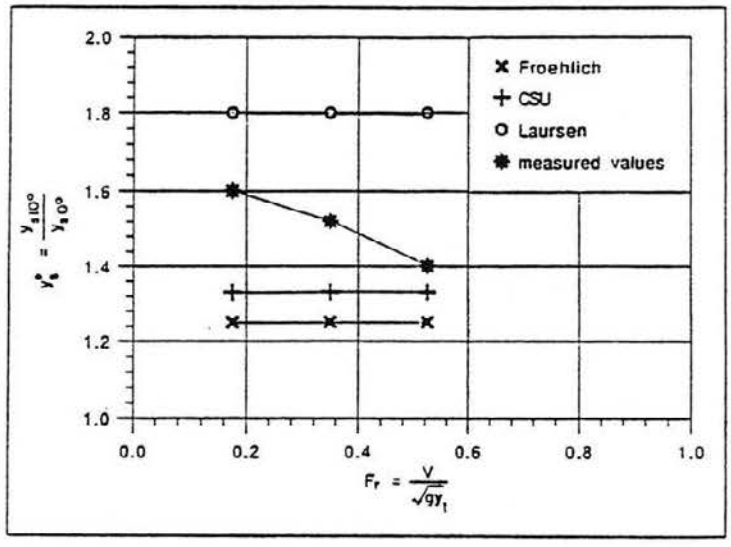

Figure 11. Effect of pier alignment on pier scour.

Possible Armoring Effect

Two samples of the bed material from the surface of the front part of the scour hole were taken and analyzed after the tests. The sieve analyses before and after Run no. 3 indicate that the amount of particles smaller than approximately 2 mm on the scour hole surface had significantly diminished while all the particles smaller than 0.5 mm had been totally washed out. The tests results, however, do not indicate significant armoring effects.

Comparison with Prototype Scour Depth

At a linear scale of 1:15, the Froude number analogy gives a velocity scale 1:3.87. The prototype conditions for which field data were available (Richardson et al., 1988) are closely modeled in Run no. 3. The measured scour depth in the experiments scaled to 4.57 m of scour depth at the prototype scale which compares with the field measured scour depth of 4.27 m.

CONCLUSIONS

The following considerations can be drawn from these laboratory experiments on velocity and scour depth measurements around a model of the Schoharie bridge pier:

1. The time-average point velocity distribution in cross and plan sections shows two areas of increased velocities alongside the pier. The recorded values were as high as 1.6 times the mean upstream approach velocity.

2. With the initial bed surface at the same elevation as the top of the footing, scour depth calculations based on pier width are more appropriate than the footing width.

3. The measured local scour depths are in reasonable agreement with the local scour depths calculated from three scour equations. All equations perform better at higher values of the Froude number (Fr > 0.3).

4. The ratio y_s^* of the angled pier scour depth $y_{s(10°)}$ to the aligned pier scour depth $y_{s(0°)}$ decreases with increasing Froude number as shown in Fig. 11. Although few experiments are considered, the detected trend is nevertheless significant.

5. The ratio of the maximum velocity fluctuations to the mean undisturbed upstream velocity decreases as the mean flow velocity increases. Values as high as 1.8 times the mean approach velocity were measured around the angled pier.

6. From the measurements reported at the prototype scale of 1:15, the run with an aligned pier and the maximum velocity (3.48 m/s) gave a scour depth at the prototype scale of 4.57 m which compares with the field measured scour depth of 4.27 m.

APPENDIX I. REFERENCES

Froehlich, D.C., 1987, "Local Scour at Bridge Piers from Onsite Measurements", U.S. Geological Survey, Water Resources Division.

Laursen, E.M., 1980, "Predicting Scour at Bridge Piers and Abutments", General Report No. 3, University of Arizona.

Richardson, E.V., Simons, D. and P.Y. Julien, 1990, "Highways in the River Environment", U.S. Department of Transportation, FHWA-HI-90.016.

Richardson, E.V., Ruff, J.F. and T.E. Brisbane, 1988, "Schoharie Creek Bridge Model Study", Proceedings of the ASCE, Hydraulic Division Spec. Conference, Colorado Springs, Colorado, August.

Santoro, V.C., 1989, "Experimental Study on Scour and Velocity Field around Bridge Piers", Thesis in partial fulfillment of the requirements for Master of Science degree, Colorado State University, Fort Collins, Colorado, July.

APPENDIX II. NOTATIONS

b	pier width
b'	projected width of the pier in perpendicular direction to the main flow
D_{50}	mean sediment size
Fr	Froude number
l	length of the pier
n	Manning roughness coefficient
Q	total discharge
V	mean approach flow velocity
y_1	upstream flow depth
y_2	flow depth in the contracted reach
y_c	contraction scour
y_s	maximum depth of scour below mean bed level
y_{sc}	calculated local scour depth
y_{sm}	measured local scour depth
$y_{s10°}$	scour depth at an angle $\alpha = 10°$
$y_{s0°}$	scour depth at an angle $\alpha = 0°$
y_s^*	ratio of $y_{s10°} / y_{s0°}$
W	width of the channel
α	angle of attack of the flow
ϕ	pier shape factor, $\phi = 1$ for round-nosed piers
τ_o	bed shear stress
τ_c	critical shear stress

SCOUR DOWNSTREAM OF GRADE-CONTROL STRUCTURES

By Noel E. Bormann[1] and Pierre Y. Julien,[2] Members, ASCE

ABSTRACT: A theoretical investigation of local scour downstream of grade-control structures based on two-dimensional jet diffusion and particle stability is experimentally verified. Turbulent jet diffusion reduces fluid velocity near the bed particles and equilibrium scour is obtained when noncohesive bed particles cannot be removed from the scour hole. Equilibrium scour depth is written as a function of velocity, flow depth and particle size. The theoretically derived equation is remarkably similar to the regression equations reported in the literature. The experimental investigation uses a large-scale physical model with unit discharge up to 2.5 m^2/s (27 sq ft/sec) and scour depths exceeding 1.4 m (4.6 ft). When combined with previous data sets at smaller scales, a total of 231 scour-depth measurements cover a wide variety of conditions: wall to vertical jets, small to large flow submergence, and various face angle slopes. The agreement between calculated scour depths and laboratory measurements is satisfactory considering the wide variety of configurations analyzed.

INTRODUCTION

Grade-control structures prevent excessive channel-bed degradation in alluvial channels. The erosive action of flowing water, however, causes significant downstream local scour, which may undermine these structures. Structural design considerations must therefore include adequate protective measures against local scour downstream of grade-control structures. In turn, appropriate protective measures can only be designed with a full understanding the mechanics, location and extent of downstream scour.

More than 50 years of laboratory measurements of scour depths under various flow conditions and structure configurations are available. Significant studies of local scour under a two-dimensional free jet downstream of hydraulic structures include those of Schoklitsch (1932), Veronese (1937), Jaeger (1939), Eggenberger (1943), Mueller and Eggenberger (1944), Hartung (1959), Damle et al. (1966), Smith and Strang (1967), Chee and Padiyar (1969), Chee and Kung (1971), Chee et al. (1972), Martins (1975), Laursen and Flick (1983), and Akashi and Saitou (1986). Experiments with two-dimensional submerged jets have been reported by Laursen (1952), Tarapore (1956), LeFeuvre (1965), Carstens (1966), Breusers (1967a, 1967b), Rajaratnam and Subramanya (1968), Altinbilek and Basmaci (1973), Altinbilek and Okyay (1973), and Rajaratnam (1981). Most existing scour-depth equations are summarized in Mason and Arumugam (1985). Maximum scour-depth equations were typically obtained from small-scale laboratory experiments with unit discharges less than 0.093 m^2/s (1 sq ft/sec) and scour depths not exceeding 0.8 m (2.9 ft).

The purpose of this paper is twofold: (1) Derive an equilibrium scour equation based on the concepts of jet diffusion and particle stability in scour

[1]Asst. Prof., Dept. of Civ. Engrg., Gonzaga Univ., Spokane, WA 99258.
[2]Assoc. Prof., Dept. of Civ. Engrg., Colorado State Univ., Fort Collins, CO 80523.

Note. Discussion open until October 1, 1991. To extend the closing date one month, a written request must be filed with the ASCE Manager of Journals. The manuscript for this paper was submitted for review and possible publication on February 28, 1990. This paper is part of the ***Journal of Hydraulic Engineering***, Vol. 117, No. 5, May, 1991. ©ASCE, ISSN 0733-9429/91/0005-0579/$1.00 + $.15 per page. Paper No. 25829.

348

TABLE 2. Summary of Local Scour Equations: $D_s + D_p = Kq^a U_o^b \Delta H^c Y_i^d \beta'^e / g^f d_s^i$

Investigator (1)	K (2)	a (3)	b (4)	c (5)	d (6)	e (7)	f (8)	i (9)
Schoklitsch (1932)	0.5	0.57	0	0.2	NA	NA	NA	0.32
Veronese (1937a)	0.2	0.54	0	0.225	NA	NA	NA	0.42
Veronese (1937b)	1.9	0.54	0	0.225	NA	NA	NA	NA
Jaeger (1939)	0.6	0.50	0	0.25	0.33	NA	NA	0.33
Eggenberger (1943)	1.4	0.60	0	0.50	NA	NA	NA	0.40
Mueller and Eggenberger (1944)	—[a]	0.60	0	0.50	NA	NA	0.8	0.40
Hartung (1959)	1.4	0.64	0	0.36	NA	NA	NA	0.32
Damle et al. (1966)	0.6	0.50	0	0.50	NA	NA	NA	NA
Chee and Padiyar (1969)	2.1	0.67	0	0.18	NA	NA	NA	0.06
Chee and Kung (1971)	1.7	0.60	0	0.20	NA	NA	NA	0.10
Chee et al. (1972)	1.9	0.60	0	0.20	NA	−0.4	NA	0.10
Martins (1975)	1.5	0.60	0	0.10	NA	NA	NA	NA
Chee and Yuen (1985)	0.6	0.45	0.55	NA	NA	1.0[b]	NA	0.10
Mason and Arumugam (1985)[c]	3.27	0.60	0	0.05	0.15	NA	0.30	0.10
Bormann (1988a)	0.7	0.45	1.0	NA	0.12	0.66[b]	0.73	0.30
Eq. 12	—[d]	0.60	1.0	NA	NA	1.0[b]	0.8	0.4

[a]K depends on jet configuration.
[b]Uses sin β'.
[c]Summary of many previous equations, values of exponent vary with H.
[d]Constant depends on inlet geometry and sediment properties.
Note: NA = not applicable.

earlier are in metric units. Most empirical scour-depth studies listed in Table 2 are concerned with vertically impinging jets, and only three studies (Chee and Kung 1971; Chee et al. 1972; and Yuen 1984) relate to nonvertical free-jet conditions. Jaeger (1939), Eggenberger (1943), and Mueller and Eggenberger (1944) studied horizontal jets entering tailwater. Other studies of submerged slightly inclined jets have established the similarity of scour-hole geometry and dependence on flow conditions (e.g., Farhoudi and Smith 1985; Rajaratnam 1981). The equation of Mason and Arumugam (1985), developed from an extensive literature review, appears to be representative of previous investigations using vertical free jets. The empirical equation of Chee and Yuen (1985), and a summary of Yuen (1984), attempts to incorporate jet diffusion into the prediction of local scour caused by two-dimensional jets. An empirical equation developed by Bormann (1988a) accounts for jet diffusion and is applicable to free and submerged jets at any orientation. Eq. 12 proposed here reflects both jet diffusion and the stability of sediment particles in a scour hole.

Examination of Table 2 leads to several conclusions: (1) The agreement of exponent a is remarkable; (2) the value of exponent i is quite similar to approximately half of the equations listed, the other half have values of 0.1; and (3) the proposed Eq. 12 is comparable to the other equations listed in Table 2.

Large-Scale Experiments

A large-scale experimental investigation with unit discharges ranging from 0.3 to 2.5 m^2/s (3 to 27 sq ft/sec) and maximum scour depths reaching 1.4

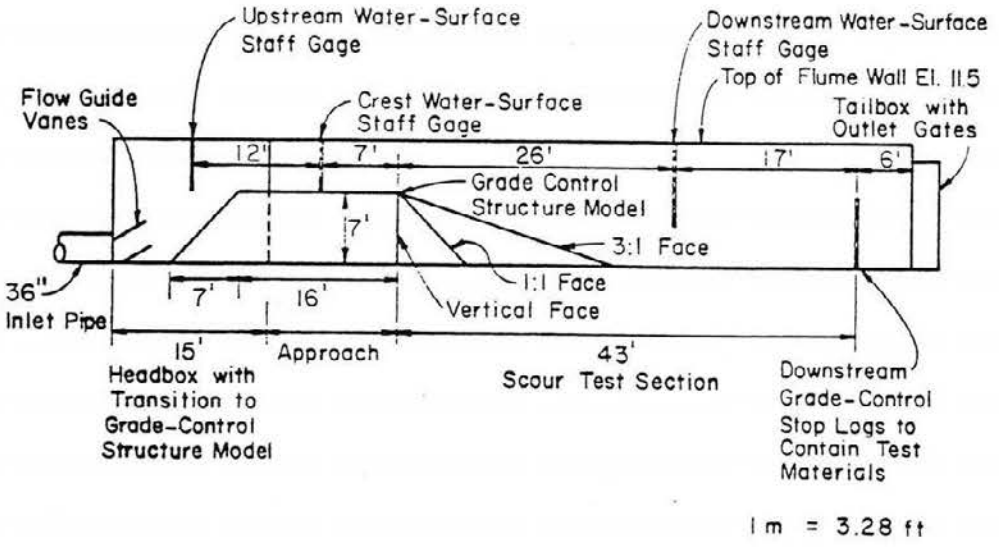

FIG. 3. Sketch of Large-Scale Test Flume

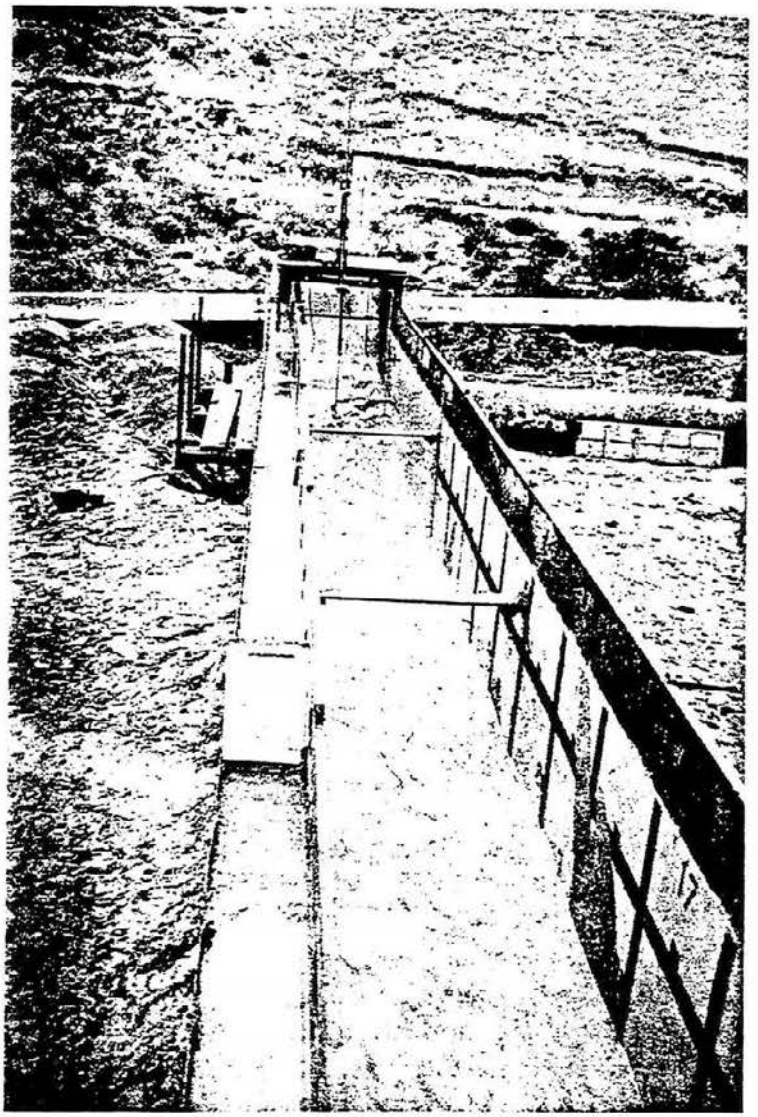

FIG. 4(*a*). Test Flume at Low Flow

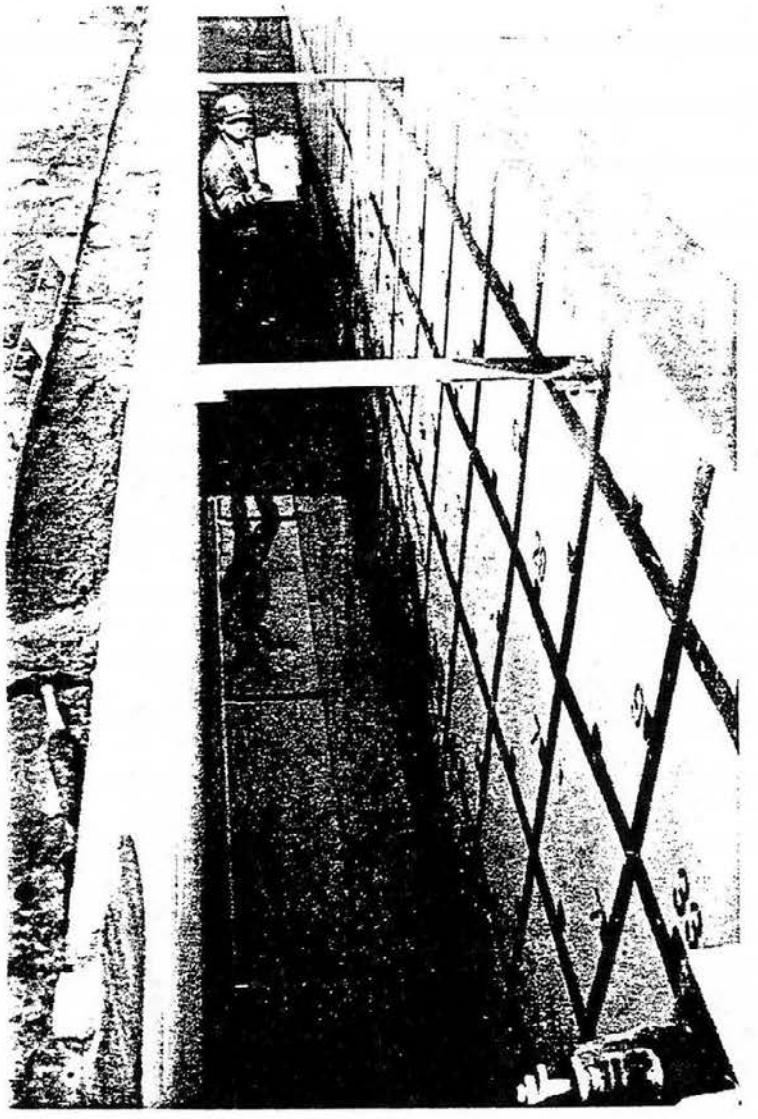

FIG. 4(*b*). Test Flume with Scour Depth Approaching 2 m

m (4.6 ft), was carried out using a large outdoor flume at the Colorado State University Engineering Research Center. The installation consisted of a headbox/inlet, an approach section, a scour-test section, and a tailbox/outlet (see Fig. 3). A 0.91-m (3-ft) diameter mixed flow pump supplied up to 2.7 m^3/s (75 cu ft/sec) to the flume test section. The flume had an overall depth of 3.5 m (11.5 ft), an overall length of 27.4 m (90 ft), and a width of 0.91 m (3 ft). The elevation of the grade-control structure model crest was set at 2.13 m (7 ft) above the flume floor. When scaled according to the Froude similitude criteria, the model scale is much larger than any previously reported tests. In fact, at this scale, the model tests overlap some prototype scour values, as discussed in Bormann (1988b).

The scour test section is defined from the crest of the grade-control structure model. A steel plate was welded to the flume walls to form the various structure face slopes tested. The scour test section exceeded 13 m (43 ft) from the crest to the downstream grade-control for the model. Downstream stop logs controlled the drop height from the crest to the sediment bed level. The water in the flume flowed over the stop logs into the tailbox, which

TABLE 3. Summary of Experimental Data

Test number (1)	Y_o (m) (2)	U_o (m/s) (3)	D_p (m) (4)	Y_t (m) (5)	D_s (m) (6)	X_s (m) (7)	d_{90} (mm) (8)	d_{50} (mm) (9)	λ radian (10)	Relative submergence (%) (11)	q (m^2/s) (12)	β′ radian (13)	L_s (m) (14)
1	0.94	2.38	0.15	1.25	1.12	6.10	1.58	0.30	0.79	90	2.25	0.21	6.23
2	0.94	2.38	0.15	1.25	1.02	6.10	1.58	0.30	0.79	90	2.25	0.19	6.21
3	0.94	2.38	0.15	0.25	1.02	6.10	1.58	0.30	0.79	90	2.25	0.19	6.21
4	0.57	3.92	0.15	0.98	1.46	6.10	1.58	0.30	0.79	71	2.22	0.26	6.31
5	0.57	3.92	0.15	0.88	1.40	7.93	1.58	0.30	0.79	63	2.22	0.19	8.08
6	0.88	1.95	0.15	1.07	1.01	6.71	1.58	0.30	0.79	86	1.72	0.17	6.81
7	0.88	1.95	0.15	1.07	1.10	4.88	1.58	0.30	0.79	86	1.72	0.25	5.04
8	0.88	1.95	0.15	1.07	1.08	5.49	1.58	0.30	0.79	86	1.72	0.22	5.62
9	0.48	3.58	0.15	0.82	1.16	5.49	1.58	0.30	0.79	67	1.71	0.23	5.64
10	0.48	3.58	0.15	0.82	1.07	5.49	1.58	0.30	0.79	66	1.71	0.22	5.62
11	0.48	3.58	0.15	0.82	1.14	6.10	1.58	0.30	0.79	66	1.71	0.21	6.23
12	0.48	3.58	0.15	0.82	1.28	6.10	1.58	0.30	0.79	66	1.71	0.23	6.26
13	1.19	1.52	0.25	1.50	0.72	4.27	1.58	0.30	0.79	93	1.81	0.22	4.38
14	0.75	2.38	0.25	1.09	0.98	7.32	1.58	0.30	0.79	70	1.78	0.17	7.42
15	0.46	3.84	0.25	0.92	1.30	6.10	1.58	0.30	0.79	56	1.78	0.25	6.29
16	1.16	2.07	0.25	1.44	0.55	6.10	1.58	0.30	0.79	91	2.40	0.13	6.15
17	0.55	4.23	0.25	0.91	1.32	6.71	1.58	0.30	0.79	52	2.32	0.23	6.89
18	1.17	1.65	0.05	1.28	0.66	4.27	1.58	0.30	0.79	93	1.93	0.17	4.33
19	0.79	2.87	0.05	0.94	1.08	6.71	1.58	0.30	0.79	70	2.27	0.17	6.80
20	0.54	4.27	0.05	0.71	1.21	6.71	1.58	0.30	0.79	51	2.32	0.19	6.82
21	0.52	3.73	0.05	0.86	0.97	4.88	1.58	0.30	0.79	71	1.94	0.21	4.98
22	0.53	3.76	0.05	0.74	1.26	7.93	1.58	0.30	0.79	62	1.99	0.16	8.03
23	1.13	2.19	0.23	1.46	0.96	4.27	1.71	0.45	0.79	92	2.47	0.27	4.43
24	0.58	3.97	0.23	1.08	1.06	6.71	1.71	0.45	0.79	70	2.32	0.19	6.83
25	0.55	4.23	0.23	0.88	1.39	7.93	1.71	0.45	0.79	53	2.32	0.20	8.09
26	1.04	1.37	0.23	1.26	0.70	3.66	1.71	0.45	0.79	92	1.42	0.25	3.77
27	0.43	3.40	0.23	0.87	0.89	4.88	1.71	0.45	0.79	70	1.46	0.22	5.00
28	0.40	3.70	0.23	0.66	1.10	4.88	1.71	0.45	0.79	47	1.46	0.27	5.06
29	0.69	0.88	0.23	0.93	0.27	2.44	1.71	0.45	0.79	96	0.61	0.20	2.49
30	0.34	1.71	0.23	0.59	0.29	3.05	1.71	0.45	0.79	72	0.58	0.17	3.09
31	0.20	3.00	0.23	0.45	0.56	3.66	1.71	0.45	0.79	46	0.60	0.21	3.74
32	0.19	3.11	0.23	0.39	0.62	3.05	1.71	0.45	0.79	33	0.59	0.27	3.17
33	0.25	1.36	0.23	0.48	0.10	1.83	1.71	0.45	0.79	72	0.34	0.18	1.86
34	0.14	2.47	0.23	0.39	0.15	1.83	1.71	0.45	0.79	48	0.34	0.20	1.87
35	0.12	2.80	0.23	0.30	0.39	2.44	1.71	0.45	0.79	20	0.33	0.25	2.52
36	0.12	2.87	0.23	0.28	0.93	1.83	1.71	0.45	0.79	15	0.33	0.56	2.16
37	1.17	2.01	0.38	1.65	0.58	4.27	1.71	0.45	1.57	95	2.36	0.22	4.37
38	0.58	3.97	0.38	1.22	0.94	8.54	1.71	0.45	1.57	70	2.32	0.15	8.64
39	0.85	1.71	0.38	1.30	0.25	1.22	1.71	0.45	1.57	94	1.46	0.48	1.37
40	0.43	3.41	0.38	1.03	0.59	6.10	1.71	0.45	1.57	73	1.46	0.16	6.17
41	0.39	3.77	0.38	0.78	1.05	5.49	1.71	0.45	1.57	45	1.46	0.25	5.67
42	0.35	4.22	0.38	0.60	1.43	4.88	1.71	0.45	1.57	24	1.48	0.36	5.20
43	0.16	3.90	0.38	0.79	0.31	4.27	1.71	0.45	1.57	68	0.62	0.16	4.32
44	0.20	2.96	0.38	0.58	0.47	3.05	1.71	0.45	1.57	42	0.59	0.27	3.17
45	0.18	3.27	0.38	0.48	0.64	3.05	1.71	0.45	1.57	20	0.58	0.32	3.21
46	0.16	3.74	0.38	0.39	0.88	4.27	1.71	0.45	1.57	1	0.60	0.29	4.45
47	0.31	0.91	0.38	0.71	0.28	0.61	1.71	0.45	1.57	91	0.29	0.83	0.90
48	0.22	1.39	0.38	0.60	0.14	3.05	1.71	0.45	1.57	70	0.30	0.17	3.09
49	0.12	2.45	0.38	0.51	0.18	3.05	1.71	0.45	1.57	42	0.31	0.18	3.10
50	0.11	2.61	0.38	0.44	0.28	1.83	1.71	0.45	1.57	20	0.29	0.35	1.94
51	0.09	3.20	0.38	0.29	1.39	1.22	1.71	0.45	1.57	1	0.30	0.97	2.15
52	0.26	1.13	0.08	0.45	0.23	1.22	1.71	0.45	1.57	95	0.29	0.24	1.26

TABLE 3. (*Continued*)

(1)	(2)	(3)	(4)	(5)	(6)	(7)	(8)	(9)	(10)	(11)	(12)	(13)	(14)
53	0.14	2.09	0.08	0.29	0.36	1.83	1.71	0.45	1.57	70	0.29	0.23	1.88
54	0.12	2.45	0.08	0.24	0.46	2.44	1.71	0.45	1.57	50	0.30	0.22	2.50
55	0.46	1.34	0.08	0.78	0.11	0.61	1.71	0.45	1.57	94	0.62	0.29	0.64
56	0.17	3.71	0.08	0.47	0.40	2.44	1.71	0.45	1.57	70	0.63	0.19	2.48
57	0.22	2.68	0.08	0.37	0.53	3.05	1.71	0.45	1.57	56	0.59	0.20	3.11
58	1.01	1.46	0.08	1.18	0.29	1.83	1.71	0.45	1.57	94	1.47	0.20	1.86
59	0.38	3.86	0.08	0.69	0.77	4.27	1.71	0.45	1.57	70	1.45	0.20	4.35
60	0.25	1.36	0.23	0.48	0.12	1.83	1.71	0.45	1.57	71	0.34	0.19	1.86
61	0.14	2.50	0.23	0.38	0.21	1.83	1.71	0.45	1.57	44	0.34	0.24	1.88
62	0.12	2.80	0.23	0.29	0.42	1.83	1.71	0.45	1.57	19	0.32	0.34	1.94
63	0.62	0.94	0.23	0.87	0.17	1.83	1.71	0.45	1.57	95	0.59	0.22	1.87
64	0.35	1.66	0.23	0.58	0.40	3.66	1.71	0.45	1.57	70	0.58	0.17	3.71
65	0.20	2.92	0.23	0.45	0.52	3.66	1.71	0.45	1.57	45	0.59	0.20	3.73
66	0.19	3.11	0.23	0.39	0.62	2.44	1.71	0.45	1.57	33	0.59	0.33	2.58
67	1.10	1.34	0.23	1.34	0.37	3.05	1.71	0.45	1.57	93	1.47	0.19	3.11
68	0.34	4.45	0.23	0.89	0.70	4.88	1.71	0.45	1.57	74	1.53	0.19	4.96
69	0.40	3.59	0.23	0.67	1.04	4.27	1.71	0.45	1.57	49	1.44	0.29	4.45
70	1.08	1.34	0.00	1.15	0.28	1.83	1.71	0.45	1.57	94	1.45	0.15	1.85
71	0.31	4.65	0.00	0.65	0.70	3.05	1.71	0.45	1.57	70	1.45	0.23	3.13
72	0.67	0.88	0.00	0.70	0.16	0.61	1.71	0.45	1.57	94	0.59	0.25	0.63
73	0.21	2.84	0.00	0.33	0.52	3.05	1.71	0.45	1.57	61	0.60	0.17	3.09
74	1.18	2.01	0.00	1.19	0.60	3.05	1.71	0.45	1.57	89	2.37	0.19	3.11
75	0.54	3.79	0.00	0.79	0.89	4.27	1.71	0.45	1.57	62	2.04	0.21	4.36
76	1.18	1.89	0.08	1.30	0.47	3.05	1.71	0.45	1.57	91	2.23	0.18	3.10
77	0.56	3.89	0.08	0.90	1.16	6.10	1.71	0.45	1.57	70	2.18	0.20	6.22
78	1.16	1.98	0.23	1.41	0.59	3.66	1.71	0.45	1.57	91	2.31	0.22	3.75
79	0.61	4.05	0.23	1.05	0.94	6.10	1.71	0.45	1.57	68	2.45	0.19	6.21
80	1.13	2.16	0.23	1.47	0.59	4.27	1.71	0.45	0.32	91	2.44	0.19	4.35
81	1.10	1.34	0.23	1.35	0.30	1.83	1.71	0.45	0.32	94	1.47	0.28	1.90
82	0.42	3.36	0.23	0.85	0.71	4.27	1.71	0.45	0.32	70	1.42	0.22	4.37
83	0.62	0.94	0.23	0.99	0.15	1.22	1.71	0.45	0.32	96	0.59	0.30	1.28
84	0.24	2.53	0.23	0.58	0.57	2.44	1.71	0.45	0.32	71	0.61	0.32	2.56
85	0.19	2.91	0.23	0.44	1.52	5.49	1.71	0.45	0.32	44	0.55	0.31	5.76
86	0.16	2.08	0.23	0.46	0.48	2.44	1.71	0.45	0.32	69	0.33	0.28	2.54
87	0.13	2.41	0.23	0.37	0.56	2.44	1.71	0.45	0.32	44	0.32	0.31	2.56
88	0.11	2.65	0.23	0.28	0.97	3.66	1.71	0.45	0.32	18	0.29	0.32	3.85

controlled the tailwater depth in the test section. A point gage mounted on a mechanical carriage was used to measure the scoured bed elevations in the center of the flume. Water-surface elevations were measured using three staff gages. Fig. 4 shows two photographs of the experimental flume. In Fig. 4(*a*), a small test flow of 0.28 m^2/s (3.1 sq ft/sec) is shown. Fig. 4(*b*) shows the flume after a test flow of 2.32 m^2/s (25 sq ft/sec). The structure slope is set at 3H:1V and scour depth in this particular run exceeded 1.98 m (6.5 ft) and reached the flume's bottom panel.

Details on model operation, data collection procedures and accuracy are available in Bormann (1988a). The data set contains 99 tests, of which 11 were deleted because scour exposed the flume bottom, leaving 88 equilibrium scour-depth measurements summarized in Table 3. The parameters listed in Table 3 are sketched in Fig. 1, while d_{50} and d_{90} denote the standard sieve diameter for which 50% and 90% of the particles are finer. Flow submergence is calculated by dividing the tailwater depth above the structure crest

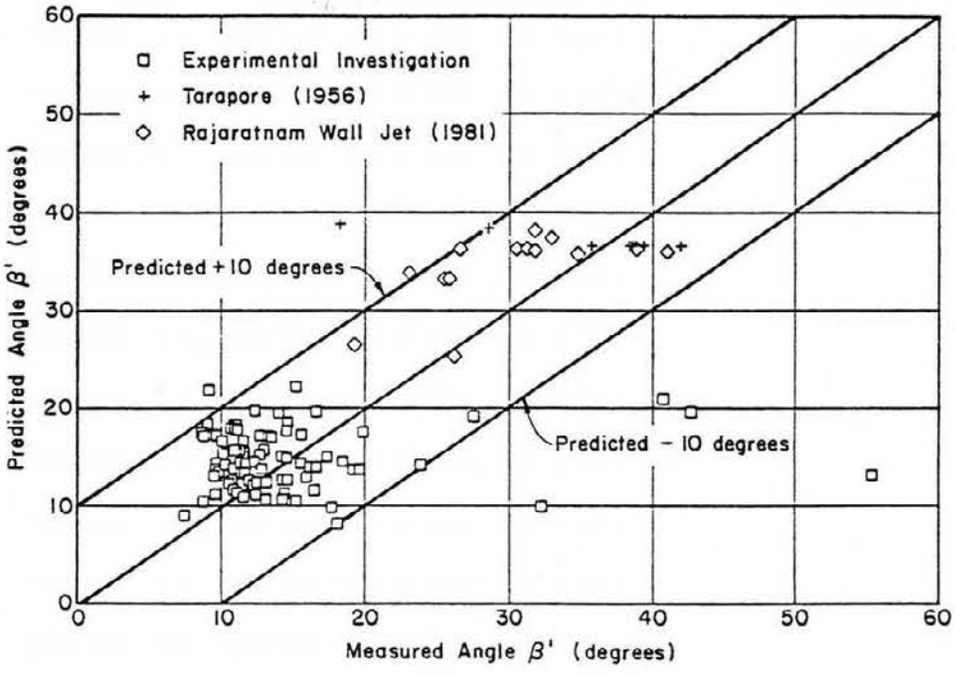

FIG. 5. Comparison of Measured and Calculated Jet Angle β′

by the flow depth on the structure. Note that the flow depth on the structure differs from the thickness of the jet entering tailwater because the pressure distribution is not hydrostatic.

The data set in Table 3 has been combined with other experimental data sets to determine the jet diffusion angle β′. Tarapore (1956) and Rajaratnam (1981) obtained a measurement of β′ for deeply submerged jets, while Table 3 covers tailwater depths not exceeding the inflow water depth. The data set including 109 data points covers a wide spectrum of submergence conditions, both for reattached wall jets with variable drop height and for wall jets with zero drop height. The angle β′ in radians is obtained by regression analysis:

$$\beta' = 0.316 \sin \lambda + 0.15 \ln \left(\frac{D_p + Y_o}{Y_o} \right) + 0.13 \ln \left(\frac{Y_t}{Y_o} \right)$$

$$- 0.05 \ln \left(\frac{U_o}{\sqrt{gY_o}} \right) \quad \ldots\ldots\ldots\

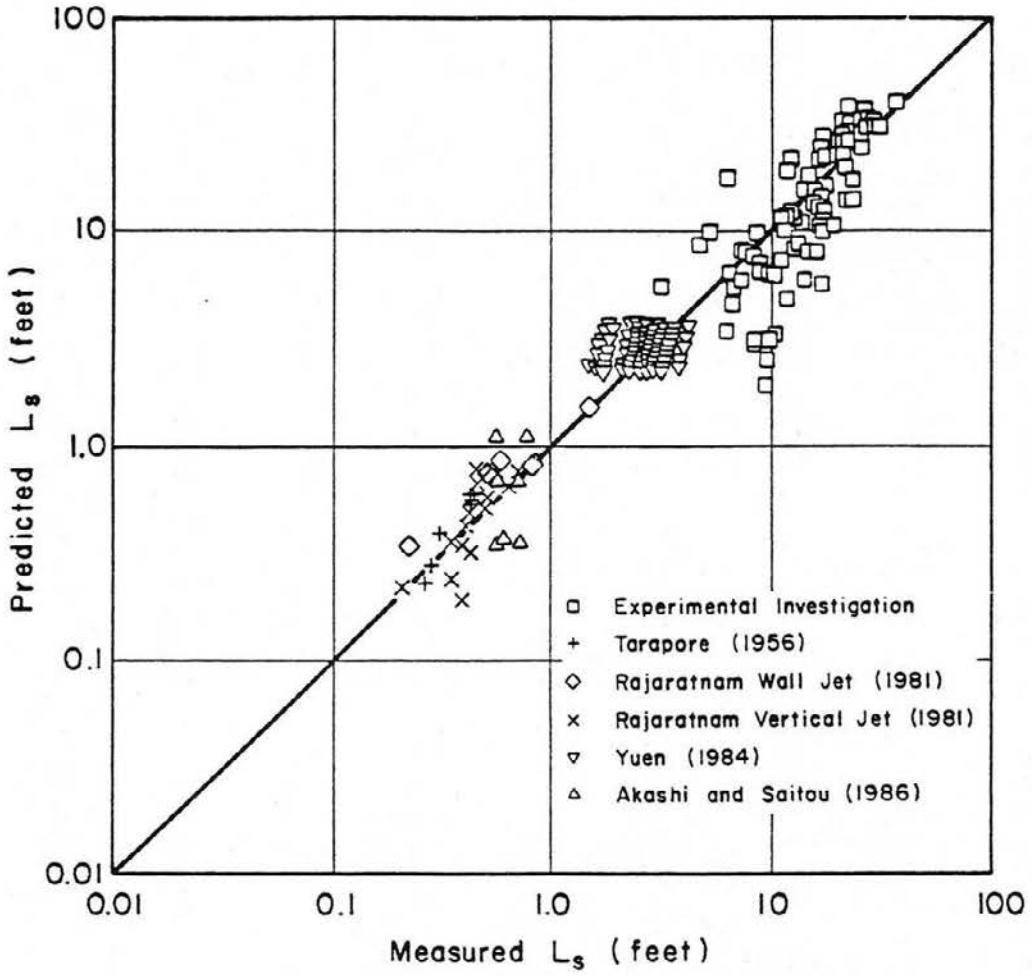

FIG. 6. Comparison of Measured and Calculated Diffusion Length L_s

tical jets, wall jets, free overfall jets, submerged jets and partially submerged flow over large scale drop structures with vertical and inclined (3H:1V and 1H:1V) face slopes. Fig. 6 compares observed diffusion lengths L_s with the theoretical values calculated from Eq. 10. The following numerical values of the parameters were selected based on the evaluation of relevant flow and particle conditions: $x = 0.5$, $\alpha = \beta'$, $\gamma_s = 2.7\gamma$, $B = 2.0$, $d_s = d_{90}$, $C_d = 1.8$, and $\phi = 25°$. Note that the parameter $x = 0.5$ determines the values of the exponents of Eq. 10 which were previously discussed in Table 2. The remaining parameters influence the diffusion length L_s and the scour depth D_s solely through the parameter K from Eq. 12. Identical values of K can be obtained with a different set of parameters. Fig. 7 compares the observed scour depths with the calculated scour depths from Eq. 11.

It is found from Figs. 6 and 7, that the diffusion length L_s can be determined more accurately than the scour depth D_s. This expected result stems from the fact that scour depth from Eq. 11 is relatively sensitive to the angle β' at low values of β'. Further research on the separation zone, the Coanda effect, and the natural instability and oscillations of plunging jets may theoretically provide better estimates of β'.

Conclusions

Local scour downstream of grade-control structures is examined theoret-

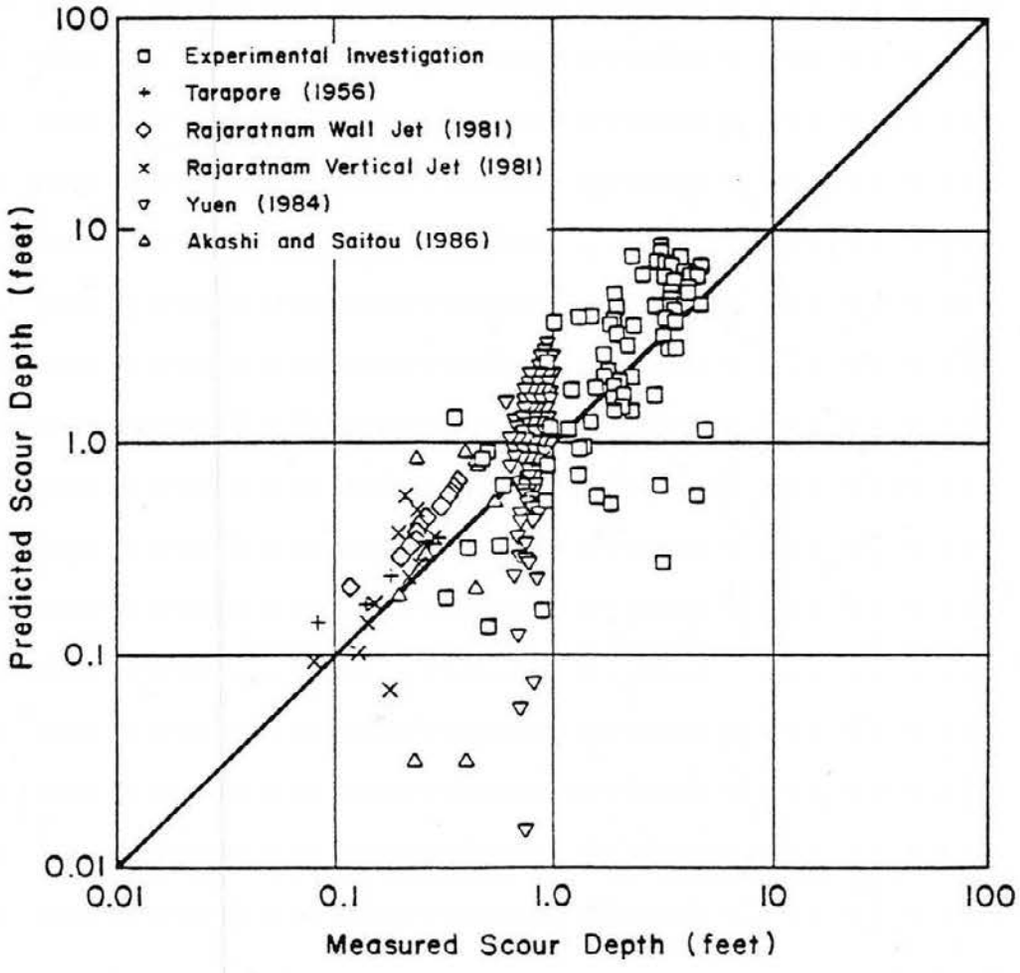

FIG. 7. Comparison of Measured and Calculated Scour Depth D_s

ically by analogy between the local scour process and jet diffusion in a plunge pool. After considering the jet trajectory, jet diffusion and stability of sediment particles in the scour hole, it is found that the exponents of the proposed equilibrium scour-depth relationship (Eq. 11) agree well with those of empirical relationships listed in Table 2. The large-scale experiments considerably extend the range of conditions for which local scour data is available. Scour depths exceeding 1.4 m (4.6 ft) were measured at unit flow discharges of 2.5 m^2/s (27 sq ft/sec). Analysis of 231 scour-depth measurements showed that the length of jet diffusion in Fig. 6 can be determined with reasonable accuracy, while Eq. 14 determines the jet angle β' with a mean prediction error of about $\pm 5°$. This explains the scatter shown in Fig. 7 for the equilibrium scour depth calculated from Eq. 11. The agreement between measured and calculated scour depths from Eq. 11 is reasonable, considering that a wide variety of conditions including vertical jets, wall jets, free overfall jets, submerged jets and flow over large-scale grade-control structures are shown in Fig. 7.

ACKNOWLEDGMENTS

The experimental investigation was completed while the first writer was employed at Simons, Li and Associates, Inc. Permission to use the data collected in this project funded by the Pima County Arizona Department of

360

Transportation and Flood Control District is gratefully acknowledged. The authors are thankful to E. V. Richardson and D. B. Simons for their encouragement and support during the course of this investigation.

APPENDIX I. REFERENCES

Akashi, N., and Saitou, T. (1986). "Influence of water surface on scour from vertical submerged jets." *J. Hydrosci. Hydr. Engrg.*, 55–69.

Albertson, M. L., Dai, Y. B., Jensen, R. A., and Rouse, H. (1950). "Diffusion of submerged jets." *Trans.*, ASCE, 115(2409), 639–697.

Altinbilek, H. D., and Basmaci, Y. (1973). "Localized scour at the downstream of outlet structures." *Proc., Int. Congress on Large Dams,* Madrid, Spain, 105–121.

Altinbilek, H. D., and Okyay, S. (1973). "Localized scour in a horizontal sand bed under vertical jets." *Proc., 15th Congress of Int. Association for Hydr. Res.*, Istanbul, Turkey, 99–106.

Beltaos, S., and Rajaratnam, N. (1973). "Plane turbulent impinging jets." *J. Hydr. Res.*, 11(1), 29–59.

Bogardi, J. (1974). *Sediment transport in alluvial streams*. Akademiai Kaido, Budapest, Hungary.

Bormann, N. E. (1988a). "Equilibrium local scour downstream of grade-control structures," thesis presented to Colorado State University, at Fort Collins, Colo., in partial fulfillment of the requirements for the degree of Doctor of Philosophy.

Bormann, N. E. (1988b). "Physical model of local scour at grade-control structures." *Proc., ASCE Nat. Conf. on Hydr. Engrg.*, ASCE, 1129–1134.

Bourque, C., and Newman, B. G. (1960). "Reattachment of a two-dimensional incompressible jet to an adjacent flat plate." *Aeronautical Quarterly,* 11, 201–232.

Breusers, H. N. C. (1967a). "Time scale of two-dimensional local scour." *Proc., 12th Congress of the Int. Association of Hydr. Res.*, Fort Collins, Colo., 3(32), 275–282.

Breusers, H. N. C. (1967b). "Two-dimensional local scour in loose sediment." *Closure of estuarine channels in tidal regions (Delft Hydr. Pub. No. 64).*

Carstens, M. R. (1966). "Similarity laws for localized scour." *J. Hydr. Div.*, ASCE, 92(3), 13–34.

Chee, S. P., and Kung, T. (1971). "Stable profiles of plunge basins." *J. Am. Water Res. Assoc.*, 7(2), 303–308.

Chee, S. P., and Padiyar, P. V. (1969). "Erosion at the base of flip buckets." *Engrg. J.*, 52(111), 22–24.

Chee, S. P., Strelchuk, D. L., and Kung, T. (1972). "Configurations of water basin for energy dissipation." *86th Annual Congress of Engrg. Institute of Canada,* Saskatoon.

Chee, S. P., and Yuen, E. M. (1985). "Erosion of unconsolidated gravel beds." *Can. J. Civ. Engrg.*, 12, 559–566.

Damle, P. M., et al. (1966). "Evaluation of scour below ski jump buckets of spillways." *Golden Jubilee Symp.*, Central Water and Power Res. Station, Poona, India, 1, 154–163.

Eggenberger, W. (1943). "Die Kolkbildung bei einen Uberstromen und beider Kombination Uberstromen-Unterstromen," thesis presented to ETH, at Zurich, Switzerland, in partial fulfillment of the requirements for the degree of Doctor of Philosophy (in German).

Farhoudi, J., and Smith, K. V. H. (1985). "Local scour profiles downstream of hydraulic jumps." *J. Hydr. Res.*, 23(4), 343–358.

Hartung, W. (1959). "Die Kolkbildung hinter Überstromen wehren im Hinblick auf eine beweglich Sturzbettgestaltung." *Die Wasser Wirtschaft,* 49(1), 309–313, (in German).

Jaeger, C. (1939). "Uber die Aehnlichkeit bei flussaulichen Modellversuchen." *Wasserkraft und Wasserwirtschaft,* 34(23/24), 269, (in German).

Kobus, H., Leister, P., and Westrich, B. (1979). "Flow field and scouring effects of steady and pulsating jets impinging on a movable bed." *J. Hydr. Res.*, 17(3), 175–192.

Laursen, E. M. (1952). "Observations on the nature of scour." *Proc., 5th Hydr. Conf., Bull. 34,* Univ. of Iowa, Iowa City, Iowa, 179–197.
Laursen, E. M., and Flick, M. W. (1983). "Scour at sill structures." *Report FHWA/AZ83/184,* Arizona Transp. and Traffic Inst., Tempe, Ariz.
LeFeuvre, A. R. (1965). "Sediment transport functions with special emphasis on localized scour," thesis presented to Georgia Institute of Technology, at Atlanta, Ga., in partial fulfillment of the requirements for the degree of Doctor of Philosophy.
Martins, R. (1975). "Scouring of rocky riverbeds and free-jet spillways." *Int. Water Power Dam Constr.,* 27(5), 152–153.
Mason, P. J., and Arumugam, K. (1985). "Free jet scour below dams and flip buckets." *J. Hydr. Engrg.,* ASCE, 111(2), 220–235.
Mueller, R., and Eggenberger, W. (1944). "Experimentelle und theoretische Untersuchungen uber das Kolkproblem." *Mitt. Versuchanstalt Wasserbau,* No. 5, ETH, Zurich (in German).
Neill, C. R. (1968). "Note on initial movement of coarse uniform bed material." *J. Hydr. Res.,* 6(2), 173–176.
Newman, B. G. (1961). "The deflection of plane jets by adjacent boundaries—Coanda effect." *Boundary Layer and Flow Control,* Vol. 1, G. V. Lachman, ed., Pergamon Press, New York, N.Y.
Rajaratnam, N. (1981). "Erosion by plane turbulent jets." *J. Hydr. Res.,* 19(4), 339–358.
Rajaratnam, N., and Subramanya, K. (1968). "Plane turbulent reattached wall jets." *J. Hydr. Div.,* ASCE, 94(1), 95–112.
Schoklitsch, A. (1932). "Kolkbildung unter Uberfallstrahlen." *Wasserwirtschaft,* 343, (in German).
Smith, C. D., and Strang, D. K. (1967). "Scour in stone beds." *Proc., 12th Congress of the Int. Association for Hydr. Res.,* 65–73.
Stevens, M. A., and Simons, D. B. (1971). "Stability analysis for coarse granular material." *River Mechanics,* Vol. 1, H. W. Shen, ed., Fort Collins, Colo.
Straub, L. G. (1953). "Dredge-fill closure of Missouri River at Fort Randall." *Proc., Minnesota Hydr. Convention,* Int. Association for Hydr. Res.
Tarapore, Z. S. (1956). "Scour below a submerged sluice gate," thesis presented to the University of Minnesota, at Minneapolis, Minn., in partial fulfillment of the requirements for the degree of Master of Science.
Veronese, A. (1937). *Erosion of a bed downstream from an outlet.* Colorado A&M College, Fort Collins, Colo.
Yuen, E. M. (1984). "Clearwater scour by high velocity jets," thesis presented to the University of Windsor, at Windsor, Ontario, in partial fulfillment of the requirements for the degree of Master of Science.

Appendix II. Notation

The following symbols are used in this paper:

A', B', C', P, P' = points of interest below grade-control structures;
a, b, c, d, e, f, i = exponents of scour-depth equation;
B = coefficient of friction relationship;
C_d = jet diffusion coefficient;
C_f = local friction coefficient;
D_p = drop height of structure;
D_s = equilibrium scour depth;
d_s = sediment size;
d_{50}, d_{90} = standard sieve diameter for which 50%, 90% of particles are finer, respectively;
g = gravitational acceleration;
ΔH = head drop across structure;

K = constant in scour equation;
L_s = diffused length of jet;
q = unit water discharge;
R^2 = coefficient of determination;
U_b = diffused near bed jet velocity;
U_o = jet velocity entering tailwater;
X_s = horizontal distance to point of maximum scour;
x = exponent of friction relationship;
Y_b = jet thickness at location of maximum scour;
Y_o = jet thickness entering tailwater;
Y_t = tailwater depth;
α = maximum side angle of scour hole;
β, β' = jet angle near surface and near bed, respectively;
γ, γ_s = specific weight of water and sediment, respectively;
θ_{cr} = critical Shields number;
λ = face angle of structure;
μ, ν = dynamic and kinematic water viscosity, respectively;
ρ, ρ_s = mass density of water and sediment, respectively;
τ_b = critical shear stress at an upsloping angle α;
τ_{cr} = critical shear stress for horizontal bed; and
ϕ = submerged angle of repose of bed sediment.

Criterion Delineating the Mode of Headcut Migration

By O. R. Stein,[1] Associate Member, ASCE, and P. Y. Julien,[2] Member, ASCE

Abstract: Two modes of headcut migration are generally recognized: (1) Rotating headcuts that tend to flatten as they migrate; and (2) stepped headcuts that tend to retain nearly vertical faces. A mathematical description of the sediment detachment potential immediately upstream and downstream of the headcut is used to delineate these modes of migration. The delineating parameter is the ratio of the time required to erode the headcut face from above to the time required to undermine the headcut face from below. This erosional time-scale ratio is a dimensionless function of flow, sediment, and geometry parameters. For the limiting case of homogeneous cohesive soils, the time-scale ratio is a simple function of a Froude number and the aspect ratio of drop height to normal flow depth. This relationship is calibrated using original laboratory experiments of headcut migration in initially vertical headcuts and verified by independent field experiments of headcuts propagating in four different homogeneous cohesive soils.

Introduction

A headcut is a natural, nearly vertical drop in channel bed elevation. The dissipation of flow kinetic energy at the drop causes excessive erosion and results in headcut upstream migration, which deepens and tends to widen the channel. Headcuts migrating in gullies may undermine upstream structures and, on a smaller scale, often define the breakpoint between overland and channel flow, and therefore play an important role in drainage network evolution. Headcuts propagating in small channels called rills contribute significantly to total upland soil losses due to erosive storms (Nearing et al. 1989). Several investigations (Blong 1970; 1985; Egboka and Okpoko 1984; Piest et al. 1975; Patton and Schumm 1975; Daniels and Jordan 1966; Kohl 1988) have focused on headcut migration in the field. Most data were collected after erosive storms and indicated that a nearly vertical face is maintained; however, information on the flow characteristics representing headcut migration was not reported. Therefore, understanding of the physical processes governing the formation, propagation, and degradation of headcuts as they migrate is very limited.

Several laboratory flume studies have observed headcut migration in specific bed materials. A knickpoint, which is a headcut in noncohesive sand, becomes indistinguishable from the rest of the channel as it propagates upstream, as shown by Brush and Wolman (1960). The data of Leopold et al. (1964) reveal the same result for cohesive soil, provided that the ratio of initial headcut drop height to flow depth in subcritical flow is less than one. Using stratified cohesive and noncohesive bed material, Holland and Pickup (1976) defined two headcut migration modes: (1) Rotating headcuts

[1]Asst. Prof., Dept. of Civ. and Agric. Engrg., Montana State Univ., Bozeman, MT 59717.

[2]Assoc. Prof., Dept. of Civ. Engrg., Colorado State Univ., Fort Collins, CO 80523.

Note. Discussion open until June 1, 1993. To extend the closing date one month, a written request must be filed with the ASCE Manager of Journals. The manuscript for this paper was submitted for review and possible publication on August 20, 1992. This paper is part of the ***Journal of Hydraulic Engineering***, Vol. 119, No. 1, January, 1993. ©ASCE, ISSN 0733-9429/93/0001-0037/$1.00 + $.15 per page. Paper No. 1888.

that alter their shape through migration, i.e., the Brush and Wolman (1960) observations; and (2) stepped headcuts that tend to maintain a nearly vertical face, i.e., the majority of field observations. Gardner (1983) reports similar observations and provides an excellent summary of geomorphological theories on headcut advancement.

The aim of this paper is to develop and test a criterion that separates stepped headcuts from rotating headcuts. The criterion was derived from the analysis of the erosion processes immediately upstream and downstream from a headcut. The criterion was tested with laboratory and field experiments of headcut migration, given steady uniform flow over a preexisting headcut geometry.

The approach used was to examine the changes in flow and sediment transport characteristics in the vicinity of the headcut. Flow upstream from the headcut was treated as an approach to a free overfall and flow downstream was examined as an impinging jet. Both flow conditions increase the applied bed shear stress, and erosion is calculated from a sediment detachment function based on excess shear stress. A headcut tends to migrate in a rotating mode if upstream erosion dominates, and a stepped mode if downstream erosion dominates. A criterion separating these modes of migration, defined as the ratio of upstream and downstream erosion time scales is tested with original laboratory experiments and independent field observations for the case of homogeneous cohesive soils.

Flow Characteristics

Two-dimensional flow over a headcut of drop height D_h in a wide rectangular channel of constant slope S is illustrated in Fig. 1. Steady flow of unit discharge q is uniform at a normal flow depth h_n and has a nearly hydrostatic pressure distribution upstream from the headcut. The pressure distribution is less than hydrostatic at the brink, causing the flow to accelerate through a distance L, approximately equal to two to four times h_n, upstream from the headcut. In this accelerated flow region, the depth gradually decreases from the normal flow depth h_n to a depth h_u at the brink, where the average flow velocity is V_u. It is considered that the water falls freely through a drop height D_h and accelerates from V_u at the brink to V_o when entering the impingement region. The jet impinges on the downstream water surface at a distance X_n downstream from the headcut face. At some distance downstream from the brink, the flow has been completely restored to normal depth.

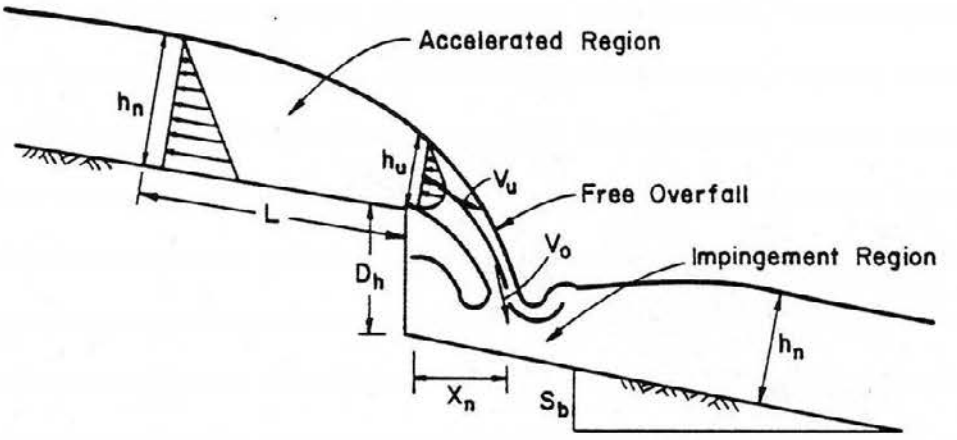

FIG. 1. Initial Headcut Hydraulics

Accelerated-Flow Region

The upstream normal flow depth h_n, and the corresponding normal flow velocity $V_n = q/h_n$, can be written as a power function of slope S and flow Reynolds number R (Julien and Simons 1985)

$$h_n = aS^b R^c \quad \text{..... (1)}$$

in which the values of the coefficients a, b, and c are listed in Table 1. Hager (1983) and Hager and Hutter (1984) proposed an energy equation to determine changes in pressure and flow depth through the accelerated flow region. The following equation for both flow depth h_u and velocity V_u at the brink compares favorably with data from previous studies (Rouse 1936, 1937; Delleur et al. 1956; Rajaratnam and Muralidhar 1968):

$$\frac{V_n}{V_u} = \frac{h_u}{h_n} = \frac{F^2}{F^2 + 0.4} \quad \text{..... (2)}$$

in which F = upstream Froude number; h_u = flow depth at the brink; and V_u = velocity at the brink. The shear stress at the brink $\tau_u = C_u \rho V_u^2$ is compared to the normal shear stress $\tau_n = C_u \rho V_n^2$ in (3). Assuming that the upstream friction coefficient C_u remains constant, and using (2), one obtains

$$\frac{\tau_u}{\tau_n} = \frac{C_u \rho}{C_u \rho} \frac{V_u^2}{V_n^2} = \left(1 + \frac{0.4}{F^2}\right)^2 \quad \text{..... (3)}$$

The shear stress at the brink τ_u is greater than the normal shear stress τ_n as given by the second term in parentheses of (3).

Free Overall Region

The free-falling nappe is accelerating from the brink to the impingement point. The velocity increases from V_u at the brink to V_o at the tailwater impingement point X_n. According to the equation of conservation of energy for free-falling fluid and assuming a small tailwater depth, the use of (2) yields

$$V_o = \sqrt{V_u^2 + 2gD_h} = V_n \left(1 + \frac{0.4}{F^2}\right) \sqrt{1 + \frac{2gD_h}{V_u^2}} \quad \text{..... (4)}$$

and

TABLE 1. Summary of Flow Characteristics, Depth = $h_n = aS^b R^c$

Type of flow (1)	a (2)	b (3)	c (4)
Laminar (k = constant)	$(k\nu^2/8g)^{1/3}$	−1/3	1/3
Turbulent, smooth boundary	$(0.22\nu^2/8g)^{1/3}$	−1/3	7/12
Turbulent (n = constant)	$(n\nu)^{6/10}$	−3/10	6/10
Turbulent (f = constant)	$(f\nu^2/8g)^{1/3}$	−1/3	2/3

$$\frac{X_n}{D_h} = V_u \sqrt{\frac{2}{gD_h}} = \sqrt{2} \sqrt{\frac{h_n}{D_h}} \left(\frac{F^2 + 0.4}{F} \right) \quad \ldots\ldots\ldots\ldots\ldots\ldots\ldots\ldots (5)$$

The two parameters V_o and X_n determine the velocity and location of the impact point of the jet entering the impinging region.

Impingement Region

Flow in the impingement region can be likened to that of an impinging plane jet. A general flow diagram for a jet produced by a free-falling nappe entering a plunge pool is shown in Fig. 2. At impact with the water surface, the jet has an initial thickness y_o, average velocity V_o, and impact angle χ. For some distance along the jet centerline, which defines the length of the potential core, diffusion has not affected velocity and the maximum velocity remains V_o. Beyond this potential core the maximum velocity is reduced by diffusion. Diffusion of an impinging turbulent jet and its interaction with impervious boundaries have been described by Beltaos and Rajaratnam (1973) and Beltaos (1974, 1976) and with porous boundaries by Kobus et al. (1979) and Bormann and Julien (1991).

Details of the relation between the diffusing jet below a headcut and scour hole development with time are given by Stein (1990) and Stein et al. (in press 1993). In summary, the maximum shear stress acting on the bed is in the vicinity of the intersection between the jet centerline and the bed, and is a function of the maximum velocity near the bed. The maximum bed shear stress in the impingement region occurs while the bed is within the jet potential core in which the maximum velocity remains V_o; therefore the maximum shear stress in the impingement region can be expressed as $\tau_d = C_d \rho V_o^2$.

The ratio of the maximum downstream shear stress to the normal shear stress is obtained from (2) and (4)

$$\frac{\tau_d}{\tau_n} = \frac{C_d \rho V_o^2}{C_u \rho V_n^2} = \frac{C_d}{C_u} \left[\left(1 + \frac{0.4}{F^2} \right)^2 + \left(\frac{2}{F^2} \frac{D_h}{h_n} \right) \right] \quad \ldots\ldots\ldots\ldots\ldots\ldots (6)$$

The shear stress ratio τ_d/τ_u is then given from the ratio of (6) and (3)

$$\frac{\tau_d}{\tau_u} = \frac{C_d}{C_u} \left[1 + \frac{2D_h}{h_n} \left(\frac{F}{F^2 + 0.4} \right)^2 \right] \quad \ldots\ldots\ldots\ldots\ldots\ldots\ldots\ldots\ldots (7)$$

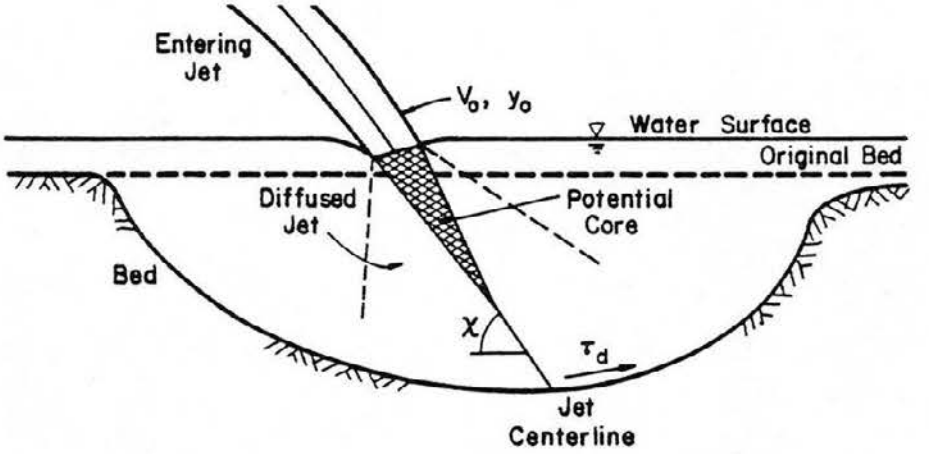

FIG. 2. Hydraulics of Impingement Region

This ratio is always larger than unity when $C_d \geq C_u$, which indicates greater shear stress at the jet impingement point than at the brink of the headcut.

Headcut Migration Mode

Rotating and stepped headcuts depend on the relative erosion rate in the accelerated and impingement regions. As illustrated in Fig. 3, the morphology of rotating and stepped headcuts depends on the time scales T_u and T_d of upstream and downstream scour. The upstream time scale T_u denotes the time for upstream vertical scour to reach the toe of the vertical face. Likewise, the downstream time scale T_d denotes the time for the impingement scour to develop horizontally and reach the toe of the vertical face. It is hypothesized that the ratio T_u/T_d can be used to delineate the mode of headcut migration. Conceptually, rotating headcuts would be obtained if $T_u < T_d$ or $T_u/T_d < 1$ if upstream erosion is dominant. Similarly, stepped headcuts would be maintained as $T_u > T_d$ or $T_u/T_d > 1$ if downstream erosion is dominant.

The time scales can be related to geometry and soil erosion characteristics. As given by Foster and Meyer (1975), the detachment rate of sediment particles per unit area E (in units of M/L^2T) depends on the applied shear stress τ exceeding the critical shear stress τ_c as

$$E = \kappa(\tau - \tau_c)^{\xi} = \kappa\left[\tau\left(1 - \frac{\tau_c}{\tau}\right)\right]^{\xi} \quad \ldots\ldots\ldots\ldots\ldots\ldots\ldots\ldots\ldots\ldots (8)$$

in which κ and ξ = empirical coefficients. Sediment detachment from the bed is also directly proportional to the bulk density of the soil B (in units of M/L^3) and the time change in bed elevation y; therefore $E_u = B_u(\partial y/\partial t)$. Integrating this expression from $y = 0$ at $t = 0$ to $y = D_h$ at $t = T_u$

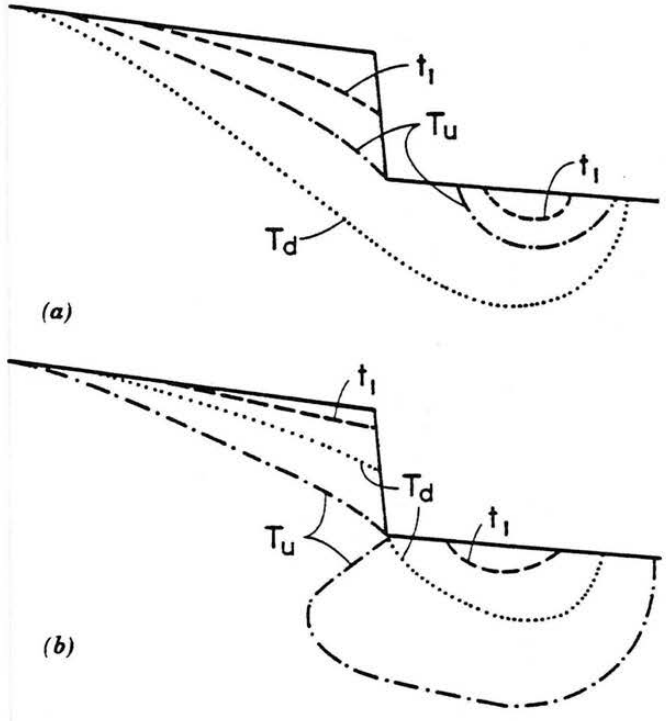

FIG. 3. Sketches of Headcut Migration: (a) Rotating Headcut $T_u < T_d$; and (b) Stepped Headcut $T_u > T_d$

368

yields the upstream sediment detachment $E_u = A_u B_u D_h / T_u$ in which A_u is an empirical coefficient and the subscript u denotes upstream conditions. Substituting this relation into (8) yields an expression for the upstream time scale T_u

$$T_u = \frac{A_u B_u D_h}{\kappa_u \tau_u^{\xi_u} \left(1 - \frac{\tau_{cu}}{\tau_u}\right)^{\xi_u}} \quad \ldots\ldots\ldots\

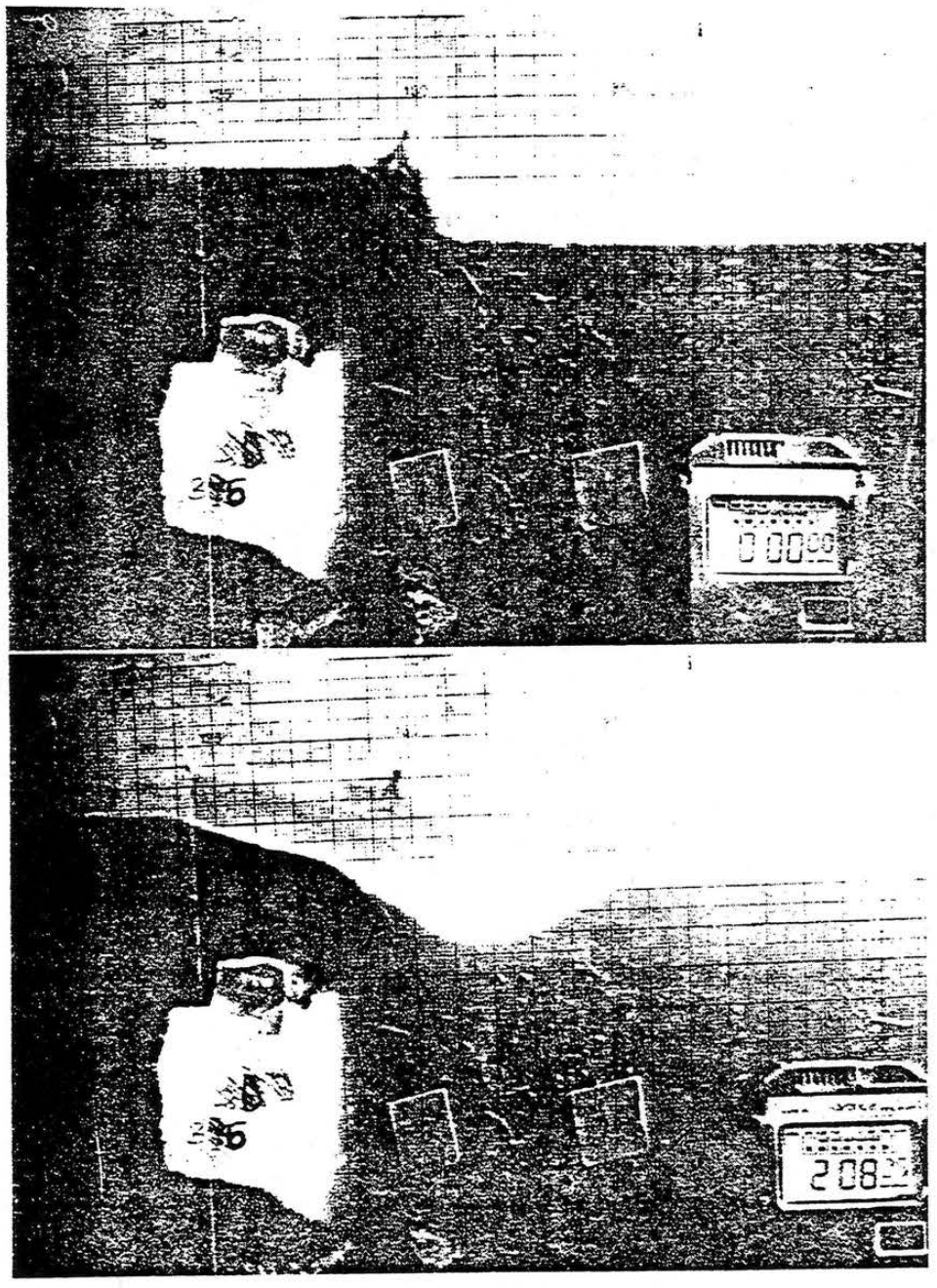

FIG. 4. Photographs of Typical Rotating Headcut

scale ratio describing the mode of headcut migration. It can be used to explain qualitative observations when sediments control headcut migration. For example, if the downstream soil is more erodible ($\tau_{cd} < \tau_{cu}$, $\kappa_d > \kappa_u$, or $\xi_d > \xi_u$) as in the case of stratified sediments, or if a surface compaction zone exists ($B_u > B_d$), the time-scale ratio is greater than one and the headcut tends to migrate in a stepped mode. However, in the particular case of homogeneous soils, in which $\tau_{cu} = \tau_{cd}$, $B_u = B_d$, $\kappa_u = \kappa_d = \kappa$, and $\xi_u = \xi_d = \xi$, and when the applied shear stress greatly exceeds the critical shear stress $\tau_u >> \tau_{cu}$ and $\tau_d >> \tau_{cd}$, so that both terms in parentheses in (11) approach unity, headcut migration becomes a function of hydraulics and geometry only. This is a limiting case, where clear cut differences in soil properties cannot explain headcut migration. After substituting (5) and (7) into (11) with the aforementioned assumptions, one obtains

370

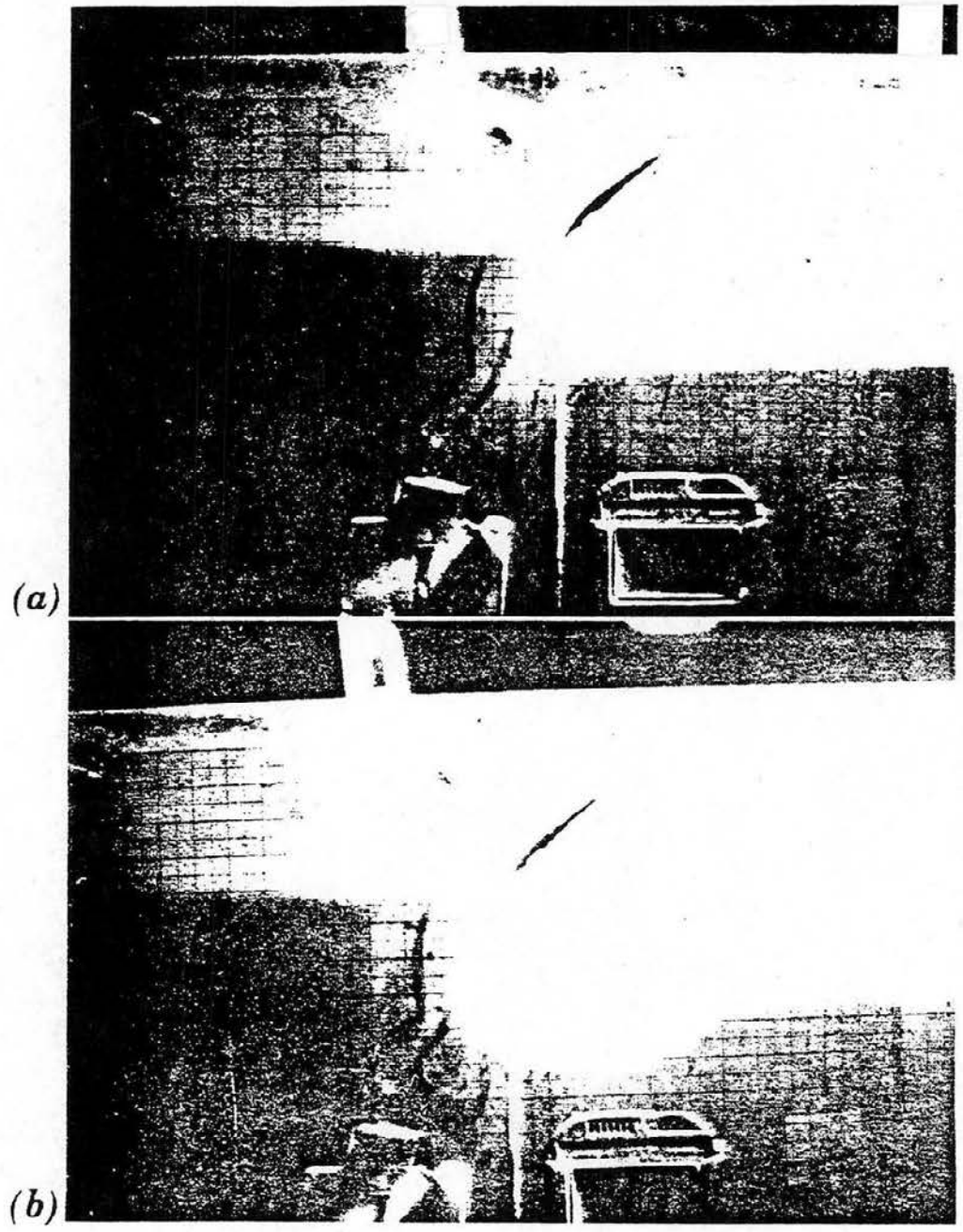

FIG. 5. Photographs of Typical Stepped Headcut

$$\frac{T_u}{T_d} \cong \frac{\Phi}{\Omega}\left[1 + \Phi^2\right]^{\xi} \quad \ldots\ldots (12)$$

in which

$$\Phi = \sqrt{2}\sqrt{\frac{D_h}{h_n}}\left(\frac{\mathsf{F}}{\mathsf{F}^2 + 0.4}\right) \quad \ldots\ldots (13a)$$

$$\Omega = 2\frac{A_d}{A_u}\left(\frac{C_u}{C_d}\right)^{\xi} \quad \ldots\ldots (13b)$$

The separation between rotating and stepped headcuts is obtained from (12) when $T_u = T_d$, thus

TABLE 3. Summary of Field Experiments (Kohl 1988; Elliot et al. 1989)

Run (1)	q ($m^3/s \cdot m$) (2)	D_h (mm) (3)	S (4)	h_n (mm) (5)	D_h/h_n (6)	Froude number (7)	Calculated T_u/T_d (8)	Observed result (9)
Pal6R2	0.0298	27	0.059	6.35	4.3	1.18	1.29	Stepped
Pie22	0.0113	78	0.066	5.85	13.3	0.71	10.23	Stepped
Pie3R0	0.0103	30	0.071	5.80	5.2	0.62	2.74	Stepped
Pie3R4	0.0351	55	0.071	8.60	6.4	1.14	2.36	Stepped
Pie310	0.0405	24	0.071	13.05	1.8	0.79	0.68	Uncertain
Sve2R2	0.0315	33	0.045	4.80	6.9	1.33	2.02	Stepped
Sve22	0.0197	28	0.045	4.70	6.0	0.93	2.73	Stepped
Sve3R4	0.0457	32	0.046	6.55	4.9	1.30	1.34	Stepped
Sve32	0.0248	23	0.046	4.15	5.5	1.23	1.73	Stepped
Sve36	0.0525	50	0.046	5.90	8.5	1.46	2.28	Stepped
Sve6R2	0.0317	68	0.038	4.85	14.0	1.51	4.26	Stepped
Sve62	0.0144	25	0.038	5.15	4.9	0.80	2.34	Stepped
Bar22	0.0123	38	0.086	6.60	5.7	0.78	2.93	Stepped
Bar3R2	0.0234	29	0.089	7.25	4.0	1.01	1.47	Stepped
Bar6R0	0.0087	42	0.077	5.25	8.0	0.37	3.37	Stepped

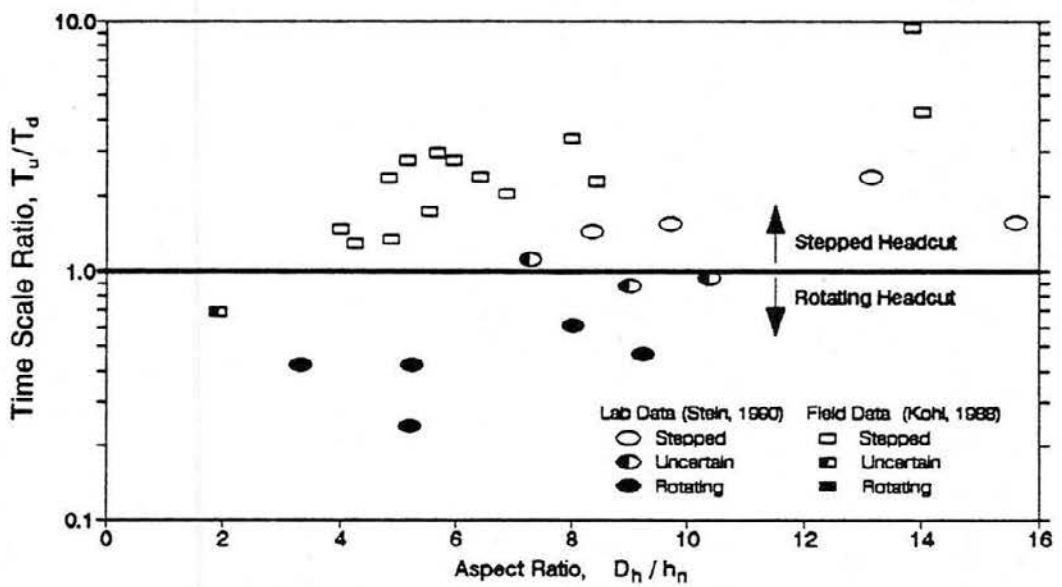

FIG. 6. Headcut Migration Criterion T_u/T_d versus Aspect Ratio

$$\Phi_c(1 + \Phi_c^2)^{\xi} = \Omega \quad \ldots\ldots (14)$$

in which Φ_c = critical value of Φ when the headcut is at the threshold between rotating and stepped migration. Separation lines between rotating and stepped headcuts can also be obtained by plotting the aspect ratio $\Psi = (D_n/h_n)$ versus the Froude number. The critical value of the aspect ratio $\Psi_c = D_h/h_n|_c$ determined from (12), (13), and (14) is

$$\Psi_c = \frac{\Phi_c^2}{2}\left(\frac{F^2 + 0.4}{F}\right)^2 \quad \ldots\ldots (15)$$

EXPERIMENTS

The headcut migration formulations of (12)–(15), applicable for the case of homogeneous cohesive soil, were calibrated using the experimental laboratory data of Stein (1990) and tested using field data on soil erodibility and headcut migration as reported by Kohl (1988) and Elliot et al. (1989).

372

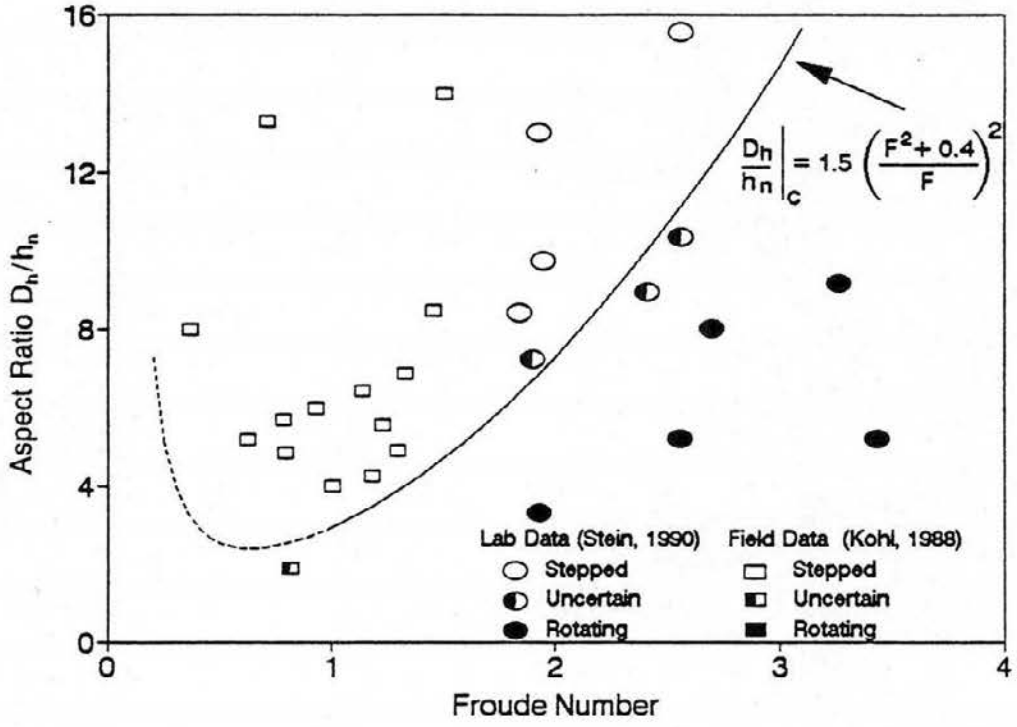

FIG. 7. Headcut Migration Criterion D_h/h_n versus Froude Number

Laboratory Experiments

A flume 10.4 cm wide and 2 m long was used for all laboratory experiments, and the bed material was a natural soil (Norka series collected in Colorado) susceptible to rill erosion and headcuts. A particle size analysis indicated the soil was 46.3% sand, 27.5% silt, and 26.2% clay with a mean particle size of $d_{50} = 0.046$ mm. To maintain uniform cohesive soil conditions and remove large pieces of organic matter, the air-dried soil was passed through a 0.420-mm sieve that destroyed large aggregates, but allowed the soil to retain cohesive properties upon rewetting.

Known weights of soil were placed in the flume and leveled after settling by manually shaking the small flume. The volume of each layer thus placed was measured to determine bulk density. Because the soil was sieved finely, a very uniform and constant bulk density of 1,320 ± 10 kg/m^3 was achieved. The final test bed, which was 23.3 cm thick, was slowly saturated by applying successive head increments of 4–8 cm to a reservoir below the flume floor. The head of each increment was held constant from 3 to 12 h, and at least 48 h elapsed between the start of wetting and the beginning of a run sequence. The final pressure head was set equal to the soil surface elevation to ensure full saturation. As many runs as possible were conducted in one flume packing, after which the uneroded soil was removed, air-dried, and resieved for future use.

Each run corresponds to a unique combination of flow rate, bed slope, and drop height. The drop height was formed by removing a block of soil between a cross section within the flume and the flume exit. The upstream and downstream bed surfaces were vertically offset by the drop height and flat between the flume sidewalls. Each run was inititated immediately after headcut formation and the cohesive properties of the soil maintained a vertical face while saturated. For all runs, the width to depth ratio was at least 16:1, and flow and headcut migration were observed to have minimal variation in width—therefore conditions were essentially two-dimensional.

Headcut migration was measured by photographing the longitudinal bed profile changes through the flume sidewall, which was imprinted with an x-y grid.

A total of 12 runs listed in Table 2 provide the data required to determine the time-scale ratio in (12), as well as the observed result from these runs. Reynolds numbers varied from 907 to 2,979, slopes from 0.014 to 0.059, and drop heights from 10 to 60 mm. The headcut in run 28 migrated about 400 mm in approximately 15 min. Runs 30–40 were abbreviated runs terminated when either upstream or downstream erosion dominated. Fig. 4 illustrates typical laboratory observations of a rotating headcut where the upstream erosion time scale is shorter than the downstream time scale, and Fig. 5 exemplifies a stepped headcut where the downstream time scale is shorter. The mode of headcut migration was visually determined from experiments and compared with computed time-scale ratios from (12). The predicted time-scale ratios T_u/T_d calculated from (12) with a value of $\xi = 1$ and $\Omega = 6.9$ varied from 0.24 to 2.37. The corresponding value of Φ_c from (14) is $\Phi_c = 1.7$.

Field Experiments

As part of experiments conducted to calibrate a newly developed upland erosion model (Elliot et al. 1989), rills preformed in 33 different agricultural soils were eroded by applying flow with and without rainfall simulation. On most rills several headcuts freely developed, and their formation and migration distance were recorded by Kohl (1988). The large data set was reduced to 15 headcuts on four different soil types by considering rills that developed only one headcut greater than 1 cm high. The headcut morphology data of Kohl (1988) and the pertinent hydraulic data of Elliot et al. (1989) are summarized in Table 3. The first three letters in the run nomenclature represent the soil type; the next digit represents the rill number: an R represents the presence of rainfall; and the last digit represents the nominal applied flow rate in gallons per minute. Reported Reynolds numbers varied from 987 to 4,539, slopes from 0.038 to 0.089, and drop heights from 23 to 78 mm.

Results

The laboratory and field data contained in Tables 2 and 3 are graphically represented in Fig. 6 as a plot of the calculated value of T_u/T_d from (12) versus aspect ratio D_h/h_n. The time-scale ratio varies over nearly two orders of magnitude from 0.24 to 10.23, and the aspect ratio varies from 1.8 to 15.6. A time-scale ratio of unity effectively separates stepped headcuts from rotating headcuts, accepting a narrow range of uncertainty ($0.8 \lessapprox T_u/T_d \lessapprox 1.2$), i.e., when upstream and downstream erosion rates are nearly identical. Under these conditions a knickpoint with an approximately 1:1 slope may migrate for some distance upstream, as observed in run 28. Laboratory headcuts in runs with time-scale ratios of less than approximately 0.8 were observed to rotate as they migrated, and undercutting of the headcut face was observed for laboratory runs with time-scale ratios greater than approximately 1.2. The observed result occurred more rapidly the greater the magnitude between the computed time-scale ratio and unity. The data have also been plotted in terms of aspect ratio versus Froude number in Fig. 7. The curve from (15) with $\Phi_c = 1.7$ effectively separates rotating and stepped headcuts. With only one exception, the reported field observations of stable headcut migration plot in the stepped-mode range.

Conclusions

A general formulation for the mode of headcut migration compares upstream and downstream erosion time scales as given in (11). This formulation is developed from a consideration of upstream and downstream sediment detachment that can be related to headcut hydraulics, sediment parameters, and geometry. A time-scale ratio T_u/T_d greater than one tends to form stepped headcuts, and rotating headcuts tend to form when $T_u/T_d < 1$. The tendency is more pronounced the further the ratio is from unity. For homogeneous cohesive soils, this time-scale ratio is written as a function of the drop height, flow depth, and Froude number, as given in (12) and (13). Separation between rotating and stepped headcuts can be achieved by comparing aspect ratio (D_h/h_n) and Froude number, as given in (15). The experiments validate the use of (12) and (15) for delineating stepped and rotating headcuts in homogeneous cohesive soils (Figs. 6 and 7, respectively). A numerical value of $\Omega = 6.9$ properly delineates rotating from stepped headcuts for laboratory and field measurements.

Acknowledgments

This study was undertaken primarily at the U.S. Department of Agriculture–Hydro-Ecosystems Group in Fort Collins, Colo. and special appreciation goes to D. DeCoursey. Additional funding at the Center for Geosciences under grant No., ARO/DAAL 03-86-K-0175 and the Montana Agricultural Experiment Station (No. J-2651) is gratefully acknowledged. The writers wish to thank W. J. Elliot, G. R. Foster, and K. D. Kohl for their insight and suggestions for improvement on final drafts of this manuscript.

Appendix I. References

Beltaos, S. (1974). "Turbulent impinging jets," PhD dissertation, University of Alberta, Edmonton, Alberta, Canada.

Beltaos, S. (1976). "Oblique impingement of plane turbulent jets." *J. Hydr. Div.*, ASCE, 102(9), 1177–1192.

Beltaos, S., and Rajaratnam, N. (1973). "Plane turbulent impinging jets." *J. Hydr. Res.*, 11(1), 29–59.

Blaisdell, F. W., Anderson, C. L., and Hebaus, G. G. (1981). "Ultimate dimensions of local scour." *J. Hydr. Div.*, ASCE, 107(3), 327–337.

Blaisdell, F. W., and Anderson, C. L. (1988a). "A comprehensive generalized study of scour at cantilevered pipe outlets pt. 1." *J. Hydr. Res.*, 26(4), 357–376.

Blaisdell, F. W., and Anderson, C. L. (1988b). "A comprehensive generalized study of scour at cantilevered pipe outlets pt. 2." *J. Hydr. Res.*, 26(5), 509–524.

Blong, R. J. (1970). "The development of discontinuous gullies in a pumice catchment." *Am. J. Sci.*, 268(4), 369–383.

Blong, R. J. (1985). "Gully sidewall development in New South Wales Australia." *Soil erosion and conservation*, S. A. El-Swaify, W. C. Moldenhauer, and A. Lo, eds., Soil Conservation Soc. Am., Ankeny, Iowa, 574–584.

Bormann, N. E., and Julien, P. Y. (1991). "Scour downstream of grade control structures." *J. Hydr. Engrg.*, ASCE, 117(5), 579–584.

Brush, L. M. Jr., and Wolman, M. G. (1960). "Knickpoint behavior in noncohesive material: a laboratory study." *Geol. Soc. Am. Bull.*, 71(1), 59–73.

Chee, S. P., and Kung, T. (1971). "Stable profiles of plunge basins." *Water Res. Bull.* 7(2), 303–308.

Daniels, R. B., and Jordan, R. H. (1966). "Physiographic history and the soils, entrenched stream of systems and gullies Harrison County Iowa." *USDA Tech. Bull. 1348*, U.S. Dept. of Agric., Washington, D.C.

Delleur, J. W., Dooge, J. C. I., and Gent, K. W. (1956). "Influence of slope roughness on the free overfall." *J. Hydr. Div.*, ASCE, 82(4), 1038-30–1038-35.
Egboka, B. C. E., and Okpoko, E. I. (1984). "Gully erosion in the Agula-Nanka region of Anambra State, Nigeria." *Challenges in African hydrology and water resources, Pub. No. 144*, Int. Assoc. Hydro. Sci., Delft, The Netherlands, 335–347.
Elliot, W. J., Liebenow, A. N., Laflen, J. M., and Kohl, K. D. (1989). "A compendium of soil erodibility data from WEPP cropland soil field erodibility experiments 1987 and 1988." *USDA-ARS National Soil Erosion Research Lab. Rept. No. 3*, Purdue Univ., West Lafayette, Ind.
Foster, G. R., and Meyer, L. D. (1975). "Mathematical simulation of upland erosion using fundamental erosion mechanics." *Present and Prospective Technol. for Predicting Sediment Yields and Sources (Proc., 1972 Sediment Yield Workshop USDA-ARS, ARS-S40)*, U.S. Dept. of Agriculture Sedimentation Lab, Oxford, Miss. 190–207.
Gardner, T. W. (1983). "Experimental study of knickpoint and longitudinal profile evolution in cohesive, homogeneous material." *Geol. Soc. Am. Bull.*, 94(5), 664–672.
Hager, W. H. (1983). "Hydraulics of plane free overfall." *J. Hydr. Engrg.*, ASCE, 109(12), 1683–1697.
Hager, W. H. (1984). Errata to "Hydraulics of Plane Free Overfall." *J. Hydr. Engrg.*, ASCE, 110(12), 1687–1688.
Hager, W. H., and Hutter, K. (1984). "Approximate treatment of plane channel flow." *Acta Mechanica*, 51(1–2), 31–48.
Holland, W. N., and Pickup, G. (1976). "Flume study of knickpoint development in stratified sediment." *Geol. Soc. Am. Bull.*, 87(1), 76–82.
Julien, P. Y., and Simons, D. B. (1985). "Sediment transport capacity of overland flow." *Trans., American Society of Agricultural Engineers*, 28(3), 755–762.
Kobus, H., Liester, P., and Westrich, B. (1979) "Flow field and scouring effects of steady and pulsating jets impinging on a moveable bed." *J. Hydr. Res.*, 17(3), 175–192.
Kohl, K. D. (1988). "Mechanics of rill headcutting," PhD dissertation, Iowa State University, Ames, Iowa.
Leopold, L. D., Wolman, M. G., and Miller, J. P. (1964). *Fluvial processes in geomorphology*. W. H. Freeman and Co., San Francisco, Calif.
Nearing, M. A., Foster, G. R., Lane, L. J., and Finkner, S. C. (1989). "A processed-based soil erosion model for USDA water erosion prediction project technology." *Trans., American Society of Agricultural Engineers*, 32(5), 1587–1593.
Patton, P. C., and Schumm, S. A. (1975). "Gully erosion, northwestern Colorado: A threshold phenomenon." *Geology*, 3(2), 88–90.
Piest, R. F., Bradford, J. M., and Wyatt, G. M. (1975). "Soil erosion and sediment transport from gullies." *J. Hydr. Div.*, ASCE, 101(1), 65–80.
Rajaratnam, N. (1981). "Erosion by plane turbulent jets." *J. Hydr. Res.*, 19(4), 339–359.
Rajaratnam, N., and Muralidhar, D. (1968). "Characteristics of the rectangular free overfall." *J. Hydr. Res.*, 6(3), 233–258.
Rouse, H. (1936). "Discharge characteristics of the free overfall." *Civ. Engrg.*, ASCE, 6(4), 257–260.
Rouse, H. (1937). "Pressure distribution and acceleration at the free overfall." *Civ. Engrg.*, ASCE, 7(7), 518.
Stein, O. R. (1990). "Mechanics of headcut migration in rills," PHD dissertation. Colorado State University, Fort Collins, Colo.

APPENDIX II. NOTATION

The following symbols are used in this paper:

a, b, c = coefficient and exponents from Table 1;
A_d, A_u = empirical coefficients in detachment equation;

B = soil bulk density;
C = coefficient of friction;
D = maximum depth of jet scour at arbitrary time;
D_h = initial drop height of headcut;
d_{50} = mean sediment size;
E = detachment of sediment particles;
f = Darcy-Weisbach friction factor;
F = Froude number;
g = gravitational acceleration;
h = flow depth at general cross section;
h_n = normal flow depth;
h_u = flow depth at free overfall brink;
k = resistance parameter for laminar flow;
L = length of accelerated flow region;
n = Manning resistance coefficient;
q = unit flow discharge;
R = Reynolds number;
S = bed slope gradient;
T_d = time scale for downstream scour;
T_u = time scale for upstream scour;
t_1 = arbitrary time $<T_u$ and $<T_d$;
V_o = initial velocity of jet;
V_n = average normal flow velocity;
V_u = average flow velocity at brink;
X_n = longitudinal distance form brink to tailwater impingement;
y_o = jet thickness;
κ, ξ = constants of sediment detachment equation;
ν = fluid density;
ρ = fluid density;
τ = shear stress at general cross section;
τ_c = critical shear stress for erosion initiation;
τ_d = shear stress in impingement region;
τ_n = normal flow shear stress;
τ_u = shear stress at brink;
Φ = function of aspect ratio and Froude number;
Φ_c = critical value of Φ;
χ = angle of jet at tailwater impingement;
Ψ_c = ratio of drop height to normal flow depth at Φ_c; and
Ω = function of empirical coefficients.

Subscripts

d = downstream; and
u = upstream.

Mechanics of jet scour downstream of a headcut

Mécanisme de l'affouillement dû à un jet en aval d'une petite chute

O. R. STEIN
Department of Civil and Agricultural Engineering, Montana State University, Bozeman, MT, USA 59717

P. Y. JULIEN
Department of Civil Engineering, Colorado State University, Fort Collins, CO, USA 80523

C. V. ALONSO
USDA-ARS Hydro-Ecosystems Research Group, Fort Collins, CO, USA 80522

SUMMARY

Scour immediately downstream of a headcut is analyzed by considering the effect of jet diffusion on sediment detachment. The analytical development results in equations for:

1. the equilibrium scour depth;
2. the rate of scour hole development.

These equations are applicable for a variety of jet configurations and any bed material including cohesive soils. The equations are tested in laboratory simulated headcuts on bed materials consisting of two non-cohesive uniform sands and one cohesive natural soil. The agreement between measured and predicted rates of scour depth increase shows that scour does not increase as a semi-logarithmic function of time. The rate of scour depth increase is very rapid for depths less than 95% of the equilibrium scour depth. Graphical solutions for the rate of scour depth increase are in agreement with the experimental measurements.

RÉSUMÉ

Le mécanisme d'érosion immédiatement en aval d'une chute est analysé en considérant l'effet du jet sur l'arrachement des sédiments. Un système d'équations a été établi qui permet de calculer:

1. la profondeur d'affouillement à l'équilibre;
2. le développement dans le temps de la fosse d'affouillement.

Ces équations peuvent s'appliquer à une grande variété de configurations d'écoulement et de matériaux mobiles y compris les sols cohésifs. Les équations ont été calées sur des essais en laboratoire avec des matériaux mobiles consistant d'une part en un mélange de deux sables non cohésifs de granulométrie uniforme et d'autre part un sol naturel cohésif. La comparaison entre mesures et calculs montre que la profondeur d'affouillement n'évolue pas selon une loi semi-logarithmique en fonction du temps. L'accroissement de la profondeur d'affouillement est très rapide pour des profondeurs inférieurs à 95% de la valeur limite. Les solutions graphiques donnant l'acroissement de la profondeur d'affouillement sont en bon accord avec les valeurs expérimentales.

Revision received December 27, 1992. Open for discussion till June 30, 1994.

1 Introduction

Scour from impinging jets has long been a research focus because it is the driving mechanism causing scour below grade control structures and dam spillways. Most investigations have considered the equilibrium scour depth in non-cohesive bed material, equilibrium scour depth being reached when the sediment particles detached from the bed cannot leave the scour hole. Jet impingement also exerts the dominant erosive action on cohesive soil below headcuts in rills and gullies. Relatively little attention has been paid to this process, which is important in terms of soil erosion characteristics and dendritic drainage network evolution, as headcuts often define the upstream end of rills and gullies.

The primary objective of this study is to examine the scour caused by free overfall jets in small scale channels such as rills. The analysis stems from the theoretical investigation of jet diffusion characteristics in a plunge pool and the erosion characteristics of the impinging jet on both cohesive and non-cohesive particles. First, a theoretical description of jet diffusion, flow velocities, shear stresses and sediment detachment characteristics is presented. This theory is then compared to a laboratory data set. The data set focuses on the changes in scour profiles with time produced by a free falling nappe for both cohesive and non-cohesive material.

2 Diffusion of free overfall jets

The flow diagram shown in Fig. 1 illustrates a jet produced by a free falling nappe entering a plunge pool. The jet, with an origin at the water surface and initial thickness y_o, enters the plunge pool at an angle χ and nearly uniform average velocity U_o.

Free jets, unaffected by a boundary, spread laterally and diffuse throughout the surrounding fluid decreasing in average velocity, as analyzed by Albertson et al. (1950). The zone in which the centerline velocity remains constant at U_o defines the potential core, of length J_p from the jet origin. Beyond this distance, the velocity U remains a maximum along the jet centerline but the entire velocity field is reduced by diffusion.

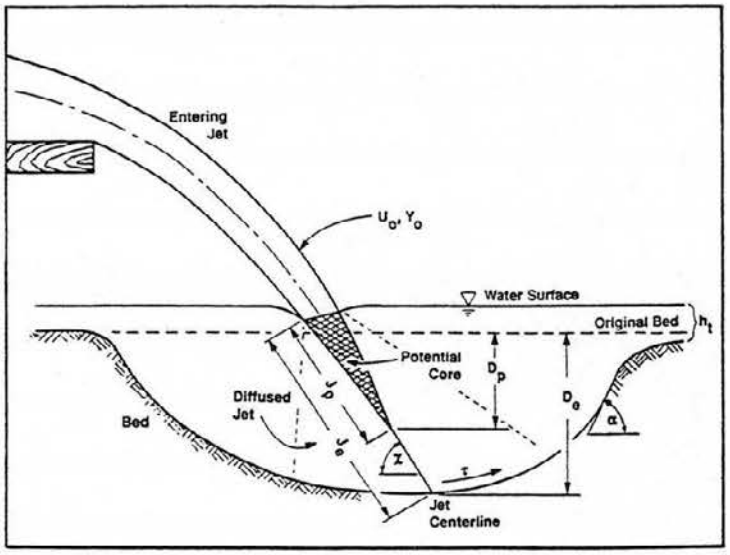

Fig. 1. Plunge pool definition sketch.
Schéma de définition de la fosse de dissipation.

The generally accepted formulation for the centerline velocity where $J > J_p$ (Rajaratnam, 1976) is:

$$\frac{U}{U_o} = C_d \sqrt{\frac{y_o}{J}}: \qquad J > J_p \tag{1}$$

where J is the distance from the origin along the centerline and the diffusion constant $C_d \approx 2.47$ is similar to the value (≈ 2.28) suggested by Albertson et al. (1950). Turbulence and non-uniform flow velocity at the jet origin influences both C_d and J_p. The length of the potential core can be simply obtained by solving equation (1) when $U = U_o$ at $J = J_p$:

$$J_p = C_d^2 y_o \tag{2}$$

Impinging jets, deflected by a flat impervious boundary, were analyzed by Beltaos (1972, 1974). His results (Beltaos 1976a, 1976b; Beltaos and Rajaratnam 1973, 1974, and 1977) identify three distinct regions in an impinging jet. The flow is analogous to a free jet for some distance from the origin and analogous to a wall jet beyond some lateral distance along the boundary from impingement. Between these regions, the boundary forces the jet to deflect causing the velocity streamlines to curve and an excess static pressure to develop. Beltaos defined the impingement region as the region in which streamlines resemble neither a free nor wall jet. His expressions for the maximum velocity in the free jet and impingement regions can be converted to the form of equation (2) in which only the value of the coefficient C_d varies. These values are 2.50 in the free jet region and 2.72 in the impingement region suggesting that an impervious boundary increases the effective diffusion constant.

Robinson (1989a,b) measured shear stress distributions along a flat impervious boundary produced by an impinging jet beneath a free overfall. His data shows that time averaged shear stress can be as much as one order of magnitude less than the maximum instantaneous value suggesting that turbulence cannot be neglected when considering jet scour.

2.1 *Equilibrium scour depth*

Most studies on the equilibrium scour depth from impinging jets have taken a rather empirical approach. Mason and Arumugam (1985) combined many previous model and prototype data sets including Cola, 1965; Hartung and Häusler, 1973; Martins, 1973, 1975 and concluded that none of the existing equations accurately predict equilibrium scour depth over the combined data sets. They attributed this to the limited dependent variables and wide range of hydraulic conditions existing in this data set.

Other researchers have used jet hydraulics to explain laboratory observations. Kobus et al. (1979) described two distinct scour hole shapes, also noted by Akashi and Saitou (1986), dependent on a dimensionless porosity factor and particle Reynolds number. Rajaratnam (1981, 1982) expanded Rajaratnam's and Beltaos' previous studies on impervious impingement to erodible beds. Mih and Kabir (1983) used Rajaratnam's analysis to study the interaction between natural streambed jet scour and armoring.

Chee and Yuen (1985) used dimensional analysis and previous relations of Beltaos (1976a) to predict the equilibrium scour depth from a large data set of jet impingement on gravel beds at various angles from 45° to 90°. They concluded that the jet impinges on the bed at the same angle as upon tailwater entry and suggested the following relationship for equilibrium scour depth D_e measured from the original unscoured bed:

$$D_e = J_e \sin\chi - h_t \tag{3}$$

380

where J_e is the jet centerline length from tailwater entry to bed impingement at equilibrium, h_t is the tailwater depth above the original unscoured bed and χ is the jet impingement angle.
Bormann (1988) and Bormann and Julien (1991) provide a unifying methodology for prediction of non-cohesive equilibrium scour depth produced by a large variety of jet configurations from deeply submerged wall jets to impinging unsubmerged jets by relating the jet hydrodynamic forces to particle stability. This is the explicit approach taken by Chee and Yuen (1985) and implicitly taken by Rajaratnam (1981, 1982) but Bormann generalizes and adds an approach similar to Stevens and Simons (1971) to account for particle stability on a sloping bed. He used equation (3) to determine D_e after the equilibrium scour length J_e is determined from the following:

$$J_e = \left[\frac{\varrho \sin\phi}{2g(\varrho_s - \varrho)\sin(\phi + \alpha)}\right]^{0.8} \frac{C_d^2 U_o^{1.6} y_o^{0.6}}{d_{50}^{0.4}} \tag{4}$$

where ϱ and ϱ_s are fluid and particle mass densities respectively, d_{50} is the mean sediment size, g the gravitational acceleration, α is the average angle of the scour hole and ϕ is the sediment angle of repose. Bormann's analysis shows relatively good agreement between measured and predicted equilibrium scour length J_e. Comparatively more scatter is obtained for predicted versus measured equilibrium scour depth D_e because of the difficulty in determining the jet impingement angle under various flow conditions.

2.2 *Rate of scour*

Rouse (1940) first suggested that scour depth increases linearly with the log of time. This approximation assumes that the scour depth increases infinitely with time and invalidates the concept of equilibrium scour depth. Laursen (1952) convincingly argued for the concept of equilibrium scour depth using the Shields parameter threshold. At some time, however long, the scour hole will have eroded to the point that the maximum average shear stress of the diffused jet equals the critical shear stress of the given bed material. This analysis of course ignores the effect on scour of turbulent bursts, which as Robinson (1989a, b) reports may have significant magnitude.
Despite the incompatibility between the concept of equilibrium scour depth and the semi-logarithmic time relationship, this rate model has also been used by Breusers (1967), Rajaratnam (1981), and Popova and Vedeneyev (1988). These predictive equations generally underestimate the scour depth at very short times and this discrepancy exists for a longer period of time for larger scale models. Additionally, scatter about the regression equations tends to increase at the longest measured times, possibly because at long times the magnitude of applied bed shear stress is approaching the critical shear stress of the bed material and turbulent fluctuations become the dominant erosive force.
Blaisdell et al. (1981) regressed an identical scour depth with time data set using semi-log, log-log and hyperbolic functions. The semi-logarithmic equation gave the poorest fit even when early data points are removed. The hyperbolic function has a computable equilibrium scour depth and gives the best fit, however the nature of this equation requires determination of a focal point which must be determined by trial and error. It is interesting to note that the predicted equilibrium depth using the hyperbolic function is reached 30,644 years after scour initiation, indicating that equilibrium scour depth may be reached only after extremely long times.

3 Analytical development

This section provides the analytical development for:
1. the evaluation of the equilibrium scour depth;
2. the time evolution of scour.

The development is quite general encompassing most previously published methods for equilibrium scour depth. It is applicable for any time during the scour process, and a variety of jet configurations and bed materials including cohesive particles.

3.1 *Equilibrium scour depth* D_e

The maximum shear stress acting upon the bed in the impingement region τ can be related to the maximum velocity in the impingement region U by introducing a coefficient of friction C_f.

$$\tau = C_f \varrho U^2 \tag{5}$$

Combining equations (1) and (5), with consideration of equation (2), gives the maximum applied bed shear stress τ, which within the potential core is constant at $\tau = \tau_o$:

$$\tau_o = C_f \varrho U_o^2 \qquad J \leq J_p \tag{6}$$

$$\tau = C_d^2 C_f \varrho U_o^2 \frac{y_o}{J} \qquad J > J_p \tag{7}$$

where J is the distance along the jet centerline from tailwater impingement to the eroding bed, J_p is the length of the jet potential core, U_o and y_o are the jet velocity and jet thickness at tailwater impingement, C_d is the diffusion coefficient and C_f is the friction coefficient.

The applied shear stress is a maximum when the eroding bed is within the potential core (equation (6)). When the bed is eroded beyond the depth of the potential core, the applied shear stress τ is inversely proportional to J (equation (7)) and decreases until τ approaches the critical shear stress for the bed material τ_c. This condition describes the equilibrium scour depth D_e. Equations (3) and (7) can be combined for the equilibrium scour depth when $\tau = \tau_c$, $J = J_e$ and the depth of tailwater is insignificant ($h_t \ll D_e$).

$$D_e = \frac{C_d^2 C_f \varrho U_o^2 y_o}{\tau_c} \sin\chi \tag{8}$$

This equation is a general expression for the equilibrium scour depth produced by an impinging jet for any jet configuration and bed material.

3.2 *Rate of scour*

The sediment detachment rate per unit area E (mass/time/area) at the point of maximum scour can be determined from sediment continuity as the product of sediment bulk density B (mass of solids/total volume) times change in scour depth D with time t. An excess shear equation is often used to determine the detachment rate in erosion models (Foster et al., 1977). Equating sediment continuity with the excess shear equation yields:

$$E = B \frac{\partial D}{\partial t} = z(\tau - \tau_c)^s \tag{9}$$

382

where $\varkappa$ and ξ are experimentally determined constants. Within the potential core, $\tau = \tau_o$, the change in scour depth D with time is given from equations (6) and (9):

$$\frac{dD}{dt} = \frac{\varkappa}{B}(C_f \varrho U_o^2 - \tau_c)^{\xi} \tag{10}$$

Integration of equation (10) from $t = 0$ to $t = T_p$ yields the time T_p at which the bed elevation is just at the tip of the potential core. The depth D_p corresponding to T_p is obtained by combining equations (2) and (3), with the assumption that the tailwater depth is insignificant ($h_t \ll D_e$).

$$T_p = \frac{BD_p}{\varkappa(C_f \varrho U_o^2 - \tau_c)^{\xi}} \tag{11}$$

$$D_p = C_d^2 y_o \sin\chi \tag{12}$$

Equations (10–12) show that scour depth D increases linearly with time t as long as the bed is within the potential core, $D \leq D_p$. Beyond the potential core, $\tau_c < \tau < \tau_o$, equation (7) shows that the maximum shear stress decreases with J due to increasing erosion of the scour hole. From equations (3), (6), (7), (9) and (12) and assuming $h_t \ll D_e$, a non-linear ordinary differential equation is obtained:

$$\frac{dD}{dt} = \frac{\varkappa}{B}\left[\frac{\tau_o D_p}{D} - \tau_c\right]^{\xi} \tag{13}$$

The equilibrium scour depth D_e is obtained when the time change in scour depth is zero, thus from equation (13):

$$\frac{D_e}{D_p} = \frac{\tau_o}{\tau_c} \tag{14}$$

Introduction of a dimensionless depth $D^* = D/D_e$, and dimensionless time $T^* = t/T_r$ where T_r is a reference time formulated from hydraulic and sediment parameters:

$$T_r = \frac{BD_e}{\varkappa\tau_o^{\xi}}\left(\frac{D_e}{D_p}\right)^{\xi} = \frac{BD_e}{\varkappa\tau_c^{\xi}} \tag{15}$$

the variable separable non-linear ordinary differential equation (13) transforms to:

$$\int_{D_p^*}^{D^*} \frac{D^{*\xi}}{(1-D^*)^{\xi}}\,dD^* = \int_{T_p^*}^{T^*} dT^* \tag{16}$$

where $D_p^* = D_p/D_e$ and $T_p^* = T_p/T_r$.

There is debate as to the proper value of the sediment detachment exponent ξ. The value of 1.5, as originally proposed by Foster et al. (1977), is derived from non-cohesive sediment transport equations, but more recent studies on cohesive soil detachment (Nearing et al., 1989; Hanson, 1989; Stein and Julien, 1991) have suggested or measured a value of 1.0. Solutions to equation (16) for $D^* \geq D_p^*$ and values of $\xi = 1$, 1.5, and for comparison as an upper limit $\xi = 2$, are provided in equations (17a), (17b) and (17c), respectively.

$$T^* - T_p^* = -D^* - \ln(1-D^*)\Big|_{D_p^*}^{D^*} \tag{17a}$$

$$T^* - T_p^* = (D^* - D^{*2})^{0.5}\left(1 - \frac{2}{D^* - 1}\right) - 1.5 \arcsin(2D^* - 1)\Big|_{D_p^*}^{D^*} \tag{17b}$$

$$T^* - T_p^* = D^* - 1 + \frac{1}{1 - D^*} + 2\ln(1 - D^*)\Big|_{D_p^*}^{D^*} \tag{17c}$$

The normalized time T_p^* corresponding to the depth of potential core scour is shown to be a function of depth or shear stress by combining equations (11), (14) and (15):

$$T_p^* = D_p^*\left(\frac{D_p^*}{1 - D_p^*}\right)^{\xi} = \frac{\tau_c}{\tau_o}\left(\frac{\tau_c}{\tau_o - \tau_c}\right)^{\xi} \tag{18}$$

This equation when combined with equation (17) provides a relation between maximum scour depth and time applicable when the bed is beyond the potential core.

The equivalent dimensionless form within the potential core ($T^* \leq T_p^*$) is obtained by combining equations (10), (14) and (15):

$$T^* = D^*\left(\frac{D_p^*}{1 - D_p^*}\right)^{\xi} \quad \text{when} \quad D^* \leq D_p^* \tag{19}$$

Solutions to equations (17), (18) and (19) are plotted, in terms of D^* versus T^*, in Fig. 2 for $\xi = 1$, 1.5 and 2 and $D_p^* = 0.0$, 0.4 and 0.8 respectively. Note that values of $D^* \leq D_p^*$ correspond to depths within the potential core and equation (19) applies. Values of $D^* \geq D_p^*$ correspond to depths beyond the potential core and equations (17) and (18) apply. As readily seen from Fig. 2 scour depth increases rapidly initially, especially for large values of D_p^*. Scour rate decreases rapidly as the equilibrium scour depth is approached and depth asymptotically approaches the equilibrium scour depth. For any value of D_p^* and ξ, scour depth is within 95% of the equilibrium depth when $T^* \geq 10$ and within 99.9% when $T^* \geq 100$. For many input values these percentages are reached considerably earlier in the scour process. Also note that at no time during the scour process does depth increase with the log of time, however this approximation is valid at intermediate times which may explain its use in many previous studies.

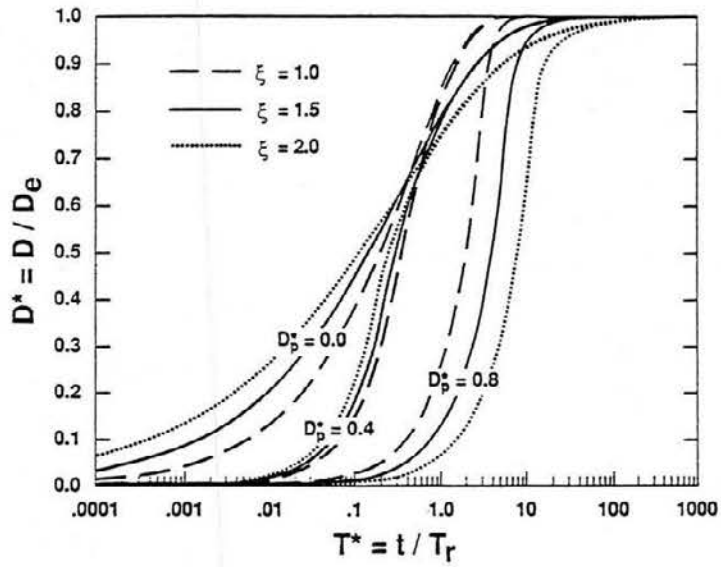

Fig. 2. Theoretical scour depth versus time.
Profondeur d'affouillement théorique en fonction du temps.

4 Laboratory experiments

Several laboratory experiments were conducted in the Hydraulics Laboratory at Colorado State University to test the theoretical relationships developed in the previous section.

4.1 *Materials and methods*

An impinging jet, similar to that which may occur below a natural headcut, was created by a free overfall at the end of a 100.0 cm long plexiglas plate set within a 10.4 cm wide by 200.0 cm long and 33.0 cm high plexiglas flume. The flume was set at 3.7% slope for all experimental runs. Each run on a given bed material represents a unique jet configuration determined by varying either the discharge or drop height between the plexiglas plate and erodible bed test section. Discharge was controlled by a pressure regulator and measured by a turbine meter in the non-recirculating flume supply line. Drop height was controlled by an exit plate set downstream from the 40.0 cm test section. Tailwater depth was therefore the normal flow depth for the given downstream hydraulic condition.

Two-dimensional scour profiles from a jet impinging on three different saturated bed materials were measured in the flume at sequential times throughout the scour process. Eight runs on a coarse sand with a mean diameter d_{50} of 1.5 mm, six runs on a fine sand $d_{50} = 0.15$ mm, and ten runs on a cohesive soil $d_{50} = 0.045$ mm were conducted. The particle size distribution of each material is given in Fig. 3. The cohesive soil is a typical agricultural soil collected from a field in eastern Colorado, USA (Norka, fine silty, mixed mesic, Aridic Argiustoll 5–9% slope). To make soil conditions as uniform as possible, and to remove large pieces of organic matter, the air dried soil was passed through a 0.420 mm sieve. This destroyed all but the natural soil's micro-aggregate structure and allowed it to retain cohesive properties upon re-wetting.

The set-up procedure for each run consisted of filling the flume test section including a volume underneath the upstream plexiglas plate with the desired bed material in 5 cm layers. The bed material was then slowly saturated from the bottom up. This method produced a uniform bulk density and water content for each bed material.

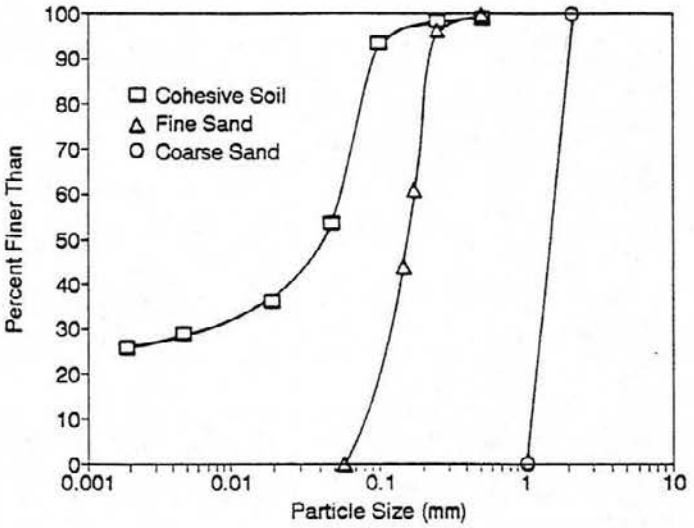

Fig. 3. Bed particle size distribution.
Granulométrie du matériau de fond.

Determining bed profile changes both quickly and accurately was critical to this study. A point gauge was used to determine initial, selected intermediate and final bed profiles. It is impossible to measure the entire profile at any instant during the run by this method, therefore a photographic technique was developed. A translucent acetate imprinted with a millimeter grid was adhered to the flume sidewall. An approximate 35 x 22 cm area of the test section was photographed through the acetate at intervals ranging from 5 sec. initially to 10 min. at the longest times, depending on the rate of profile change. Typically 30 to 40 profiles were taken per run. Accurate bed and water surface profiles, taken at virtually instantaneous selected times by this photographic technique, were digitized to store the x, y, t coordinates of the bed profiles. These coordinates were used to determine bed profiles, volume of eroded material, and maximum depth of scour at instantaneous times. Details of the experimental set-up, data collection and run specifics are given in Stein (1990).

4.2 *Results and discussion*

Typical scour profiles determined from the photographic technique for the cohesive soil (Run 8) and fine sand $d_{50} = 0.15$ mm (Run 26) over a period of approximately 2.5 hours are shown in Figs. 4a and 4b respectively. As expected, the scour rate is most rapid initially and decreases with time.

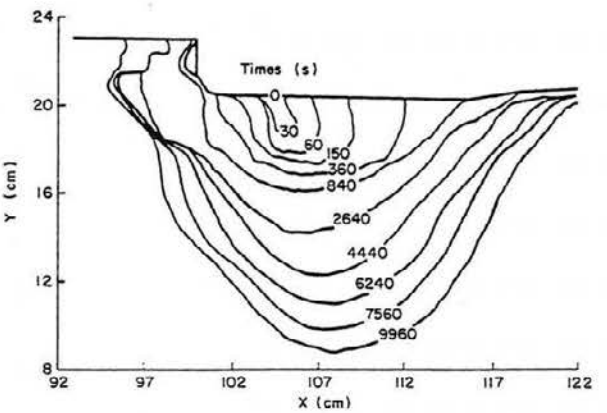

Fig. 4a.
Cohesive soil scour profiles versus time.

Profiles d'affouillement en sol cohésif en fonction du temps.

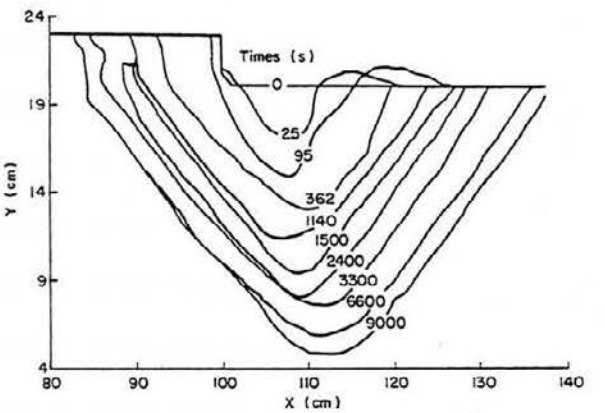

Fig. 4b.
Fine sand scour profiles versus time.

Profils d'affouillement avec du sable fin en fonction du temps.

The profile shape for all runs is approximately symmetrical about the maximum depth of scour with a slight skewness in the downstream direction. Maximum depth of scour is in the vicinity of the calculated centerline of the impinging jet, but unlike results of Chee and Yuen (1985) this maximum is consistently shifted in the upstream direction.

4.2.1 Equilibrium scour depth

Virtually all theoretically guided predictive equations for equilibrium scour depth can be simplified to equation (8). The validity of this equation was tested using the three bed materials. Bormann's method (equations (3) and (4)) was used without modification for non-cohesive sands (Runs 14–21, $d_{50} = 1.5$ mm, $\phi = 34°$; Runs 22–27, $d_{50} = 0.15$ mm, $\phi = 25°$) while equation (8) with

$\tau_c = 0.32$ Pascal was used for the cohesive bed material (Runs 1–13). This value was determined from an independent set of experiments as reported by Stein and Julien, (1991). A value of 2.6 was taken for the diffusion constant C_d. This value is higher than used by Bormann (1.8–2.3) but is lower than that given by Beltaos (2.72) for diffusion in the impingement region. Bormann's experiments often had a poorly defined jet and Beltaos' were for a plane, impervious boundary. The jet in the present experiments was well defined but boundaries are neither plane (except for $t = 0$) nor impervious. The coefficient of friction was determined from a Blasius flow assumption $C_f = (0.22/8)(q/\nu)^{-0.25}$ where q is unit discharge and ν is the kinematic viscosity.

The various parameters needed to determine the predicted equilibrium scour depth D_e from equations (3) and (4) or (8), the time T_M at which the run was terminated and the corresponding maximum measured depth D_{eM} are given in Table 1. All runs were terminated after a maximum 2.75 hr and for several runs this time was not sufficiently long for the equilibrium scour depth to be reached. A comparison between measured and predicted equilibrium scour depths should include this time factor when appropriate. Therefore, the expected equilibrium depth was adjusted D_{eP} to correspond to the measured time T_M using the appropriate formulation of equation (17) determined from scour rate data as detailed in the following section. This adjustment was most necessary for the largest equilibrium depths on the cohesive soil runs. The D^* value corresponding to D_{eP} (D_{eP}/D_e) varied from 0.27 to 0.88, 0.82 to 0.92 and 0.98 to 1.00 for cohesive soil, fine sand and coarse sand runs respectively. The adjusted equilibrium depth D_{eP} is compared to the measured depth D_{eM} in Fig. 5. These values are also given in Table 1. As can be seen from Fig. 5 almost all measured maximum depths are within 20% of the expected maximum depth, a considerable improvement over most previously published correlations.

Table 1. Experimental values of ultimate scour depth parameters
Valeurs expérimentales des paramètres caractérisant la profondeur limite d'affouillement

Run	D_h (mm)	q ($m^3/s \cdot m$)	U_o (m/s)	y_o (mm)	χ (o)	D_e (mm)	T_M (s)	D_{eP} (mm)	D_{eM} (mm)
13	10	0.00157	0.68	2.3	41	68	7200	60	77
12	10	0.00489	0.93	5.2	28	159	6000	101	112
7	20	0.00154	0.81	1.9	51	94	6240	72	81
3–4	20	0.00225	0.87	2.6	46	125	8340	98	84
11	20	0.00346	0.95	3.6	41	173	9000	123	130
6	20	0.00450	1.01	4.4	38	211	6000	122	122
8	40	0.00172	1.04	1.7	59	145	9960	113	119
1	40	0.00230	1.07	2.1	56	180	745	49	51
10	40	0.00354	1.14	3.1	51	249	9000	157	128
9	40	0.00458	1.19	3.8	48	302	4080	136	142
21	20	0.00162	0.82	2.0	50	47	9000	47	45
20	20	0.00257	0.89	2.9	45	63	4080	62	58
19	20	0.00347	0.95	3.7	41	76	1800	75	73
18	20	0.00493	1.04	4.8	37	96	1800	94	82
14	40	0.00168	1.03	1.6	59	68	1800	67	38
15	40	0.00235	1.08	2.2	55	83	1800	81	57
16	40	0.00353	1.14	3.1	51	106	1800	104	74
17	40	0.00480	1.20	4.0	47	129	5220	129	97
22	20	0.00166	0.82	2.0	50	99	9000	91	103
23	20	0.00232	0.87	2.7	46	122	9000	112	132
24	20	0.00349	0.95	3.7	41	161	9000	143	163
27	40	0.00175	1.04	1.7	59	140	9000	115	134
26	40	0.00242	1.08	2.2	55	172	9000	151	162
25	40	0.00337	1.13	3.0	51	212	9000	193	175

Table 2. Experimental values of scour depth evolution parameters
Valeurs expérimentales des paramètres caractérisant l'évolution de la profondeur d'affouillement

Run	B (kg/m^3)	D_p (m)	D_e (m)	D_p^*	τ_0 (Pa)	x [1]	ξ	T_r (s)
13	1290	0.010	0.068	0.15	2.21	0.04	1.0	6615
12	1290	0.017	0.159	0.11	3.12	0.04	1.0	15509
7	1290	0.010	0.094	0.11	3.14	0.04	1.0	9220
3–4	1290	0.013	0.125	0.10	3.27	0.04	1.0	12253
11	1290	0.016	0.173	0.09	3.52	0.04	1.0	16921
6	1290	0.019	0.211	0.09	3.74	0.04	1.0	20607
8	1290	0.010	0.145	0.07	4.99	0.04	1.0	14167
1–2	1290	0.012	0.180	0.07	4.97	0.04	1.0	17617
10	1290	0.016	0.249	0.07	5.06	0.04	1.0	24343
9	1290	0.019	0.302	0.06	5.18	0.04	1.0	29531
21	1350	0.010	0.047	0.22	3.15	0.98	1.5	115
20	1350	0.014	0.063	0.22	3.33	0.98	1.5	140
19	1350	0.016	0.076	0.21	3.52	0.98	1.5	161
18	1350	0.019	0.096	0.20	3.83	0.98	1.5	192
14	1350	0.009	0.068	0.14	4.99	0.98	1.5	163
15	1350	0.012	0.083	0.15	4.97	0.98	1.5	184
16	1350	0.016	0.106	0.15	5.06	0.98	1.5	216
17	1350	0.020	0.129	0.15	5.21	0.98	1.5	247
22	1670	0.010	0.099	0.11	3.16	0.30	1.5	2837
23	1670	0.013	0.122	0.11	3.28	0.30	1.5	3354
24	1670	0.016	0.161	0.10	3.53	0.30	1.5	4172
27	1670	0.010	0.140	0.07	4.99	0.30	1.5	3858
26	1670	0.012	0.172	0.07	4.97	0.30	1.5	4433
25	1670	0.016	0.212	0.07	5.04	0.30	1.5	5155

[1] Units dependent on value of ξ; s/m if $\xi = 1.0$, $s^2/m^{0.5} \cdot kg^{0.5}$ if $\xi = 1.5$

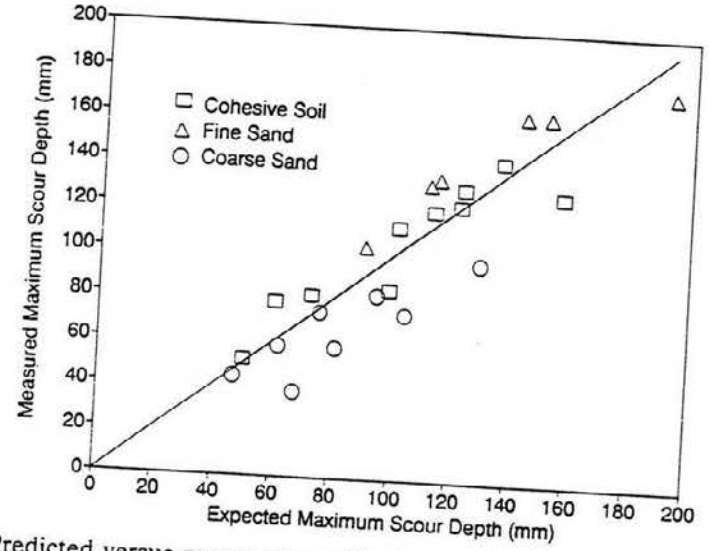

Fig. 5. Predicted versus measured equilibrium scour depth.
Profondeur d'affouillement à l'équilibre. Comparaison calcul-mesures.

4.2.2 Rate of scour

The applicability of equations (17), (18) and (19) for scour depth increase was tested using the same runs as described for equilibrium depth. The depth of potential core scour $D_p^* = D_p/D_e$ varies slightly in the experiments from 0.06 to 0.15 for cohesive soil, 0.07 to 0.11 for fine sand and 0.14 to 0.22 for the coarse sand. As seen in Fig. 2, D_p^* strongly influences scour rate, but within the small experimental range is insignificant. The raw data were normalized using the reference time T_r calculated assuming $\xi = 1$, 1.5 and 2. The parameter $\varkappa$ was adjusted for each bed material and ξ value to provide the best fit between theory and experimental results. Plots of the measured increase in normalized scour depth D^* with normalized time T^* for ten cohesive soil runs, six fine sand runs and seven coarse sand runs are compared with predicted values in Figs. 6, 7 and 8, respectively. The sand runs have the best fit when $\xi = 1.5$ and $\varkappa = 0.98$ ($s^2 \cdot kg^{-0.5} \cdot m^{-0.5}$) for the

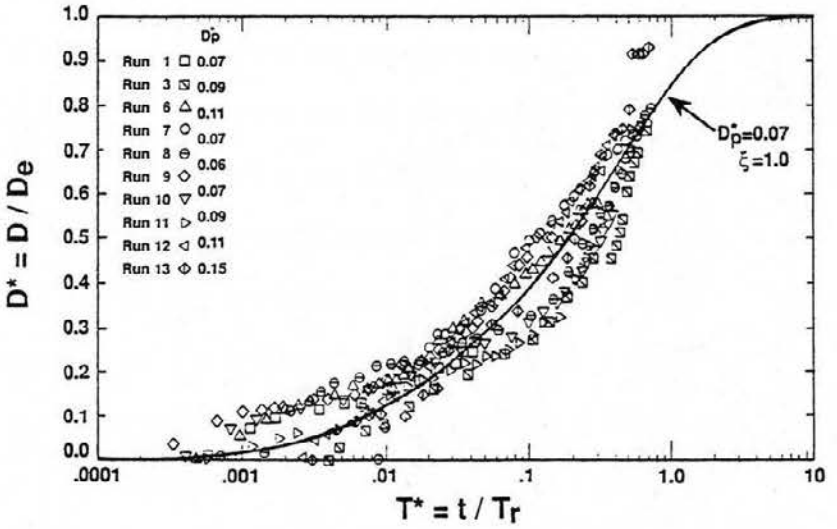

Fig. 6. Predicted versus measured scour depth evolution; cohesive soil.
Evolution de la profondeur d'affouillement; sol cohésif. Comparaison calcul-mesures.

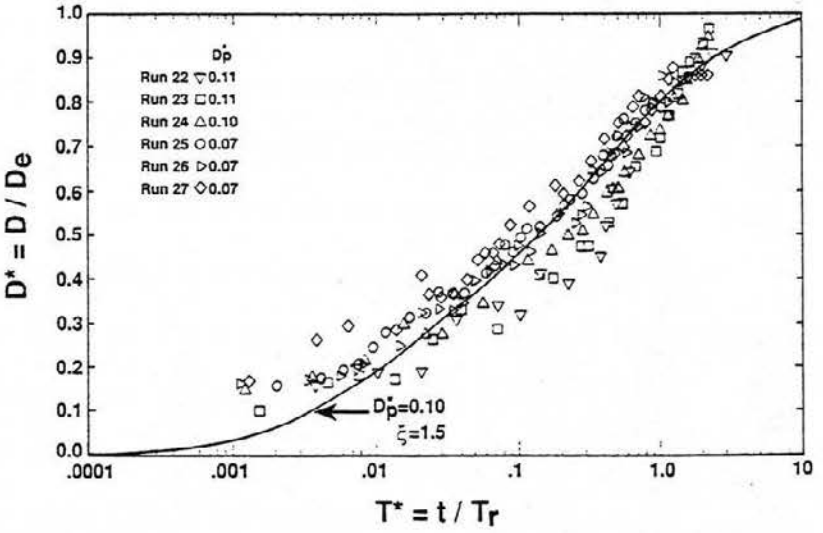

Fig. 7. Predicted versus measured scour depth eveolution; fine sand.
Evolution de la profondeur d'affouillement; sable fin. Comparaison calcul-mesures.

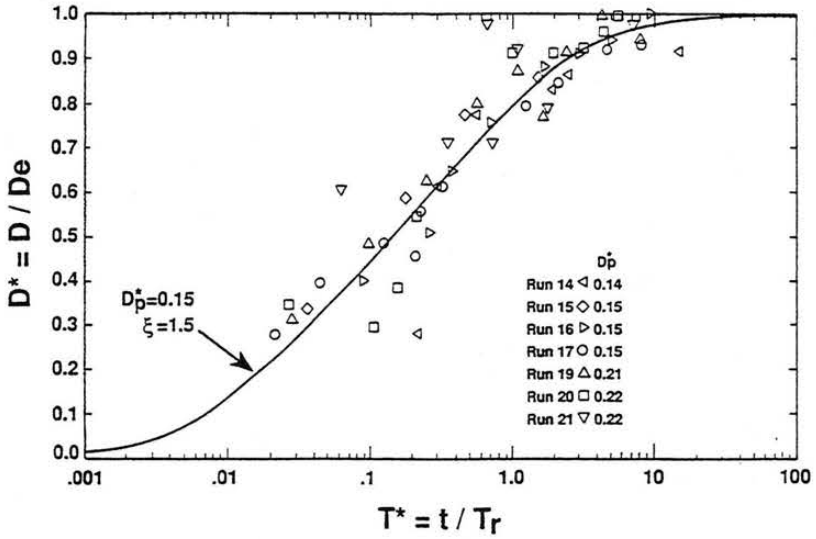

Fig. 8. Predicted versus measured scour depth evelution; coarse sand.
Evolution de la profondeur d'affouillement; sable grossier. Comparaison calcul-mesures.

coarse sand and 0.30 for the fine sand. The cohesive soil runs have the best fit with $\xi = 1.0$ and $x = 0.04$ (s · m^{-1}). As discussed in Stein and Julien (1991), these data support previously proposed or measured values of the experimental constant ξ. The change in measured scour depth is not linear with the log of time for any bed material or value of the experimental constants, x and ξ. The present analysis with the proper choice of constants is a marked improvement over the semi-logarithmic linear model.

5 Conclusions

The change in maximum scour depth with time produced by an impinging jet proceeds at a rate dependent on the position of the bed relative to the jet origin, which in general corresponds to the tailwater elevation, but in this study, with an extremely shallow tailwater depth, corresponds to the original bed elevation. The rate can be analytically determined by relating the maximum velocity of a diffusing jet at a specific time with the generally accepted excess shear sediment detachment equation while considering sediment continuity at the eroding bed's surface. Initially during the scour process, while the bed surface is within the jet's potential core ($D^* \leq D_p^*$), the rate is constant and given by equation (10). Thereafter ($D^* \geq D_p^*$), the scour rate decreases with time as given by equation (13). The scour depth asymptotically approaches an equilibrium depth D_e calculated from equation (8). Using the proper normalizing parameters $D^* = D/D_e$ and $T^* = t/T_r$, with T_r from equation (15), the rate of scour can be calculated for any bed material, jet configuration and time within the scour process using equations (17–19). A graphical representation of these equations, as shown in Fig. 2, reveals that, regardless of input parameters, scour depth is within 95% of the equilibrium depth for $T^* \geq 10$. This condition is reached sooner for a larger critical shear stress and/or a smaller jet.

The validity of the developed equations has been tested in the laboratory with non-cohesive and cohesive bed materials. Agreement between measured and predicted equilibrium scour depths is generally within 20% as shown in Fig. 5. This agreement is generally better than previously

published results for non-cohesive material and has the advantage of being equally applicable to cohesive bed materials. Correlation between the measured and predicted scour rate is equally good with the proper choice of the excess shear sediment detachment parameters, as shown in Figs. 6, 7 and 8. The results indicate that the value of the sediment detachment exponent ξ is 1.5 for non-cohesive sand and 1.0 for cohesive soil and thus supports previously published conclusions. The usage of an impinging jet holds promise as an improved method for the determination of all experimental parameters of the excess shear sediment detachment equation.

Acknowledgements

This study has been primarily funded by the USDA-ARS Hydro-Ecosystems Research Group. Additional support is provided by the ARO Center for Geosciences at Colorado State University (Grant ARO/DAAL 03-86-K-0175) and the Montana State Agricultural Experiment Station (Paper no. J-2703). Our appreciation goes to all groups.

List of symbols

B soil bulk density
C_d diffusion constant of a jet
C_f coefficient of friction
d_{50} mean sediment size
D maximum depth of jet scour at a given time t
D^* normalized maximum scour depth (D/D_e)
D_e equilibrium depth of jet scour
D_{eM} measured scour depth at time T_M
D_{eP} predicted scour depth at time T_M
D_h drop height of the headcut
D_p depth of scour corresponding to potential core tip
D_p^* normalized depth of potential core tip (D_p/D_e)
E sediment detachment rate per unit area
g gravitational acceleration
h_t depth of tailwater
J distance along a jet centerline
J_e distance along a jet centerline to impingement at equilibrium
J_p length of a jet potential core
q unit flow discharge
t time
T^* normalized time (t/T_r)
T_M time at which the maximum scour depth was measured
T_p time corresponding to potential core scour depth D_p
T_p^* normalized time (T_p/T_r)
T_r reference time
U maximum diffused jet velocity
U_o initial jet velocity
y_o initial jet thickness
$\varkappa, \xi$ constants of sediment detachment equation

α average angle of scour hole boundary
ν fluid kinematic viscosity
ϱ fluid density
ϱ_s particle density
τ_c critical shear stress for erosion initiation
τ shear stress in the impingement region
τ_o shear stress in the potential core
ϕ angle of repose of submerged sediment
χ jet angle at tailwater impingement

References

1. ALBERTSON, M. L., DAI, Y. B., JOHNSON, R. A. and ROUSE, H. (1950), Diffusion of Submerged Jets, Trans. ASCE 115, pp. 639–697.
2. AKASHI, N. and SAITOU, T. (1986), Influence of Water Surface on Scour From a Vertical Submerged Jet, J. of Hydroscience and Hydr. Engr. 4(2) pp. 55–69.
3. BELTAOS, S. (1972), Normal Impingement of Plane Turbulent Jets on Sooth Walls, M.S. Thesis, University of Alberta, Edmonton, Alberta, Canada.
4. BELTAOS, S. (1974), Turbulent Impinging Jets, Ph.D. Dissertation, University of Alberta, Edmonton, Alberta, Canada.
5. BELTAOS, S. (1976a), Oblique Impingement of Plane Turbulent Jets, J. Hydr. Div., ASCE 102(HY9), pp. 1177–1192.
6. BELTAOS, S. (1976b), Oblique Impingement of Circular Turbulent Jets, J. Hydr. Res. 14(1), pp. 17–36.
7. BELTAOS, S. and RAJARATNAM, N. (1973), Plane Turbulent Impinging Jets, J. Hydr. Res. 11(1), pp. 29–59.
8. BELTAOS, S. and RAJARATNAM, N. (1974), Impinging Circular Turbulent Jets, J. Hydr. Div., ASCE 100(HY10), pp. 1313–1328.
9. BELTAOS, S. and RAJARATNAM, N. (1977), Impingement of Axisymmetric Developing Jets, J. Hydr. Res. 15(4), pp. 311–325.
10. BLAISDELL, F. W., ANDERSON, C. L. and HEBAUS, G. G. (1981), Ultimate Dimensions of Local Scour, J. Hydr. Div., ASCE 107(HY3), pp. 327–337.
11. BORMANN, N. E. (1988), Equilibrium Local Scour Depth Downstream of Grade Control Structures, Ph.D. Dissertation, Colorado State University, Fort Collins, Co.
12. BORMANN, N. E. and JULIEN, P. Y. (1991), Scour Downstream of Grade Control Structures, J. Hydr Engr. 117(5), pp. 579–594.
13. BREUSERS, H. N. C. (1967), Time Scale of Two Dimensional Local Scour, Inter. Asso. Hydr. Res. Proc., 12th Congress, Vol. 3, pp. 275–282, Paper No. C32.
14. CHEE, S. P. and YUEN, E. M. (1985), Erosion of Unconsolidated Gravel Beds, Can. J. Civ. Engr. 12, pp. 559–566.
15. COLA, R. (1965), Energy Dissipation of a High-Velocity Vertical Jet Entering a Basin, Inter. Asso. Hydr. Res. Proc., 11th Congress, Vol. 1, Paper No. 1.52.
16. FOSTER. G. R., MEYER, L. D. and ONSTAD, C. A. (1977), An Erosion Equation Derived From Basic Erosion Principles, Trans. ASAE 20(4), pp. 678–682.
17. HANSON, G. L. (1989), Channel Erosion Study of Two Compacted Clays, Trans. ASAE 32(5), pp. 485–490.
18. HARTUNG, F. and HÄUSLER, E. (1973), Scours, Stilling Basins and Downstream Protection Under Free Overfall Jets at Dams, 11th Inter. Comm. Large Dams Trans., Vol II Q41, Paper R3, pp. 39–56.
19. KOBUS, H., LEISTER, P. and WESTRICH, B. (1979), Flow Field and Scouring Effects of Steady and Pulsating Jets Impinging on a Moveable Bed, J. Hydr. Res. 17(3), pp. 175–192.
20. LAURSEN, E. M. (1952), Observations on the Nature of Scour, Proc. 5th Hydr. Conf., University of Iowa, Iowa City, Iowa Bul. 34, pp. 179–197.
21. MARTINS, R. (1973), Contribution to the Knowledge on the Scour Action of Free Jets on Rocky River-Beds, 11th Inter. Comm. Large Dams Trans., Vol. II Q41, Paper R44, pp. 799–814.
22. MARTINS, R. (1975), Scouring of Rocky River-Beds by Free-Jet Spillways, Inter. Water Pow. Dam Constr. 27(4), pp. 152–153.
23. MASON, P. J. and ARUMUGAM, K. (1985), Free Jet Scour Below Dams and Flip Buckets, J. Hydr. Engr. 111(2), pp. 220–235.

24. MIH, W. C. and KABIR, J. (1983), Impingement of Water Jets on Nonuniform Streambed, J. Hydr. Engr. 109(4), pp. 536-548.
25. NEARING, M. A., FOSTER, G. R., LANE, L. J. and FINKNER, S. A. (1989), A Process-Based Soil Erosion Model for USDA Water Erosion Prediction Project Technology, Trans. ASAE 32(5), pp. 1587-1593.
26. POPOVA, K. S. and VEDENEYEV, Y. E. (1988), Time Variation in the Depth of Local Scour Downstream of Dams, Fluid Mech. - Soviet Res. 17(3), pp. 123-134.
27. RAJARATNAM, N. (1976), Turbulent Jets: Development in Water Science #5, Elsevier Scientific Publishing Co., Amsterdam, The Netherlands.
28. RAJARATNAM, N. (1981), Erosion by Plane Turbulent Jets. J. Hydr. Res. 19(4), pp. 339-359.
29. RAJARATNAM, N. (1982), Erosion by Unsubmerged Plane Water Jets. In: Applying Research to Hydraulic Practice, ASCE Conf., Jackson, MS, pp. 280-288.
30. ROBINSON, K. M. (1989a), Stress Distribution at an Overfall, Trans. ASAE 32(1), pp. 75-80.
31. ROBINSON, K. M. (1989b), Hydraulic Stress on an Overfall Boundary, Trans. ASAE 32(4), pp. 1269-1274.
32. ROUSE, HUNTER (1940), Criteria for Similarity in the Transportation of Sediment, Proc. 1st Hydraulic Conf., State University of Iowa, Iowa City, Iowa, pp. 33-49.
33. STEIN, O. R. (1990), Mechanics of Headcut Migration in Rills, Ph.D. Dissertation, Colorado State University, Fort Collins, CO 80523.
34. STEIN, O. R. and JULIEN, P. Y. (1991), Measurement of Rill Erosion Sediment Detachment, ASAE Paper No. 91-2086, Presented Internat. Summer Meetings, June 23-26, Albuquerque, NM, USA.
35. STEVENS M. A. and SIMONS, D. B. (1971), Stability Analysis for Coarse Granular Material. In: River Mechanics, Vol. 1, (Chap. 17), H. W. Shen (ed.), Fort Collins, CO.

SEDIMENT CONCENTRATION BELOW FREE OVERFALL

By O. R. Stein,[1] Associate Member, ASCE, and P. Y. Julien,[2] Member, ASCE

ABSTRACT: Time-varying sediment concentration exiting a plunge pool is analyzed by considering the effect of free-overfall jet diffusion on sediment detachment and scour. The analysis results in dimensionless relationships between scour volume, sediment concentration, maximum scour depth, and time. Sediment concentration is at a maximum near the initiation of scour, when the eroding bed is at the tip of the impinging jet's potential core. Thereafter, sediment concentration decreases as a function of time and scour-hole geometry, expressed as maximum scour depth. Dimensionless geometric relationships show that the scour volume per unit width can be expressed as twice the square of the maximum scour depth at the corresponding time for the cohesive and noncohesive soils tested. Analytical relationships between sediment concentration and time are verified by laboratory experiments of scour below a free overfall on two sand-bed materials (one coarse and one fine) and on one cohesive soil, each replicated several times. The agreement between measured and predicted values is best for the noncohesive sands.

INTRODUCTION

A free overfall is associated with an abrupt break in channel bed slope such as below grade-control structures, dam outlets, cantilevered pipes, and head cuts incised in ephemeral streams. The scour potential in the region immediately downstream from the free overfall is well documented. For example, Bormann and Julien (1991) have examined scour below grade-control structures; Blaisdell and Anderson (1988a,b) studied the scour potential below cantilevered pipes; Holland and Pickup (1976), Begin et al. (1980a,b), Gardner (1983), and Stein and Julien (1993) examined the sediment production and migration of head cuts. A summary of an empirical approach for the analysis of scour below hydraulic structures is provided by Mason and Arumugam (1985). Scour dimensions have also been related to impinging-jet diffusion (Kobus et al. 1979; Rajaratnam 1981, 1982; Chee and Yuen 1985). Most research efforts have focused on predicting scour depth, which may affect the structure at the free overfall, as opposed to volumetric scour dimensions and sediment concentration, which may affect downstream morphology and water quality as well as the structure but are much more difficult to measure in an actively eroding plunge pool.

The aim of this paper is to determine relationships between time, scour depth, scour-hole volume, and sediment concentration generated by flow at a free overfall, independent of possible soil mass wasting contributions to downstream sediment load. The analysis describes the change with time of sediment detachment and transport within a developing plunge pool at the soil/water interface. The approach relates downstream sediment con-

[1]Asst. Prof., Dept. of Civ. and Agric. Engrg., Montana State Univ., Bozeman, MT 59717.

[2]Assoc. Prof., Dept. of Civ. Engrg., Colorado State Univ., Fort Collins, CO 80523.

Note. Discussion open until February 1, 1995. To extend the closing date one month, a written request must be filed with the ASCE Manager of Journals. The manuscript for this paper was submitted for review and possible publication on May 23, 1993. This paper is part of the *Journal of Hydraulic Engineering*, Vol. 120, No. 9, September, 1994. ©ASCE, ISSN 0733-9429/94/0009-1043/$2.00 + $.25 per page. Paper No. 6224.

394

centration to diffusion of an impinging jet. Jet diffusion is used to determine the time change in maximum scour depth. In turn, dimensionless relationships between scour depth and volume are developed. Finally, sediment concentration rate is related to scour volume changes. The analysis results in graphic relationships between sediment concentration and time. These relationships are tested using laboratory measurements of sediment concentration leaving a scour hole created by the impingement of a free overfall jet on three bed materials: two relatively uniform sand sizes and one cohesive soil.

JET DIFFUSION AND SCOUR HOLE GEOMETRY

The plunge pool created by the impingement of a two-dimensional plane jet on an erodible bed, as produced below a free overfall, is shown in Fig. 1. The jet, with an origin at the water surface and initial thickness y_0, enters the plunge pool at an angle χ and nearly uniform average velocity U_0. Free jets, unaffected by a boundary, spread longitudinally and diffuse throughout the surrounding fluid, decreasing in average velocity as analyzed by Albertson et al. (1950). The zone in which the centerline velocity remains constant at U_0 defines the potential core, of length J_p from the jet origin. Beyond this distance, the velocity U remains a maximum along the jet centerline but the entire flow velocity field is reduced by diffusion.

The generally accepted formulation for the centerline velocity U where $J > J_p$ (Rajaratnam 1976) is:

$$\frac{U}{U_0} = C_d \sqrt{\frac{y_0}{J}}; \qquad J > J_p \tag{1}$$

where J = the distance from the origin along the centerline, and the diffusion constant $C_d \approx 2.47$ is similar to the value (≈ 2.28) suggested by Albertson et al. (1950). Tubulence and nonuniform flow velocity at the jet origin

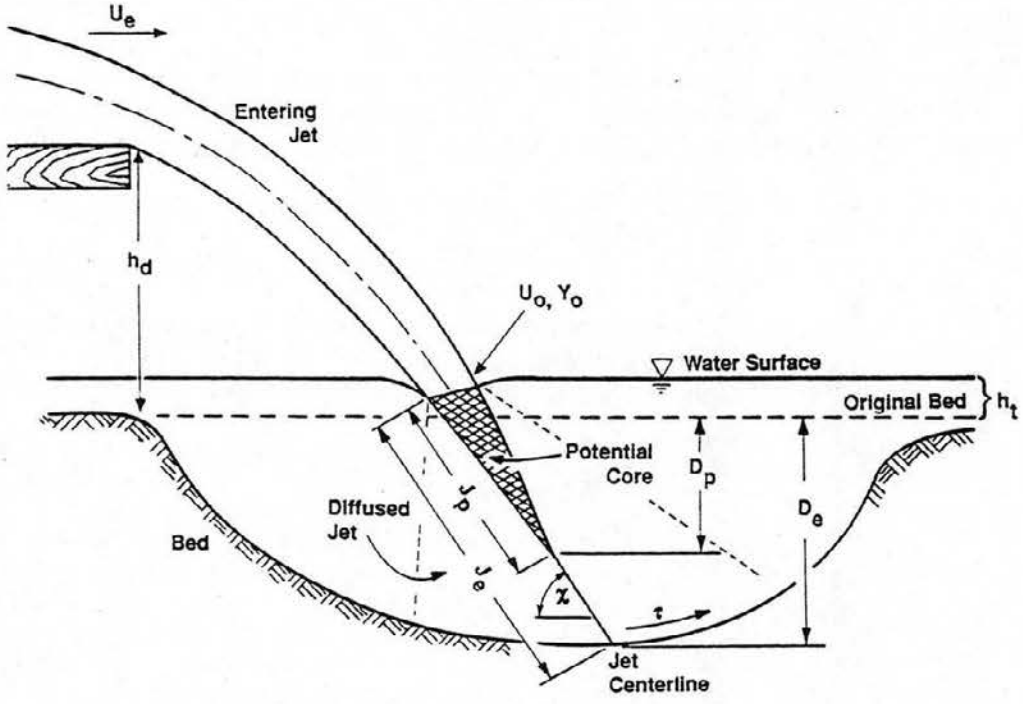

FIG. 1. Plunge-Pool Definition

influences both C_d and J_p. The length of the potential core can be obtained by solving (1) when $U = U_0$ at $J = J_p$:

$$J_p = C_d^2 y_0 \tag{2}$$

Impinging jets, deflected by a flat impervious boundary, were analyzed by Beltaos (1972, 1974). His results for plane jets (Beltaos and Rajaratnam 1973; Beltaos 1976) identify three distinct regions in an impinging jet. The flow in analogous to a free jet for some distance from the origin and analogous to a wall jet beyond some longitudinal distance along the boundary from impingement. Between these regions, the jet is deflected by the boundary, causing the velocity streamlines to curve and an excess static pressure to develop. Beltaos defined the impingement region as the region in which streamlines resemble neither a free nor wall jet. His expressions for the maximum velocity in the free jet and impingement regions can be converted to the form of (1) in which only the value of the coefficient C_d varies. These values are 2.50 in the free-jet region and 2.72 in the impingement region, suggesting that an impervious boundary increases the effective diffusion constant.

Scour-hole geometry is usually represented by maximum depth:

$$D = J \sin \chi - h_t \tag{3}$$

where D = the maximum depth at an arbitrary time; and h_t = the tailwater depth. Many studies have found that other scour-hole dimensions can be related to depth (Chee and Kung 1971; Rajaratnam 1981; Blaisdell et al. 1981; Blaisdell and Anderson 1988b). Rouse (1940) first suggested that scour depth increases linearly with the log of the time. This approximation assumes that the scour depth increases infinitely with time and invalidates the concept of equilibrium or ultimate scour depth. Laursen (1952) convincingly argued for the concept of equilibrium scour depth using the Shields parameter threshold. At some time, however long, the scour hole will have eroded to the point that the shear stress of the diffused jet equals the critical shear stress of the bed material. This analysis of course ignores the effect on scour of turbulent bursts, which as Robinson (1989a,b) reports may be an order of magnitude higher than the time-averaged shear stress.

ANALYTICAL DEVELOPMENT

Scour Depth versus Time

The sediment detachment rate per unit area E (mass/time/area) at the point of maximum scour can be determined from sediment continuity as the product of sediment bulk density B (mass of solids/total volume) and the change in scour depth D with time t. An excess shear equation is often used to determine the detachment rate in erosion models (Foster et al. 1977). Equating sediment continuity with the excess shear equation yields:

$$E = B \frac{dD}{dt} = \kappa(\tau - \tau_c)^{\xi} \tag{4}$$

where τ = the applied shear stress; τ_c = the critical shear stress of the bed material; and κ and ξ = experimentally determined constants.

The maximum shear stress τ acting on the bed in the scour hole can be related to the maximum diffused jet velocity in the plunge pool U by introducing a coefficient of friction C_f.

$$\tau = C_f \rho U^2 \tag{5}$$

Combining (1) and (5), with consideration of (2), gives the maximum applied bed shear stress τ, which within the potential core is constant at $\tau = \tau_0$:

$$\tau_0 = C_f \rho U_0^2; \qquad J \leq J_p \tag{6}$$

$$\tau = C_d^2 C_f \rho U_0^2 \frac{y_0}{J}; \qquad J > J_p \tag{7}$$

where J = the distance along the jet centerline from tailwater impingement to the eroding bed; J_p = the length of the jet potential core; U_0 and y_0 = the jet velocity and jet thickness at tailwater impingement; C_d = the diffusion coefficient, and C_f = the friction coefficient. The equilibrium scour depth D_e occurs when $\tau = \tau_c$; therefore, from (3) and (7), and assuming tailwater depth is insignificant ($h_t \approx 0$):

$$D_e = \frac{C_d^2 C_f \rho U_0^2 y_0}{\tau_c} \sin \chi \tag{8}$$

Similarly, from (2) and (3), the depth of scour when the bed is just at the tip of the potential core D_p is:

$$D_p = C_d^2 y_0 \sin \chi \tag{9}$$

From (3), (4), (6), (7), and (9), and assuming $h_t \ll D_e$, a nonlinear ordinary differential equation, applicable when the bed is beyond the potential core, is obtained:

$$\frac{dD}{dt} = \frac{\kappa}{B}\left(\frac{\tau_0 D_p}{D} - \tau_c\right)^{\xi}; \qquad D \geq D_p \tag{10}$$

Integration of (4) from $t = 0$ to $t = T_p$ with τ constant at τ yields the time of potential core scour, which corresponds to the depth $D = D_p$:

$$T_p = \frac{B D_p}{\kappa(\tau_0 - \tau_c)^{\xi}} \tag{11}$$

The equilibrium scour depth D_e is obtained when the time change in scour depth is zero; thus from (10):

$$\frac{D_e}{D_p} = \frac{\tau_0}{\tau_c} \tag{12}$$

The time T_p and corresponding depth D_p delineate the break between potential core hydraulics and jet-diffusion hydraulics control of sediment detachment. For shorter times and shallower depths, when the bed is within the potential core, the scour rate [(4)] is independent of time because shear stress is constant [(6)]. Thereafter, as scour depth increases, shear stress [(7)] and scour rate [(10)] decrease. The scour rate beyond the potential core [(10)] can be rewritten in a dimensionless form:

$$\frac{dD^*}{dT^*} = \left(\frac{1 - D^*}{D^*}\right)^{\xi}; \qquad D^* \geq D_p^* \tag{13}$$

by combining (10) and (12) and introducing dimensionless depths $D^* =$

D/D_e and $D_p^* = D_p/D_e$, and dimensionless time $T^* = t/T_r$, where T_r is a reference time of convenience with no physical significance, formulated by combining the dimensional hydraulic and sediment parameters of (10):

$$T_r = \frac{BD_e}{\kappa\tau_0^{\xi}}\left(\frac{D_e}{D_p}\right)^{\xi} = \frac{BD_e}{\kappa\tau_c^{\xi}} \tag{14}$$

Eq. (13) shows that the change in scour depth with time can be expressed as function of the ratio of maximum scour depth at the corresponding time to the equilibrium scour depth. Solutions to (13), in terms of T^* versus D^*, are dependent on value of the sediment-detachment exponent ξ. For values of $\xi = 1.0$ and 1.5, respectively, solutions are (Stein et al. 1993):

$$T^* - T_p^* = -D^* - \ln(1 - D^*)\Big|_{D_p^*}^{D^*} \tag{15a}$$

$$T^* - T_p^* = (D^* - D^{*2})^{0.5}\left(1 - \frac{2}{D^* - 1}\right) - 1.5\arcsin(2D^* - 1)\Big|_{D_p^*}^{D^*} \tag{15b}$$

where $T_p^* = T_p/T_r$ = the dimensionless time of potential core scour. The exponent value $\xi = 1.5$ is based on sediment transport equations and applicable to noncohesive-sediment detachment. Recent studies (Nearing et al. 1989; Hanson 1989; Stein and Julien 1991) on cohesive-soil detachment have suggested or measured a value of $\xi = 1.0$.

Sediment Concentration versus Scour Volume, Scour Depth, and Time

Owing to the conservation of mass, the sediment concentration leaving the two-dimensional scour hole can be expressed as the change in scour volume with time:

$$C = \frac{B}{\rho q}\frac{dV}{dt} \tag{16}$$

where C = the sediment concentration (mass solids/mass water); B = the bed-material bulk density; V = the scoured volume per unit width; ρ = the fluid mass density; q = the unit flow rate; and t = the time from the initiation of scour. Substituting the dimensionless $T^* = t/T_r$ and $V^* = V/D_e^2$ into (16) yields:

$$C = \frac{\kappa D_e \tau_c^{\xi}}{\rho q}\frac{dV^*}{dT^*} \tag{17}$$

where D_e = the equilibrium scour depth; κ and ξ = experimental sediment detachment parameters; and τ_c = the critical shear stress of the bed material.

A power function relating scour volume and scour depth $V^* = \alpha D^{*\beta}$ where α and β are experimentally determined constants yields:

$$\frac{dV^*}{dT^*} = \phi D^{*(\beta-1)}\frac{dD^*}{dT^*} \tag{18}$$

where $\phi = \alpha\cdot\beta$ = a scour-hole shape function; and $D^* = D/D_e$.

Sediment concentration and scour depth are then related by combining (13), (17) and (18):

$$C = \frac{\kappa D_e \tau_c^{\xi}}{\rho q} \phi D^{*(\beta-1)} \left(\frac{1 - D^*}{D^*}\right)^{\xi}, \qquad D^* \geq D_p^* \tag{19}$$

The maximum sediment concentration occurs when scour is within the potential core, when $D^* = D_p^*$; thus from (19):

$$C_{\max} = \frac{\kappa D_e \tau_c^{\xi}}{\rho q} \phi D_p^{*(\beta-1)} \left(\frac{1 - D_p^*}{D_p^*}\right)^{\xi} \tag{20}$$

Defining $C^* = C/C_{\max}$, combination of (19) and (20) yields:

$$C^* = \frac{C}{C_{\max}} = \left(\frac{D_p^*}{D^*}\right)^{1+\xi-\beta} \left(\frac{1 - D^*}{1 - D_p^*}\right)^{\xi}, \qquad D^* \geq D_p^* \tag{21}$$

Eqs. (19)–(21) show that the sediment concentration leaving the scour hole is a function of the corresponding normalized scour depth D^*, the scour-hole geometry through the shape function ϕ and the sediment-detachment potential of the flow. Of primary interest is the relationship between sediment concentration and time, achieved by combining (15) and (21). Graphic solutions to (15) and (21), comparing C^* and T^* as well as the relationship between scour volume and scour depth expressed in (18) are tested using laboratory data of scour below a free overfall for two different-sized noncohesive soils and one cohesive soil.

EXPERIMENTS

Several laboratory experiments were conducted in the Hydraulics Laboratory at Colorado State University to test the theoretical relationships developed in the previous section. An impinging jet was created by a free overfall at the end of a 100.0-cm-long acrylic-plastic plate set within an acrylic-plastic flume 10.4 cm wide by 200.0 cm long and 33.0 cm high. The flume was set at 3.7% slope for all experimental runs. Each run on a given bed material represents a unique jet configuration determined by varying either the discharge or drop height between the acrylic-plastic plate and erodible bed test section. Discharge was controlled by a pressure regulator and measured by a turbine meter in the nonrecirculating flume supply line. Drop height was controlled by placement of a nonerodible plate in the bed material downstream from the 40.0-cm test section. There was a smooth transition between the test bed and plate; therefore tailwater depth was the normal flow depth in the downstream section.

Two-dimensional scour profiles from a jet impinging on three different saturated bed materials were measured in the flume at sequential times throughout the scour process. Eight runs (14–21) on a coarse sand with a mean diameter d_{50} of 1.5 mm, six runs (22–27) on a fine sand $d_{50} = 0.15$ mm, and nine runs (3–13) on a cohesive soil $d_{50} = 0.045$ mm were conducted. The particle size distribution of each material is given in Fig. 2. The cohesive soil is a typical agricultural soil (Norka series) collected in eastern Colorado. To maintain uniform cohesive-soil conditions and to remove large pieces of organic matter, the air-dried soil was passed through a 0.420-mm sieve, which destroyed large aggregates but allowed the soil to retain cohesive properties upon rewetting.

The setup procedure for each run consisted of filling the flume test section including a volume underneath the upstream acrylic-plastic plate with the desired bed material in 5-cm layers. The bed material was then slowly

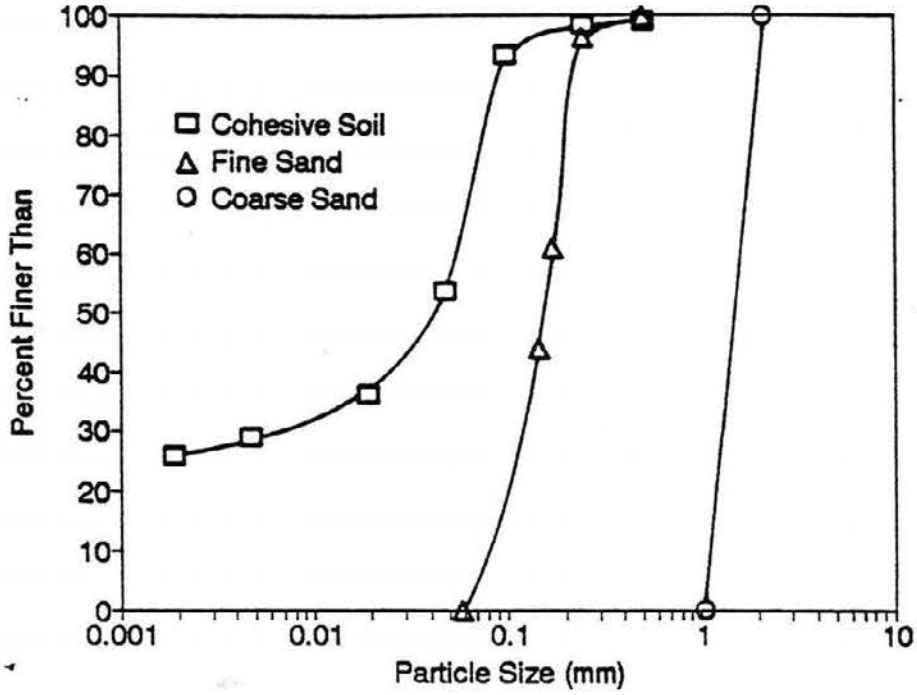

FIG. 2. Bed-Particle-Size Distribution

saturated from the bottom up. This method produced a uniform bulk density and water content for each bed material.

Bed profiles were measured using a photographic technique. A translucent acetate imprinted with a millimeter grid was adhered to the flume sidewall. An approximate 35 by 22 cm area of the test section was photographed through the acetate at intervals ranging from 5 s at initial times to 10 min at the longest times, depending on the rate of profile change. Typically, 30–40 profiles were taken per run. The profile photographs were digitized to store their x-, y-, and t-coordinates. These coordinates were used to determine bed profiles, volume of eroded material, and maximum depth of scour at instantaneous times.

Approximately 20–30 sediment concentration samples were collected in 2.5-L buckets at the flume exit per run. The time intervals between samples ranged from 30 s to 15 min, in a manner similar to photographic intervals. Each sample, of approximately 2000 mL, represents a concentration value averaged over a period of time that was greater for runs with lower flow rates (range approximately 4–11 s). Because the bed was steep (3.7%) and the reach downstream from the 40-cm test bed was armored with a plate, measured sediment concentration was seldom affected by either erosion or deposition downstream from the scour hole; however, there was a small delay between the time sediment exited the scour hole and was measured at the flume exit, corresponding to the time required to transport the sediment over the approximate 1-m length. The total sample volume was weighed to the nearest gram and allowed to settle for 24 h, after which the water was decanted. The remaining sample was allowed to evaporate at room temperature for an additional 24–48 h and weighed to the nearest 0.01 g. Sediment concentration was calculated by dividing the dry sediment weight by the difference between total sample and dry sediment weight. Details of the experimental setup, data collection, and run specifics are given in Stein (1990).

406

RESULTS

A total of 23 runs on three different bed materials were conducted in which the change in time of both sediment concentration and scour-hole geometry were measured. Typical scour profiles, in which the x-axis is parallel with the bed, for the cohesive soil (run 8) and fine sand $d_{50} = 0.15$ mm (run 26) over a period of approximately 2.5 h are shown in Figs. 3(*a*) and 3(*b*), respectively. Unlike these bed types, the coarse sand exhibited the shape noted by both Kobus et al. (1979) and Akashi and Saitou (1986) in which a steep-sided active scour hole is contained within a scour hole with sediment particles at the angle of repose. For all runs, maximum depth of scour is in the vicinity of the calculated centerline of the impinging jet, but, unlike results of Chee and Yuen (1985), this maximum is consistently shifted in the upstream direction. For most of the sand runs (but none of the cohesive-soil runs), a small mound of sediment developed just downstream from the scour hole at initial times, when detachment within the

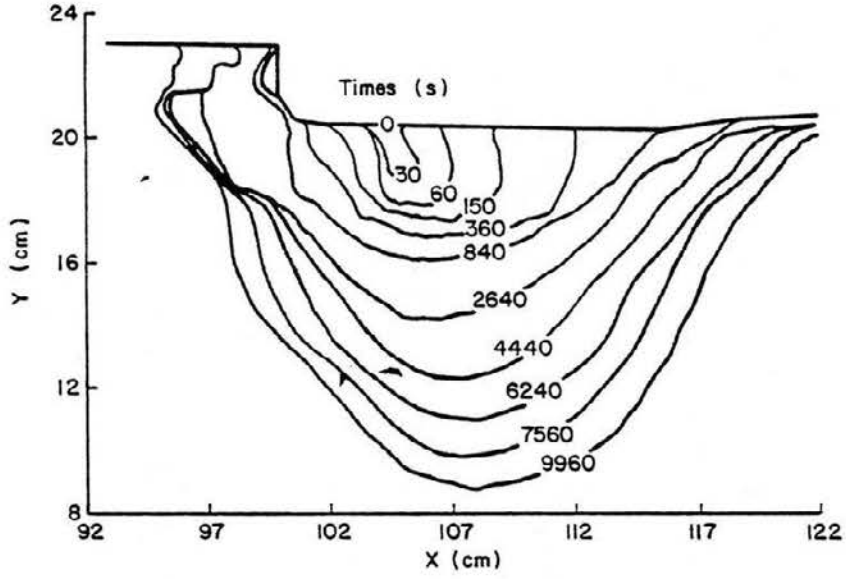

FIG. 3(*a*). Cohesive-Soil Scour Profiles versus Time

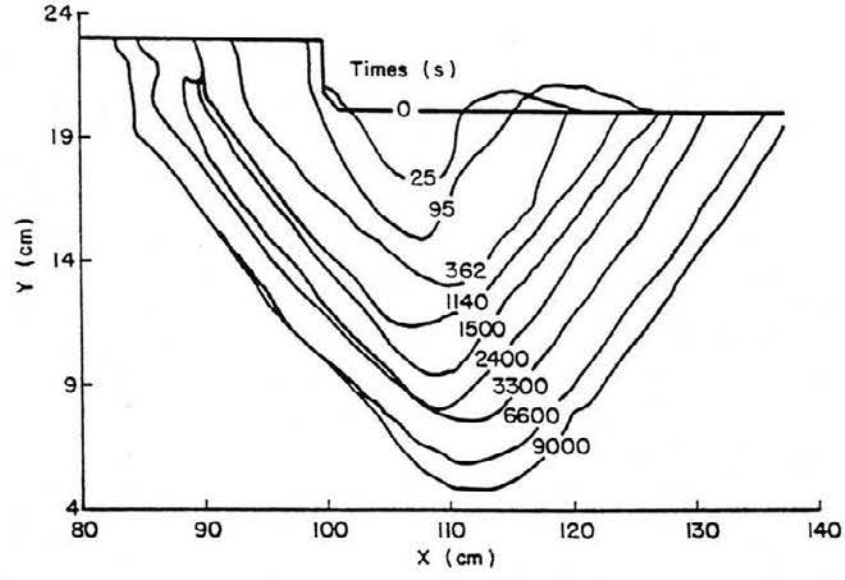

FIG. 3(*b*). Fine-Sand Scour Profiles versus Time

scour hole exceeded the downstream channel's sediment transport capacity [Fig. 3(*b*)]. As the scour hole grew larger and detachment capacity sufficiently decreased, the mound eroded and all sediment detached in the scour hole was transported to the flume exit. While the effect of the mound on tailwater depth and sediment concentration is not considered in the analysis, its effect is short-lived (less than 150 s).

A regression analysis of V^* versus D^* was performed to determine the shape function $\phi = \alpha \cdot \beta$ and exponent β. The resulting coefficients as well as bulk density B and the experimental sediment detachment parameters κ, ξ, and τ_c, which were independently determined from the scour-depth measurements (Stein and Julien 1991; Stein et al. 1993), are shown in Table 1. Two distinct shapes are noted for the coarse sand, dependent on the drop height creating the impinging jet, as could be expected from the analysis of Kobus et al. (1979). For a lower drop height, the active scour hole was less

TABLE 1. Experimental Scour Shape and Sediment-Detachment Parameters

Material (1)	α (2)	β (3)	κ^a (4)	ξ (5)	τ_c (Pa) (6)	B (kg/m³) (7)
Coarse-sand shape 1	1.60	2.11	0.98	1.5	0.74	1,350
Coarse-sand shape 2	0.94	1.79	0.98	1.5	0.74	1,350
Fine sand	2.33	2.10	0.30	1.5	0.35	1,670
Cohesive soil	1.83	1.76	0.04	1.0	0.32	1,290

[a]Units dependent on value of ξ: κ in s/m if $\xi = 1.0$; κ in $s^2/m^{0.5} \cdot kg^{0.5}$ if $\xi = 1.5$.

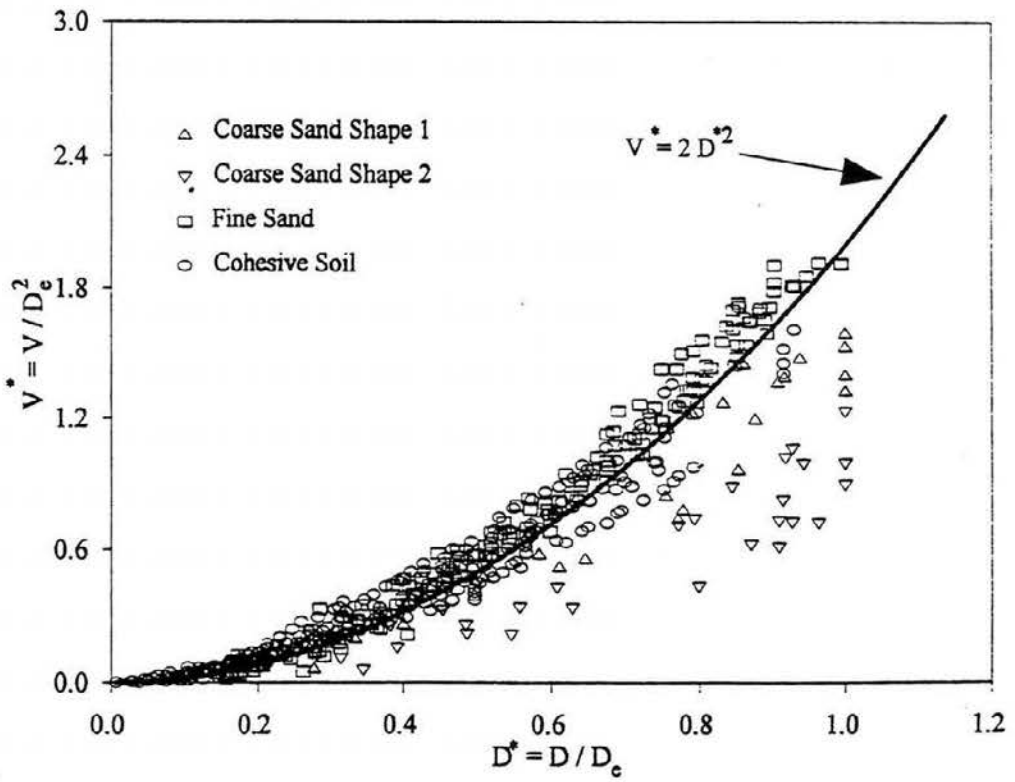

FIG. 4. Measured-Scour-Hole Volume versus Measured Depth

402

pronounced and the scour hole grew longer for a given depth. The fine-sand and cohesive-soil scour profiles were unaffected by drop height. From the regression coefficients, an assumption that $\alpha \simeq \beta \simeq 2$—therefore $\phi \simeq 4$ appears reasonably valid for all bed materials and scour-hole shapes, especially for the fine sand and cohesive soil. The data for all 23 runs, which include three different bed materials, are compared with the approximate assumption that $V^* = 2 \cdot D^{*2}$ in Fig. 4.

The pertinent hydraulic variables q, U_0, y_0, and χ and other normalizing parameters D_p, D_e, D_p^*, T_p, T_r, T_p^*, and C_{max} required to compare sediment concentration, scour volume, scour depth, and time are given in Table 2. Jet velocity, thickness, and impingement angle were determined from a simple free-falling nappe relationship:

$$U_0 = \sqrt{u_e^2 + 2gh_d} \tag{22a}$$

$$y_0 = \frac{q}{U_0} \tag{22b}$$

$$\chi = \tan^{-1}\left(\frac{\sqrt{2gh_d}}{u_e}\right) \tag{22c}$$

where u_e = the velocity at the brink of the free overfall; g = the gravitational acceleration; and h_d = the drop height between the brink and downstream bed. A value of 2.6 was taken as the diffusion constant C_d. The coefficient of friction was determined from a Blasius flow assumption, i.e.

$$C_f = \frac{0.22}{8}\left(\frac{q}{\nu}\right)^{-0.25} \tag{23}$$

where q = unit discharge; ν = the kinematic viscosity; and q/ν = the Reynolds number.

Theoretical and experimental results of the relation between sediment concentration and time are compared for eight coarse-sand runs, six fine-sand runs and nine cohesive-soil runs in Figs. 5, 6, and 7, respectively. The theory is developed from a solution of (15) and (21) using normalizing parameters in Tables 1 and 2 plus $\beta = 2$ and $\phi = 4$. The depth of potential core scour $D_p^* = D_p/D_e$ varies slightly in the experiments from 0.06 to 0.15 for cohesive soil, 0.07 to 0.11 for fine sand, and 0.14 to 0.22 for the coarse sand. The term D_p^* influences solutions to (15), but as seen in Figs. 5–7 is insignificant within the experimental range.

For the runs with sand (Figs. 5 and 6), agreement between predicted and measured sediment concentration versus time is good throughout the entire scour process. Sediment concentration is near the predicted maximum initially, while scour is occurring within the potential core, and decreases as the scour hole and diffusion length of the impinging jet grows. The predicted maximum sediment concentration for the cohesive soil (Fig. 7) is considerably less than measured. At initial times for the cohesive-soil tests, measured sediment concentration values were unavoidably enhanced by additional scour in the test bed downstream from the free overfall. However, as the scour hole developed, the remaining test bed stabilized and the experimental conditions matched the theory developed in (15) and (21). At these longer scour times, theory approximates the measured sediment concentration, in a fashion similar to the sand runs. The time of potential core scour ($C \simeq C_{max}$) is very small, averaging 3.7, 10.6, and 135.0 s for the

1. he fine-
eight. From
er ore $\phi \approx$
io shapes,
runs, which
ap oximate

normalizing
ur ediment
i Table 2.
ined from a

(22a)

(22b)

(22c)

gr itational
d mstream
e coefficient
e.

(23)

d q/v = the

er iediment
ns, six fine-
ectively. The
n malizing
c potential
0.06 to 0.15
or ie coarse
F s. 5–7 is

ore cted and
ou he entire
naximum ini-
d reases as
Th predicted
7) is consid-
il sts, mea-
ce by addi-
ll. However,
iz and the
a (21). At
equment con-
o*ntial core
5. s for the

TABLE 2. Experimental Hydraulic Parameters

Run (1)	$q \times 10^6$ ($m^3/s \cdot m$) (2)	U_0 (m/s) (3)	y_0 (mm) (4)	χ (5)	D_p (mm) (6)	D_c (mm) (7)	D_R^* (8)	T_p (s) (9)	T_r (s) (10)	T_p^* (11)	C_{max} (g/g) (12)
(*a*) Cohesive Soil d_{50} = 0.045 mm											
13	1,570	0.6818	2.3	41	10	68	0.15	174	6,615	0.026	0.0017
12	4,890	0.9339	5.2	28	17	159	0.11	194	15,509	0.013	0.0014
7	1,540	0.8105	1.9	51	10	94	0.11	114	9,220	0.012	0.0026
3	2,250	0.8672	2.6	46	13	125	0.10	139	12,253	0.011	0.0024
11	3,460	0.9500	3.6	41	16	173	0.09	164	16,921	0.010	0.0022
6	4,500	1.0120	4.4	38	19	211	0.09	176	20,607	0.009	0.0020
8	1,720	1.0363	1.7	59	10	145	0.07	66	14,167	0.005	0.0037
10	3,540	1.1420	3.1	51	16	249	0.07	111	24,343	0.005	0.0031
9	4,580	1.1939	3.8	48	19	302	0.06	128	29,531	0.004	0.0029
(*b*) Coarse Sand d_{50} = 1.5 mm											
21	1,620	0.8173	2.0	50	10	47	0.22	4	115	0.032	0.1274
20	2,570	0.8905	2.9	45	14	63	0.22	4	140	0.032	0.1166
19	3,470	0.9506	3.7	41	16	76	0.21	5	161	0.030	0.1122
18	4,930	1.0358	4.8	37	19	96	0.20	5	192	0.026	0.1093
14	1,680	1.0337	1.6	59	9	68	0.14	1	163	0.009	0.1176
15	2,350	1.0757	2.2	55	12	83	0.15	2	184	0.010	0.1064
16	3,530	1.1415	3.1	51	16	106	0.15	3	216	0.012	0.0933
17	4,800	1.2043	4.0	47	20	129	0.15	3	247	0.012	0.0899
(*c*) Fine Sand d_{50} = 0.15 mm											
22	1,660	0.8206	2.0	50	10	99	0.11	10	2,837	0.003	0.0384
23	2,320	0.8724	2.7	46	13	122	0.11	14	3,354	0.004	0.0361
24	3,490	0.9518	3.7	41	16	161	0.10	16	4,172	0.004	0.0340
27	1,750	1.0383	1.7	59	10	140	0.07	5	3,858	0.001	0.0716
26	2,420	1.0799	2.2	55	12	172	0.07	7	4,433	0.002	0.0656
25	3,370	1.1331	3.0	51	16	212	0.07	9	5,155	0.002	0.0606

404

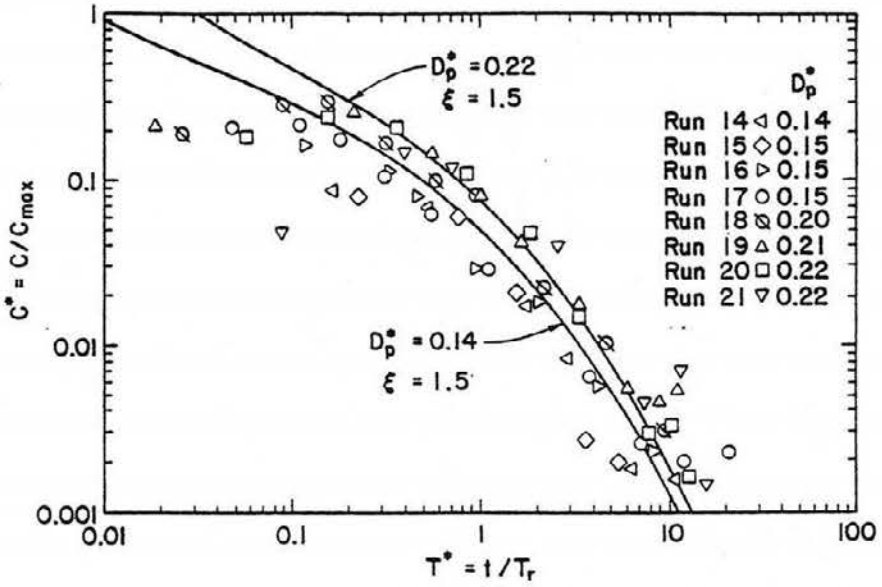

FIG. 5. Predicted versus Measured Sediment Concentration: Coarse Sand

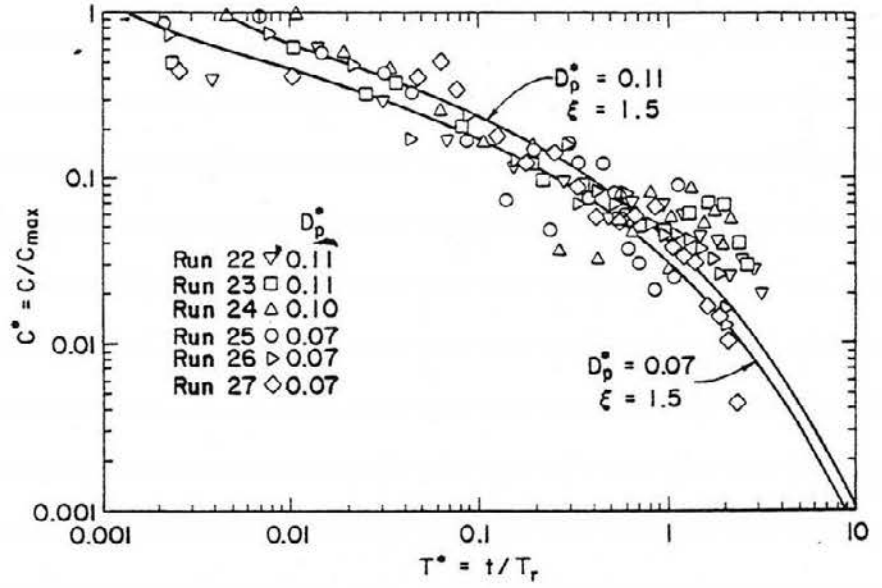

FIG. 6. Predicted versus Measured Sediment Concentration: Fine Sand

coarse sand, fine sand, and cohesive soil, respectively. Also, agreement between measured sediment concentration and time is enhanced for all cases if the regression coefficients in Table 1 are used rather than using $\beta = 2$ and $\phi = 4$. However, use of the approximate values allows a common shape factor to be used for all bed materials while still maintaining an acceptable accuracy level.

PROCEDURE

The following example illustrates the procedure for the calculation of sediment concentration and scour geometry changes with time.

The parameters are: flow such that $U_0 = 1.19$ m/s, $y_0 = 0.0021$ m, and $\chi = 65°$ (as would be caused by a 0.0025-m²/s flow approaching a 6-cm drop at 0.5 m/s); and the bed material is sand, $d_{50} = 0.15$ mm, such that $\kappa =$

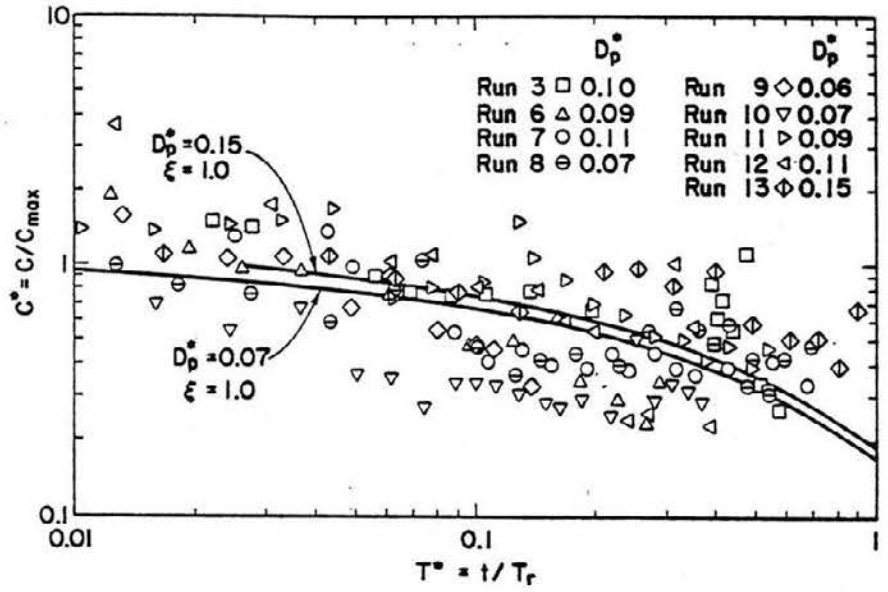

FIG. 7. Predicted versus Measured Sediment Concentration: Cohesive Soil

$0.30\ s^2/kg^{0.5} \cdot m^{0.5}$, $\xi = 1.5$, and $\tau_c = 0.35\ N/m^2$, with a bulk density of 1,900 kg/m^3. (See Table 1 for parameter ranges.)

The following must be determined: the expected equilibrium scour depth, the maximum sediment concentration, the sediment concentration when the scour depth is 0.1 m, and the sediment concentration at $t = 5$ min $= 300$ s.

Solution

Expected Equilibrium Scour Depth

From (23), calculate the coefficient of friction:

$$C_f = \frac{0.22}{8}\left(\frac{0.0025}{1 \times 10^{-6}}\right)^{-0.25} = 0.0039 \tag{24}$$

From (6), calculate the maximum applied shear stress:

$$\tau_0 = 0.0039 \times \frac{1{,}000\ \text{kg}}{\text{m}^3} \times \frac{1.19^2\ \text{m}^2}{\text{s}^2} = \frac{5.52\ \text{N}}{\text{m}^2} \tag{25}$$

From (8) and assuming $C_d = 2.6$, calculate the equilibrium scour depth:

$$D_e = \frac{2.6^2 \times 0.0039 \times \dfrac{1{,}000\ \text{kg}}{\text{m}^3} \times \dfrac{1.19^2\ \text{m}^2}{\text{s}^2} \times 0.0021\ \text{m}}{\dfrac{0.35\ \text{kg}}{\text{ms}^2}} \sin 65° = 0.20\ \text{m} \tag{26}$$

Maximum Sediment Concentration

From (9), calculate the potential core scour depth:

$$D_p = 2.6^2 \times 0.0021\ \text{m} \times \sin 65° = 0.013\ \text{m} \tag{27a}$$

406

$$D_p^* = \frac{0.013 \text{ m}}{0.20 \text{ m}} = 0.065 \tag{27b}$$

From (20) and taking $\phi = 4$ and $\beta = 2$, calculate the maximum sediment concentration:

$$C_{max} = \frac{\dfrac{0.30 \text{ s}^2}{\text{kg}^{0.5}\text{ m}^{0.5}} \times 0.20 \text{ m} \times \dfrac{0.35^{1.5} \text{ kg}^{1.5}}{\text{m}^{1.5}\text{ s}^3}}{\dfrac{1{,}000 \text{ kg}}{\text{m}^3} \times \dfrac{0.0025 \text{ m}^2}{\text{s}}} \times 4$$

$$\times 0.065 \times \left(\frac{1 - 0.065}{0.065}\right)^{1.5} = \frac{0.071 \text{ g sediment}}{1 \text{ g water}} \tag{28}$$

Assuming the specific weight of sediment is 2.65, sediment concentration expressed in milligrams per liter is:

$$C_{max} = \frac{10^6 \times 2.65 \times 0.071}{2.65 + 0.071} = \frac{69{,}100 \text{ mg}}{\text{L}} \tag{29}$$

Sediment Concentration with 0.1-m Scour Depth

Check that $D > D_p$ (0.1 m > 0.013 m; yes) and calculate D^*:

$$D^* = \frac{0.1 \text{ m}}{0.20 \text{ m}} = 0.50 \tag{30}$$

From (14), calculate the reference time:

$$T_r = \frac{\dfrac{1{,}900 \text{ kg}}{\text{m}^3} \times 0.20 \text{ m}}{\dfrac{0.30 \text{ s}^2}{\text{kg}^{0.5}\text{ m}^{0.5}} \times \dfrac{0.35^{1.5} \text{ kg}^{1.5}}{\text{m}^{1.5}\text{ s}^3}} = 6{,}120 \text{ s} \tag{31}$$

From (11), calculate the time of potential core scour:

$$T_p = \frac{\dfrac{1{,}900 \text{ kg}}{\text{m}^3} \times 0.013 \text{ m}}{\dfrac{0.30 \text{ s}^2}{\text{kg}^{0.5}\text{ m}^{0.5}} \times (5.52 - 0.35)^{1.5} \dfrac{\text{kg}^{1.5}}{\text{m}^{1.5}\text{ s}^3}} = 7.00 \text{ s} \tag{32}$$

From (21), calculate the sediment concentration:

$$\frac{C}{C_{max}} = \left(\frac{0.065}{0.50}\right)^{0.5} \left(\frac{1 - 0.50}{1 - 0.065}\right)^{1.5} = 0.14 \tag{33a}$$

$$C = 0.14 \times 0.071 = \frac{0.0099 \text{ g sediment}}{1 \text{ g water}} = \frac{9{,}860 \text{ mg}}{\text{L}} \quad \text{when } D = 0.1 \text{ m} \tag{33b}$$

Sediment Concentration at t = *5 min*

Check that $t > T_p$ (300 s > 7.0 s; yes) and calculate T^*:

(27*b*)

inium sediment

se nent (28)
water

it ncentration

(29)

te D^*:

(30)

(31)

7.00 s (32)

4 (33*a*)

ien $D = 0.1$ m

(33*b*)

*:

$$T^* = \frac{300 \text{ s}}{6{,}120 \text{ s}} = 0.049 \tag{34}$$

From Fig. 6 with $D_p^* = 0.065$ and $T^* = 0.049$, read $C^* = 0.25$; therefore

$$C = 0.25 \times 0.071 = \frac{0.018 \text{ g sediment}}{1 \text{ g water}} = \frac{17{,}300 \text{ mg}}{\text{L}} \quad \text{when } t = 300 \text{ s} \tag{35}$$

Alternatively, with $D_p^* = 0.065$ and $T^* = 0.049$, solve (15*b*) iteratively for D^* and use (21) to solve for concentration.

CONCLUSIONS

The sediment concentration exiting a scour hole below a free overfall is directly related to the sediment detachment potential of a jet impinging on an erodible bed. At any given time, sediment concentration is directly related to the corresponding maximum scour depth as shown in (19). When the eroding bed is within the impinging jet's potential core, concentration is near a maximum as given in (20). Thereafter, concentration decreases with depth as given by (21). Sediment concentration also decreases with time as expressed in (15) and (21) and shown in Figs. 5–7.

The validity of the relationships between sediment concentration and time, developed in (15) and (19)–(21), is tested in the laboratory with noncohesive and cohesive bed materials. Agreement between measured and predicted sediment concentration is good throughout the scour process when scour occurs in noncohesive soils, as shown in Figs. 5 and 6. For the case of scour in cohesive soils, theory approximates experimental results at longer times, as shown in Fig. 7. The shape of the scour hole influences the relationships between sediment concentration and scour depth [(21)] and sediment concentration and time (Figs. 5–7). An assumption that the scour-hole volume per unit width is twice the square of scour depth at the corresponding time is shown to be reasonably valid for all bed materials in Fig. 4.

ACKNOWLEDGMENTS

This study has been primarily funded by the U.S. Department of Agriculture–Agricultural Research Service's Great Plains Research Group. Additional support is provided by the Army Research Office Center for Geosciences at Colorado State University (grant ARO/DAAL 03-86-K-0175) and the Montana State Agricultural Experiment Station (paper J-2869). Our appreciation is extended to all groups.

APPENDIX I. REFERENCES

Albertson, M. L., Dai, Y. B., Johnson, R. A., and Rouse, H. (1950). "Diffusion of submerged jets." *Trans.*, ASCE, 115, 639–697.

Akashi, N., and Saitou, T. (1986). "Influence of water surface on scour from a vertical submerged jet." *J. Hydrosci. and Hydr. Engrg.*, 4(2), 55–69.

Begin, Z. B., Meyer, D. F., and Schumm, S. A. (1980a). "Knickpoint migration due to base level lowering." *J. Wtrway., Port., Coast. and Oc. Div.*, ASCE, 106(3), 369–389.

Begin, Z. B., Meyer, D. F., and Schumm, S. A. (1980b). "Sediment production of

alluvial channels in response to base level lowering." *Trans.*, American Society of Agricultural Engineers, 23(5), 1183–1188.
Beltaos, S. (1972). "Normal impingement of plane turbulent jets on sooth walls," MS thesis, University of Alberta, at Edmonton, Alberta.
Beltaos, S. (1974). "Turbulent impinging jets," PhD dissertation, University of Alberta, at Edmonton, Alberta.
Beltaos, S. (1976). "Oblique impingement of plane turbulent jets." *J. Hydr. Div.*, ASCE, 102(9), 1177–1192.
Beltaos, S., and Rajaratnam, N. (1973). "Plane turbulent impinging jets." *J. Hydr. Res.*, 11(1), 29–59.
Blaisdell, F. W., and Anderson, C. L. (1988a). "A comprehensive generalized study of scour at cantilevered pipe outlets, Pt. 1." *J. Hydr. Res.*, 26(4), 357–376.
Blaisdell, F. W., and Anderson, C. L. (1988b). "A comprehensive generalized study of scour at cantilevered pipe outlets, Pt. 2." *J. Hydr. Res.*, 26(5), 509–524.
Blaisdell, F. W., Anderson, C. L., and Hebaus, G. G. (1981). "Ultimate dimensions of local scour." *J. Hydr. Div.*, ASCE, 107(3), 327–337.
Bormann, N. E., and Julien, P. Y. (1991). "Scour downstream of grade control structures." *J. Hydr. Engrg.*, ASCE,117(5), 597–594.
Chee, S. P., and Kung, T. (1971). "Stable profiles of plunge basins." *Water Res. Bull.*, 7(2), 303–308.
Chee, S. P., and Yuen, E. M. (1985). "Erosion of unconsolidated gravel beds." *Can. J. Civ. Engrg.*, 12(3), 559–566.
Foster, G. R., Meyer, L. D., and Onstad, C. A. (1977). "An erosion equation derived from basic erosion principles." *Trans.*, American Society of Agricultural Engineers, 20(4), 678–682.
Gardner, T. W. (1983). "Experimental study of knickpoint and longitudinal profile in cohesive, homogeneous material." *Geol. Soc. Amr. Bull.*, 94(5), 664–672.
Hanson, G. J. (1989). "Channel erosion study of two compacted clays." *Trans.*, American Society of Agricultural Engineers, 32(5), 485–490.
Holland, W. N., and Pickup, G. (1976). "Flume study of knickpoint development in stratified sediment." *Geol. Soc. Amr. Bull.*, 87(1), 76–82.
Kobus, H., Liester, P., and Westrich, B. (1979). "Flow field and scouring effects of steady and pulsating jets impinging on a moveable bed." *J. Hydr. Res.*, 17(3), 175–192.
Laursen, E. M. (1952). "Observations on the nature of scour." *Proc. 5th Hydr. Conf.*, University of Iowa, Iowa City, Iowa, 179–197.
Mason, P. J., and Arumugam, K. (1985). "Free jet scour below dams and flip buckets." *J. Hydr. Engrg.*, ASCE, 111(2), 220–235.
Nearing, M. A., Foster, G. R., Lane, L. J., and Finkner, S. A. (1989). "A process-based soil erosion model for USDA water erosion prediction project technology." *Trans.*, American Society of Agricultural Engineers, 32(5), 1587–1593.
Rajaratnam, N. (1976). "Turbulent jets." *Development in Water Science 5*. Elsevier Scientific Publishing Co., Amsterdam, the Netherlands.
Rajaratnam, N. (1981). "Erosion by plane turbulent jets." *J. Hydr. Res.*, 19(4), 339–359.
Rajaratnam, N. (1982). "Erosion by unsubmerged plane water jets." *Proc. Applying research to hydraulic practice*, ASCE, New York, N.Y., 280–288.
Robinson, K. M. (1989a). "Hydraulic stress on an overfall bounday." *Trans.*, American Society of Agricultural Engineers, 32(4), 1269–1274.
Robinson, K. M. (1989b). "Stress distribution at an overfall." *Trans.*, American Society of Agricultural Engineers, 32(1), 75–80.
Rouse, H. (1940). "Criteria for similarity in the transportation of sediment." *Proc. 1st Hydraulic Conf.*, State University of Iowa, Iowa City, Iowa, 33–49.
Stein, O. R. (1990). "Mechanics of headcut migration in rills," PhD dissertation, Colorado State University, at Fort Collins, Colo.
Stein, O. R., and Julien, P. Y. (1991). "Measurement of rill erosion sediment detachment." *Paper No. 91-2086*, American Society of Agricultural Engineers, St. Joseph, Mo.

Stein, O. R., and Julien, P. Y. (1993). "A criterion delineating the mode of headcut migration." *J. Hydr. Engrg.*, ASCE, 119(1), 37–50.
Stein, O. R., Julien, P. Y., and Alonso, C. V. (1993). "Mechanics or jet scour downstream of a headcut." *J. Hydr. Res.*, 31(6), 723–738.

APPENDIX II. NOTATION

The following symbols are used in this paper:

B = soil bulk density;
C = sediment concentration;
C_d = diffusion constant of jet;
C_f = coefficient of friction;
C_{max} = sediment concentration at tip of potential core;
D = maximum depth of jet scour at given time t;
D^* = normalized scour depth (D/D_e);
D_e = equilibrium depth of jet scour;
D_p = depth of scour corresponding to potential core tip;
D_p^* = normalized depth of potential core tip (D_p/D_e);
d_{50} = mean sediment size;
E = sediment detachment rate per unit area;
g = gravitational acceleration;
h_d = drop height;
h_t = tailwater depth;
J = distance along jet centerline;
J_e = distance along jet centerline to impingement at equilibrium;
J_p = length of jet potential core;
q = unit-flow discharge;
T^* = normalized time (t/T_r);
T_p = time of potential core scour;
T_p^* = normalized time of potential core score (T_p/T_r);
T_r = reference time;
t = time;
u_e = velocity at the brink of overfall;
U = maximum diffused jet velocity;
U_0 = initial jet velocity;
V = scour-hole volume;
V^* = normalized scour-hole volume (V/D_e^{*2});
y_0 = initial jet thickness;
α, β = experimental scour-shape factors;
κ, ξ = experimental parameters of sediment-detachment function;
ν = fluid kinematic viscosity;
ρ = fluid density;
τ_c = critical shear stress for erosion initiation;
τ = shear stress in scour hole;
τ_0 = shear stress in potential core;
ϕ = scour-hole shape factor = $\alpha \cdot \beta$; and
χ = jet angle at tailwater impingement.

410

ADVANCES IN PREDICTING RESERVOIR SEDIMENTATION

M. Frenette[1] and P. Y. Julien[2]

Advances in reservoir sedimentation have been obtained through evaluation of case studies. The determination of the incoming sediment load, trap efficiency and life expectancy are of primary importance in the design of reservoirs. The feasibility of large projects, with reservoir capacity exceeding 3 km^3, can be jeopardized with sedimentation problems. Recent investigations of the Peligre dam in Haiti reveal a three-fold increase in the incoming sediment load. Moreover, trap efficiency predictions from conventional methods can be significantly less than actual measurements because of flocculation of clay particles.

INTRODUCTION

Reservoir sedimentation is of great consequence. Up to one third of the impounding capacity of a newly built reservoir can be lost within one year in China (Qian, 1982).

Reservoir sedimentation is a complex process which varies with sediment production, rate of transportation and mode of deposition. The concept of life expectancy of reservoirs represents a challenge for the planners since the sediment problems arise from geological sources, cutting and burning of brushland and forest, over grazed grasslands, cropland cultivation and natural hazards including landslides, bank erosion, gullies formation, etc. Sediment transport and sedimentation depend on the river regime, flood frequencies, reservoir geometry, flocculation potential and density current.

Existing methods for predicting reservoir sedimentation have been tested in the light of thorough investigations of several reservoirs. In this paper, a brief outline of the existing technology is followed with a discussion of two cases studies: Peligre dam in Haiti and Molineros dam in Boliva.

TECHNOLOGY FOR PREDICTING RESERVOIR SEDIMENTATION

Sediments eroded from upland areas, gullies, streambanks and stream beds are transported in the fluvial system until the hydraulic conditions are conducive to deposition. Sediment is carried either as bed load or suspended load. As the stream approaches the reservoir, the sediment transport capacity decreases due to flow deceleration and deposition takes place. The coarse material forms deltas at the head of the reservoir; the intermediate size fractions settle throughout the reservoirs; the clay fractions may form density currents which generally move through the reservoir toward the foot of the dam (Fig. 1).

Storage losses in terms of live and dead storages, trap efficiency, control measures and the operation of the dam must be considered with: the inflow hydrograph, the sediment inflow, the sediment characteristics, the reservoir configuration, the regional geography and land use.

1. Professor of Civil Engineering, Laval University, Québec, Canada.
2. Assistant Professor of Civil Engineering, Colorado State University, Fort Collins, Colorado and former graduate student at Laval University.

THIRD INTERNATIONAL SYMPOSIUM ON RIVER SEDIMENTATION
The University of Mississippi, March 31-April 4, 1986

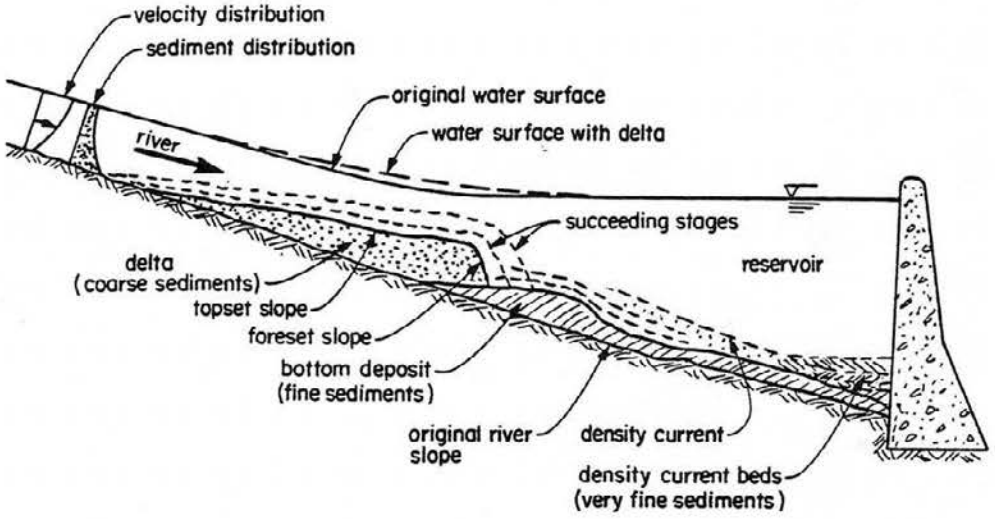

Figure 1. A typical flow and deposition pattern of a reservoir.

Determination of Incoming Sediment Load

The incoming sediment load is usually measured at gaging stations. Flow and sediment measurements define the sediment rating curve. The annual suspended sediment yield is obtained from the sediment rating curve and the flow duration curve. Experience indicates that the method is not reliable: when the period of record is short; when data at high flows are insufficient; and when the sediment rating curve shows considerable scatter. Often then, the rating curves are different during the rising limb and the recession limb of the hydrograph. Flood flows carry most of the sediments and in order to give full weight to the total sediment inflow, observations must normally concentrate during the flood period. Unfortunately, in many cases, measurements are not available during extreme events.

Difficulties in measuring bed load call for the use of bed load formulas such as the Meyer-Peter Muller, Einstein-Brown, Ackers-White formulas. Armoured beds in mountainous streams are frequent and the composition of the bed load is different from that of the bed material. In some cases consolidated clay is found underneath a thin layer of alluvium covering the bed which is washed out at high flows. The calculated load is then larger than the measured load since the transport capacity of the stream is greater than the availability of sediments. The ratio of bed load to suspended load can sometimes be taken as 10 percent. This ratio can also be higher if the suspended load is reduced.

When wash load is dominant, mathematical models can be used to predict, from Universal Soil Loss Equation (USLE) or other equations, soil losses by overland flow and sediment yield from watersheds. Models based can be used when sufficient data is available from topographic, land use and agricultural maps, aerial photographs and field surveys. Two models (LAVSED-I and LAVSED-II) have been recently developed to predict sediment yield from large watersheds. Mathematical models based on physical characteristics of watershed figure among the most powerful tools because the rate of sediment transport can be predicted for alternative watershed conditions (Frenette and Julien, 1985).

Trap Efficiency of the Reservoir

Defined as the ratio of the deposited sediment to the total sediment inflow, the trap efficiency primarily depends on the sediment load characteristics and the detention time of the inflow and the age of the reservoir. The detention time depends upon the: type of reservoir; ratio between the storage capacity and inflow; shape of the reservoir basin; type of operation of the dam.

For large reservoirs empirical relationships have been developed by Brune and Allen (1941), Churchill (1948), Brune (1953), Brown (1958) and Chen (1975). Brune's model relates the percentage of deposited sediment with the capacity inflow ratio, which is nothing else than the detention time. Churchill correlated trap efficiency with a sediment index equal to the ratio of the retention period to the mean velocity of flow through the reservoir. Brown related the relationship of sediment trapped (in percent) to the ratio of the original storage capacity to the watershed area.

Chen (1975) presents a series of curves for various particle sizes, in mm, relating the trap efficiency to the ratio of the basin area A, in m^2, to the outflow ratio Q_o, in cm. This is shown in Figure 2 and compared with Brune and Churchill's methods. The results indicate that the two well known methods tend to underestimate trap efficiency for coarser material, but overestimate for finer material. The average size diameter, however, is well represented.

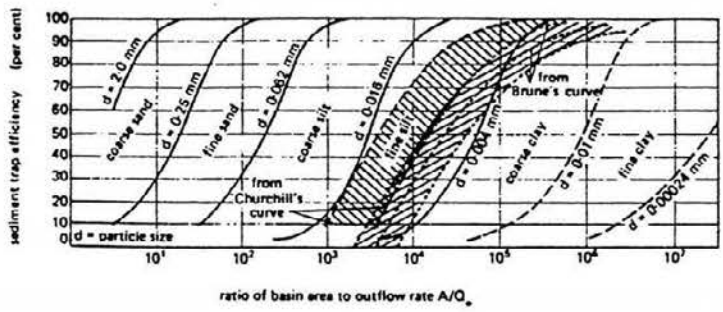

Figure 2. Chen's trap efficiency curve from "Design of Sediment Retention Curve" at Urban Hydrology and Sediment Control Symposium, Lexington, USA, 1975. (Graf, 1984)

In 1971, Borland introduced a new approach showing the relation between the fraction of material deposited and the settling velocity of the suspended material:

$$TE = 1 - \exp\,[-1{,}055\ Lw/Vd] \qquad (1)$$

in which TE = fraction of sediment deposited in the reservoir; L = total length of the reservoir; w = fall velocity of the sediment; V = mean velocity of the flow in the reservoir and d = flow depth.

Karaushev (1966) developed a similar theory for the trap efficiency of small reservoirs:

$$TE = 1 - [1 - (C/I)]\ e\left[\frac{-\phi\ (C/I)}{1 - (C/I)}\right] \qquad (2)$$

$\phi = \bar{w}\ T_s/h$

$\bar{w}$ = mean fall velocity of the transported sediment

T_s = duration of spill over period (second)

h = mean depth of the reservoir

C/I = capacity inflow ratio.

These equations can be used in mathematical models related to reservoir sedimentation, since they both take into consideration the major parameters involved in the processes of silting.

4/12

Patterns of Deposition

Prediction of the deposition patterns entail not only volume determination, but the location in the reservoir where the volume is depleted. A few relationships exist such as the area increment method by Borland and Miller (1962), which states that the total volume of sediment, V_s, to be distributed in a reservoir consists of the portion which is uniformly distributed vertically over the height $(H - h_o)$ plus the portion, V_o, below the new zero elevation of the reservoir:

$$V_s = A_o (H - h_o) + V_o \tag{3}$$

where: A_o = area correction factor in acres

H = reservoir depth at the dam in feet

h_o = new zero elevation varying with the rate of sedimentation.

The method approximates the actual sediment deposition pattern which can vary widely from the real pattern since various factors are not taken into account.

A second method developed by Borland and Miller (Empirical Area - Reduction Method) is based on the accumulation data for 30 reservoirs in USA. The method takes into consideration the shape of the reservoir: Gorge type, hill, flood plain - foothill and lake type. This method gives an indication of the way in which the sediment will be distributed. Application by Borland and Miller indicates favorable comparison with field observation, but the method still does not include all the factors. Among the most recent methods, figure the Garde et al. model for predicting progressive delta profiles using topset and foreset slopes. Graf (1971, 1984), Yücel and Graf (1973), Lopez (1978) Rice (1981) and Simons and Li (1982) present recent modeling attempts taking into consideration the flow and sediment characteristics, bed load relationships, reservoir geometry and reservoir operation for predicting the volume and pattern of deposition in reservoir.

Unit Weight of the Deposit Material

The conversion of the incoming weight of sediment (ppm, g/ℓ, kg/m^3) to volume necessitates knowledge of the average unit weight. For material coarser than 0.1 mm this imposes no problem as the unit weight of such deposit varies within a narrow range around 1300 kg/m^3. With the presence of finer material, the problem becomes more complicated since the unit weight is function of time due to the consolidation of the material and exposure to the air. Until now the Miller (1953) formula has been widely used in estimating the unit weight of new deposits. After T years of uniform settling, the unit weight is given by:

$$W_t = W_i + 0.43\ k\ [(\frac{T}{T-1})\ (\ell n\ T) - 1] \tag{4}$$

where: W_t = unit weight after T years

W_i = initial weight (kg/m)

k = Lane-Koelzer factor

T = time (years).

Application of these methods to several reservoirs showed results somewhat different from those expected. Advances in reservoir sedimentation are discussed as dictated from the analysis of case studies. The analysis of two reservoirs is presented in the following: Peligre Dam in Haiti and Molineros Reservoir in Bolivia.

PELIGRE DAM IN HAITI (Case Study No 1)

The only dam in Haiti, Peligre, was built in 1956. It is located on the Artibonite river about 50 km north-east of the capital Port-au-Prince. The height of the dam (Figure 3) is 44 m creating an artificial lake of 607 hm^3, with 77 percent of active storage (Figure 4). A schematic diagram of the reservoir is shown on Figures 5 and 6. Initially built for flood control and irrigation, hydropower generation was included in 1972 in order to provide electricity to the capital Port-au-Prince. Food from the irrigation projects also serves almost exclusively the population of Port-au-Prince.

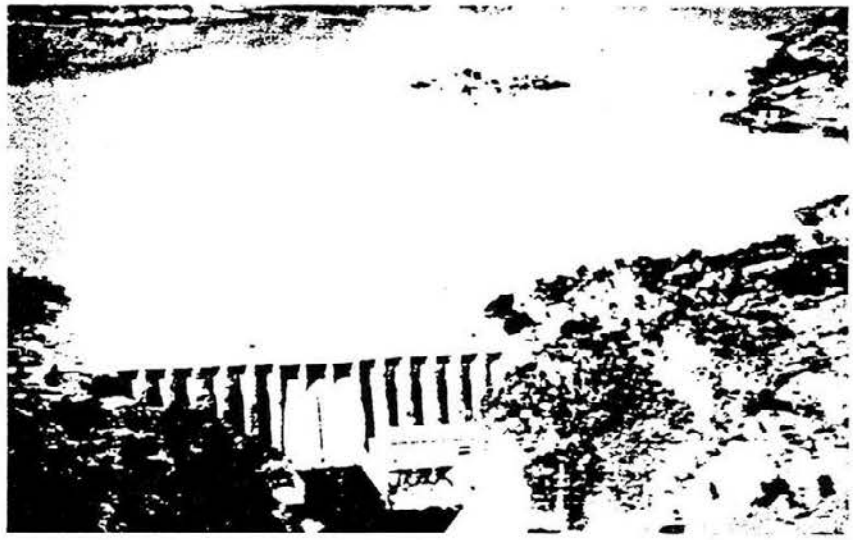

Figure 3. Peligre dam and reservoir.

Figure 4. Sedimentation upstream the reservoir.

Based on data collected in 1925 and 1926, the planners have estimated the annual rate of silting in the reservoir at 3.5 hm^3/yr corresponding to an expected life of about 180 years. Survey of the reservoir in 1961, five years after the construction of the dam, confirmed the predicted rate of sedimentation with a total accumulated volume of 16.6 hm^3 (3.32 hm^3/yr). But in 1977 a quick drawdown due to a severe drought has shown a total stokage of sediment higher than normal. An immediate survey was undertaken and repeated in 1979 to indicate that the accumulation of sediment in the reservoir had increased drastically since 1961, reflecting a significant reduction of the life expectancy.

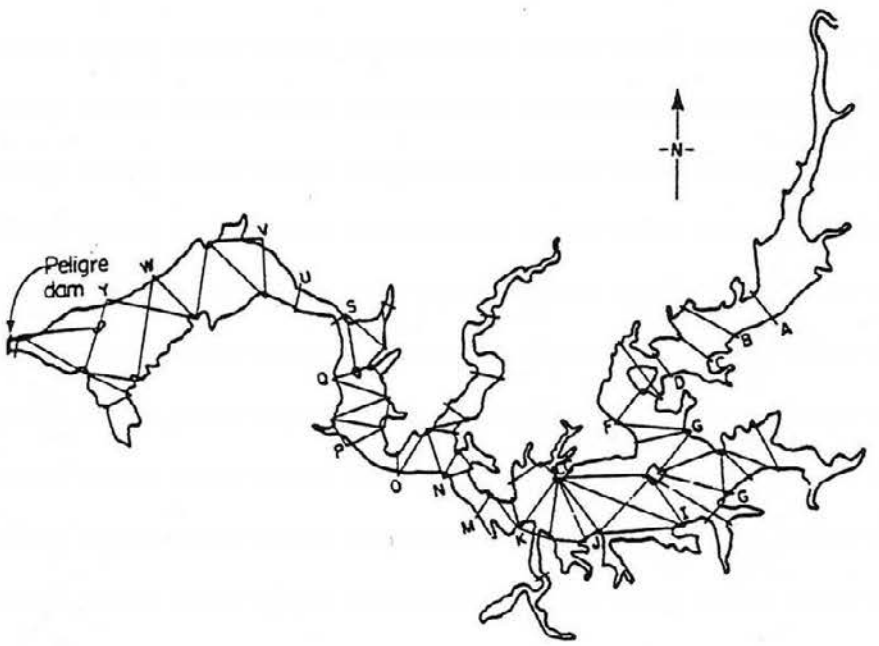

Figure 5. Localization of cross sections for the reservoir survey.

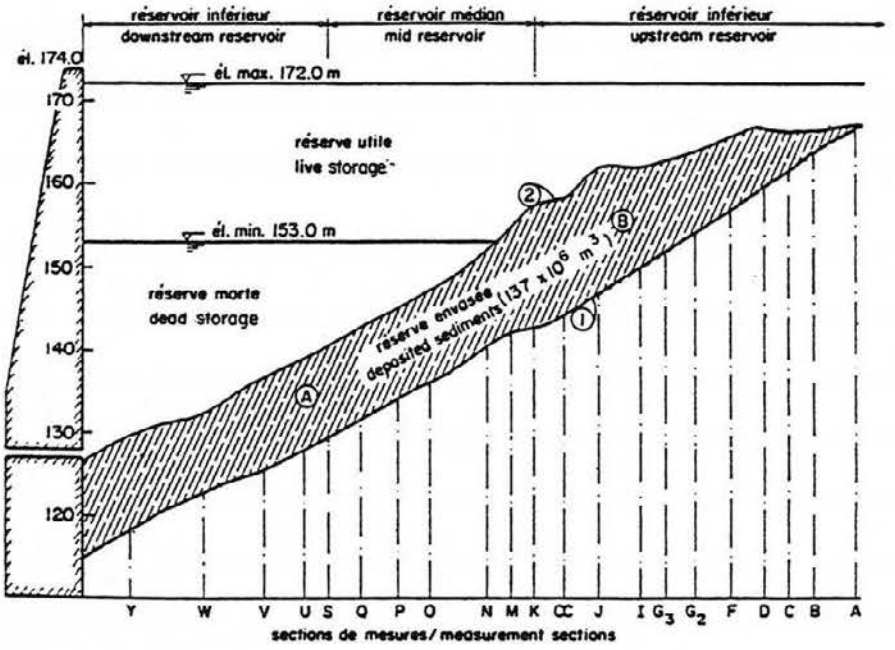

Figure 6. Deposition patterns of Peligre reservoir: (1) initial bed in 1956; (2) bed profile in 1979; (A) clay 85 percent; (B) clay 25 percent, silt 60 percent and fine sand 15 percent.

Hydrology and Sediment Inflow

The Artibonite river basin above the dam has a total drainage basin of 6615 km^2. The mean monthly precipitation varies from 25 mm in December and January to 300 mm/month during the rainy period (May to September). The resulting 54 years mean annual flow is 78 m^3/s, equivalent to 11.8 ℓ/s/km^2. Variation of the mean annual flow entering the reservoir from 1920 to 1979 is shown in Figure 7. The results indicate a general increase of the hydrological events (average and extremes) since 1945. This phenomenon arose from

415

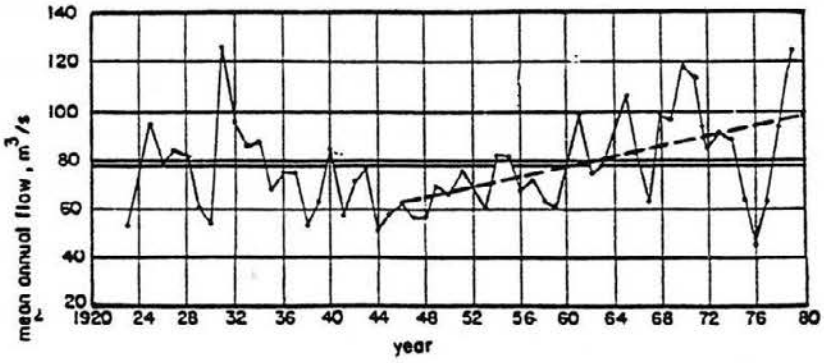

Figure 7. Mean annual flow at the dam site: 78 m^3/s and average progression since 1944.

many disturbances in the watershed as shown in Table I indicating the percentage of deforestation, cultivation and erosion between 1956 and 1978, as determined from aerial photographs. This changes the runoff and infiltration processes and consequently the hydrological regime. As mentioned before, the sediment inflow observed in 1925-26 gave an average of 3.5×10^6 m^3/yr. Table II presents the observed concentration and sediment load calculated for each station at the entrance and outlet of the reservoir from 1977 to 1979.

Table I. Changes in land use between 1956 and 1978.

Sub-basin	Slope > 30%	Slope < 30%	Forest cover (km^2) 1956	Forest cover (km^2) 1978	Agriculture (km^2) 1956	Agriculture (km^2) 1978	Deforested, eroded or rock (km^2) 1956	Deforested, eroded or rock (km^2) 1978
Samana ($118\ km^2$)	64 (54.0%)	54 (46.0%)	40.4 (34.2%)	7 (6.0%)	25.7 (21.8%)	36 (30.4%)	52 (44.0%)	75 (63.6%)
Thomondes ($225\ km^2$)	116 (52.0%)	109 (48.0%)	32 (14.2%)	21.4 (9.5%)	64 (28.5%)	57.3 (25.5%)	129 (57.3%)	146.3 (65.0%)

Table II. Results of sediment investigation in 1925-26, 1977-79.

Sediment concentration observed in 1977 (mg/ℓ)	Minimum	Average	Maximum
Inflow:			
Gaging station Los Abeille	0	± 5000	27,000
Gagin station Los Cayemite	0	± 1000	8,400
Outflow:			
Gagin station Domond	0	4	59

Sediment load estimated between 1977-79	
Incoming sediment load (total)	30×10^6 t
Outgoing sediment load (total)	0.20×10^6 t
Total accumulation (3 years)	29.8×10^6 t
Mean annual load	9.94×10^6 t/yr

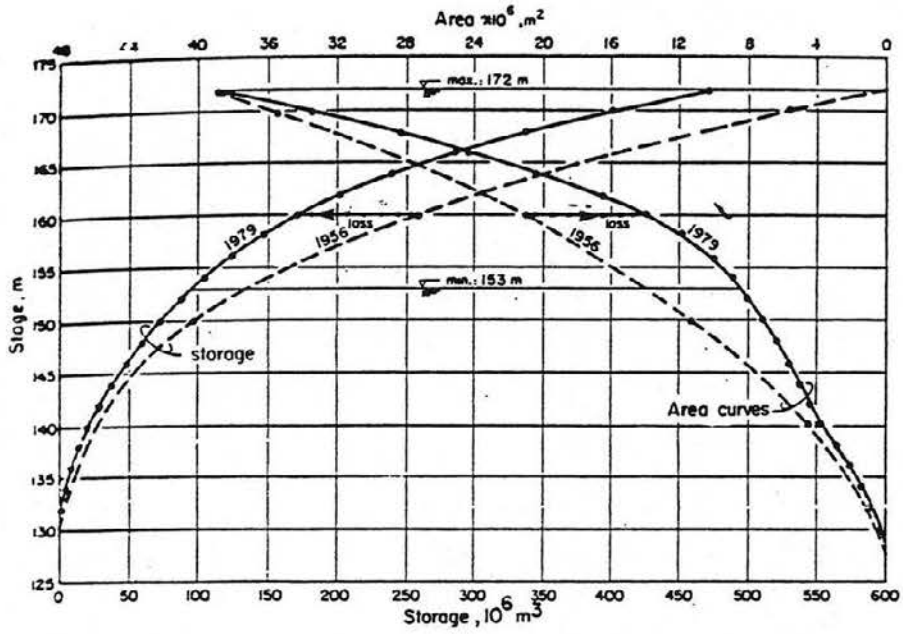

Figure 8. Curves of areas and volumes in 1956 and 1979.

Survey of the Reservoir

Surveys of the reservoir sedimentation made in 1961, 1977 and 1979 gave an accumulation of 16.6 hm^3, 105 hm^3 and 135 hm^3. The corresponding increases in the sedimentation rate are: 1956-61, 3.3 hm^3/yr; 1961-77, 6.3 hm^3/yr; and 1977-79, 10 hm^3/yr. Interestingly, the 1956-61 period gave approximately the same rate of silting as observed in 1925-26.

The pattern of deposition in the reservoir based on the 1979 survey (Fig. 6) shows a regular shape with a gradual segregation of sand, silt and clay. Sands are observed mainly in the upper part of the reservoir in the delta formation and clay near the dam. The incoming load is fine and the median diameter of the deposit at the topset of the delta is also small varying between 0.0085 to 0.022 mm. This is due mainly to the flocculation phenomena. In fact, trap efficiency of the reservoir, based on the conventional methods (Brune, Churchill, Borland) indicated that only 50 to 60 percent of the sediment should settle in the reservoir whereas field observations (Table II) give nearly 100 percent. Laboratory tests performed on flocculation or detention time of particles in water gave a large deviation between flocculated and deflocculated rates of silting depending on the water quality and concentration of sediment (Fig. 9). Water quality tests has confirmed the high potential of flocculation caused by high percentages of calcareous.

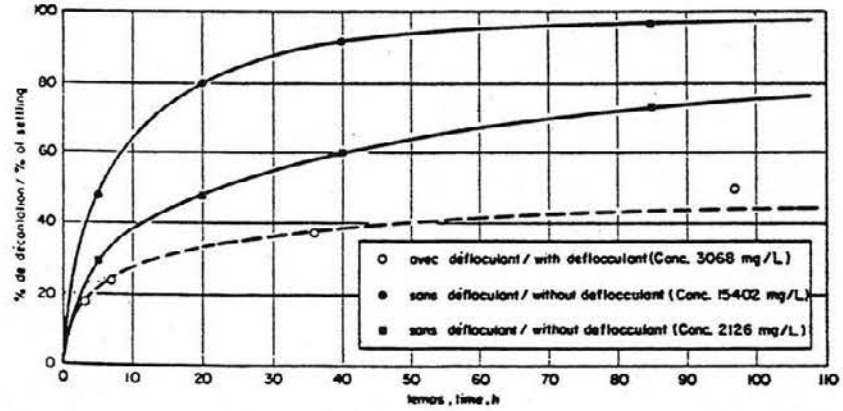

Figure 9. Settling of sediments with time.

417

The unit weight of the first layers of the deposit was established by field observation at 750 kg/m^3, while near the original bed (old layer) the unit weight reaches 1300 kg/m^3, with an average of 1025 kg/m^3 (Fig. 10).

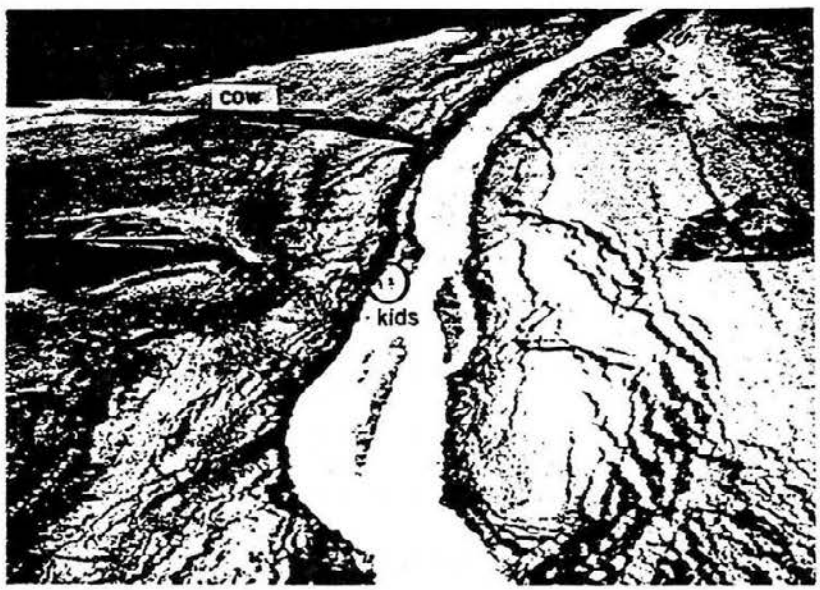

Figure 10. Channel formation and bank failure in the middle reach of the reservoir (section M.N.).

Mathematical Modeling: Silting in the Reservoir

The mathematical model used for the calculation of the incoming load, e.g. sediment silting in the reservoir is relatively simple. Regression analysis was made between the flow discharge and sediment discharge in order to estimate the yearly load since 1956, first year of operation of the reservoir. However, changes in watershed increased progressively the rate of the incoming sediment load. A correction coefficient was introduced to model the increased sediment load. Calibration was based on the three reservoir surveys. In addition, progressive compaction was also considered in the model taking the initial unit weight observed and Miller's formula (Eq. 4).

The results of the model showed that the specific degradation of the watershed defined as $e_m = E/S$, E being the incoming sediment load and S the watershed area has increased at a rate of 18 percent (24 years of simulation) respecting the following equation:

$$e_m = 281.4 + 52.8\ T \qquad t/km^2/year \qquad (T:\ \text{in years}) \qquad (5)$$

Figure 11 yields the specific results obtained each year between 1956 and 1979. The results obtained by the estimates presented above, with an increasing sediment load facilitated the definition of settling in reservoir according to the time period, pattern of deposition and compaction phenomena. Considering the computation for several alternatives the results obtained by the simulation are shown in Figure 12:

Curve no 1: the total volume of sediment in the reservoir, if the watershed characteristics in 1979 would have prevailed in 1956 and if the compaction of the sediment did not occur in the reservoir (Total Volume T.V. = 207.6 hm);

Curve no 2: the accumulated volume of sediment in reservoir taking into consideration the progressive degradation of watershed and the compaction of the sediment deposit (e.g. real conditions (T.V. = 135 hm^3);

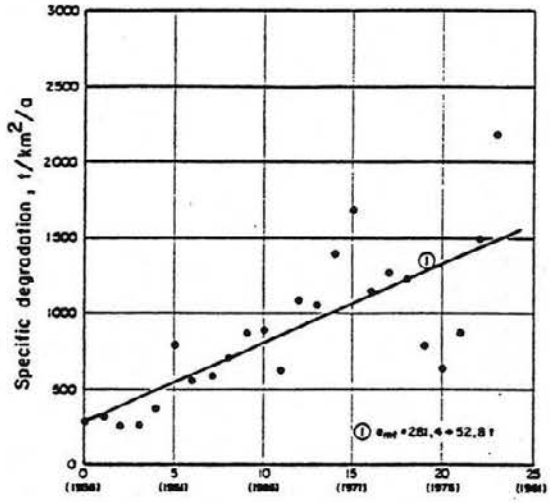

Figure 11. Increasing of the specific degradation since 1956.

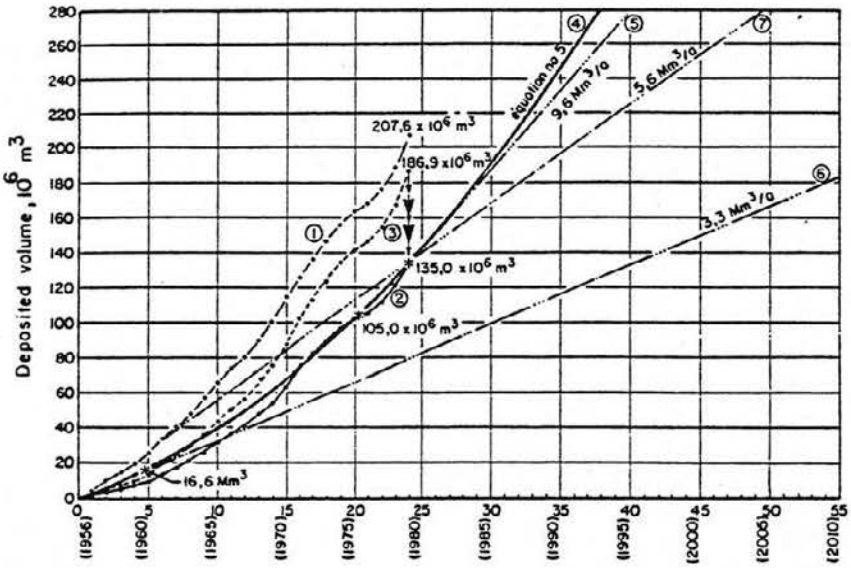

Figure 12. Simulation of the accumulation of sediments in reservoir since 1956.

Curve no 3: idem to Curve no 2, without compaction (T.V. = 187 hm^3);

Curve no 4: the historical progression of silting obtained by the model following a quadratic form:

$$V\ (hm^3) = 2.71\ T + 0.121\ T^2 \qquad (T \text{ in years since } 1956) \qquad (6)$$

Curve no 5: average sediment load entering the reservoir based on data obtained between 1977-1979 (Q_s = 9.9 hm^3/yr);

Curve no 6: initial load considered for the design of the dam: (Q_s = 3.3 hm^3/yr);

Curve no 7: average volume of sediment from 1956-1977 (Q_s = 5.6 hm^3/yr).

From comparison of these curves with the reservoir surveys, curve number 4 represents more adequately the past rate of silting of the reservoir. The important increase in sediment yield has reduced drastically the life expectancy of the reservoir (see Table III).

Table III. Perspective of sediment in the reservoir.

Sedimentation of the reservoir (active storage)	Design Value (year)	Mathematical Model (curve no 4)
20%	1997	1979
30%	2011	1985
50%	2039	1995

Discussion

The case history of the Peligre dam in Haiti shows that the determination of sediment deposition in reservoir is dependent upon reliable raw data. This requires a well established sediment monitoring program including regular reservoir surveys. The simple model indicates very well the increase in silting rate with an average increase of about 18 percent per year. Correspondingly a quadratic growth curve is more appropriate than a straight line for predicting sediment yield. Thus, the rate of sediment inflow almost tripled from 1956 to 1979.

MOLINEROS PROJECT IN BOLIVIA (Case Study No 2)

The Molineros project, although very compact, has a very large reservoir capacity located south-east of Cochabama in the Bolivian Andes. The site of the project is on the Caine River. The gorge at the dam site has a length of nearly 7 km and a depth that exceeds 300 meters (Figure 13). While the discharge, head and location are generally suitable for hydropower plants large sediment loads transported in the Caine River have postponed the project, viable otherwise, since 1972. The reevaluation of the project in 1983 was consisting in a 132 MW surface powerhouse dam of 200 m high, storing 2980 hm^3 as live storage. The shape of the reservoir is long (45 km) and narrow, thus presenting many singularities which could affect sedimentation in the reservoir. The reservoir has been subdivided in six reaches as shown in Figure 13. Detailed volumes and relative capacity of each reach are presented in the table, Figure 13.

Hydrology

The Caine River basin has a total drainage area of 9530 km^2. Steep slopes covered with only 20 percent of ground cover and easily eroded sand stone, silt stone, shales and marls are responsible for the large sediment load in the Caine River. The mean annual watershed precipitation is 630 mm, varying from 1115 mm in the rainy regions to 400 mm in the dryest regions. Over the whole basin, the wet season - December to March - represents near 80 percent of the total rainfall. The resulting 30 years mean annual flow is 47.2 m^3/s which represents a specific runoff value of 5 $\ell/s/km^2$. Flood flow determination done by means of different probability distribution laws - best fitting being the Log-Pearson III law, Fig. 14 a - which give, for a return period of 1000 and 10,000 years, 3750 m^3/s and 4150 m^3/s respectively (PMF Value = 4950 m^3/s).

Erosion and Sediment Discharge

Some current studies involving the geology mapping and the soil erosion in the Caine River basin concluded that two tributaries, the Tapacari and the Arque Rivers, draining together 35 percent of the whole basin, convey the largest part of sediments, estimated at about 60 percent of the total load. Multiple rating curves were considered: rising and recession periods, seasonal periods, rainy and dry periods. For the 11 years of observation (1972-82) it was impossible to proceed to the calibration for each period. Discharges arising from peak storms during dry period, however, do not give the same sediment relationships whether they occur in a severe area of erosion or in a more stable area. In the upper limit, the average concentration of solids corresponds to a value of 150 g/ℓ (Fig. 15).

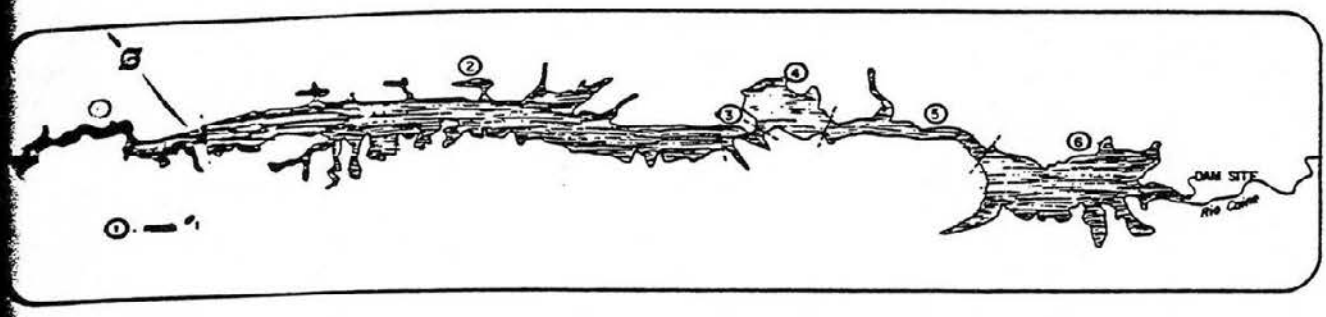

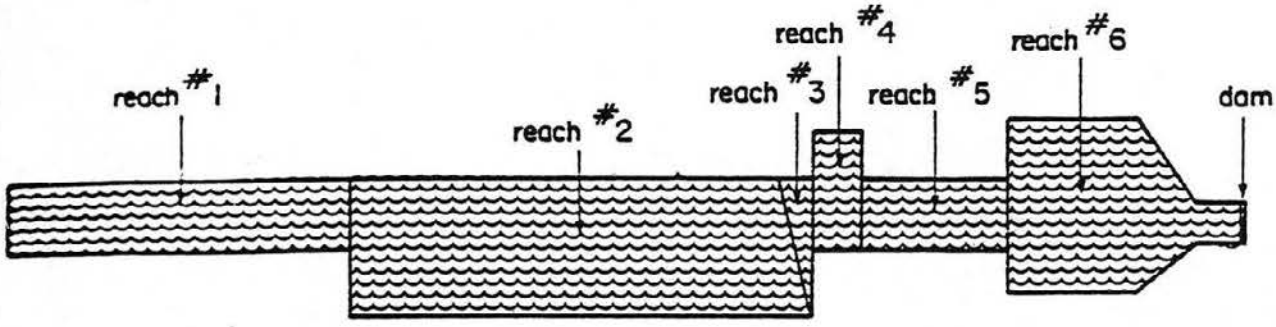

reach Nº	maximum length , km	maximum depth , m	average area , km^2	average volume, $10^6 m^3$
1	13,0	85,0	11 802	474,4
2	15,3	130,0	25 339	1562,4
3	1,1	134,0	762	58,7
4	1,7	138,0	1 199	92,0
5	5,4	152,0	4371	299,3
6	8,0	200,0	7031	493,2

Figure 13. Shape and schematic view of the Molinero's reservoir.

In addition to the rating curve studies related to the morphological changes of the watershed due to erosion a set of duration curves for water and sediments are shown in Figure 16.

According to the hydraulic and sediment balance it was found that (Fig. 16):

- 98 percent of the annual sediment load Q_s correspond to a discharge above 100 m^3/s, occurring less than 17 percent of the time ($Q_{.17}$).
- 95 percent of Q_s correspond to a discharge above 160 m^3/s ($Q_{.08}$).

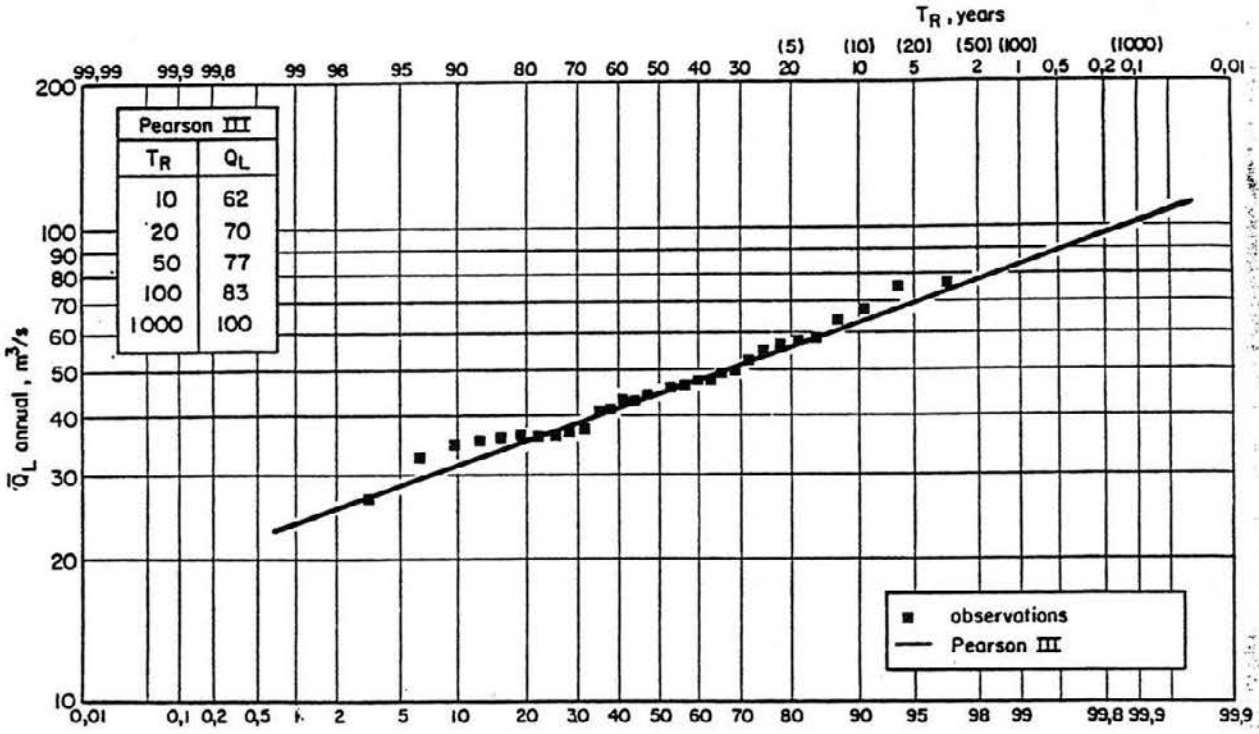

Figure 14a. $\bar{Q}_L$ annual vs. probability (1952-1982).

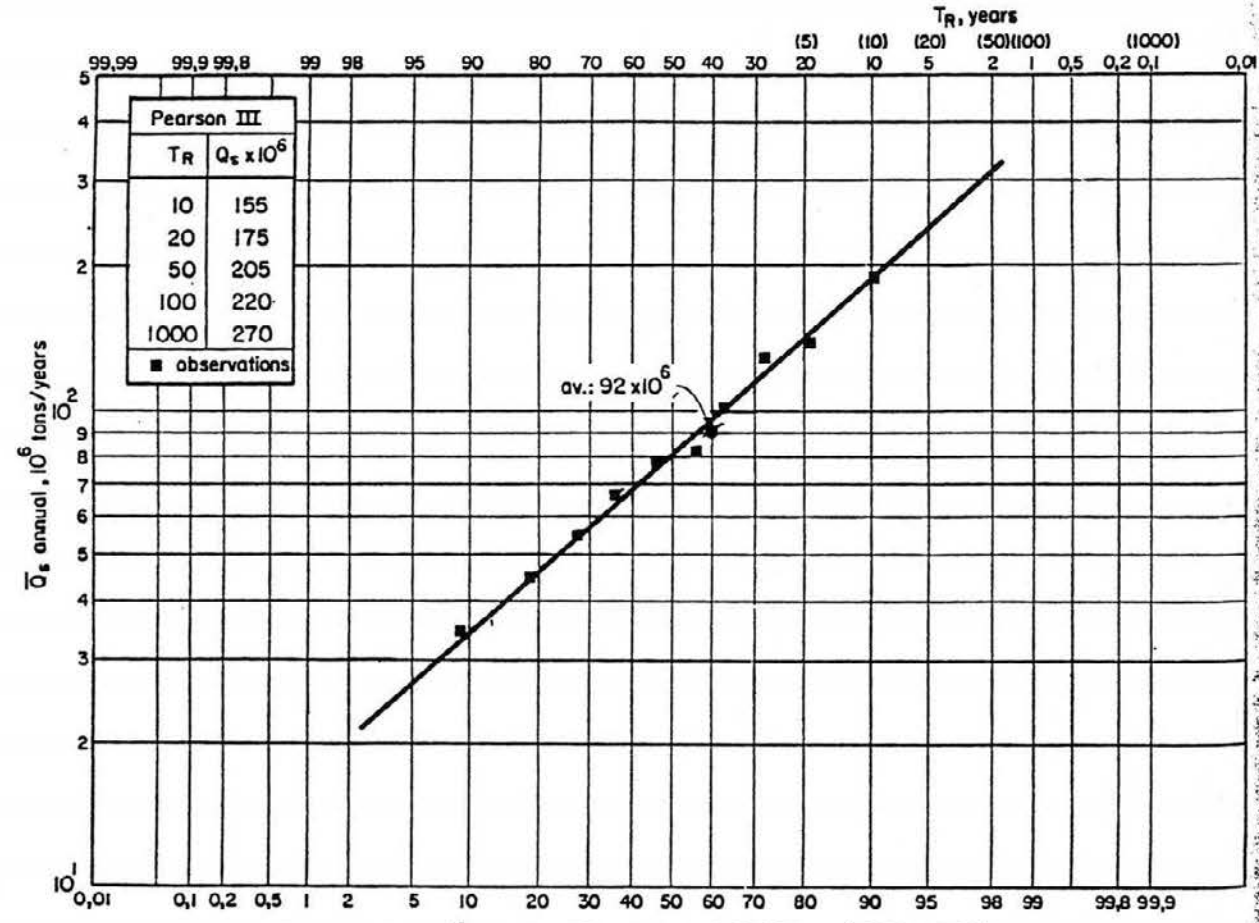

Figure 14b. $\bar{Q}_s$ annual vs. probability (1973-1982).

422

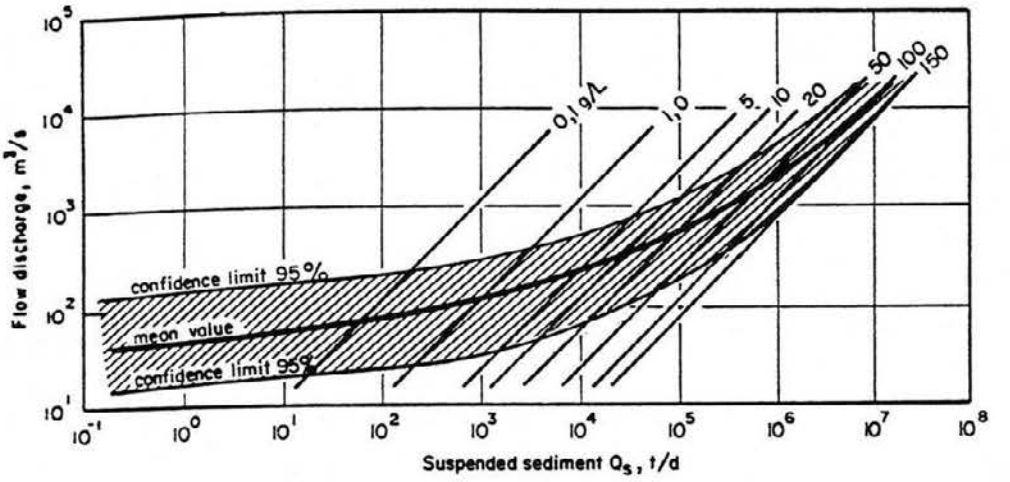

Figure 15. Caine River sediment rating curve at Molineros station, period 1972-1982.

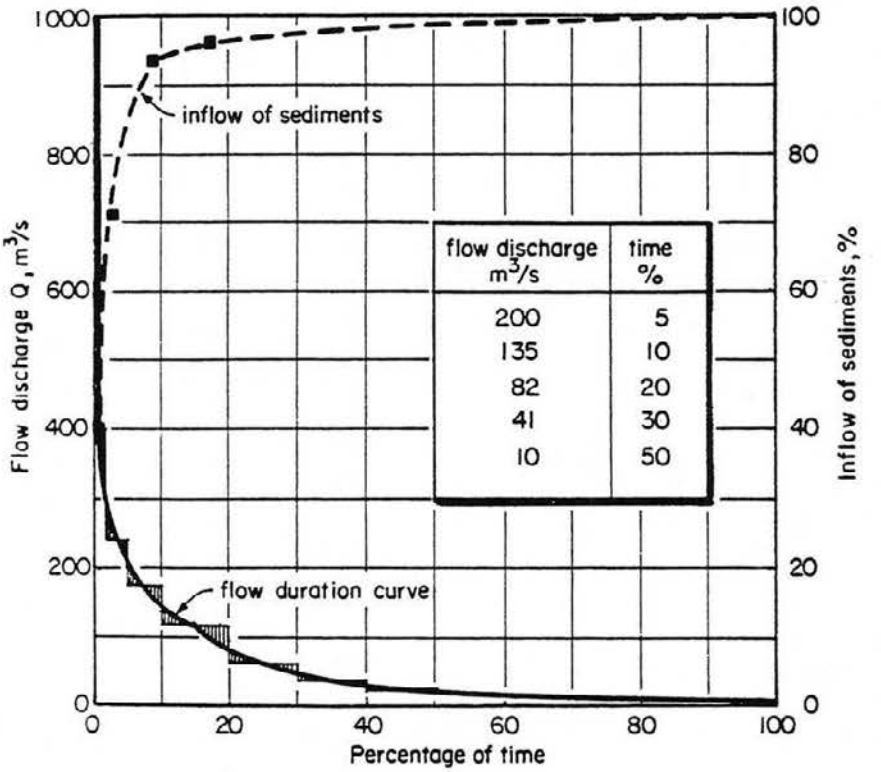

Figure 16. Flow duration curve and inflow of sediment, Molineros project, period 1972-1982.

- 50 percent of Q_s correspond to a discharge above 275 m^3/s ($Q_{.02}$).
- 40 percent of Q_s correspond to a discharge above 1000 m^3/s ($Q_{.01}$).

Considering the average and sediment discharge duration frequency for each classes, the average load of sediment at the dam site was estimated at 110 x 10^6 t/yr, of which 15 percent is assumed to represent the bed load. In fact, due to the slope of the river ($\bar{S}$ = 0.004) cobbles, gravels and sands are observed in the bed of the Caine river. On the other hands, laboratory tests gave the following results for the grain size distribution of the suspended load:

- 25 percent of sand $w \cong 7 \times 10^{-3}$ m/s

- 65 percent of silt $w \cong 4 \times 10^{-4}$ m/s

- 10 percent of clay $w \cong 4 \times 10^{-6}$ m/s

(w = settling velocity)

Investigation of the Long-Term Mean Sediment Discharge

The annual suspended sediment load has been correlated to the peak discharges an mean annual flows. The results of this comparison are presented in the Figure 17 (a, b, c, d). The results presented here are representative only of the suspended sediment par of the total sediment discharge. Bed-material transport is essentially unmeasured an therefore undefined, but assumes to correspond to 15 percent of the suspended load.

This computation of the average suspended sediment yield for long-term periods usin a relationship between the annual suspended sediment discharge and the annual water dis charge presents accurate results as long as there is no disturbance in the watershed Changes in land use may increase the erosion and change the rating curve. The bes results obtained correspond to the relation of the sediment discharge and the product o the annual peak flow with the mean annual water discharge (results not shown here).

Trap Efficiency

Considering the characteristics of each individual reach of the reservoir and th annual flow, the settling potential for every size fraction was studied with using th Borland formula. Table IV shows the results for the mean annual flow (49.5 m^3/s), indi cating that the sand and silt fraction can settle out completely in any of the individu reaches while the clay fraction (less than 10 percent) presents some difference. For th overall reservoir the trap efficiency is almost 100 percent, as also given by other empir ical approaches (Brune, Churchill ...). The formation of density currents is highl probable and up to 20 percent of the inflow of fine sediments is expected to move to th dam with the density current.

Table IV. Cumulative trap efficiency for each reach using Borland's method.

Water level: 2.020 m

REACH #	L (m)	V (m/s)	(c) ($\times 10^6$ m^3)	A ($\times 10^3$ m^2)	d (m)	TE SAND	TE SILT	TE CL
1	13,300	1.04×10^{-3}	474.4	11,802	40.2	100	100	73
1,2	28.650	5.20×10^{-4}	2,036.8	37.141	54.8	100	100	98
1,2,3	29.700	5.24×10^{-4}	2,095.5	37.903	55.3	100	100	98
1,2,3,4	31.300	5.29×10^{-4}	2,187.5	39.102	55.9	100	100	98
1,2,3, 4,5	36.600	5.45×10^{-4}	2,486.8	43,473	57.2	100	100	99
1,2,3, 4,5,6	44,350	5.51×10^{-4}	2,980.0	50,504	59.0	100	100	99

4624

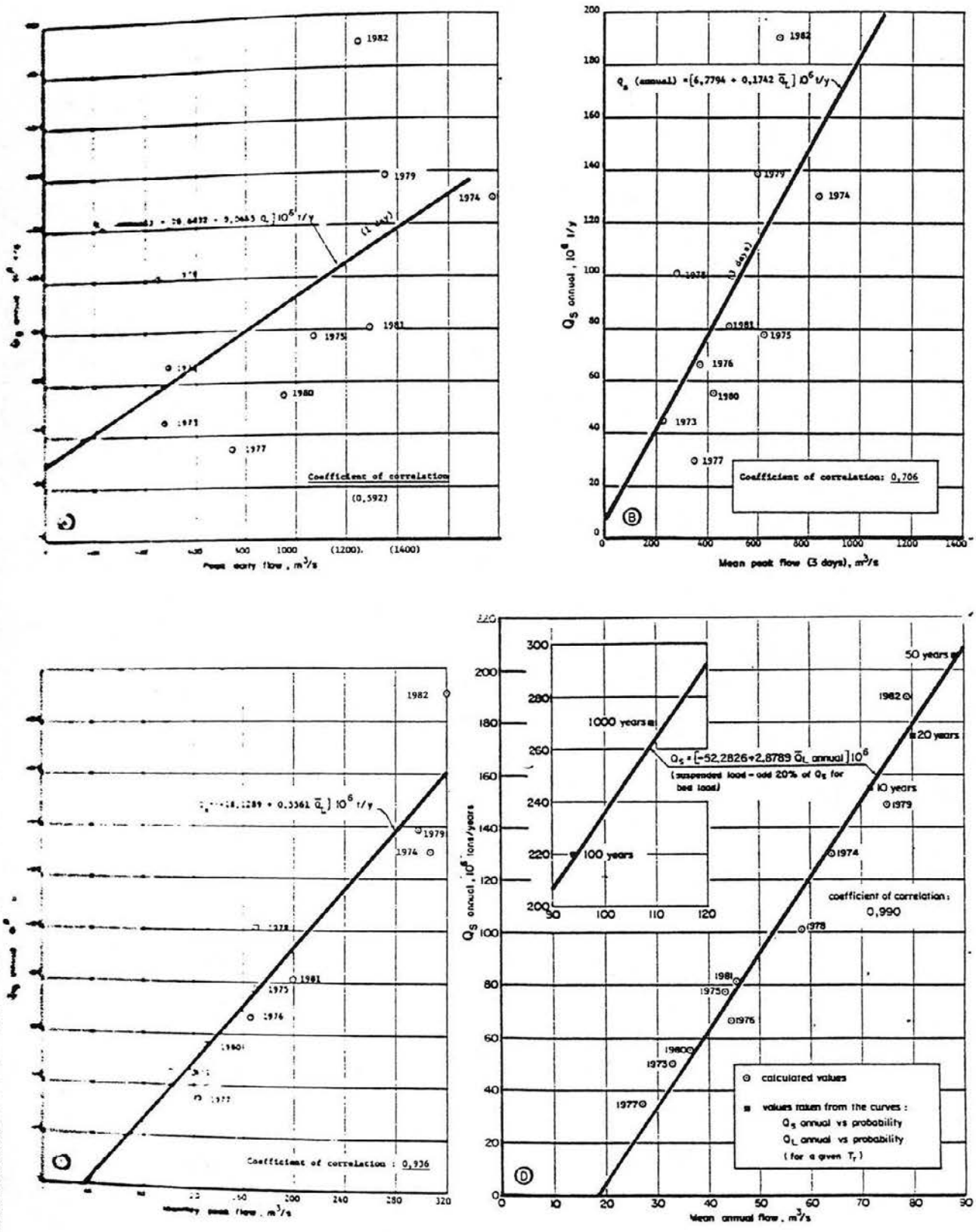

Figure 17. Relations between flow discharges and sediments inflow.

Life Expectancy of the Reservoir

The amount of sediment flowing into the future reservoir being very large (Specific Degradation 1195 t/km^2/yr) as already described, it became necessary to examine some counter-measures for solving the sediment problems such as the reduction of sediment inflow into the reservoir and possible flushing sediments beyond the predetermined sediment level.

Specific weight of the reservoir deposit has been estimated using Lane and Koelzer, Trask and Colby's methods. Over a long period, the unit weight was estimated to 1300 kg/m^3 in the delta formation (including the bottom deposit) and 1100 kg/m^3 in the density current beds.

Preliminary evaluations of the rates of silting are shown in Figure 18, computed with two assumptions regarding density currents. The advantage of a density current being related to deposition near the dam in the dead storage area. On the other hand the delta formation reduces significantly the live storage of the reservoir. As shown in the figures the rate is constant without density currents while an inflexion point appears at 66 percent of accumulation if a density current occurs. This percentage corresponds to 80 percent of the relative life expectancy of the reservoir.

Finally, Figure 19 gives an idea of the rate of silting assuming that the dam would have been built in 1952 (back to the first streamflow records), in 1973 and 1985. Important statements can then be made, showing that the rate of the sediment inflow is increasing slightly with time, respecting the following relation:

$$Q_s = [59.6\ T + 2.55\ T^2] \times 10^6\ (t/yr) \qquad (T = \text{time in year starting in 1973})$$

In summary, taking a constant rate, the reservoir should have been completely filled with sediment in 30.5 years if built in 1952, and 35 years if built in 1973, but reduce to 24.4 years according to the quadratic curve if built in 1973 and 18 years if built in 1985.

Discussion

This review 1983 of the sediment discharge of the Molineros project in Boliva, after a first investigation in 1972 still lead to the same conclusion: "While the flows and heads are generally suitable for hydropower plants of various sizes the large volume of sediments still postpone the project, viable otherwise, since 1972." Further studies are carried on in order to extend the life expectancy of the reservoir.

In comparison with Tarbela dam on the Indus river, Lowe and Fox (1982) estimated the annual sediment load at 200 x 10^6 t/yr for an average peak flow of 8500 m^3/s (maximum recorded in 112 years = 18,690 m^3/s). The rate of erosion in Boliva, on the Caine river, is more severe than in the case of Tarbela dam (about twice), considering that the average concentration of solids (kg/m^3) in the Indus river (at Tarbela site) is about 3.3 percent while 7.0 percent at Molineros dam.

Conclusion

Current technology for predicting reservoir sedimentation has been critically reviewed in the light of thorough investiations of case studies. The determination of the incoming sediment load, trap efficient, unit weight of sediment deposits and life expectancy are shown to be of primary importance in the design of reservoirs.

The feasibility of the Molineros project in Bolivia has been shown to depend mainly on the rate of silting in the reservoir. It is demonstrated in this analysis that although the total reservoir capacity is close to 3 km^3, the life expectancy of the reservoir varies from 18 to 35 years depending on the alternatives examined in this prefeasibility investigation.

426

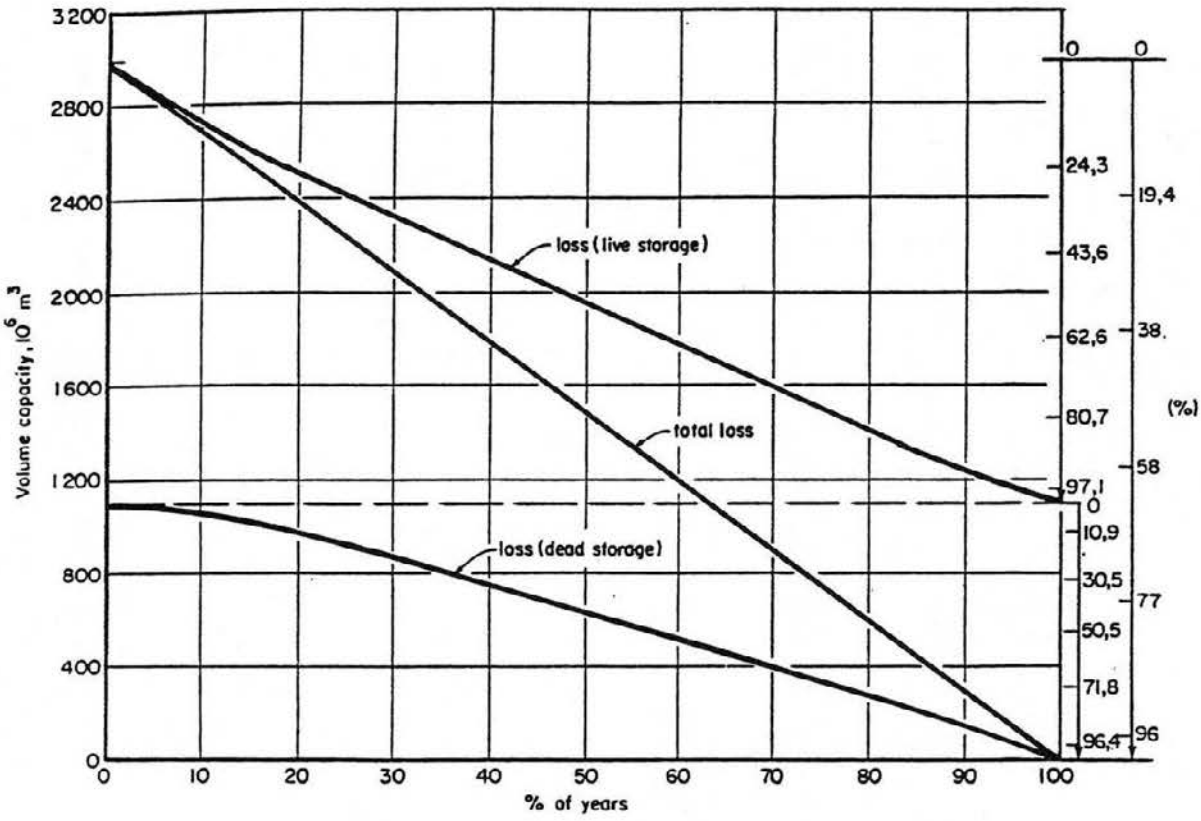

Figure 18a. Filling up of reservoir (level 2020m) without density current.

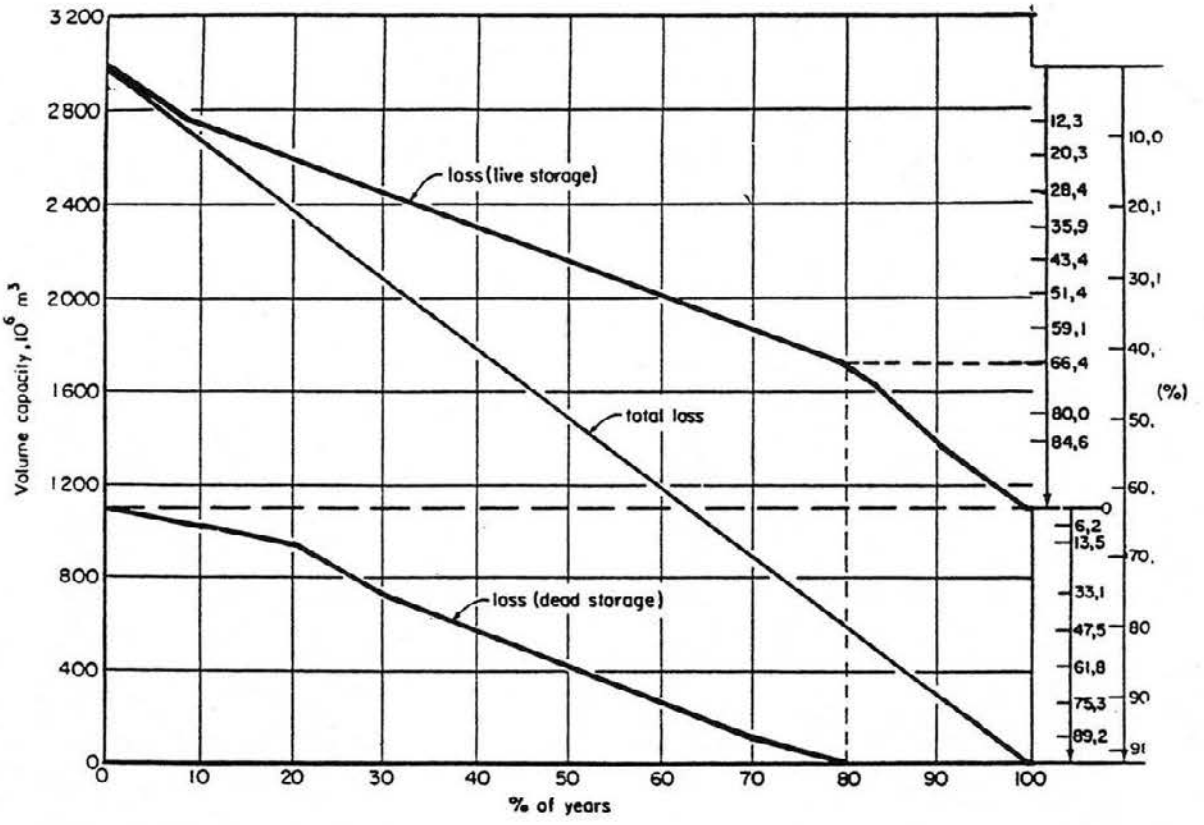

Figure 18b. Filling up of reservoir (level 2020 m) with density current.

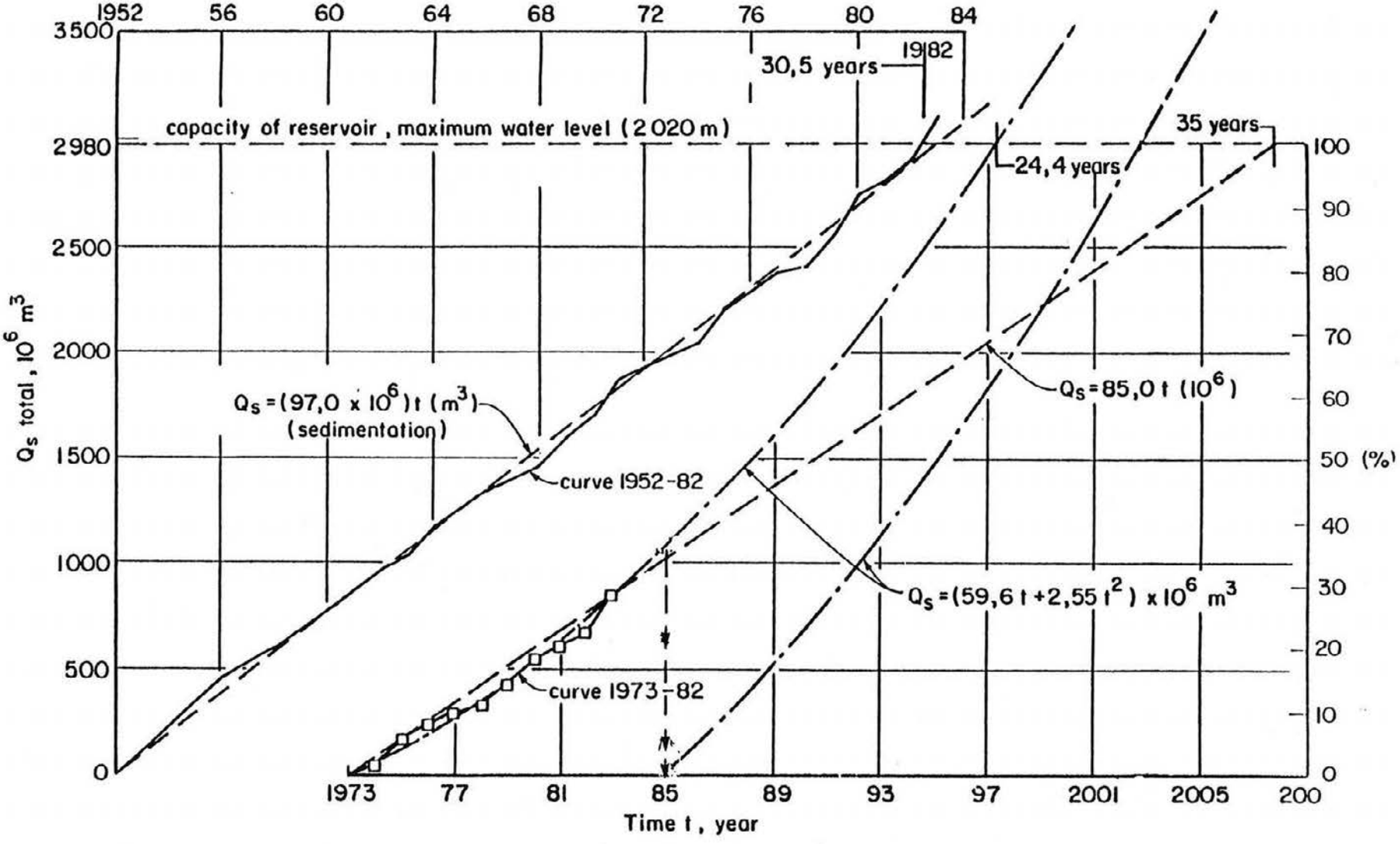

Figure 19. Cumulative curves Q_s vs. time (total sediment load).

The Peligre dam in Haiti reveals several key features to be considered in the design of reservoirs. The threefold increase in specific degradation, due to changes in land use in the upland areas, since the construction of the dam in 1956 jeopardizes the life expectancy of the reservoir. Among other considerations, the trap efficiency as predicted by conventional methods was considerably less than the measurements because of the increased settling potential relative to flocculation of clay particles. Interestingly, the measurements are in contradiction with Chen's recommendations (Fig. 2) regarding trap efficiency of fines particles, when flocculation occurs.

References

Borland, W. M., (1971) Reservoir Sedimentation, Chap. 29 in River Mechanics, Water Resources Publications, Fort Collins, USA, 38 p.

Borland, W. M., (1975) Sedimentation Engineering, ASCE, Manual No. 54, pp. 587-605.

Borland, W. M. and Miller, C. R., (1962) "Stabilization of Five Mile and Muddy Creek", presented at the May 1962 ASCE Meeting held at Omaha, Neb.

Brown, C. B., (1958) Sediment Transportation, Engineering Hydraulics Wiley, New York, USA.

Brune, G. M., (1953) "Trap Efficiency of Reservoirs", Trans. AGU, Vol. 34, No. 3, pp. 407-418.

Chen, (1975) "Design of Sediment Retention Curve", Urban Hydrology and Sediment Control Symposium, Lexington, USA.

Churchill, M. A., (1948) Discussion of "Analysis and Use of Reservoir Sedimentation Data" by L. C. Gottschalk: Proc. Federal Inter-Agency Sedimentation Conf., Denver, Colorado, pp. 139-140.

Dehoux, M., (1961) "Etude de la sédimentation du lac Péligre", rapport interne, Electricité d'Haiti, Port-au-Prince, Haiti.

Frenette, M., Souriac, J.-C., and Tournier, J.-P., (1982) "Modélisation de l'alluvionnement de la retenue de Péligre, Haiti", 14th International Congress on Large Dams, Rio de Janeiro, Brazil, pp. 93-115.

Frenette, M., Tournier, J.-P., and Nzakimuena, T. J., (1982) "Cas historique de sédimentation du barrage Péligre, Haiti", Canadian Journal of Civil Engineering, Vol. 9, No. 2, pp. 206-223.

Frenette, M. and Julien, P. Y., (1985) "Computer Modeling of Soil Erosion and Sediment Yield from Large Watersheds", Proceedings of the 27th Annual Convention of the Institution of Engineers, Peshawar, Pakistan, 21 p.

Frenette, M. and Julien, P. Y., (1986) LAVSED-I - Un modèle pour prédire l'érosion des bassins et le transfert de sédiments fins dans les cours d'eau", Canadian Journal of Civil Engineering, April (In Press).

Graf, W. H., (1971) Hydraulic of Sediment Transport, McGraw Hill, New York, USA.

Graf, W. H., (1984) "Hydraulics of Reservoir Sedimentation", Communication du Laboratoire d'hydraulique #51, EPFL, Lausanne, 40 p.

Hydrotech Inc., (1983) "Molineros Hydropower Project on Caine River", Preliminary analysis of sediment data, sedimentological spect, 121 p.

Julien, P. Y. and Frenette, M., (1986) "LAVSED II - A Model for Predicting Suspended Load in Northern Streams", Canadian Journal of Civil Engineering, April (In Press).

Julien, P. Y. and Frenette, M., (1985) "Modeling of Rainfall Erosion", Journal of Hydraulic Engineering, ASCE, Vol. 111(10), Oct., pp. 1344-1359.

Karaushev, A., (1965) "A Method of Calculating Sedimentation in Reservoirs", Soviet Hydrology, AGU, No. 3.

Knappen, Tippets, Abbett Eng. Co., (1950) "Artibonite Valley, Development for Irrigation, Flood Control, Drainage, Hydro-electric Power", Internal Report, NY.

Lalonde, Girouard, Letendre et Ass. Ltee, (1977) "Projet inventaire des ressources hydrauliques", Rapport d'études sédimentologiques, Montréal, Québec.

Lalonde, Girouard, Letendre et Ass., (1980) "Etudes sédimentologiques du réservoir Péligre", Rapport préliminaire, Montréal, Québec.

Lopez, J. L., (1978) "Mathematical Modeling of Sediment Deposition in Reservoir", Ph.D. dissertation, Colorado State University, Fort Collins.

Lowe III, J. and Fox, I. H. R., (1982) "Sedimentation in Tarbela Reservoir", 14th International Congress on Large Dams, Rio de Janeiro, Brazil, 3-7 May, 1982, pp. 317-340.

Miller, C. R., (1953) "Determination of the Unit Weight of Sediment for Use in Sediment Volume Computations", USBR.

Quian, N., (1982) "Reservoir Sedimentation and Slope Stability, Technical and Environmental Effects", General report Q54, 14th Congress on Large Dams, Rio de Janeiro, 1982.

Rice, T. L., (1981) "Reservoir Sedimentation Modeling", Ph.D. Dissertation, Colorado State University, Fort Collins.

Simons, Li and Ass., (1982) Engineering Analysis of Fluvial Systems, Fort Collins, Colorado.

Yücel O. and Graf, W. H., (1973) "Bed Load Deposition in Reservoir", Proceedings 15th Congress of IAHR, Istanbul, Turkey, 1973.

Bull. Soc. géol. France, 1993, t. 164, n° 5, pp. 649-660

Experiments on stratification of heterogeneous sand mixtures

by PIERRE Y. JULIEN*, YONGQIANG LAN** and GUY BERTHAULT***

Key words. – Stratification, Sediment mixtures, Lamination.

Abstract. – Superposed strata in sedimentary rocks are believed to have been formed by successive layers of sediments deposited periodically with interruptions of sedimentation. This experimental study examines possible stratification of heterogeneous sand mixtures under continuous (non-periodic and non-interrupted) sedimentation. The three primary aspects of stratification are considered : lamination, graded-beds, and joints. (1) Experiments on segregation of eleven heterogeneous mixtures of sand size quartz, limestone and coal demonstrate that through lateral motion of a sand mixture, the fine particles fall between the interstices of the rolling coarse particles. Coarse particles gradually roll on top of fines and microscale sorting is obtained. Microscale segregation similar to lamination is observed on plane surfaces, as well as under continuous settling in columns filled with either air or water. (2) The formation of graded-beds is examined in a laboratory flume under steady flow and a continuous supply of heterogeneous sand particles. Under steady uniform flow and plane bed with sediment motion, the coarse particles of the mixture roll on a laminated bed of mostly fine sand particles. In non-uniform flow, the velocity decrease caused by a tailgate induces the formation of a stratum of coarse particles propagating in the downstream direction. On top of this cross-stratified bed, fine particles settle through the moving bed layer of rolling coarse sand particles and form a near horizontally laminated topset stratum of finer particles. Over time, a thick stratum of coarse particles thus progresses downstream between two strata of laminated fine particles, continuously prograding upward and downstream. (3) Laboratory experiments on the desiccation of natural sands also show preferential fracturing, or joints, of crusty deposits at the interface between strata of coarse and fine particles.

Rather than successive sedimentary layers, these experiments demonstrate that stratification under a continuous supply of heterogeneous sand particles results from : segregation for lamination, non-uniform flow for graded-beds, and desiccation for joints. Superposed strata are not necessarily identical to successive layers.

Expériences sur la stratification de mélanges sableux hétérogranulaires

Mots-clés. – Stratification, Mélanges hétérogranulaires, Lamination.

Résumé. – Les strates dans les roches sédimentaires sont généralement assimilées à des couches sédimentaires successives déposées avec arrêt périodique de la sédimentation. Cette étude expérimentale examine la possibilité de stratification de mélanges de sables hétérogranulaires en sédimentation continue (sans interruption et périodicité de la sédimentation). Les trois aspects principaux de la stratification sont considérés : lamination, lits stratifiés, et joints. (1) Les expériences sur la ségrégation de onze mélanges hétérogranulaires de quartz, calcaires et charbons démontrent que lors du mouvement latéral de sables hétérogènes, les particules fines tombent dans les interstices entre particules grossières en mouvement. Les particules grossières roulent sur les fines et la ségrégation est obtenue à l'échelle microscopique. Cette ségrégation microscopique similaire à la lamination est observée sur des surfaces planes, tout comme en sédimentation continue en colonnes d'air ou d'eau. (2) La formation de lits stratifiés est examinée au laboratoire dans un canal avec écoulement permanent et alimentation continue de particules hétérogranulaires. A partir d'un écoulement permanent et uniforme sur un lit hétérogranulaire plan, les grosses particules du mélange roulent sur la surface d'un dépôt laminé de particules fines. En écoulement permanent non-uniforme, la diminution de vitesse d'écoulement provoquée par l'insertion d'un seuil à l'aval du canal induit la formation d'une strate deltaïque de particules grossières en progression vers l'aval. Une strate laminée de particules fines se forme simultanément au dessus du lit stratifié obliquement. Une strate de particules grossières en progression vers l'aval se forme donc continuellement entre deux strates laminées de particules fines en progradation verticale et vers l'aval. (3) Les expériences en laboratoire sur la dessiccation de sables naturels montre des fractures préférentielles, ou joints, à l'interface des strates de grosses et de fines particules dans les dépôts séchés à l'air.

Ces expériences démontrent que la stratification de mélanges sableux sous alimentation continue en sédiments hétérogranulaires résulte de : la ségrégation produisant la lamination, l'écoulement non-uniforme produisant les lits stratifiés, et la dessication produisant les joints. Les strates superposées ne sont donc pas nécessairement le résultat de couches sédimentaires successives.

I. – INTRODUCTION

As stratification usually describes layering in rocks, a single layer of homogeneous lithology is referred to as a stratum. Stratification has often been associated with intermittent sedimentary layers. Superposed strata in sedimentary rocks are believed to have been formed by successive layers of sediment deposited periodically with interruptions of sedimentation.

McKee *et al.* [1967] reported on the sedimentary structure, texture and shape of the massive sand deposits developed during the Bijou Creek flood in July 1965. Stratified sand deposits up to 12 feet (3.8 m) in thickness formed within a few hours. The violent flood deposited superposed thick horizontal strata of fine and coarse sands, characteristic of the upper flow regime with internal layering in the form of microscale lamination. Is stratification resulting from successive intermittent layers in such rapid and quite continuous sedimentary flow ? The primary features of interest in the Bijou Creek sand deposits are : (1) lamination seen as a microscale sorting of coarse and fine particles at a vertical scale not exceeding 10 mm ; (2) graded-beds or strata of coarse and fine particles of thickness exceeding 10 mm ; and (3) horizontal joints between sediment deposits.

* Associate Professor, Civil Engineering Department, Engineering Research Center, Colorado State University, Fort Collins, Colorado 80523, USA.
** Engineering Research Center, Colorado State University, Fort Collins, Colorado 80523, USA.
*** 28 boul. Thiers, Meulan, 78250, France.
Manuscrit déposé le 26 octobre 1992 ; accepté le 15 avril 1993.

TABL. I. – Summary of hypotheses explaining the origin of horizontal lamination.
TABL. I. – *Synthèse des hypothèses expliquant l'origine des laminae horizontales.*

	Reference	Summary of Hypothesis
1.	Kuenen & Menard (1952) Kuenen (1953, 1957)	Velocity pulsations in turbidity current.
2.	Ksiazkiewicz (1952)	Diluted secondary turbidity currents suspended above bed.
3.	Ten Haaf (1956)	Sorting action of vortices by turbulence in turbidity currents.
4.	Hsü (1959)	Settling and laminar flow of fluidized sediment along bed.
5.	Unrug (1959) Wood & Smith (1959)	Settling from tail of turbidity current with a non-uniform concentration.
6.	Bouma (1962) & Lombard (1963)	Small turbulent eddies. Current velocity pulses with settling or traction.
7.	Moss (1963) Kuenen (1966)	Grains of similar susceptibility to transport tend to deposit together. i.e. spatial & temporal selection of similar grains due to grain interaction under quasi-steady flow condition - the "like-seek-like" principle.
8.	Allen (1964)	Pulsating sediment supply due to separate large scale eddies. Upper regime plane bed.
9.	Walker (1965)	Intermittent supply of mixed sediment to top of viscous sublayer followed by differential settling through; for finer grained laminae. Coarser grained laminae under upper regime plane bed.
10.	Sanders (1965)	Settling and traction during current velocity fluctuation. Not upper regime plane bed.
11.	Jopling (1967)	Attributed laminae to the superposition of longitudinal segregations of bedload grains under aggradation of a upper regime plane bed.
12.	Pettijohn (1957,1975)	Transitory phases or minor chance fluctuations in velocity of depositing current.
13.	Middleton (1970)	Smaller grains filter down between larger ones during flow, thus displacing the larger ones towards the free surface.
14.	Smith (1971) McBride et al. (1975)	Migration of very low relief bedforms (diminished ripples and dunes).
15.	Frostick & Reid (1977)	Combine the ideas of Pettijohn, Moss and Kuenen.
16.	Bridge (1978)	Described possible lamination formation due to the effect of single burst-sweep cycle on a plane bed.
17.	Hesse & Chough (1980)	Suggested that a horizontal lamination formed with multiple burst and sweep events on plane bed.
18.	Allen (1984)	Laminae form due to the shifting distribution of boundary shear stress as large eddies move downstream over a plane bed.
19.	Bridge & Best (1988)	Laminae form by both migration of low-relief bedwaves and the turbulent bursting process.
20.	Paola, Wiele & Reinhart (1989)	Extremely low amplitude bedforms. Initial deposition from small scale turbulent fluctuations in shear stress followed by sieving out mechanism resulting in a smooth surface process termed glazing.

432

Hjulstrom [1935] defined a relationship between velocity and motion of particles of different sizes. Various hypotheses formulated to explain the origin of near-horizontal lamination in unidirectional flow were compiled by Bridge [1978], and Cheel and Middleton [1986], and are summarized in table I. Allen [1984] stated that many authors have qualitatively recognized the importance of some periodic or quasi-periodic phenomenon, either located in the flow or in the uppermost levels of the bed. Velocity pulses, large eddies and turbulent fluctuations have had a wide appeal [Kuenen and Menard, 1952; Kuenen, 1953, 1957; Ten Haaf, 1956; Pettijohn, 1957, 1975; Bouma, 1962; Lombard, 1963; Allen, 1964].

Bridge [1978] proposed the "burst-sweep cycle" in the turbulent boundary layers to explain the vertical sorting that defines laminae. Accordingly, bursts would cause upward dispersion of the suspended load throughout the flow, also some of the saltating load would carry coarser grains due to higher shear stress. As bed shear stress decreases, the dispersed particles settle down to form a laminated layer. Allen [1984] suggested a model based on the larger coherent structures of the turbulent boundary layers to explain the formation of horizontal laminae under plane bed in the upper flow regime. Cheel and Middleton [1986] suggested that the probable mechanism for the formation of FU (fining-upward) and CU (coarsening-upward) laminae was the burst-sweep process. Unrug [1959], and Wood and Smith [1959] saw parallel lamination as caused by the segregation of the coarser grains into distinct clouds within the flow. Hsü [1959] attributed lamination to laminar flow at the bed.

On the basis of field observations or laboratory experiments, other investigators have explained parallel laminations by the travel of extremely flat symmetrical to strongly asymmetrical bed waves [Jopling, 1965, 1967; Jopling and Walker, 1968; Smith, 1971; McBride *et al.*, 1975; Allen, 1982], although not always in the context of an upper-stage plane bed. Paola *et al.* [1989], along with Bridge and Best [1988], explained that lamination results from the superposition of two processes : (1) high-frequency erosion and deposition due to turbulence; and (2) migration of low-amplitude bed forms that is neither upper- nor lower flow-regime.

A "like-seeks-like" mechanism of grain sorting in the bedload layer was advocated by Moss [1962, 1963] and Kuenen [1966]. Interestingly, Kuenen [1966] reported that : "current pulsations are so numerous that they should produce ten to a hundred times more laminae than are present." He also stated in his abstract : "the selective concentration is due to the tendency of particles moving along the bottom to join stationary ones of equal weight, density and shape..." He added that "in spite of extremely uniform discharge without pulsation, lamination developed in nearly all experiments." Guy *et al.* [1966] noted the sorting of coarse and fine sand particles in laboratory flumes. Middleton [1970] proposed that grading arose because smaller grains tended to filter down between the larger ones during flow, thus displacing the larger grains toward the free surface. This segregation mechanism is also referred to as "kinematic sieving" in Allen [1982]. A sorting process was also advocated by Frostick and Reid [1977]. Berthault [1986, 1988] found that the thickness of laminae in still water increased as the difference between the size of particles became greater, and the laminae thickness also increased with flow velocity of running water.

The fundamental study reported herein focuses on laboratory experiments addressing three key issues in sediment stratification : (1) lamination (thinner than 10 mm) resulting from segregation of heterogeneous sand mixtures; (2) graded-beds (thicker than 10 mm) of heterogeneous sand mixtures that may result from steady non-uniform flow and continuous settling; and (3) horizontal joints at the interface between strata. The use of sand mixtures with coarse and fine particles of different colors ensures a better visualization of the sediment sorting besides providing an assessment of the distribution of different particle sizes. This article summarizes several laboratory reports by Julien and Chen [1989a,b] and Julien and Lan [1989, 1990a, 1990b] on recent laboratory experiments carried out in the Hydraulic Laboratory of the Engineering Research Center at Colorado State University.

II. – Experiments on segregation and lamination

Laboratory experiments on segregation of sand size mixtures of quartz, limestone and coal were carried out to examine how clearly various mixtures of particles of different sizes, density and shape can separate into thin layers of coarse and fine particles not exceeding a few millimeters in thickness : (1) under horizontal motion; and (2) through settling in air and water.

A) Sediment mixtures

Thirteen different sand size materials, have been used in the experiments. For each material, the particle size distribution, mass density, angle of repose, angularity and color are summarized in table II. Note that D_{10}, D_{25}, D_{50},

Tabl. II. – Characteristics of sands tested.

Tabl. II. – *Caractéristique des sables utilisés.*

Sand	Color	Mass density g/cm³	Angle of repose in air (degree)	Angle of repose in water (degree)	Angularity	Particle diameter				
						D_{10} (mm)	D_{25} (mm)	D_{50} (mm)	D_{75} (mm)	D_{90} (mm)
B2040	black	2.70	39.5	38	angular	.38	.48	.57	.67	.76
B3060	black	2.70	37	36	angular	.14	.20	.33	.55	.62
ERC #1	white	2.45	35	32	rounded	.08	.11	.13	.15	.18
ERC #2	white	2.65	37	34	rounded	.72	.90	1.20	1.50	1.90
ERC #3	white	2.65	37.5	35	rounded	.48	.55	.63	.73	.82
ERC #4	white	2.65	--	--	--	.09	.13	.16	.19	.29
ERC #5	beige	2.65	42.5	35	rounded	.15	.29	.55	.97	--
limestone #1	white	2.65	--	--	rounded	--	.31	.39	.47	--
limestone #2	white	2.65	37	34	rounded	--	.76	.91	1.00	--
coal #1	black	1.30	--	--	angular	--	.26	.41	.57	--
coal #2	black	1.30	40	40	very angular	--	--	.25	--	--
coal #3	black	1.30	--	--	angular	--	--	.66	--	--
coal #4	black	1.30	--	--	angular	--	--	1.24	--	--

433

D_{75} and D_{90} represent the particle size for which 10 %, 25 %, 50 %, 75 % and 90 %, respectively, of the particles are finer. The measured angle of repose increases as the subjective (angular *vs.* rounded) microscopic observation of angularity increases. Both parameters indicate that ERC #1, ERC #2, ERC #3, ERC #5, limestone #1, and limestone #2 are rounded, while coal #1, coal #3, coal #4, B2040 and B3060 are angular. Equal weights of materials of different sizes and colors were mixed to form a total of eleven mixtures listed in table III.

B) Experiments on segregation

Simple experiments were conducted to investigate possible segregation of sediment particles on a transparent horizontal plexiglas plate 30 × 40 cm^2. A small volume (not exceeding 10 cm^3) of a given homogeneous sand mixture was poured onto the plate which was then gently agitated manually for a few minutes in the horizontal direction of the plexiglas plate. Pictures were then taken above and below the plate to examine whether segregation occurs. The same procedure was repeated for each sand mixture. Typical experimental results, shown on figure 1, demonstrate how easy it is to segregate these two types of particles with the finer white particles (ERC #1) underneath (see fig. 1a), and the coarser black particles (B2040) on top (see fig. 1b).

The experimental results for the segregation of 12 different mixtures scrutinized by Julien and Lan [1990b] are summarized in table III. The pattern of particle segregation generally includes three types : (1) no segregation ; (2) fine particles on top of coarse particles ; and (3) coarse particles on top of fine particles (fig. 1). Segregation of particles always takes place if the two types of particles in the mixture have different sizes or densities. The particle segregation diagram on figure 2 illustrates the three types of particle segregation according to particle diameter D_{50} and mass density ρ of the data from table III.

The most fundamental mechanism explaining the segregation of heterogeneous sand mixtures of constant mass density starts from a uniform mixture of coarse and fine particles as sketched in figure 3. Only the lateral motion of the mixture in any direction is necessary to induce segregation. During lateral motion of the sand mixture in figure 3a, the fine particles fall through the interstices between coarse particles and reach the bottom of the moving

TABL. III. – Horizontal segregation of sand mixtures.

TABL. III. – *Ségrégation horizontale des mélanges sableux.*

#	Mixture†	Content‡	Observation
A	ERC #1 & B2040	$\rho_2 \equiv \rho_1$, $D_2 \neq D_1$	Clear segregation. Coarse black particles on top of fine white particles (see Fig. 1).
B	ERC #3 & B2040	$\rho_2 \equiv \rho_1$, $D_2 \equiv D_1$	No apparent segregation.
C	ERC #1 & B3060	$\rho_2 \neq \rho_1$, $D_2 \neq D_1$	Clear segregation. Coarse black particles on top of fine white particles.
D	ERC #1 & coal #1	$\rho_2 \neq \rho_1$, $D_2 \neq D_1$	Clear segregation. Coarse black particles on top of fine and white particles.
E	ERC #3 & coal #3	$\rho_2 \neq \rho_1$, $D_2 = D_1$	Clear segregation. Coarse coal particles on top of fine white particles.
F	limestone #1 & B3060	$\rho_2 \equiv \rho_1$, $D_2 \equiv D_1$	No clear segregation of particles.
G	limestone #2 & coal #1	$\rho_2 \neq \rho_1$, $D_2 \neq D_1$	Clear segregation. Fine black particles on top of coarse white particles.
H	ERC#2 & coal #1	$\rho_2 \neq \rho_1$, $D_2 \neq D_1$	No clear segregation is observed.
I	limestone #1 & coal #2	$\rho_2 \neq \rho_1$, $D_2 \neq D_1$	Clear segregation. Fine black particles on top of coarse limestone particles.
J	limestone #1 & B2040	$\rho_2 \equiv \rho_1$, $D_2 \neq D_1$	Clear segregation. Coarse black particles on top of limestone particles.
K	B3060 & ERC #3	$\rho_2 \neq \rho_1$, $D_2 \neq D_1$	Clear segregation. Coarse white particles on top of fine black particles.

† Mixtures are comprised of equal weight of each material.

‡ Mass density ρ, particle diameter D, different $\neq$, same $=$, comparable $\equiv$, (e.g. $D_2 = D$, same particle diameter $\rho_2 \neq \rho$, different mass density)

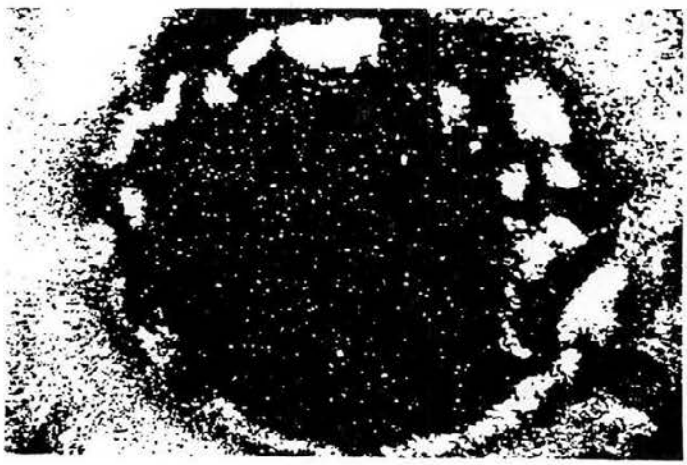

FIG. 1a. – Clear segregation of mixture ERC#1 & B2040, from above.

FIG. 1a. – *Ségrégation nette du mélange ERC#1 & B2040, vue de dessus.*

FIG. 1b. – Clear segregation of mixture ERC#1 & B2040, from underneath.

FIG. 1b. – *Ségrégation nette du mélange ERC#1 & B2040, vue de dessous.*

layer, while the coarse particles start rolling on top of the fine particles (fig. 3b). After a certain time, the fine particles stabilize at the bottom of the moving layer while the coarse particles remain mobile on top (fig. 3c). In order to obtain segregation with particles of the same mass density, it is important that the fines be sufficiently small to fall between the interstices of the coarse particles, and also, the coarse particles must be able to roll on top of the small ones. Particles of equivalent sizes and different densities also segregate with lighter particles on top of heavier particles.

Segregation is possible without bedforms and without turbulence, in that regard the segregation process is very different from the "glazing" process suggested by Paola *et al.* [1989]. Middleton [1970] and Allen [1982] also debated whether the dispersive shear stress arising from inter-particle collisions exerts a significant influence on segregation. Given that the dispersive stress is proportional to the square of the rate of deformation, we repeated our experiments under extremely low rates of deformation without inter-particle impact, thus negligible dispersive stress. The similar patterns that developed demonstrate that the segregation process results from the displacement of smaller grains between the coarser grains rather than from high speed inertial impact between particles.

C) Experiments on lamination

The objective of these experiments in a settling column was to examine possible repetitive segregation, or lamination, of various heterogeneous sand mixtures settling in air and in water. The visualization of the repetitive segregation under continuous settling of these mixtures falling into a column filled with air or water is possible through the plexiglas sidewalls of a square cylindrical settling column 10 cm × 10 cm × 84 cm (shown in fig. 4). A valve was installed at both ends of the cylinder to supply or drain water

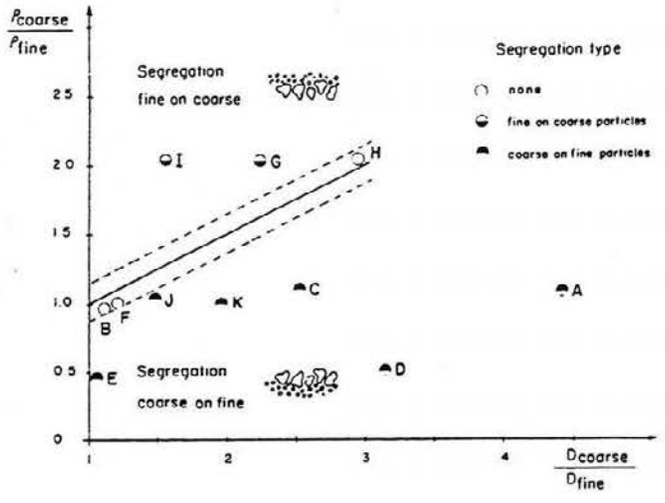

FIG. 2. – Particle segregation diagram.

FIG. 2. – *Diagramme de ségrégation des particules.*

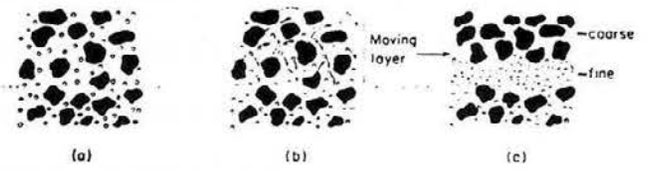

FIG. 3. – Sketch of the segregation process with constant particle mass density, before (a), during (b), and after (c) motion.

FIG. 3. – *Schéma du processus de ségrégation des particules de densité constante, avant* (a), *durant* (b), *et après* (c) *mouvement.*

during and/or after experiments. Photographs were taken from the sides of the column and the sorting characteristics of various mixtures with different densities, sizes and shapes were documented. A homogeneous mixture was poured at a constant rate (given in table IV) into the cone at the top of the cylinder. The valve controlling the settling rate was then opened to let the mixture settle directly near the center of the stationary cylinder.

During most experiments in air, the splashing of particles after impact was significant, owing to high fall velocities of the particles. The saltating distance of particles reached 5 cm from the point of impact. In many instances, no

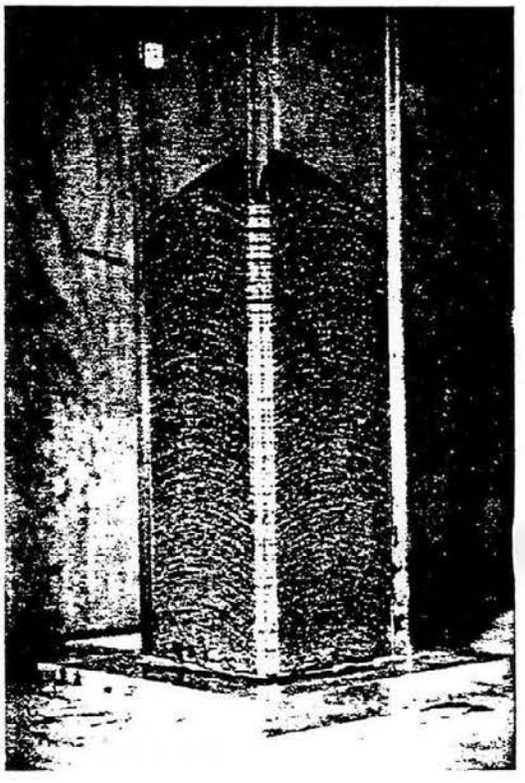

FIG. 4. – Example of clear lamination in air (mixture #C).

FIG. 4. – *Exemple de lamination nette à l'air (mélange #C).*

laminae formed when rolling of one type of particles on the other was not obvious. Splashing was reduced by raising the base height of the settling column. Clear repetitive segregation, or lamination, was shown in at least two experiments. In such cases as mixture #C, black particles roll on top of white particles before landsliding, resulting in clear lamination with thickness less than 0.5 cm.

The experimental results for each of ten different mixtures of quartz, limestone and coal are summarized in table IV for both runs in air and in water, respectively. Generally speaking, mixtures forming laminae in air often form laminae in water. However, cases such as mixtures #D and #I do not form laminae in water because coal particles settle very slowly in water. When the cylinder was slightly inclined at an angle of approximately 5°, the experiment with mixture #C highlights the importance of the rolling distance of the moving layers. Lamination becomes clearer as the rolling distance increases. The laminae thickness, however, remains unaffected by the inclination angle of the cylinder.

These experiments on lamination, summarized in table IV, support the following conclusions :

1) laminae can develop in either : (a) mixtures of the same density but different particle size – mixture #C ; (b) mixtures of the same size but different particle density – mixture #E ; or (c) mixtures of different particle density and different particle size – mixture #D ;

2) laminae can be produced in both air and water. In air, splashing of the particles becomes predominant as the mixture gets coarser due to higher fall velocity. Splashing is greatly reduced in water, although the turbulence induced by the settling of coarser particles enhances suspension of finer particles. The settling of such mixtures becomes more uniform in that no laminae can be found because the segregation mechanism does not take place ;

3) under a continuous supply of sediment, lamination is found to be essentially the result of the mechanical interaction between particles of different size, shape and density. The segregation process of heterogeneous sand mixtures under lateral motion, sketched in figure 3, is the primary cause of lamination. Segregation results from the rolling of one particle over the other, and lamination is possible without fluid turbulence and without the migration of low amplitude bedforms. Superposed laminae cannot be identified to discontinuous sedimentation into successive layers.

III. – Experiments on graded-beds

Laboratory experiments on graded-beds were conducted to determine whether stratification of heterogeneous sand mixtures is possible under steady flow and a continuous supply of sand particles. As opposed to segregation and lamination where sorting of particles occurs at a scale not exceeding a few millimetres, the graded-beds experiments determine whether graded-beds of coarse and fine sands, at a scale exceeding 10mm, are possible. The flow conditions examined in the laboratory flume are : i.e. upper regime plane bed, flow conditions similar to those of Bijou Creek during the 1965 flood.

A) Experimental procedure

Laboratory experiments on graded-beds were carried out in a tilting plexiglas flume (0.15 m wide, 0.15 m deep, and 2.40 m long) shown on figure 5. The flume recirculates both water and sediment in order to provide a continuous supply of heterogeneous sand particles under steady flow conditions during the course of each experiment. Particular design consideration of the headbox and the entrance profile of the flume ensured complete sediment mixing and steady inflow of sediment.

Four types of sands identified in table I as ERC #2, ERC #4, B2040 and B3060 were selected to prepare two sand mixtures identified as SM2 (equal weights of B2040 and ERC #4), and SM3 (equal weights of B3060 and ERC #2). These mixtures have been used by Julien and Chen [1989a], and by Julien and Lan [1990b].

TABL. IV. – Settling lamination in air and water.
TABL. IV. – *Lamination des dépôts à l'air et submergés.*

	Mixture	Characteristic		In Air Settling Rate (cm/s)	In Air Lamination	In Water Settling Rate (cm/s)	In Water Lamination
B	B2040 & ERC #3	$\rho_2 \equiv \rho_1$	$D_2 \equiv D_1$	2.05	not clear	1.02	none
C	ERC #1 & B3060	$\rho_2 \neq \rho_1$	$D_2 \neq D_1$	9.14	clear	9.11	not clear
D	ERC #1 & coal #1	$\rho_2 \neq \rho_1$	$D_2 \neq D_1$	7.00	clear	9.0	none
E	ERC #3 & coal #3	$\rho_2 \neq \rho_1$	$D_2 = D_1$	4.01	not clear	0.80	clear
F	limestone #1 & B3060	$\rho_2 \equiv \rho_1$	$D_2 \equiv D_1$	9.00	none	0.84	not clear
G	limestone #2 & coal #1	$\rho_2 \neq \rho_1$	$D_2 \neq D_1$	5.20	none	1.05	none
H	ERC #2 & coal #1	$\rho_2 \neq \rho_1$	$D_2 \neq D_1$	9.00	none	0.75	none
I	limestone #1 & coal #2	$\rho_2 \neq \rho_1$	$D_2 \neq D_1$	3.44	not clear	1.30	none
J	limestone #1 & B2040	$\rho_2 \equiv \rho_1$	$D_2 \neq D_1$	1.62	not clear	0.76	clear
L	limestone #2 & B3060	$\rho_2 \equiv \rho_1$	$D_2 \neq D_1$	9.00	none	0.90	none

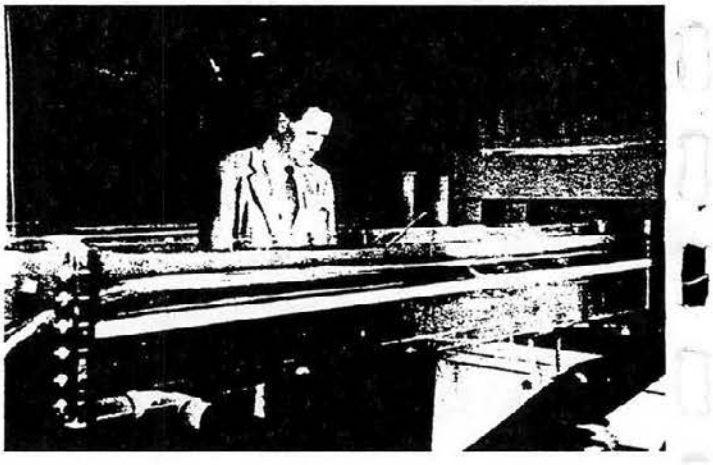

FIG. 5. – Small recirculating flume.
FIG. 5. – *Petit canal de recirculation.*

TABL. V. – Summary of graded-bed measurements.

TABL. V. – *Compilation des mesures sur lits stratifiés.*

Step	Discharge Q (cm^3/s)	Flow Depth h (cm)	Average Velocity V_m (cm/s)	Upstream Velocity V_u (cm/s)	Downstream Velocity V_d (cm/s)	H-Lam † (cm)	Froude Number Fr	Delta Thickness (cm)
Run:SM2A (Horizontal) D_{50} = 0.28 mm								
SM2A-1	2650	2.9	57.5	53.2	33.2	0.27	.99	1.9
SM2A-2	3470	3.9	57.4	47.6	40.0	0.8	.59	0.8
SM2A-3	3949	4.0	63.6	50.0	46.3	1.1	.64	0.4
SM2A-4	4480	4.1	70.4	54.5	52.5	1.2	.74	0.2
Run:SM2D (Horizontal) D_{50} = 0.28 mm								
SM2D-1	2750	3.4	52.1	46.7	26.2	0.4	.81	2.9
SM2D-2	4026	4.0	64.9	57.5	37.6	0.5	1.07	2.3
Run:SM2C (Pos. slope S = +0.005) D_{50} = 0.28 mm								
SM2C-1	2778	3.7	48.4	42.0	35.5	0.6	.65	0.8
SM2C-2	3470	3.8	58.9	50.0	41.4	0.7	.93	0.9
SM2C-3	4007	4.5	57.4	50.0	45.3	0.7	.75	0.5
SM2C-4	4428	4.4	64.9	53.8	50.0	0.9	.98	0.4
Run: SM2B (Adv. Slope S = -0.005) D_{50} = 0.28 mm								
SM2B-1	3334	4.0	53.7	45.7	36.4	0.7	.73	1.2
SM2B-2	3601	4.1	56.6	50.0	41.5	0.6	.80	0.9
SM2B-3	3644	4.0	58.7	50.0	42.7	0.7	.88	0.8
SM2B-4	3988	4.1	62.7	52.5	42.1	0.8	.98	1.2
Run:SM3A (Horizontal) D_{50} = 0.62 mm								
SM3A-1	3558	3.9	58.8	50.0	44.0	0.7	.90	0.8
SM3A-2	3850	3.9	63.6	49.6	45.1	1.1	1.06	0.5
SM3A-3	4304	4.4	63.1	49.6	42.0	1.2	.92	1.0
SM3A-4	4939	4.5	70.8	54.9	51.4	1.3	1.14	0.4

† Horizontally laminated deposit thickness

Prior to each experiment, the flume slope was set (horizontal, positive, or adverse slope). The flow rate was controlled by a gate valve and measured by a Venturi orifice. The flow of water and sediment first ran freely near critical flow conditions without downstream gate control until reaching the equilibrium plane bed with sediment transport. Starting from equilibrium plane conditions, the deposition of sand in the flume in non-uniform flow was induced by inserting a first tailgate, 0.15 m wide and 0.02 m high, at the downstream end of the flume. The water depth and the thickening of sediment deposits were measured through the transparent sidewall of the flume. Local velocity measurements upstream and downstream of the delta were taken using a Ultrasonic Doppler Velocimeter Model UDV-89 with an accuracy of + 0.003 m/sec or 2 % of reading, whichever was greater. Measurements of discharge, surface velocity and depth were taken and compiled in table V, and the progression of the deltaic sediment deposits was recorded. The new deposit reached the downstream end of the flume about 20 to 30 minutes after inserting the tailgate and new equilibrium conditions were then obtained. After completing the measurements, the second gate was inserted to form a second deposit and the documentation procedure was repeated.

B) Experimental results

This experimental procedure clearly demonstrated the formation of stratified graded beds. A schematic description of the formation of graded beds is sketched on figure 6. Under initial steady uniform flow conditions and a continu-

437

ous supply of heterogenous sand size particles, coarse particles roll on a bed of fine sand particles. The plane bed laminated deposit is comprised mostly of fine sand particles. The insertion of a single tailgate induces first the formation of a deltaic stratum of coarse black particles which propagates in the downstream direction. On the delta, fine particles cover the top set slope, while coarse particles roll on a laminated bed of fine particles. Coarse particles settle on the foreset slope of the delta, which progresses in the downstream direction as shown in figure 7. On the top of the delta, the fine white particles in the moving layer of rolling black particles deposit on the topset deposit of fine white particles. The thickness of the laminated topset deposit gradually increases until the delta foreset reaches the downstream end of the flume. Typical cross-sectional and longitudinal views of the deposit after a single tailgate in figures 8a and 8b clearly illustrates the stratified nature of the deposit of coarse black particles between two laminated deposits of finer white particles.

Elaborate descriptions of the deposits for each run (4 sets with mixture SM2 identified as SM2A to SM2D and one set with mixture SM3 noted SM3A) are found in Julien and Chen [1989a]. Flume bed slopes are given in table V for each set of runs. The horizontally laminated (H-Lam) layer thickness was examined in terms of depth-averaged velocities upstream V_u and downstream V_d at the tip of the delta in table V. It was found that for the runs SM2A, V_u varies slightly, although V_d and H-Lam significantly increase with discharge, while the delta thickness decreases with discharge. At a comparable discharge, the runs SM2D showed an expected increase in delta thickness with gate height. With positive slope, runs SM2C, the results were similar to those with horizontal slope (SM2A) except that the thickness of deposits was less sensitive to changes in discharge. Under adverse slopes, runs SM2B, the thickness variability with discharge was also less significant.

These results primarily show that the delta thickness increases as V_d decreases, while V_u remains fairly constant ($V_u \approx 50$ cm/s). The effect of slope shows that the delta and H-Lam thicknesses vary with discharge for horizontal slope. Results are uncertain for both positive and adverse slopes.

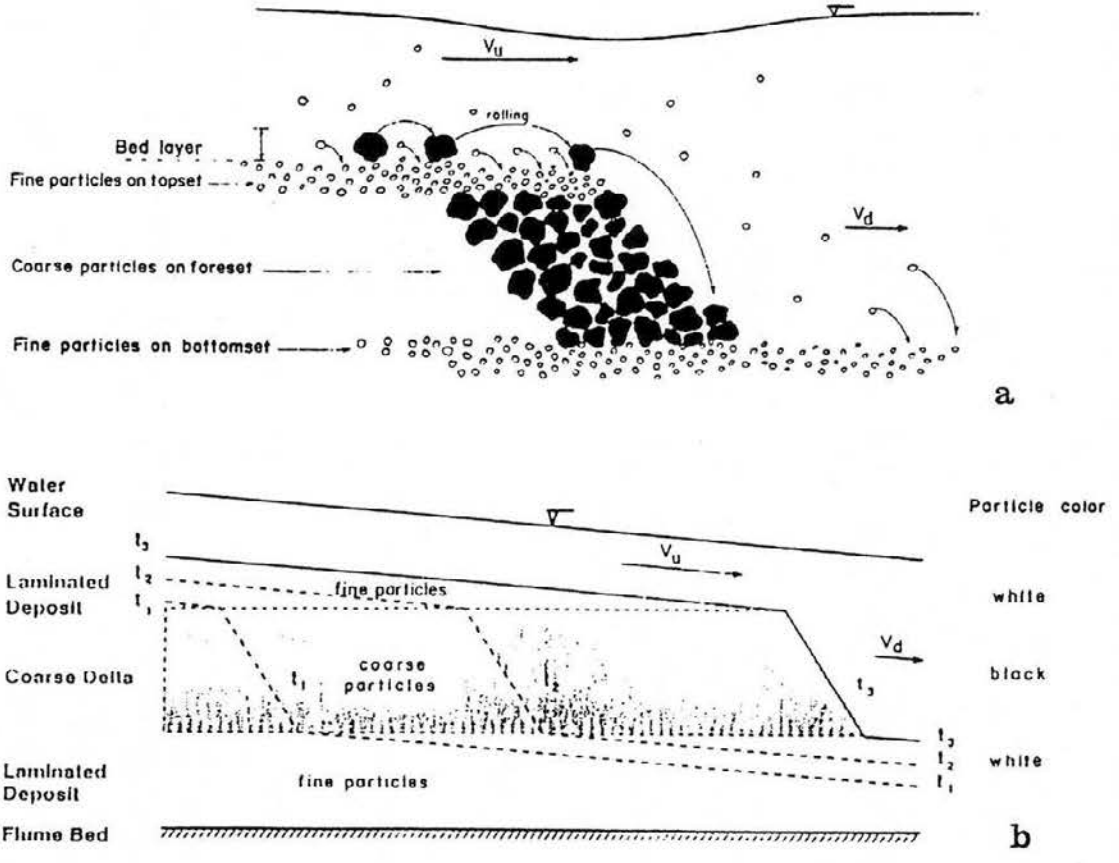

FIG. 6a. – Schematic formation of graded-beds.

FIG. 6a. – *Schéma de formation de lits stratifiés.*

FIG. 6b. – Time sequence of deposit formation for $t_1 < t_2 < t_3$.

FIG. 6b. – *Séquence de formation des dépôts pour* $t_1 < t_2 < t_3$.

438

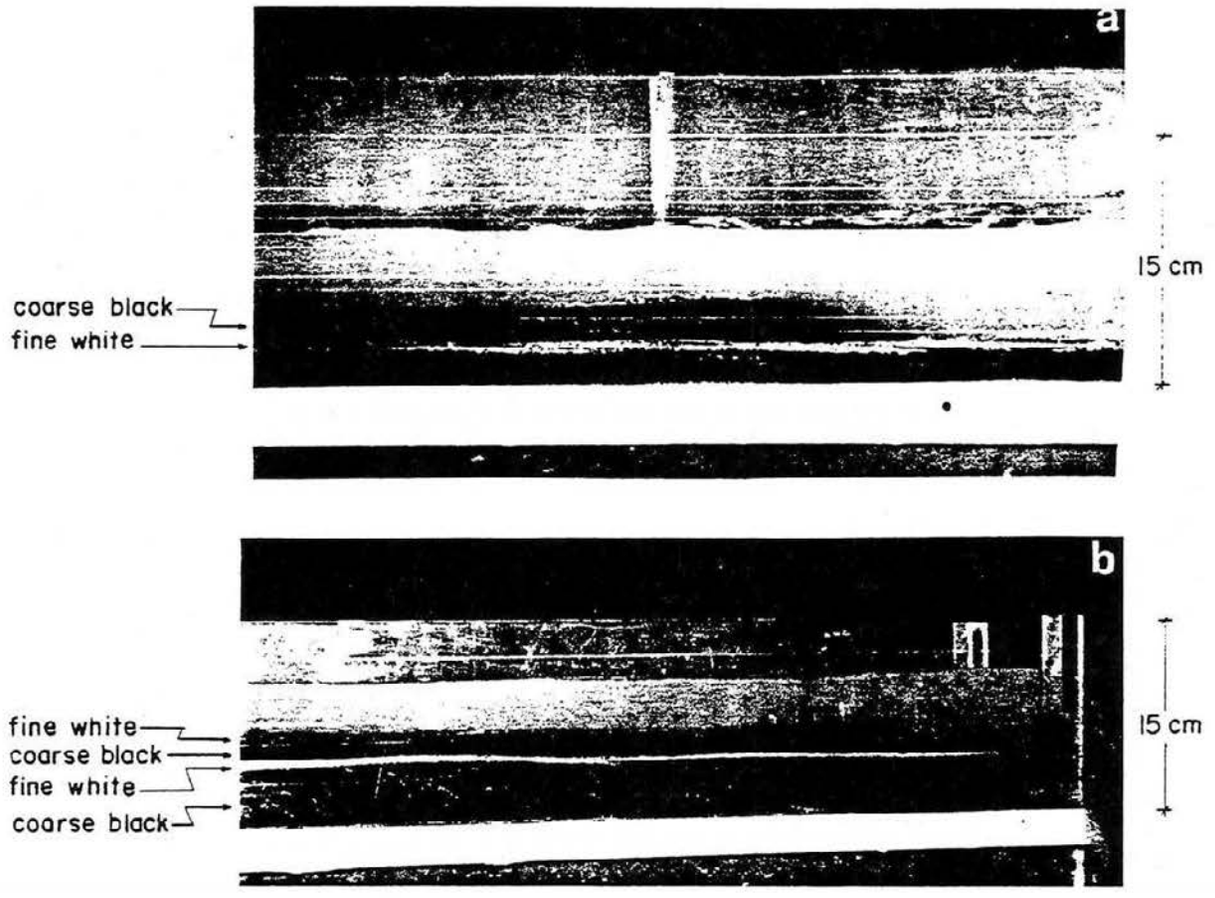

FIG. 7a. – Example of graded-beds with first tailgate.
FIG. 7a. – *Exemple de lits stratifiés avec premier seuil.*
FIG. 7b. – Example of graded-beds with second tailgate.
FIG. 7b. – *Exemple de lits stratifiés avec second seuil.*

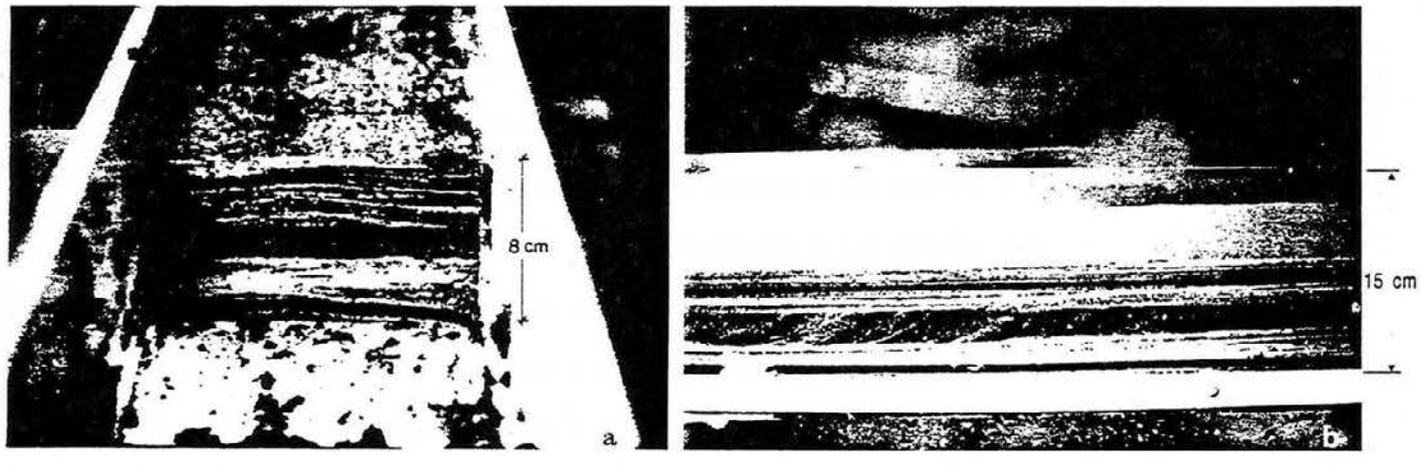

FIG. 8a. – Typical cross-sectional view of deposit.
FIG. 8a. – *Coupe transversale typique du dépôt.*

FIG. 8b. – Typical longitudinal view of deposit (flow from right to left).
FIG. 8b. – *Coupe longitudinale typique du dépôt (écoulement vers la gauche).*

In summary, the velocity change in the downstream direction induces selective settling of particles of different sizes, thus forming graded-beds which develop in the downstream direction. These observations of graded-bed formation highlight the simultaneous development of topset and foreset deposits as sketched in figures 6 and 7. A laminated stratum of fine particles forms on top and at the base of a cross-stratified foreset stratum of coarse particles. The time sequence of the formation of this stratified deposit shows that sets of laminae develop vertically upward and propagate downstream as the cross-stratified bed of coarse particles progresses in the downstream direction. At a microscopic scale on the surface of the deposit, the coarse particles roll on a bed of fine particles in a manner very similar to the segregation process sketched in figure 3 and described in the first part of this experimental program. The experiments demonstrate that stratified deposits can form in steady non-uniform flow under a continuous supply of fine and coarse sediment particles.

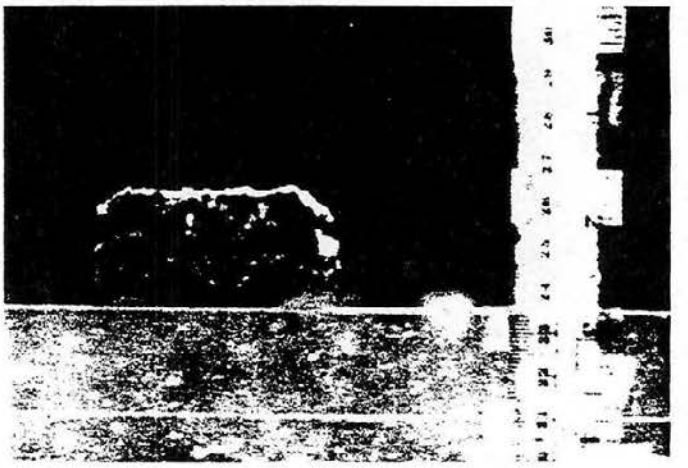

FIG. 9. – Horizontal fracturing of the Bijou Creek sand.
FIG. 9. – *Fractures horizontales du sable de Bijou Creek.*

IV. – EXPERIMENTS ON JOINTS FROM DESICCATION

The purpose of laboratory experiments on horizontal stratification joints was to examine, through desiccation, the possible appearance of vertical cracks and horizontal planes of preferential fracturing. The experiments focused on depositional and drying characteristics of the Bijou Creek natural sand in a small recirculating flume. This study was limited to deposits under steady flow and continuous supply of natural sand over a plane bed without bed forms [Julien and Chen, 1989b].

A) Experimental procedure

The sediment used in this experiment was the natural sand from the surface of the main channel bed of Bijou Creek near Hoyt, Colorado. The sample was taken near the locality III in the investigation of McKee *et al.* [1967]. Prior to the experiments, this natural sand was sieved to remove pebbles and organic material. The particle size ranged from fine to very coarse sand (D_{10} = 0.34 mm, D_{50} = 0.75 mm, and D_{90} = 1.65 mm), and the silt and clay content (passing the sieve #230) is only 0.1 percent of the sediment. The sediment size distribution was similar to that reported by McKee *et al.* [1967].

The procedure used was similar to that of the flume experiments discussed in the previous section. The graded-beds left in the flume after the experiment were exposed to solar lights for seven days until complete desiccation of the deposit.

B) Experimental results

No vertical cracks were found in the stratified deposit after seven days under solar lights, which may be attributed to the low silt and clay content (less than 1 %) of the hard crusted deposit. The horizontal planes, or joints, between the crusted finer sands and the coarser sands separated easily as shown in figure 9. These joints separating particles of different sizes constitute preferential planes for the propagation of fractures in dried sediment deposits. These experiments simply support previous observations that joints can result from desiccation and not necessarily from periods without sediment settling.

V. – CONCLUSIONS

This fundamental study demonstrates the usefulness of laboratory experiments in the analysis of stratification of heterogeneous sand mixtures. Upper flow regime conditions similar to the Bijou Creek flood can be reproduced in the laboratory, and clear stratification of heterogeneous mixtures is evidenced by using coarse and fine sand grains of different colors.

Lamination essentially results from the mechanical segregation of heterogeneous particles in a moving layer. Lamination is possible without turbulence and without the migration of low amplitude bedforms. Through lateral movement of particles of constant mass density, finer particles fall within the interstices of rolling coarser particles. Coarse particles then roll on top of fines and microscale segregation of particles is then obtained. The degree of segregation depends on particle size distribution, density and possibly angularity of heterogeneous sand mixtures (see fig. 2). Repetitive segregation is also possible in settling columns where lamination is clearly observed both in air and water. Sufficient space, or rolling distance, is required for clear lamination to develop in moving layers of heterogeneous particles. Particles of comparable size but different densities segregate similarly with heavier particles falling between lighter particles.

The graded-bed experiments clearly demonstrate the simultaneous formation of stratified deposits under steady flow conditions and a continuous supply of heterogeneous particles. The deposition process involves the formation of a stratum of coarse particles between laminated deposits fine particles as a result of velocity changes in non-uniform flow. The time sequence of the deposit formation shows

454

that sets of laminae develop vertically upward and progress in the downstream direction. At a microscopic scale, at the surface of the deposit, coarse particles roll on a deposit of fine particles as a result of particle segregation.

Desiccation experiments on the Bijou Creek sand deposits in laboratory flumes, indicate preferential fracturing of the crusty deposit along horizontal planes, or stratification joints, separating graded-beds of coarse and fine particles. On the other hand, no vertical cracks were observed in the experiments, which may be explained by the low clay content of the Bijou Creek sand.

In summary, these experiments demonstrate that stratification of heterogeneous sand mixtures can result from : segregation for lamination, non-uniform flow for graded-beds, and desiccation for joints. Therefore, superposed strata are not necessarily identified to successive sedimentary layers.

Acknowledgment. – The writers would like to thank Mrs. Berné, Postma and editorial advisor Mr. Séguret for their insightful suggestions in the review of this publication.

Références

ALLEN J.R.L. (1964). – Primary current lineation in the Lower Old Red Sandstone (Devonian) Anglo-Welsh basin. – *Sedimentology*, **3**, 89-108.

ALLEN J.R.L. (1982). – Sedimentary structures, their character and physical basis. – *Dev. Sediment.*, **30B**, II, 593 p.

ALLEN J.R.L. (1984). – Parallel lamination developed from upper-stage plane bed : a model based on the large coherent structures of turbulent boundary layer. – *Sediment. Geol.*, **39**, 227-242.

BERTHAULT G. (1986). – Sedimentology-experiments on lamination of sediments. – *C.R. Acad. Sci.*, Paris, **303**, II, 17, 1569-1574.

BERTHAULT G. (1988). – Sedimentation of heterogranular mixture-experimental lamination in still and running water. – *C.R. Acad. Sci.*, Paris, **306**, II, 717-724.

BOUMA A.M. (1962). – Sedimentology of some flysch deposits : a graphic approach to facies interpretation. – Elsevier, Amsterdam, 168 p.

BRIDGE J.S. (1978). – Origin of horizontal lamination under turbulent boundary layer. – *Sediment. Geol.*, **20**, 1-16.

BRIDGE J.S. & BEST J.L. (1988). – Flow, sediment transport and bedform dynamics over the transition from dunes to upper-stage planebeds : implications for the formation of planar laminae. – *Sedimentology*, **35**, 753-763.

CHEEL R.J. & MIDDLETON G.V. (1986). – Horizontal laminae formed under upper flow regime plane bed conditions. – *J. Geol.*, **94**, 489-504.

FROSTICK L.E. & REID I. (1977). – The origin of horizontal laminae in ephemeral stream channel-fill. – *Sedimentology*, **24**, 1-9.

GUY H.P., SIMONS D.B. & RICHARDSON E.V. (1966). – Summary of alluvial channel data from flume experiments 1956-1961. – *U.S. Geol. Surv., Paper* **462-I**, 96 p.

HESSE R. & CHOUGH S.K. (1980). – The Northwest Atlantic Mid-Ocean Channel of the Labrador Sea : II. Deposition of parallel laminated levee muds from the viscous sublayer. – *Sedimentology*, **27**, 697-711.

HJULSTRÖM F. (1935). – The morphological activity of rivers as illustrated by River Fyris. – *Bull. Geol. Inst.*, Uppsala, **25**, Chap. III.

HSÜ K.J. (1959). – Flute- and groove-casts in the Prealpine flysch, Switzerland. – *Am. J. Sci.* **257**, 529-536.

JOPLING A.V. (1965). – Laboratory study of the distribution of grain size in cross-bed deposits. *in* : G.V. MIDDLETON, Ed., Primary sedimentary structure and their hydrodynamic interpretation. – *Spec. Publs., SEPM*, **12**, 53-65.

JOPLING A.V. (1967). – Origin of laminae deposited by the movement of ripples along a streambed : a laboratory study. – *J. Geol.*, **75**, 287-305.

JOPLING A.V. & WALKER R.G. (1968). – Morphology and origin of ripple-drift cross-lamination, with examples from the Pleistocene of Massachusetts. – *J. Sediment. Petrol.*, **38**, 971-984.

JULIEN P.Y. & CHEN Y.C. (1989a). – Experimental study of horizontal lamination in a circulating flume. – Civil Engr. Rpt. CER88-89PYJ-YCC14, Colorado State University, Fort Collins, CO, 63 p.

JULIEN P.Y. & CHEN Y.C. (1989b). – Experimental study of the deposition and drying of Bijou Creek Sand in a recirculating flume. – Civil Engr. Rpt. CER89-90PYJ-YCC4, Colorado State University, Fort Collins, CO, 35 p.

JULIEN P.Y. & LAN Y.Q. (1989). – Experimental formation of alluvial channel in wide rectangular flume. – Civil Engr. Rpt. CER89-90PYJ-YQL2, Colorado State University, Fort Collins, CO, 29 p.

JULIEN P.Y. & LAN Y.Q. (1990a). – Sedimentation of heterogranular mixtures in a vertical cylinder. – Civil Engr. Rpt. CER89-90PYJ-YQL13, Colorado State University, Fort Collins, CO, 48 p.

JULIEN P.Y. & LAN Y.Q. (1990b). – Laboratory experiments on lamination, stratification and desiccation. – Civil Engr. Rpt. CER89-90-PYJ-YQL-15, Colorado State University, Fort Collins, CO, 177 p.

KSIAZKIEWICZ M. (1952). – Graded and laminated bedding in the Carpathian flysch. – *Ann. Soc. Geol. Pologne.*, **22**, 399-499.

KUENEN Ph.H. (1953). – Significant features of graded bedding. – *Bull. Am. Assoc. Pet. Geol.*, **74**, 523-545.

KUENEN Ph.H. (1957). – Sole markings of graded greywacke beds. – *J. Geol.*, **65**, 231-258.

KUENEN Ph.H. (1966). – Experimental turbidite lamination in a circular flume. – *J. Geol.*, **74**, 523-545.

KUENEN PH.H. & MÉNARD H.W. (1950). – Turbidity currents as a cause of graded-bedding. – *J. Geol.*, **58**, 2, 91-127.

KUENEN PH.H. & MÉNARD H.W. (1952). – Turbidity currents, graded and non-graded deposits. – *J. Sediment. Petrol.*, **22**, 86-96.

LOMBARD A. (1963). – Laminities : a structure of flysch-type sediments. – *J. Sediment. Petrol.*, **33**, 14-22.

MCBRIDE E.F., SHEPHERD R.G. & CRAWLEY R.A. (1975). – Origin of parallel, near-horizontal laminae by migration of bed forms in a small flume. – *J. Sediment. Petrol.*, **45**, 132-139.

MCKEE E.D., CROSBY E.J. & BERRYHILL H.L. JR. (1967). – Flood deposits, Bijou Creek, Colorado, June, 1965. – *J. Sediment. Petrol.*, **37**, 829-851.

MIDDLETON G.V. (1970). – *Geol. Assoc. Can., Spec. Pap.*, 7, 253-272.

MOSS A.J. (1962). – The physical nature of common sandy and pebbly deposits, part I. – *Am. J. Sci.*, **260**, 337-373.

MOSS A.J. (1963). – The physical nature of common sandy and pebbly deposits, part II. – *Am. J. Sci.*, **261**, 197-243.

PETTIJOHN F.J. (1957). – Sedimentary rocks. – Harper and Row, New York, N.Y., 2nd ed., 718 p.

PETTIJOHN F.J. (1975). – Sedimentary rocks. – Harper and Row, New York, N.Y., 3rd ed., 628 p.

PAOLA C., WIELE S.M. & REINHART M.A. (1989). – Upper-regime parallel lamination as a result of turbulent sediment transport and low-amplitude bed forms. – *Sedimentology*, **36**, 47-59.

SANDERS J.E. (1965). – Primary sedimentary structures formed by turbidity currents and related re-sedimentation mechanisms. *In :* G.V. MIDDLETON Ed., Primary sedimentary structures and their hydrodynamic interpretation. – *Soc. Econ. Paleontol. Mineral. Spec. Publ.*, **12**, 192-329.

SMITH N.D. (1971). – Pseudo-planar stratification produced by very low amplitude sandwave. – *J. Sediment. Petrol.*, **41**, 69-73.

TEN HAAF E. (1956). – Significance of convolute lamination. – *Geol. Mijnb.*, **18**, 188-194.

UNRUG R. (1959). – On the sedimentation of the Lgota beds, Biesle area, western Carpathians. – *Rocz. Pol. Tow. Geol.*, **29**, 218-223.

WALKER R.G. (1965). – The origin and significance of the internal sedimentary structures of turbidities. – *Proc. Yorksh. Geol. Soc.*, **35**, 1-32.

WOOD A & SMITH A.J. (1959). – Sedimentation and sedimentary history of the Aberystwyth Grits (Upper Llandoverian). – *Q. J. Geol. Soc. London*, **114**, 163-195.

Interaction entre le débit et les populations de tacons (*Salmo salar*) de la rivière Matamec, Québec

M. Frenette, M. Caron et P. Julien

Département de Génie civil, Université Laval, Ste-Foy (Qué.) G1K 7P4

et R. J. Gibson

Ministère des Pêches et des Océans, Case postale 5667, St-Jean, T.-N. A1C 5X1

Frenette, M., M. Caron, P. Julien et R. J. Gibson. 1984. Interaction entre le débit et les populations de tacons (*Salmo salar*) de la rivière Matamec, Québec. Can. J. Fish. Aquat. Sci. 41: 954–963.

Partant de l'hypothèse qu'en rivière, la population de jeunes saumons (*Salmo salar*), appelés tacons après la première année, est reliée directement aux caractéristiques physiques des habitats, variables selon le débit, une analyse par régression linéaire multiple a été effectuée entre les estimations de population de tacons de la rivière Matamec (Côte Nord du golfe Saint-Laurent) et les débits minima, moyens et maxima pour des périodes mensuelles et saisonnières. Les variables les plus significatives ont été obtenues pour le débit minimal d'avant crue (aux environ d'avril) et le débit moyen du mois d'août de l'avant dernière année (2 ans auparavant) et le débit moyen du mois de juillet de l'année précédente. Ces débits correspondent à des périodes biologiques critiques concernant la présence des jeunes saumons en rivière et furent utilisés dans le développement d'un modèle de prédiction. La calibration a porté sur des données couvrant la période 1971–77. Les prédictions obtenues sont significatives à 95 %, lorsque les trois paramètres indépendants sont utilisés conjointement et atteignent plus de 66 % lorsqu'un seul paramètre est considéré. Dans l'ensemble, il est montré que le débit est un facteur limitant de grande importance influençant directement la survie des saumons dans les cours d'eau.

Given the hypothesis that in a river, the population of young salmon (*Salmo salar*), called parr after the first year, is directly related to the discharge-variable physical characteristics of the habitats, a multiple linear regression analysis was carried out between the parr population estimates in the Matamec River (north shore of the Gulf of St. Lawrence) and the minimum, average, and maximum discharges for monthly and seasonal periods. The most significative variables were obtained for the minimum discharge before flooding (around April), the average August discharge of the year before last (2 yr before), and the average July discharge of the previous year. These discharges corresponded to critical biological periods for the young salmon present in the river and were used to develop a prediction model that was loaded with data covering the period 1971–77. The predictions obtained were 95% significant when the three independant parameters were used jointly and reached more than 66% when only one parameter was taken into account. Overall, it is shown that the discharge is an important limiting factor directly influencing salmon survival in streams.

Reçu le 2 mai 1983
Accepté le 9 mars 1984

Received May 2, 1983
Accepted March 9, 1984

Le potentiel biologique d'une rivière à saumon (*Salmo salar*) est limité par plusieurs facteurs d'ordre hydrologique, autant que biologique ou physique sans omettre les influences humaines tels la pêche, le déboisement, la pollution ou la construction de barrage.

Sur le plan purement biologique ou hydrobiologique il y a lieu de distinguer le cycle vital de l'espèce. Ce cycle débute par la période d'incubation dans les frayères survenant en période d'étiage hivernal, et le stade de l'alevin qui émerge des graviers plus ou moins avec l'arrivée de la crue du printemps. Puis vient le stade de tacon, d'une durée moyenne de trois ans, pendant laquelle le cours d'eau est soumis à toute une gamme de débits allant des étiages d'hiver et d'été aux crues de printemps et d'automne. Il y a enfin la migration des saumoneaux vers la mer qui survient, règle générale en période de crue. Au cours de cette période passée en rivère le saumon juvénile est aussi soumis à plusieurs facteurs influencés en grande partie par l'hydrologie du cours d'eau. Citons en exemple la température de l'eau, l'abondance de nourriture, la compétition inter ou intra-spécifique, l'exondation des frayères et des habitats de nutrition en période d'étiage et la prédation par les oiseaux aquatiques, plus élevée en période de basses eaux.

Sur le plan physique et hydrodynamique il y a le cadre de vie caractérisé par la physique même des habitats et la dynamique du milieu. Ainsi des facteurs tel que vitesse d'écoulement superficie d'eau libre, géométrie des habitats (fosses, frayères etc.) sont directement influencés par le régime hydrologique des cours d'eau.

Or, malgré un milieu de vie aussi variable et complexe, il est reconnu que les espèces ont pu développer, au cours des années des comportements qui leur permettent de s'adapter aux changements continuels du milieu physique et dynamique dans lequel ils habitent. Cet énoncé présuppose donc qu'il doit exister des liens entre l'hydrologie et la population de saumon dans le cours d'eau.

Parmi les auteurs qui ont tenté d'établir ces liens hydro

biologiques citons dans l'ordre chronologique: Wicket (1951, 1958), Smoker (1953), Havey et Davis (1970), Havey (1974), Becker et al. (1982) et Chadwick (1982). Tous ont démontré qu'il existait des rapprochements entre les antécédants hydrologiques et la population des saumons. Plusieurs des études s'adressent aux saumons adultes du Pacifique, mais sous plusieurs aspects, leurs comportements sont similaires à ceux des saumons de l'Atlantique. D'autres aux juvéniles en reliant de façon globale les populations à la précipitation ou au volume d'eau ruisselé annuellement, sans mettre en évidence les périodes les plus critiques pour la survie des salmonidés.

Les objectifs visés au cours de cette recherche sont donc: (1) approfondir le sujet, en mettant une emphase particulière sur les périodes hydrologiques les plus critiques de survie des saumons juvéniles et (2) développer un modèle de prédiction visant à estimer les populations de jeunes saumons dans un cours d'eau. Le réciproque de cette étude est que le modèle permet de déterminer l'influence des interventions humaines telle une modification de débit sur le potentiel biologique d'un cours d'eau et de définir le débit requis pour assurer ou augmenter le potentiel d'un cours d'eau.

Matériel et méthodes

Il est intéressant de constater, au niveau des principes que la majorité des facteurs susceptibles d'affecter la productivité biologique d'un cours d'eau sont contrôlés par un dénominateur commun, soit le débit liquide.

La méthodologie utilisée au cours de cette recherche a donc consisté à étudier, d'une part l'évolution des paramètres géométriques des cours d'eau en fonction du débit, selon les principes de régime d'équilibre, et d'autre part, à tenter de définir la gamme de débits les plus significatifs susceptibles d'affecter les populations de jeunes saumons dans les cours d'eau. À cet effet une analyse par régression linéaire entre les populations de tacons et les débits minima, moyen et maxima pour les périodes journalières, hebdomadaires, mensuelles et saisonnières a été réalisée à partir des données s'échelonnant de 1971 à 1977. Puis il y a eu intégration des résultats, consistant à trouver les explications hydrobiologiques justifiant les résultats les plus significatifs de la régression.

Description du site d'études

Afin d'éviter toute influence extérieure et de s'en tenir à un milieu naturel strictement sain (sans influence humaine), les études ont été effectuées sur la rivière Matamec, Québec, un tributaire du Saint-Laurent, dont le bassin constitue une réserve écologique. La rivière Matamec (fig. 1) est située approximativement à la rencontre des coordonnées 50°18′N et 65°57′O et draîne une superficie de 684 km sur la Côte Nord du golfe Saint-Laurent.

Ce bassin d'origine précambrienne est couvert presque entièrement d'une forêt boréale composée essentiellement de conifères. Le tronçon inférieur de la rivière draîne le lac Matamec d'une superficie de 16,2 km^2 et franchit une distance de 9,6 km avant de se jeter dans le golfe. La présence de cinq chutes le long de son parcours lui confère un profil longitudinal en escalier. L'omble de fontaine (*Salvelinus fontinalis*) et le saumon de l'Atlantique (*Salmo salar*) sont les deux principales espèces du cours d'eau.

Caractéristiques hydrologiques et hydrauliques

La reconstitution des débits journaliers de la rivière Matamec

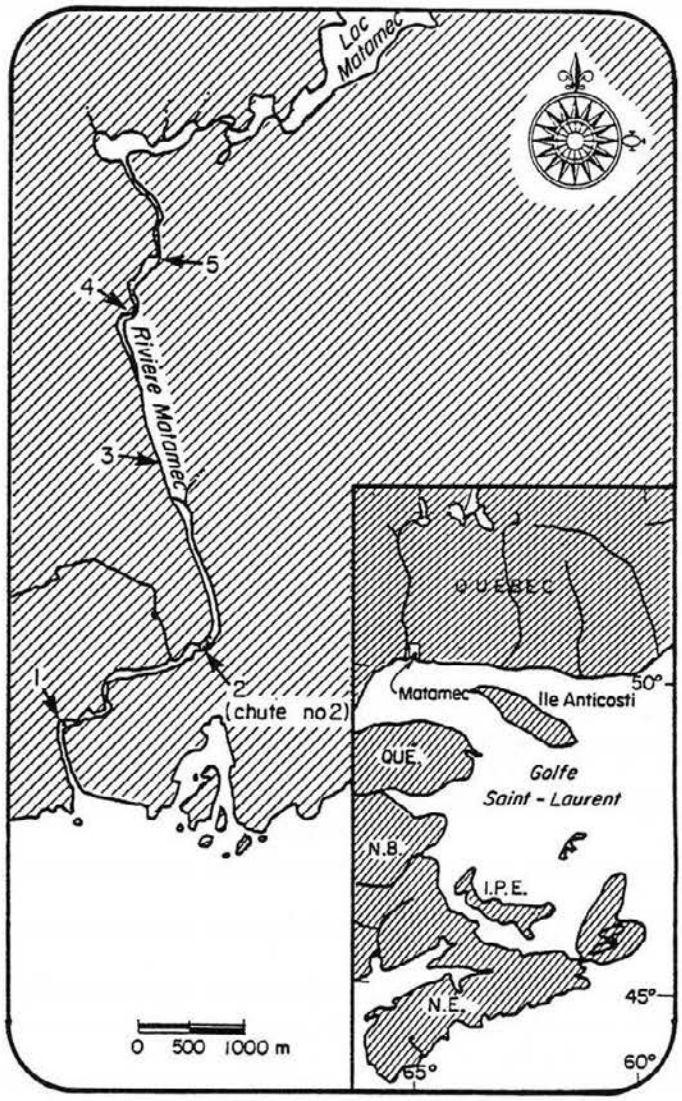

FIG. 1. Plan de localisation de la rivière Matamec.

pour la période comprise entre 1957 et 1978 et les caractéristiques hydrauliques correspondantes sont actuellement connues (Frenette et Julien 1981). Le tableau 1 ci-après fourni un sommaire des divers débits annuels et saisonniers en fonction de différentes périodes de récurrences et de durées. La courbe de débits classés exprimant le décroissant du débit en fonction de la fréquence de dépassement apparaît à la fig. 2, tandis que la fig. 3 fourni l'hydrogramme moyen journalier et les extrêmes mensuels.

Le débit moyen interannuel à la sortie du lac Matamec est de l'ordre de 13,5 m^3/s, alors que les moyennes mensuelles varient de quelques mètres cubes (en moyenne 1 à 4) à la fin de l'hiver à plus de 60 m^3/s, parfois, au printemps.

Selon la théorie de Léopold et Maddock (1953) la variation moyenne, à une section donnée, des caractéristiques hydrauliques d'un cours d'eau, pouvant s'ajuster librement, se définit comme suit:

(1) Largeur moyenne : $b = \alpha Q^{1/10}$

(2) Profondeur moyenne : $h = \beta Q^{2/5}$

(3) Section moyenne : $A = bh = \alpha\beta Q^{1/2}$

(4) Vitesse moyenne : $v = Q/A = (1/\alpha\beta)Q^{1/2}$

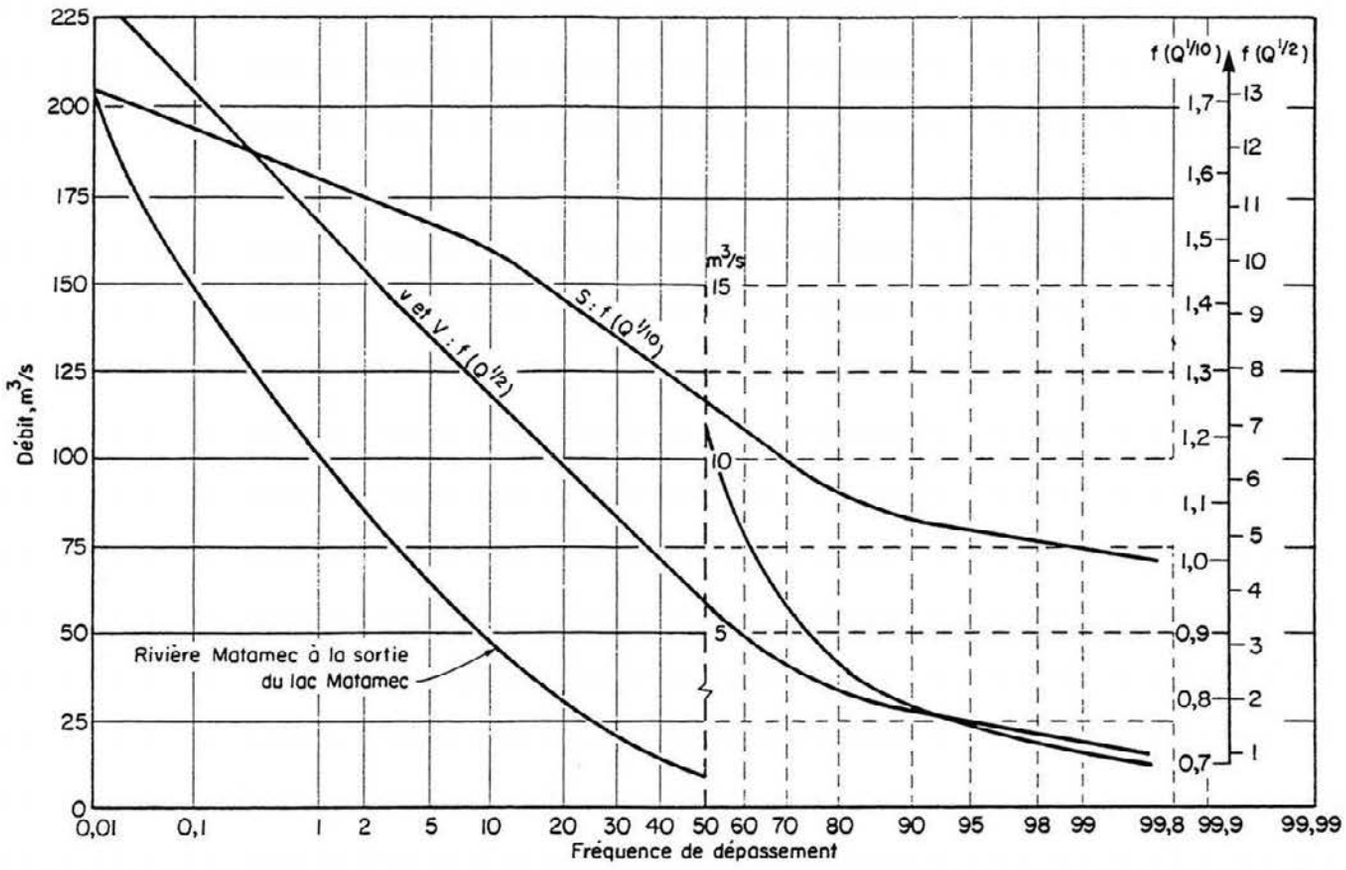

FIG. 2. Courbes des débits journaliers classés de la rivière Matamec et variation de la superficie d'eau libre (S), du volume d'eau écoulé (V) et de la vitesse d'écoulement (v) en fonction du temps de récurrence.

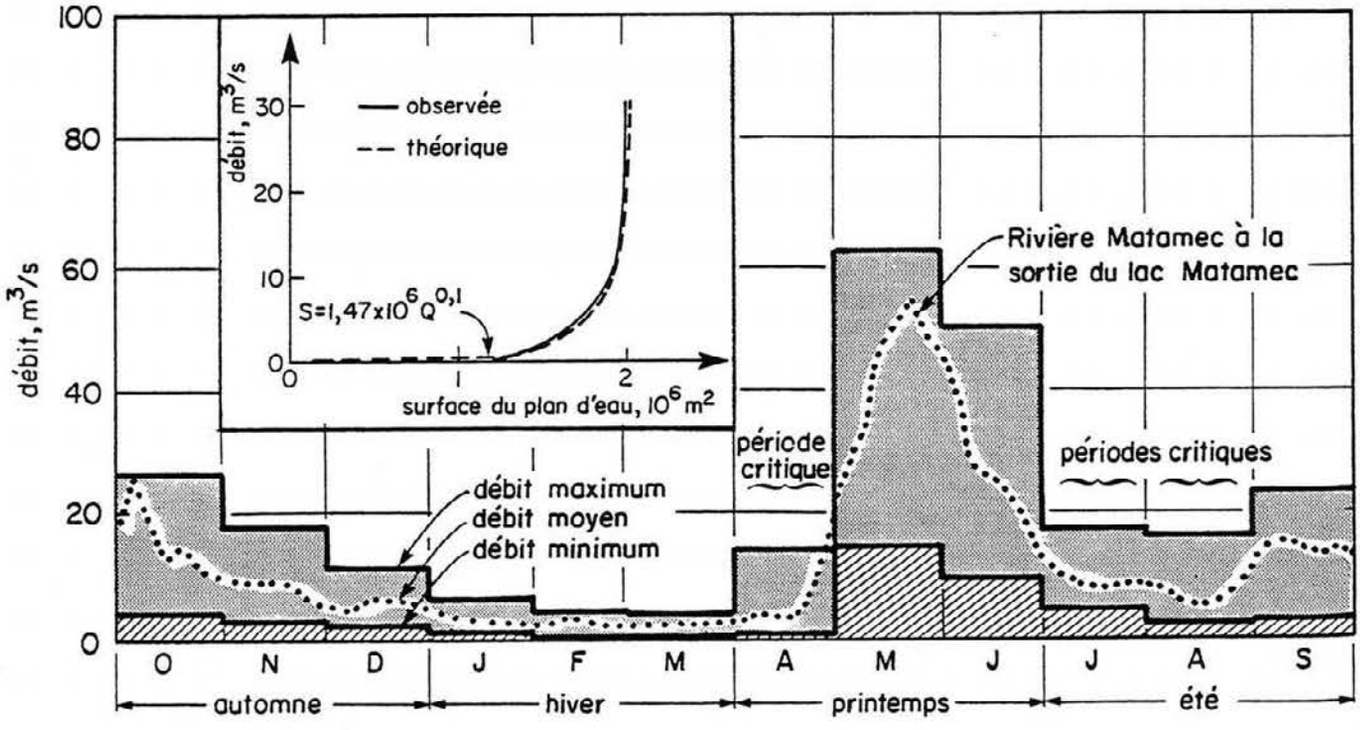

FIG. 3. Hydrogrammes de la rivière Matamec et variation de la surface du plan d'eau en fonction du débit.

TABLEAU 1. Sommaire des statistiques de débit (m^3/s) à la sortie du lac Matamec (station 072502).

	Nombre de jours consécutifs	Minima			Maxima			
		20 ans	10 ans	Moyen	Moyen	Moyen	10 ans	20 ans
Annuel	1	0,79	0,85	1,13	13,5	70,8	84,9	113,2
	15	0,85	0,99	1,27		52,4	65,1	70,8
	30	0,91	1,06	1,39		40,0	50,0	57,5
	60	0,99	1,13	1,56		34,0	41,0	43,9
Hiver	1	0,82	0,85	1,27	2,4	5,1	12,7	17,6
(1 janvier au	15	0,85	0,99	1,56		4,0	9,1	12,5
31 mars)	30	0,90	1,10	1,68		3,7	6,1	9,7
	60	1,13	1,27	1,84		3,4	5,4	6,8
Printemps	1	0,99	1,13	1,34	25,5	69,4	84,9	116,1
(période	15	1,13	1,27	2,26		56,6	70,8	77,9
de fonte)	60	15,8	18,1	22,65		36,8	42,5	45,3
Été	1	1,56	1,84	3,11	12,5	36,0	65,1	79,3
(1 juillet au	15	1,84	2,12	3,96		25,5	35,4	39,6
13 septembre)	30	2,45	2,65	5,05		19,5	27,0	30,5
	60	4,25	4,25	7,64		14,1	20,4	22,6
Automne	1	1,98	2,12	3,11	11,3	36,8	73,6	93,4
(1 octobre au	15	2,12	2,41	3,96		24,1	39,4	48,1
31 décembre)	30	2,30	2,75	5,05		16,0	30,5	36,5
	60	3,82	4,39	8,21		14,2	21,2	25,5

où α et β sont des coefficients numériques spécifiques à chaque cours d'eau.

Par extension, la surface au miroir ou superficie d'eau libre et le volume d'eau d'un tronçon donné de rivière "L" sont définis par :

(5) Surface au miroir : $S = bL = \alpha' Q^{1/10}$

(6) Volume d'eau : $V = Sh = \alpha' \beta Q^{1/2}$

avec $\alpha' = \alpha L$.

Eu égard aux saumons, les relations les plus importantes sont celles se rattachant à la surface d'eau libre, au volume d'eau et aux vitesses moyennes d'écoulement, soient les équations 4, 5 et 6. On obtient :

(7) v et $V : f_1(Q^{1/2})$

(8) $S : f_2(Q^{1/10})$.

La variation de ces paramètres en fonction des probabilités de débit apparaît sur la courbe des débits classés (fig. 2). On constate ainsi que dans les deux premiers cas (vitesse et volume d'écoulement) que la décroissance est graduelle et continue en fonction du débit. La surface d'eau libre, par contre, présente une courbe à deux paliers avec deux points d'inflexion majeurs correspondant au débit $Q10\,\%$ ($Q = 30\ m^3/s$) et $Q85\,\%$ ($Q = 3\ m^3/s$).

Cette dernière constatation prend toute son importance si l'on se réfère aux travaux d'Allen (1969) et d'Elson (1975) qui définissent la relation entre les populations des salmonidés et les superficies d'eau libre d'un cours d'eau; d'où l'interaction qui doit exister entre le débit et la population de saumons adultes ou juvéniles dans les cours d'eau.

Dans le cas de la rivière Matamec, la variation de la superficie d'eau libre, pour l'ensemble des tronçons fluviaux (rapides exclus) entre l'estuaire et le lac Matamec, observée en fonction du débit inférieure à $30\ m^3/s$, est présentée à la fig. 3. La relation correspondante est :

(9) $S = 1{,}47 \times 10^6 Q^{0{,}10}$.

Un excellent ajustement est ainsi constaté entre les caractéristiques physiques du plan d'eau et l'équation de Léopold et Maddock indiquant par là une diminution rapide de la surface au miroir en période d'étiage, notamment si le débit devient inférieur à 8 ou $10\ m^3/s$. Ce débit correspondant à une valeur légèrement inférieure à la moyenne interannuelle estimée à $13{,}5\ m^3/s$ et au débit moyen d'été évalué à $12{,}5\ m^3/s$ (voir tableau 1).

Corrélation des débits avec la population de saumons juvéniles

Plusieurs chercheurs ont réalisé des études biologiques sur la population de saumons de la rivière Matamec. Ces études étaient principalement orientées, d'une part, vers une compréhension des relations existant entre les saumons juvéniles, les ombles de fontaine et leurs habitats et, d'autre part, vers l'évaluation de la productivité d'une rivière à saumon dans la région boréale du Canada (Gibson 1973, 1978a). Dans cette perspective, la population de tacons de saumons au pied de la deuxième chute a été estimée à partir de 1971 par Gibson (1975, 1977) en utilisant la méthode modifiée de marquage et de recapture de Schnabel (Ricker 1975). En raison de sa représentativité pour la rivière Matamec, le site au pied de la deuxième chute a été soumis à un échantillonnage plus intensif que les autres sites sur la même rivière. Les populations de tacons âgés d'un ou deux ans (notés 1+ ou 2+) sont montrées au tableau 2. Il peut être observé, à l'exception de l'année 1977, que la population de tacons 2+ y est toujours supérieure à celle de tacons 1+, et pour cette raison les populations sont analysées séparément dans notre travail.

Les populations de tacons ont été corrélées d'abord avec les débits moyens à la sortie du lac Matamec (km 9,6) sur une base annuelle, saisonnière et mensuelle et ensuite avec les débits minima saisonniers couvrant une période de 1, 7, 15, 30 et 60 jours consécutifs. De plus, pour que les débits coïncident avec

446

TABLEAU 2. Estimations de population de tacons au pied de la deuxième chute de la rivière Matamec. Données estimées par la méthode marquage–recapture de Schnabel. Les intervalles de confiance à 95 % sont indiqués entre parenthèses.

Année	Tacons 1+ (tacons/ha)	Tacons 2+ (tacons/ha)
1971	200 (140–320)	590 (510–700)
1972[a]	690	1 330
1973	510 (300–1 660)	1 750 (1 420–2 290)
1974	260 (200–360)	450 (350–630)
1975[a]	100	190
1976	140 (110–200)	230 (220–260)
1977	690 (510–920)	430 (320–600)
1978	250 (170–390)	840 (570–1 290)

[a]Ces estimations de population de tacons 1+ et 2+ ont été déterminées à partir de la population totale et de la répartition moyenne en chacune des classes d'âge.

les diverses étapes de croissance antérieure, les populations de tacons ont été corrélées aux débits écoulés 0, 1 et 2 années auparavant.

Les analyses effectuées se divisent en trois parties. D'abord, la régression a été effectuée entre la population totale de tacons et chacun des débits mentionnés. Par la suite les populations de tacons 1+ et de tacons 2+ ont été corrélées séparément avec les débits montrant les coefficients de corrélation les plus élevés avec la population totale.

Afin de relier la population totale de tacons aux différents débits précités, un très grand nombre d'équations de régression linéaire de la forme suivante ont été ajustées par la méthode des moindres carrés :

$$(10) \quad \hat{y} = a + bx$$

où $\hat{y}$ = variable dépendante (population de tacons), x = variable indépendante (débit) et a et b = paramètres d'ajustement.

Plusieurs de ces équations n'ont pu être retenues à cause de la faible valeur du coefficient de corrélation; par contre, certaines équations ont permis d'obtenir un niveau de corrélation relativement élevé. Dans le but de sélectionner les équations à une seule variable explicative les plus valables, un test sur le coefficient de détermination a permis de vérifier si la variance expliquée diffère significativement de la variance résiduelle (A. Brown, Presses de l'Université Laval, Québec, comm. pers.).

Dans le cas étudié, l'équation de régression linéaire à une seule variable obtenue pour un échantillon de sept paires de valeurs est jugée significative lorsque le coefficient de détermination $R^2 \geqslant 0{,}57$.

Résultats

Population totale de tacons

Parmi les nombreux ajustements obtenus, deux équations ont révélé que le coefficient de détermination était supérieur à la valeur critique requise par le test. La première relie la population totale de tacons au débit minimum durant une période de 30 jours consécutifs qui a précédé la crue du printemps deux années auparavant (mentionnons que ce débit correspond globalement au débit moyen du mois d'avril). La seconde relie la population totale de tacons au débit moyen d'août, écoulé deux années auparavant. Les données de base sont présentées au tableau 3 et les équations obtenues sont les suivantes :

$$(11) \quad \hat{P}_t = 119{,}5 + 208{,}4Q_1 \quad (R^2 = 0{,}66)$$

$$(12) \quad \hat{P}_t = -1176 + 361{,}0Q_2 \quad (R^2 = 0{,}69)$$

où $\hat{P}_t$ = population totale de tacons, Q_1 = débit minimum, avant la crue printanière, durant une période de 30 jours consécutifs, survenu deux ans auparavant et Q_2 = débit moyen du mois d'août deux ans auparavant.

Les courbes correspondantes sont présentées respectivement aux fig. 4A et 4B, les intervalles de confiance ayant été déterminés à partir de la loi de distribution de Student–Fisher (Spiegel 1980).

L'équation de régression multiple à deux variables explicatives a également été obtenue pour la population totale de tacons (fig. 4) :

$$(13) \quad \hat{P}_t = -966 + 124{,}0Q_1 + 23\,594Q_2 \quad (R^2 = 0{,}85).$$

TABLEAU 3. Données de population de tacons et de débits mensuels ayant montré les meilleures corrélations. Les débits observés sont indiqués entre parenthèses.

Année	Q min. avant-crue 30 jours consécutifs	Q moyen juillet (m^3/s)	Q moyen août (m^3/s)	Population de tacons observée		
				Tacons 1+ (nb/ha)	Tacons 2+ (nb/ha)	Totale (nb/ha)
1969	3,00	10,67	6,85			
1970	4,53	10,56	8,49			
1971	11,01	4,78	8,61	200	590	790
1972	4,33	9,03	3,96	687	1 333	2 020
1973	3,06	12,83	5,63	510	1 750	2 260
1974	1,84	10,76 (9,77)	4,95 (3,99)	260	450	710
1975	4,42	14,04 (14,10)	5,27 (7,67)	100	190	290
1976	10,14	4,36	9,82	140	230	370
1977	2,89	8,01	9,57	690	430	1 120
1978	1,72	12,5	3,55	250	840	1 090

447

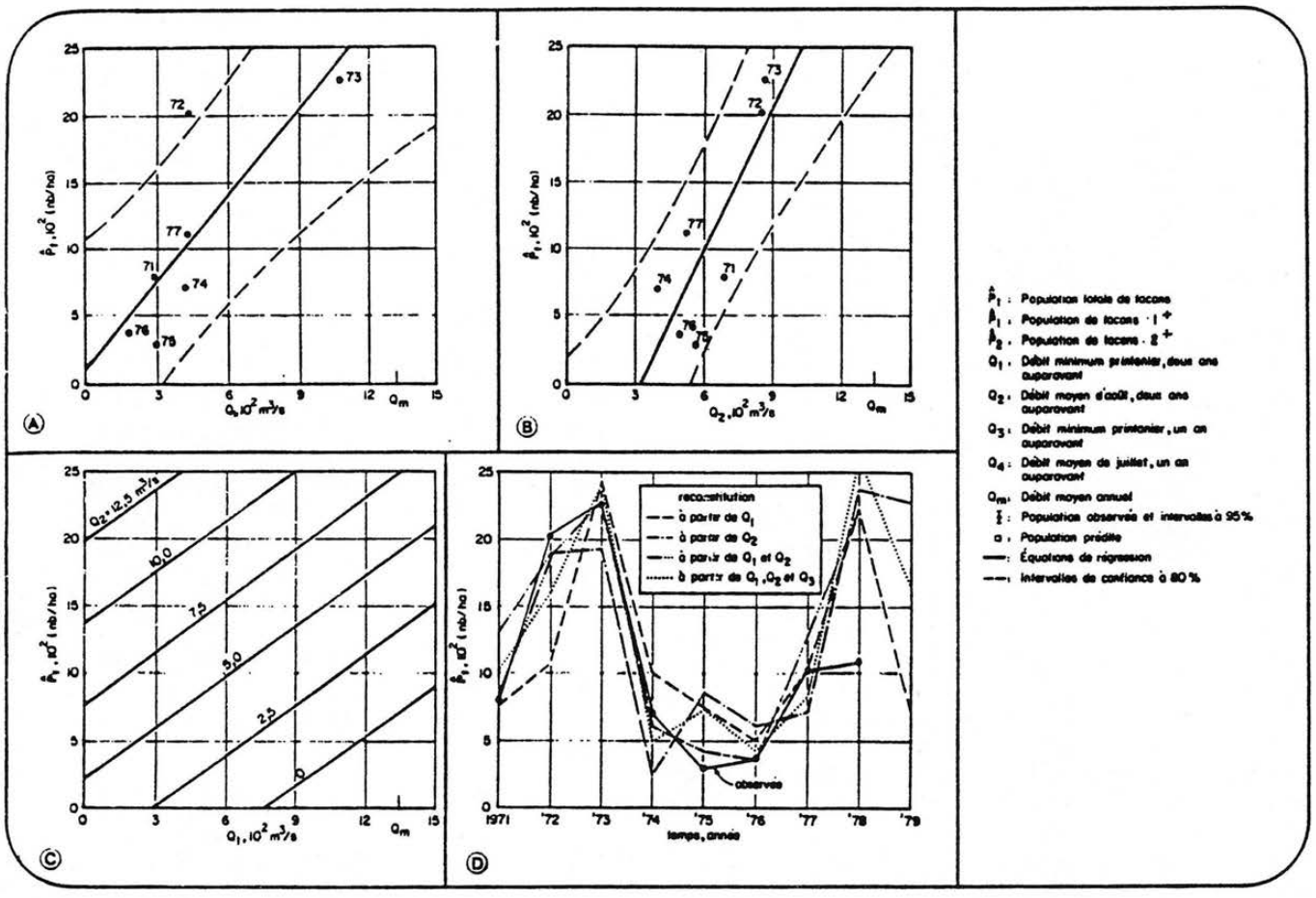

FIG. 4. Population totale de tacons vs (A) Q_1, (B) Q_2, (C) Q_1 et Q_2 et (D) débits observés et reconstitués pour la période 1971–79.

Le coefficient de corrélation de cette équation représentée à la fig. 4C est de 0,91. Afin de vérifier si cette équation est plus significative que les équations à une seule variable, le coefficient de corrélation a été corrigé en fonction du nombre de degrés de liberté (Draper et Smith 1966). Cette analyse a permis de démontrer que l'addition d'une seconde variable améliore significativement le coefficient de corrélation.

Population de tacons 2+ et 1+

Afin de compléter l'analyse de ces résultats, les débits ayant montré les meilleures corrélation ($R > 0,6$) avec la population totale ont été utilisés comme données de base pour analyser distinctement les populations de tacons 1+ et de tacons 2+.

Pour la population de tacons 2+ ($\hat{P}_2$), les meilleures équations de régression obtenues sont les suivantes :

(14) $\hat{P}_2 = -64,6 - 168,5Q_1 \quad (R^2 = 0,72)$ (fig. 5A)

(15) $\hat{P}_2 = -1109 + 291,0Q_2 \quad (R^2 = 0,76)$ (fig. 5B)

(16) $\hat{P}_2 = -940 + 190,4Q_1 + 100,3Q_2 \quad (R^2 = 0,92)$ (fig. 5C)

où $\hat{P}_2$ = population de tacons 2+ et Q_1, Q_2 = définis précédemment.

Là encore, l'analyse du coefficient de corrélation corrigé montre que la corrélation linéaire multiple apporte une amélioration réelle au coefficient de corrélation.

En ce qui concerne la population de tacons 1+ ($\hat{P}_1$), les équations équivalentes obtenues sont les suivantes :

(17) $\hat{P}_1 = 12,8 + 63,6Q_3 \quad (R^2 = 0,77)$ (fig. 6A)

(18) $\hat{P}_1 = 954,3 - 63,6Q_4 \quad (R^2 = 0,81)$ (fig. 6B)

(19) $\hat{P}_1 = 572,7 + 28,3Q_3 - 38,9Q_4 \quad (R^2 = 0,85)$ (fig. 6C)

où $\hat{P}_1$ = population de tacons 1+, Q_3 = débit minimum printanier durant une période de 30 jours survenue un an auparavant et Q_4 = débit moyen de juillet, un an auparavant.

Contrairement au cas précédent, l'augmentation du coefficient de corrélation, en introduisant une seconde variable explicative, n'est pas améliorée pour les tacons 1+.

Prédiction des populations de tacons dans la rivière Matamec

À partir des équations de régression obtenues, il a été possible de prédire distinctement la population de tacons 1+ et 2+ pour la période 1971–79 tel que montré aux fig. 4D, 5D et 6D. En ce qui concerne la population totale de tacons, une équation de régression multiple à trois variables explicatives a été établie :

(20) $\hat{P}_t = -1017 + 154,0Q_1 + 143,4Q_2 + 87,6Q_3 \quad (R^2 = 0,96).$

De façon à avoir une vision plus globale des prédictions, la population totale de tacons a été estimée en considérant deux approches différentes : (1) en supposant des débits régularisés

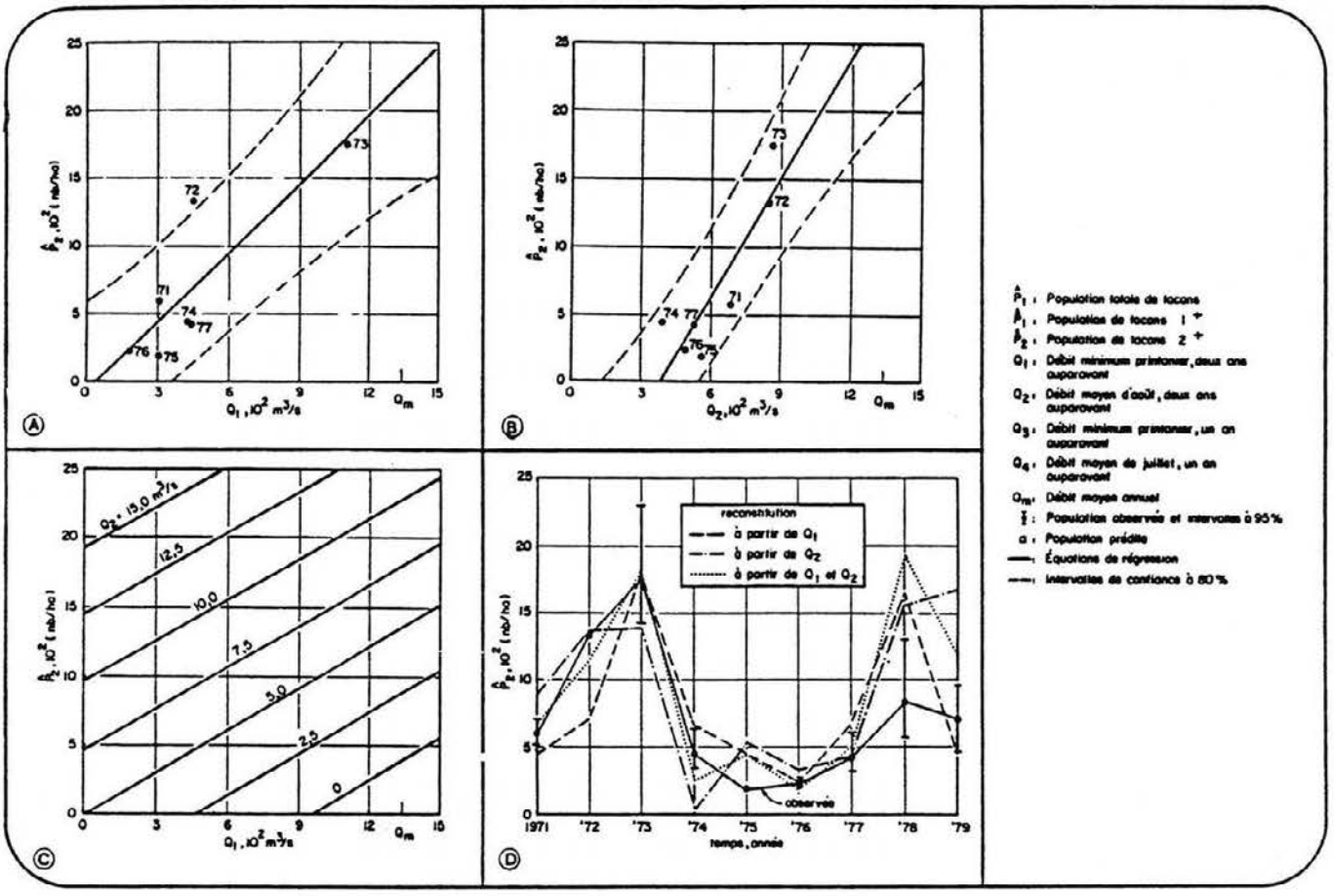

FIG. 5. Population de tacons 2+ vs (A) Q_1, (B) Q_1 et Q_2, (C) Q_1 et Q_2 et (D) débits observés et reconstitués pour la période 1971–79.

durant les périodes critiques, ajustés aux valeurs minimales suivantes : 5, 10 et 13,5 m^3/s respectivement, la dernière valeur correspondant à la moyenne interannuelle; (2) en reconstituant les populations depuis 1957 selon les débits naturels observés chaque année durant les périodes critiques. Les résultats comparés aux observations de 1971 à 1977 sont reportés à la fig. 7.

Discussion

En liant l'habitat des tacons au plan d'eau d'une rivière, il est mis en évidence dans un premier temps qu'il existe une étroite relation (éq. 5) entre le débit liquide et la surface au miroir d'un cours d'eau, notamment en période d'étiage, relation qui fournit une première explication des résultats.

Cette étude met aussi en évidence les relations existant entre les populations de jeunes saumons (tacons) et les caractéristiques hydrologiques d'une rivière. Les résultats traduisent assez clairement que les débits affectent de façon importante la productivité d'un rivière. En effet, l'analyse par régression linéaire indique que la population juvénile dans la rivière Matamec pour la période de 1971 à 1978, est principalement corrélée aux débits minima précédant la crue printanière et aux valeurs moyennes de débit en juillet et en août. Il est intéressant de noter que le débit minimum d'avant crue correspond à toute fin pratique au débit moyen du mois d'avril.

Plus particulièrement, cette étude démontre que la population totale de tacons est reliée significativement au débit minimum printanier et au débit moyen du mois d'août, écoulés deux années auparavant. La population de tacons 2+ est également corrélée significativement à ces deux mêmes débits caractéristiques tandis que la population de tacons 1+ est reliée aux débits minimum printanier et moyen de juillet écoulés l'année précédente. À la lumière de ces résultats, la survie des jeunes saumons dans une rivière serait fortement influencée par les conditions hydrologiques et hydrauliques du cours d'eau à la période d'éclosion des œufs et d'alevinage ainsi que durant la période de croissance estivale (juillet et août), lorsque les niveaux d'eau deviennent faibles.

En conséquence, les débits en période de pré-émergence des alevins de même que les débits des mois de juillet et août apparaissent les plus critiques pour la survie des alevins et des tacons. Notons que Becker et al. (1982) ont trouvé pour le saumon chinook (*Oncorhynchus tshawytscha*) que la tolérance d'exondation décroît à partir de l'état embryonnaire et que les alevins pré-émergés sont les moins tolérants à supporter l'exondation.

Par ailleurs sachant que l'abondance de la nourriture est directement reliée aux superficies d'eau libre donc aux débits d'écoulement il semble bien évident que l'insuffisance de nourriture associée aux caractéristiques d'étiage des mois de juillet et d'août entraînent une plus grande vulnérabilité des alevins et des tacons qui doivent faire face aux prédateurs, au surpeuplement et à la compétition pour des habitats propices.

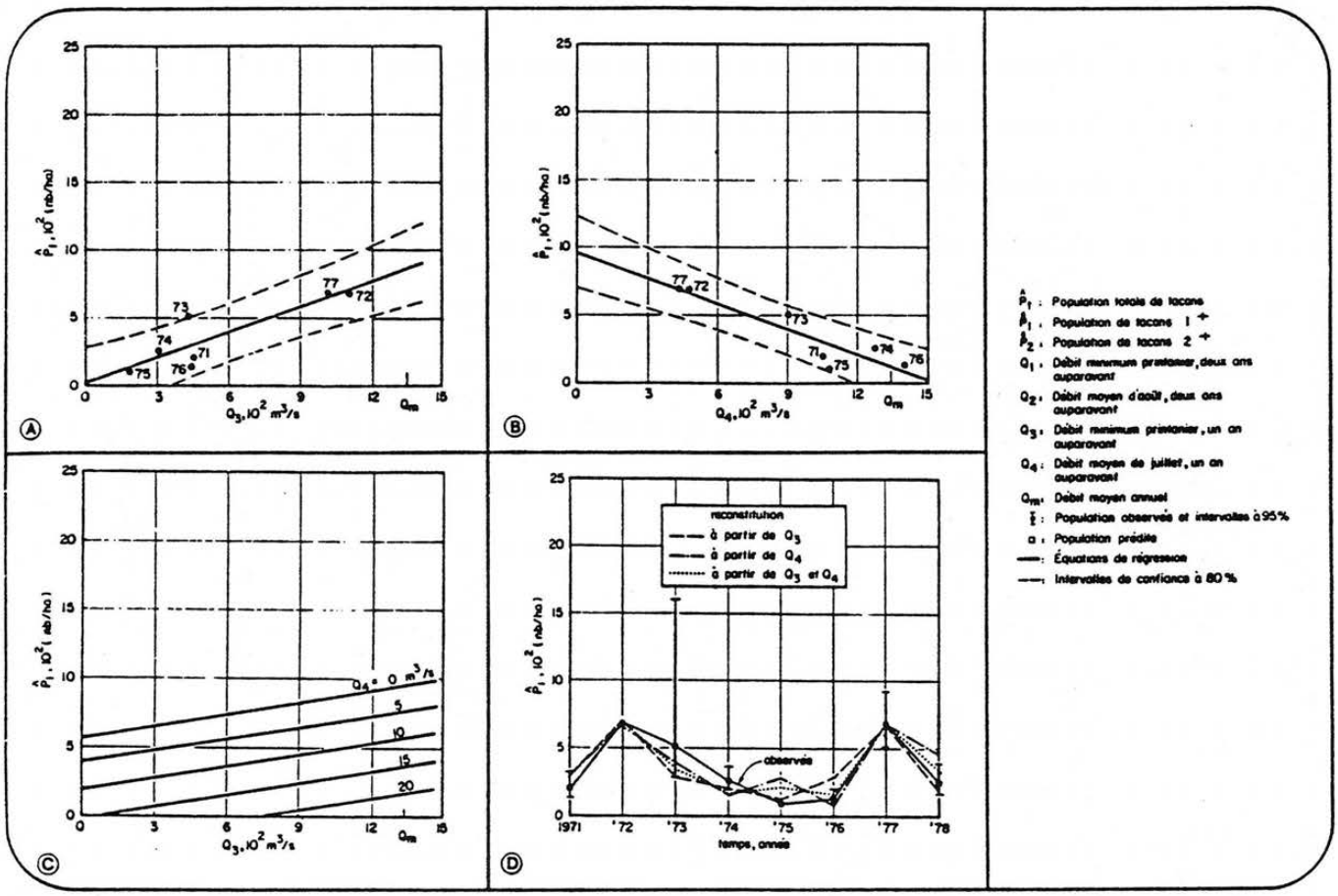

FIG. 6. Population de tacons 1+ vs (A) Q_3, (B) Q_4, (C) Q_3 et Q_4 et (D) débits observés et reconstitués pour la période 1971–78.

Les corrélations effectuées entre les populations de tacons et les débits d'étiage hivernal (débits les plus faibles de l'année) se sont avérées aucunement significatives. Une explication possible est qu'au cours de cette période, les jeunes saumons se nourissent très peu et se cachent dans le gravier ou au fond des fosses profondes dans un état plus ou moins léthargique (Allen 1940; Gibson 1978b). Ces remarques ne s'appliquent pas nécessairement aux œufs en état d'incubation dans les frayères, lesquels risquent d'être partiellement exondées en hiver en période d'étiage extrême, mais tel que démontré par Becker et al. (1982) le pourcentage de survie des œufs embryonnaires est tout près de 100 % à la fin de l'hiver même s'il y a exondation de courte durée.

Les faibles corrélations obtenues pour les autres périodes de l'année, en dehors des mois critiques (exemples : en mai, en juin ou à l'automne) révèlent une suffisance au niveau des habitats par rapport aux populations en présence.

Cette analyse des populations basée sur les données hydrauliques a permis de développer un premier outil de prédiction sur les périodes critiques de survie des jeunes saumons dans un cours d'eau.

À partir des résultats de simulation sur modèle, il est intéressant de noter l'influence qu'aurait eu une régularisation des eaux à la sortie du lac Matamec sur les populations potentielles de la rivière (voir fig. 7). La simulation depuis 1957 montre par exemple une diminution naturelle de la population moyenne de tacons. Ainsi, il est probable qu'une diminution d'au-delà de 50 % de tacons dans la rivière en 20 ans soit attribuable aux conditions naturelles de débit durant les périodes critiques. Bien sûr, la confirmation d'un tel résultat nécessiterait plusieurs autres années d'observation, néanmoins la tendance actuelle demeure révélatrice. Il est à noter ici, que l'ensemble du régime hydrologique n'a probablement pas subi de modifications au cours de cette période, bien que d'apparence contraire d'après la courbe de la fig. 6. Il faut en effet se rappeler que le modèle est basé sur des débits spécifiques propres à des périodes mensuelles bien déterminées agissant comme facteur limitant sur le potentiel biologique et non sur l'ensemble des événements hydrologiques.

Le corollaire de cette recherche est assez évident : pour augmenter le potentiel biologique d'un cours d'eau, il faut maintenir les superficies d'eau libre en période critique soit par une régularisation des eaux au moyen de lacs artificiels, ou barrages régulateurs, soit en créant des plans d'eau avec des seuils à l'intérieur même des cours d'eau. La première solution nous apparaît la meilleure car elle n'entraîne pas de diminution du champ de vitesses ce qu'entraîne la deuxième solution. À l'inverse, sachant que le déboisement a pour effet d'accentuer les débits extrêmes de crue et d'étiage, il y a donc lieu d'entrevoir une réduction des populations de tacons dans les cours d'eau suite à un déboisement intensif, strictement en regard des caractéristiques d'écoulement.

En bref, la présente recherche met bien en évidence qu'une grande majorité des facteurs susceptibles d'influencer la pro-

450

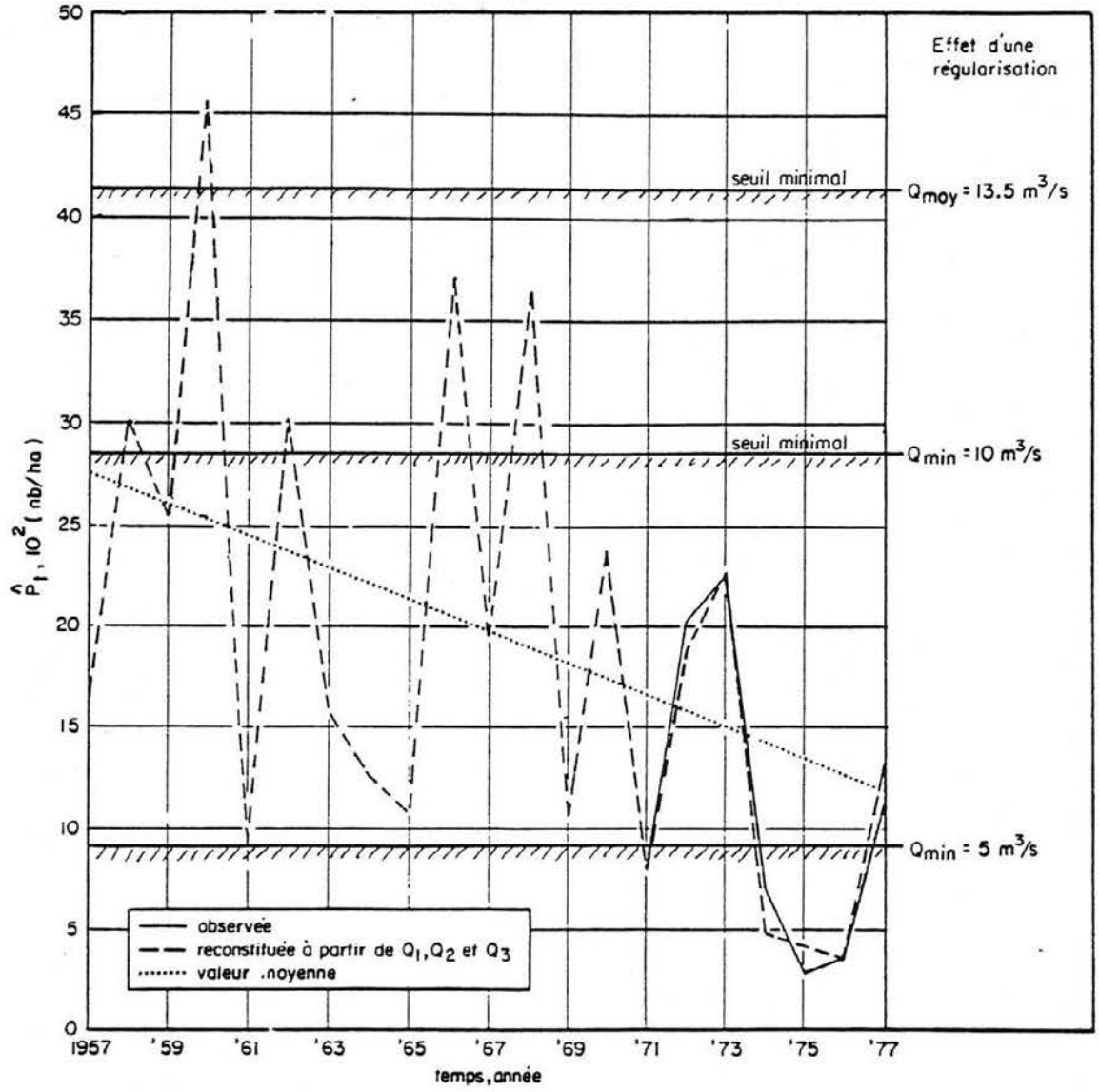

FIG. 7. Population totale de tacons observée et reconstituée à partir de Q_1, Q_2 et Q_3 pour la période 1957–77.

ductivité d'une rivière à saumon sont associés à un dénominateur commun, soit le débit d'écoulement, et que l'équilibre hydro-biologique qui en dépend peut dès lors être influencé dans un sens ou dans l'autre selon les modifications apportées à ce débit.

Il est cependant à noter que les résultats de cette étude proviennent uniquement d'analyse de données de la rivière Matamec. Toutefois, étant donné que les débits significatifs correspondent aux régimes d'équilibre définient par Léopold et Maddock et à des périodes critiques dans le cycle de vie des salmonidés, et, que les caractéristiques hydrologiques (hydrogramme, débit classé) sont bien représentatives des rivières à saumon, il nous apparaît évident que des relations similaires existent sur d'autres cours d'eau. Dans ce sens, cette recherche constitue un développement significatif en vue de définir les périodes critiques de survie de l'espèce voire même en vue d'en améliorer les populations.

Remerciements

Nous désirons exprimer nos remerciements à l'Institut Océanographique Woods Hole pour leur contribution financière et pour l'hospitalité reçue à la station de recherche de Matamec, de même qu'aux ministères de l'Environnement Québec et du Loisir, Chasse et Pêche pour l'étroite collaboration entretenue depuis plusieurs années. Plus particulièrement, nous tenons à exprimer notre reconnaissance à M. Yvon Côté, biologiste, pour ses remarques et conseils pratiques concernant le présent article.

Références

ALLEN, K. R. 1940. Studies on the biology of the early stages of the salmon (*Salmo salar*). J. Anim. Ecol. 9: 1–23.

1969. Limitations on production in salmonid populations in streams. p. 3–18. *Dans* T. G. Northcote [éd.] Symposium on Salmon and Trout in Streams. H. R. MacMillan Lectures in Fisheries, Univ. British Columbia. Vancouver, B.C.

BECKER ET AL. 1982. Effects of dewatering on chinook salmon reeds: tolerance of four development phases to daily dewaterings. Trans. Am. Fish. Soc. 111: 624–637.

CHADWICK. 1982. Stock–recruiting relationship for Atlantic salmon (*Salmo salar*) in Newfoundland rivers. Can. J. Fish. Aquat. Sci. 39: 1496–1501.

DRAPER, N. R., ET H. SMITH. 1966. Applied regression analysis. John Wiley & Sons, New York, NY. 107 p.

ELSON, P. F. 1975. Atlantic salmon rivers, smolt production and optima spawning: an overview of natural production. Int. Atl. Salmon Found Spec. Publ. Ser. 6: 96–119.

FRENETTE, M., ET P. JULIEN. 1981. Recueil de données sur les caractéristiques hydro-physiques du bassin de la rivière Matamec. Rapp. GCS-81-03, Département de Génie civil, Université Laval, Ste-Foy (Qué.).

GIBSON, R. J. 1973. Interactions of juvenile Atlantic salmon (*Salmo salar*) and brook trout (*Salvelinus fontinalis*). Int. Atl. Salmon Found. Spec. Publ. Ser. 4(1): 181–202.

1975. Matamek Annual Report for 1975. WHOI-75-62. Woods Hole Oceanographic Institution, Woods Hole, MA.

1977. Matamek Annual Report for 1976. WHOI-77-28. Woods Hole Oceanographic Institution, Woods Hole, MA.

1978a. Matamek Annual Report for 1977. WHOI-78-92. Woods Hole Oceanographic Institution, Woods Hole, MA.

1978b. The behavior of juvenile Atlantic salmon (*Salmo salar*) and brook trout (*Salvelinus fontinalis*) with regard to temperature and water velocity. Trans. Am. Fish. Soc.

HAVEY, K. A. 1974. Effects of regulated flows on standing crops of juvenile salmon and other fishes at Barrows Stream, Maine. Trans. Am. Fish. Soc. 103: 1–9.

HAVEY, K. A., ET R. M. DAVIS. 1970. Factors influencing standing crops and survival of juvenile salmon at Barrows Stream, Maine. Trans. Am. Fish. Soc. 99: 299–311.

LÉOPOLD, L. B., ET T. MADDOCK. 1953. The hydraulic geometry of stream channels and some physiographic implications. USGS Prof. Pap. 252: 57 p.

RICKER, W. E. 1975. Computation and interpretation of biological statistics of fish populations. Bull. Fish. Res. Board Can. 191: 382 p.

SMOKER, W. A. 1953. Stream flow and silver salmon production in western Washington. Wash. Dep. Fish. Res. Pap. 1: 5–12.

SPIEGEL, M. R. 1980. Théorie et application de la statistique. Série Schaum McGraw-Hill, New York, NY.

WICKETT, W. P. 1951. The coho salmon population of Nile Creek. Fish. Res. Board Can. Progr. Rep. Pac. Coast Stn. 89: 88–89.

1958. Review of certain environmental factors affecting the production of pink and chum salmon. J. Fish. Res. Board Can. 15: 1103–1126.